A STUDY OF THE EFFECTS OF RARE-EARTH ELEMENTS ON THE MICROSTRUCTURAL EVOLUTION AND DEFORMATION BEHAVIOR OF MAGNESIUM ALLOYS AT TEMPERATURES UP TO 523K

By

Ajith Chakkedath

A DISSERTATION

Submitted to
Michigan State University
in partial fulfillment of the requirements
for the degree of

Materials Science and Engineering – Doctor of Philosophy

2016

ABSTRACT

A STUDY OF THE EFFECTS OF RARE-EARTH ELEMENTS ON THE MICROSTRUCTURAL EVOLUTION AND DEFORMATION BEHAVIOR OF MAGNESIUM ALLOYS AT TEMPERATURES UP TO 523K

By

Ajith Chakkedath

Due to their high specific strength, lightweight magnesium (Mg) alloys are being increasingly used for applications, such as the automotive industry, where weight savings are critical. In order to develop new alloys and processing methods to achieve higher strength and better formability to compete with currently used metal alloys, it is important to understand the effects of alloying elements, processing, and temperature on the microstructure, mechanical properties, and the deformation behavior.

In this dissertation, a systematic investigation on the effects of Nd additions (0-1wt.%) and temperature (298-523K) on the microstructure and the activity of different deformation modes in as-cast and cast-then-extruded Mg-1Mn (wt.%) alloys were performed. For this study, an in-situ testing technique which combines tension and compression testing inside a scanning electron microscope (SEM) with electron backscatter diffraction (EBSD) analysis was employed.

The main findings of this work were that the microstructure, strength, and the distribution of the deformation modes varied significantly as a function of Nd content, temperature, and processing. An increase in the Nd content resulted in a weaker texture after extrusion in Mg-1Mn alloys. A combination of slip and twinning mechanisms controlled the tensile deformation in the extruded alloys at ambient temperatures. With an increase in temperature, the twinning activity decreased, and slip mechanisms dominated the deformation. In the extruded Nd-containing alloys, basal <a> slip dominated the deformation, especially at elevated temperatures,

suggesting that Nd additions strengthen basal <a> slip. This resulted in excellent elevated-temperature strength retention in extruded Mg-1Mn-1Nd alloy, and a decrease in the Nd content to 0-0.3wt.% resulted in a decrease in the tensile strength at elevated temperatures. In extruded Mg-1Mn, contraction twinning dominated the tensile deformation and this alloy exhibited a lower elongation-to-failure (ε_f) than the other alloys at 323K. With an increase in strain, these twins evolved into $\{10\bar{1}1\} - \{10\bar{1}2\}$ double twins. Crystal plasticity modeling and simulation of the contraction twins and double twins showed that the activity of these twin modes is detrimental to the ε_f of Mg alloys due to the strain localization that happens within the twinned volume due to the enhanced activity of basal <a> slip. This agreed with the experimental observations. Compared to the extruded materials, the as-cast alloys exhibited significantly larger grain sizes and lower tensile strengths. The deformation in the as-cast alloys was dominated by a combination of basal <a> slip and extension twinning at all test temperatures.

A novel methodology which combines in-situ annealing inside a SEM with EBSD analysis was developed and employed to understand the effects of dilute Ce additions (0.2-0.6wt.%) on the recrystallization behavior in Mg-2Zn (wt.%) alloys. Texture weakening in these alloys resulted from the formation of an enhanced number of grain boundaries with $< hkil >$ rotation axis during recrystallization. The developed testing methodology will be valuable for future recrystallization studies on Mg and other alloy systems.

Overall, the insights gained from this dissertation will have a broad impact on understanding the deformation behavior and microstructural evolution of RE-containing Mg alloys, and such insights can serve as guidance for the development of new alloys and processes. The information and data provided in this dissertation can also serve as inputs for the development of accurate crystal plasticity models.

To my younger brother, Akhil.

ACKNOWLEDGEMENTS

First of all, I would like to thank my advisor Dr. Carl Boehlert for giving me the opportunity to perform this work. He has provided invaluable guidance throughout my PhD work. I greatly appreciate his patience to personally show how to operate the research equipment and his willingness to discuss about the research at any time. He also provided me with many opportunities to present my work at technical conferences both in USA and abroad. In addition, he supported me to visit Spain and Germany for academic purposes during this time. Moreover, apart from academics, he showed me how to be a good mentor, how to be helpful to others, and how to be a nice person overall. I am sure the values I learned from him over the past four years will be helpful for the success of my career in the future.

I would also like to thank my committee members, Dr. Thomas Bieler, Dr. Philip Eisenlohr, Dr. Tamara Reid Bush, and my previous committee member Dr. Jeff Sakamoto for their guidance in the completion of my degree. Dr. Bieler and Dr. Eisenlohr always led instructive and helpful discussions during the weekly group meeting as well as during personal meeting. The constructive suggestions by Dr. Reid Bush and Dr. Sakamoto, especially during the comprehensive exam, were helpful for me to be on the right track.

I would like to thank Dr. Per Askeland for his assistance with operating and trouble-shooting the electron microscopes and other materials analysis equipment. I would also like to thank Dr. Paloma Hidalgo-Manrique for her assistance while conducting research at IMDEA Materials Institute, Spain. I would also like to thank Dr. Martin Crimp for the insightful discussions during the group meeting.

I would like to acknowledge that the funding for this research was supported by National Science Foundation Division of Material Research (Grant No. DMR1107117) through the Materials World Network program. I would like to thank our collaborators from Spain, Dr. Maria Teresa Perez-Prado and Dr. Javier Llorca at IMDEA Materials Institute for their useful discussions. I would also like to thank our collaborators from Germany, Dr. Jan Bohlen, Dr. Sangbong Yi, and Dr. Dietmar Letzig at Magnesium Innovation Center MagIC, for processing and providing the materials for this study. I would also like to thank Mr. David Hernandez Escobar at Technical University of Madrid, Spain for helping me to conduct some experiments and perform data analysis during the summer of 2015.

I would like to thank the current and former members of the "metals group", who have directly and indirectly helped me in my research, including Dr. Zhe Chen, Dr. Hongmei Li, Dr. James Seal, Dr. Bite Zhou, Dr. Dongdi Yin, Dr. Rocío Muñoz Moreno, Dr. Vicente Herrera, Mr. Yang Su, Mr. Harsha Phukan, Mr. Chen Zhang, Mr. Aboozar Mapar, Mr. Quan Zhou, Mr. Huan Wang, Mr. Di Kang, Mr. Vahid Khademi, Ms. Uchechi Okeke, Ms. Aida Amroussia, Mr. Tias Maiti, Mr. Bret Dunlap, Mr. Minming Wang, Mr. Aritra Chakraborty, and Mr. Zhuowen Zhao. I would also like to thank those who have sacrificed their time to help me in any respect during my time here at Michigan State University.

Finally, my gratitude goes to my parents for not saying "no" to most of the decisions I have taken in my life so far. Last but not least, I would like to dedicate this work to my younger brother, Akhil, who is just there on the other side of the planet.

TABLE OF CONTENTS

LIST OF TABLES xi

LIST OF FIGURES xiii

KEY TO SYMBOLS AND ABBREVIATIONS xxxi

CHAPTER 1 INTRODUCTION 1
1.1 Rationale and research objective 1
1.2 Work performed 7

CHAPTER 2 BACKGROUND AND LITERATURE REVIEW 11
2.1 Fundamentals of Mg and Mg alloys 11
2.1.1 Crystal structure 11
2.1.2 Alloying 12
(a) Manganese (Mn) 13
(b) Neodymium (Nd) 13
(c) Cerium (Ce) 15
2.2 Processing of Mg alloys 16
(a) Cast alloys 16
(b) Wrought alloys 17
2.3 Texture and microstructure 18
(a) The effect of particles 20
(b) The effect of non-basal slip activity, shear bands, interfaces, and grain boundaries 21
2.4 Deformation mechanisms 24
2.4.1 Dislocation slip 25
2.4.2 Twinning 25
2.5 Deformation behavior 31
(a) Changes in lattice parameters 34
(b) Changes in SFE 35
(c) Changes in grain size 35

CHAPTER 3 EXPERIMENTAL PROCEDURES 37
3.1 Material 37
3.2 Microstructural characterization 38
3.2.1 Metallography preparation 38
3.2.2 Scanning electron microscopy 39
3.2.3 Electron backscatter diffraction 40
3.2.4 Transmission electron microscopy 42
3.2.5 Energy dispersive spectroscopy 42
3.3 In-situ mechanical testing 43
3.3.1 Sample configuration 43
3.3.2 In-situ tension and compression testing 44
3.4 Slip/twin trace analysis and Schmid factor calculation 47

3.5 CRSS ratio estimation 52
3.6 Crystal plasticity modeling and simulation 53
3.7 In-situ annealing/recrystallization 55

CHAPTER 4 RESULTS 58
4.1 Extruded Mg-1Mn (M1) 59
4.1.1 Microstructure and texture 59
4.1.2 In-situ tension 61
4.1.2.1 323K tension 62
4.1.2.2 423K tension 76
4.1.2.3 523K tension 84
4.2 As-cast Mg-1Mn-0.5Nd (MN10) 91
4.2.1 Microstructure and texture 91
4.2.2 In-situ tension 98
4.2.2.1 323K tension 99
4.2.2.2 423K tension 106
4.2.2.3 523K tension 113
4.3 Extruded Mg-1Mn-0.3Nd (MN10) 121
4.3.1 Microstructure and texture 121
4.3.2 In-situ tension 124
4.3.2.1 323K tension 127
4.3.2.2 423K tension 132
4.3.2.3 523K tension 137
4.3.3 In-situ compression 141
4.3.3.1 323K compression 142
4.3.3.2 423K compression 146
4.3.3.3 523K compression 149
4.4 As-cast Mg-0.9Mn-0.8Nd (MN11) 152
4.4.1 Microstructure and texture 152
4.4.2 In-situ tension 157
4.4.2.1 323K tension 159
4.4.2.2 423K tension 163
4.4.2.3 523K tension 168
4.5 Extruded Mg-1Mn-0.9Nd (MN11-300), Mg-1Mn-1Nd (MN11-275) 174
4.5.1 Microstructure and texture 174
4.5.2 In-situ tension 179
4.5.2.1 323K tension 181
4.5.2.1.1 Estimated CRSS ratios 186
4.5.2.2 423K tension 187
4.5.2.3 523K tension 192
4.5.3 In-situ compression 197
4.5.3.1 298K compression 199
4.5.3.2 423K compression 205
4.5.3.3 523K compression 209
4.6 Rolled Mg-2Zn-0.2Ce and Mg-2Zn-0.6Ce (ZE20) 213
4.6.1 Microstructure and texture 213

4.6.2 In-situ annealing/recrystallization of Mg-2Zn-0.2Ce....215
4.6.3 In-situ annealing/recrystallization of Mg-2Zn-0.6Ce....220

CHAPTER 5 DISCUSSION....226
5.1 Microstructure....226
5.2 Texture....229
5.3 Mechanical properties....230
5.4 Deformation mechanisms....232
5.4.1 Extruded M1....232
5.4.1.1 Crystal plasticity modeling and simulation of twins....246
5.4.2 As-cast MN10 and MN11....251
5.4.3 Extruded MN10 and MN11....253
5.5 Recrystallization in rolled ZE20....261

CHAPTER 6 SUMMARY AND CONCLUSIONS....266
6.1 Summary....266
6.2 Conclusions....266
6.2.1 Extruded M1....266
6.2.2 As-cast MN10....268
6.2.3 Extruded MN10....269
6.2.4 As-cast MN11....270
6.2.5 Extruded MN11....270
6.2.6 Rolled ZE20....271
6.3 Summary of the novel aspects of this work....272
6.4 Recommendations for future work....274

APPENDICES....276
Appendix A Methodology for slip/twin trace analysis and Schmid factor calculation....277
Appendix B Matlab™ code for slip trace analysis and Schmid factor calculation....279
Appendix C Methodology for speculating slip activity based on orientation gradients within deformed grains....282

BIBLIOGRAPHY....293

LIST OF TABLES

Table 1.1 Characteristics of Mg and Mg based alloys compared to other commonly used structural materials based on Fe, Al, Ti, and plastics [Lütjering et al. 2003, King 2007, Kulekci 2008, Callister 2009] 3

Table 1.2 Comparison of the cost and the market penetration of some lightweight components for automotive applications [Zaluzec 2014, personal communication] 4

Table 2.1 Letters representing the alloying elements according to the ASTM specification, 'Standard Practice for Codification of Unalloyed Magnesium and Magnesium-Alloys, Cast and Wrought' 2011 13

Table 3.1 Chemical composition of the materials studied (in weight percent) 37

Table 3.2 Testing conditions of the investigated specimens 45

Table 3.3 The list of slip and twin systems in Mg considered for the trace analysis 47

Table 4.1 M1 tensile property comparison between different test conditions 61

Table 4.2 The chemical composition of the 10 Mn-rich precipitates analyzed inside the grains in the as-cast MN10 microstructure. The values are in wt% 93

Table 4.3 The chemical composition of the 8 Nd-rich precipitates analyzed inside the grains in as-cast MN10 microstructure. The values are in wt% 94

Table 4.4 The chemical composition of the as-cast MN10 matrix. The values are in wt% 95

Table 4.5 The chemical composition of the 5 Mn-rich precipitates analyzed at the grain boundaries in as-cast MN10 microstructure. The values are in wt% 95

Table 4.6 As-cast MN10 tensile property comparison between different test conditions 98

Table 4.7 The chemical composition of the 9 Mn-rich precipitates analyzed inside the grains in the extruded MN10 microstructure. The values are in wt% 123

Table 4.8 The chemical composition of the 6 Nd-rich precipitates analyzed inside the grains in the extruded MN10 microstructure. The values are in wt% 123

Table 4.9 The chemical composition of the extruded MN10 matrix. The values are in wt% ...123

Table 4.10 MN10 extruded tensile property comparison between different test conditions 125

Table 4.11 MN10 extruded compression property comparison between different test conditions 142

Table 4.12 The chemical composition of the 4 Mn-rich precipitates analyzed inside the grains in the as-cast MN11 microstructure. The values are provided in wt% 154

Table 4.13 The chemical composition of the 3 Nd-rich precipitates analyzed at the grain boundaries in the as-cast MN11 microstructure. The values are in wt% 155

Table 4.14 The chemical composition of the as-cast MN11 matrix. The values are in wt% 156

Table 4.15 As-cast MN11 tensile property comparison between the different test conditions ..158

Table 4.16 The chemical composition of the five Mn-rich precipitates analyzed in the extruded MN11-300 microstructure. The values are in wt% 177

Table 4.17 The chemical composition of the four Nd-rich precipitates analyzed in the extruded MN11-300 microstructure. The values are in wt% 177

Table 4.18 The chemical composition of the extruded MN11-300 matrix. The values are in wt% 177

Table 4.19 MN11-300 and MN11-275 tensile property comparison for samples tested between 323-523K 181

Table 4.20 The bootstrapped mean CRSS ratios and the corresponding 90% confidence intervals (listed in parenthesis) for prismatic <a> slip, pyramidal <c+a> slip, and extension twinning in the MN11-300 and MN11-275 alloys estimated using the tensile deformation results at 323K 187

Table 4.21 MN11-300 extruded compression test property comparison for samples tested at 298K, 423K, and 523K 199

Table 5.1 Summary of the average grain size of M1, MN10, and MN11 with different processing histories 227

Table 5.2 Summary of the type, approximate size, and the location of the precipitates in the microstructure for M1, MN10, and MN11 227

LIST OF FIGURES

Figure 1.1 The increase in the Mg die casting use during 1991–2008 owing almost entirely due to the automotive use [King 2007] 2

Figure 1.2 Examples of automotive components made of Mg alloys: (a) engine block (b) wheel (c) door frame (d) oil pan (e) steering wheel and (f) seat frames [Kulekci 2008] 6

Figure 1.3 Some automotive components made of Mg alloys and obtained weight reduction [Tański et al. 2010] 6

Figure 1.4 Inverse pole figures (IPF) showing the crystallographic texture of extruded round bars of Mg-1Mn with Ce, Y, and Nd additions. The left and right IPFs were obtained from materials extruded with an extrusion rate (profile exit rate) of 1m/min and 10m/min, respectively. The other extrusion parameters are same for all materials (See Section 3.1 for details). The intensity levels for the IPF are 1.0, 1.5, 2.0, 3.0, 5.0, 7.0,…, multiples of a random distribution. I_{max} is the maximum intensity values observed. The data is adopted from Bohlen et al. 2010 8

Figure 2.1 The unit cell of the HCP crystal structure of Mg. The lattice constants "c" and "a" are indicated 11

Figure 2.2 The Mn-rich region of the Mg-Mn phase diagram [Nayeb-Hashemi et al. 1985] 14

Figure 2.3 The Mg-Nd binary phase diagram [Nayeb-Hashemi et al. 1988a] 15

Figure 2.4 The Mg-Ce binary phase diagram [Nayeb-Hashemi et al. 1988b] 16

Figure 2.5 Schematic representation of the strong basal texture formation in conventional Mg alloys after extrusion [Chen 2012] 20

Figure 2.6 The atomic radius of RE elements (r_a) and solubility of RE elements in solid Mg (G) as a function of the atomic number of the RE element (N_a) [Rokhlin 2003, Rokhlin 2006] 22

Figure 2.7 Illustration of the three commonly observed slip systems in Mg: (a) $\{0001\} < 11\bar{2}0 >$ basal <a> slip, (b) first order $\{10\bar{1}0\} < 11\bar{2}0 >$ prismatic <a> slip, and (c) Second order $\{11\bar{2}2\} < 11\bar{2}3 >$ pyramidal <c+a> slip 27

Figure 2.8 Illustration of the two commonly observed twin systems in Mg: (a) $\{10\bar{1}2\} < 10\bar{1}1 >$ extension twinning and (b) $\{10\bar{1}1\} < 10\bar{1}2 >$ contraction twinning 27

Figure 2.9 Schematic illustration of the $\{10\bar{1}1\} - \{10\bar{1}2\}$ double twin formation in Mg. The 56° misorientation about $< 11\bar{2}0 >$ formed due to the contraction twinning, the 86° misorientation about $< 11\bar{2}0 >$ formed due to the subsequent extension twinning, and the effective misorientation of 38° about $< 11\bar{2}0 >$ with respect to parent grain due to the double twinning event are indicated 29

Figure 2.10 Experimentally observed variation in CRSS values of different deformation mechanisms with temperature in Mg and alloys adapted from Chapuis et al. [2011], Obara et al. [1973], Yoshinaga et al. [1963], Yoshinaga et al. [1964], Kelley et al. [1968], Wonziewicz et al. [1967], Reed-Hill et al. [1957], and Flynn et al. [1961]. The computationally calculated CRSS values (dotted lines) were adapted from Barnett [2003] 32

Figure 3.1 Photograph of the (a) MN10 as-cast material and (b) M1 extruded rod. Note that some material from the as-cast billet in (a) was removed for testing purposes 39

Figure 3.2 Photograph of an EDM cut test specimen representative of those used for the tension and compression experiments. The sample dimensions are indicated 43

Figure 3.3 Photograph of the testing stage placed inside the Tescan Mira3 SEM chamber 46

Figure 3.4 Example of slip trace analysis performed on the grain indicated as "A" in (a). The sequential SE SEM images taken during the 523K tensile experiment on extruded MN10 is given in (a) to (d), and the approximate strain values at which the images were taken are indicated in the images. The blue line in (c) indicate the experimentally observed slip band direction. (e) The EBSD IPF map in the normal direction for grain "A" with the HCP unit cell showing the grain orientation. (f) The calculated slip traces for the 12 possible slip systems. Note that only basal <a> slip systems (slip system numbers 1-3) matched the experimentally observed slip traces. (g) Tabulated slip system chart showing the Schmid factors for all the possible 12 slip systems. The basal <a> slip system number 3, $(0001)[\bar{1}\bar{1}20]$, highlighted as bold in (g), was determined to be the active slip system with a Schmid factor of 0.44 50

Figure 3.5 Photograph of the heating stage used for the in-situ annealing experiments. Note that the sample (not shown) for the in-situ annealing/recrystallization experiment was placed directly on top of the heating element during the experiments 56

Figure 4.1 (a) SE SEM and (b) BF TEM image showing the microstructure of extruded M1. The extrusion direction is horizontal in (a) 60

Figure 4.2 The grain size distribution of the extruded M1 60

Figure 4.3 Representative texture of extruded M1 microstructure in the form of $\{0001\}$ and $\{10\bar{1}0\}$ pole figures in the normal direction 61

Figure 4.4 Representative stress vs. displacement plots for extruded M1 samples tensile tested at 323K, 423K, and 523K. The stress drops indicates the stress relaxation that occurred when the tests were interrupted for imaging. The displacement values included displacements in both the gage section and the grip regions 62

Figure 4.5 (a) EBSD IPF map in the normal direction before deformation and (b) the corresponding $\{0001\}$ and $\{10\bar{1}0\}$ pole figures from the gage section of the M1 specimen tensile tested at 323K. The area marked by the black box in (a) indicates the region in which trace analysis was performed 63

Figure 4.6 Sequential SE SEM images for the M1 specimen tensile tested at 323K: (a) undeformed, (b) ~0.7% strain, (c) ~5.2% strain, and (d) ~9.9% strain. In (c) and (d), the slip/twin traces are color coded for basal <a> slip (blue), prismatic <a> slip (red), pyramidal <c+a> slip (orange), and contraction twinning (purple) 64

Figure 4.7 SE SEM images of the same area in the gage section of the M1 specimen tensile tested at 323K (a) before deformation and (b) at ~9.9% strain. (c) and (d) shows the EBSD IPF maps in the normal direction for the same area shown in (a) and (b). Extension twins were observed in grains marked A and B in (a) and (c). The extension twins are indicated by black arrows in (b) and (d). In (d), the HCP unit cells are overlaid showing the misorientation between the parent grain and the twinned region and the rotation angles are indicated 67

Figure 4.8 (a) SE SEM image of a contraction twin observed in the M1 specimen tensile tested at 323K. The twin shown in (a) was formed at ~5.2% - ~9.9% strain. The EBSD IPF map in the normal direction of the region highlighted by black box in (a) is given in (b). In (b), the HCP unit cells are overlaid showing the misorientation between the parent grain and the twinned region and the rotation angles are indicated 68

Figure 4.9 A histogram of the Schmid factor distribution of basal <a>, prismatic <a>, pyramidal <c+a> slip systems, and extension and contraction twin systems for the M1 323K tension experiment 69

Figure 4.10 The individual grain orientations in which different deformation modes were observed for the M1 tensile test at 323K, plotted in a (a) unit triangle along the tensile direction and (b) {0001} pole figure along the normal direction. The line connects the grain orientations on both sides of the cracks observed 70

Figure 4.11 (a) SE SEM image of a $\{10\bar{1}1\}-\{10\bar{1}2\}$ double twin observed in M1 specimen tensile tested at 323K. The twin shown in (a) was formed at ~5.2% – ~9.9% strain. The EBSD IPF map in the normal direction of the same region shown in (a) is given in (b). In (b), the HCP unit cells are overlaid showing the misorientation between the parent grain and the twinned region and the rotation angles are indicated 71

Figure 4.12 The evolution of contractions twins into $\{10\bar{1}1\}-\{10\bar{1}2\}$ double twins observed in the M1 specimen tensile tested at 323K: (a) SE SEM image and (b) corresponding EBSD IPF map along the normal direction of the area highlighted by the black box in (a). The area highlighted by the black box in (b) is shown in (c). In (c), the HCP unit cells are over laid showing the misorientation between the parent grain and the twinned region, and the common $<11\bar{2}0>$ direction is highlighted by red lines. In (c), the purple line, the black line, and the yellow line highlights the contraction twin boundary, the extension twin boundary, and the misorientation caused by $\{10\bar{1}1\}-\{10\bar{1}2\}$ double twinning, respectively, and the rotation angles are indicated. In (c), note that the four regions formed due to the twinning events are marked as A, B, C, and D 73

Figure 4.13 (a) SE SEM image of the gage section of the M1 specimen tensile tested at 323K after fracture. The SE SEM image of the crack highlighted by the black box is shown in (b). In

(b) the orientation of the grain in which crack was observed is indicated in the form of HCP unit cell and the orientation of the contraction twin trace parallel to the crack is given. In (c) SE SEM image of the crack shown in (b) is given with the sample tilted 70° with respect to the beam 74

Figure 4.14 SE SEM image of the fracture surface of the extruded M1 specimen tensile tested at 323K approached at an angle of 45° tilted along the tensile direction. The angle of view is indicated 75

Figure 4.15 SE SEM image of the microstructure of the same area of a M1 specimen: (a) after "light" mechanical polishing and (b) after further mechanical polishing by applying more force (the mechanical polishing forces were not measured). (c) EBSD IPF map in the normal direction of the area highlighted by the black box in (b) depicting the extension twins which formed during the second polishing step. The unit cell orientations of the extension twins and the matrix are provided in (c). In (d), the orientation of the grains in which extension twins were formed during mechanical polishing in the M1 specimen tensile tested at 423K is provided in the form of {0001} pole figure in the normal direction 77

Figure 4.16 (a) EBSD IPF map in the normal direction before deformation and (b) the corresponding {0001} and $\{10\bar{1}0\}$ pole figures from the gage section of M1 specimen tensile tested at 423K. The area on which trace analysis was performed is marked in 4.16a. The grains in which extension twins were formed during polishing are highlighted by black arrows in (a) ……78

Figure 4.17 Sequential SE SEM images for M1 tensile tested at 423K: (a) undeformed, (b) ~0.9% strain, (c) ~5.7% strain, and (d) ~15.6% strain. In (c) and (d), slip/twin traces are color coded for basal <a> slip (blue), prismatic <a> slip (red), pyramidal <c+a> slip (orange), and contraction twin (purple). The tensile axis and extrusion direction was horizontal. The grains in which extension twins were formed on the surface during mechanical polishing are marked by black arrows in (a) 80

Figure 4.18 EBSD IPF maps in the normal direction for the same area in the tensile tested sample for M1 at 423K (a) 0% strain and (b) ~15.6% strain. A contraction twin was observed in the grain marked "A" in (a). In (b) the HCP unit cells are overlaid showing the rotation between the parent and the twin orientations, and the misorientation angle is indicated 82

Figure 4.19 A histogram of the Schmid factor distribution of basal <a> slip, prismatic <a> slip, pyramidal <c+a> slip, extension twin, and contraction twin systems identified for the M1 specimen tensile tested at 423K 83

Figure 4.20 The individual grain orientations in which different deformation modes were observed for M1 tensile test at 423K, plotted in (a) unit triangle along the tensile direction and (b) {0001} pole figure along the normal direction. The lines connect the grain orientations on both sides of the cracks observed 84

Figure 4.21 (a) EBSD IPF map in the normal direction before deformation and (b) the corresponding {0001} and $\{10\bar{1}0\}$ pole figures from the gage section of M1 specimen tensile

tested at 523K. The area on which trace analysis was performed is marked in 4.21a 85

Figure 4.22 Sequential SE SEM images for the M1 specimen tensile tested at 523K: (a) undeformed, (b) ~0.5% strain, (c) ~4.1% strain, and (d) ~7.8% strain. In (c) and (d), slip traces are color coded for basal <a> slip (blue), prismatic <a> slip (red), and pyramidal <c+a> slip (orange). The tensile axis and extrusion direction was horizontal 86

Figure 4.23 A histogram of the Schmid factor distribution of basal <a> slip, prismatic <a> slip, and pyramidal <c+a> slip systems identified for the M1 specimen tensile tested at 523K. Note that no twinning activity was observed in the area analyzed 89

Figure 4.24 The individual grain orientations in which different deformation modes were observed for M1 tensile test at 523K deformed to ~7.8% strain, plotted in (a) unit triangle along the tensile direction and (b) {0001} pole figure along the normal direction. The lines connect the grain orientations on both sides of the cracks observed 90

Figure 4.25 SE SEM image of the as-cast MN10 microstructure 91

Figure 4.26 The grain size distribution of the as-cast MN10 92

Figure 4.27 (a) SE SEM image showing the Mn-rich precipitates aligned parallel to the basal planes and (b) DF TEM image of the Mn-rich precipitates in the MN10 as-cast microstructure. In (a), the orientation of the grains is indicated as HCP unit cells as obtained from EBSD analysis 93

Figure 4.28 DF TEM images of (a) Mn-rich and (b) Nd-rich precipitates observed in the MN10 as-cast microstructure 94

Figure 4.29 DF TEM image of a grain boundary in MN10 as-cast microstructure in which Mn-rich precipitates were observed. The SAD patterns from both grains are shown in the inset 96

Figure 4.30 Representative texture of as-cast MN10 in the form of {0001} and $\{10\bar{1}0\}$ pole figures 97

Figure 4.31 EBSD IPF map of the areas from which the pole figures shown in Figure 4.30 was obtained 97

Figure 4.32 Representative stress vs. displacement plots for as-cast MN10 sample tensile tested at 323K, 423K, and 523K. The stress drops indicate the stress relaxation that occurred when the tests were interrupted for imaging. The displacement values include displacements in both the gage section and the grip region. Approximate local strain values are indicated in the plot 99

Figure 4.33 EBSD IPF map in the normal direction of the as-cast MN10 specimen tensile-tested at 323K (a) before deformation and (b) after deformation to ~9.9% strain. The extension twins observed in the undeformed microstructure are marked by black arrows in (a) 100

Figure 4.34 Sequential SE SEM images for the MN10 as-cast specimen tensile tested at 323K: (a) undeformed, (b) ~0.8% strain, (c) ~4.1% strain, and (d) ~8.2% strain. In (c) and (d), the slip traces are color coded for basal <a> slip (blue), prismatic <a> slip (red), and pyramidal <c+a> slip (orange). The corresponding Schmid factor values are given in (c) and (d) 101

Figure 4.35 EBSD IPF map of the region highlighted by a black box in Figure 4.33b. The extension twin boundaries are highlighted by black lines and the $(10\bar{1}2) - (01\bar{1}2)$ double twin boundaries are highlighted by white lines. The HCP unit cells are overlaid indicating the misorientation between parent grain and the twinned region 103

Figure 4.36 High magnification SE SEM image of the area highlighted by the black box in Figure 4.34c. The basal <a> slip observed within the extension twinned region at ~4.1% strain is marked along with its corresponding Schmid factor value 105

Figure 4.37 A histogram of the Schmid factor distribution of basal <a>, prismatic <a>, pyramidal <c+a>, and extension twins observed in the MN10 as-cast specimen tensile tested at 323K 105

Figure 4.38 The individual grain orientations in which different deformation modes were observed for the MN10 as-cast specimen tensile tested at 323K, plotted in (a) unit triangle along the tensile direction and (b) {0001} pole figure along the normal direction 106

Figure 4.39 EBSD IPF map in the normal direction of the MN10 as-cast specimen tensile-tested at 423K (a) before deformation and (b) after deformation to ~9.4% strain. The extension twins observed in the undeformed microstructure are marked by black arrows in (a) 107

Figure 4.40 Sequential SE SEM images for the MN10 as-cast specimen tensile tested at 423K: (a) undeformed, (b) ~1.1% strain, (c) ~6.0% strain, and (d) ~9.4% strain. In (c) and (d), the slip traces are color coded for basal <a> slip (blue), prismatic <a> slip (red), and pyramidal <c+a> slip (orange). The corresponding Schmid factor values are given in (c) and (d) 108

Figure 4.41 EBSD IPF map of the region highlighted by the black box in Figure 4.39b. The extension twin boundaries are highlighted by black lines and the $(10\bar{1}2) - (01\bar{1}2)$ double twin boundaries are highlighted by yellow lines. The HCP unit cells are overlaid indicating the misorientation between parent grain and the twinned region 110

Figure 4.42 High magnification SE SEM image of the area highlighted by the black box in Figure 4.40c. The prismatic <a> slip observed within the extension twinned region at ~6.0% strain is marked along with its corresponding Schmid factor value 111

Figure 4.43 A histogram of the Schmid factor distribution of basal <a>, prismatic <a>, pyramidal <c+a>, and extension twins observed in the MN10 as-cast specimen tensile tested at 423K 112

Figure 4.44 The individual grain orientations in which different deformation modes were observed for the MN10 as-cast specimen tensile tested at 423K, plotted in (a) unit triangle along the tensile direction and (b) {0001} pole figure along the normal direction 113

Figure 4.45 EBSD IPF map in the normal direction of the as-cast MN10 specimen tensile-tested at 523K (a) before deformation and (b) after deformation to ~10.7% strain. The extension twins observed in the undeformed microstructure are marked by black arrows in (a) 114

Figure 4.46 Sequential SE SEM images for the MN10 as-cast specimen tensile tested at 323K: (a) undeformed, (b) ~0.7% strain, (c) ~3.9% strain, and (d) ~10.7% strain. In (c) and (d), the slip traces are color coded for basal <a> slip (blue), prismatic <a> slip (red), and pyramidal <c+a> slip (orange). The corresponding Schmid factor values are given in (c) and (d) 115

Figure 4.47 EBSD IPF map of the regions highlighted in Figure 4.45b by (a) the black box "A" showing the extension twin (b) the black box "B" showing the $(10\bar{1}2) - (01\bar{1}2)$ double twin and (c) the black box "C" showing the contraction twin. The extension twin, $(10\bar{1}2) - (01\bar{1}2)$ double twin, and contraction twin boundaries are highlighted by black, white, and purple lines, respectively. The HCP unit cells are overlaid indicating the misorientation between the parent grain and the twinned region 117

Figure 4.48 High magnification SE SEM image of the area highlighted by a black box in Figure 4.46c. The basal <a> slip observed within the extension twinned region at ~3.9% strain is marked along with its corresponding Schmid factor value 118

Figure 4.49 A histogram of the Schmid factor distribution of basal <a>, prismatic <a>, pyramidal <c+a>, extension twins, and contraction twins observed in the MN10 as-cast specimen tensile tested at 523K 119

Figure 4.50 The individual grain orientations in which different deformation modes were observed for the MN10 as-cast specimen tensile tested at 523K, plotted in (a) unit triangle along the tensile direction and (b) {0001} pole figure along the normal direction 120

Figure 4.51 (a) SE SEM and (b) BF TEM image showing the microstructure of extruded MN10. The extrusion direction is horizontal. The extrusion direction is horizontal and out of the plane of paper in (a) and (b), respectively 122

Figure 4.52 The grain size distribution of extruded MN10 122

Figure 4.53 Representative texture of extruded MN10 microstructure in the form of $\{0001\}$ and $\{10\bar{1}0\}$ pole figures in the normal direction 124

Figure 4.54 Representative stress vs. displacement plots for extruded MN10 samples tensile tested at 323K, 423K, and 523K. The stress drops indicate the stress relaxation that occurred when the tests were interrupted for imaging. The displacement values included displacements in both the gage section and the grip regions. The approximate strain values are indicated and "X" indicates when fracture occurred 126

Figure 4.55 Sequential SE SEM images for the extruded MN10 tensile tested at 323K: (a) ~2.7% strain, (b) ~7.7% strain, (c) ~12.2% strain, and (d) ~21.6% strain. A grain boundary crack observed in this area at ~7.7% strain is indicated by the arrow. It is noted that no obvious slip

traces were observed 128

Figure 4.56 EBSD IPF map in the normal direction of the same area from the gage section of the extruded MN10 tensile tested specimen at 323K (a) before deformation and (b) at ~6.4% strain. An extension twin observed in this region is indicated by the black arrow in (b). The HCP unit cells are overlaid showing the misorientation between the parent grain and the twinned region and the rotation angles are indicated in (b) 130

Figure 4.57 A histogram of the Schmid factor distribution of extension and contraction twin systems for the extruded MN10 323K tension experiment 131

Figure 4.58 The individual grain orientations in which different deformation modes were observed for extruded MN10 tensile test at 323K, plotted in a (a) unit triangle along the tensile direction and (b) {0001} pole figure along the normal direction. The lines connect the grain orientations on both sides of the cracks observed 132

Figure 4.59 Sequential SE SEM images for the extruded MN10 tensile tested at 423K: (a) 0% strain, (b) ~8.3% strain, (c) ~22.0% strain, and (d) ~39.6% strain. Basal <a> slip observed in this region is highlighted by blue line and corresponding Schmid factor value is indicated in (d) ...133

Figure 4.60 EBSD IPF map in the normal direction of the same area from the gage section of the extruded MN10 tensile tested specimen at 423K (a) before deformation and (b) at ~17.8% strain. An extension twin observed in this region is indicated by the black arrow in (b). The HCP unit cells are overlaid showing the misorientation between the parent grain and the twinned region and the rotation angles are indicated in (b) 135

Figure 4.61 A histogram of the Schmid factor distribution of extension and contraction twin systems for the extruded MN10 423K tension experiment 136

Figure 4.62 The individual grain orientations in which different deformation modes were observed for extruded MN10 tensile test at 423K, plotted in a (a) unit triangle along the tensile direction and (b) {0001} pole figure along the normal direction 137

Figure 4.63 Sequential SE SEM images for the extruded MN10 tensile tested at 523K: (a) 0% strain, (b) ~6.8% strain, (c) ~22.3% strain, and (d) ~27.4% strain. Basal <a> slip and pyramidal <c+a> slip observed in this region are highlighted by blue and orange lines, respectively. The corresponding Schmid factor values are indicated in (c) and (d) 138

Figure 4.64 A histogram of the Schmid factor distribution of basal <a> slip, prismatic <a> slip, and pyramidal <c+a> slip for the extruded MN10 specimen tensile tested at 523K. No twinning was observed in the area analyzed 140

Figure 4.65 The individual grain orientations in which different deformation modes were observed for extruded MN10 tensile test at 523K, plotted in a (a) unit triangle along the tensile direction and (b) {0001} pole figure along the normal direction 141

Figure 4.66 Representative stress vs. displacement plots for extruded MN10 samples compression tested at 323K. The displacement values included displacements in both the gage section and the grip regions. The approximate strain values are indicated 142

Figure 4.67 {0001} pole figures in the normal direction from the gage section of the MN10 extruded specimen compression tested at 323K (a) before and (b) after deformation (deformed to ~6.9% strain) 143

Figure 4.68 EBSD IPF map in the normal direction of the same area from the gage section of the extruded MN10 compression tested specimen at 323K (a) before deformation and (b) at ~6.9% strain. Extension twin boundaries (86°±5° misorientation about $< 11\bar{2}0 >$, twin plane $\{10\bar{1}2\}$±5° tolerance) are highlighted in black in (b) 144

Figure 4.69 A histogram of the Schmid factor distribution of extension twins for the extruded MN10 323K compression experiment 145

Figure 4.70 The individual grain orientations in which extension twins were observed for extruded MN10 compression test at 323K, plotted in a (a) unit triangle along the compression direction and (b) {0001} pole figure along the normal direction 145

Figure 4.71 {0001} pole figures in the normal direction from the gage section of the MN10 extruded specimen compression tested at 423K (a) before and (b) after deformation 146

Figure 4.72 EBSD IPF map in the normal direction of the same area from the gage section of the extruded MN10 compression tested specimen at 423K (a) before deformation and (b) at ~8.1% strain. Extension twin boundaries (86°±5° misorientation about $< 11\bar{2}0 >$, twin plane $\{10\bar{1}2\}$±5° tolerance) are highlighted in black in (b) 147

Figure 4.73 A histogram of the Schmid factor distribution of extension twins for the extruded MN10 423K compression experiment 148

Figure 4.74 The individual grain orientations in which different extension twins were observed for extruded MN10 compression test at 423K, plotted in a (a) unit triangle along the compression direction and (b) {0001} pole figure along the normal direction 148

Figure 4.75 {0001} pole figures in the normal direction from the gage section of the MN10 extruded specimen compression tested at 523K (a) before and (b) after deformation 149

Figure 4.76 EBSD IPF map in the normal direction of the same area from the gage section of the extruded MN10 compression tested specimen at 523K (a) before deformation and (b) at ~4.0% strain. Extension twin boundaries (86°±5° misorientation about $< 11\bar{2}0 >$, twin plane $\{10\bar{1}2\}$±5° tolerance) are highlighted in black in (b) 150

Figure 4.77 A histogram of the Schmid factor distribution of extension twins for the extruded MN10 523K compression experiment 151

Figure 4.78 The individual grain orientations in which extension twins were observed for extruded MN10 compression test at 523K, plotted in a (a) unit triangle along the compression direction and (b) {0001} pole figure along the normal direction 151

Figure 4.79 SE SEM image of as-cast MN11 microstructure 152

Figure 4.80 The grain size distribution of as-cast MN11. A total of ~220 grains were measured 153

Figure 4.81 (a) SE SEM image showing the Mn-rich precipitates aligned parallel to the basal <a> planes and (b) DF TEM image of the Mn-rich precipitates in the MN11 as-cast microstructure. In (a), the orientation of the grains is indicated as HCP unit cells as obtained from the EBSD analysis 154

Figure 4.82 (a) BF TEM image of a Nd-rich precipitate observed within grains and (b) DF TEM image of Nd-rich precipitates observed at the grain boundaries in the MN11 as-cast microstructure. The SAD patterns from the two grains on either side of the grain boundary are shown in inset in (b) 155

Figure 4.83 Representative texture of as-cast MN11 in the form of {0001} and $\{10\bar{1}0\}$ pole figures 156

Figure 4.84 EBSD IPF map of the five different areas from which the pole figures shown in Figure 4.83 were obtained for as-cast MN11 157

Figure 4.85 Representative stress vs. displacement plots for the as-cast MN11 sample tensile tested at 323K, 423K, and 523K. The stress drops indicate the stress relaxation that occurred when the tests were interrupted for imaging. The displacement values incorporate displacements in both the gage section and the grip region. Approximate local strain values are indicated in the plot 158

Figure 4.86 EBSD IPF map in the normal direction of the as-cast MN11 specimen tensile-tested at 323K (a) before deformation and (b) after deformation to ~8.3% strain 159

Figure 4.87 Sequential SE SEM images for the MN11 as-cast specimen tensile tested at 323K: (a) undeformed and (b) ~8.3% strain. In (b) the basal <a> slip traces observed in this region are highlighted and the corresponding Schmid factor values are provided 160

Figure 4.88 EBSD IPF map of the region highlighted by the black box in Figure 4.86b. The extension twin boundaries are highlighted by black lines. The HCP unit cells are overlaid indicating the misorientation between the parent grain and the twinned region 161

Figure 4.89 A histogram of the Schmid factor distribution of basal <a> slip and extension twins observed in the MN11 as-cast specimen tensile tested at 323K 162

Figure 4.90 The individual grain orientations in which different deformation modes were

observed for the MN11 as-cast specimen tensile tested at 323K, plotted in (a) unit triangle along the tensile direction and (b) {0001} pole figure along the normal direction 162

Figure 4.91 EBSD IPF map in the normal direction of the MN11 as-cast specimen tensile-tested at 423K (a) before deformation and (b) after deformation to ~8.1% strain 163

Figure 4.92 Sequential SE SEM images for the MN11 as-cast specimen tensile tested at 423K: (a) undeformed, (b) ~0.5% strain, (c) ~3.6% strain, and (d) ~8.1% strain. In (c) and (d), the slip traces are color coded for basal <a> slip (blue), and the corresponding Schmid factor values are given 164

Figure 4.93 EBSD IPF map of the region highlighted by the black box in Figure 4.91b. The extension twin boundaries are highlighted by black lines. The HCP unit cells are overlaid indicating the misorientation between the parent grain and the twinned region 166

Figure 4.94 A histogram of the Schmid factor distribution of basal <a>, prismatic <a>, pyramidal <c+a>, and extension twins observed in the MN11 as-cast specimen tensile tested at 423K 167

Figure 4.95 The individual grain orientations in which different deformation modes were observed for the MN11 as-cast specimen tensile tested at 423K, plotted in (a) unit triangle along the tensile direction and (b) {0001} pole figure along the normal direction 168

Figure 4.96 EBSD IPF map in the normal direction of the as-cast MN11 specimen tensile-tested at 523K (a) before deformation and (b) after deformation to ~6.7% strain 169

Figure 4.97 Sequential SE SEM images for the MN11 as-cast specimen tensile tested at 523K: (a) undeformed, (b) ~0.7% strain, (c) ~3.6% strain, and (d) ~6.7% strain. In (c) and (d), the slip traces are color coded for basal <a> slip (blue), prismatic <a> slip (red), and pyramidal <c+a> slip (orange). The corresponding Schmid factor values are provided in (c) and (d) 170

Figure 4.98 EBSD IPF map of the region highlighted in Figure 4.96b by the black box showing the extension twin. The extension twin boundaries are highlighted by black lines. The HCP unit cells are overlaid indicating the misorientation between parent grain and the twinned region ..172

Figure 4.99 A histogram of the Schmid factor distribution of basal <a>, prismatic <a>, pyramidal <c+a>, and extension twins observed in the MN11 as-cast specimen tensile tested at 523K 173

Figure 4.100 The individual grain orientations in which different deformation modes were observed for the MN11 as-cast specimen tensile tested at 523K, plotted in (a) unit triangle along the tensile direction and (b) {0001} pole figure along the normal direction 173

Figure 4.101 SE SEM images showing the microstructure of extruded (a) MN11-300 and (b) MN11-275. The extrusion direction is horizontal 174

Figure 4.102 The grain size distribution of the extruded (a) MN11-300 and (b) MN11-275 175

Figure 4.103 BF TEM images of (a) a Mn-rich precipitate and (b) a Nd-rich precipitate observed inside the grains in the extruded MN11-300 microstructure. In (c), a BF TEM image of a grain boundary is shown. The Mn-rich and Nd-rich precipitates are highlighted and the SAD pattern from both grains is given in the inset in (c) 176

Figure 4.104 Representative texture of (a) MN11-300 and (b) MN11-275 microstructure in the form of $\{0001\}$ and $\{10\bar{1}0\}$ pole figures in the normal direction 178

Figure 4.105 Representative stress vs. displacement plots for MN11-300 (solid lines) and MN11-275 (dotted lines) samples tensile tested at 323K, 423K, and 523K. The stress drops indicate the stress relaxation occurred when the tests were interrupted for imaging. "X" indicates fracture 180

Figure 4.106 Sequential SE SEM images for the extruded MN11-300 specimen tensile tested at 323K: (a) 0% strain, (b) ~9.0% strain, (c) ~17.5% strain, and (d) ~29.7% strain. A basal <a> slip observed in this region is highlighted by blue line and the corresponding Schmid factor value is indicated in (d) 182

Figure 4.107 EBSD IPF map in the normal direction of the same area from the gage section of the extruded MN11-275 tensile tested specimen at 323K (a) before deformation and (b) at ~14.0% strain. An extension twin observed in this region is indicated by the black arrow in (b). The HCP unit cells are overlaid showing the misorientation between the parent grain and the twinned region and the rotation angles are indicated in (b) 184

Figure 4.108 Histogram of the Schmid factor distribution of different deformation modes observed in extruded (a) MN11-300 and (b) MN11-275 specimens tensile tested at 323K 185

Figure 4.109 The individual grain orientations in which different slip modes were observed for extruded MN11-300 sample tensile test at 323K, plotted in a (a) unit triangle along the tensile direction and (b) {0001} pole figure along the normal direction 186

Figure 4.110 Sequential SE SEM images for the extruded MN11-300 specimen tensile tested at 423K: (a) 0% strain, (b) ~7.8% strain, (c) ~18.7% strain, and (d) ~30.6% strain. Basal <a> slip traces observed in this region are highlighted by blue line and corresponding Schmid factor values are indicated in (d) 188

Figure 4.111 EBSD IPF map in the normal direction of the same area from the gage section of the extruded MN11-275 tensile tested specimen at 423K (a) before deformation and (b) at ~17.3% strain. An extension twin observed in this region is indicated by a black arrow in (b). The HCP unit cells are overlaid showing the misorientation between the parent grain and the twinned region and the rotation angles are indicated in (b) 190

Figure 4.112 Histogram of the Schmid factor distribution of different deformation modes observed in extruded (a) MN11-300 and (b) MN11-275 specimens tensile tested at 423K 191

Figure 4.113 The individual grain orientations in which different slip modes were observed for

extruded MN11-300 sample tensile test at 423K, plotted in a (a) unit triangle along the tensile direction and (b) {0001} pole figure along the normal direction 192

Figure 4.114 Sequential SE SEM images for the extruded MN11-300 sample tensile tested at 523K: (a) 0% strain, (b) ~8.3% strain, (c) ~19.2% strain, and (d) ~42.5% strain. Basal <a> slip traces observed in this region are highlighted by blue lines and the corresponding Schmid factor values are indicated in (d) 193

Figure 4.115 EBSD IPF map in the normal direction of the same area from the gage section of the extruded MN11-275 tensile tested specimen at 523K (a) before deformation and (b) at ~13.9% strain. An extension twin observed in this region is indicated by the black arrow in (b). The HCP unit cells are overlaid showing the misorientation between the parent grain and the twinned region and the rotation angles are indicated in (b) 195

Figure 4.116 Histogram of the Schmid factor distribution of different deformation modes observed in the extruded (a) MN11-300 and (b) MN11-275 specimens tensile tested at 523K ……..196

Figure 4.117 The individual grain orientations in which different deformation modes were observed for extruded MN11-300 tensile test at 523K, plotted in a (a) unit triangle along the tensile direction and (b) {0001} pole figure along the normal direction 197

Figure 4.118 Representative stress vs. displacement plots for extruded MN11-300 samples compression tested at 298K, 423K, and 523K. The displacement values included displacements in both the gage section and the grip regions. The approximate strain values are indicated. The dotted line shows the stress vs. displacement plot for the MN11-300 specimen compression tested to study the evolution of twins. The stress drops indicated when the test was paused for imaging 198

Figure 4.119 {0001} pole figures in the normal direction from the gage section of the MN11-300 extruded specimen compression tested at 298K (a) before and (b) after deformation (~6.1% strain) 199

Figure 4.120 EBSD IPF map in the normal direction of the same area from the gage section of the extruded MN11-300 compression tested specimen at 298K (a) before deformation and (b) at ~6.1% strain. Extension twin boundaries (86°±5° misorientation about $< 11\bar{2}0 >$, twin plane $\{10\bar{1}2\}$±5° tolerance) are highlighted in black in (b) 201

Figure 4.121 A histogram of the Schmid factor distribution of extension twins for the extruded MN11-300 298K compression sample 202

Figure 4.122 The individual grain orientations in which extension twins were observed for extruded MN11-300 compression test at 298K, plotted in a (a) unit triangle along the compression direction and (b) {0001} pole figure along the normal direction 202

Figure 4.123 {0001} pole figures in the normal direction from the gage section of the MN11-300

extruded specimen compression tested at 298K to study the evolution of extension twins, at (a) 0%, (b) ~0.8%, (c) ~4.9%, and (d) ~10.5% strain 203

Figure 4.124 EBSD IPF map along the normal direction of an extension twin observed in MN11-300 specimen compression tested at 298K, at (a) 0%, (b) ~0.8%, and (c) ~4.9% strain, indicating the twin evolution. The HCP unit cells are overlaid showing the misorientation between the parent grain and the twinned region and the rotation angles are indicated in (b). Both the compression direction and then extrusion direction are horizontal 204

Figure 4.125 A histogram of the Schmid factor distribution of extension twins for the extruded MN11-300 298K compression experiment performed to study the evolution of extension twins 204

Figure 4.126 The individual grain orientations in which extension twins were observed for extruded MN11-300 compression test at 298K performed to study the evolution of extension twins, plotted in a (a) unit triangle along the compression direction and (b) {0001} pole figure along the normal direction 205

Figure 4.127 {0001} pole figures in the normal direction from the gage section of the MN11-300 extruded specimen compression tested at 423K (a) before and (b) after deformation (5.9% strain) 206

Figure 4.128 EBSD IPF map in the normal direction of the same area from the gage section of the extruded MN11-300 compression tested specimen at 423K (a) before deformation and (b) at ~5.9% strain. Extension twin boundaries (86°±5° misorientation about $< 11\bar{2}0 >$, twin plane $\{10\bar{1}2\}$±5° tolerance) are highlighted in black in (b) 207

Figure 4.129 A histogram of the Schmid factor distribution of extension twins for the extruded MN11-300 423K compression sample 208

Figure 4.130 The individual grain orientations in which different extension twins were observed for extruded MN11-300 compression test at 423K, plotted in a (a) unit triangle along the compression direction and (b) {0001} pole figure along the normal direction 208

Figure 4.131 {0001} pole figures in the normal direction from the gage section of the MN11-300 extruded specimen compression tested at 523K (a) before and (b) after deformation (~4.8% strain) 209

Figure 4.132 EBSD IPF map in the normal direction of the same area from the gage section of the extruded MN11-300 compression tested specimen at 523K (a) before deformation and (b) at ~4.8% strain. Extension twin boundaries (86°±5° misorientation about $< 11\bar{2}0 >$, twin plane $\{10\bar{1}2\}$±5° tolerance) are highlighted in black in (b). The grains in which multiple twin variants were observed are marked as “A” and “B” in (a) and (b) 211

Figure 4.133 A histogram of the Schmid factor distribution of extension twins for the extruded MN11-300 523K compression sample 212

Figure 4.134 The individual grain orientations in which extension twins were observed for extruded MN11-300 compression test at 523K, plotted in a (a) unit triangle along the compression direction and (b) {0001} pole figure along the normal direction 212

Figure 4.135 The EBSD IPF map of the microstructure and the texture in the form of {0001} pole figures along the normal direction for (a) as-rolled Mg-2Zn-0.2Ce, (b) Mg-2Zn-0.2Ce after annealing, (c) as-rolled Mg-2Zn-0.6Ce, and (d) Mg-2Zn-0.6Ce after annealing. The annealing was carried out at 673K for 60s for both materials. The rolling direction is vertical. It is noted that the images shown above were taken from different sections of the material, thus they do not represent the same microstructural patches before and after annealing 214

Figure 4.136 EBSD IPF maps and the corresponding {0001} pole figures in the normal direction depicting the microstructural evolution in rolled Mg-2Zn-0.2Ce as a function of annealing temperature. I_{max} is the maximum intensity values observed in the pole figures. It is noted that it took ~5-15 minutes to get to the annealing temperature and the EBSD orientation map was acquired in ~45 minutes for each subsequent heating step. The rolling direction is horizontal ……..217

Figure 4.137 The grain orientation spread maps of the microstructural patch analyzed for rolled Mg-2Zn-0.2Ce as a function of temperature. It is noted that it took ~5-15 minutes to get to the annealing temperature and the EBSD orientation map was acquired in ~45 minutes for each subsequent heating step. The rolling direction is horizontal 219

Figure 4.138 The number fraction of the $< hki0 >$ and $< hkil >$ type misorientation axis of the newly formed grain boundaries during the four heating cycles between 423K and 548K in the microstructural patch analyzed for rolled Mg-2Zn-0.2Ce 220

Figure 4.139 EBSD IPF maps and the corresponding {0001} pole figures in the normal direction depicting the microstructural evolution in rolled Mg-2Zn-0.6Ce as a function of annealing temperature. I_{max} is the maximum intensity values observed in the pole figures. It is noted that it took ~5-15 minutes to get to the annealing temperature and the EBSD orientation map was acquired in ~55 minutes for each subsequent heating step. The rolling direction is horizontal ……..221

Figure 4.140 The grain orientation spread maps of the microstructural patch analyzed for rolled Mg-2Zn-0.6Ce as a function of annealing temperature. It took ~5-15 minutes to get to the annealing temperature and the EBSD orientation map was acquired in ~55 minutes for each subsequent heating step. The rolling direction is horizontal 224

Figure 4.141 The number fraction of the $< hki0 >$ and $< hkil >$ type misorientation axis of the newly formed grain boundaries during the six heating cycles between 423K and 598K in the microstructural patch analyzed for rolled Mg-2Zn-0.6Ce 225

Figure 5.1 Approximate tensile YS values of M1, MN10, and MN11 as a function of test temperature 232

Figure 5.2 The Schmid factor distribution for all variants of basal <a> slip, prismatic <a> slip, and pyramidal <c+a> slip for all grains in a representative un-deformed extruded M1 microstructure calculated based on a uniaxial stress state assumption (tensile axis parallel to extrusion direction). The distribution was obtained using EDAX TSL OIM Analysis 6.1 software 234

Figure 5.3 The relative distribution of different deformation modes observed in the extruded M1 specimen tensile tested at 323K, 423K, and 523K 236

Figure 5.4 The global Schmid factor values of the contraction twin variants identified in the extruded M1 specimen tensile tested at 323K overlaid with the Schmid factor values for the contraction twin variant and pyramidal <c+a> slip variant with the highest Schmid factor in the same grain 238

Figure 5.5 The pole figures indicating the $\{10\bar{1}3\}$ poles for (a) the region marked "C" (double twinned region) and (b) "D" (matrix) in Figure 4.12c for the 323K tension-tested extruded M1 specimen deformed to ~9.9% strain. The common poles are circled 240

Figure 5.6 The Schmid factor values calculated based on a uniaxial stress state assumption for different deformation modes in the regions indicated as "A", "B", "C", and "D", in Figure 4.12c for the 323K tension-tested extruded M1 specimen deformed to ~9.9% strain. Note that "A" and "D" represent the matrix, "B" represents the primary $\{10\bar{1}1\}$ contraction twinned region, and "C" represents the $\{10\bar{1}1\} - \{10\bar{1}2\}$ double twinned region 241

Figure 5.7 The Schmid factor map for basal <a> slip, calculated based on a uniaxial stress state assumption, for the area shown in Figure 4.12b for the 323K tension-tested extruded M1 specimen deformed to ~9.9% strain 243

Figure 5.8 The unit cells indicating the Burger's vectors for the 3 variants of basal <a> slip in the twinned volume (a) indicated as "B" and (b) indicated as "C" in Figure 4.12c for the 323K tension-tested extruded M1 specimen deformed to ~9.9% strain. The basal <a> slip variants and the corresponding global Schmid factors calculated based on a uniaxial stress state assumption are listed 243

Figure 5.9 The global Schmid factor values of the pyramidal <c+a> slip variants identified in the extruded M1 specimen tensile tested at 523K overlaid with the Schmid factor values for the contraction twin variant and pyramidal <c+a> slip variant with the highest Schmid factor in the same grain 245

Figure 5.10 (a) the stress and (b) strain response of the contraction twin and the parent grain, shown in Figure 4.12c, when pulled along the Y axis, after 4.0% strain (see Section 3.6 for the details of the simulation) 247

Figure 5.11 The accumulated shear from different slip systems in the contraction twin and parent grain after 4.0% strain along the Y direction simulated using the crystal plasticity model given in Section 3.6. Z is the normal direction 247

Figure 5.12 (a) the stress and (b) strain response of the $\{10\bar{1}1\} - \{10\bar{1}2\}$ double twin and the parent grain, shown in Figure 4.12c, when pulled along the Y axis. The maximum strain was 5.0% (see Section 3.6 for the details of the simulation) 249

Figure 5.13 The accumulated shear from different slip systems in the $\{10\bar{1}1\} - \{10\bar{1}2\}$ double twin and parent grain after 5.0% strain along the Y direction simulated using the crystal plasticity model given in Section 3.6. Z is the normal direction 249

Figure 5.14 The change in the orientation of the matrix and (a) the contraction twin and (b) the $\{10\bar{1}1\} - \{10\bar{1}2\}$ double twin before and after the crystal plasticity simulations in the form of 0001 pole figures along the normal direction. The red dots indicate the orientation before deformation and the black dots indicate the orientation after (a) 4.0% and (b) 5.0% strain 251

Figure 5.15 The relative distribution of the different deformation modes identified in as-cast MN10 and MN11 tensile tested at 323K, 423K, and 523K 252

Figure 5.16 The relative distribution of the different deformation modes identified in extruded MN10, MN11-275, and MN11-300 tensile tested at 323K, 423K, and 523K 255

Figure 5.17 The EBSD IPF map for extruded MN10 tensile tested at 323K after 6.4% strain. The grains are partitioned using the orientations for which basal <a> slip traces were observed during the tensile test at 523K. The pole figures for the grain highlighted by the white box are overlaid with the simulated arcs for different slip systems. By analyzing the streaks in the pole figures, it is likely that basal <a> slip system number 2 with a Schmid factor of 0.37 was active 260

Figure 5.18 The EBSD IPF map in the normal direction, the corresponding texture in the form of {0001} pole figures, and the misorientation angle distribution in the final annealed microstructure in rolled (a) Mg-2Zn-0.2Ce, (b) Mg-2Zn-0.6Ce, and (c) AZ31. The grain boundaries highlighted by white lines in the EBSD IPF correspond to $< 11\bar{2}0 >$ and $< 10\bar{1}0 >$ type, and the black ones correspond to $< 10\bar{1}1 >$ type rotation axis. I_{max} is the maximum texture intensity values observed. The rolling direction is horizontal. The EBSD data was post-processed using a clean-up procedure in which multiple iteration of grain dilation with a grain tolerance angle of 5 degrees and minimum grain size of 5 pixels was performed. Furthermore, the EBSD data were partitioned with a grain tolerance angle of 5 degrees and a minimum grain size of 15-25 pixels 262

Figure 5.19 The distribution of the grain boundaries with $< 11\bar{2}0 >$, $< 10\bar{1}0 >$, and $< 10\bar{1}1 >$ type rotation axis in Mg-2Zn-0.2Ce, Mg-2Zn-0.6Ce, and AZ31 in the final annealed microstructure 263

Figure C.1 The SEM image and the corresponding EBSD IPF of the area in which basal <a> slip traces were observed (see blue line in upper right hand side image) after 8.2% strain in the as-cast MN10 tensile-tested at 323K. The pole figures obtained from this region are overlaid with the simulated arcs for different slip systems. The Schmid factors for different slip systems are also listed. The bold slip system was identified based on the slip trace analysis. By comparing

the streaks observed in the pole figures with the simulated arcs for different slip systems, basal <a> slip on system 3 was identified to be active in this grain 283

Figure C.2 The SEM image and the corresponding EBSD IPF of the area in which prismatic <a> slip traces were observed after 8.2% strain in the as-cast MN10 tensile-tested at 323K. The pole figures obtained from the area highlighted by the black box are overlaid with the simulated arcs for different slip systems. The Schmid factors for different slip systems are also listed. The bold slip system was chosen based on the slip trace analysis. By comparing the streaks observed in the pole figures with the simulated arcs for different slip systems, prismatic <a> slip was identified to be active in this grain 285

Figure C.3 The SEM image and the EBSD IPF map of the grain in which obvious slip traces were not observed after 8.2% strain in as-cast MN10 tensile-tested at 323K. The pole figures obtained from the grain are overlaid with the simulated arcs for different slip systems. The Schmid factors for different slip systems are also listed. By comparing the streaks observed in the pole figures with the simulated arcs for different slip systems, multiple variants of pyramidal <c+a> slip system were probably active in this grain 287

KEY TO SYMBOLS AND ABBREVIATIONS

Ag	Silver
Al	Aluminum
Approx.	Approximate
ASTM	American Society for Testing and Materials
BF	Bright-field
Bi	Bismuth
Ca	Calcium
Cd	Cadmium
Ce	Cerium
CI	Confidence Index
CRSS	Critical resolved shear stress
Cu	Copper
$\dot{\gamma}_0$	Reference shear rate
γ	Shear
DF	Dark-field
EBSD	Electron backscatter diffraction
EDM	Electro-discharge machining
EDS	Energy dispersive X-ray spectroscopy
ε_f	Elongation-to-failure
F	Deformation gradient
Fe	Iron

F_e	Elastic deformation gradient
FEPA	Federation of European Producers of Abrasives
F_p	Plastic deformation gradient
Gd	Gadolinium
HCP	Hexagonal close-packed
ICTS	Spanish National Centre for Electron Microscopy
In	Indium
IPF	Inverse pole figure
La	Lanthanum
Li	Lithium
$\frac{1}{m}$	Stress exponent
MagIC	Magnesium Innovation Center
Mg	Magnesium
Mn	Manganese
n	Slip normal vector
Nd	Neodymium
ND	Normal direction
Pb	Lead
PSN	Particle stimulated nucleation
q	Hardening matrix
RD	Rolling or reference direction
RE	Rare-earth
RT	Room temperature

s	Unit slip direction
SAD	Selective area diffraction
SE	Secondary electron
SEM	Scanning electron microscope
SFE	Stacking fault energy
Si	Silicon
SiC	Silicon carbide
Sr	Strontium
T	Temperature
TD	Transverse or tensile direction
TEM	Transmission electron microscope
Ti	Titanium
Tl	Thallium
τ	Resolved shear stress
τ_{cr}	Slip resistance
UTS	Ultimate tensile strength
wt.%	Weight percent
Y	Yttrium
YS	Yield strength
Zn	Zinc
Zr	Zirconium

CHAPTER 1

INTRODUCTION

1.1 Rationale and research objective

Magnesium (Mg) and its alloys are the lightest engineering metals used for structural applications. As shown in Table 1.1, Mg exhibits a density of ~1.8 g/cm^3. At the same time, Mg alloys exhibit high specific strength and stiffness values compared to other commonly used structural materials, see Table 1.1. These properties make Mg attractive for applications where weight savings are critical. Table 1.1 compares the characteristics of Mg and Mg based alloys with other commonly used structural materials based on Fe, Al, Ti, and plastics. Although Ti typically exhibits a higher specific strength value than Mg, the higher cost of Ti makes it less attractive for high volume applications.

Mg and Mg alloys are employed in a variety of applications, including automotive, aerospace, electronics, biomedical, and sporting goods. However, currently the large scale application of Mg alloys is mainly concentrated in the automotive industry [King 2007]. Figure 1.1 shows the massive increase in the Mg die casting use over the years 1991-2008. This rapid increase is almost entirely due to the automotive use and this is forecasted to continue over the coming years [King 2007].

Auto-manufacturers are forced to expand the use of Mg due to the greater legislative demand for reduced emission and better fuel economy. Studies suggest that weight reduction is the most cost effective way to meet these requirements [Kulekci 2008]. Figure 1.2 shows examples of automotive components made of Mg alloys [Kulekci 2008] and Figure 1.3 depicts the weight reduction obtained by using components made of Mg alloys in a vehicle [Tański et al.

2010]. It is estimated that every 10% reduction in mass results in a 6.6-8% increase in fuel efficiency [Beals et al. 2007] and a 22-70% weight reduction is possible by using Mg alloys in automotive components [Kulekci 2008]. As shown in Table 1.1, Mg is ~75% lighter than Fe and ~35% lighter than Al, and it has high strength-to-weight ratio which can be further improved by alloying. From the manufacturing point of view, the outstanding fluidity of Mg allows the manufacturing of net-shape components. With Mg it is possible to manufacture thinner and more complicated shapes with good dimensional capabilities, especially using die casting. Furthermore, Mg has better damping characteristics and better machinability compared with Al. These attributes of Mg along with weight reduction possibilities makes it attractive to the automotive industry where weight savings are a premium [King 2007]. Being the sixth most abundant element with readily exploitable resources available worldwide, Mg has the potential to fulfill the future demands [King 2007].

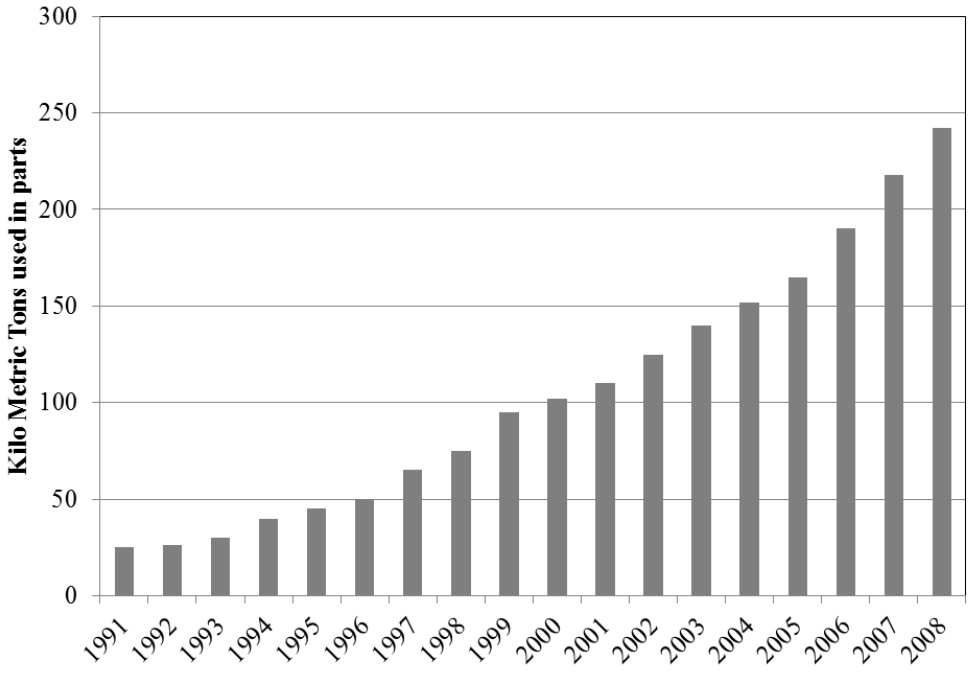

Figure 1.1 The increase in the Mg die casting use during 1991-2008 owing almost entirely due to the automotive use [King 2007].

However, Mg alloys are used in automobiles much less than alloys based on Fe and Al. Table 1.2 compares the cost and the market penetration of some lightweight components for automotive applications [Zaluzec 2014, personal communication]. As shown in Table 1.2, among the Mg components used today, most of it is produced by a casting method. In order to improve the use of Mg in high volume applications, it is critical to increase the quantity of wrought products, even though the additional steps involved in the wrought processing increase the total price of the product (the final cost of conventional Mg alloy extrusions are more than three times than that for Al [King 2007]). In order to realize this, a clear advantage of the wrought product, such as improvement in mechanical property and formability, needs to be demonstrated. Rare-earth (RE) containing Mg alloys exhibit several desirable properties, as described in the following sections, which makes it readily useful for cast or wrought applications. However, as shown in Table 1.2, the cost of components made out of such alloys are very high ($4-4.5/lb saved) to be considered for high volume general applications. Thus, RE-containing Mg alloys are currently restricted for low volume specialty applications. This is partly due to the high cost of RE elements itself. Nevertheless, more research is required to develop new alloys and processes that are cost effective in order to reduce the final cost of Mg products, so that they can compete with traditional materials.

Table 1.1 Characteristics of Mg and Mg based alloys compared to other commonly used structural materials based on Fe, Al, Ti, and plastics [Lütjering et al. 2003, King 2007, Kulekci 2008, Callister 2009].

	Mg	Al	Fe	Ti	Plastics
Density (g/cm^3)	1.8	2.8	7.2	4.5	1.0-1.7
Melting point (°C)	650	660	1536	1670	100-150
Tensile strength (MPa)	240	320	1000	1000	40-60
Specific strength ($MPa/(Mg/m^3)$)	130	100	40	190	30-80
Elastic modulus (GPa)	45	68	205	115	1.5-3.0
Specific stiffness ($GPa^{1/3}/(Mg/m^3)$)	2.0	1.5	0.75	1.1	1.1-1.5
Comparative price	Medium	Medium	Low	High	Low

Table 1.2 Comparison of the cost and the market penetration of some lightweight components for automotive applications [Zaluzec 2014, personal communication].

Component	Cost ($/lb saved)	Applications	Implementation
Al engine	<1	General	High volume
Mg die castings	<1	General	High volume
Ultra-High Strength Steel body	<1	General	Emerging
Al closures	1.5-2.5	As-needed	High volume
Sheet Molding Compound body panel	1.5-2.5	As-needed	High volume
Al body	2-3.5	As-needed	Emerging
Al brake rotors	2-4	As-needed	Emerging
RE-containing Mg alloys (cast/wrought)	4-4.5	Specialty	Low volume
Ti exhaust system	4.5-7	Specialty	Low volume
Carbon composite body	4.5-8	Specialty	Low volume

The poor formability at room temperature (RT) limits some wrought Mg alloy products [Polmear 1994, King 2007, Chino et al. 2008a, Kulekci 2008]. Mg exhibits a hexagonal close-packed (HCP) structure. This non-symmetric structure partly complicates the deformation behavior of Mg. Among the available slip systems, the critical resolved shear stress (CRSS) for basal slip is significantly lower than that of non-basal slip systems at ambient temperatures, and the non-basal slip activity becomes significant only at elevated temperatures (typically greater than 473K) [Hutchinson et al. 2010]. The easily activated basal <a> slip provides only two independent modes of deformation [Yoo 1981]. Thus, at ambient temperatures, the von-Mises criterion of five independent slip systems required for homogeneous plastic deformation cannot be satisfied and an increase in formability can be expected only at elevated temperatures [von-Mises 1928]. Thus, wrought Mg alloy products are typically processed at elevated temperatures in the range of 573-673K. This requirement further adds cost to the price of the finished product. In addition, Mg deforms by simultaneous activation of slip and twinning, especially at ambient temperatures. The prevalence of various twinning mechanisms during deformation can lead to premature fracture [Barnett 2007]. Moreover, Mg alloys tend to form a strong crystallographic

texture during wrought processing, and this leads to anisotropic deformation behavior and mechanical properties [Nave et al. 2004, Stanford et al. 2008], which can be undesirable.

Being a relatively new material considered for engineering applications, there is a lack of both fundamental knowledge and practical experience in the application of Mg alloys. So, the research and development of new alloys, understanding of processing-microstructure-property relationships, and the establishment of the database are all very important for the widespread application of Mg alloys. It is important to provide a detailed characterization of the microstructure, mechanical properties, and deformation behavior of new Mg alloys, which will improve the understanding of processing-microstructure-property relationships. In addition, fundamental studies on the deformation mechanisms and its effect on the formability of Mg alloys are essential for the development of new alloys that can compete with commercially-used Al alloys. It was recently observed that wrought Mg alloys containing RE elements exhibit relatively weak crystallographic texture and have better formability than conventional wrought Mg alloys [Chino et al. 2008b, Bohlen et al. 2010]. However, the mechanisms responsible for weak crystallographic texture formation in RE-containing Mg alloys are not known yet. Therefore, an investigation and comparison of the microstructure, texture evolution, mechanical properties, and the deformation behavior of both conventional and RE-containing Mg alloys with different processing histories is beneficial. The overarching goal of this research is to understand the effects of processing, RE alloying, and temperature on the microstructure, crystallographic texture, mechanical properties, and deformation behavior of a few newly developed Mg alloy systems. In addition to that, one target was to be able to understand why RE additions result in texture weakening during wrought processing.

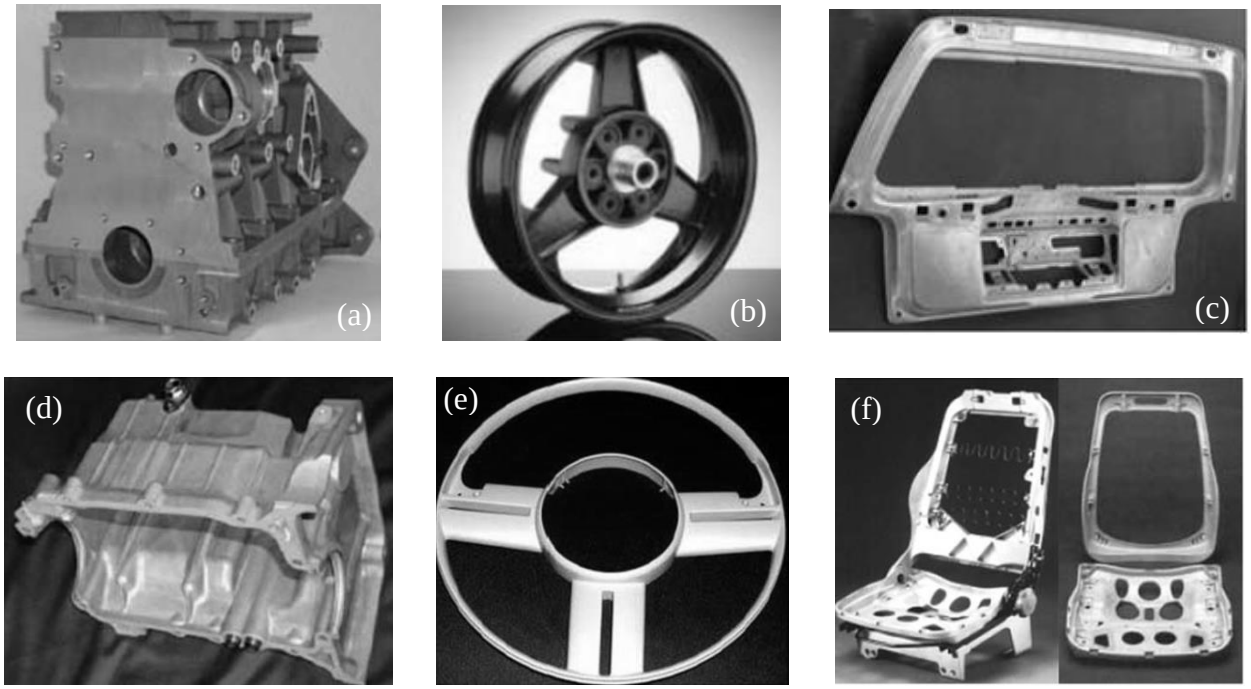

Figure 1.2 Examples of automotive components made of Mg alloys: (a) engine block (b) wheel (c) door frame (d) oil pan (e) steering wheel and (f) seat frames [Kulekci 2008].

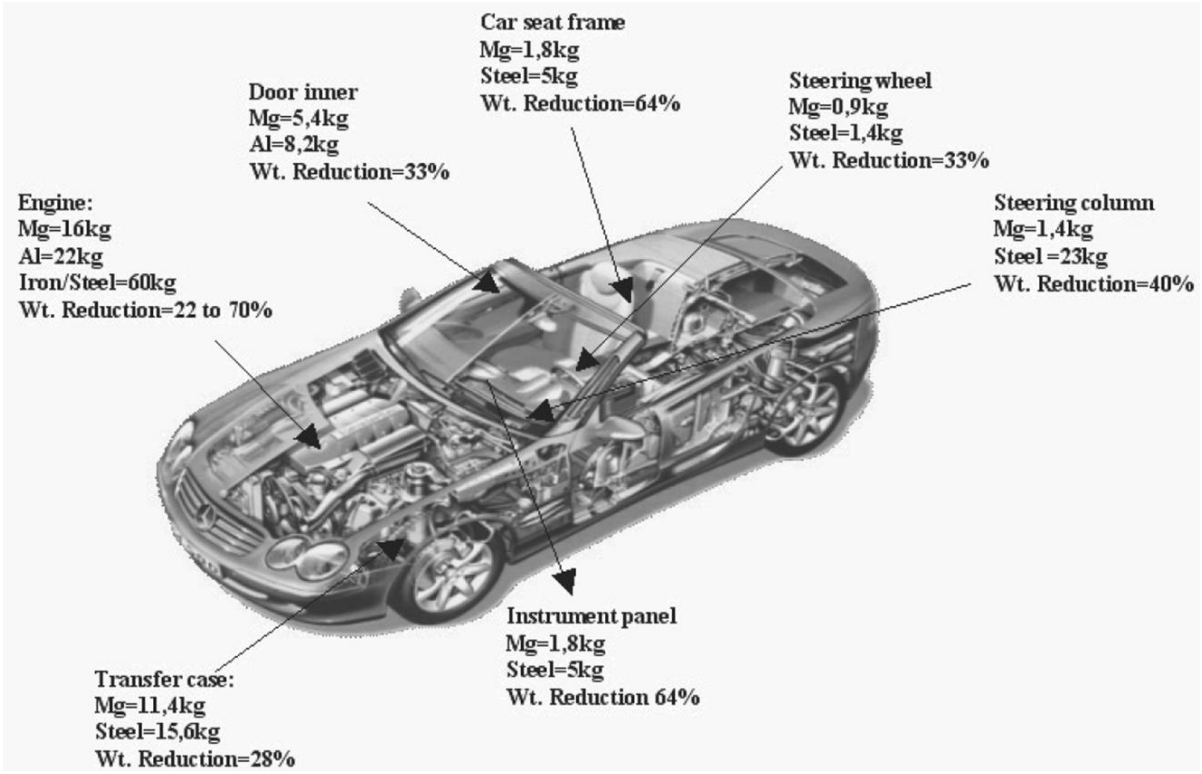

Figure 1.3 Some automotive components made of Mg alloys and obtained weight reduction [Tański et al. 2010].

1.2 Work performed

Recently it was discovered that Nd is a stronger texture modified than either Ce or Y [Bohlen et al. 2010]. In particular, a set of Mg-1Mn (wt.%)[1] alloys was extruded with either 1wt.% Ce, Y, or Nd. The dramatic effects of the resulting texture differences are illustrated in Figure 1.4. The reason for this discrepancy is currently not understood. Moreover, the effect of Nd on the deformation behavior of Mg alloys, especially at elevated temperatures, is not clear. Thus, Nd was the RE alloying addition targeted in this work.

In this dissertation work, the deformation behavior of Mg alloys with different amount of Nd additions and different processing histories were studied. The alloys studied were extruded Mg-1Mn (M1), as-cast and cast-then-extruded Mg-1Mn-0.3Nd (MN10), and as-cast and cast-then-extruded Mg-1Mn-1Nd (MN11). In addition, the recrytstallization and texture evolution in hot rolled Mg-2Zn-0.2Ce and Mg-2Zn-0.6Ce (ZE20) sheets were studied. The materials were supplied by Dr. Jan Bohlen, Dr. Sangbong Yi, and Dr. Dietmar Letzig of Magnesium Innovation Centre (MagIC), Helmholtz Centre, Geesthacht, Germany.

In Chapter 2, a background on Mg and Mg alloys is provided, including the fundamental crystal structure, alloying, processing, texture and microstructure, and the available deformation mechanisms. A review on the current understanding of the deformation behavior, with a focus on RE-containing Mg alloys, is also provided.

---

[1] Henceforth, all alloy compositions are given in weight percent unless otherwise mentioned.

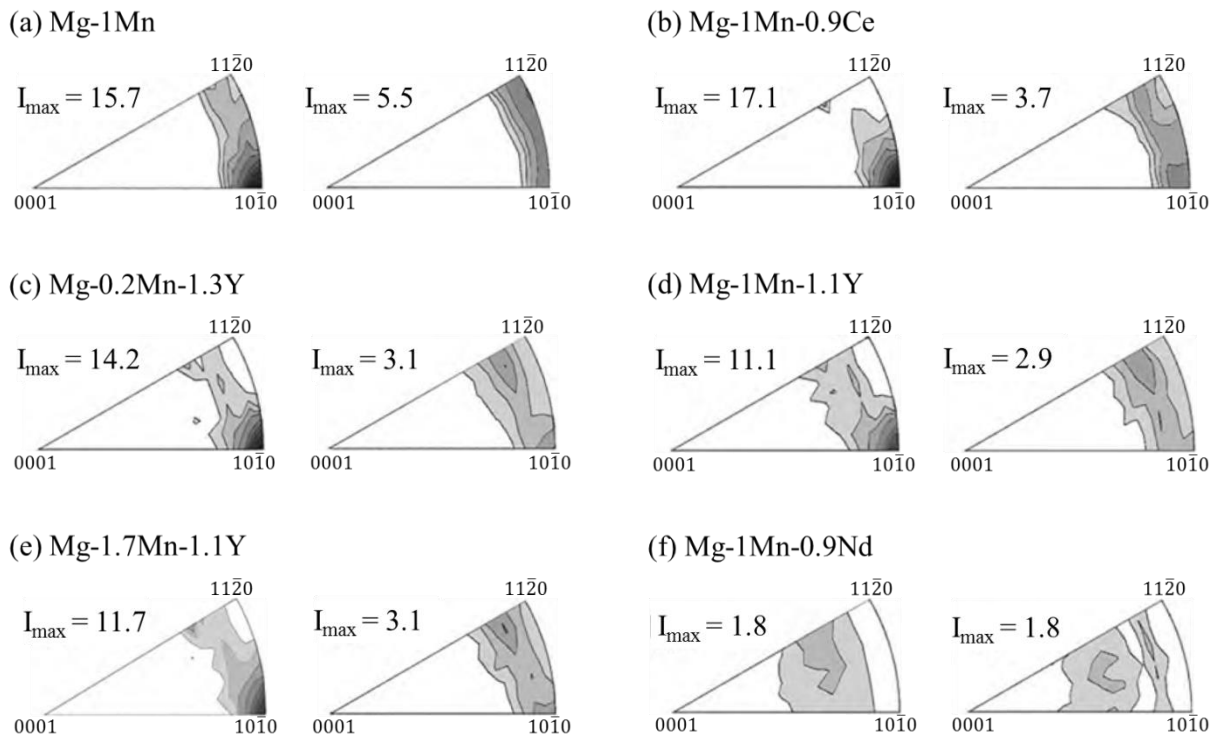

Figure 1.4 Inverse pole figures (IPF) showing the crystallographic texture of extruded round bars of Mg-1Mn with Ce, Y, and Nd additions. The left and right IPFs were obtained from materials extruded with an extrusion rate (profile exit rate) of 1m/min and 10m/min, respectively. The other extrusion parameters are same for all materials (See Section 3.1 for details). The intensity levels for the IPF are 1.0, 1.5, 2.0, 3.0, 5.0, 7.0,…, multiples of a random distribution. I_{max} is the maximum intensity values observed. The data is adopted from Bohlen et al. 2010.

In Chapter 3, the materials and experimental procedures used in this dissertation work are described. The bulk alloy composition and the processing histories are provided for each material. The details of the techniques used for microstructural characterization, in-situ specimen preparation, and in-situ mechanical testing are presented. The methodology used for slip/twin trace analysis, Schmid factor calculation, and CRSS ratio estimation are also provided. In addition, the details of the crystal plasticity modeling and simulations used to study the deformation behavior of twins are presented. Furthermore, the details of the novel in-situ annealing methodology developed to study the recrystallization behavior are described.

In Chapter 4, the results from the microstructure and texture characterization and the in-situ tension/compression experiments for each material are presented. The grain size and texture was characterized using scanning electron microscopy (SEM) and electron backscatter diffraction (EBSD). The chemical composition of precipitates was measured using transmission electron microscopy (TEM) combined with energy dispersive spectroscopy (EDS). TEM was also used to understand the distribution and morphology of the precipitates. In-situ tension/compression experiments were performed at 298K, 323K, 423K, and 523K. The surface deformation evolution was captured by the in-situ collected secondary electron (SE) images. EBSD was performed both before and after deformation. The active deformation systems for each testing condition of each material were determined by trace analysis. In the case of the extruded MN11, the CRSS ratios of different deformation systems were estimated. Finally, the results from the in-situ annealing/recrystallization experiments performed on rolled ZE20 were presented.

In Chapter 5, a discussion of the microstructure, strength, and deformation behavior of the studied materials is presented. The differences in the microstructure and texture of each material are discussed. How these differences affect the mechanical properties of each material at different temperatures is discussed. Furthermore, the relative activity of the different deformation systems at different testing conditions for each material is compared and discussed. The distribution of the deformation activity was also characterized as a function of strain level and this was the first time that such work had been performed on this alloy system. In the case of extruded M1, the effect of contraction twins and $\{10\bar{1}1\}-\{10\bar{1}2\}$ double twins on the limited elongation-to-failure (ε_f) at ambient temperatures was discussed in the light of crystal plasticity simulations. This combined in-situ experimental/modeling work was able to elucidate

the sequential steps involved in the evolution of double-twinning, which had previously only been able to be addressed speculatively using ex-situ experiments. In addition, the recrystallization behavior of rolled ZE20 was discussed and compared with a rolled conventional Mg alloy, AZ31.

In Chapter 6, the conclusions of this dissertation are presented and potential future work is suggested. In particular, new insights were obtained as to why Nd is such a strong texture modifier. The characterized distribution of the deformation modes was helpful in this regard. It is noteworthy, that through this dissertation work, the in-situ SEM methodology was improved upon and a new methodology, involving a slightly different setup, for characterizing the microstructural evolution of Mg alloys during annealing was developed. It is expected that both these methodologies will be heavily used in years to come to further understand processing-microstructure-property relationships of Mg alloys.

CHAPTER 2

BACKGROUND AND LITERATURE REVIEW

2.1 Fundamentals of Mg and Mg alloys

2.1.1 Crystal structure

Pure Mg exhibits a HCP crystal structure, which belongs to $P6_3/mmc$ space group, under atmospheric pressure and at RT. The arrangement of atoms in a unit cell of Mg is shown in Figure 2.1. The lattice parameters are typically a = 0.32nm and c = 0.52nm giving the real c/a ratio of 1.624, which is slightly lower than the ideal value of 1.633 for the HCP structure [Yoo 1981, Avadesian et al. 1999].

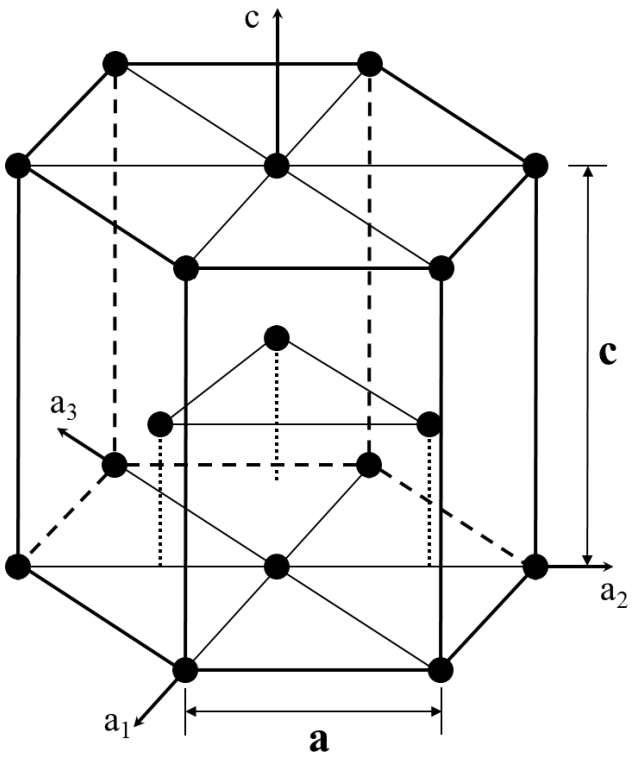

Figure 2.1 The unit cell of the HCP crystal structure of Mg. The lattice constants "c" and "a" are indicated.

2.1.2 Alloying

Mg is generally used for engineering applications after being alloyed with other metals. The major factors that dominate the physical metallurgy of Mg alloys are the hexagonal lattice structure, with a c/a = 1.624 and the atomic diameter of 0.32 nm. The atomic diameter favors a diverse range of solute elements that range within ±15% the diameter of Mg [Polmear 1994]. Depending on the type of the elements added, the alloys can be broadly classified into conventional alloys, which contain elements such as Mn, Al, Zn, Si, Ca, and RE-containing Mg alloys, which contain elements such as Nd, Ce, Sr, Y, Gd, La.

The nomenclature of Mg alloys according to ASTM standards ('Standard Practice for Codification of Unalloyed Magnesium and Magnesium-Alloys, Cast and Wrought' 2011) is to list the abbreviation letters representing the alloying element, and then list the rounded figures representing the weight percent of the corresponding element, respectively. The letters representing different alloying elements are summarized in Table 2.1. It is noted that in this study, Neodymium (Nd) is labeled as "N", which is not consistent with the ASTM standards, because Nd is a RE element and labeled as "E" according to the standard code. A few alloying elements related to the alloys investigated in this study are introduced, and their effects are mentioned in the next section.

Table 2.1 Letters representing the alloying elements according to the ASTM specification, 'Standard Practice for Codification of Unalloyed Magnesium and Magnesium-Alloys, Cast and Wrought' 2011.

Alloying element	Abbreviation letter
Aluminum (Al)	A
Copper (Cu)	C
Rare-earths	E
Strontium (Sr)	J
Zirconium (Zr)	K
Manganese (Mn)	M
Silver (Ag)	Q
Silicon (Si)	S
Gadolinium (Gd)	V
Yttrium (Y)	Y
Zinc (Zn)	Z

(a) Manganese (Mn)

The addition of Mn enhances the corrosion resistance of Mg alloys [Avedesian et al. 1999]. In addition, since Mn is essential for humans, it is considered as a choice as an alloying element for biomedical Mg alloys [Gu et al. 2010]. Mn is usually used together with other alloying elements such as Al and/or Zn, however, some binary alloys are used for extrusions specifically for biomedical applications [Gu et al. 2010]. Figure 2.2 shows the Mn-rich region for the Mg-Mn phase diagram [Nayeb-Hashemi et al. 1985]. Based on the phase diagram, the solubility of Mn in Mg is low, and with decreasing temperature, precipitation of α-Mn from supersaturated solid solution is expected [Mezbahul-Islam et al. 2014].

(b) Neodymium (Nd)

RE elements are generally added to increase the creep resistance, high-temperature strength, and corrosion resistance [Avedesian et al. 1999]. Figure 2.3 shows the Mg-Nd binary phase diagram [Nayeb-Hashemi et al. 1988a]. Specifically, Nd enhances the material strength

particularly at high temperatures [Gupta et al. 2011]. This is due to the potential of Nd to generate thermally-stable precipitates within the grain structure and grain boundaries [Lyon et al. 2007]. Nevertheless, the solubility of RE elements in Mg is generally very limited [Mezbahul-Islam et al. 2014]. In addition, RE elements can serve as texture modifier for Mg alloys. Specifically, it is observed that dilute additions of Nd modifies the texture of wrought products, and Nd has shown to be a stronger texture modifier compared with other RE elements such as Ce and Y (See Figure 1.4) [Bohlen et al. 2010].

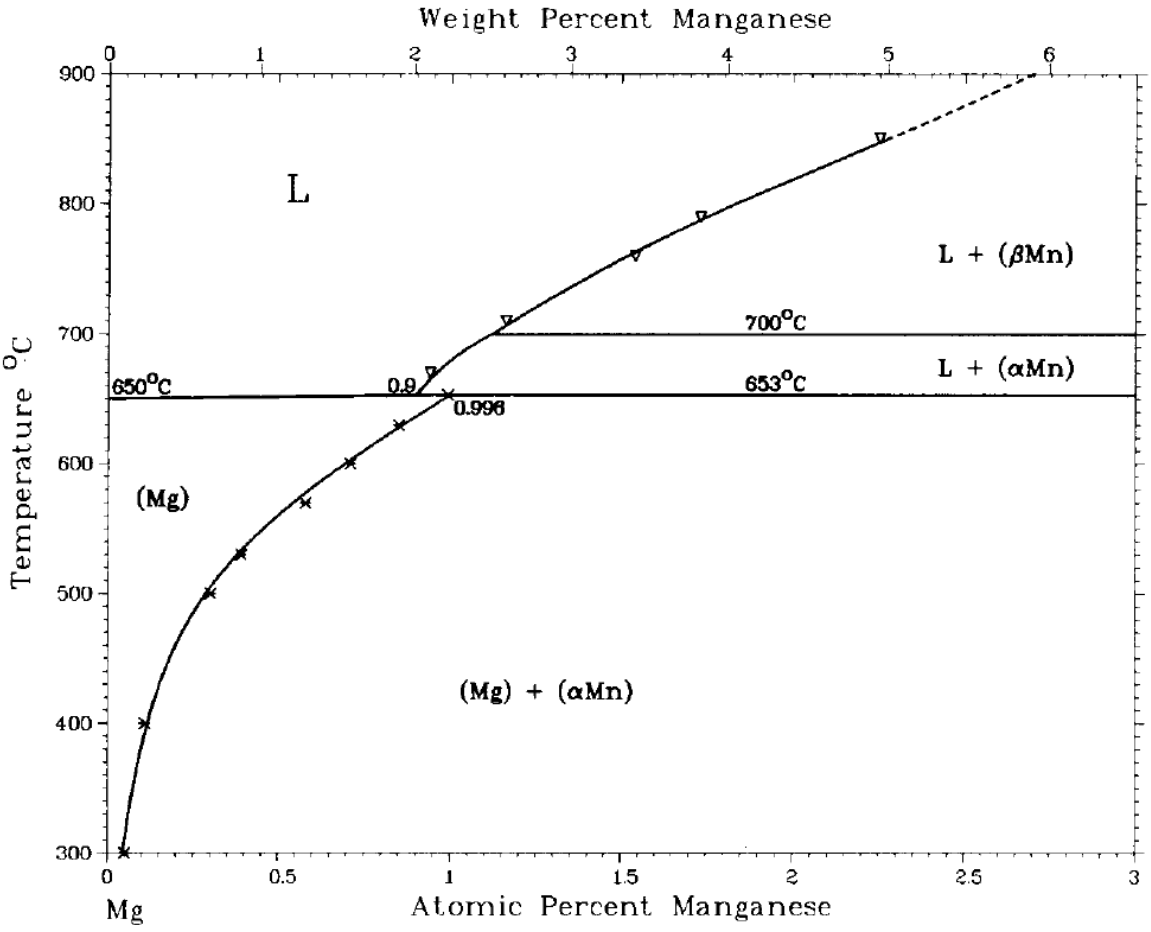

Figure 2.2 The Mn-rich region of the Mg-Mn phase diagram [Nayeb-Hashemi et al. 1985].

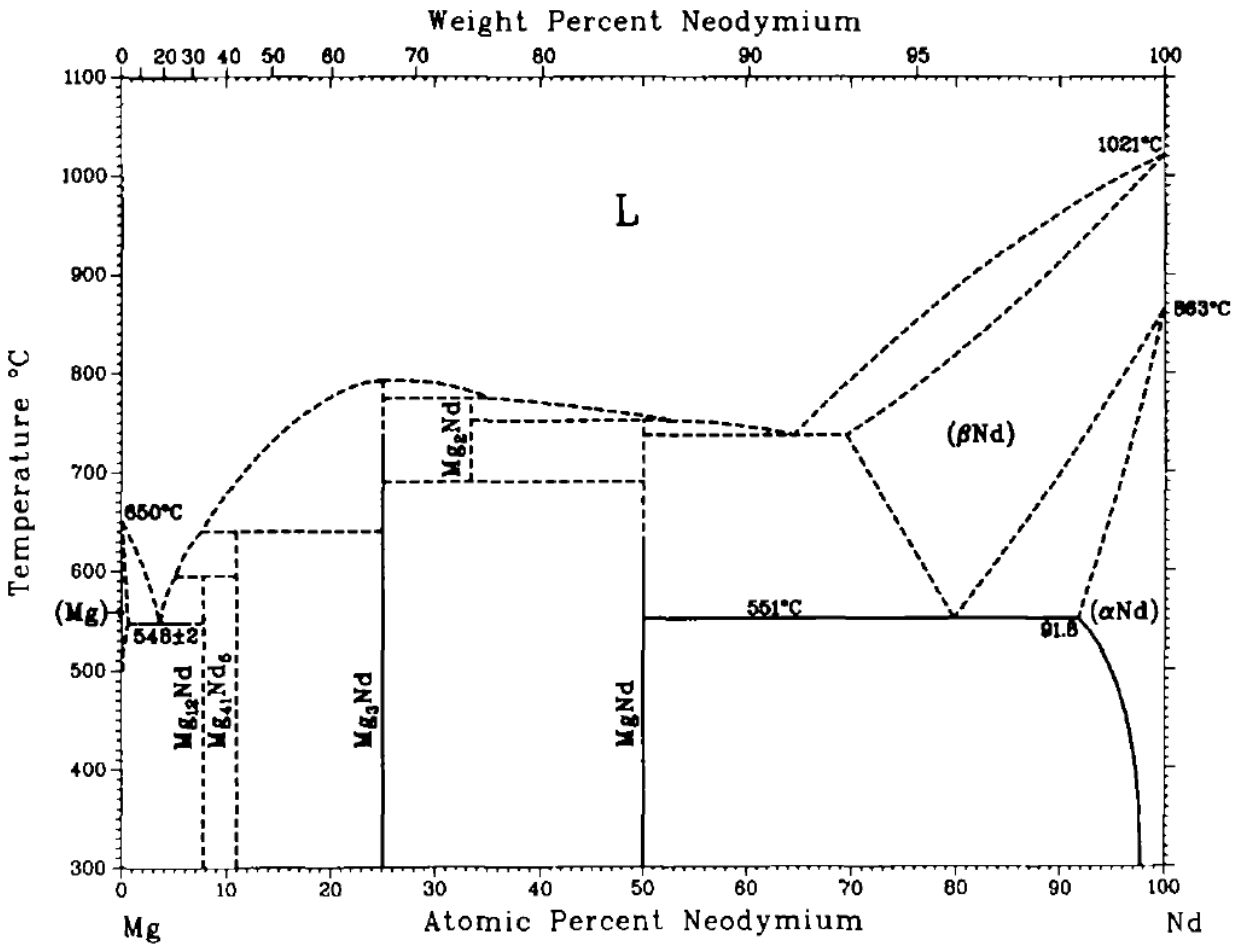

Figure 2.3 The Mg-Nd binary phase diagram [Nayeb-Hashemi et al. 1988a].

(c) Cerium (Ce)

The addition of Ce enhances the elongation-to-failure in Mg alloys [Mishra et al. 2008]. Although not as strong of a texture-modifier as Nd, Ce additions assist in the weakening of texture in wrought Mg alloys (See Figure 1.4) [Bohlen et al. 2010]. Being a relatively low-cost element compared to other RE elements, Ce-containing wrought Mg alloys are attractive for high volume automotive applications [King 2007]. Figure 2.4 shows the Mg-Ce binary phase diagram [Nayeb-Hashemi et al. 1988b]. Similar to other RE elements, the solubility of Ce in Mg is very limited [Mezbahul-Islam et al. 2014].

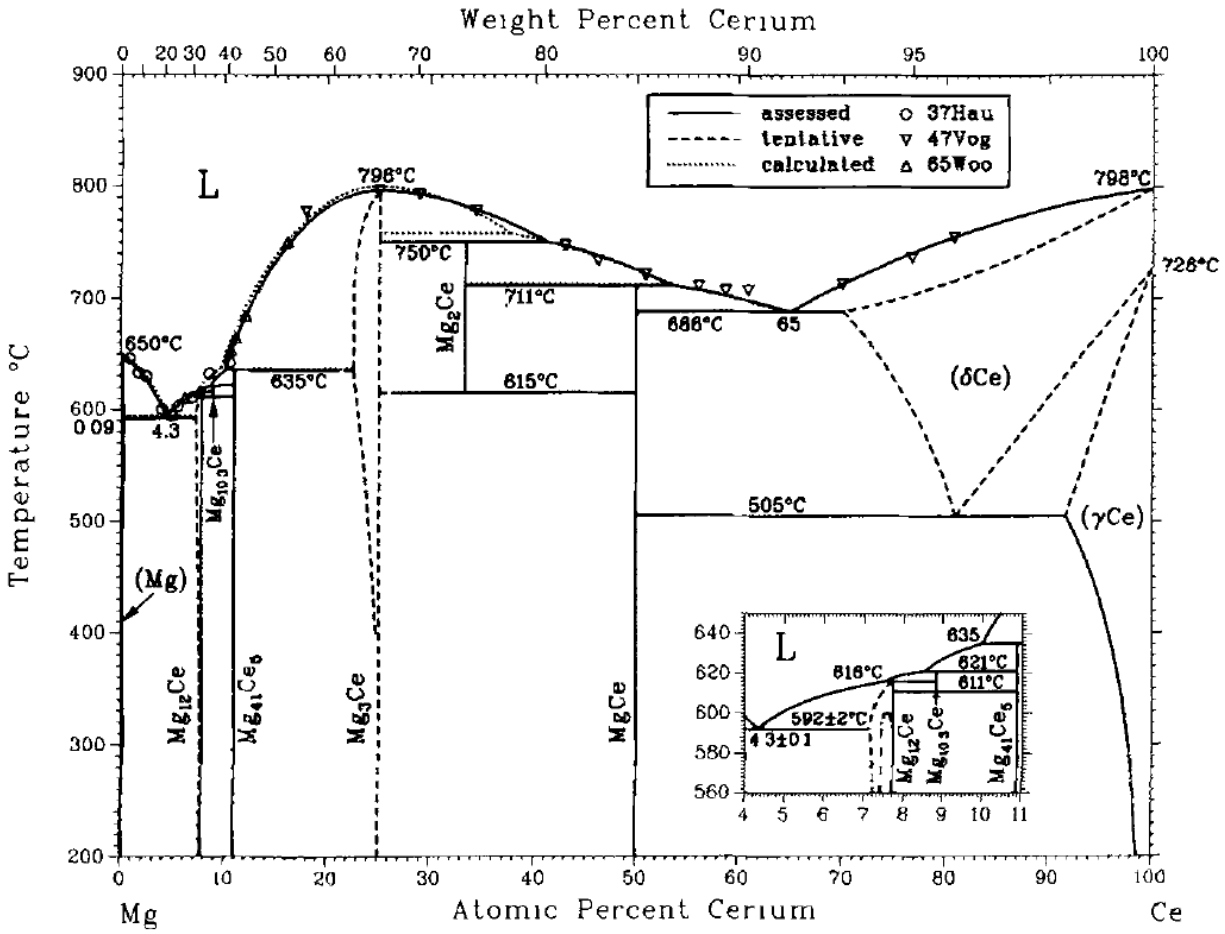

Figure 2.4 The Mg-Ce binary phase diagram [Nayeb-Hashemi et al. 1988b].

2.2 Processing of Mg alloys

Based on the processing method, Mg alloys can be classified in to cast and wrought alloys. The major attributes of both types of alloys are discussed below:

(a) Cast alloys

Most of the Mg components made today are produced by a casting method. Reliable alloys have been developed with the addition of RE elements. Still the high temperature properties (T>448K) of cast Mg alloys are not always satisfactory and this needs further research

and development. The distribution, amount, and shape of the intermetallic phases formed during solidification are the major factors that influence the deformation behavior and mechanical properties of Mg cast alloys. RE elements have an advantage over other elements as they can form thermally-stable intermetallic compounds [Hort et al. 2006]. The attributes of Mg alloys that are favorable to the casting process are high fluidity, low specific heat per unit volume, low density, reduced tendency of sticking to the mold material, and absence of reaction with steel dies, which enables the use of pressure die casting that ensures good shape reproducibility [Polmear 1994, Dobrzanski et al. 2007, King 2007]. The majority of the cast Mg alloys used in commercial applications are die cast. Some Mg alloys are also compatible with gravity casting, squeeze casting and the thixotropic casting processes [Polmear 1994]. It is noted that the RE elements in the cast alloys have a tendency to segregate [Zou et al. 2005]. This could lead to segregation with respect to RE elements, such as stringers of precipitates, in the wrought microstructure [Bohlen et al. 2010].

(b) Wrought alloys

Wrought materials are mainly manufactured by extrusion, rolling, or press forging at temperatures ranging from 573K to 773K. Because of the limited number of active deformation mechanisms available at RT, the processing of wrought alloys is carried out at elevated temperatures [Polmear 1994]. Among wrought processes, extrusion is of great importance. It is observed that hydrostatic extrusion can reduce the processing temperature significantly [Letzig et al. 2008]. Other major drawbacks of extruded alloys are the low extrusion speed and the strong texture generated during the fabrication process which induces yield strength asymmetry [Bettles et al. 2005]. It is observed that RE containing wrought Mg alloys exhibit good mechanical properties and are more easy to process compared to conventional Mg alloys [Rokhlin 2003,

Bettles et al. 2005, Bohlen et al. 2010]. In short, the study of texture, microstructure, and alloying composition of wrought Mg alloys is very important to develop alloys that can compete with the already established wrought aluminum alloys. For example, the wrought Al alloy 2024, which is commonly used for applications requiring high strength to weight ratio exhibit a specific YS value of ~27kNm/Kg (the YS at RT is ~76MPa and the density is ~2.8g/cm^3) and ε_f value of ~12% [Friedrich et al. 2006]. In order to be an attractive candidate for lightweight applications, Mg alloys need to exhibit better properties on a density-normalized basis compared to currently used Al alloys. The mechanical properties of the materials studied in this work will be compared with that for Al alloy 2024 in Section 5.3.

2.3 Texture and microstructure

Conventional Mg alloys tend to exhibit low formability partially due to their large mechanical anisotropy [Ball et al. 1994, Ulacia et al. 2010]. Figure 2.5 shows a schematic representation of strong basal texture in conventional Mg alloys after extrusion [Chen 2012]. This anisotropy can be reduced by alloying Mg with RE elements, and weaker wrought textures result [Bohlen et al. 2007, Chino et al. 2008a, Chino et al. 2008b, Cottam et al. 2008, Mackenzie et al. 2008, Mishra et al. 2008, Stanford et al. 2008, Bohlen et al. 2010, Stanford 2010a, Stanford et al. 2010, Al-Samman et al. 2011, Jiang et al. 2011, Robson et al. 2011, Sandlobes et al. 2011]. However, the origin of such weak textures is not clear. The effect of RE elements, such as lanthanum (La), Y, Gd, Ce, and Nd, on the texture of wrought Mg alloys has been reported in a number of studies [Bohlen et al. 2007, Bohlen et al. 2010, Hantzsche et al. 2010, Stanford et al. 2010]. It was found that for extruded binary Mg-RE alloys, dilute addition of RE elements (specifically, 0.02 at.% for Y, 0.01 at.% for La, 0.015 at.% for Gd, and 0.016 at.% for Ce) resulted in a texture similar to that of pure Mg (extrusion axis tilted 14° from the arc $[10\bar{1}0]$ –

$[11\bar{2}0]$) [Stanford et al. 2010]. With increasing RE addition, the texture initially shifts toward a "conventional texture" (extrusion axis perpendicular to the c-axes), while the so-called "RE texture" (extrusion axis aligned with the $[10\bar{1}0]$ and the $[\bar{1}2\bar{1}1]$ directions) was only observed with sufficiently high RE concentration (specifically, 0.03 at.% for La, 0.06 at.% for Gd, and 0.04 at.% for Ce) [Stanford et al. 2010]. For rolled Mg alloys, the addition of RE elements resulted in a texture in which the c-axes are shifted significantly both toward the rolling direction (RD) and transverse direction (TD), which is different from the conventional texture in which the c-axes are mostly aligned with the normal direction (ND) and only slightly shifted towards RD [Bohlen et al. 2007].

Typically, these changes in texture are accompanied by a decrease in the texture intensity, and the degree of texture weakening depends on the alloying element and the amount of the alloying element [Bohlen et al. 2007, Bohlen et al. 2010, Hantzsche et al. 2010, Stanford 2010]. Although Nd has been shown to be a stronger texture modifier compared with other RE elements (See Figure 1.4), a systematic study has yet to be performed to understand the effect of Nd content on the texture. It would be expected that as the Nd content decreases, a more conventional wrought texture would be exhibited. However, prior to this study, it was not clear how much Nd is required for texture modification and this question was a target of this dissertation research.

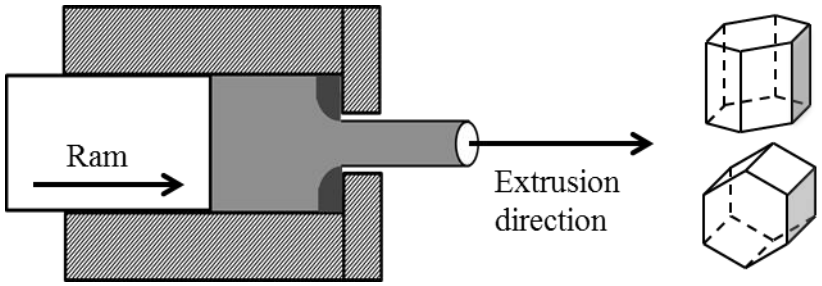

Figure 2.5 Schematic representation of the strong basal texture formation in conventional Mg alloys after extrusion [Chen 2012].

The established Mg-RE phase diagrams suggest that different RE elements will affect Mg alloys differently [Rokhlin 2003, Rokhlin 2006]. The atomic radius and solubility of different RE elements in solid Mg at different temperature as a function of atomic number is given in Figure 2.6 [Rokhlin 2003, Rokhlin 2006]. The solubility of different RE elements in solid Mg, which changes regularly in accordance with the sizes of the corresponding atomic radii, differs within a wide range (See Figure 2.6), and this determines the difference in the influence of RE elements on the characteristics of the Mg alloys [Rokhlin 2006]. The fact that the solubility of RE elements in Mg decreases with a decrease in temperature (See Figure 2.6) suggests that RE elements in Mg tend to form supersaturated solid solutions.

Although the principal effect of RE elements on the texture modification during recrystallization is somewhat understood, the mechanisms responsible for texture weakening in RE-containing Mg alloys, which are most likely connected with the presence of solutes and/or precipitates, are not well understood. Different mechanisms proposed in the literature for texture weakening observed in RE containing Mg alloys are reviewed in the following sections.

(a) The effect of particles

Ball and Pragnell [1994], were the first to observe texture weakening in extruded RE

containing Mg alloys, such as Mg-5.2Y-1.7Nd-1RE-0.6Zr. They concluded that the weak random texture observed after extrusion was due to Particle Stimulated Nucleation (PSN). However, in a more recent study by Stanford and Barnett [2008], it was observed that PSN was not the controlling mechanism for texture weakening during extrusion in Mg alloys with dilute RE additions, such as Mg-1.6Gd and Mg-0.2La, and the texture modification was attributed to the oriented nucleation of grains at the shear bands. The authors reported that in Mg-1.6Gd no precipitates were observed and the precipitates observed in Mg-0.2La were far too small to produce PSN [Stanford et al. 2008]. It is interesting to note that La is not soluble in Mg (for practical purposes) while Gd is a fully soluble alloying addition at the concentrations (<0.25 at.%) studied by the authors (See Figure 2.6). However, other alloys such as Mg-1.5Mn are known to form nano-sized precipitates [Stanford et al. 2008]. Hantzche et al. [2010], reported that texture weakening occurs even in the absence of precipitates in the case of largely soluble RE elements such as Y. This solute-related phenomenon has been confirmed in other extruded Mg-RE alloys [Stanford et al. 2008, Stanford 2010]. It could be concluded that texture weakening can take place in single-phase solid solution alloys with no precipitates, and even if PSN is active, it is not the sole mechanism responsible for texture weakening.

(b) The effect of non-basal slip activity, shear bands, interfaces, and grain boundaries

Akhtar and Teghtsoonian [1969] studied the effect of dilute additions of non-RE elements, such as Zn and Al, on the slip activity and observed that the CRSS of non-basal slip decreases and the CRSS of basal <a> slip increases with increasing solute content. The authors observed the same tendency for the CRSS of basal <a> slip with other non-RE element additions, such as indium (In), lead (Pb), bismuth (Bi), cadmium (Cd), thallium (Tl), and lithium (Li), and attributed the extent of solid-solution strengthening to the size of solute and valency

differences between the solute and the solvent [Akhtar et al. 1972]. It was reported that the amount of RE (specifically Ce, Nd, and Y) addition required for sufficient texture weakening is connected with the solid solubility of the respective element in Mg, and the texture weakening was attributed to the appearance of deformation bands and the restriction of grain growth by solute segregation and/or particles [Hantzsche et al. 2010]. Hadorn et al. [2012] recently examined the role of solute in texture modification in Mg-Y alloys and the promotion of non-basal slip and suppression of grain boundary mobility were proposed to be the solid-solution based mechanisms responsible for texture weakening. Barnett et al. [2004] proposed that the severe shear banding observed during cold rolling plays an important role in the texture weakening phenomenon observed in Mg-0.2Ce.

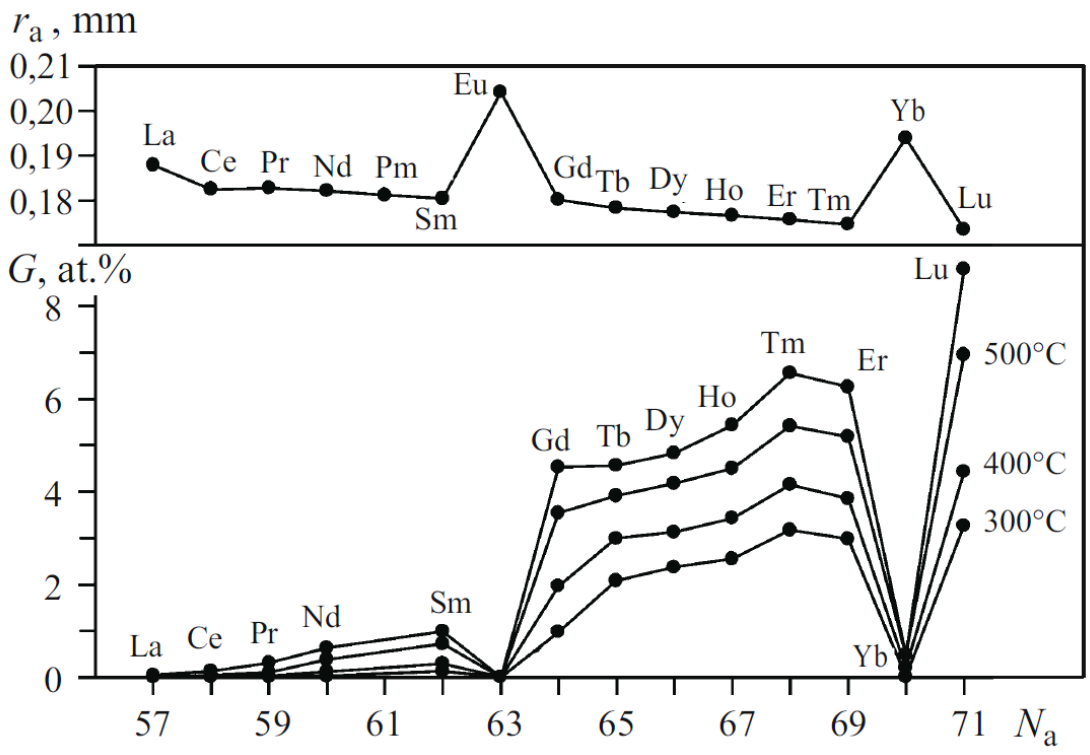

Figure 2.6 The atomic radius of RE elements (r_a) and solubility of RE elements in solid Mg (G) as a function of the atomic number of the RE element (N_a) [Rokhlin 2003, Rokhlin 2006].

Significant solute segregation at grain boundaries was observed in Mg-0.28Y (at.%), while Mg-0.39Zn (at.%) did not show significant solute enrichment at grain boundaries [Hadord et al. 2012]. Similar tendency of solute enrichment at grain boundaries was observed previously in Mg-4.65Gd [Stanford et al. 2010]. It is interesting to note that Zn addition does not modify the texture in Mg while Y and Gd are texture modifiers. Nie et al. [2013] recently reported the periodic segregation of solutes at fully coherent twin boundaries after compression and subsequent heat treatment in Mg-Zn, Mg-Gd, and Mg-Gd-Zn solid solution alloys. It is interesting to note that a fully coherent twin boundary has low interfacial energy compared to partially-coherent interfaces such as high-angle grain boundaries. Nie et al. [2013] attributed the strengthening effect observed in such alloys after heat treatment to the strong pinning effect of solutes at interfaces. In a recent study, Stanford et al. [2011] observed a significant increase in the local concentration of RE solutes at the grain boundaries compared to the matrix in an alloy with modified texture and proposed that the segregation of solute to the grain boundaries plays a significant role in the texture modification in RE-containing Mg alloys.

In general, it is not clear whether the texture weakening observed in Mg-RE alloys is due to atomic effects or microstructural effects or a combination of both. Considering the dilute amounts of RE additions required for significant texture weakening and the propensity of solutes to segregate to low-energy interfaces in Mg alloys, it is likely that the effect of RE elements on interfaces plays a critical role in texture modification as well as the deformation behavior. However, the mechanisms responsible for texture modification in different RE-containing Mg alloys needs to be investigated as the difference in behavior caused by different RE elements in Mg is not fully understood. In this context it is worthwhile to note that Nd was found to be a much stronger texture modifier than Ce or Y in extruded Mg-1Mn [Bohlen et al. 2010]. By

stronger texture modifier it means Nd results in the formation of a weaker texture (i.e. more random) not like the conventional alloys type wrought texture (i.e. strong basal texture). Even though the maximum equilibrium solid solubility of Nd in Mg is relatively low (~3.6 wt.%) [Hehmann et al. 1990, Rokhlin 2003, Rokhlin 2006], a systematic study on the presence or absence of precipitates in Mg-1Mn alloys with dilute Nd additions (≤ 1 wt.%) is lacking to date. In a recent study on extruded Mg-1Mn-1Nd [Hidalgo-Manrique et al. 2014], the presence of thermally-stable Mn-containing particles and the strong tendency of Nd to segregate to boundaries were revealed, and these factors were proposed to be the main mechanisms controlling the texture and grain size. In the same study, it was also observed that the extruded Mg-1Mn-1Nd contains a large amount of Nd in the solid solution which tends to precipitate during thermal treatment. In this context it is desirable to study the effect of Nd additions in the matrix as well as at the interfaces in Mg-1Mn-xNd alloys.

2.4 Deformation mechanisms

The deformation of Mg occurs by the simultaneous activation of crystallographic slip and deformation twinning. The dominance of a specific slip or twinning system in Mg is highly dependent on the deformation temperature. The ease of particular slip/twin under specific conditions is usually related to their CRSS values. Although widespread values of the CRSS have been reported for the various slip and twinning systems of Mg alloys (See Section 2.6 for more details), it is generally accepted that the CRSS follows the trend $CRSS_{basal\ <a>\ slip} < CRSS_{extension\ twin} < CRSS_{prismatic\ <a>\ slip} < CRSS_{pyramidal\ <c+a>\ slip}$ at RT. As a result, basal <a> slip and extension twinning are the dominant deformation mechanisms in randomly-oriented polycrystals at low temperatures (including RT) and low strain rates. The characteristics of the commonly observed slip and twinning mechanisms in Mg alloys are given in the following

sections.

2.4.1 Dislocation slip

Generally, independent modes of slip can happen on two basal $\{0001\}$ planes and two prismatic planes $\{10\bar{1}0\}$, with "a" Burger's vector, $< 11\bar{2}0 >$. A slip system with "c+a" Burger's vector, $< 11\bar{2}3 >$, on the pyramidal plane $\{11\bar{2}2\}$ alone can provide five independent modes [Avedesian et al. 1999]. The commonly observed slip systems in Mg are schematically represented in Figure 2.7. It is noted that the $\{0001\}$ basal plane is the close-packed plane and the $< 11\bar{2}0 >$ directions (<a> directions) are the close-packed directions in Mg. According to von-Mises criterion, for a polycrystal to be ductile it should have at least five independent slip systems [von-Mises 1928]. As the basal <a> slip, which is the only slip system active at room temperature, does not have five independent slip systems, the mechanical processing of Mg alloys is difficult at room temperature [Yoo 1981]. This is also one of the reasons behind the strong texture formed in wrought alloys. The strong texture makes the material behave differently in compression and tension modes. It is observed that the yield stress in compression is almost half that in tension along the strain axis in wrought products [Ball et al. 1994]. This tensile-compressive asymmetry has negative impact on the applications of wrought alloys as one needs to consider both tensile and compression strengths during the design of components and an asymmetry might be undesirable in some of the applications.

2.4.2 Twinning

In addition to dislocation slip, twinning, which can provide 0 to 5 independent modes, also play an important role in the deformation behavior of Mg. Two major twin systems observed in Mg alloys are $\{10\bar{1}2\} < 10\bar{1}1 >$ "extension twinning" and $\{10\bar{1}1\} < 10\bar{1}2 >$

"contraction twinning" [Avedesian et al. 1999]. Twinning is a polar mechanism [Christian et al. 1995]. As a result, $\{10\bar{1}2\} < 10\bar{1}1 >$ twinning is active only when the deformation conditions are such that an extension along the <c> axis takes place. In turn, $\{10\bar{1}1\} < 10\bar{1}2 >$ twinning takes place when the deformation gives rise to compression along the <c> axis. Hence the name extension twinning and contraction twinning. Twinning leads to reorientation of the lattice. Extension twinning and contraction twinning ideally causes a misorientation of 86° and 56° about $< 11\bar{2}0 >$, respectively [Avedesian et al. 1999]. In general, twinning is favored at high strain rates and low temperatures [Christian et al. 1995]. Figure 2.8 illustrates the commonly observed twin systems in Mg.

The wrought processing of Mg alloys often results in the formation of a crystallographic texture in which the c-axis is preferentially aligned perpendicular to the processing direction [Bohlen et al. 2010]. Further processing on this material can place the c-axis of the majority of the crystals under compression. It is important to note that the most easily activated deformation systems in Mg, basal <a> slip and extension twinning, cannot accommodate compressive strain along the c-axis. The slip systems that can accommodate strain along the c-axis are prohibitive at ambient temperatures in conventional Mg alloys due to their high CRSS values [Hutchinson et al. 2010, Chapuis et al. 2011]. Thus, various contraction twinning mechanisms are expected to activate when polycrystalline Mg alloys with strong basal texture are deformed at ambient temperatures. Thus, the significance of twinning mechanisms on the ambient temperature deformation behavior of polycrystalline Mg alloys is of commercial interest.

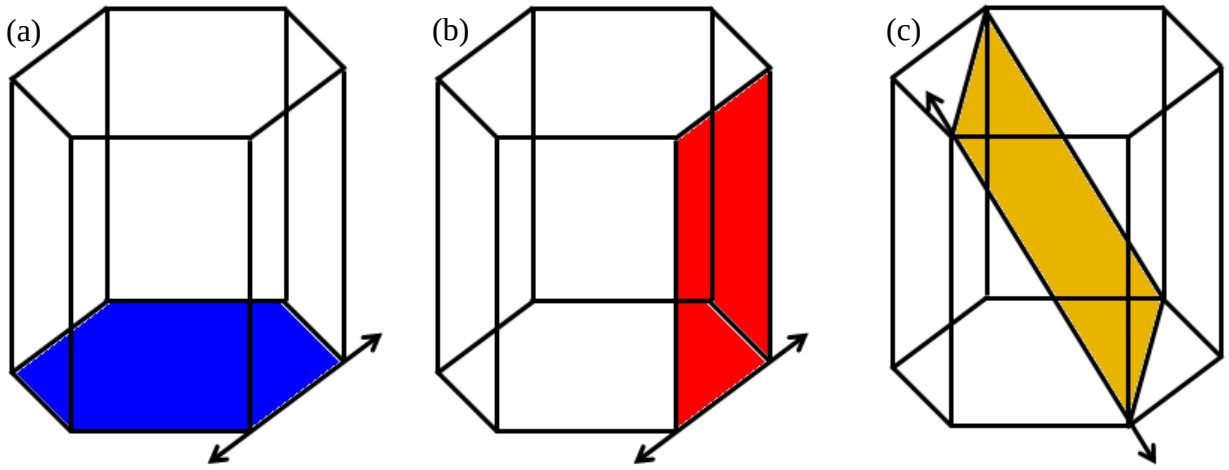

Figure 2.7 Illustration of the three commonly observed slip systems in Mg: (a) $\{0001\} < 11\bar{2}0 >$ basal <a> slip, (b) first order $\{10\bar{1}0\} < 11\bar{2}0 >$ prismatic <a> slip, and (c) Second order $\{11\bar{2}2\} < 11\bar{2}3 >$ pyramidal <c+a> slip.

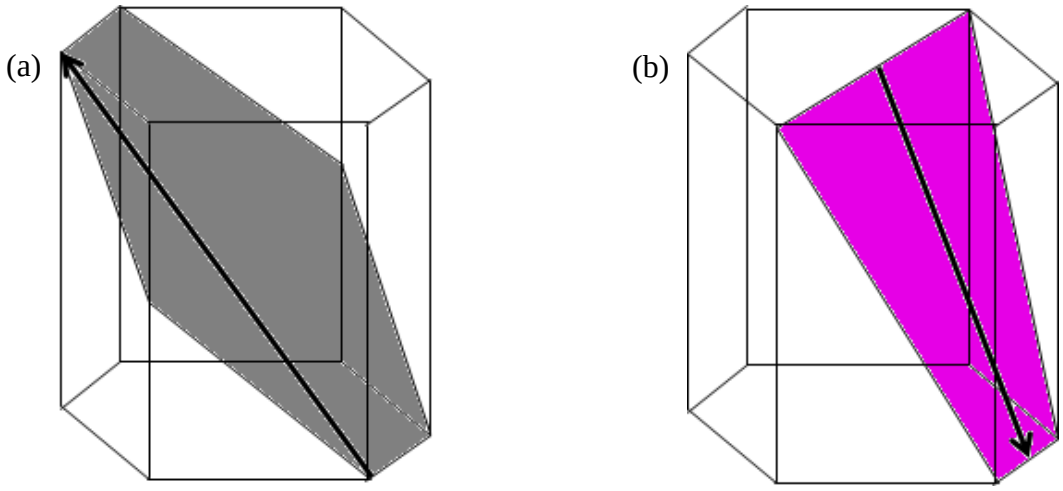

Figure 2.8 Illustration of the two commonly observed twin systems in Mg: (a) $\{10\bar{1}2\} < 10\bar{1}1 >$ extension twinning and (b) $\{10\bar{1}1\} < 10\bar{1}2 >$ contraction twinning.

Previous studies have reported the activation of various types of twinning modes, such as $\{10\bar{1}1\}$, $\{30\bar{3}4\}$, $\{10\bar{1}3\}$, $\{10\bar{1}5\}$, $\{10\bar{1}4\}$, $\{11\bar{2}4\}$, when the c-axis was placed under compression in Mg single crystals, and these twinning modes were often associated with crack initiation sites and fracture planes [Reed-Hill et al. 1957a, Reed-Hill et al. 1957b, Yoshinaga et

al. 1963, Hartt et al. 1967, Wonsiewicz et al. 1967, Kelley et al. 1968, Yoshinaga et al. 1973]. Complex double twinned structures have also been observed in Mg single crystals when the c-axis is compressed [Wonsiewicz et al. 1967, Hartt et al. 1968]. The primary twinning mode was reported to be either on $\{10\bar{1}1\}$ or $\{10\bar{1}3\}$ planes, and secondary twinning happens on $\{10\bar{1}2\}$ planes inside the primary twinned volume [Couling et al. 1959]. In the case of $\{10\bar{1}1\} - \{10\bar{1}2\}$ double twin, the 56° misorientation about $< 11\bar{2}0 >$ caused by the activation of the $\{10\bar{1}1\}$ contraction twin and the subsequent misorientation of 86° about $< 11\bar{2}0 >$ caused by the activation of the $\{10\bar{1}2\}$ extension twin result in an effective misorientation of 38° about $< 11\bar{2}0 >$ with respect to the parent grain. Figure 2.9 illustrates the formation $\{10\bar{1}1\} - \{10\bar{1}2\}$ double twin in Mg. For $\{10\bar{1}1\} - \{10\bar{1}2\}$ double twins, the formation of voids at the twin interior-matrix interface has been identified as a fracture initiation site [Hartt et al. 1968]. It was reported that this type of double twinning mechanism could result in the preferential alignment of the crystal for easy activation of basal <a> slip [Couling et al. 1959]. This could lead to the softening of the twinned volume compared to the parent region, which in turn could result in the formation of localized "shear bands" ultimately leading to shear failure [Couling et al. 1959]. However, there is ambiguity about the source of large deformation inside the double twinned regions. It was suggested that the ease of activity of basal <a> slip within the twin volume causes shear localization and results in large surface step formation [Hartt et al. 1967, Wonsiewicz et al. 1967]. At the same time, non-basal slip and grain boundary shear was reported to be responsible for the shear deformation inside the twinned region in some of the earlier studies [Wonsiewicz et al. 1967, Hartt et al. 1968, Kelley et al. 1968].

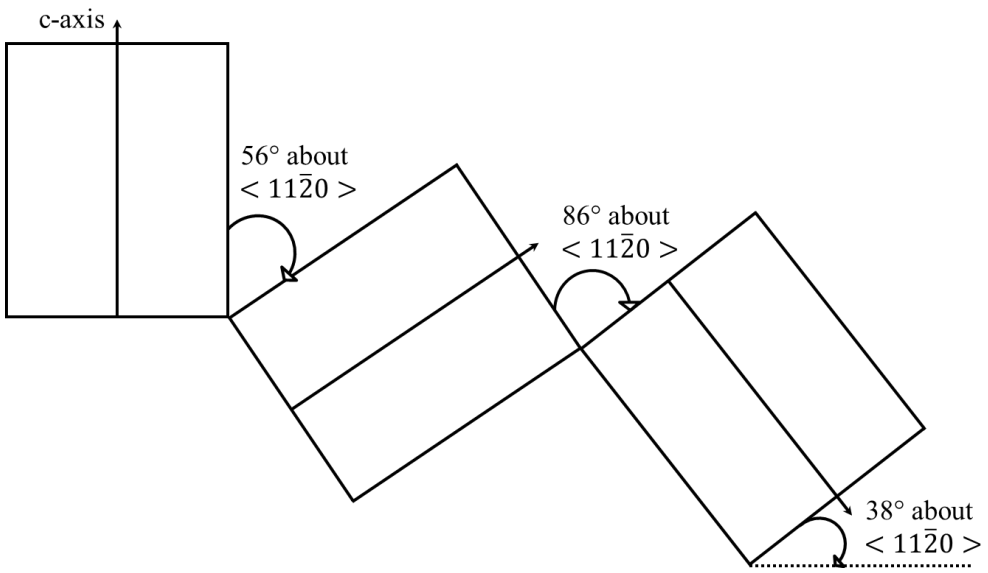

Figure 2.9 Schematic illustration of the $\{10\bar{1}1\} - \{10\bar{1}2\}$ double twin formation in Mg. The 56° misorientation about $< 11\bar{2}0 >$ formed due to the contraction twinning, the 86° misorientation about $< 11\bar{2}0 >$ formed due to the subsequent extension twinning, and the effective misorientation of 38° about $< 11\bar{2}0 >$ with respect to parent grain due to the double twinning event are indicated.

In addition, earlier studies have reported the activation of twinning systems, such as $\{30\bar{3}4\}$ and $\{11\bar{2}1\}$, in polycrystalline Mg alloys [Couling et al. 1956]. Compression bands related to twinning modes, such as $\{10\bar{1}1\}$ and $\{10\bar{1}5\}$, was suggested as an important deformation mechanism which determines the cold workability of polycrsyatlline Mg alloys [Omori 1979]. However, there has been some ambiguity in these earlier reports because twin types were determined and assigned mostly based on trace analysis of habit planes using optical microscopy. In addition, while there are many reports of twinning based shear band formation and fracture in single crystals, there is limited information about the same in Mg polycrystals in the literature.

Recent studies have reported the observation of a complex double twinning phenomenon in wrought Mg, and wrought alloys such as Mg-0.2Ce, AZ31, AZ61, AM30, ZK60, and ZM20 [Barnett et al. 2004, Nave et al. 2004, Jiang et al. 2006, Barnett 2007, Barnett et al. 2008, Ando et al. 2010, Ma et al. 2011, Ando et al. 2014, Martin et al. 2015, Niknejad et al. 2016]. Barnett suggested that $\{10\bar{1}1\} - \{10\bar{1}2\}$ double twinning might cause shear failure at low strain due to the combined effect of strain softening and localized twin-sized void formation [Barnett 2007]. The formation of large surface steps accompanied by narrow banded twins of type $\{10\bar{1}1\} - \{10\bar{1}2\}$ (with identical plane of shear) after tensile deformation were reported in rolled AZ31 [Koike et al. 2005, Ando et al. 2007, Ando et al. 2010]. This suggests localized deformation within the double twinned volume, which might assist in the nucleation of cracks. Thus, the premature failure of AZ31 at ambient temperature could be attributed to the formation of $\{10\bar{1}1\} - \{10\bar{1}2\}$ twins [Barnett, 2007, Ando et al. 2010]. Niknejad et al. [2016] observed the formation of transgranular cracks with orientations identical to the $\{10\bar{1}1\} - \{10\bar{1}2\}$ double twin habit planes in AZ61, and attributed this phenomenon to the shear localization within the double twin volume due to massive basal <a> slip activity leading to early transgranular crack/void initiation and subsequent fracture. The decreased elongation-to-failure which results in limited cold workability of Mg was in part attributed to this phenomenon.

There is ambiguity in the literature about the temperature dependence of twinning in Mg single crystals. It was reported that twins with a habit near $\{10\bar{1}3\}$ and $\{30\bar{3}4\}$ readily form at elevated temperatures [Reed-Hill et al. 1957]. In single crystals, it was reported that the CRSS for twinning decreases with an increase in temperature [Yoshinaga et al. 1963]. Wonsiewicz et al. [1967] reported that the twinning activity initially increased and then decreased with an increase in temperature in single crystals. However, there is an opposite trend observed in

polycrystals. In a recent study, it was observed that the $\{10\bar{1}1\} - \{10\bar{1}2\}$ twinning frequency decreased with an increase in temperature in extruded AM30 [Jiang et al. 2006]. However, the activity of slip mechanisms was not investigated in that study. In Mg single crystals, it was observed that pyramidal <c+a> slip was prevalent above 573K and the twinning activity decreased with an increase in temperature, and this was attributed to the decrease in CRSS values for non-basal slip at elevated temperatures [Yoshinaga et al. 1963, Obara et al. 1973]. Similarly in polycrystals, it can be expected that at elevated temperatures, the CRSS of pyramidal <c+a> slip would become lower than that of contraction twinning and the decreasing relative activity of contraction twinning might result in improved elongation-to-failure [Barnett 2007]. However, clear experimental evidence of this phenomenon is lacking. It can be inferred from the previous studies that $\{10\bar{1}1\} - \{10\bar{1}2\}$ double twinning is partly responsible for the catastrophic failure of polycrystalline Mg alloys at ambient temperatures. However, the effect of this phenomenon on the macroscopic behavior is not clear yet. In addition, a systematic study on the effect of temperature on the contribution of different slip and twinning mechanisms towards deformation is lacking in the literature.

2.5 Deformation behavior

The increase of deformation temperature is accompanied by a change of deformation mechanisms in Mg alloys [Rokhlin 2003]. In fact more slip systems are activated at elevated temperatures [Trojanova et al. 2005]. The experimentally measured and computationally calculated CRSS values of different deformation systems in Mg and Mg alloys, and their variation with respect to temperature is given in Figure 2.10. The experimental data given in Figure 2.10 is adapted from Reed-Hill et al. [1957], Flynn et al. [1961], Yoshinaga et al. [1963], Yoshinaga et al. [1964], Wonziewicz et al. [1967], Kelley et al. [1968], Obara et al. [1973], and

Chapuis et al. [2011] and the computationally calculated CRSS values are adapted from Barnett [2003]. As shown in Figure 2.10, the relative activity of prismatic <a> and pyramidal <c+a> slip systems typically increases at elevated temperatures in conventional Mg alloys. It is expected that at temperatures around 673K the CRSS of non-basal slip systems becomes closer to that of basal <a> slip, and this results in the improved formability of the material. Furthermore, the decrease in twinning activity was expected to be due to the lower CRSS values for the slip systems at elevated temperatures.

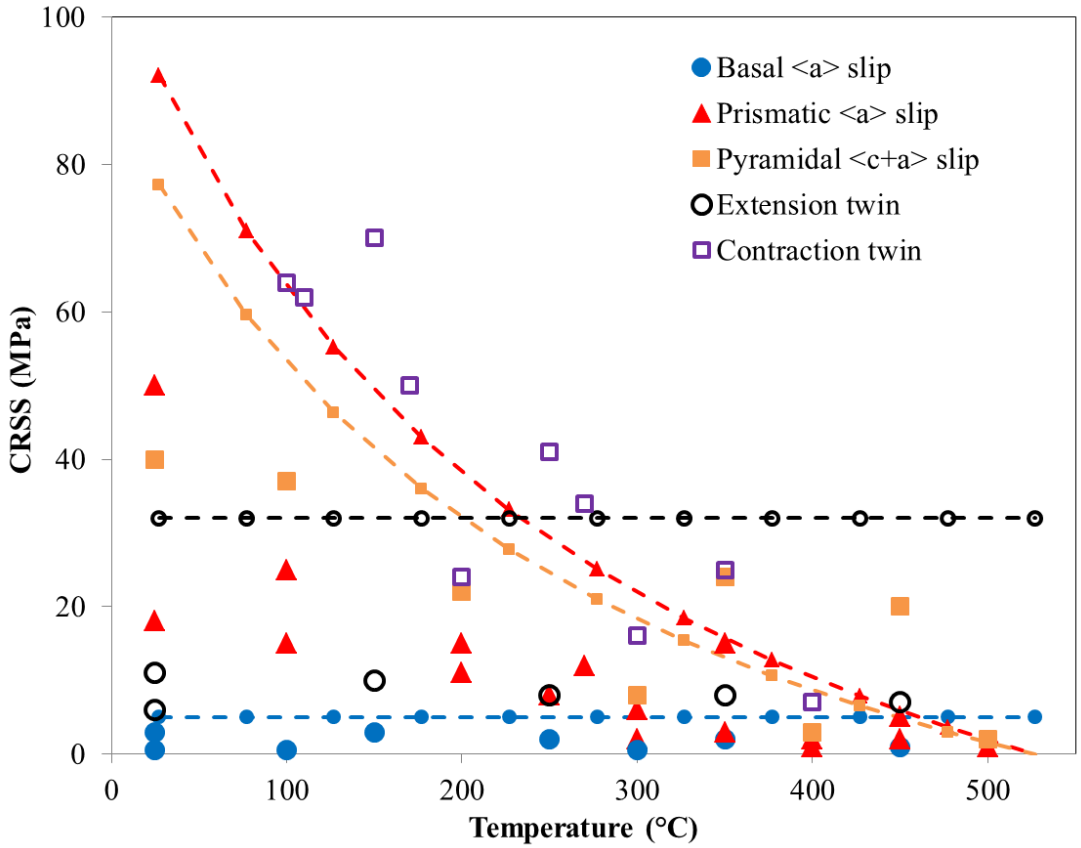

Figure 2.10 Experimentally observed variation in CRSS values of different deformation mechanisms with temperature in Mg and alloys adapted from Reed-Hill et al. [1957], Flynn et al. [1961], Yoshinaga et al. [1963], Yoshinaga et al. [1964], Wonziewicz et al. [1967], Kelley et al. [1968], Obara et al. [1973], and Chapuis et al. [2011]. The computationally calculated CRSS values (dotted lines) were adapted from Barnett [2003].

The limited cold formability of Mg and its alloys is partly attributed to its hexagonal crystallography and the associated lack of sufficient independent slip systems for uniform deformation [Yoo 1981]. However, as described in the previous section, additional mechanisms might also play a critical role in the limited ambient temperature elongation-to-failure of Mg alloys. For example, particular types of twinning-related mechanisms have been attributed to localized shear deformation which results in premature failure. In order to improve the cold formability of Mg alloys, it is critical to understand the underlying mechanisms that limit the ε_f. One of the effective ways to improve formability of Mg is to enhance the activity of non-basal slip. It has been reported that the activity of non-basal slip at low temperatures in Mg-RE alloys is enhanced, compared with conventional Mg alloys, because the CRSS of prismatic <a> and pyramidal <c+a> systems in Mg-RE alloys becomes closer to that of extension twinning and basal <a> slip [Chino et al. 2008a, Chino et al. 2008b, Mishra et al. 2008, Al-Samman et al. 2011, Robson et al. 2011]. The ambient temperature deformation of pure Mg and conventional Mg alloys are limited to mainly basal <a> slip and extension twinning, resulting in strain localization, shear banding, and premature failure of the material [Yoo 1981]. Due to their lower CRSS values compared to other deformation modes, basal <a> slip and extension twinning are the most easily activated deformation systems at ambient temperatures [Hutchinson et al. 2010, Chapuis et al. 2011]. It is generally reported in literature that the CRSS of basal <a> slip is lower than that of extension twinning. However, in a recent study, Ye et al. [2011], measured the CRSS values for extension twinning and basal <a> slip in pure Mg and Mg-0.2Ce using in-situ nano-compression experiments. It was observed that the CRSS of extension twinning was dramatically reduced by 0.2wt.% addition of Ce and the measured CRSS values for basal <a> slip and extension twinning was strikingly close [Ye et al. 2011].

It has been hypothesized that the changes in the CRSS of the various deformation systems might be attributed to the influence of RE solute elements on crystal structure features such as the lattice parameters, the stacking fault energy, and/or the width of the dislocation cores. In general, the mechanisms responsible for the activation of different deformation modes in Mg-RE alloys are not well understood. Specifically, the deformation mechanisms operative in Nd-containing alloys are still not clear, and an understanding of the effect of Nd on the tension and compression and tension-creep deformation behavior is lacking. Furthermore, no clear experimental evidence of the distribution of the deformation systems that are active under different testing conditions exists to date. Thus, there is a need to both quantify the relative activities of the different deformation modes present in Mg-RE alloys as a function of temperature and determine the relative CRSS values of the active slip systems. In this context, the different mechanisms proposed in the literature for the changes in slip and twinning activity in Mg alloys are reviewed in the following sections.

(a) Changes in lattice parameters

In materials with hexagonal structure, the c/a ratio affects the difference in CRSS values between basal and non-basal slip and a reduction in c/a ratio enhances the activity of non-basal slip [Yoo 1981]. In a recent study by Kim et al. [2012], the increase in CRSS values of basal <a> slip observed in Mg-nonRE binary alloys compared to pure Mg was attributed to the changes in lattice parameters. Studies showed that addition of Li, Y, La, Ce, Nd, Gd, and Ca (typically >0.5-1 at.%) increases the activity of non-basal slip and this was explained to be due to the decrease in c/a ratio in such alloys [Busk 1950, Hehmann et al. 1990, Agnew et al. 2011]. However, recent studies showed that c/a ratio was not altered by very small additions of Ce (Mg-0.2Ce) and Y (Mg-3Y) even though enhancement of non-basal slip was observed and it was

attributed to the changes in stacking fault energy (SFE) [Chino et al. 2008a, Chino et al. 2008b, Sandlobes et al. 2011].

(b) Changes in SFE

The first principle calculations by Datta et al. [2008] and Inoue et al. [2011] showed that the combination of high strength and large elongation observed in Mg-1Zn-2Y (at.%) alloy with sub-micron grain size, was due to the changes in SFE, which might have resulted in the increased activity of non-basal slip. Recent atomistic studies by Pei et al. [2013], showed that the generalized SFEs of slip systems in Mg were altered by Y additions. Sandlobes et al. [2011, 2012], attributed the increased ductility of Mg-Y binary alloys to the increased activity of non-basal slip due to the changes in SFEs. They also showed that neither grain refinement, precipitation hardening, shear banding, decreased c/a ratio, nor changed Peierls potentials can be responsible for higher activity of non-basal slip in Mg-Y binary alloys.

(c) Changes in grain size

Koike et al. [2003], attributed the enhanced activity of non-basal slip observed in a conventional alloy, AZ31, to grain-boundary compatibility stresses due to grain size reduction. However, it was observed that grain refinement was not responsible for the enhanced activity of non-basal deformation modes in Mg-3Y [Sandlobes et al. 2011]. Meyers et al. [2001], showed that twinning activity becomes difficult with decrease in grain size in HCP metals such as Ti and the grain size impacts twinning more than it does slip. A similar tendency of an increase in twinning activity with an increase in grain size has been observed in other HCP metals such as Zn [Ecob et al. 1983]. It is hypothesized the same would be true in Mg alloys. Barnett [2008], suggested that the number density of twins and the twin volume increases markedly with grain

size. An increase in twin volume fraction with increasing grain size was observed in AZ31 sheets during tensile deformation [Jain et al. 2008]. It was observed that a transition from twinning to slip dominated deformation occurs with decreasing grain size and/or increasing temperature in extruded AZ31 during compression deformation [Barnett et al. 2004]. However, systematic studies on the effect of grain size on the relative activity of different deformation modes in Mg-RE alloys are lacking in the literature. In the studies mentioned above, the grain size values for the wrought alloys were in the range ~5-75μm. It is noted that, the extruded materials studied in this work exhibited a similar grain size (~10-42μm) and the as-cast materials exhibited significantly higher values (~361-970μm).

It is important to note that most of the studies mentioned in this chapter were performed ex-situ. By using in-situ studies it is possible to accurately identify the activity of different deformation modes in a given microstructure as a function of strain and temperature. RE-containing Mg alloys has not been investigated extensively using in-situ studies until this work. In addition, through in-situ studies on polycrystalline microstructures, one can now estimate the CRSS values as developed by Li et al. [2013a, 2013b], and a similar methodology was used in this study. The estimated CRSS values can be used as inputs for crystal plasticity modeling and simulation of microstructural patches so one can predict optimal microstructures for certain applications and check if such microstructures can be processed efficiently. This is the holy grail of physical metallurgy, and I hope that someone can do this as a continuation of this dissertation work.

CHAPTER 3

EXPERIMENTAL PROCEDURES

3.1 Material

The materials studied in this dissertation were processed at the Magnesium Innovation Center (MagIC) in Geesthacht, Germany. The bulk chemical compositions of the as-cast and extruded M1, MN10, and MN11 alloys (named according to the ASTM standards, 'Standard Practice for Codification of Unalloyed Magnesium and Magnesium-Alloys, Cast and Wrought' 2011) were measured using spark emission spectroscopy at MagIC. Table 3.1 lists the chemical composition of all the materials studied.

The M1, MN10, and MN11 alloys were gravity cast to produce billets of either 125 or 150 mm diameter. The billets were then machined to a diameter of 93 mm and then homogenized at 623K for 15 hours prior to extrusion. Indirect extrusion was carried out at 573K and/or 548K to produce round bars of 17 mm diameter, which corresponds to an extrusion ratio of 1:30. The extrusion rate was 5.6 mm/s which corresponded to a profile exit speed of 10 m/min. Figure 3.1 show images representative of the as-cast and extruded rods. The MN11 alloys extruded at 573K and 548K are referred as MN11-300 and MN11-275, respectively.

Table 3.1 Chemical composition of the materials studied (in weight percent).

Material	Mg	Mn	Nd
Extruded M1	Balance	0.99	x
Extruded MN10	Balance	1.12	0.26
Extruded MN11-300	Balance	0.95	0.94
Extruded MN11-275	Balance	1	1
Cast MN10	Balance	0.97	0.40
Cast MN11	Balance	0.89	0.77

3.2 Microstructural characterization

3.2.1 Metallography preparation

The samples were mechanically polished using silicon carbide (SiC) planar grinding papers through 800, 1200, 2400, and 4000 grits (FEPA - Federation of European Producers of Abrasives standard) sequentially. Water was used for lubrication as well as rinsing the specimen before moving to the next grinding step. Each of these polishing steps lasted 30 seconds to 1 minute. The specimens were then polished through 6µm, 3µm, and 1µm diamond paste sequentially. Each of these polishing steps lasted 5 to 10 minutes. Ethanol was used both as a lubricant and as a cleanser for the specimen during this step. Colloidal silica solution, with a 0.04µm particle size (Struers OP-S colloidal silica solution catalog No. 40700000), was used for the final mechanical polishing step. This step lasted 5 to 15 minutes. To remove the residual colloidal silica after this step, the specimen was rinsed immediately under running water, gently wiped with a finger or a cotton swab moistened with dish washing soap, quickly rinsed and sprayed with ethanol, and blow dried with warm air by keeping the sample ~2 feet from a hair dryer. The entire cleaning process after the colloidal silica step lasted less than 5 seconds. The grinding papers, polishing cloths, and diamond paste were purchased from MetLab, Buehler, or Struers. The samples were then chemically polished using a mixture of 100ml methanol, 12ml hydrochloric acid, and 8ml nitric acid, and the sample surface was etched using a solution containing 60ml ethanol, 20ml water, 15ml acetic acid, and 5ml nitric acid. Each of the chemical polishing and etching steps typically lasted less than 5 seconds. Ethanol was used to rinse the specimen after the chemical polishing and etching. The specimen was then blow dried with warm air by keeping the sample ~2 feet from a hair dryer.

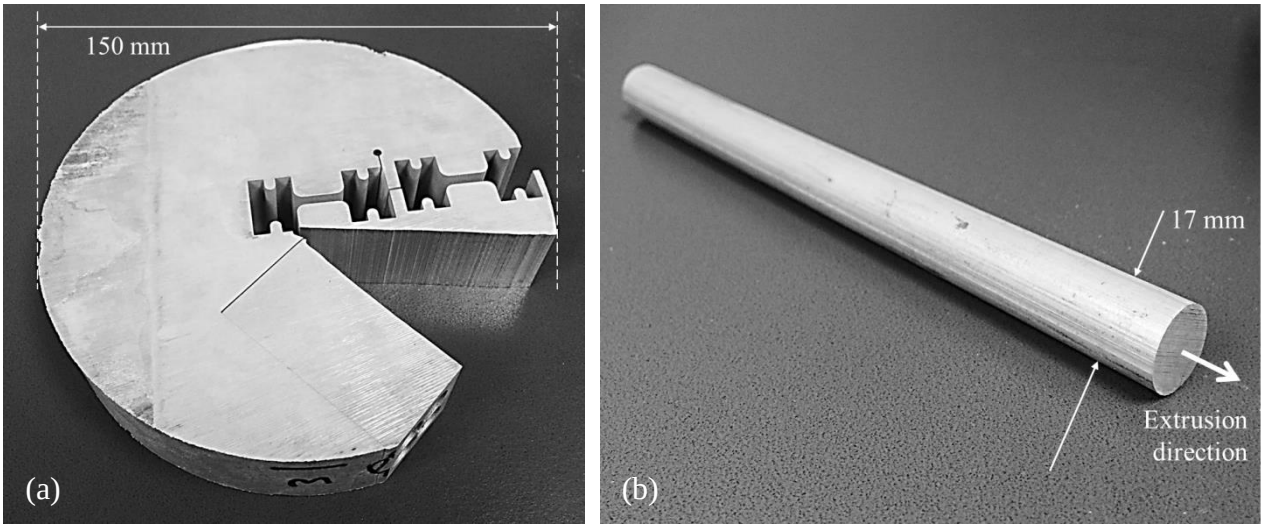

Figure 3.1 Photograph of the (a) MN10 as-cast material and (b) M1 extruded rod. Note that some material from the as-cast billet in (a) was removed for testing purposes.

3.2.2 Scanning electron microscopy

The microstructures of the different alloys investigated in this study were examined using scanning electron microscopy (SEM), primarily using secondary electron (SE) imaging. The electron beam voltage used was 25kV. The SEMs used in this dissertation work included a field emission gun Camscan 44FE SEM and a field emission gun Tescan Mira3 SEM. The Camscan 44FE SEM is located in room 3507A and the Tescan Mira3 SEM is located in room 1130 of the engineering building at Michigan State University (East Lansing, MI). The volume fraction of the second phase particles in the alloys studied were measured using ImageJ software on several SE SEM images of the microstructure. The software was used to shade the pixels that show a brightness value within a set range. Thus, due to the contrast difference, different phases in the SE SEM images were represented by pixels with different brightness. The fraction of the pixels corresponding to one phase, among the total number of pixels, was used to represent the phase volume fraction.

3.2.3 Electron backscatter diffraction

Electron backscatter diffraction (EBSD) orientation maps were acquired from the gage section of the specimens before and after deformation. Prior to deformation, the samples were polished to a mirror finish following the procedures described in Section 3.2.1. An EDAX-TSL (Mahwah, NJ) EBSD system, attached to the SEMs mentioned in Section 3.2.2, was used for this dissertation work. The specimens were tilted to 70 degrees from horizontal. For the Camscan 44FE SEM, EBSD was performed using a 25kV electron beam and a working distance of 33mm. For the Tescan Mira3 SEM, the same voltage was used, but, the working distance was in the range 15-19mm. For the extruded materials, which exhibited a relatively fine average grain size (ranging between ~10-45μm), a step size in the range of 0.75-1.75μm was used for the specimens prior to the deformation. A step size in the range of 0.6-1.5μm was used for the specimens after the deformation. A 2x2 binning was used for the undeformed specimens and a 1x1 binning setting was used for the deformed specimens. For the fine twins observed in the extruded M1 specimens after deformation, the orientation maps were obtained using a step size of 0.05-0.25μm. In the case of the as-cast materials, which exhibited a relatively large average grain size (ranging between ~350-1000μm), a step size of 5μm with a 4x4 binning setting was used for the undeformed specimens and a 3μm step size with either a 4x4 or a 2x2 binning setting was used for the deformed specimens. The data acquisition speed for the Camscan SEM EBSD system was 15-20 points per second, and 25-35 points per second for the Tescan SEM EBSD system.

After acquiring the EBSD "raw" data, post-processing "clean-up" procedures were performed to remove erroneous data points formed due to un-indexed or inappropriately indexed patterns. "Neighbor CI (Confidence Index) Correlation" and "Grain Dilation" were the two

clean-up procedures used in this study. "Neighbor CI Correlation" was accomplished by replacing the orientation of the erroneous data point with the orientation of the neighboring point that had the highest CI value. The erroneous data point was defined as a point with a CI value below a user defined threshold, usually kept between 0.01-0.05. A minimum grain size (in terms of pixels; usually between 2-5 pixels) was used to perform the "Grain Dilation". Using this procedure, any grouping of less than 2-5 pixels with a misorientation greater than 5 degrees was considered to be insufficient to be defined as a single grain. The orientations of these points were re-assigned to match the adjacent grain orientation. In some cases, multiple iterations of the clean-up procedures were performed. It is noted that the input parameters for the clean-up procedures were selected based on the overall average CI value of the raw data in an effort to minimize the number of points modified.

The EBSD data collection was performed using EDAX TSL OIM Data Collection software (Mahwah, NJ), and the crystallographic texture measurements as well as other analysis were performed using EDAX TSL OIM Analysis 6.1 software (Mahwah, NJ). For texture measurements, the EBSD data were partitioned with a grain tolerance angle of 5 degrees and a minimum grain size of 10-20 pixels. It is noted that the texture of the as-cast materials were obtained from the orientation maps acquired using the "Stage Control" mode in which a step size of 10-15μm was used. In all other cases, the "Beam Control" mode was used for data collection. The average grain size was calculated from the EBSD maps using the appropriate functions given in the EDAX TSL OIM Analysis software (Mahwah, NJ), which gives the grain diameter and/or ASTM grain number as output. The methodology used for the grain size measurement can be found in Vander Voort [1999]. The grain size was measured from coarse-step (typically 1-2μm) EBSD scans and can be expected to slightly overestimate the grain size [Barnett et al.

2004]. However, it is noted that the average grain size measured using the line-intercept method [ASTM E112-13, Standard Test Methods for Determining Average Grain Size, ASTM International, West Conshohocken, PA, 2013] on SE SEM images yielded similar values.

3.2.4 Transmission electron microscopy

Transmission electron microscopy (TEM) analysis was performed using either a JEOL JEM 3000F operated at 300kV or a JEOL JEM 2100HT operated at 200kV. Both TEMs were located at the Spanish National Centre for Electron Microscopy (ICTS) at Complutense University, Madrid, Spain. The TEM foils were prepared by polishing the samples to a thickness between 60-200μm, and then electro-polishing using a Struers TenuPol-5 double jet system and a solution of 4% Perchloric acid and 96% Ethanol as an electrolyte. The electrolyte temperature was kept below 248K. A flow rate of ~15 and a voltage of ~12V, which corresponds to a current of ~12mA, were used. Some samples were further thinned using a Gatan PIPS Ion Polishing system at 4.5-5.0keV at an incident angle of ~8 degrees with a rotation speed of ~3 rpm at RT. The electropolishing unit is located at Michigan State University and the ion polishing system is located at ICTS, Complutense University, Madrid, Spain.

3.2.5 Energy dispersive spectroscopy

Energy Dispersive Spectroscopy (EDS) analysis was performed using an OXFORD INCA XEDS microanalysis system attached to either of the TEMs mentioned in Section 3.2.4. It is noted that the EDS analysis was semi-quantitative in nature. Accurate identification of the chemical composition of the second phase particles is challenging with EDS as the results are dependent on the beam size and the size of the particles. In some cases the spectroscopic data may come from the second-phase particles as well as the primary phase. Without an accurate

knowledge of the size of the second phase particles and the thickness of the TEM samples, it is extremely difficult to draw accurate quantitative measurements from the EDS results. In this study, the data obtained from EDS was considered to be semi-quantitative.

3.3 In-situ mechanical testing

3.3.1 Sample configuration

Flat dog-bone test samples with a 3mm gage width and 10mm gage length were electro-discharge machined (EDM) for in-situ testing inside a SEM. Figure 3.2 shows a photograph of an EDM cut specimen. The specimens were then polished using the method described in Section 3.2.1. The specimen thickness after polishing was ~2mm. In the case of the extruded materials, the specimens were EDM cut such that the testing axis was parallel to the extrusion direction. Table 3.2 lists the testing conditions of the specimens investigated in this study.

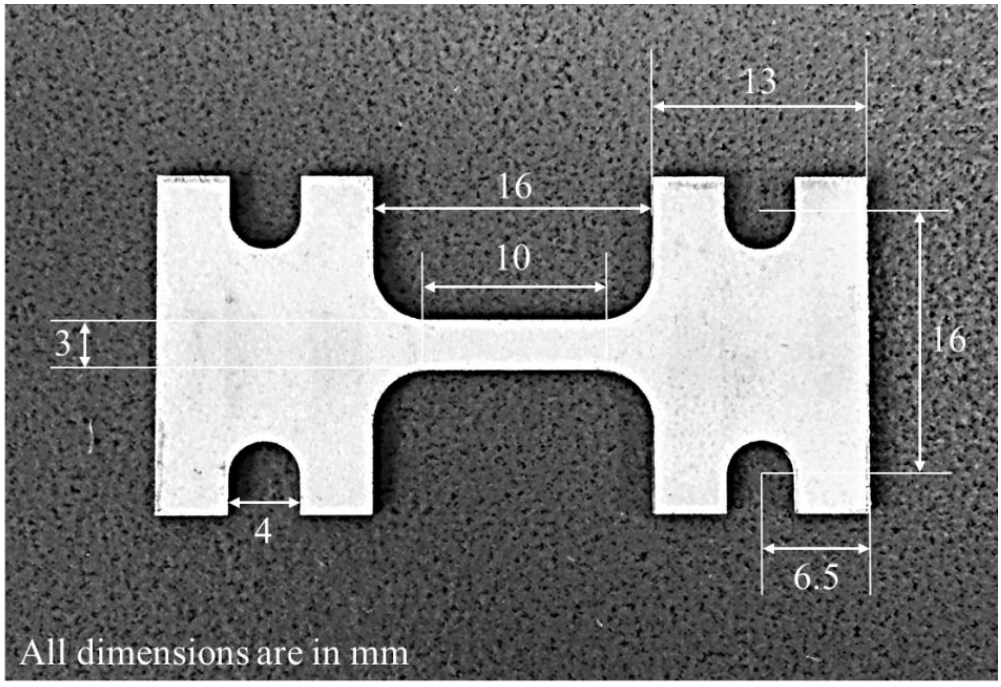

Figure 3.2 Photograph of an EDM cut test specimen representative of those used for the tension and compression experiments. The sample dimensions are indicated.

3.3.2 In-situ tension and compression testing

The in-situ SEM testing methodology allows for the capture of the deformation evolution on the specimen surface during the tension and compression experiments. A screw-driven tensile/compression stage built by Ernest F. Fullam, Inc. (originally located in Lantham, NY and later acquired by MTI Instruments, Albany, NY) was placed inside a Tescan Mira3 SEM. Figure 3.3 shows a photograph of the stage placed inside the Tescan Mira3 SEM.

In-situ tensile and/or compression tests were performed on the extruded M1, as-cast MN10, extruded MN10, as-cast MN11, and extruded MN11-275 and MN11-300 specimens at 298/323K, 423K, and 523K with a constant crosshead displacement rate of 0.004mm/s (corresponding to an approximate strain rate of $10^{-3}s^{-1}$) (See table 3.2). The displacement, time, and load data were recorded during the tests using the MTESTW version F 8.8e data acquisition and control software (Admet, Inc., Norwood, MA). SE SEM images were taken before loading and during interruptions at different displacements throughout the experiments. The tests were paused for 5-10 minutes while the images were acquired. During this pause, some stress relaxation of the specimen occurred. After imaging, the deformation was continued at the same displacement rate. The test temperature was controlled using a constant-voltage power supply to a 6mm diameter tungsten-based heating element placed just below the gage section, which radiantly heated the sample during the test. The temperature was monitored using a fine-gage K-type thermocouple spot-welded to the side of the gage section, and the temperature was maintained at ±5 degrees of the desired temperature during the experiments. The vacuum inside the SEM chamber was maintained below $2x10^{-6}$ Torr throughout the experiments.

Table 3.2 Testing conditions of the investigated specimens.

Material	Test mode	Temperature	Number of tests
M1 extruded	Tension	323K	1
M1 extruded	Tension	423K	1
M1 extruded	Tension	523K	1
MN10 cast	Tension	323K	1
MN10 cast	Tension	423K	1
MN10 cast	Tension	523K	1
MN10 extruded	Tension	323K	3
MN10 extruded	Tension	423K	2
MN10 extruded	Tension	523K	2
MN10 extruded	Compression	323K	1
MN10 extruded	Compression	423K	1
MN10 extruded	Compression	523K	1
MN11 cast	Tension	323K	1
MN11 cast	Tension	423K	1
MN11 cast	Tension	523K	1
MN11-300 extruded	Tension	323K	1
MN11-300 extruded	Tension	423K	1
MN11-300 extruded	Tension	523K	1
MN11-300 extruded	Compression	298K	2
MN11-300 extruded	Compression	423K	1
MN11-300 extruded	Compression	523K	1
MN11-275 extruded	Tension	323K	2
MN11-275 extruded	Tension	423K	3
MN11-275 extruded	Tension	523K	3

In this study, the tensile and compression data are reported in the form of engineering stress versus displacement plots. Using this testing technique, the instantaneous cross-sectional area of the sample was not measured. Instead the surface deformation is characterized through SEM imaging and using these images the local displacements along the loading direction are measured. It is noted that the displacement data collected by the MTESTW software included the deformation in the gage section as well as the grip sections. Thus, the total strain calculated using the software displacement data and the specimen gage length did not represent the actual strain of the areas monitored during the in-situ test. This displacement divided by the gage length tended to overestimate the strain achieved by the gage section alone, especially at the

elevated temperatures. Thus, the local strains, indicated in the stress vs displacement curves depicted in this work, were estimated by measuring the relative displacements of obvious microstructural features, such as second phase particles, on the SE SEM images acquired before, during, and after deformation. Therefore, the strain values reported are local strains unless otherwise specified. Some of the specimens were taken to failure, while some were not taken to failure in order to facilitate EBSD orientation mapping after deformation without further sample preparation. It is noted that the deterioration of the sample surface due to deformation (up to ~15% strain) did not significantly affect the EBSD Kikuchi pattern collection.

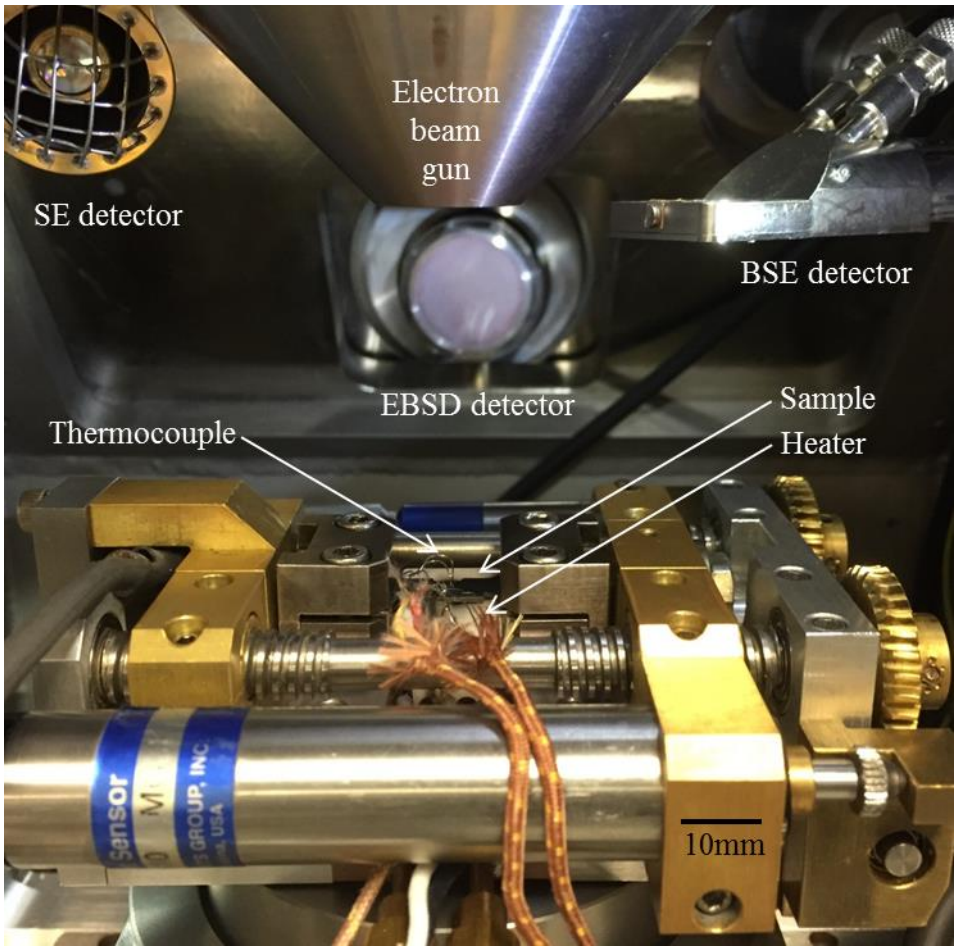

Figure 3.3 Photograph of the testing stage placed inside the Tescan Mira3 SEM chamber.

3.4 Slip/twin trace analysis and Schmid factor calculation

The active slip and twinning systems were identified using the EBSD data and the SE SEM images acquired during the tensile/compression experiments. Slip/twin-trace analysis was performed by inputting the Euler angles obtained from the EBSD orientation measurements from a grain and all possible slip/twin systems into a Matlab™ code that provided a visual representation of all the possible plane traces as output. The plane trace of each system on the sample surface was obtained by the cross product of the slip/twin plane and the grain surface normal. The Schmid factor values for the different deformation systems in each grain of interest were calculated based on the EBSD-determined orientation and the assumption of a uniaxial tension or compression stress state. A brief description of the methodology used for the slip/twin trace analysis and Schmid factor calculation is given in Appendix A.

Table 3.3 lists the slip and twin systems considered in this study. There are 3 basal <a> slip, 3 prismatic <a> slip, 6 pyramidal <c+a> slip, 6 extension twinning, and contraction twinning systems. The slip systems are numbered from 1-3, 4-6, and 7-12, respectively, for basal <a>, prismatic <a>, and pyramidal <c+a> slip systems, in the Matlab™ code (See Appendix B).

Table 3.3 The list of slip and twin systems in Mg considered for the trace analysis.

Deformation mode	Slip/twin system	Number of variants
Basal <a> slip	$\{0001\} < 11\bar{2}0 >$	3
Prismatic <a> slip	$\{10\bar{1}0\} < 11\bar{2}0 >$	3
Pyramidal <c+a> slip	$\{11\bar{2}2\} < 11\bar{2}3 >$	6
Extension twinning	$\{10\bar{1}2\} < 10\bar{1}1 >$	6
Contraction twinning	$\{10\bar{1}1\} < 10\bar{1}2 >$	6

Both slip and twinning events were identified using this trace analysis methodology. The experimentally-observed deformation systems in a given grain were identified by comparing the calculated plane traces with the slip/twin plane traces observed in the SE SEM images. It is noted that the experimentally-observed traces were always within 0-3 degrees of the chosen simulated plane trace of the corresponding deformation system. Because there are three different slip directions on the basal <a> plane (along three <a> directions), the slip direction cannot be unambiguously determined by trace analysis, so the slip system with the highest Schmid factor was assumed to be the active system when basal <a> slip trace was observed. It is noted that the Schmid factor values in this dissertation were calculated based on a uniaxial global stress state. Therefore, the Schmid factor values presented in this study refer to global Schmid factors.

Figure 3.4 illustrates an example of the slip trace analysis methodology used in this study. Figure 3.4a-d shows a 523K tensile deformed microstructural patch of an extruded MN10 specimen with 0%, ~6.8%, ~16.8, and ~27.4% strain, respectively. The grain of interest is highlighted as "A" in Figure 3.4a. In Figure 3.4e, the crystallographic orientation of the grain of interest is highlighted by the HCP unit cell in the EBSD IPF map in the normal direction. Figure 3.4f shows the slip traces of the 12 possible slip systems calculated by inputting the orientation angles acquired by EBSD into the Matlab^{TM} code (See Appendix B). Comparing the calculated sip traces with the experimentally-observed slip bands, it is clear that the calculated basal <a> slip traces (number 1, 2, and 3) matches with the observed slip bands. Figure 3.4g lists the Schmid factors of the three basal <a> slip systems, along with other slip systems. Slip number 3, $(0001)[\bar{1}\bar{1}20]$, was chosen to be the active slip system for this particular grain as it exhibited the highest Schmid factor (0.44) among all the three basal <a> slip variants. The Matlab^{TM} code used to calculate the possible slip plane traces shown in Figure 3.4f is given in Appendix B.

Twin trace analysis was performed using the same methodology. The twins identified using this approach were confirmed by comparing the EBSD-measured twin orientation with their parent orientation, as each type of twin has a unique misorientation angle and rotation axis with respect to the parent orientation. It is noted that some of the extension twins identified in this study exhibited negative values for Schmid factor. This is due to the polar nature of the twinning mechanism. For example, extension twinning is active only when the deformation conditions are such that extension along the c-axis takes place [Christian 1995]. Thus, negative Schmid factor values for extension twinning are obtained when the global stress state would favor "compression" along the c-axis for extension twinning systems.

It is noted that if a given grain displays activation of multiple slip/twin systems, this will result in multiple entries/counts in the total number of activated deformation systems. In the case of slip, if a given grain exhibits a set of parallel slip lines, such as the slip lines shown in Figure 3.4, this will be considered as one activated deformation system.

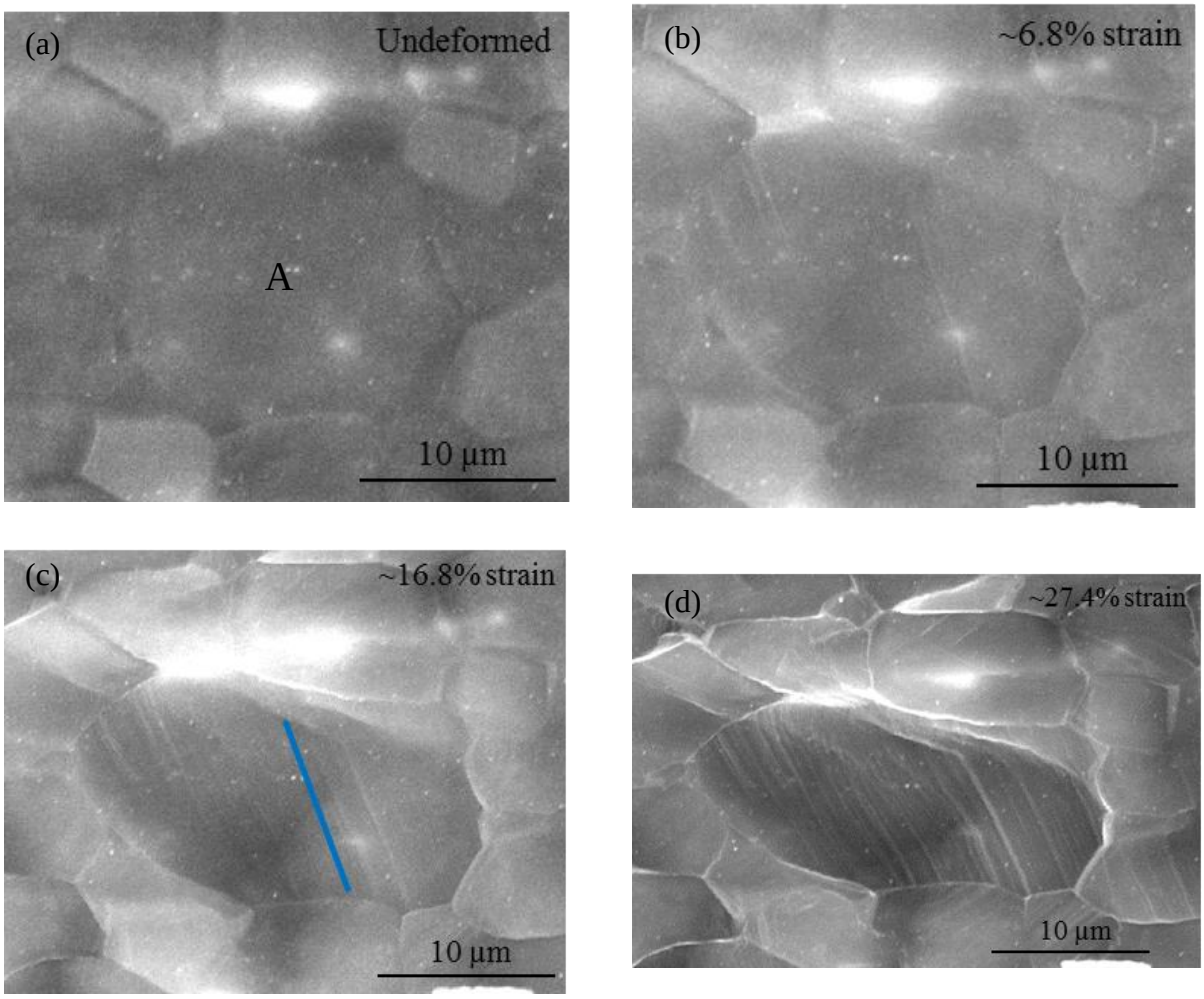

Figure 3.4 Example of slip trace analysis performed on the grain indicated as "A" in (a). The sequential SE SEM images taken during the 523K tensile experiment on extruded MN10 is given in (a) to (d), and the approximate strain values at which the images were taken are indicated in the images. The blue line in (c) indicate the experimentally observed slip band direction. (e) The EBSD IPF map in the normal direction for grain "A" with the HCP unit cell showing the grain orientation. (f) The calculated slip traces for the 12 possible slip systems. Note that only basal <a> slip systems (slip system numbers 1-3) matched the experimentally observed slip traces. (g) Tabulated slip system chart showing the Schmid factors for all the possible 12 slip systems. The basal <a> slip system number 3, $(0001)[\bar{1}\bar{1}20]$, highlighted as bold in (g), was determined to be the active slip system with a Schmid factor of 0.44.

Figure 3.4 (cont'd)

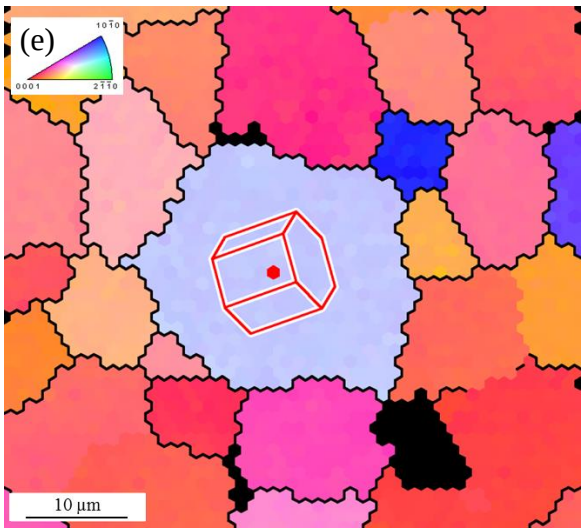

(f)

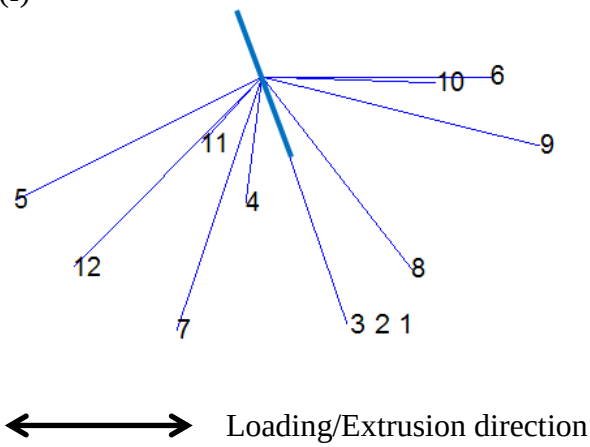

(g)

Slip system number	Slip system type	Slip system	Schmid factor
1	Basal <a>	$(0001)[\bar{2}110]$	0.21
2	Basal <a>	$(0001)[\bar{1}2\bar{1}0]$	0.22
3	**Basal <a>**	$(\mathbf{0001})[\mathbf{\bar{1}\bar{1}20}]$	**0.44**
4	Prismatic <a>	$(01\bar{1}0)[2\bar{1}\bar{1}0]$	0.11
5	Prismatic <a>	$(10\bar{1}0)[1\bar{2}10]$	0.11
6	Prismatic <a>	$(\bar{1}100)[11\bar{2}0]$	0
7	Pyramidal <c+a>	$(11\bar{2}\bar{2})[\bar{1}\bar{1}23]$	0.41
8	Pyramidal <c+a>	$(\bar{1}2\bar{1}2)[1\bar{2}13]$	0.40
9	Pyramidal <c+a>	$(\bar{2}112)[2\bar{1}\bar{1}3]$	0.21
10	Pyramidal <c+a>	$(\bar{1}\bar{1}22)[11\bar{2}3]$	0.02
11	Pyramidal <c+a>	$(1\bar{2}12)[\bar{1}2\bar{1}3]$	0.20
12	Pyramidal <c+a>	$(2\bar{1}\bar{1}2)[\bar{2}113]$	0.40

The observed slip traces were a result of dislocation motion. A limitation of the in-situ SEM testing methodology is that only the surface behavior, which is likely to have somewhat different stress constraints than the bulk microstructure, is characterized. It is noted that the slip trace analysis technique used in this work only identifies slip activity indirectly through the observation of surface slip traces. This approach has the possibility to miss the observation of some deformation systems. For example, slip systems with Burgers vectors parallel to the

sample surface will not develop observable traces. Also, diffuse slip will not lead to well-defined slip traces. Furthermore, the deformation systems observed at the surface may not reflect the subsurface activity, as the nature of constraints is different, which may affect the activation of different deformation systems. In addition, slip bands will not develop if the magnitude of slip is small. It is therefore likely that not all of the slip traces exhibited by the deformed specimens were observed, especially when one considers the amount of strain achieved by the samples. Therefore, the activation of some of the deformation systems may not have been detected.

3.5 CRSS ratio estimation

The CRSS ratios of the different deformation modes were estimated using a methodology described by Li et al. [2013a, 2013b]. A brief description of the methodology is given in this section. A least squares optimization procedure was utilized to minimize the difference between the experimentally-observed deformation systems' distributions obtained from the slip/twin trace analysis and the expected deformation systems' distributions, which accounted for the texture from all of the grains in the microstructural patch analyzed. In order to accomplish this, first the experimentally-observed deformation modes (basal <a> slip, prismatic <a> slip, pyramidal <c+a> slip, and extension twinning) in all grains from the analyzed microstructural patch were binned based on Schmid factor increments of 0.05. All possible deformation systems were predicted based on the orientation distribution of all grains in the same microstructural patch (accounting for texture), regardless of whether or not the deformation system was activated. For each grain, there are 18 possible deformation systems, including 3 basal <a> slip, 3 prismatic <a> slip, 6 pyramidal <c+a> slip, and 6 extension twinning systems. The Schmid factor values for all the possible deformation systems were calculated based on an uniaxial stress state

assumption and this distribution was also binned based on Schmid factor increments of 0.05. An optimization methodology, which uses a least-square minimization technique, was used to minimize the difference between the experimentally-observed and the predicted number of observations of the different deformation modes. The statistical resampling technique of bootstrapping was used to generate multiple equivalent datasets from which mean CRSS ratios of the different deformation systems with respect to basal <a> slip were estimated. With statistical analysis, the confidence intervals of the estimated CRSS ratios were deduced. It is noted that the CRSS ratio analysis was only performed on the extruded MN11-300 and MN11-275 specimens tensile deformed at 323K. This was because there were the most trace observations for each of the deformation modes (42 and 55 observations in MN11-300 and MN11-275, respectively). For the other materials, there were an insufficient number of traces observed to obtain statistically significant CRSS ratios.

3.6 Crystal plasticity modeling and simulation

In order to more thoroughly understand the deformation behavior of the contraction twins and the $\{\mathbf{10\bar{1}1}\}-\{\mathbf{10\bar{1}2}\}$ double twins observed during the experiments, crystal plasticity simulations of these twins were performed using the model described in this section. A material point model following the finite strain framework developed by Roters et al. [Roters, 2010], DAMASK, was used to model the deformation response of the microstructures generated. The deformation gradient $\boldsymbol{F}$ at each material point is decomposed into elastic $\boldsymbol{F_e}$ and plastic $\boldsymbol{F_p}$ components. The constitutive model used for the study is similar to phenomenological description of Peirce et al. [Peirce 1982] for cubic crystals. The state variables in this constitutive model are slip resistance $\boldsymbol{\tau_{cr}^{\beta}}$ on each slip systems, which evolves with shear $\boldsymbol{\gamma^{\xi}}$ according to relationship given by Hutchinson [Hutchinson 1976].

$$\boldsymbol{\tau_{cr}^{\xi}} = q_{\xi\beta}\left[h_0\left(1-\frac{\boldsymbol{\tau_{cr}^{\beta}}}{\tau_s}\right)^a\right]|\dot{\gamma^{\beta}}| \tag{1}$$

The slip system interactions are controlled by the hardening matrix $\boldsymbol{q_{\xi\beta}}$. With the above defined slip resistance, the shear on each system is given by

$$\boldsymbol{\dot{\gamma}^{\xi}} = \boldsymbol{\dot{\gamma}_0}\left|\frac{\boldsymbol{\tau^{\xi}}}{\boldsymbol{\tau_{cr}^{\xi}}}\right|^{\frac{\mathbf{1}}{\boldsymbol{m}}}\boldsymbol{sign}(\boldsymbol{\tau^{\xi}}) \tag{2}$$

where, $\boldsymbol{\dot{\gamma}_0}$ is the reference shear rate, $\frac{\mathbf{1}}{\boldsymbol{m}}$ the stress exponent, and $\boldsymbol{\tau^{\xi}} = s^{\xi} \otimes n^{\xi}$ the resolved shear stress. The sum of shear on all slip systems generates the plastic velocity gradient

$$\boldsymbol{L_p} \coloneqq \boldsymbol{\dot{F}_p F_p^{-1}} = \sum_{\boldsymbol{\xi=1}}^{\boldsymbol{N}} \boldsymbol{\dot{\gamma}^{\xi}}\, \boldsymbol{s^{\xi}} \otimes \boldsymbol{n^{\xi}} \tag{3}$$

where, $\boldsymbol{s^{\xi}}$ and $\boldsymbol{n^{\xi}}$ are unit slip direction and slip normal vectors, respectively.

A Fast Fourier Transform based solver along with the material point model, DAMASK developed by Eisenlohr et al. [Eisenlohr, 2013] was used as a boundary value solver. Periodic representative volume elements of the generated microstructures were discretized by 42x64x42 voxels. Boundary conditions for simulating uniaxial tensions along x-direction are,

$$\frac{\dot{\bar{F}}}{10^{-3}s^{-1}} = \begin{bmatrix} * & 0 & 0 \\ 0 & 1 & 0 \\ 0 & 0 & * \end{bmatrix} and\ \frac{\bar{P}}{Pa} = \begin{bmatrix} 0 & * & * \\ * & * & * \\ * & * & 0 \end{bmatrix} \tag{4}$$

This loadcase is then applied for 50s resulting in an average deformation gradient, $\boldsymbol{\bar{F}}$ of 1.05 discretized into 50 increments. The CRSS values for different slip systems were adapted from [Agnew et al. 2006].

3.7 In-situ annealing/recrystallization

The Mg-2Zn-0.2Ce and Mg-2Zn-0.6Ce rolled sheets used for the in-situ annealing/recrystallization experiments were processed and provided by Dr. Jan Bohlen from MagIC, Geesthacht, Germany. At this moment, the measured alloy composition and the parameters used for the hot rolling process are not provided by MagIC. Flat rectangular samples with ~10mm width and ~15mm length were cut from the as-rolled sheets using a diamond saw. The thickness of the as-received rolled sheets was ~1mm. The specimens were then mechanically polished using the methodology described in Section 3.2.1. To further improve the quality of the sample surface for EBSD, some specimens were electropolished using a Struers TenuPol-5 double jet system and a solution of 30% Nitric acid and 70% Methanol as an electrolyte. More details of the electropolishing methodology can be found in Section 3.2.4.

Figure 3.5 shows the experimental setup developed for the in-situ annealing/recrystallization experiments. To build the heating stage shown in Figure 3.5, the heating element and the cooling system from the in-situ mechanical testing stage (See Section 3.3.2) was detached and then mechanically fixed on a custom made metallic fixture. The metallic fixture was then mechanically attached to a Tescan Mira3 SEM (See Section 3.2.2) stage. The sample was placed directly on top of the heater and secured using copper tape. To monitor the temperature, a fine-gage K-type thermocouple was spot-welded to the surface of the specimen.

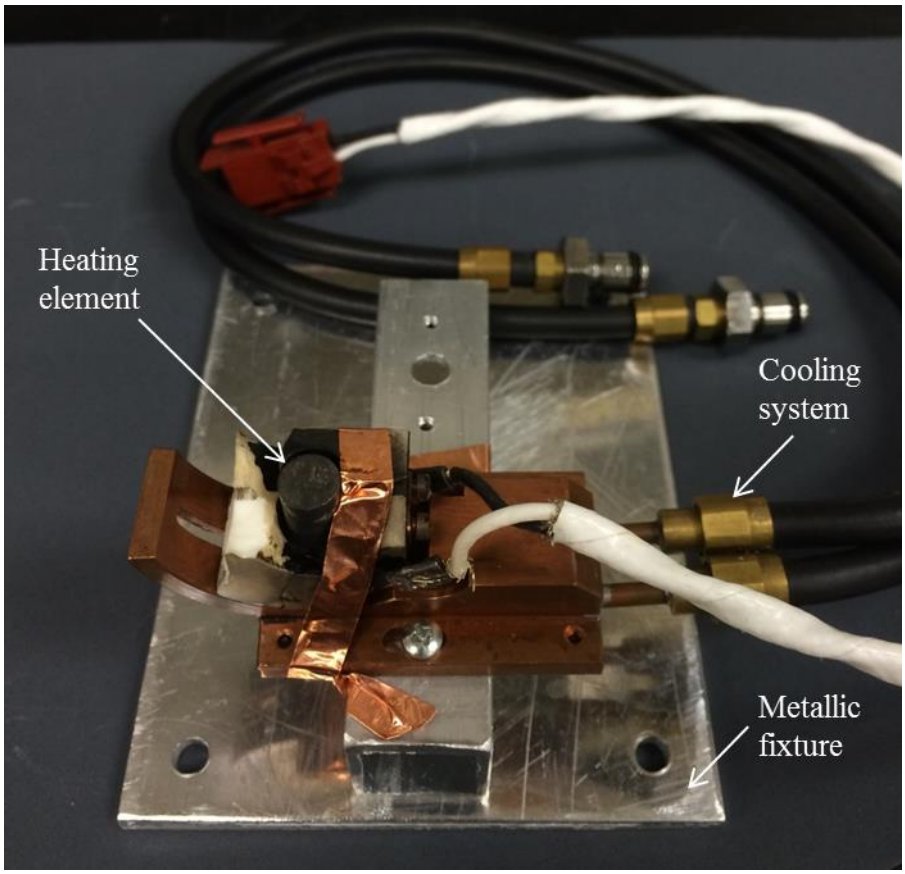

Figure 3.5 Photograph of the heating stage used for the in-situ annealing experiments. Note that the sample (not shown) for the in-situ annealing/recrystallization experiment was placed directly on top of the heating element during the experiments.

The EBSD map of a microstructural patch (typically ~100μm X ~150μm) was initially acquired at 298K. The specimen was then heated to a target temperature in the range of 423-623K. This typically took ~5-15 minutes. The sample was kept at that target temperature for ~15 minutes to homogenize and stabilize the specimen temperature. An EBSD map of the same microstructural patch was then acquired while the sample was kept at the desired temperature. The EBSD orientation mapping took ~45-55 minutes. It is noted that a significant change in microstructure was not observed during this time. A step size of 0.5μm was used. The temperature of the specimens was maintained within ±3 degrees while the EBSD maps were

acquired. The heating and the subsequent EBSD mapping cycle was then continued up to a desired temperature. The EBSD maps were typically acquired at 298K, 423K, 473K, 498K, 523K, 548K, 573K, and 598K. The EBSD data collection and analysis was performed using the methods described in Section 3.2.3. As the results of these experiments are sensitive to the parameters used for the post-processing "clean-up" procedures, criterions somewhat different from those given in Section 3.2.3 were used for the analysis of the EBSD raw data. Thus, the specific details of the user inputs used for the analysis will be mentioned alongside the results.

CHAPTER 4

RESULTS

This chapter presents the experimental results obtained from the extruded M1, as-cast and cast-then-extruded MN10, and as-cast and cast-then-extruded MN11 alloys. In addition, in this chapter, results on the recrystallization behavior of rolled ZE20 alloys will be presented. This chapter is divided into six sections, pertaining to each of the above mentioned materials. Subsections provided in each of the first five sections present the results of the characterization of the microstructure and texture, and the in-situ tensile/compression experiments at different test temperatures. The characterization of microstructure and texture was carried out by using SEM, EBSD, TEM, and EDX. The slip/twin trace analysis was performed to identify the active deformation modes for each material at the different test conditions (See Table 3.2). The result of the alloy that does not contain Nd, M1, was described first. Then, alloys containing increasing amounts of Nd additions, MN10 and MN11, were examined. Thus, the deformation behavior of the conventional alloy, without RE addition, is described first, and the influence of Nd addition is presented later. For all cases, the effect of alloy composition and processing condition on the microstructure and the deformation behavior, including the YS values and the relative activity of different deformation modes, were evaluated. Finally, in the last section, results from the in-situ annealing/recrystallization experiments on rolled ZE20 alloys are presented. These alloys were only used for understanding the recrystallization behavior. Thus, no load was applied during the experiments and the deformation behavior was not studied. A more thorough analysis, discussion, and comparison of the results will be presented in Chapter 5.

4.1 Extruded Mg-1Mn (M1)

4.1.1 Microstructure and texture

Figure 4.1a and 4.1b show representative SE SEM and Bright-field (BF) TEM images of the extruded M1 microstructure, respectively. The average grain diameter was ~42±30μm based on ASTM standards for grain size measurement [ASTM E112-13 2013, Vander Voort 1999]. Figure 4.2 shows the distribution of the grain size in extruded M1. As shown in Figure 4.1a, most of the grains were not equiaxed suggesting that the grains were not recrystallized. The extrusion direction was horizontal in Figure 4.1a. The stringers of precipitates along the extrusion direction indicate that the cast billet may not have been homogeneous with respect to the alloying elements. The volume fraction of the second phase particles measured from the SE SEM images were ~1.24%. The BF TEM image (see Figure 4.1b) shows precipitates of ~200nm diameter randomly distributed in the microstructure. TEM EDS analysis performed on the precipitates suggested a Mn-rich composition as the average measured composition was ~57Mg-43Mn (wt.%). EDS performed on the surrounding matrix suggested a composition of ~99.5Mg-0.5Mn (wt.%).

EBSD was used to investigate the texture of the extruded M1. Figure 4.3 shows the representative texture of extruded M1 in the form of $\{0001\}$ and $\{10\bar{1}0\}$ pole figures in the normal direction. The texture shown in Figure 4.3 was obtained from an area containing ~1500 grains. The pole figures show a strong basal <a> fiber texture where the basal plane normal was aligned perpendicular to the tensile direction. Such a strong basal texture is common in conventional wrought Mg alloys (Bohlen et al. 2010, Boehlert et al. 2012). Due to the strong basal texture, basal <a> slip and extension twinning exhibited low Schmid factors (typically less

than 0.25) while prismatic <a> slip, pyramidal <c+a> slip, and contraction twinning exhibited larger Schmid factors (typically higher than 0.35).

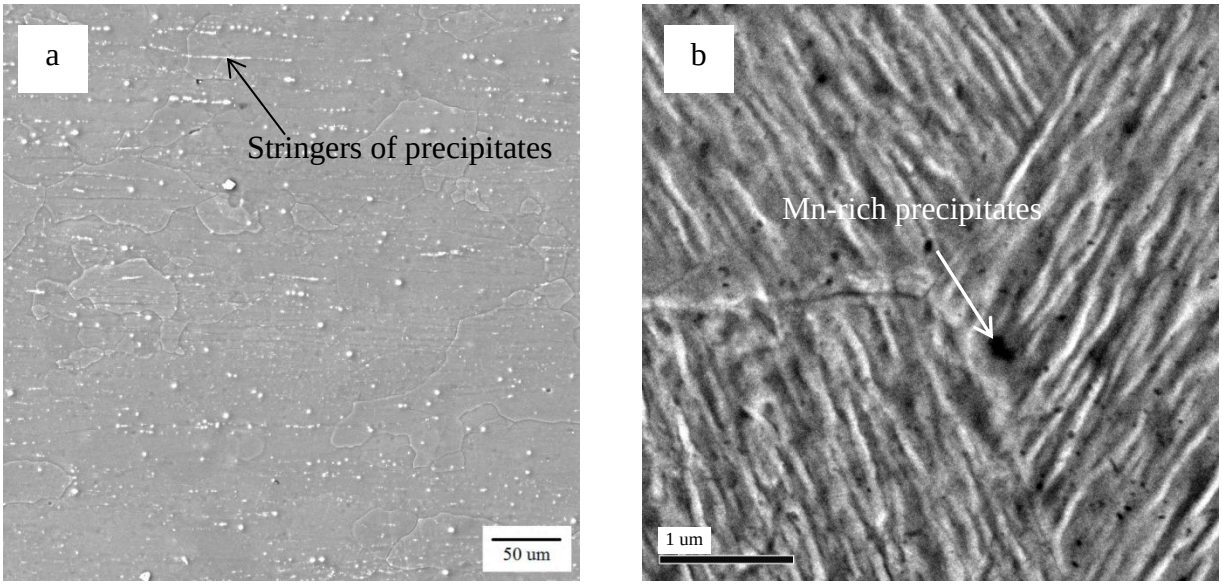

Figure 4.1 (a) SE SEM and (b) BF TEM image showing the microstructure of extruded M1. The extrusion direction is horizontal in (a).

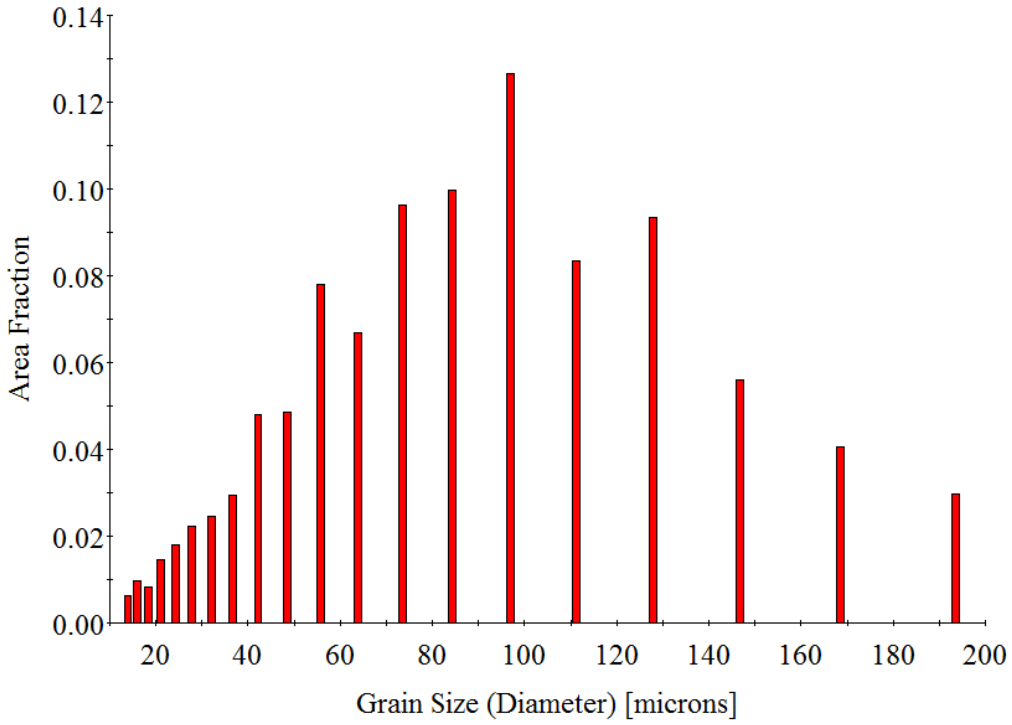

Figure 4.2 The grain size distribution of the extruded M1.

4.1.2 In-situ tension

In-situ tensile tests were performed on M1 at 323K, 423K, and 523K. One test was performed for each temperature. EBSD data were acquired before and after deformation, and slip/twin trace analysis was performed. The engineering stress versus displacement curves for the 323K, 423K, and 523K tensile tests are illustrated in Figure 4.4. The stress drops indicate the stress relaxation that occurred when the tests were paused for imaging. The specimen tested at 323K failed at ~9.9% strain. The specimens tested at 423K and 523K were not taken to failure. As shown in Figure 4.4, the YS of M1 decreased with increasing temperature. Table 4.1 lists the approximate YS and UTS obtained, and the maximum strain levels achieved for each experiment.

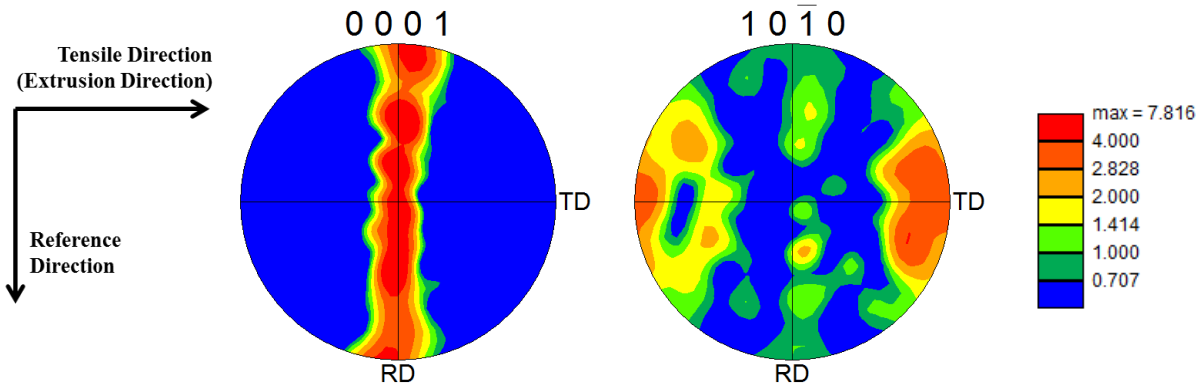

Figure 4.3 Representative texture of extruded M1 microstructure in the form of {0001} and {10$\bar{1}$0} pole figures in the normal direction.

Table 4.1 M1 tensile property comparison between different test conditions.

Test temperature	YS (MPa)	UTS (MPa)	Maximum strain (%)
323K	~154	~181	~9.9 (fractured)
423K	~75	~84	~15.6
523K	~45	~62	~7.8

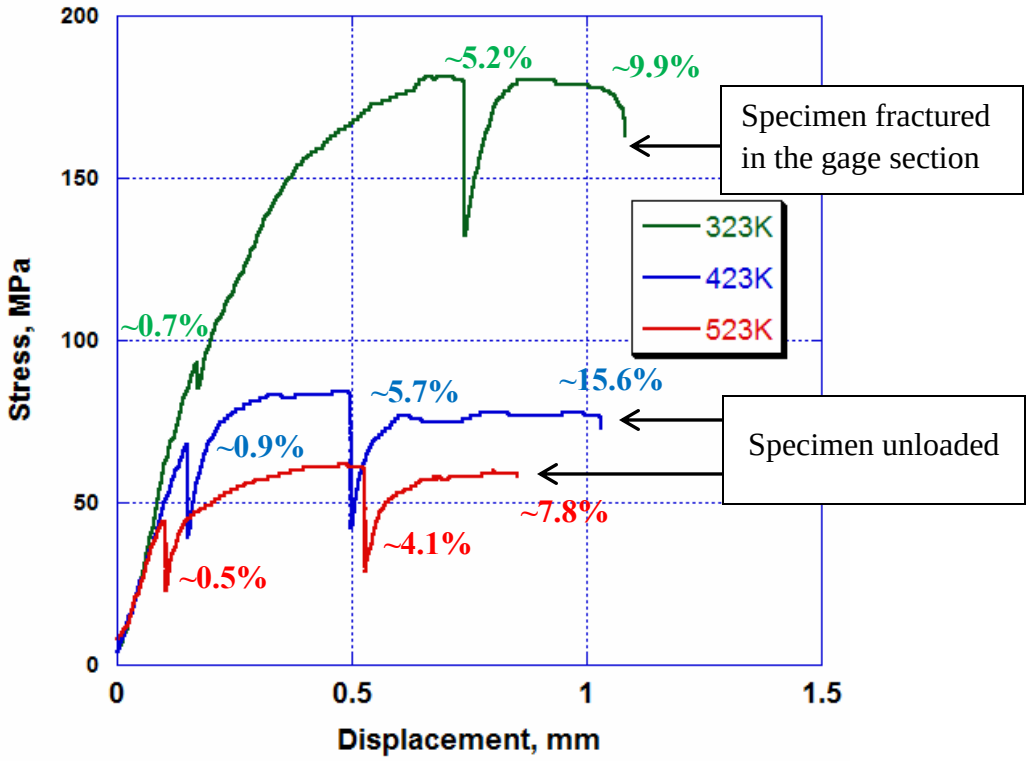

Figure 4.4 Representative stress vs. displacement plots for extruded M1 samples tensile tested at 323K, 423K, and 523K. The stress drops indicates the stress relaxation that occurred when the tests were interrupted for imaging. The displacement values included displacements in both the gage section and the grip regions.

4.1.2.1 323K tension

Figure 4.5 shows the EBSD IPF map in the normal direction and the corresponding {0001} and $\{10\bar{1}0\}$ pole figures from the gage section of the 323K tensile tested sample before deformation.

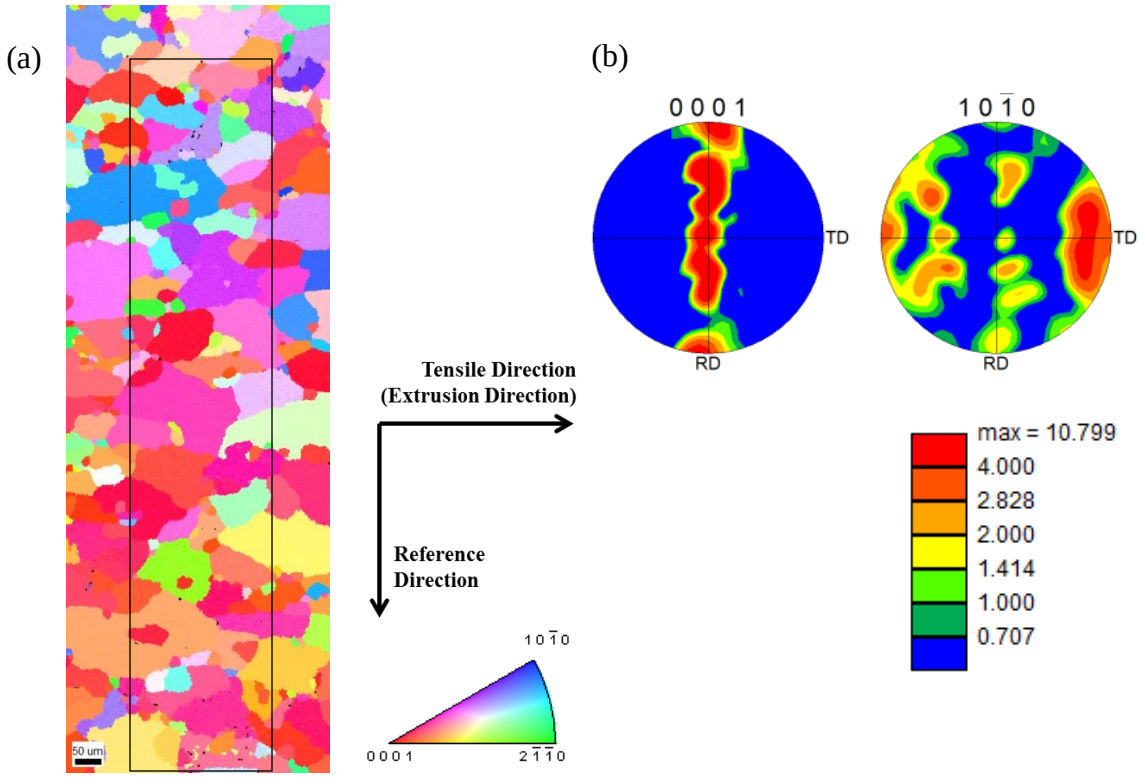

Figure 4.5 (a) EBSD IPF map in the normal direction before deformation and (b) the corresponding {0001} and {10$\bar{1}$0} pole figures from the gage section of the M1 specimen tensile tested at 323K. The area marked by the black box in (a) indicates the region in which trace analysis was performed.

Figure 4.6 shows sequential SE SEM images taken from the same area of the 323K tensile-tested specimen. No slip traces were observed before yielding at a strain level of ~0.7%. At ~5.2% strain, basal <a> slip, pyramidal <c+a> slip, and contraction twin traces (highlighted by blue, orange, and purple lines, respectively, in Figure 4.6c) were observed. Prismatic <a> slip traces were observed at ~9.9% strain. More slip/twin traces were observed at ~9.9% strain compared with ~5.2% strain (see Figure 4.6d).

(a) ε ≈ 0%

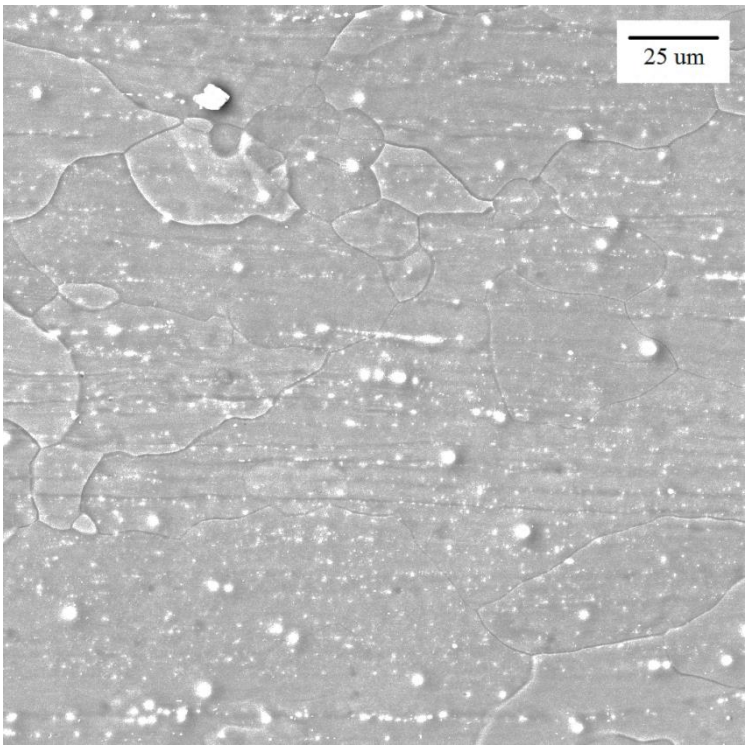

Tensile axis
↔
Extrusion direction

(b) ε ≈ 0.7%

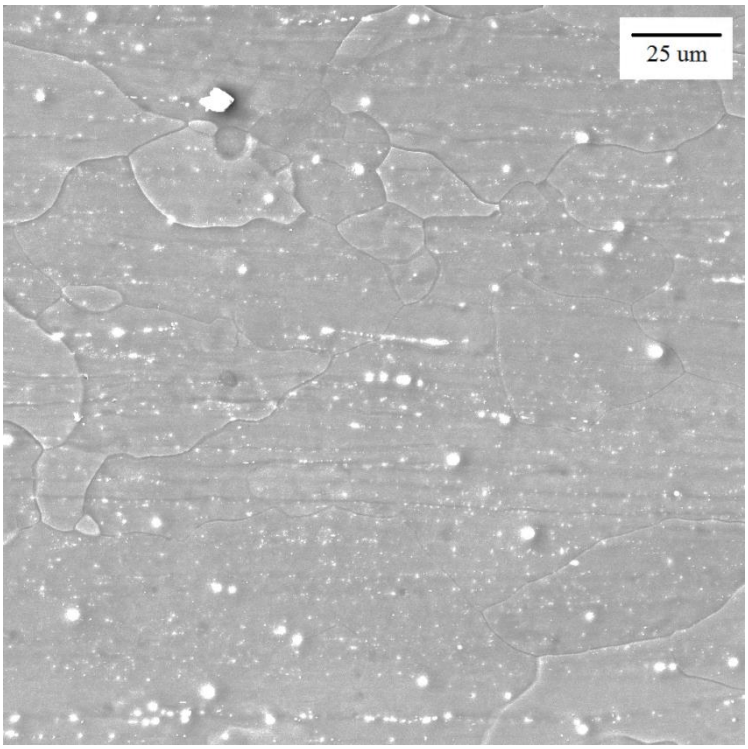

Figure 4.6 Sequential SE SEM images for the M1 specimen tensile tested at 323K: (a) undeformed, (b) ~0.7% strain, (c) ~5.2% strain, and (d) ~9.9% strain. In (c) and (d), the slip/twin traces are color coded for basal <a> slip (blue), prismatic <a> slip (red), pyramidal <c+a> slip (orange), and contraction twinning (purple).

Figure 4.6 (cont'd)

(c) ε ≈ 5.2%

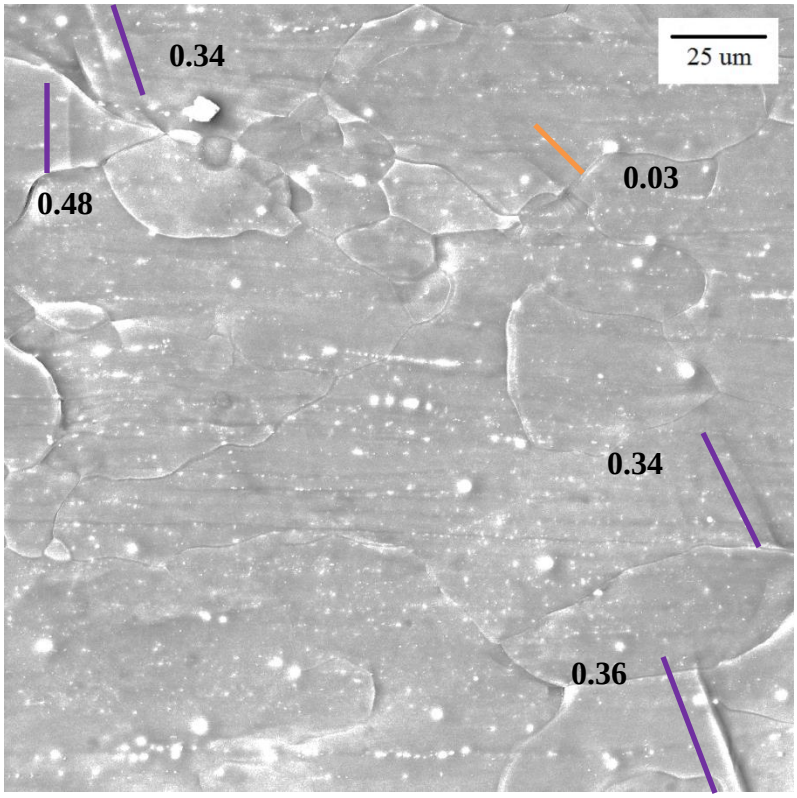

(d) ε ≈ 9.9%

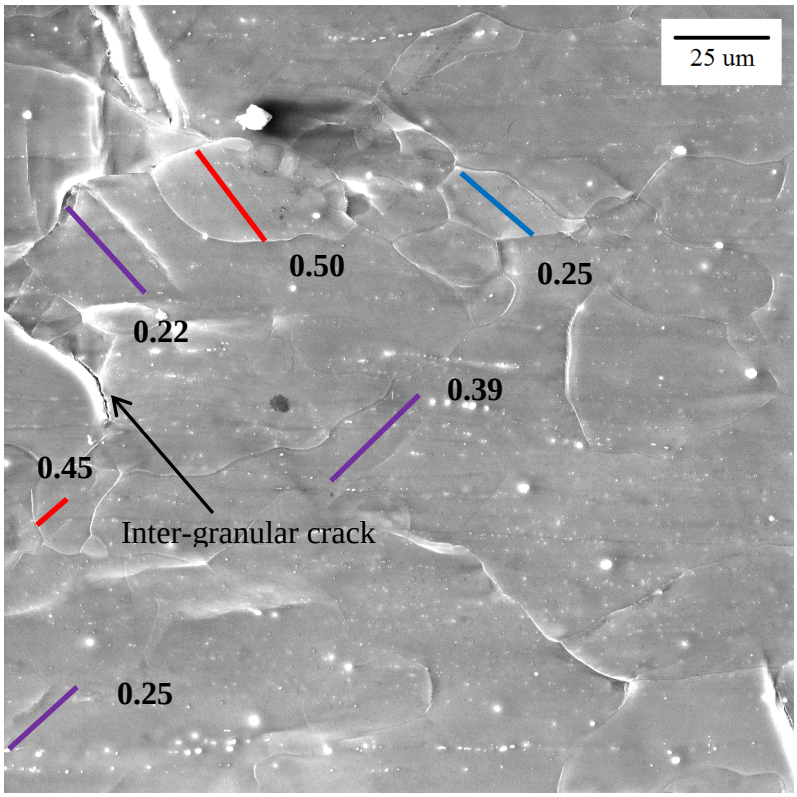

It was challenging to identify extension twins from the SE SEM images (see Figure 4.7b). Figure 4.7a and 4.7b shows the SE SEM images of the same area from the gage section. However, the EBSD IPF maps better revealed the extension twinning activity. Figure 4.7c-d shows the EBSD IPF maps in the normal direction of the same region shown in Figure 4.7a-b. Two extension twins identified in this region are indicated by the black arrows in Figure 4.7b and 4.7d. In Figure 4.7d, HCP unit cells are overlaid on the parent grains and twin regions and the corresponding misorientation across the twin habit plane boundary was indicated. The habit plane for the twins shown in Figure 4.7d was $\{10\bar{1}2\}$. Extension twinning in Mg ideally causes a rotation of 86° about $< 11\bar{2}0 >$ direction with the twin plane $\{10\bar{1}2\}$ [Yoo 1981]. All of the extension twins reported in this section were identified from the EBSD IPF maps. The morphology of the contraction twins was different from the extension twins as seen in the SE SEM images (see Figure 4.7 and Figure 4.8). This assisted in contrasting contraction twins from extension twins.

Figure 4.8 shows the SE SEM image and the corresponding EBSD IPF map in the normal direction of a contraction twin identified in the 323K tensile tested M1 sample. In Figure 4.8b, HCP unit cells are overlaid on the parent grains and twin regions and the corresponding misorientation across the twin habit plane boundary was indicated. The habit plane of the twin shown in Figure 4.8d was $\{10\bar{1}1\}$. Contraction twinning in Mg ideally causes a rotation of 56° about $< 11\bar{2}0 >$ direction with the twin plane $\{10\bar{1}1\}$ [Yoo 1981].

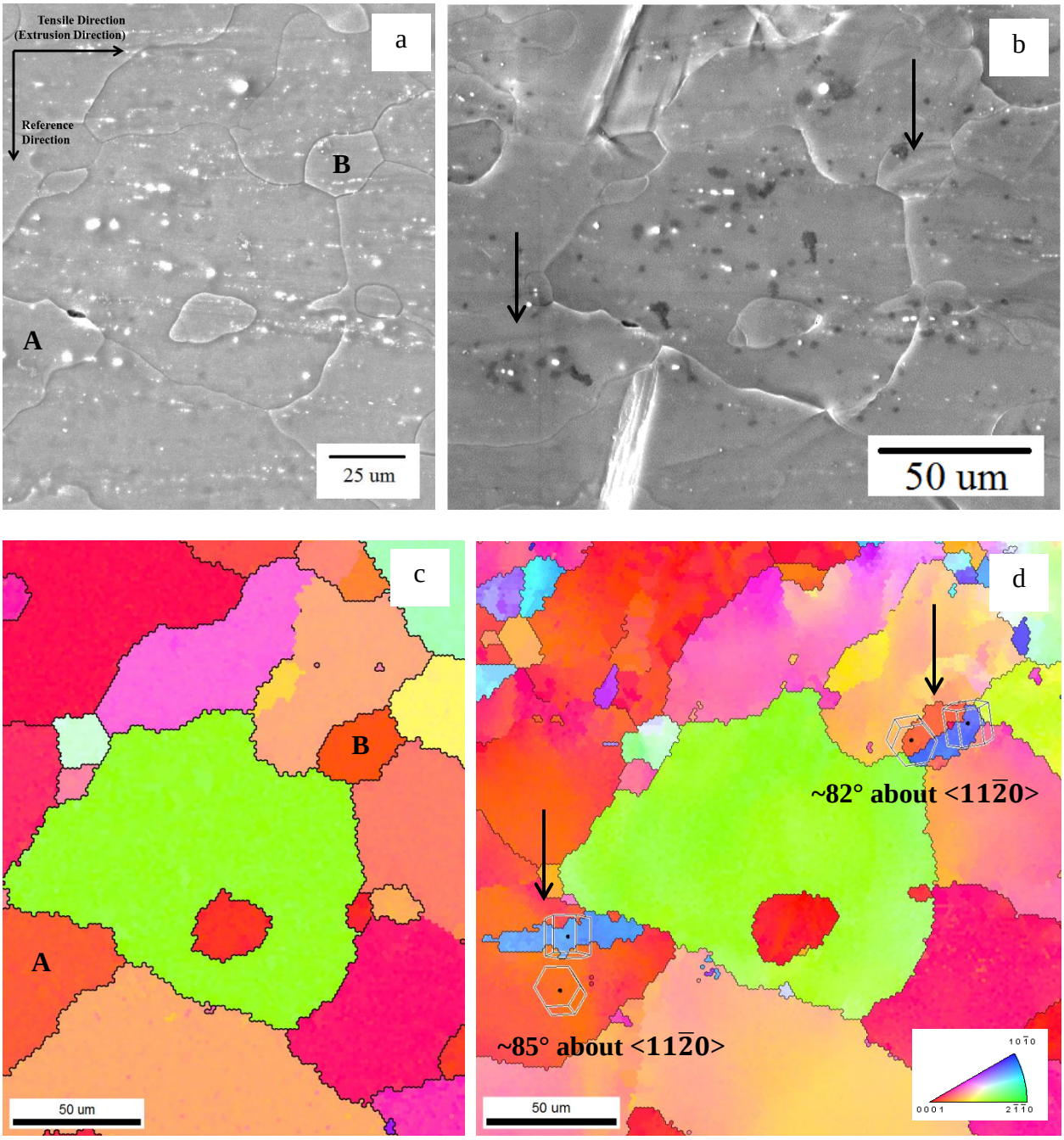

Figure 4.7 SE SEM images of the same area in the gage section of the M1 specimen tensile tested at 323K (a) before deformation and (b) at ~9.9% strain. (c) and (d) shows the EBSD IPF maps in the normal direction for the same area shown in (a) and (b). Extension twins were observed in grains marked A and B in (a) and (c). The extension twins are indicated by black arrows in (b) and (d). In (d), the HCP unit cells are overlaid showing the misorientation between the parent grain and the twinned region and the rotation angles are indicated.

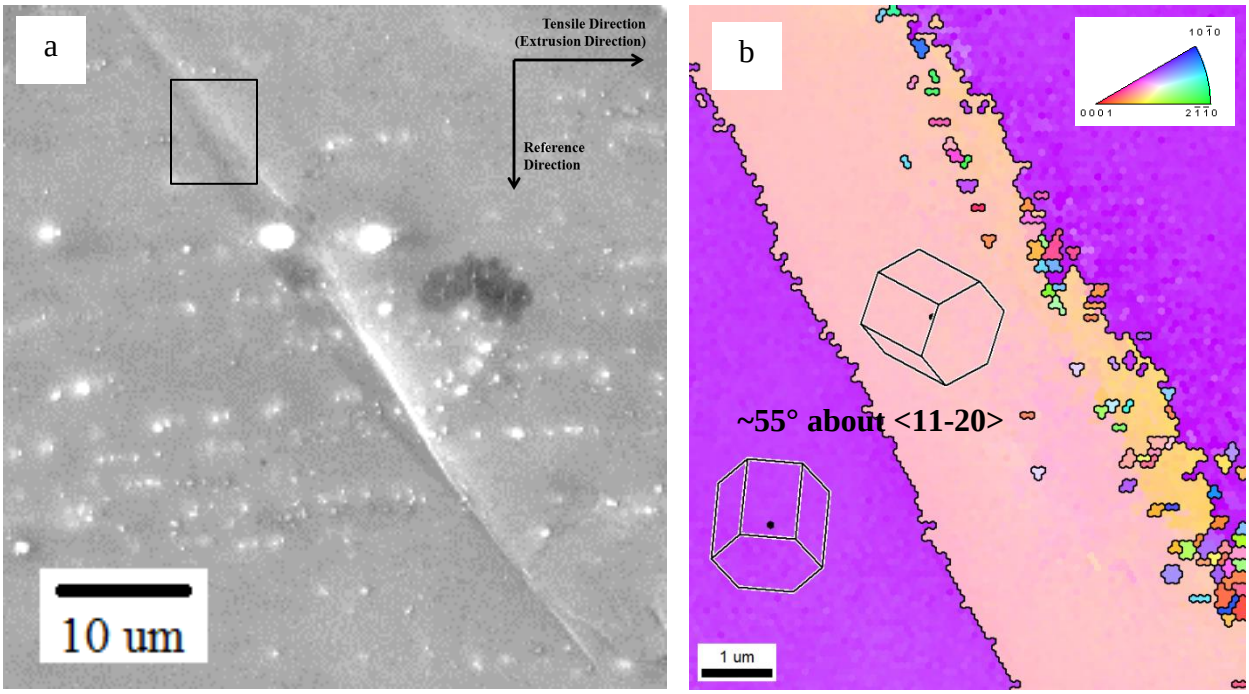

Figure 4.8 (a) SE SEM image of a contraction twin observed in the M1 specimen tensile tested at 323K. The twin shown in (a) was formed at ~5.2% - ~9.9% strain. The EBSD IPF map in the normal direction of the region highlighted by black box in (a) is given in (b). In (b), the HCP unit cells are overlaid showing the misorientation between the parent grain and the twinned region and the rotation angles are indicated.

Trace analysis was performed on ~100 grains from the area indicated in Figure 4.5. 17 slip traces and 45 twin traces were observed in this area ((17+45)/100≈62%). It is noted that multiple deformation modes were activated in 11 grains. Out of the 17 slip traces observed, 15 were matched with slip systems. The other two slip traces could not be matched with one slip system because the trace was common for multiple slip modes. Figure 4.9 plots the number of identified observations of a particular deformation mode versus the corresponding global Schmid factor range. 4 basal <a> (4/60≈7%), 5 prismatic <a> (5/60≈8%), 6 pyramidal <c+a> (6/60≈10%) slip systems were identified along with 16 extension twins (16/60≈27%), and 29 contraction twins (29/60≈48%). Thus, contraction twinning was the dominant deformation mode at 323K. Basal <a> slip was activated with Schmid factors ranging from 0.09 to 0.32. All of the

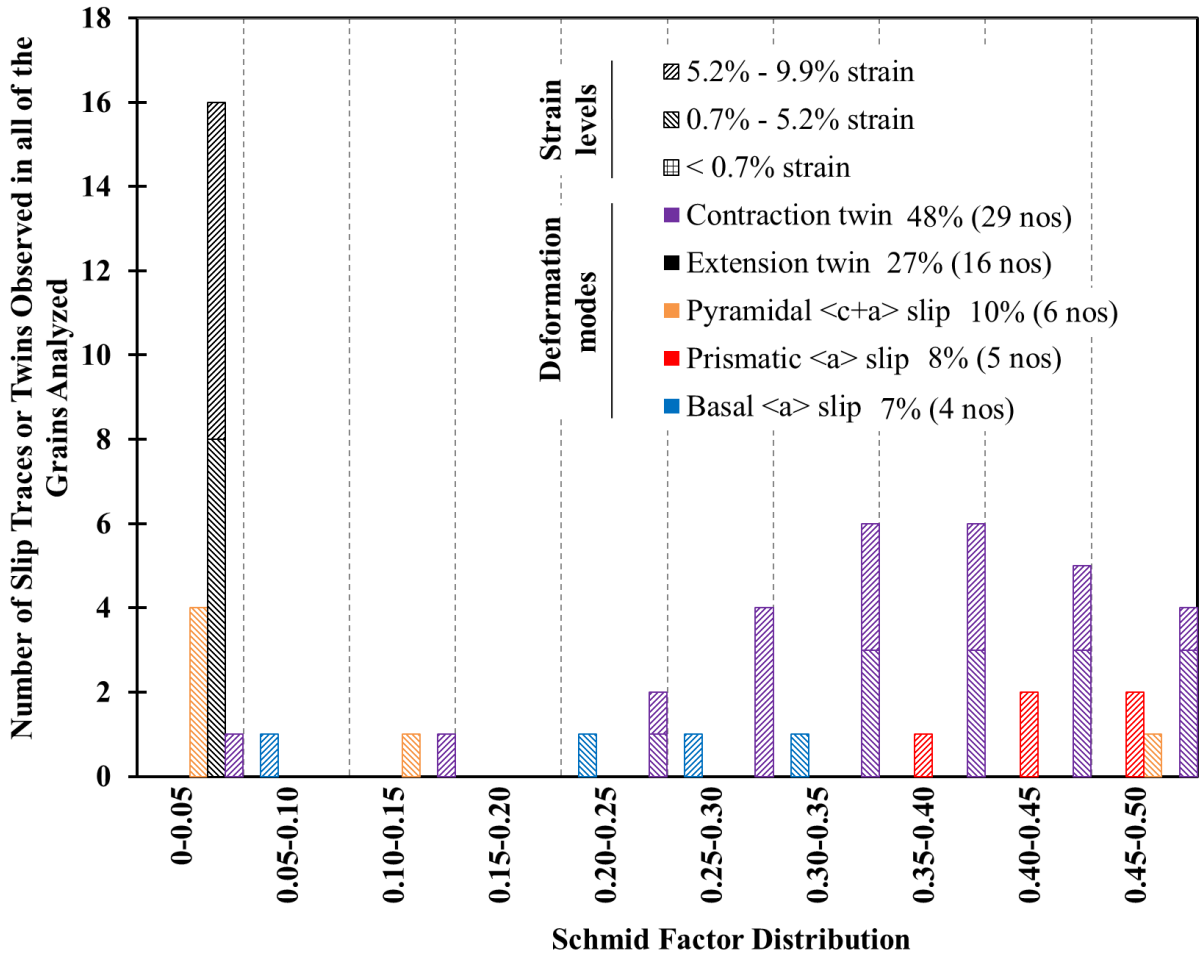

Figure 4.9 A histogram of the Schmid factor distribution of basal <a>, prismatic <a>, pyramidal <c+a> slip systems, and extension and contraction twin systems for the M1 323K tension experiment.

prismatic <a> slip was activated at high Schmid factors (>0.35). Most of the pyramidal <c+a> slip was activated at Schmid factors lower than 0.13. All of the extension twins were activated at global Schmid factors lower than 0.01. Unlike that for extension twins, most of the contraction twins were activated at global Schmid factors greater than 0.25. An intergranular crack observed at ~9.9% strain in the region analyzed is indicated in Figure 4.6d.

In Figure 4.10a, the orientation of the grains in which different deformation systems were identified was plotted in a unit triangle along the tensile direction. The orientations of two grains in which slip traces were observed, but were unable to be identified with a particular slip system, were also plotted in Figure 4.10a. The orientation of the grains on both sides of a grain boundary crack, observed at ~9.9% strain, was plotted and connected by a line in Figure 4.10a. In Figure 4.10b the same data from 4.10a is plotted in a {0001} pole figure along the normal direction.

The contraction twins identified in the M1 specimen tensile tested at 323K evolved into $\{10\bar{1}1\}-\{10\bar{1}2\}$ double twins with an increase in strain. $\{10\bar{1}1\}-\{10\bar{1}2\}$ double twins were formed due to the formation of $\{10\bar{1}2\}$ extension twins in the $\{10\bar{1}1\}$ contraction twinned region [Couling et al. 1959]. $\{10\bar{1}1\}-\{10\bar{1}2\}$ double twinning in Mg ideally causes a rotation of 38° about $< 11\bar{2}0 >$ direction [Couling et al. 1959]. The formation of $\{10\bar{1}2\}$ extension twins in the $\{10\bar{1}1\}$ contraction twinned region results in a misorientation of 56°+86°=142° about $< 11\bar{2}0 >$, which is crystallographically equivalent to 38° about $< 11\bar{2}0 >$. The habit plane of such double twins is a subject of debate [Yoshinaga et al. 1973, Cizek et al. 2008].

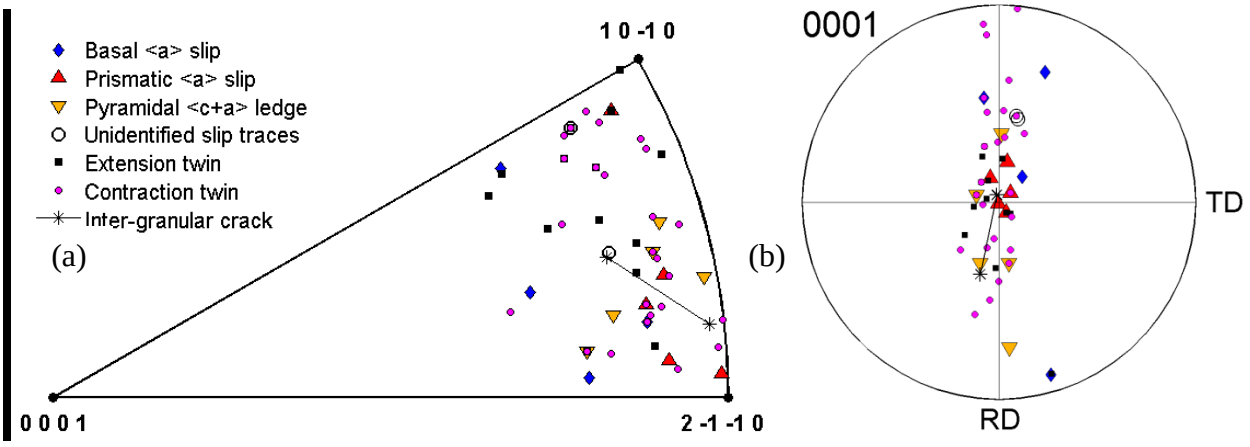

Figure 4.10 The individual grain orientations in which different deformation modes were observed for the M1 tensile test at 323K, plotted in a (a) unit triangle along the tensile direction and (b) {0001} pole figure along the normal direction. The line connects the grain orientations on both sides of the cracks observed.

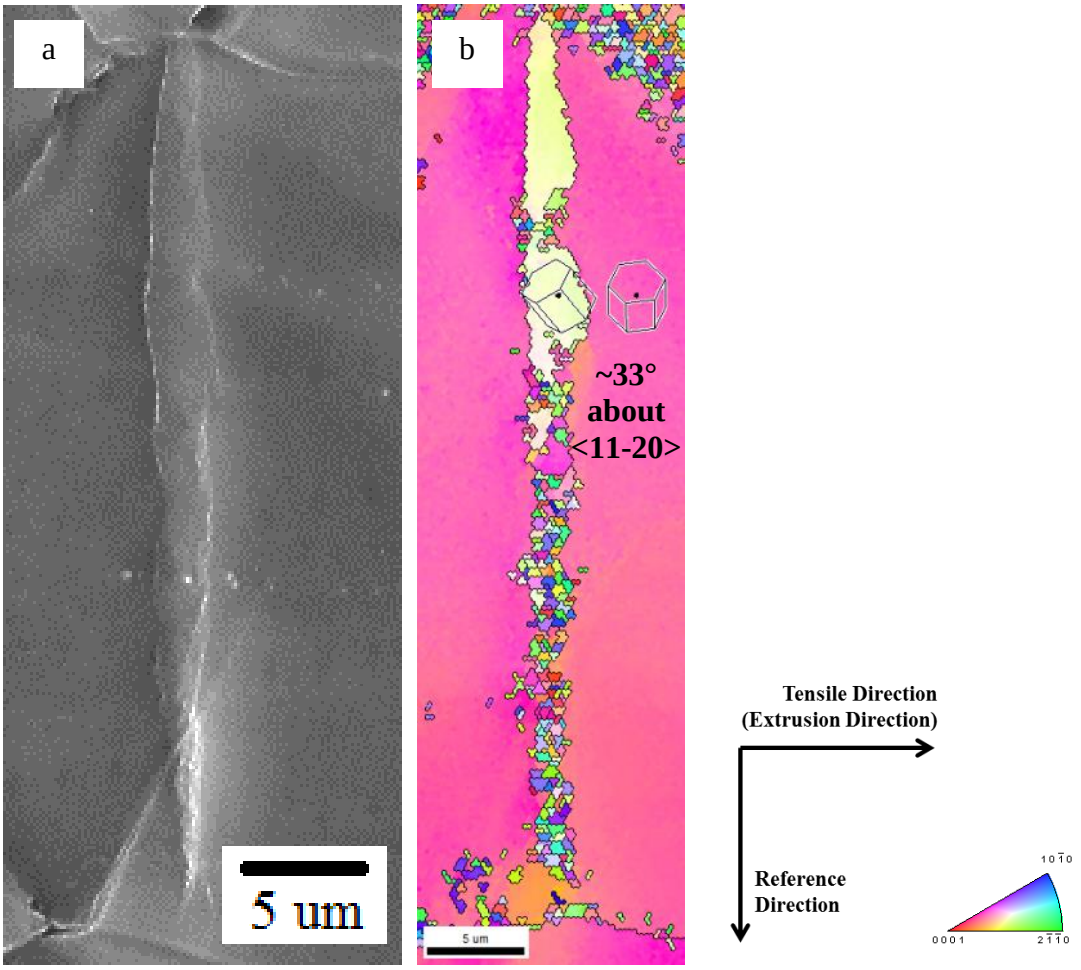

Figure 4.11 (a) SE SEM image of a $\{10\bar{1}1\} - \{10\bar{1}2\}$ double twin observed in M1 specimen tensile tested at 323K. The twin shown in (a) was formed at ~5.2% – ~9.9% strain. The EBSD IPF map in the normal direction of the same region shown in (a) is given in (b). In (b), the HCP unit cells are overlaid showing the misorientation between the parent grain and the twinned region and the rotation angles are indicated.

It was difficult to obtain EBSD orientation maps from such double twinned areas. This was expected to be due to the fine size of the double twinned regions and the high levels of strain within this region. Nevertheless, individual indexing was possible in some cases and a consistent identification of $\{10\bar{1}1\} - \{10\bar{1}2\}$ twinning resulted. Figure 4.11 shows the SE SEM image and the corresponding EBSD IPF map along the normal direction of a $\{10\bar{1}1\} - \{10\bar{1}2\}$ twin identified in the M1 specimen tensile tested at 323K. In Figure 4.11b, HCP unit cells are

overlaid on the parent grains and twin regions, and the corresponding misorientation across the twin habit plane boundary was indicated. The habit plane of the double twin shown in Figure 4.11b was $\{10\bar{1}3\}$.

In the cases where the contraction twins were not fully developed into $\{10\bar{1}1\}-\{10\bar{1}2\}$ double twins, it was possible to index $\{10\bar{1}1\}$ and $\{10\bar{1}2\}$ twinned regions, separately. Figure 4.12 shows the SE SEM image and the corresponding EBSD IP map in the normal direction of one such case observed for the M1 specimen tensile tested at 323K. In Figure 4.12c, the area highlighted by the black box in Figure 4.12b is shown by overlaying the EBSD IPF map in the normal direction over the EBSD image quality (Kikuchi band contrast) map. In Figure 4.12c, the purple line highlights the contraction twin boundary (56°±5° misorientation about $< 11\bar{2}0 >$, twin plane $\{10\bar{1}1\}$±5° tolerance), the black line highlights the extension twin boundary (86°±4° misorientation about $< 11\bar{2}0 >$, twin plane $\{10\bar{1}2\}$±4° tolerance), and the yellow line highlights the misorientation caused by $\{10\bar{1}1\}-\{10\bar{1}2\}$ double twinning (38°±5° misorientation about $< 11\bar{2}0 >$). The step size for the EBSD map shown in Figure 4.12a and 4.12c was 0.15 μ. In Figure 4.12c, the $\{10\bar{1}1\}$ contraction twin variant was identified to be $(01\bar{1}1)[01\bar{1}\bar{2}]$ with Schmid factor 0.35, and the $\{10\bar{1}2\}$ extension twin variant was $(0\bar{1}12)[01\bar{1}1]$ with Schmid factor 0.14.

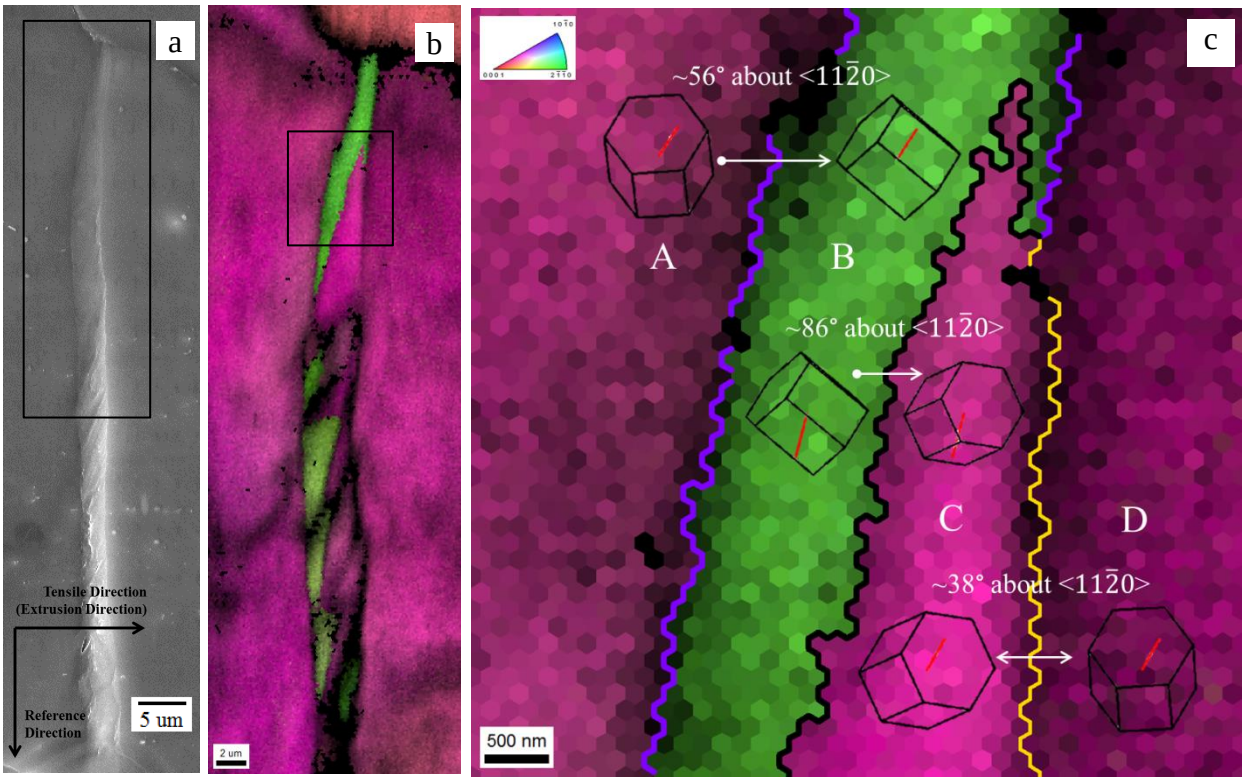

Figure 4.12 The evolution of contractions twins into $\{10\bar{1}1\} - \{10\bar{1}2\}$ double twins observed in the M1 specimen tensile tested at 323K: (a) SE SEM image and (b) corresponding EBSD IPF map along the normal direction of the area highlighted by the black box in (a). The area highlighted by the black box in (b) is shown in (c). In (c), the HCP unit cells are over laid showing the misorientation between the parent grain and the twinned region, and the common $< 11\bar{2}0 >$ direction is highlighted by red lines. In (c), the purple line, the black line, and the yellow line highlights the contraction twin boundary, the extension twin boundary, and the misorientation caused by $\{10\bar{1}1\} - \{10\bar{1}2\}$ double twinning, respectively, and the rotation angles are indicated. In (c), note that the four regions formed due to the twinning events are marked as A, B, C, and D.

It was observed that surface steps were formed in the $\{10\bar{1}1\} - \{10\bar{1}2\}$ double twinned regions (See Figure 4.12a and 4.13a). Crack formation was observed along the surface steps with increase in strain. This was expected to be due to shear localization within the $\{10\bar{1}1\} - \{10\bar{1}2\}$ double twinned volume. This will be discussed in section 5.4.1. Figure 4.13a shows the SE SEM image of the gage section along the normal direction of the 323K tensile tested M1 specimen. The steps formed in the $\{10\bar{1}1\} - \{10\bar{1}2\}$ double twinned regions were observed

over the entire gage section. However, a higher frequency of steps was observed close to the fracture surface (See Figure 4.13a). A higher magnification SE SEM image of the crack highlighted by the black box in Figure 4.13a is shown in Figure 4.13b. Figure 4.13c shows the SE SEM image of the crack shown in Figure 4.13b after the sample was tilted 70° with respect to the beam.

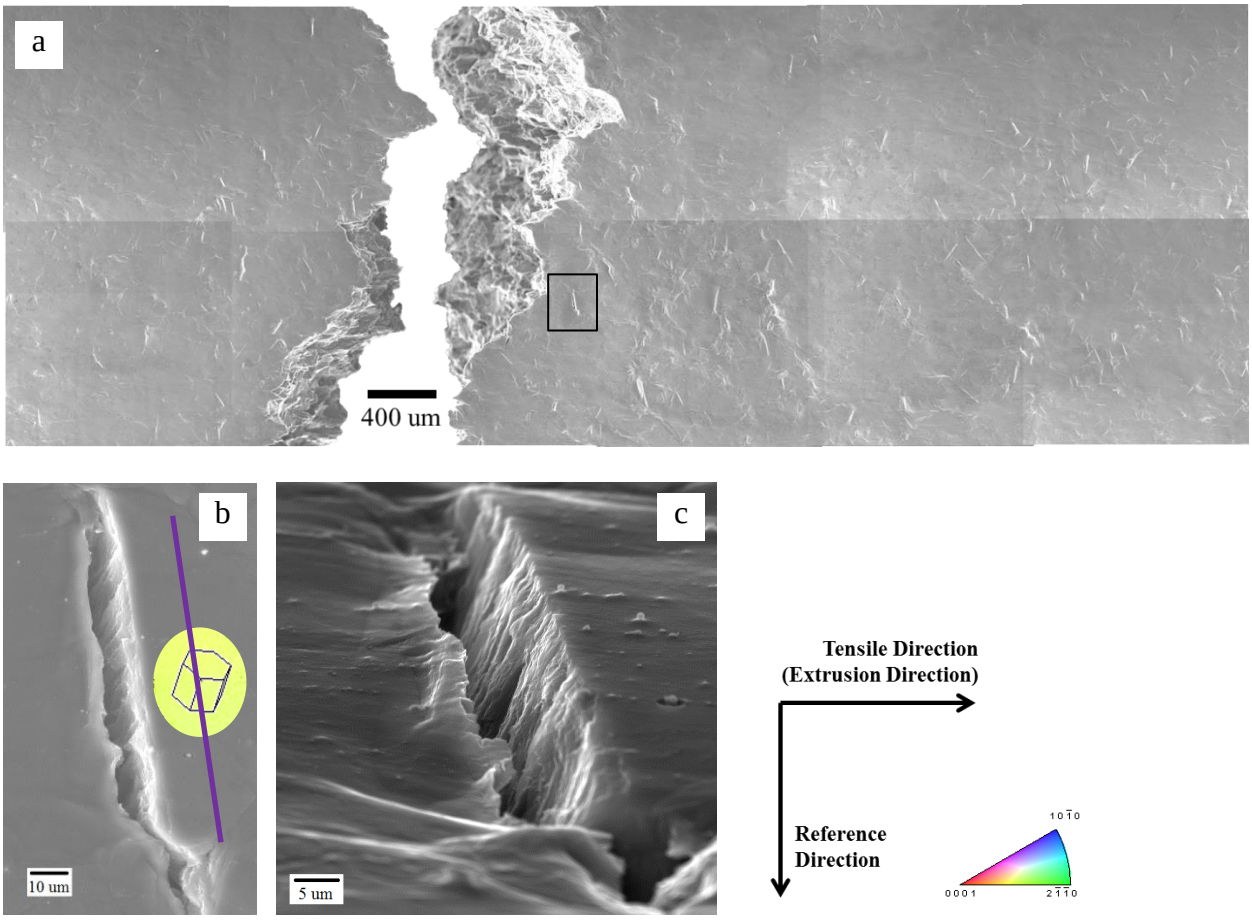

Figure 4.13 (a) SE SEM image of the gage section of the M1 specimen tensile tested at 323K after fracture. The SE SEM image of the crack highlighted by the black box is shown in (b). In (b) the orientation of the grain in which crack was observed is indicated in the form of HCP unit cell and the orientation of the contraction twin trace parallel to the crack is given. In (c) SE SEM image of the crack shown in (b) is given with the sample tilted 70° with respect to the beam.

Figure 4.14 shows the SE SEM image of the fracture surface of the M1 specimen tensile tested at 323K. The sample was tilted 45° to the tensile direction. Flat surfaces expected to be developed due to localized shear failure within the $\{10\bar{1}1\} - \{10\bar{1}2\}$ double twinned regions were observed over the entire fracture surface. The fracture surface shown in Figure 4.14 is typical for a material that has undergone failure due to shear localization. Recent studies reported similar microstructural features on the fracture surface of AZ31 and polycrystalline Mg after deformation at room temperature, and these studies concluded that these features are linked to the localized shear deformation within $\{10\bar{1}1\} - \{10\bar{1}2\}$ double twins [Ando 2014, Martin 2015].

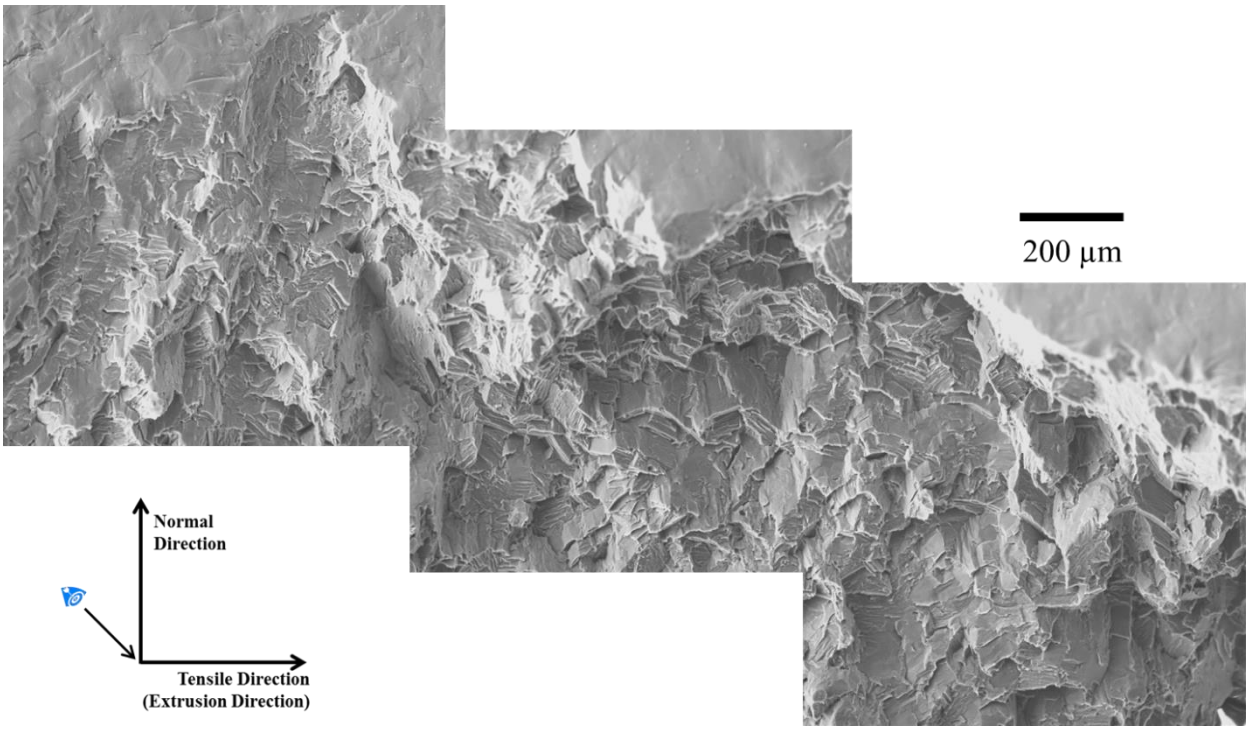

Figure 4.14 SE SEM image of the fracture surface of the extruded M1 specimen tensile tested at 323K approached at an angle of 45° tilted along the tensile direction. The angle of view is indicated.

4.1.2.2 423K tension

Before describing the 423K tension results for M1, it is noted that extension twins formed on the surface of some of the grains during mechanical polishing in the microstructure of the sample tensile tested at 423K. To understand the formation of such twins, a separate M1 sample was mechanical polished twice by applying different mechanical forces (the mechanical polishing forces were not measured), and the formation of extension twin traces is depicted in Figure 4.15. Figure 4.15a shows an SE SEM image of the microstructure after "light" mechanical polishing and Figure 4.15b shows the same area after further polishing while applying more force. Figure 4.15c shows the EBSD IPF map in the normal direction of the area highlighted by the black box in Figure 4.15b depicting the extension twins, which formed on the surface. Further analysis revealed that traces of extension twins were observed only in the grains in which the c-axis was oriented perpendicular to the normal direction. Figure 4.15d shows the orientation of the grains in which extension twins were formed during mechanical polishing in the M1 specimen tensile tested at 423K. From 4.15d, a strong dependence on the grain orientation (c-axis aligned perpendicular to the normal direction) and the formation of extension twins during polishing was observed. It is noteworthy that such grains are oriented favorably for the activation of extension twins when compressive forces are applied in the normal direction, which is the loading condition while polishing. It can be assumed that a force of approximately 50-100N was applied during the second polishing step. Considering the gage section of the tensile specimen, which is 3mm wide X 10mm long, a force of ~50-100N translates to a stress of ~2-4MPa. This applied stress is close to the CRSS values estimated for extension twinning in Mg [Chapuis et al. 2011]. This explains the formation of extension twins in the grains that are oriented favorably for the activation of extension twins.

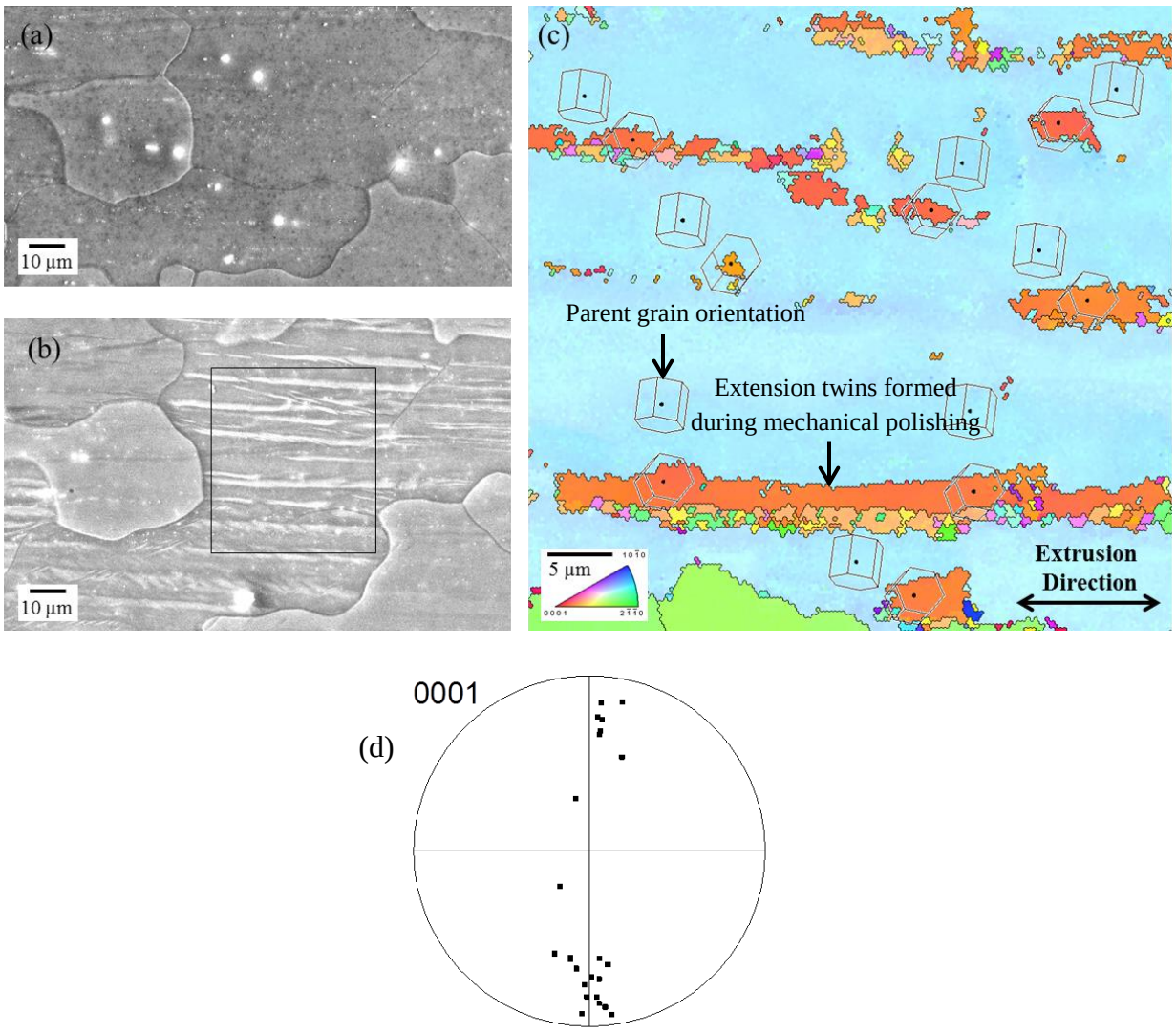

Figure 4.15 SE SEM image of the microstructure of the same area of a M1 specimen: (a) after "light" mechanical polishing and (b) after further mechanical polishing by applying more force (the mechanical polishing forces were not measured). (c) EBSD IPF map in the normal direction of the area highlighted by the black box in (b) depicting the extension twins which formed during the second polishing step. The unit cell orientations of the extension twins and the matrix are provided in (c). In (d), the orientation of the grains in which extension twins were formed during mechanical polishing in the M1 specimen tensile tested at 423K is provided in the form of {0001} pole figure in the normal direction.

Figure 4.16 shows the EBSD IPF map in the normal direction and the corresponding {0001} and $\{10\bar{1}0\}$ pole figures from the gage section of the 423K tensile tested sample before deformation. The area in which trace analysis was performed is marked in Figure 4.16a.

The grains in which extension twins were formed during mechanical polishing in the M1 specimen tensile tested at 423K are marked by black arrows in Figure 4.16a and 4.17a. As the size of these twin traces are small compared to the grain size and they only formed in a small fraction of grains, it was assumed that their effect on the bulk mechanical properties was negligible. The size and shape of these twins stayed the same during the tensile testing (see Figure 4.17). Such extension twin traces were not observed for the specimens tensile tested at 323K and 523K. This phenomenon might be due to the variations in the force applied while polishing.

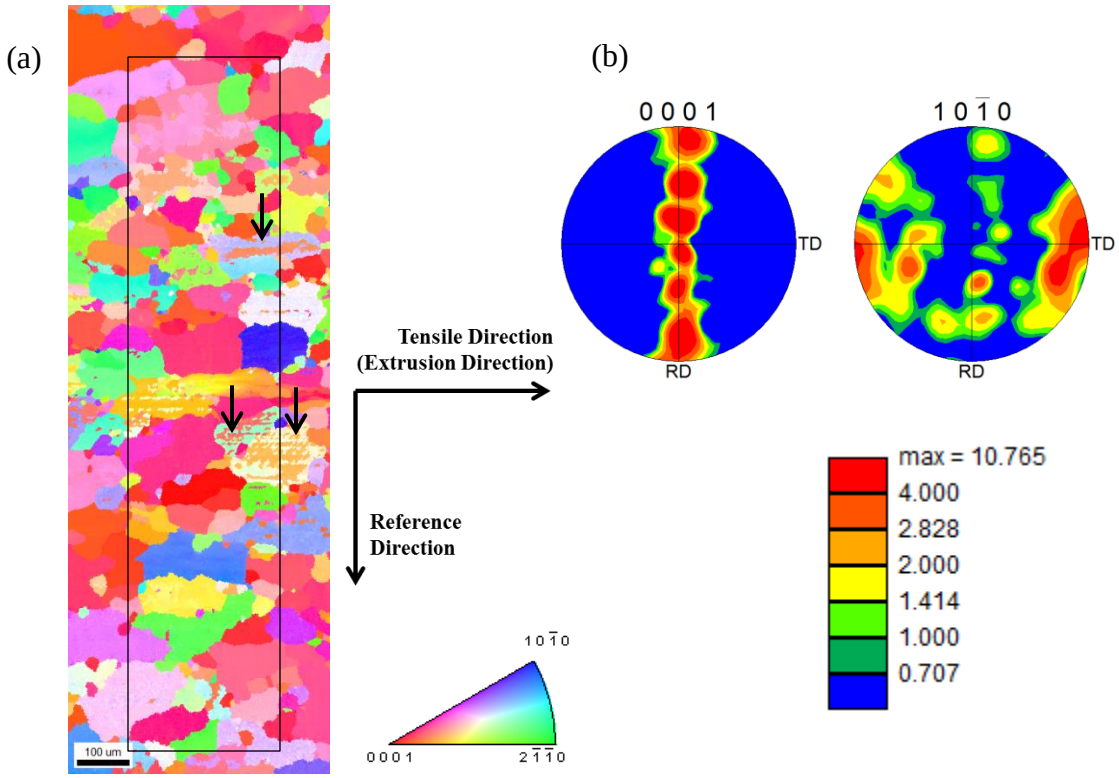

Figure 4.16 (a) EBSD IPF map in the normal direction before deformation and (b) the corresponding {0001} and {10$\bar{1}$0} pole figures from the gage section of M1 specimen tensile tested at 423K. The area on which trace analysis was performed is marked in 4.16a. The grains in which extension twins were formed during polishing are highlighted by black arrows in (a).

Figure 4.17 shows sequential SE SEM images taken from the same area of the 423K tensile tested specimen. Slip traces started to appear close to the YS (~75 MPa) and at ~0.9% strain. At ~5.7% strain, slip traces and contraction twinning were observed. The majority of the slip traces identified was for prismatic <a> and pyramidal <c+a> slip systems (highlighted by red and orange lines in Figure 4.17c, respectively) and their global Schmid factor ranged from 0.02 to 0.50. Basal <a> slip (highlighted by blue lines in Figure 4.17c) was also observed at ~5.7% strain. More slip traces were observed at ~15.6% strain (see Figure 4.17d).

Figure 4.18 shows the EBSD IPF map in the normal direction before and after deformation from the gage area of the specimen tested at 423K. In Figure 4.18, the misorientation of the twinned region with respect to the matrix is shown by the overlaid HCP unit cells and the misorientation angle is indicated.

(a) ε ≈ 0%

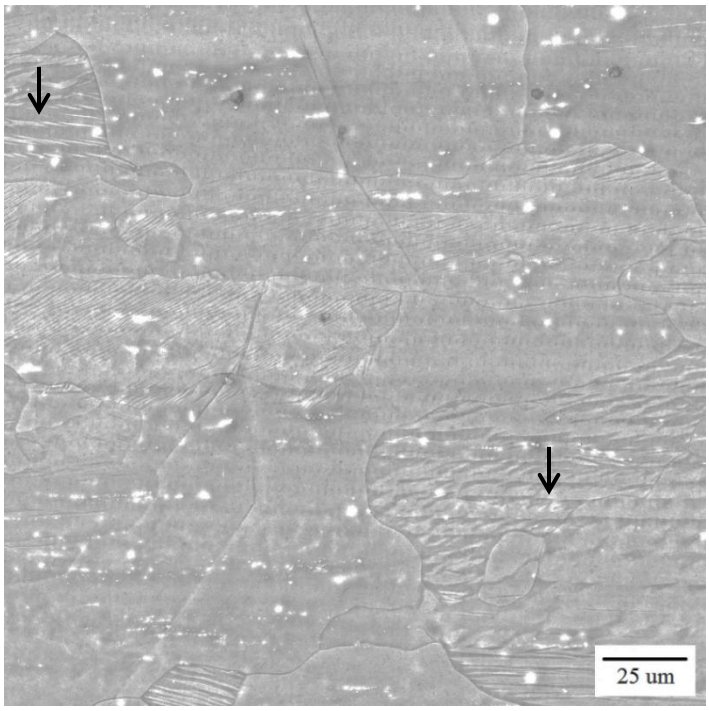

Tensile axis
↔
Extrusion direction

(b) ε ≈ 0.9%

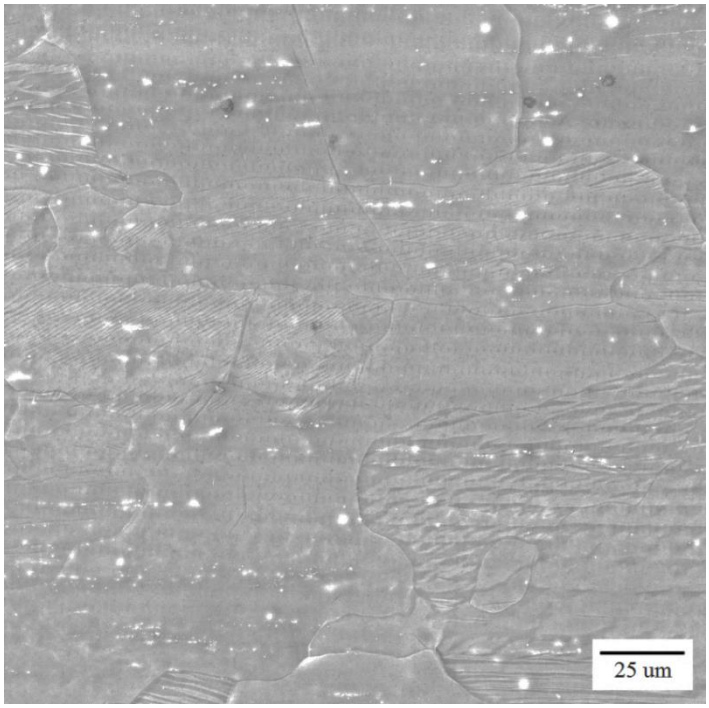

Figure 4.17 Sequential SE SEM images for M1 tensile tested at 423K: (a) undeformed, (b) ~0.9% strain, (c) ~5.7% strain, and (d) ~15.6% strain. In (c) and (d), slip/twin traces are color coded for basal <a> slip (blue), prismatic <a> slip (red), pyramidal <c+a> slip (orange), and contraction twin (purple). The tensile axis and extrusion direction was horizontal. The grains in which extension twins were formed on the surface during mechanical polishing are marked by black arrows in (a).

Figure 4.17 (cont'd)

(c) ε ≈ 5.7%

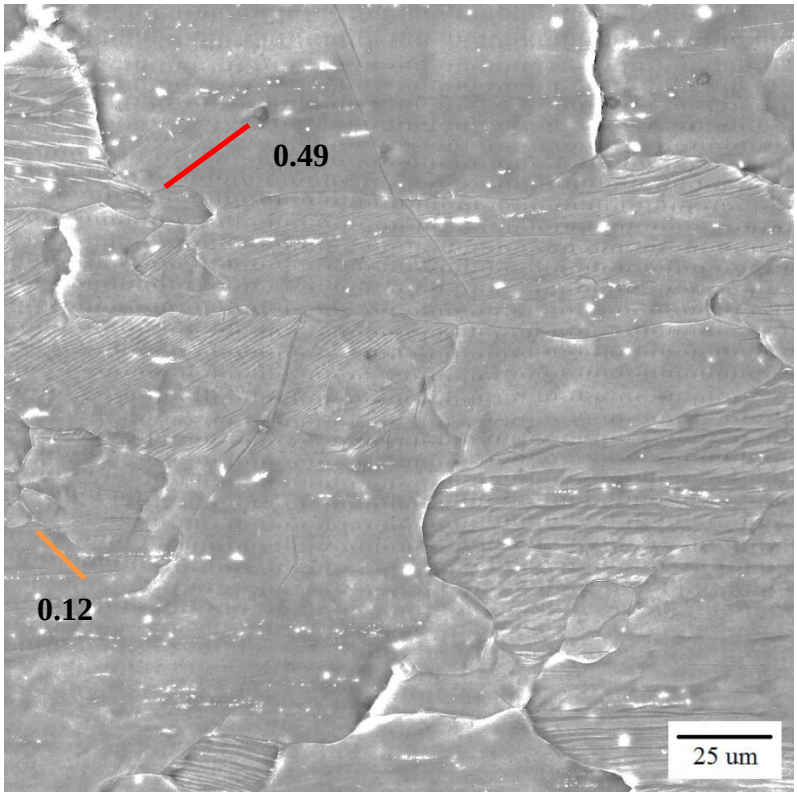

(d) ε ≈ 15.6%

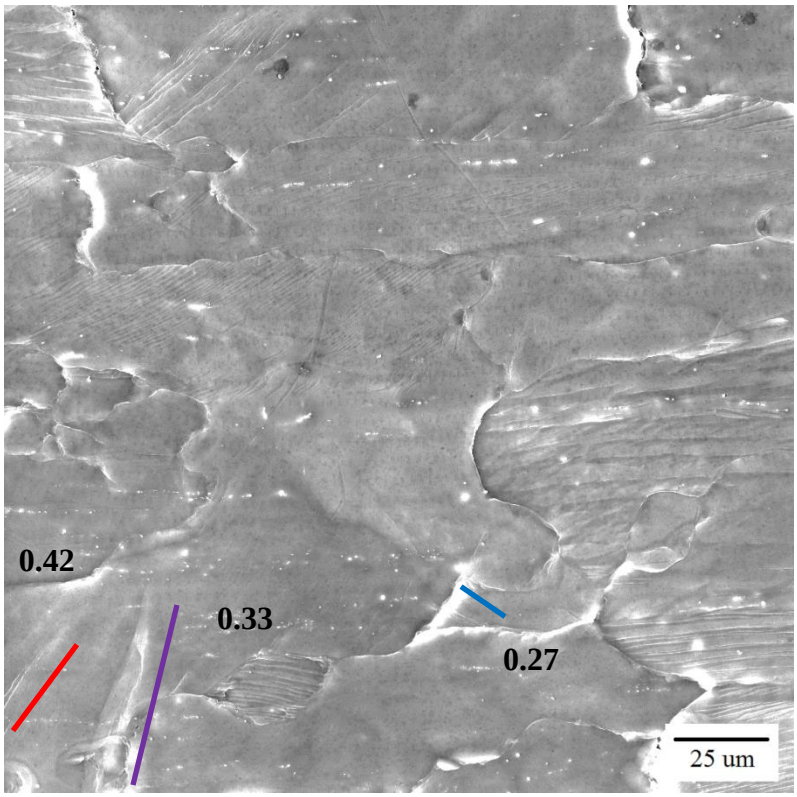

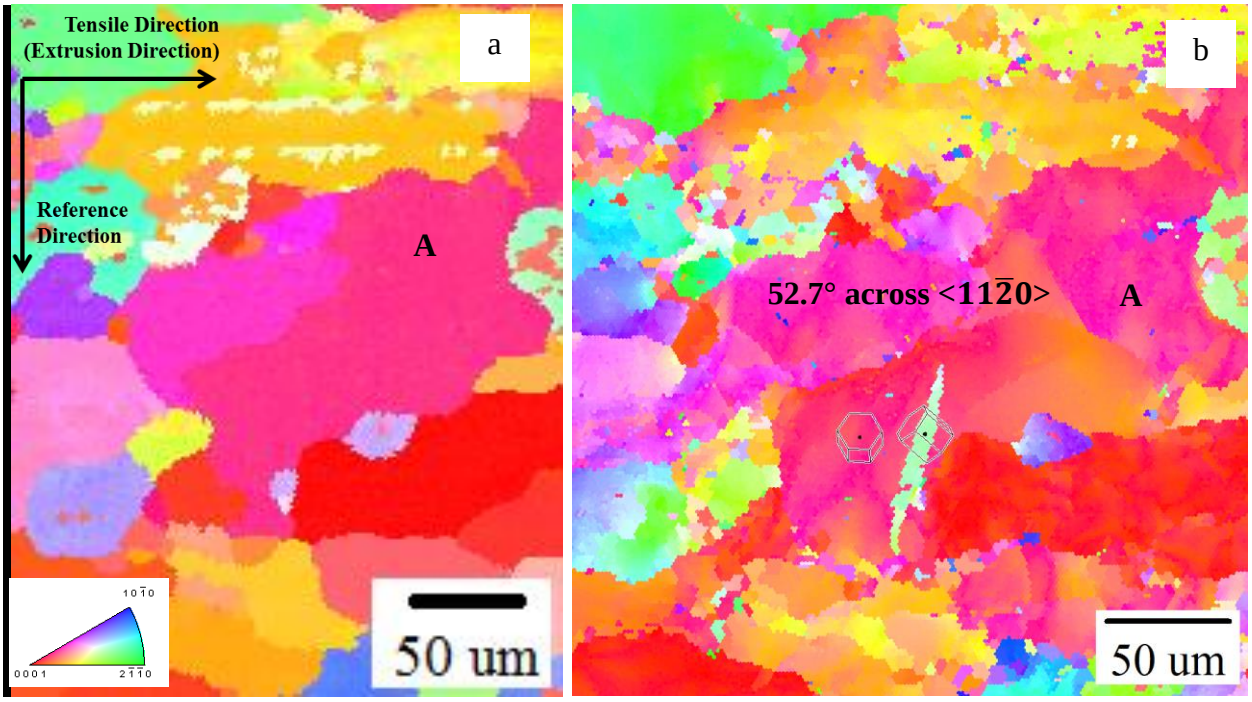

Figure 4.18 EBSD IPF maps in the normal direction for the same area in the tensile tested sample for M1 at 423K (a) 0% strain and (b) ~15.6% strain. A contraction twin was observed in the grain marked "A" in (a). In (b) the HCP unit cells are overlaid showing the rotation between the parent and the twin orientations, and the misorientation angle is indicated.

Trace analysis was performed on ~75 grains and 34 (34/75≈45%) instances of deformation activity were observed. 3 contraction twins and 2 extension twins were identified in the deformed region. Out of 29 slip traces observed, 24 were identified. The rest of the slip traces could not be identified because the trace was common for multiple slip systems. Figure 4.19 plots the number of identified observations of a particular deformation mode versus the global Schmid factor range. Basal <a> slip and pyramidal <c+a> slip were distributed over the entire Schmid factor range while all prismatic <a> slip happened at high Schmid factors (>0.40). 6 basal <a> slip (6/29≈21%), 11 prismatic <a> (11/29≈38%), and 7 pyramidal <c+a> (7/29≈24%) slip systems were identified along with 2 extension twins (2/29≈7%), and 3 contraction twins (3/29≈10%). Similar to the tensile test at 323K, extension twins were activated

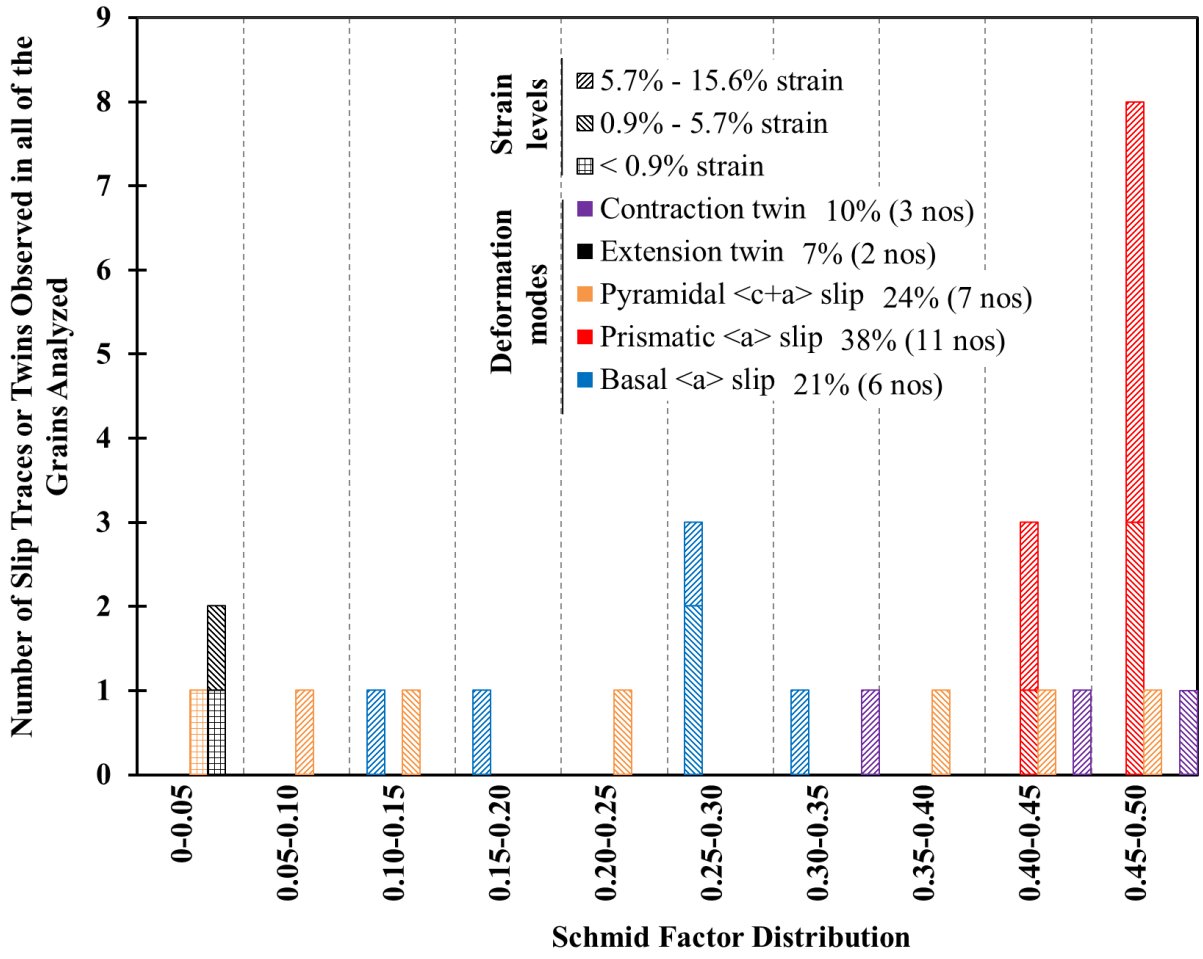

Figure 4.19 A histogram of the Schmid factor distribution of basal <a> slip, prismatic <a> slip, pyramidal <c+a> slip, extension twin, and contraction twin systems identified for the M1 specimen tensile tested at 423K.

at low Schmid factors (<0.01) and contractions twins were activated at high Schmid factors (>0.30). The deformation was controlled mainly by slip at 423K, where prismatic <a> slip was the dominant deformation mode. Basal <a> slip and pyramidal <c+a> slip exhibited similar relative activities.

Figure 4.20 shows a stereographic triangle with the grain orientations plotted for basal <a> slip, prismatic <a> slip, pyramidal <c+a> slip, extension twinning, and contraction twinning observed for the sample tensile tested to ~15.6% strain at 423K. 5 grains in which slip traces

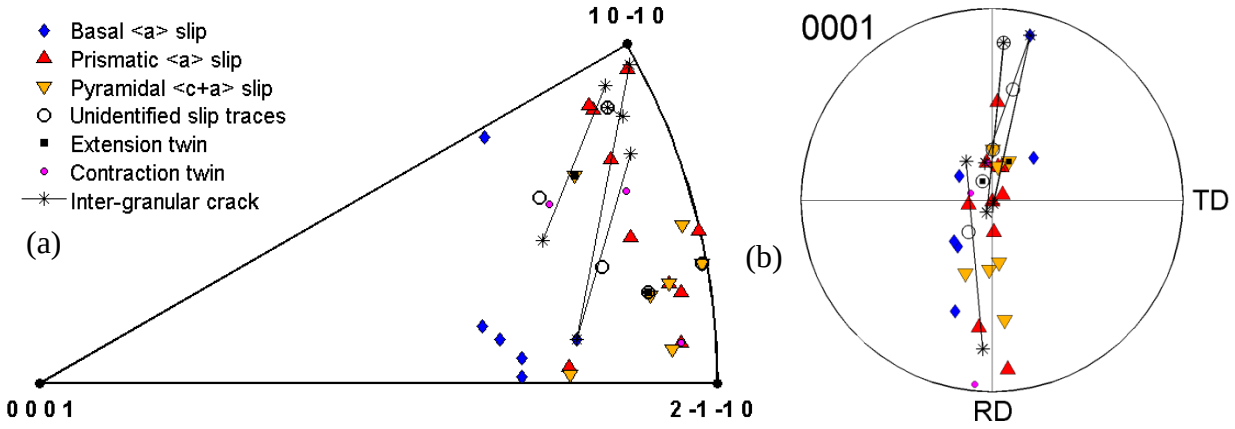

Figure 4.20 The individual grain orientations in which different deformation modes were observed for M1 tensile test at 423K, plotted in (a) unit triangle along the tensile direction and (b) {0001} pole figure along the normal direction. The lines connect the grain orientations on both sides of the cracks observed.

were observed, but were unable to be identified, were also plotted in Figure 4.20. 4 grain boundary cracks were observed in the area analyzed for trace analysis. The orientation for grains on both sides of the cracks were plotted and connected by lines in Figure 4.20. The cracks were formed between grains with significant misorientation. The c-axis of the adjacent grains was almost perpendicular to each other. It was also noted that in such cases the c-axis of the grains involved was almost perpendicular to the tensile axis (See Figure 4.20). Multiple deformation modes were observed in 5 grains. The data points for those grains can be seen overlapped in Figure 4.20.

4.1.2.3 523K tension

Figure 4.21 shows the EBSD IPF map in the normal direction and the corresponding {0001} and $\{10\bar{1}0\}$ pole figures from the gage section of the 523K tensile tested sample before deformation. The area in which trace analysis was performed is marked in Figure 4.21a.

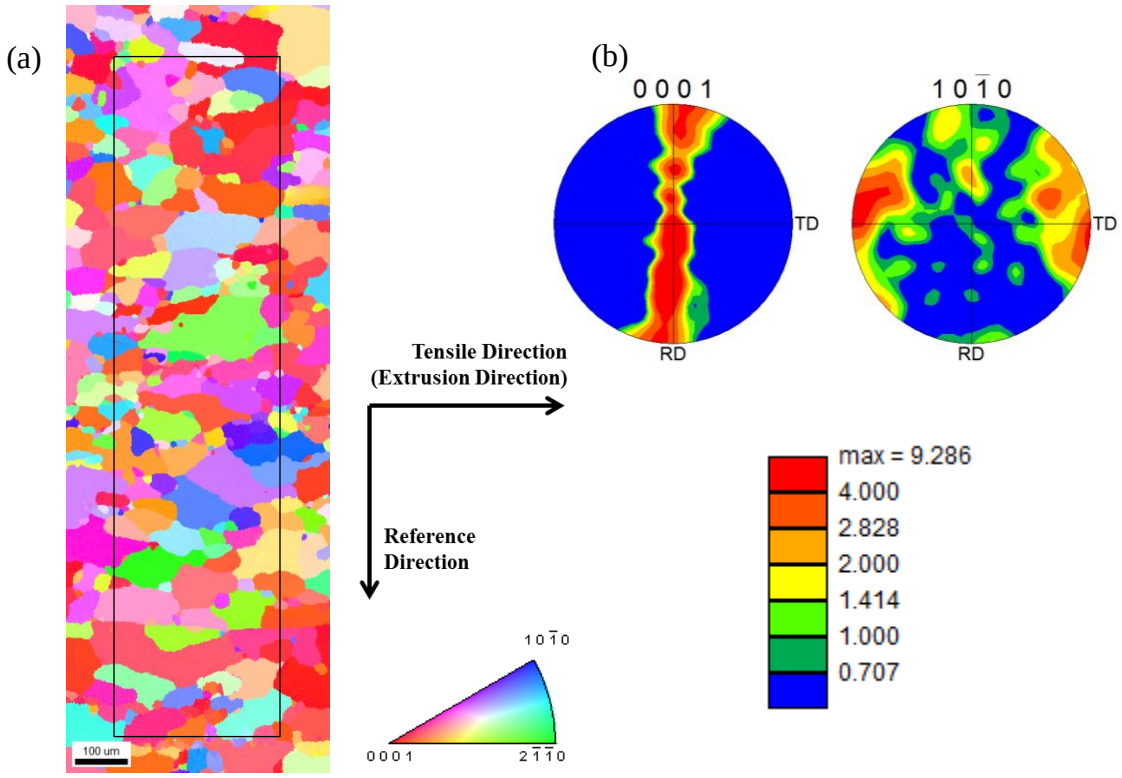

Figure 4.21 (a) EBSD IPF map in the normal direction before deformation and (b) the corresponding {0001} and {10$\bar{1}$0} pole figures from the gage section of M1 specimen tensile tested at 523K. The area on which trace analysis was performed is marked in 4.21a.

Figure 4.22 shows sequential SE SEM images taken from the same area of the 523K tensile tested specimen. Slip traces started to appear at ~0.5% strain. With an increase in strain, more slip traces were observed. Basal <a> slip, prismatic <a> slip, and pyramidal <c+a> slip systems (highlighted by blue, red, and orange lines, respectively, in Figure 4.22c) exhibited similar activities. Basal <a> slip occured at relatively low Schmid factors which ranged from 0.04 to 0.26. Almost all of the prismatic <a> slip happened at high Schmid factors (>0.39). Pyramidal <c+a> slip happened at Schmid factors ranging from 0.01 to 0.48. No extension twins or contraction twins were observed in the area analyzed.

(a) ε ≈ 0%

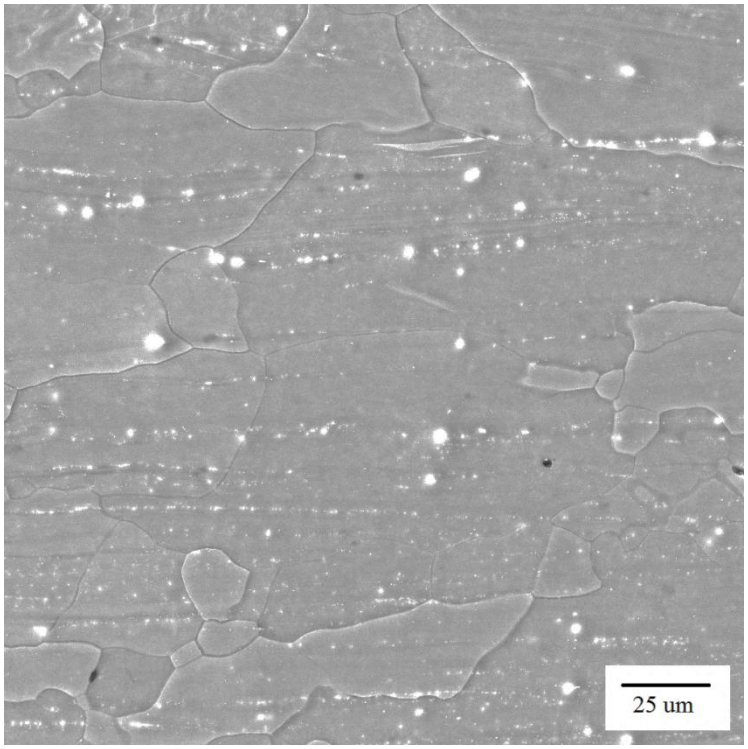

Tensile axis
↔
Extrusion direction

(b) ε ≈ 0.5%

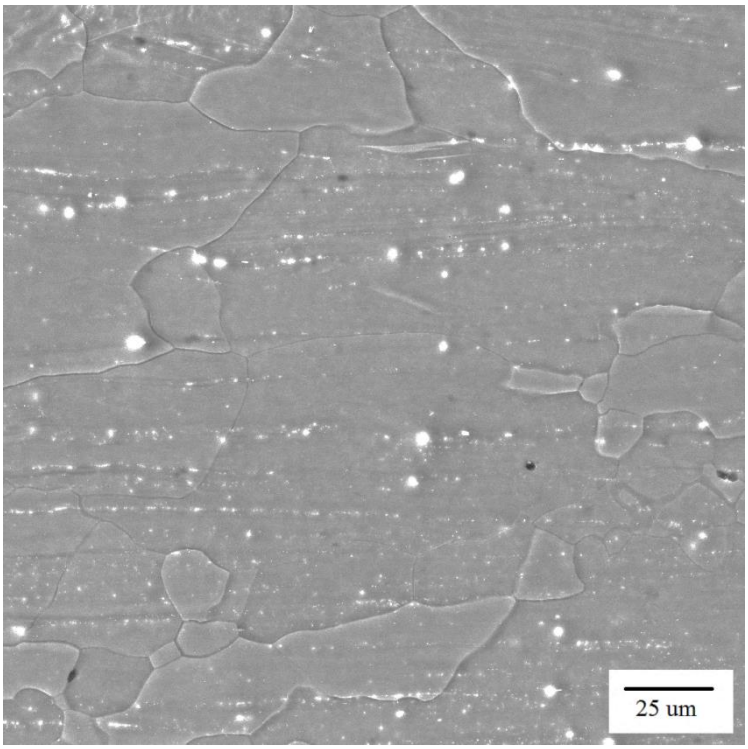

Figure 4.22 Sequential SE SEM images for the M1 specimen tensile tested at 523K: (a) undeformed, (b) ~0.5% strain, (c) ~4.1% strain, and (d) ~7.8% strain. In (c) and (d), slip traces are color coded for basal <a> slip (blue), prismatic <a> slip (red), and pyramidal <c+a> slip (orange). The tensile axis and extrusion direction was horizontal.

Figure 4.22 (cont'd)

(c) ε ≈ 4.1%

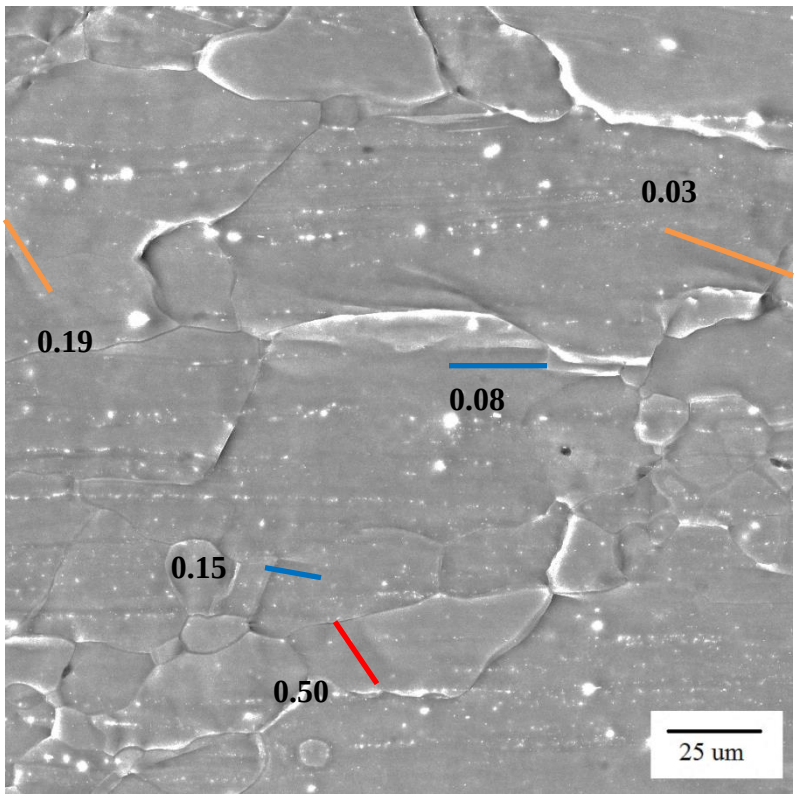

(d) ε ≈ 7.8%

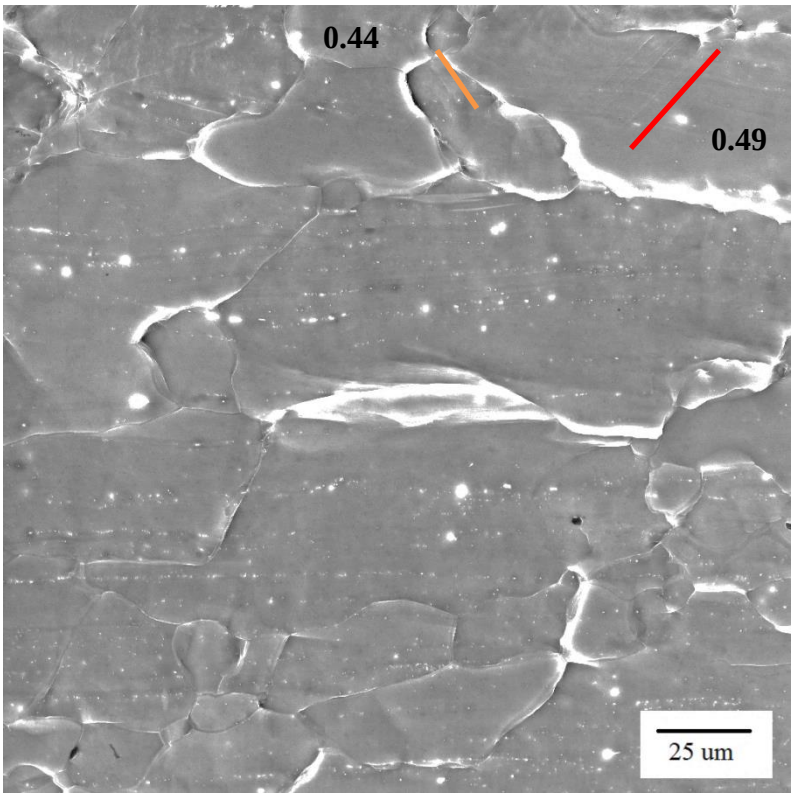

Trace analysis was performed on ~125 grains and slip traces were observed in 51 (51/125≈41%) grains. Out of 51 slip traces observed, 43 were identified. The rest of the slip traces could not be uniquely matched to one slip mode because the trace was common for multiple slip systems. Figure 4.23 plots the number of identified observations of a particular deformation mode versus the global Schmid factor range. In Figure 4.23, basal <a> slip and pyramidal <c+a> slip were distributed over the entire Schmid factor range, while almost all of the prismatic <a> slip happened at high Schmid factors (>0.35). 12 basal <a> (12/43≈28%), 16 prismatic <a> (16/43≈37%), and 15 pyramidal <c+a> (15/43≈35%) slip traces were identified. Thus, the deformation was controlled by slip at 523K, where basal <a> slip, prismatic <a> slip, and pyramidal <c+a> slip exhibited similar relative activities.

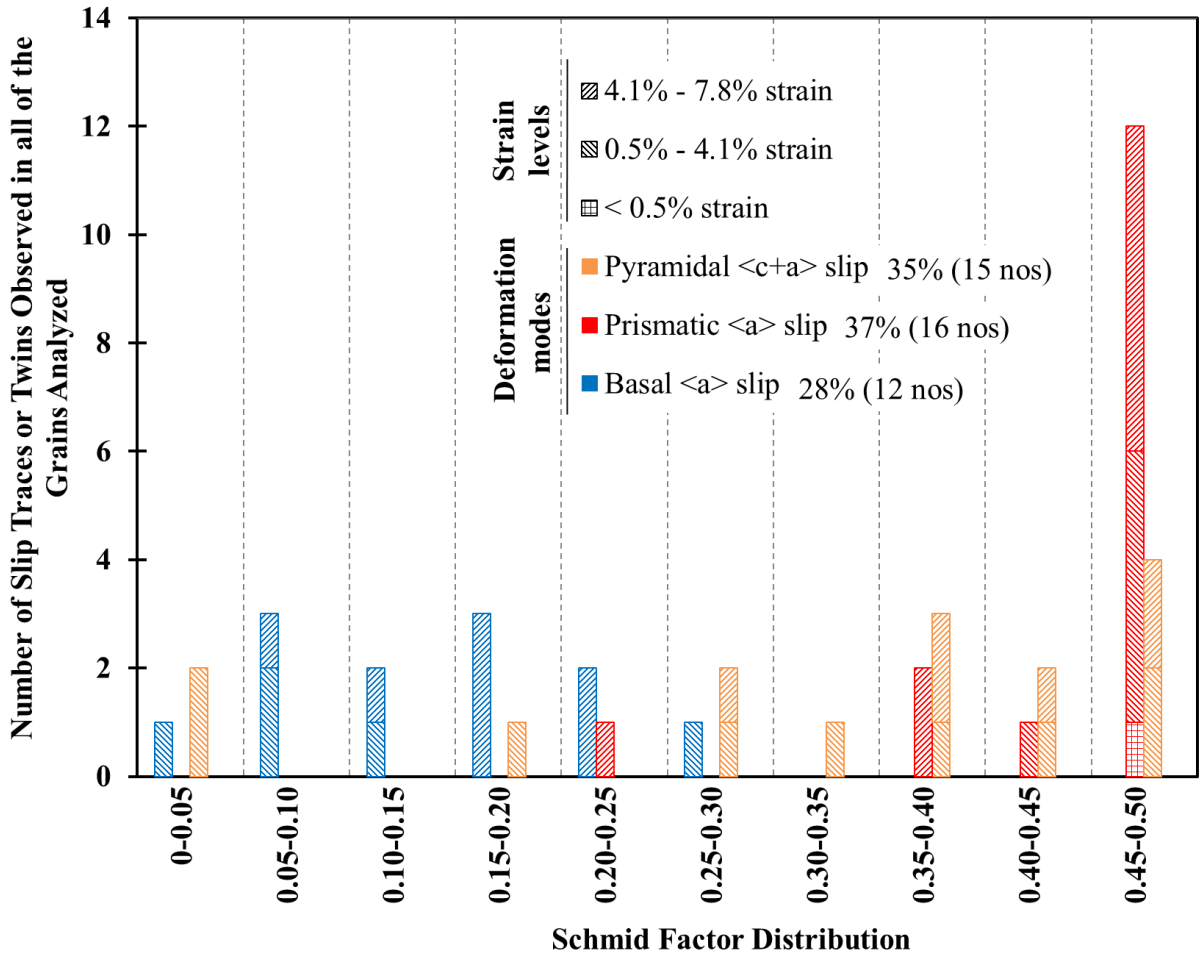

Figure 4.23 A histogram of the Schmid factor distribution of basal <a> slip, prismatic <a> slip, and pyramidal <c+a> slip systems identified for the M1 specimen tensile tested at 523K. Note that no twinning activity was observed in the area analyzed.

Figure 4.24 shows the unit triangle with the individual grain orientations plotted for the grains in which basal <a> slip, prismatic <a> slip, and pyramidal <c+a> slip traces were identified for the M1 sample tensile tested to ~7.8% strain at 523K. 8 grains in which slip traces were observed, but were unable to be uniquely matched, were also plotted in Figure 4.24. 2 grain boundary cracks were observed in the area analyzed. The orientation of the grains on both sides of the observed grain boundary cracks were plotted and connected by lines in Figure 4.24. Multiple deformation modes were observed in 4 grains.

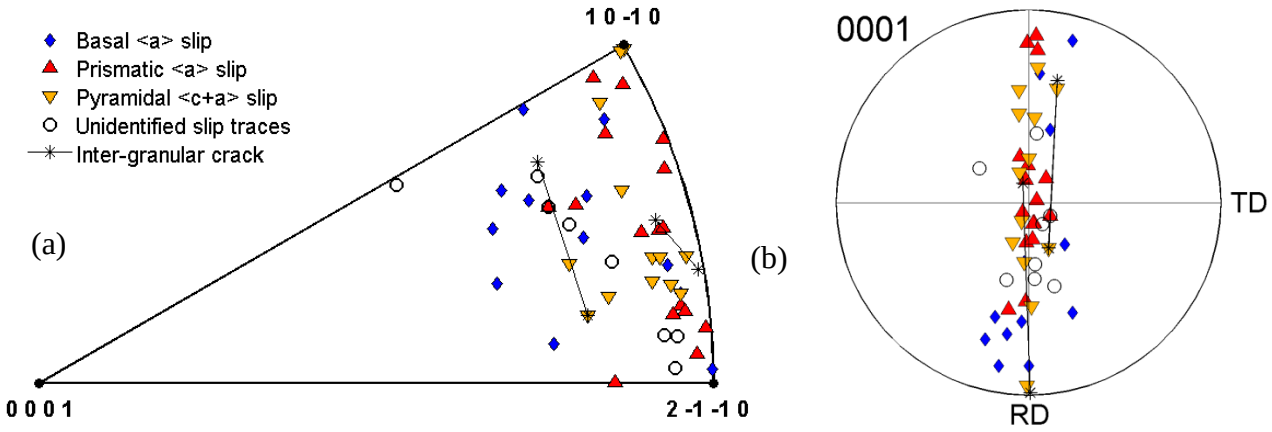

Figure 4.24 The individual grain orientations in which different deformation modes were observed for M1 tensile test at 523K deformed to ~7.8% strain, plotted in (a) unit triangle along the tensile direction and (b) {0001} pole figure along the normal direction. The lines connect the grain orientations on both sides of the cracks observed.

4.2 As-cast Mg-1Mn-0.5Nd (MN10)

4.2.1 Microstructure and texture

Figure 4.25 shows a representative SE SEM image of the as-cast MN10 microstructure. As shown in figure 4.25, equiaxed grains were observed. The average grain diameter was ~361±197μm based on ASTM standards for grain size measurement [ASTM E112-13 2013, Vander Voort 1999]. Figure 4.26 shows the grain size distribution of as-cast MN10.

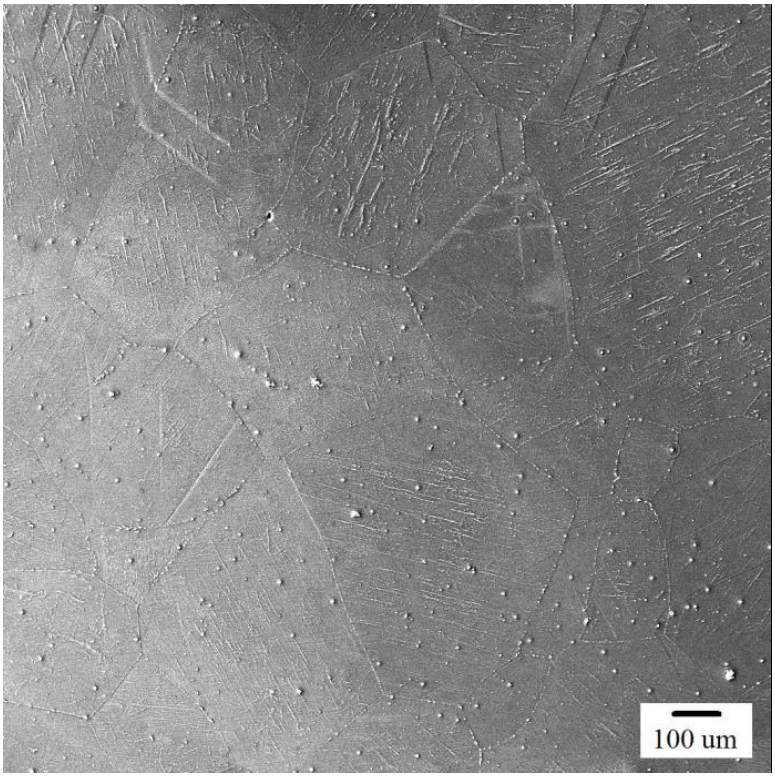

Figure 4.25 SE SEM image of the as-cast MN10 microstructure.

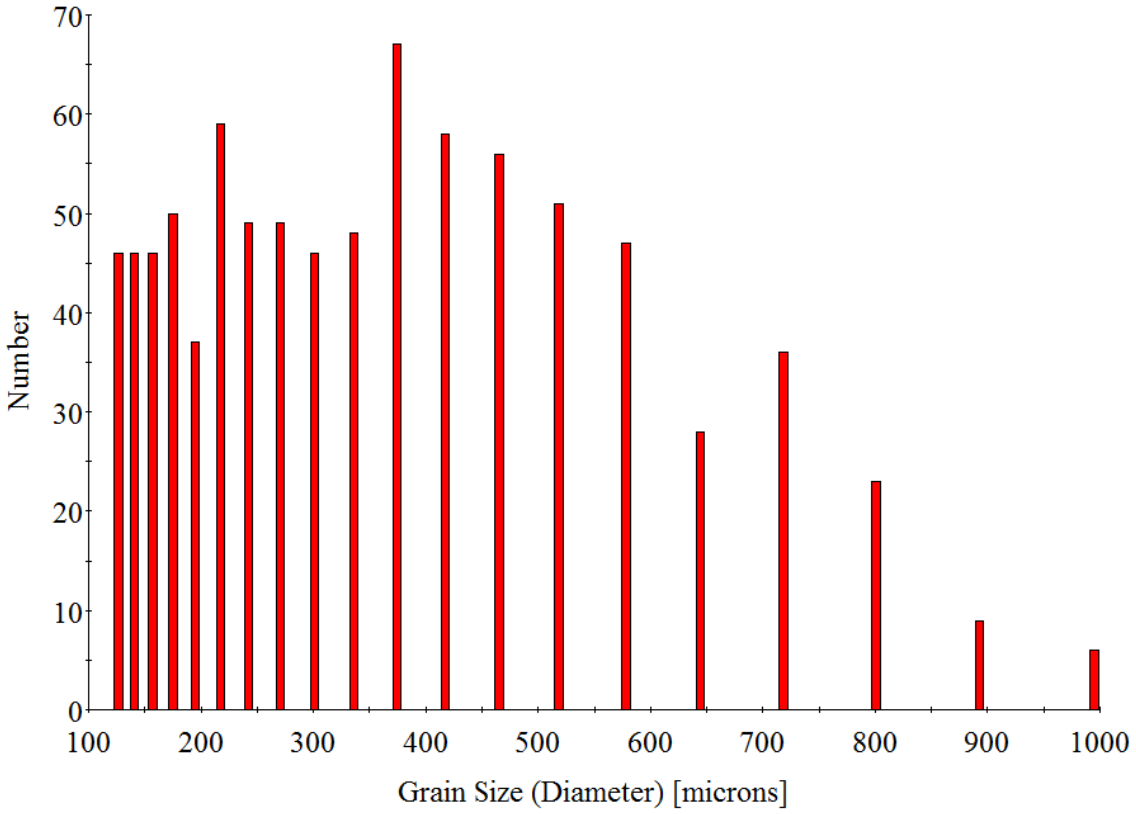

Figure 4.26 The grain size distribution of the as-cast MN10.

Stringers of precipitates were observed within grains in the MN10 as-cast microstructure. These precipitates appeared to be aligned parallel to the basal <a> planes. Figure 4.27a shows the SE SEM image of the microstructure showing the stringers of precipitates within the grains. The orientation of the grains obtained from EBSD analysis is indicated in Figure 4.27a. The volume fraction of the second phase particles measured from the SE SEM images were ~1.50%. Figure 4.27b shows the Dark-field (DF) TEM image of the Mn-rich precipitates on which EDS analysis was performed. The average composition taken from 10 measurements of Mg-Mn precipitates inside the grains was ~Mg-27Mn-1Nd (wt.%). Table 4.2 lists the chemical composition of the 10 Mn-rich precipitates analyzed.

Table 4.2 The chemical composition of the 10 Mn-rich precipitates analyzed inside the grains in the as-cast MN10 microstructure. The values are in wt%.

Observations	Mg	Mn	Nd
1	73.40	26.41	0.19
2	89.84	9.20	0.96
3	69.39	30.03	0.58
4	82.96	15.96	1.08
5	64.73	34.87	0.40
6	80.78	18.92	0.30
7	67.78	30.02	2.20
8	79.57	19.84	0.59
9	84.06	14.18	1.76
10	28.23	70.43	1.34
Average	72.07	26.99	0.94

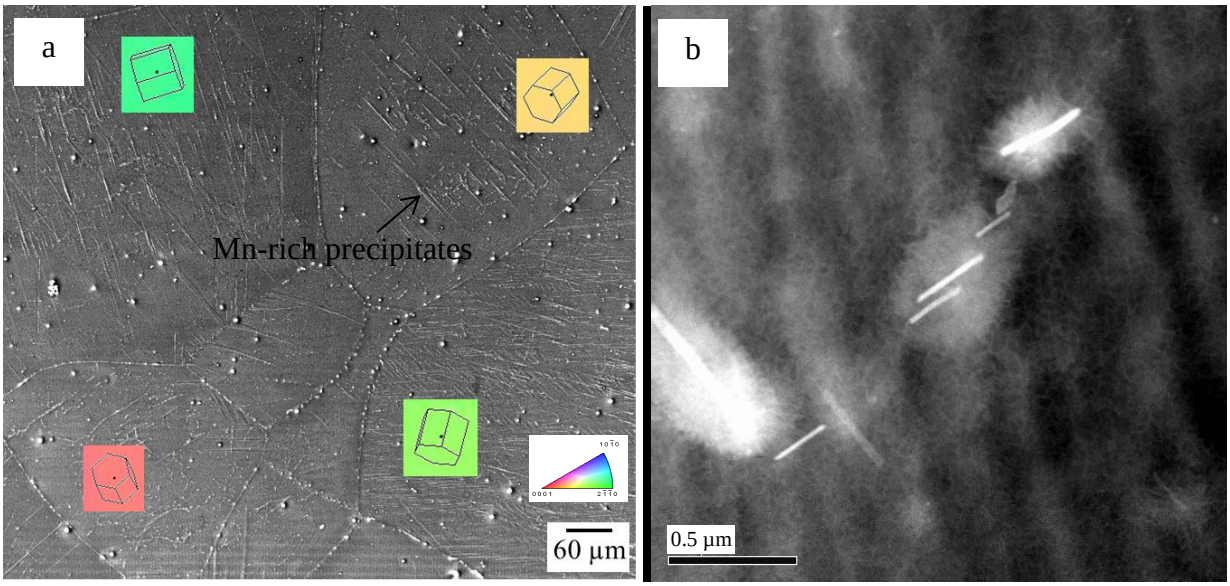

Figure 4.27 (a) SE SEM image showing the Mn-rich precipitates aligned parallel to the basal planes and (b) DF TEM image of the Mn-rich precipitates in the MN10 as-cast microstructure. In (a), the orientation of the grains is indicated as HCP unit cells as obtained from EBSD analysis.

Irregularly shaped Nd-rich and Mn-rich precipitates were observed in the MN10 as-cast microstructure in a randomly distributed fashion. Figure 4.28a and 4.28b shows the DF TEM

images of the irregularly shaped Mn-rich and Nd-rich precipitates, respectively. 8 observations on Nd-rich precipitates inside grains showed an average composition of ~Mg-17Mn-30Nd. Table 4.3 shows the chemical composition of the 8 Nd-rich precipitates analyzed.

Table 4.3 The chemical composition of the 8 Nd-rich precipitates analyzed inside the grains in as-cast MN10 microstructure. The values are in wt%.

Observations	Mg	Mn	Nd
1	46.04	35.91	18.05
2	77.85	0.04	22.12
3	50.78	23.51	25.71
4	59.87	12.86	27.27
5	64.72	8.24	27.04
6	64.06	0.90	35.05
7	45.97	0.23	53.80
8	10.73	57.68	31.58
Average	52.50	17.42	30.08

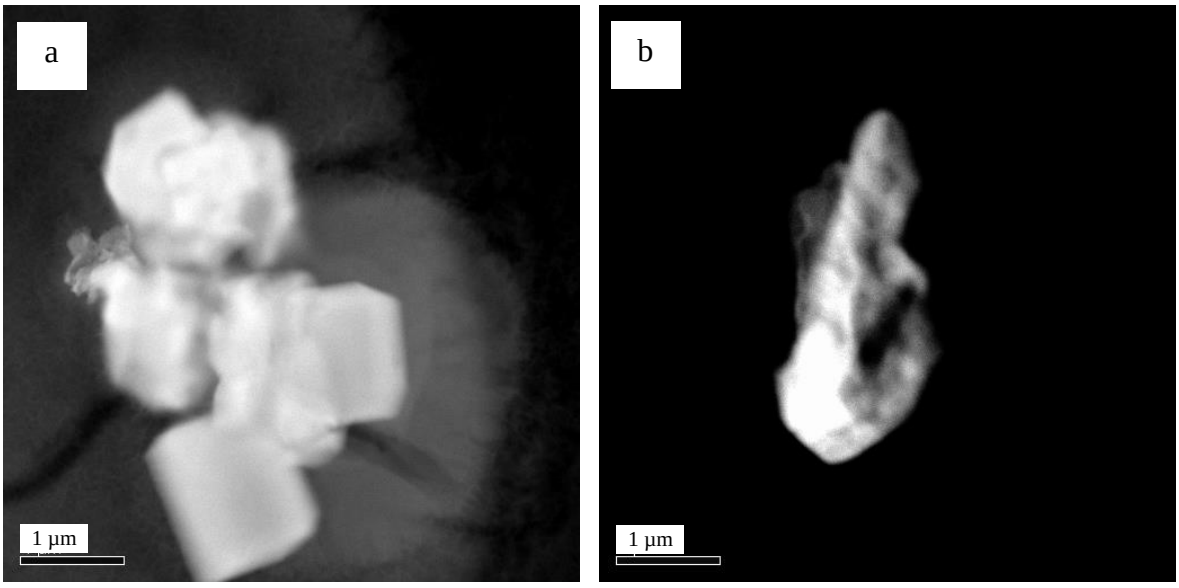

Figure 4.28 DF TEM images of (a) Mn-rich and (b) Nd-rich precipitates observed in the MN10 as-cast microstructure.

EDS performed on the matrix showed an average composition of ~Mg-1Mn-0.5Nd (wt.%) from 2 observations. Table 4.4 lists the chemical composition obtained from the 2 observations on the matrix. Mn-rich precipitates were also observed at the grain boundaries. The average composition of the precipitates at grain boundaries was ~Mg-42Mn-3Nd (wt.%) from 5 observations. Table 4.5 lists the chemical composition of the 5 Mn-rich precipitates analyzed at the grain boundaries. Figure 4.29 shows the DF TEM image of a grain boundary in MN10 as-cast microstructure in which Mn-rich precipitates were observed.

Table 4.4 The chemical composition of the as-cast MN10 matrix. The values are in wt%.

Observations	Mg	Mn	Nd
1	98.22	1.25	0.53
2	98.73	0.73	0.54
Average	98.48	0.99	0.54

Table 4.5 The chemical composition of the 5 Mn-rich precipitates analyzed at the grain boundaries in as-cast MN10 microstructure. The values are in wt%.

Observations	Mg	Mn	Nd
1	38.69	59.96	1.35
2	58.21	38.16	3.63
3	54.46	44.15	1.39
4	47.83	47.05	5.12
5	73.93	21.64	4.43
Average	54.62	42.19	3.18

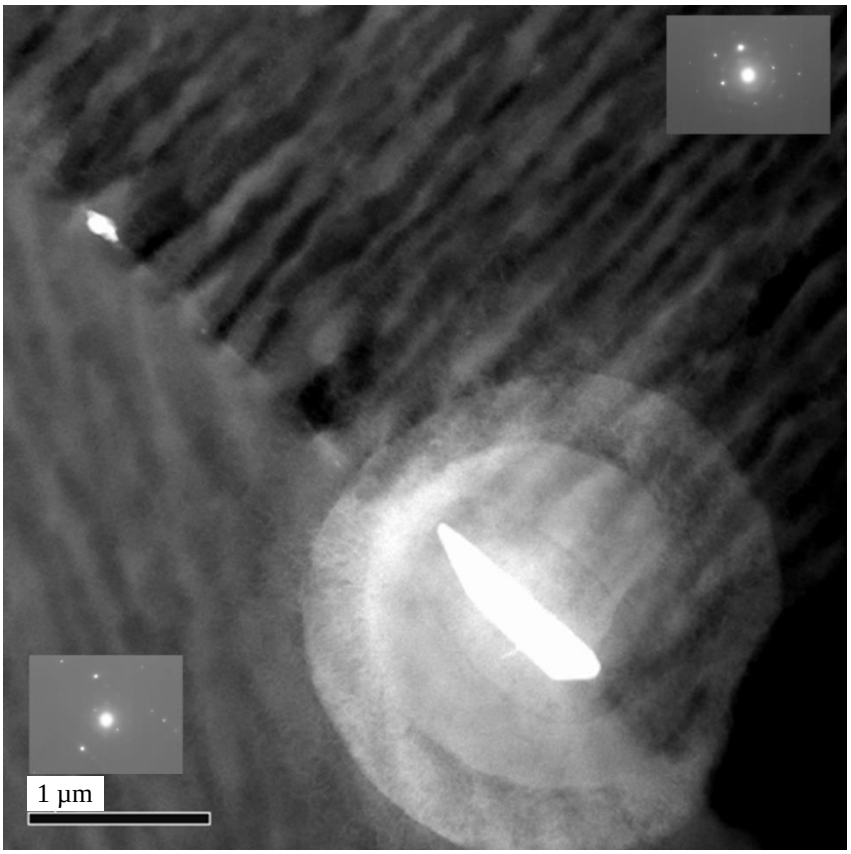

Figure 4.29 DF TEM image of a grain boundary in MN10 as-cast microstructure in which Mn-rich precipitates were observed. The selective area diffraction (SAD) patterns from both grains are shown in the inset.

Figure 4.30 shows the representative texture of as-cast MN10 in the form of {0001} and $\{10\bar{1}0\}$ pole figures obtained using EBSD. The texture shown in Figure 4.30 was obtained from an area containing ~850 grains. Figure 4.31 shows the EBSD IPF map along the normal direction of the area from which the pole figures shown in Figure 4.30 was obtained. The image shown in Figure 4.31 was obtained by combining EBSD IPF maps of the gage section of 3 separate in-situ samples with similar orientations (normal direction of the sample perpendicular to the radial direction of cast billet) but from different regions of the cast billet. The pole figures show a weak texture. This type of texture is commonly observed in as-cast Mg alloys [Agnew et al. 2001, Pérez-Prado et al. 2004].

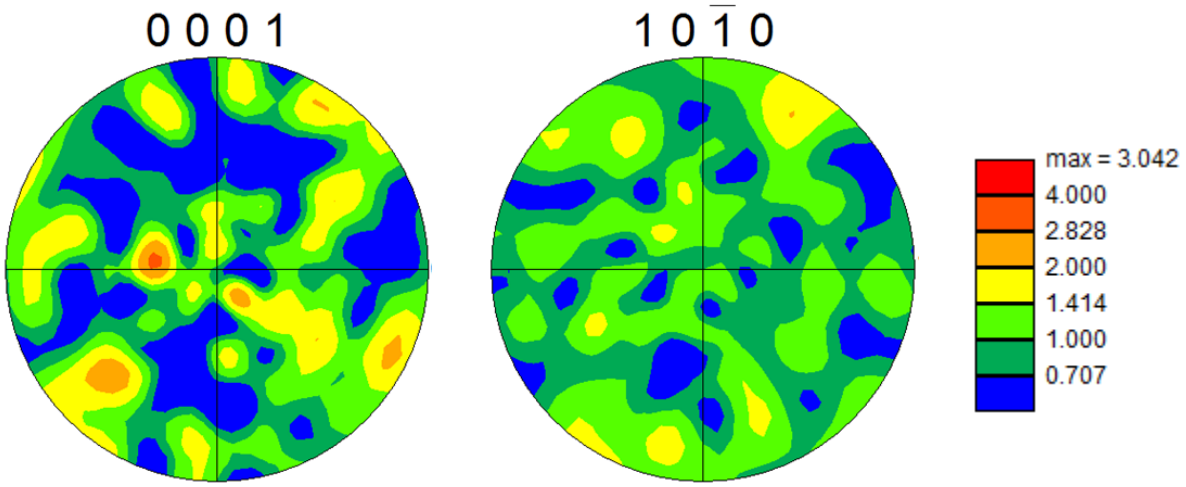

Figure 4.30 Representative texture of as-cast MN10 in the form of {0001} and {10$\bar{1}$0} pole figures.

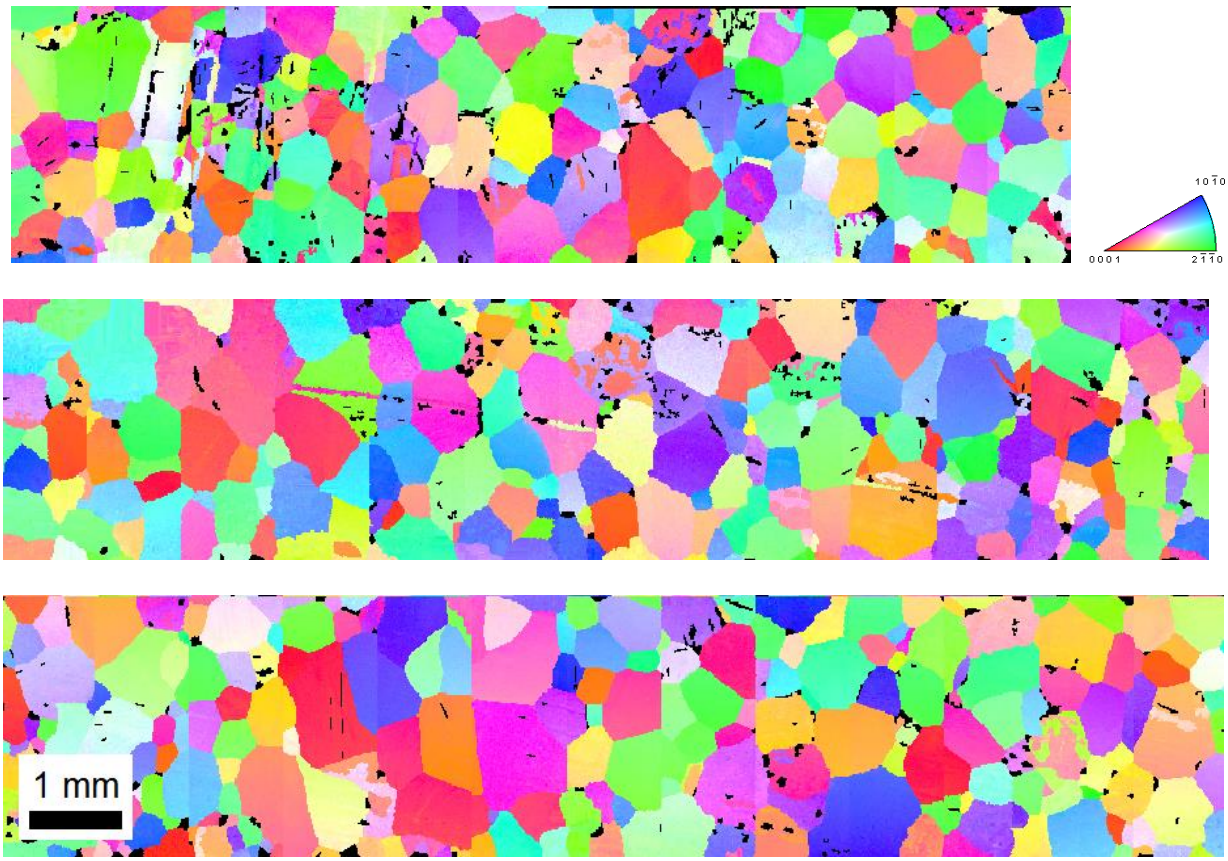

Figure 4.31 EBSD IPF map of the areas from which the pole figures shown in Figure 4.30 was obtained.

4.2.2 In-situ tension

In-situ tensile tests were performed on the as-cast MN10 at 323K, 423K, and 523K. One test was performed for each temperature. EBSD data was acquired before and after deformation, and slip/twin trace analysis was performed. Figure 4.32 shows the stress versus displacement plots for the 323K, 423K, and 523K tensile tests on the as-cast MN10. The stress drops indicate the stress relaxation that occurred when the tests were paused for imaging. None of the specimens were taken to failure in order to facilitate EBSD mapping without further sample preparation. Table 4.6 lists the approximate YS, UTS, and the maximum strain levels attained in each experiment.

Table 4.6 As-cast MN10 tensile property comparison between different test conditions.

Test Temperature	YS(MPa)	UTS (MPa)	Maximum strain (%)
323K	~36	~102	~9.9%
423K	~30	~75	~9.4%
523K	~23	~68	~10.7

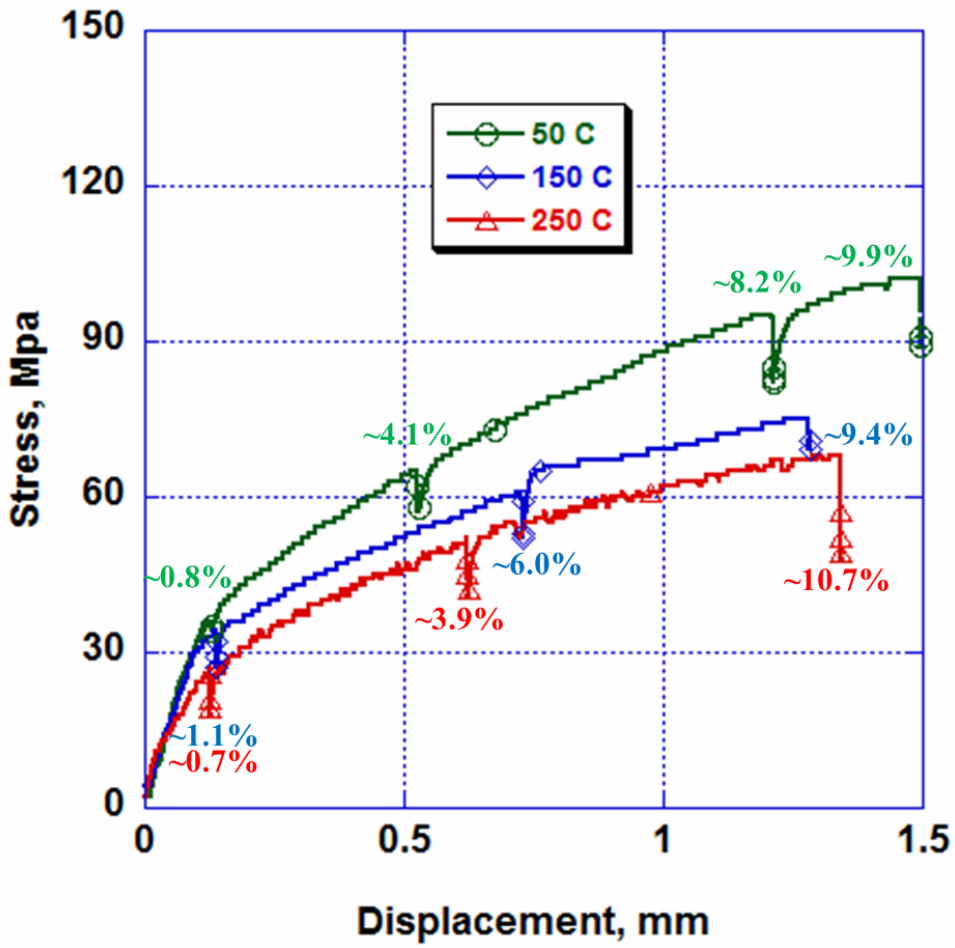

Figure 4.32 Representative stress vs. displacement plots for as-cast MN10 sample tensile tested at 323K, 423K, and 523K. The stress drops indicate the stress relaxation that occurred when the tests were interrupted for imaging. The displacement values include displacements in both the gage section and the grip region. Approximate local strain values are indicated in the plot.

4.2.2.1 323K tension

Figure 4.33 shows the EBSD IPF map in the normal direction from the gage section of the 323K tensile tested sample before and after deformation. Extension twins were observed in the undeformed microstructure (See Figure 4.33a). These twins were expected to be formed during the casting solidification process. In Figure 4.33a, the twins are marked by black arrows.

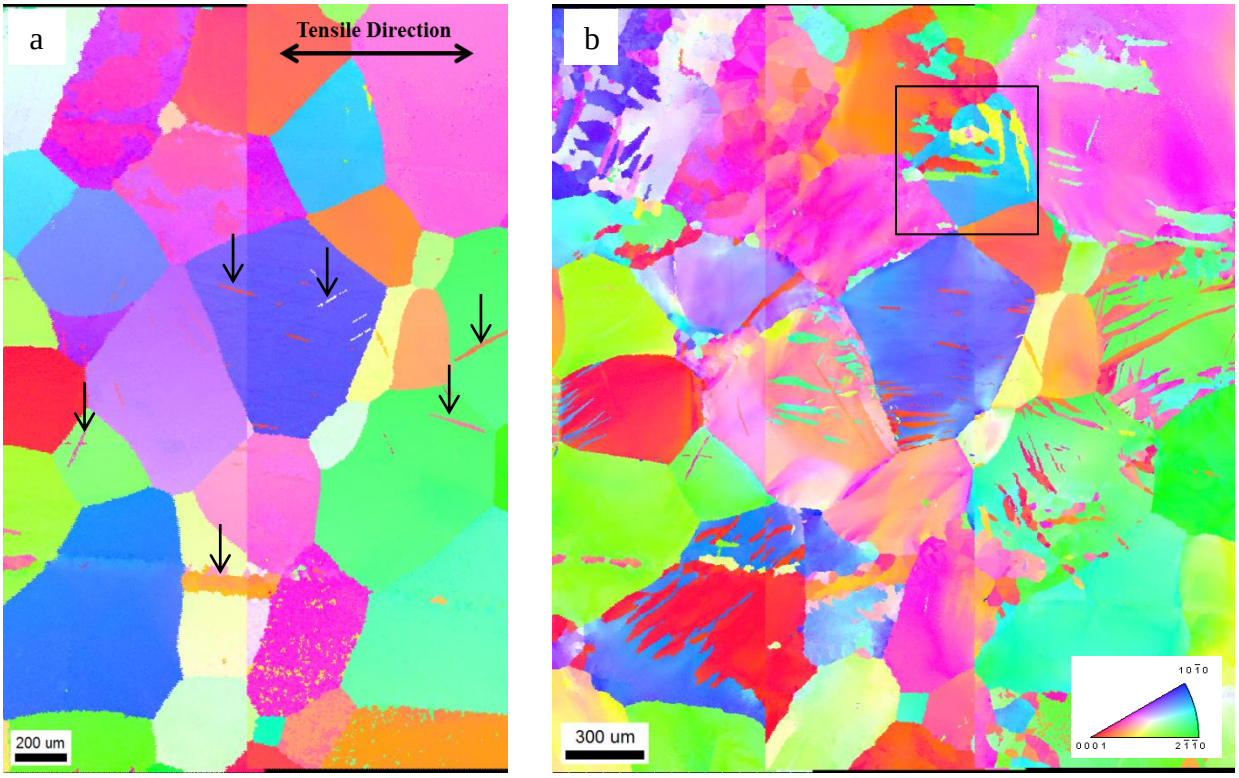

Figure 4.33 EBSD IPF map in the normal direction of the as-cast MN10 specimen tensile-tested at 323K (a) before deformation and (b) after deformation to ~9.9% strain. The extension twins observed in the undeformed microstructure are marked by black arrows in (a).

Figure 4.34 shows the sequential SE SEM images taken from the same area of the 323K tensile-tested specimen. Extension twins started to appear during the early stages of deformation at ~0.8% strain and basal <a> slip started to appear at ~4.1% strain.

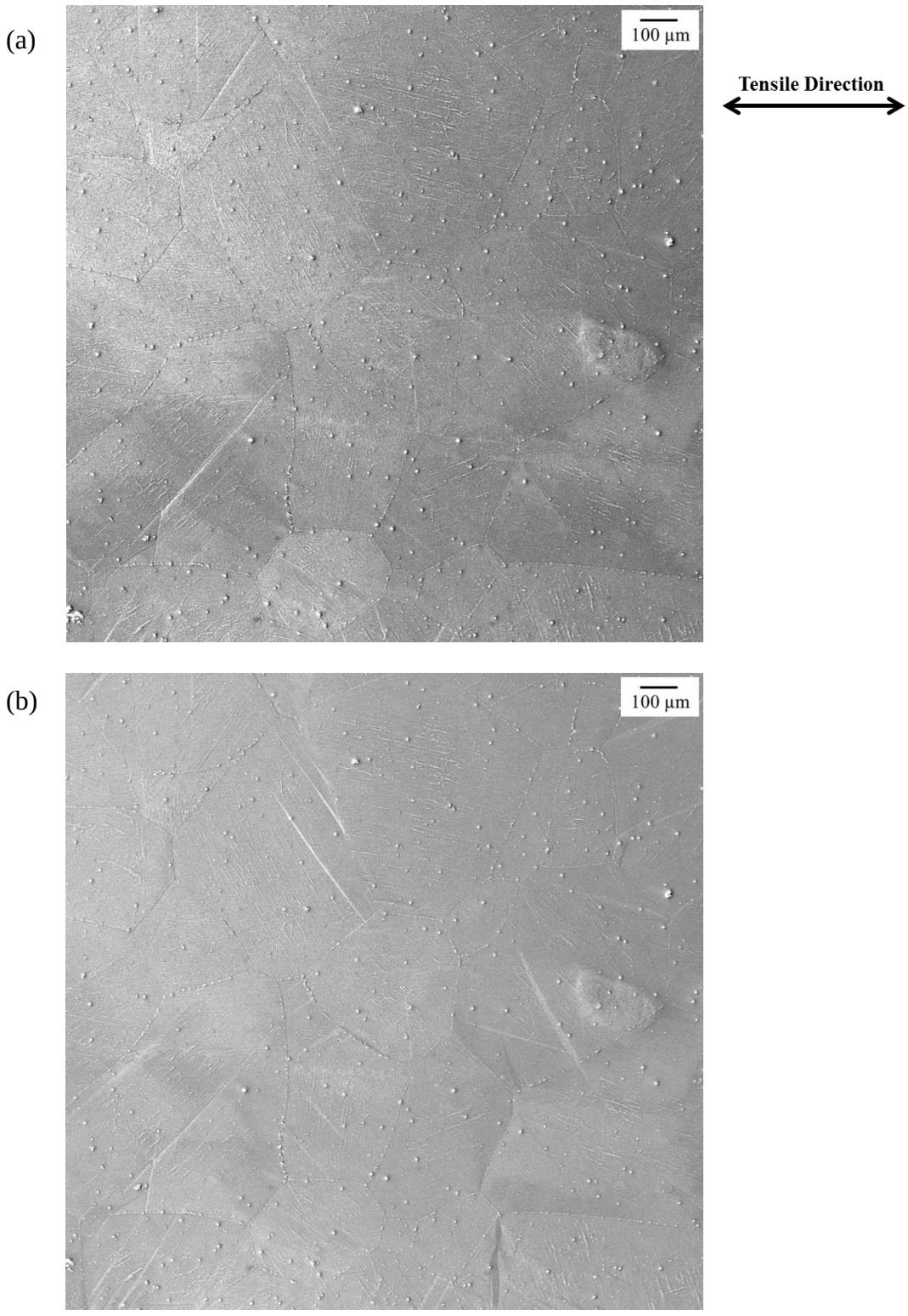

Figure 4.34 Sequential SE SEM images for the MN10 as-cast specimen tensile tested at 323K: (a) undeformed, (b) ~0.8% strain, (c) ~4.1% strain, and (d) ~8.2% strain. In (c) and (d), the slip traces are color coded for basal <a> slip (blue), prismatic <a> slip (red), and pyramidal <c+a> slip (orange). The corresponding Schmid factor values are given in (c) and (d).

Figure 4.34 (cont'd)

(c)

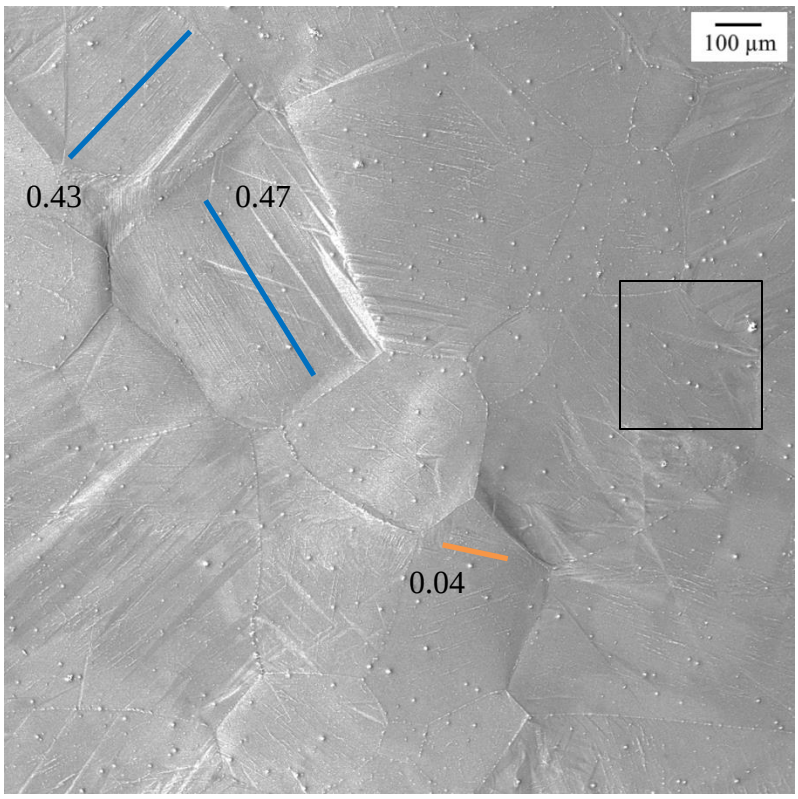

(d)

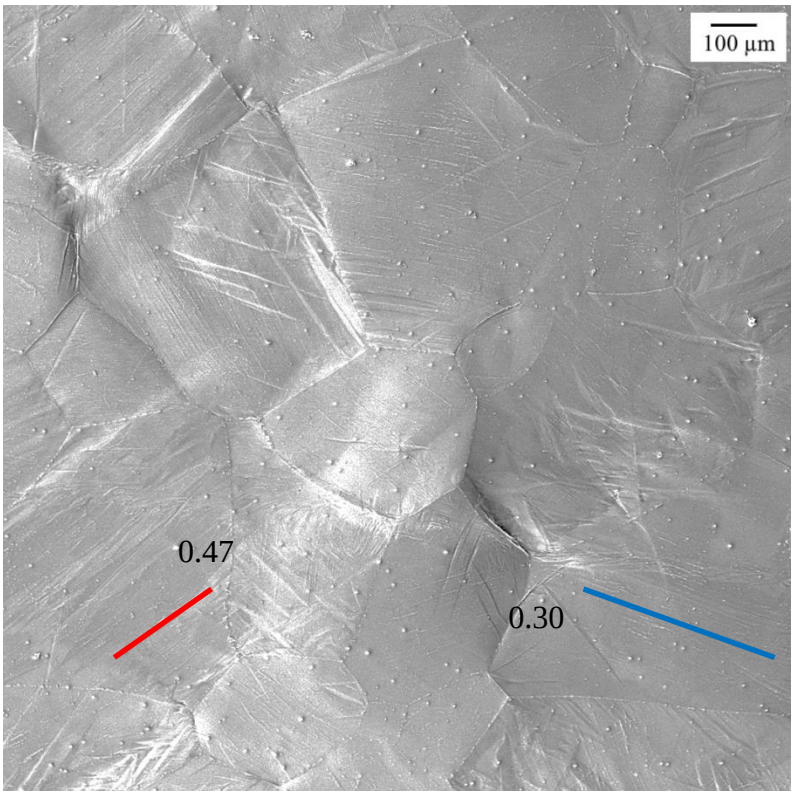

Some of the extension twins developed into $(10\bar{1}2) - (01\bar{1}2)$ double twins. Four such double twins were observed in the area analyzed. $(10\bar{1}2) - (01\bar{1}2)$ double twins ideally result in a misorientation of 60° about $< 10\bar{1}0 >$ [Mu et al. 2012]. Figure 4.35 shows the area highlighted by a black box in Figure 4.33b. The extension twins and the $(10\bar{1}2) - (01\bar{1}2)$ double twins observed in this region are highlighted in Figure 4.35. It is noted that multiple extension twin variants were activated in the grain shown in Figure 4.35.

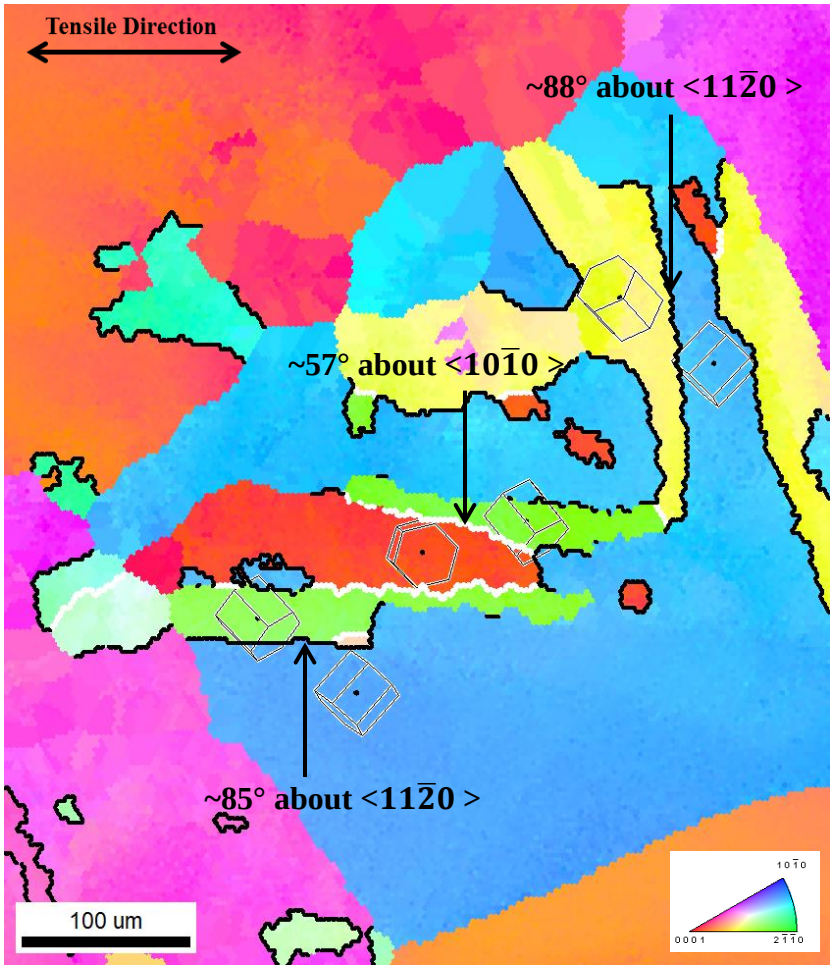

Figure 4.35 EBSD IPF map of the region highlighted by a black box in Figure 4.33b. The extension twin boundaries are highlighted by black lines and the $(10\bar{1}2) - (01\bar{1}2)$ double twin boundaries are highlighted by white lines. The HCP unit cells are overlaid indicating the misorientation between parent grain and the twinned region.

Trace analysis was performed on approximately 30 grains from the microstructural patch shown in Figure 4.33a. 10 slip traces were observed in this region in which 8 were basal <a> slip, 1 was prismatic <a> slip, and 1 was pyramidal <c+a> slip. The pyramidal slip trace was observed to be localized near the grain boundary (See Figure 4.34c and 4.34d) suggesting that its activation might be assisted by local stress heterogeneities. Four of the observed slip traces were formed inside the twinned region. Three of them were basal <a> slip and one was prismatic <a> slip. Figure 4.36 shows a high magnification image of the area marked by the black box in Figure 4.34c indicating the activation of basal <a> slip inside the extension twinned region. Wavy slip traces were observed in one grain in which pyramidal <c+a> slip was identified (See Figure 4.34c and 4.34d). Multiple slip/twin traces were observed in some of the grains.

Figure 4.37 plots the number of identified observations of a particular deformation versus the corresponding global Schmid factor range. 14 twin traces were observed and all of them were extension twins. ~79% (11 out of 14) extension twins were observed at Schmid factor values less than 0.20, and two of these were observed at Schmid factors less than 0. All of the basal <a> slip was observed at Schmid factors higher than 0.25. Extension twinning and basal <a> slip controlled the deformation in the MN10 as-cast specimen tensile tested at 323K.

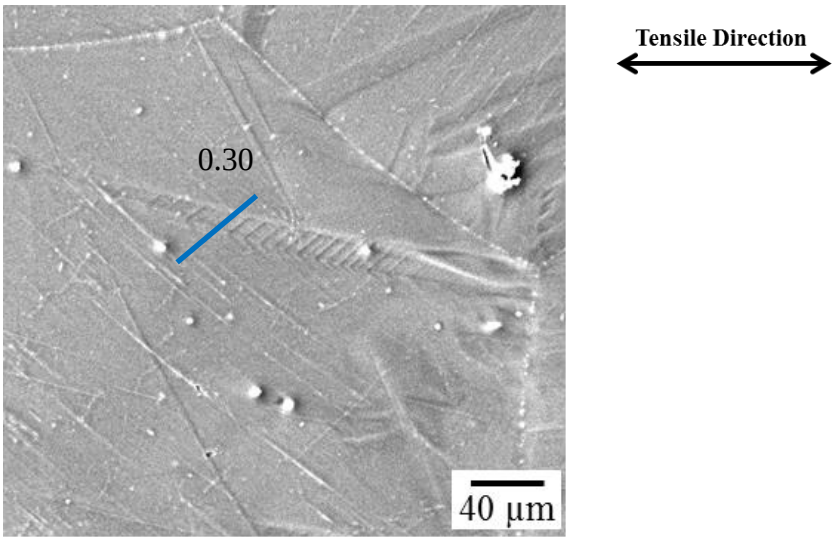

Figure 4.36 High magnification SE SEM image of the area highlighted by the black box in Figure 4.34c. The basal <a> slip observed within the extension twinned region at ~4.1% strain is marked along with its corresponding Schmid factor value.

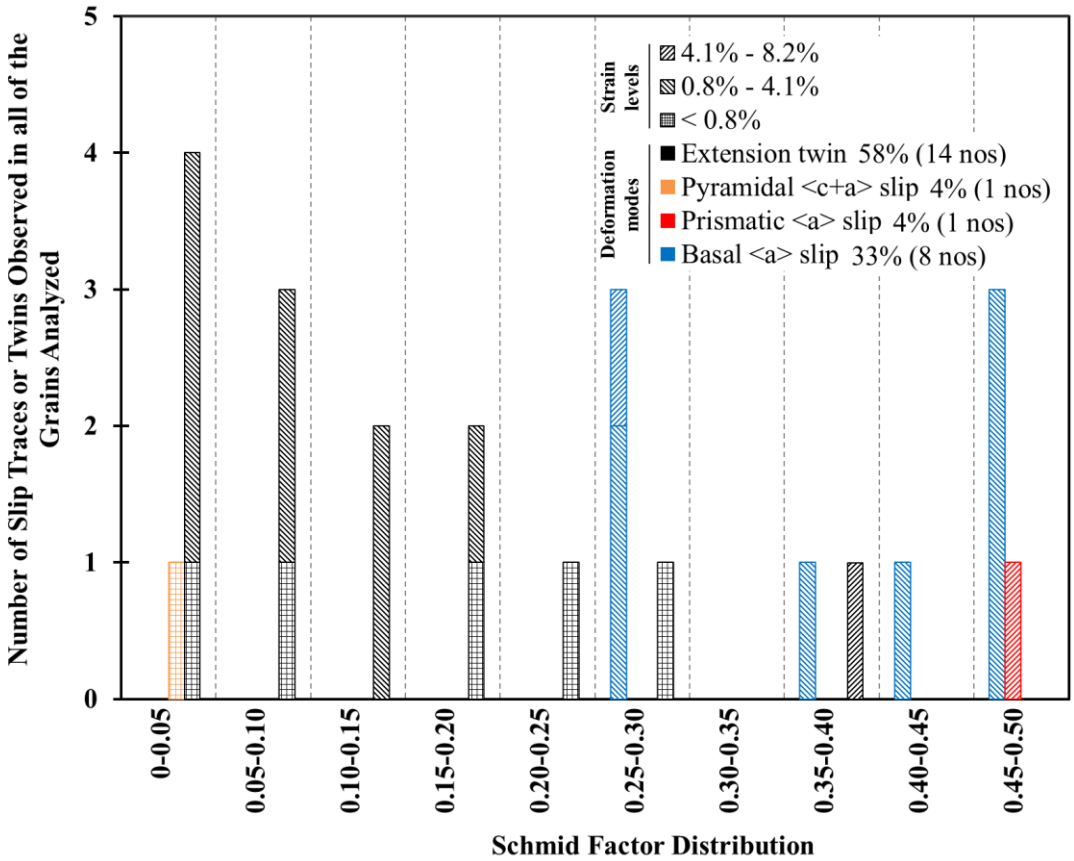

Figure 4.37 A histogram of the Schmid factor distribution of basal <a>, prismatic <a>, pyramidal <c+a>, and extension twins observed in the MN10 as-cast specimen tensile tested at 323K.

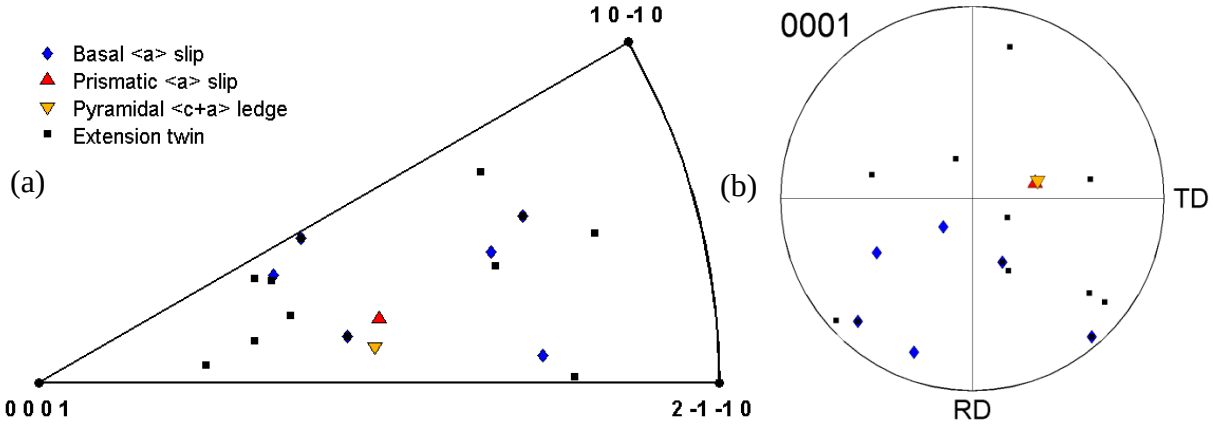

Figure 4.38 The individual grain orientations in which different deformation modes were observed for the MN10 as-cast specimen tensile tested at 323K, plotted in (a) unit triangle along the tensile direction and (b) {0001} pole figure along the normal direction.

Figure 4.38a shows the orientation of the grains in which different deformation modes were identified plotted in a unit triangle along the tensile direction for the as-cast MN10 sample tensile tested at 323K. Figure 4.38b shows the same data from Figure 4.38a plotted in a {0001} pole figure along the normal direction.

4.2.2.2 423K tension

Figure 4.39 shows the EBSD IPF map in the normal direction from the gage section of the 423K tensile tested sample before and after deformation to ~9.4% strain. Extension twins observed in the undeformed microstructure are marked by black arrows in Figure 4.39a.

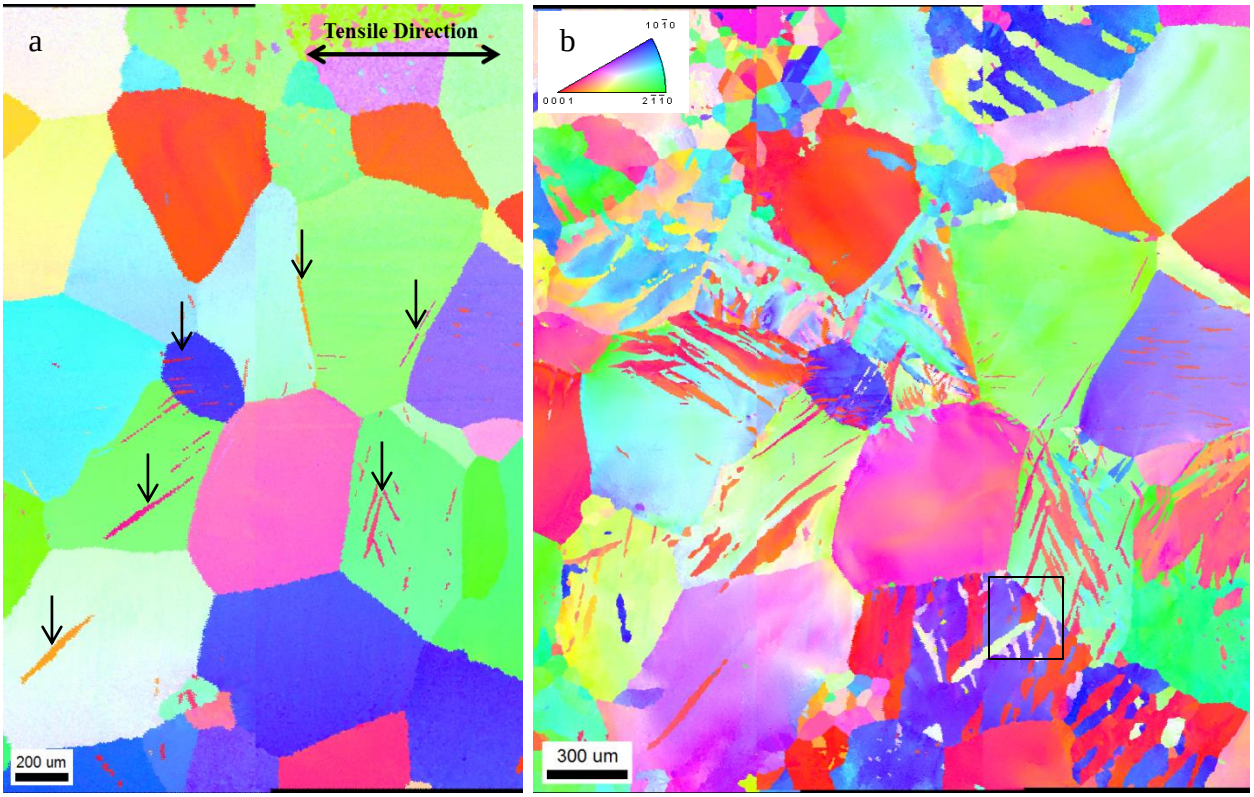

Figure 4.39 EBSD IPF map in the normal direction of the MN10 as-cast specimen tensile-tested at 423K (a) before deformation and (b) after deformation to ~9.4% strain. The extension twins observed in the undeformed microstructure are marked by black arrows in (a).

Figure 4.40 shows the sequential SE SEM images taken from the same area of the gage section of the 423K tensile-tested specimen. Extension twins started to appear at ~1.1%. Basal <a> slip, prismatic <a> slip, and pyramidal <c+a> slip were first observed at ~6.0% strain.

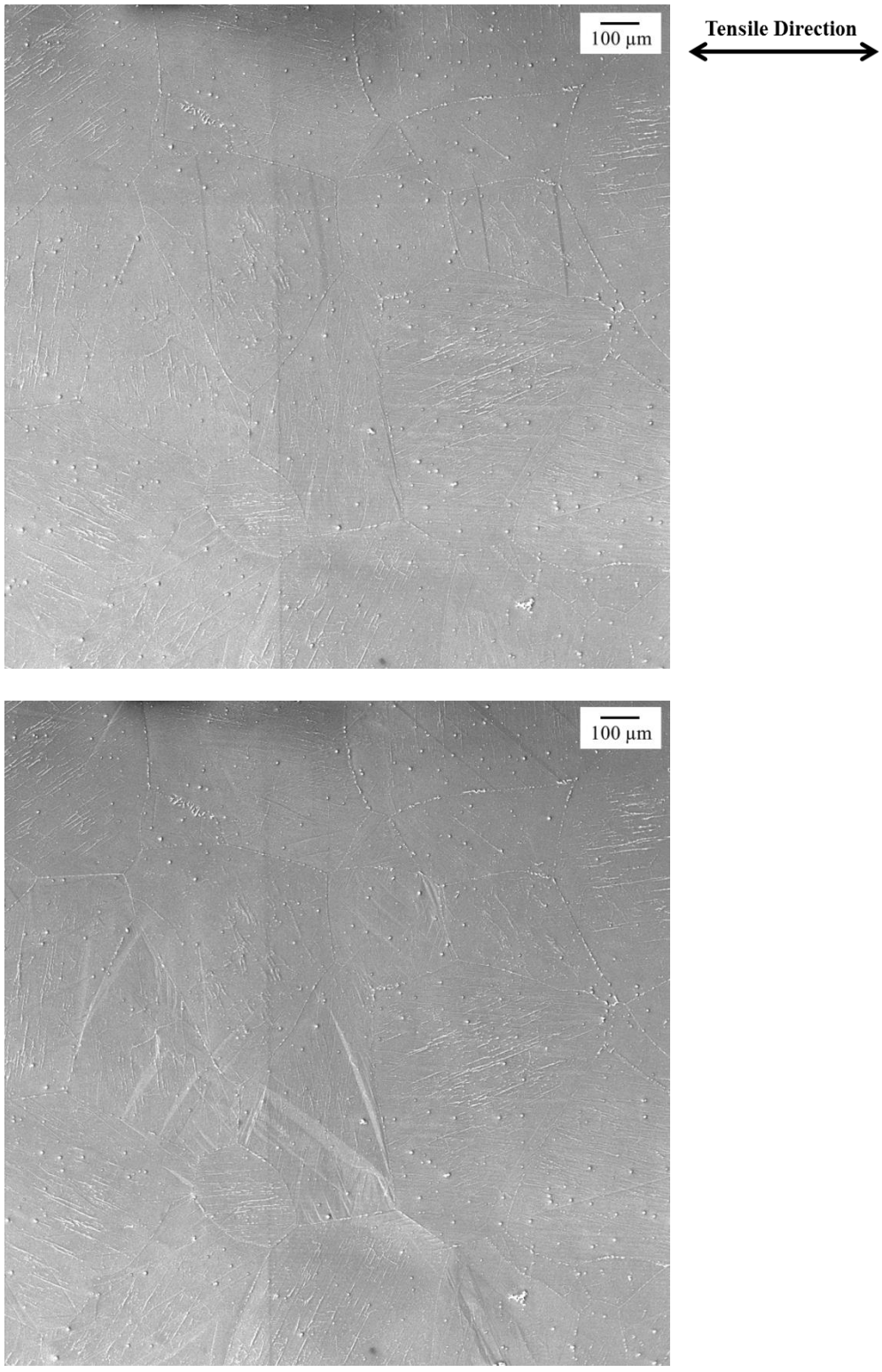

Figure 4.40 Sequential SE SEM images for the MN10 as-cast specimen tensile tested at 423K: (a) undeformed, (b) ~1.1% strain, (c) ~6.0% strain, and (d) ~9.4% strain. In (c) and (d), the slip traces are color coded for basal <a> slip (blue), prismatic <a> slip (red), and pyramidal <c+a> slip (orange). The corresponding Schmid factor values are given in (c) and (d).

Figure 4.40 (cont'd)

(c)

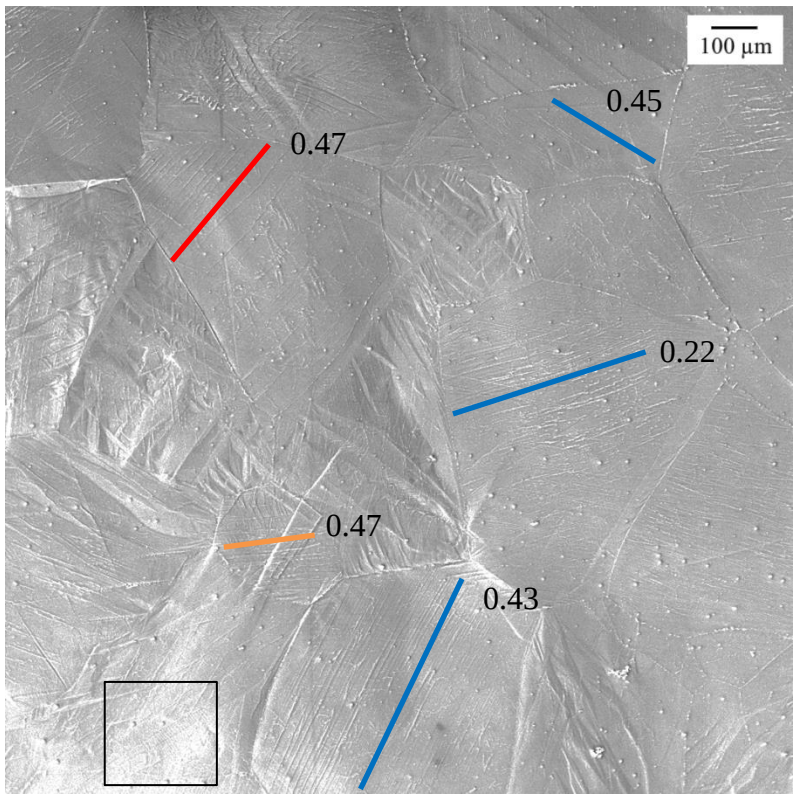

(d)

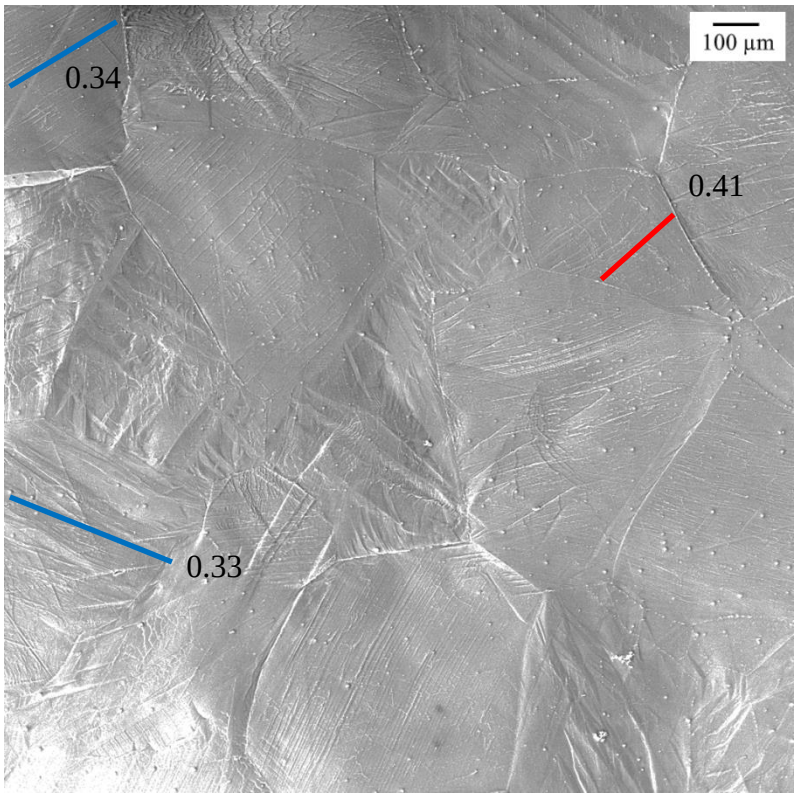

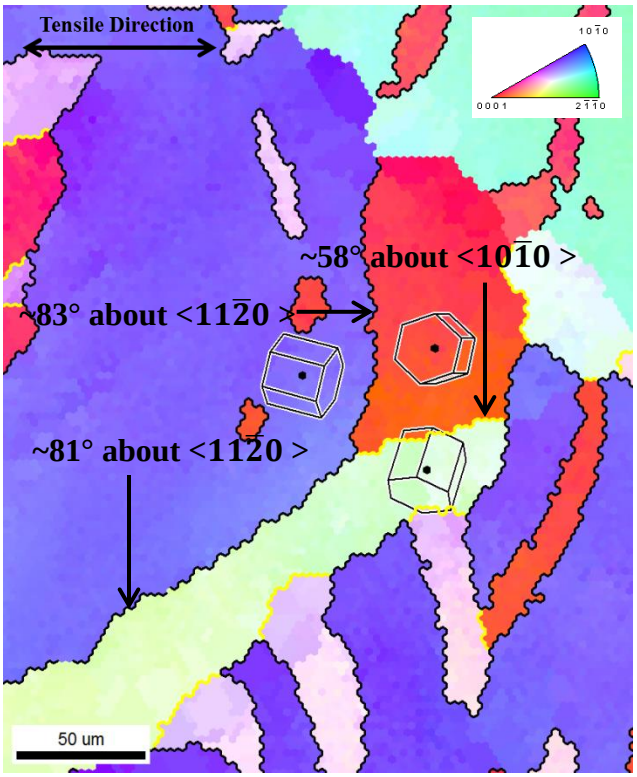

Figure 4.41 EBSD IPF map of the region highlighted by the black box in Figure 4.39b. The extension twin boundaries are highlighted by black lines and the $(10\bar{1}2) - (01\bar{1}2)$ double twin boundaries are highlighted by yellow lines. The HCP unit cells are overlaid indicating the misorientation between parent grain and the twinned region.

Four $(10\bar{1}2) - (01\bar{1}2)$ double twins were observed in the microstructural patch analyzed. Figure 4.41 shows the area highlighted by the black box in Figure 4.39b. The extension twins and the $(10\bar{1}2) - (01\bar{1}2)$ double twins observed in this region are highlighted in Figure 4.41.

Trace analysis was performed on approximately 35 grains from the microstructural patch shown in Figure 4.39a. 21 slip traces were observed in this region in which 14 were basal <a> slip, 4 were prismatic <a> slip, and 3 were pyramidal <c+a> slip. Three of the observed slip traces were formed inside the twinned region. Two of them were basal <a> slip and one was prismatic <a> slip. Figure 4.42 shows the high magnification image of the area marked by the

black box in Figure 4.40c indicating the activation of prismatic <a> slip inside the extension twinned region. Wavy slip traces were observed in 11 grains (See Figure 4.40d) suggesting that cross-slip happened during the deformation.

Figure 4.43 plots the number of identified observations of a particular deformation versus the corresponding global Schmid factor range. 16 twin traces were observed and all of them were extension twins. ~64% (9 out of 14) basal <a> slip traces were observed at Schmid factors higher than 0.30. More non-basal <a> slip activity was observed in the MN10 as-cast specimen at 423K compared to 323K. However, similar to 323K, extension twinning and basal <a> slip controlled the deformation in MN10 as-cast specimen tensile tested at 423K. It is noted that multiple slip and twin traces were observed in some of the grains analyzed.

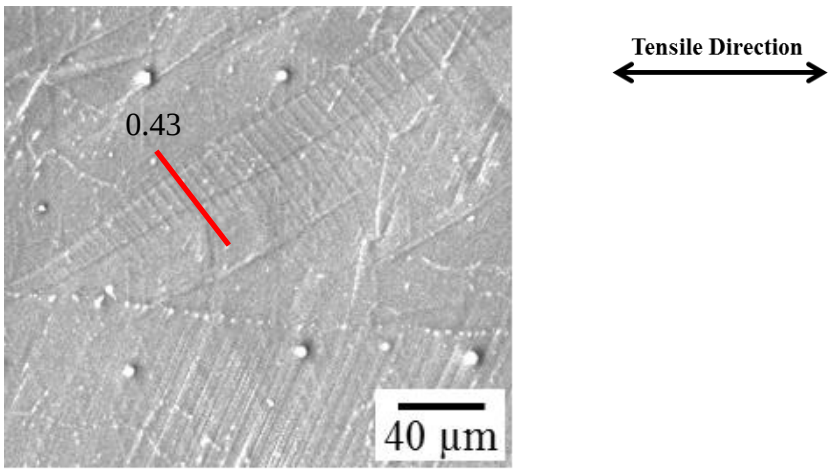

Figure 4.42 High magnification SE SEM image of the area highlighted by the black box in Figure 4.40c. The prismatic <a> slip observed within the extension twinned region at ~6.0% strain is marked along with its corresponding Schmid factor value.

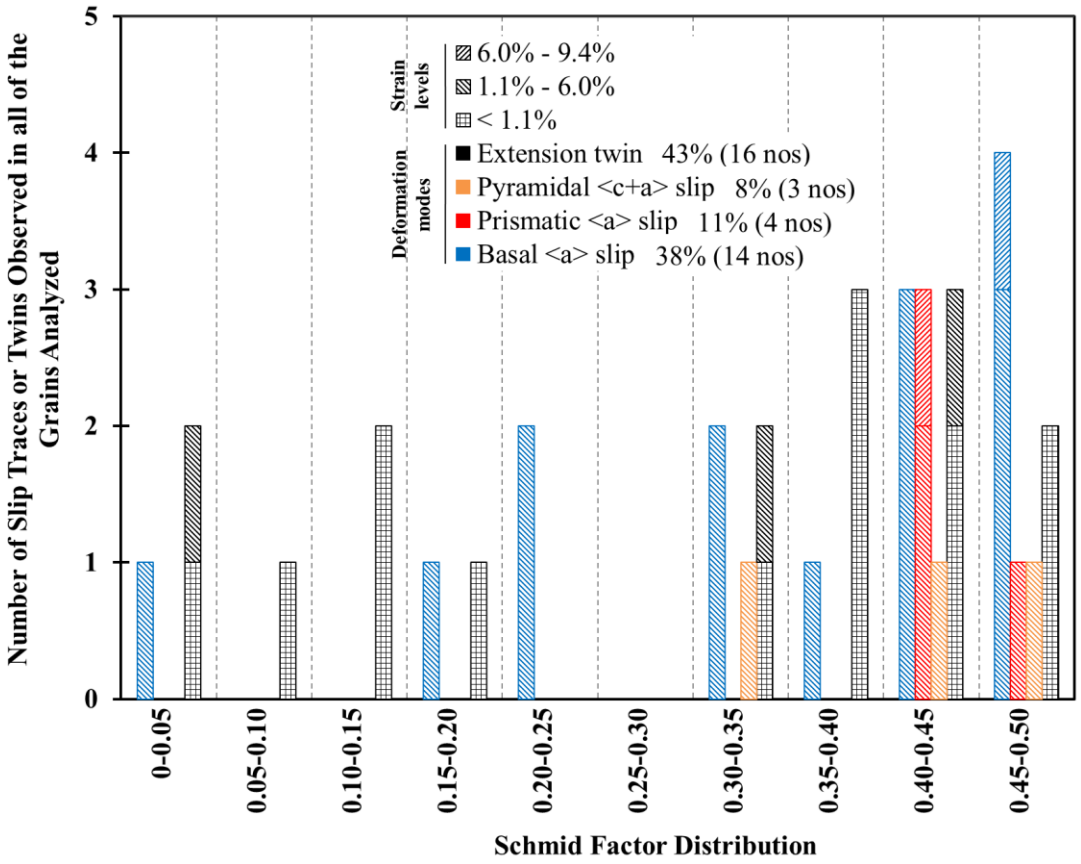

Figure 4.43 A histogram of the Schmid factor distribution of basal <a>, prismatic <a>, pyramidal <c+a>, and extension twins observed in the MN10 as-cast specimen tensile tested at 423K.

Figure 4.44a shows the orientation of the grains in which different deformation modes were identified plotted in a unit triangle along the tensile direction. Figure 4.44b shows the same data from Figure 4.44a plotted in a {0001} pole figure along the normal direction.

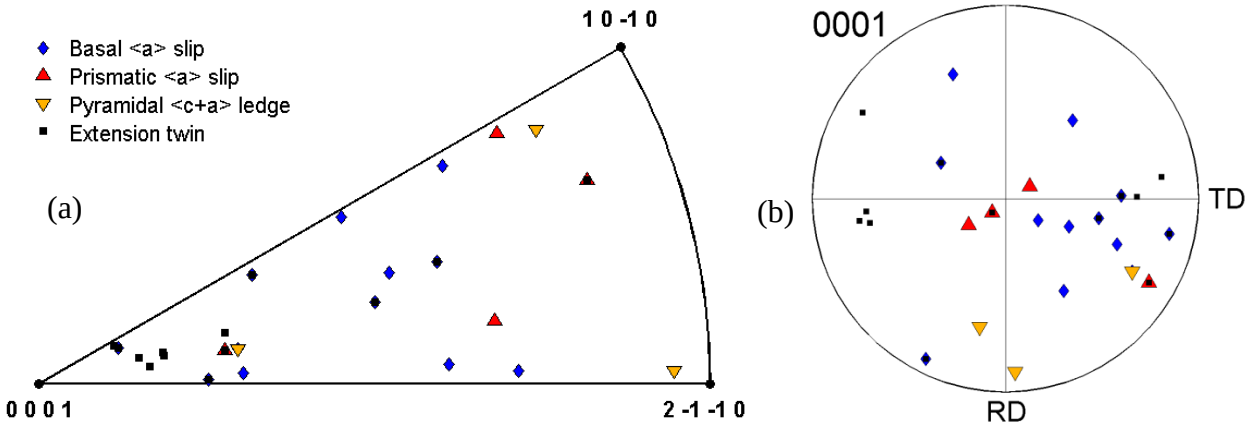

Figure 4.44 The individual grain orientations in which different deformation modes were observed for the MN10 as-cast specimen tensile tested at 423K, plotted in (a) unit triangle along the tensile direction and (b) {0001} pole figure along the normal direction.

4.2.2.3 523K tension

Figure 4.45 shows the EBSD IPF map in the normal direction from the gage section of the MN10 as-cast specimen, tensile tested at 523K, before and after deformation. Extension twins observed in the undeformed microstructure are marked by black arrows in Figure 4.45a.

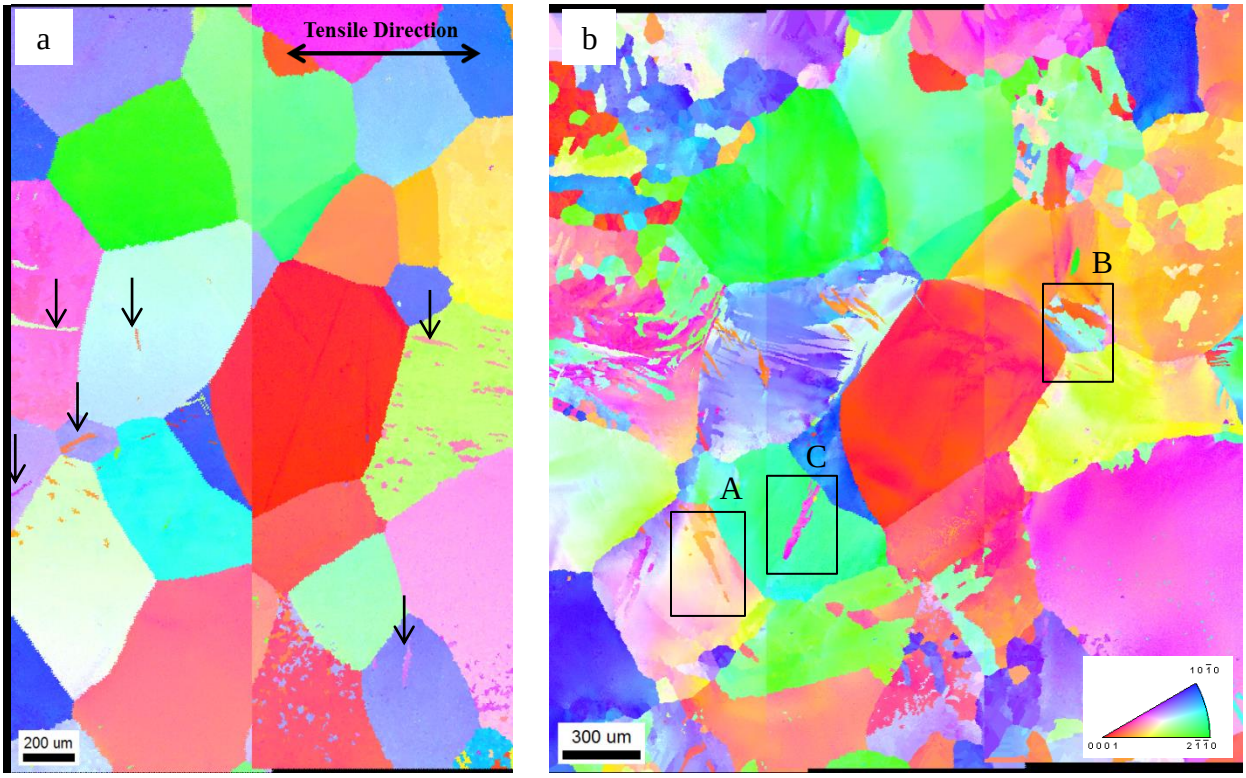

Figure 4.45 EBSD IPF map in the normal direction of the as-cast MN10 specimen tensile-tested at 523K (a) before deformation and (b) after deformation to ~10.7% strain. The extension twins observed in the undeformed microstructure are marked by black arrows in (a).

Figure 4.46 shows the sequential SE SEM images taken from the microstructural patch analyzed for slip and twin activity in the 523K tensile-tested specimen. Extension twins started to appear at the early stages of deformation at ~0.7%. Basal <a> slip and prismatic <a> slip traces were also observed at ~0.7% strain. However, a majority of the slip traces started appearing at ~3.9% strain.

Two $(10\bar{1}2) - (01\bar{1}2)$ double twins and one contraction twin were observed in the area analyzed. An extension twin, a $(10\bar{1}2) - (01\bar{1}2)$ double twin, and a contraction twin were observed in the areas highlighted by black boxes in Figure 4.45b are shown in Figure 4.47. It is noted that multiple extension twin variants were activated in some of the grains.

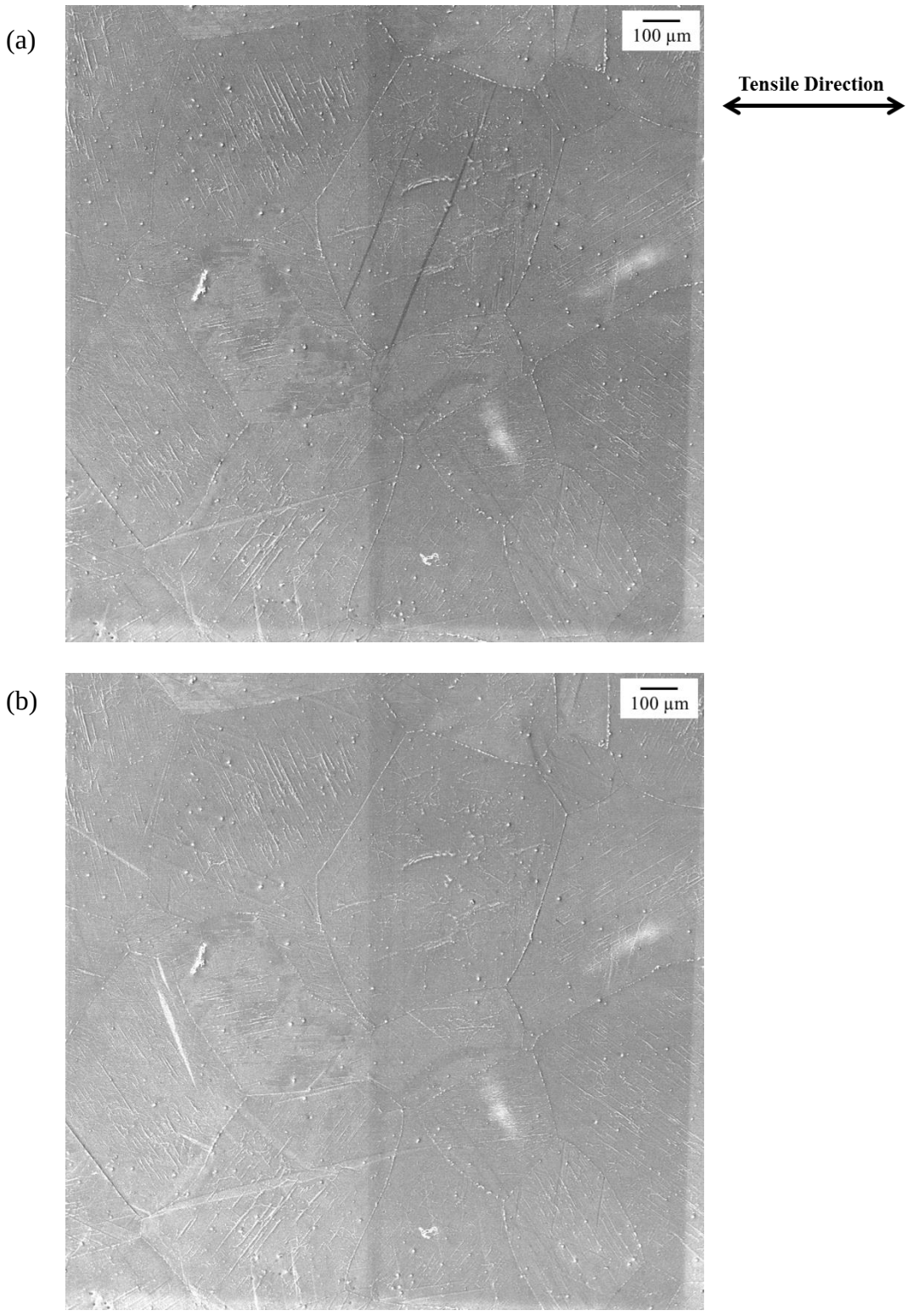

Figure 4.46 Sequential SE SEM images for the MN10 as-cast specimen tensile tested at 323K: (a) undeformed, (b) ~0.7% strain, (c) ~3.9% strain, and (d) ~10.7% strain. In (c) and (d), the slip traces are color coded for basal <a> slip (blue), prismatic <a> slip (red), and pyramidal <c+a> slip (orange). The corresponding Schmid factor values are given in (c) and (d).

Figure 4.46 (cont'd)

(c)

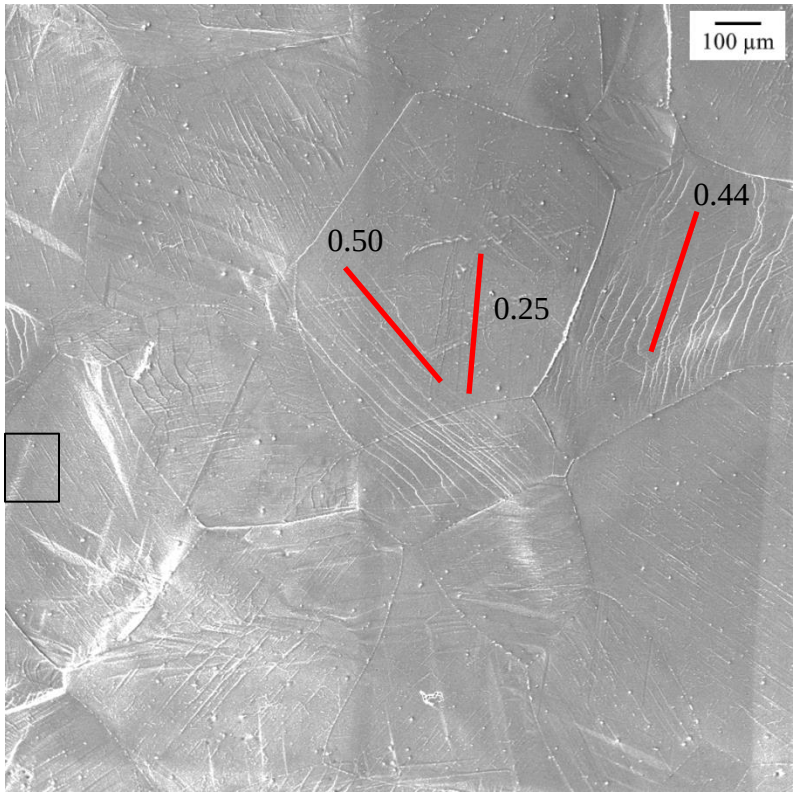

(d)

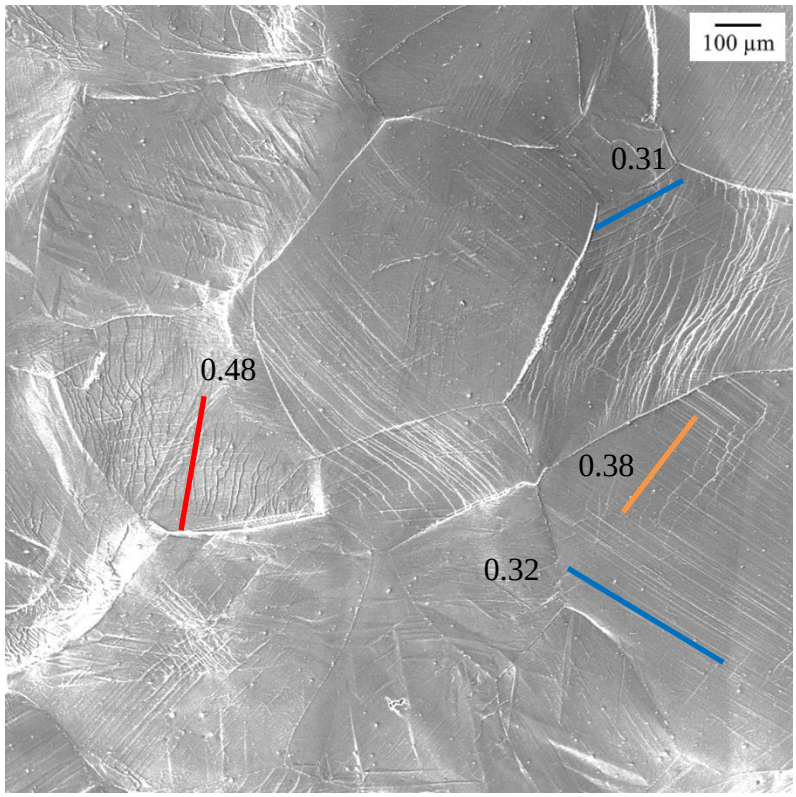

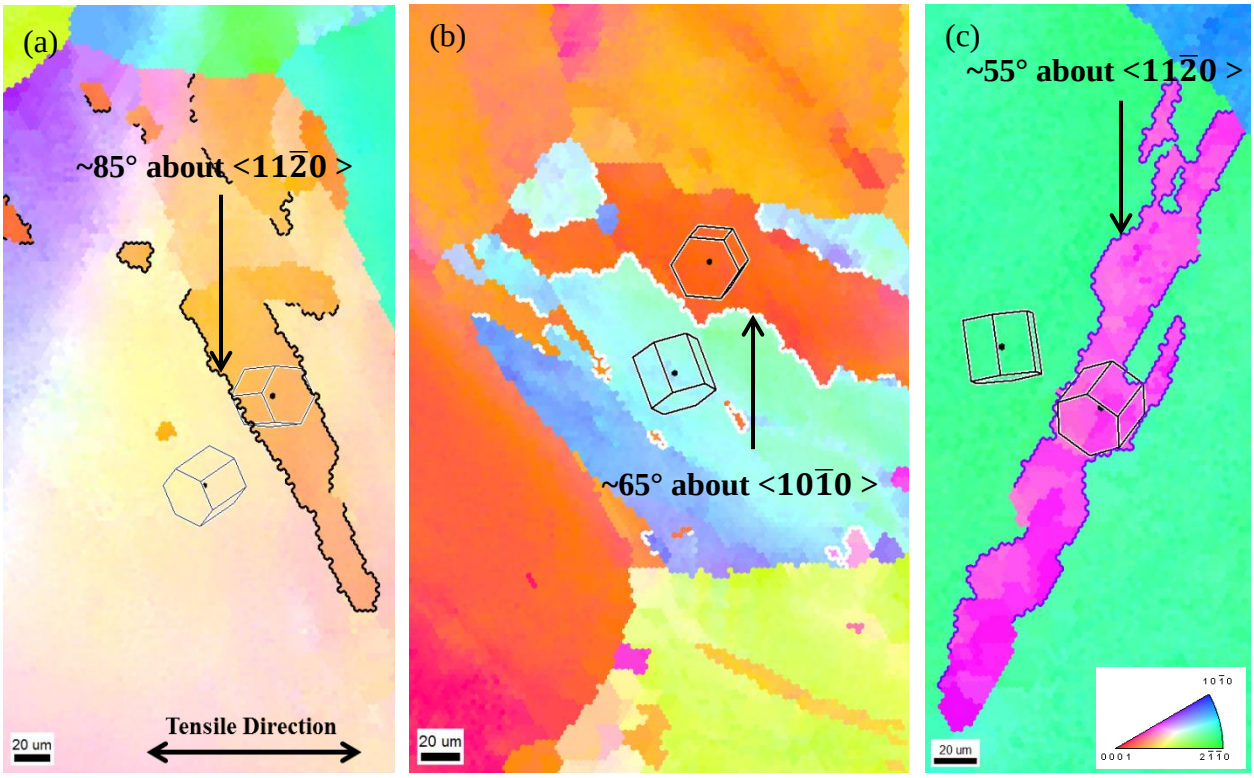

Figure 4.47 EBSD IPF map of the regions highlighted in Figure 4.45b by (a) the black box "A" showing the extension twin (b) the black box "B" showing the $(10\bar{1}2) - (01\bar{1}2)$ double twin and (c) the black box "C" showing the contraction twin. The extension twin, $(10\bar{1}2) - (01\bar{1}2)$ double twin, and contraction twin boundaries are highlighted by black, white, and purple lines, respectively. The HCP unit cells are overlaid indicating the misorientation between the parent grain and the twinned region.

Trace analysis was performed on approximately 30 grains from the microstructural patch shown in Figure 4.45a. 34 slip traces were observed in this region in which 16 were basal <a> slip, 11 were prismatic <a> slip, and 7 were pyramidal <c+a> slip. One of the observed basal <a> slip traces formed inside the twinned region. Figure 4.48 shows the high magnification image of the area marked by the black box in Figure 4.46c indicating the activation of basal <a> slip inside the extension twinned region. Wavy slip traces were observed in 18 grains and multiple slip/twin traces were observed in most of the grains analyzed. The number of slip traces observed at 523K was higher than that of at 423K and 323K.

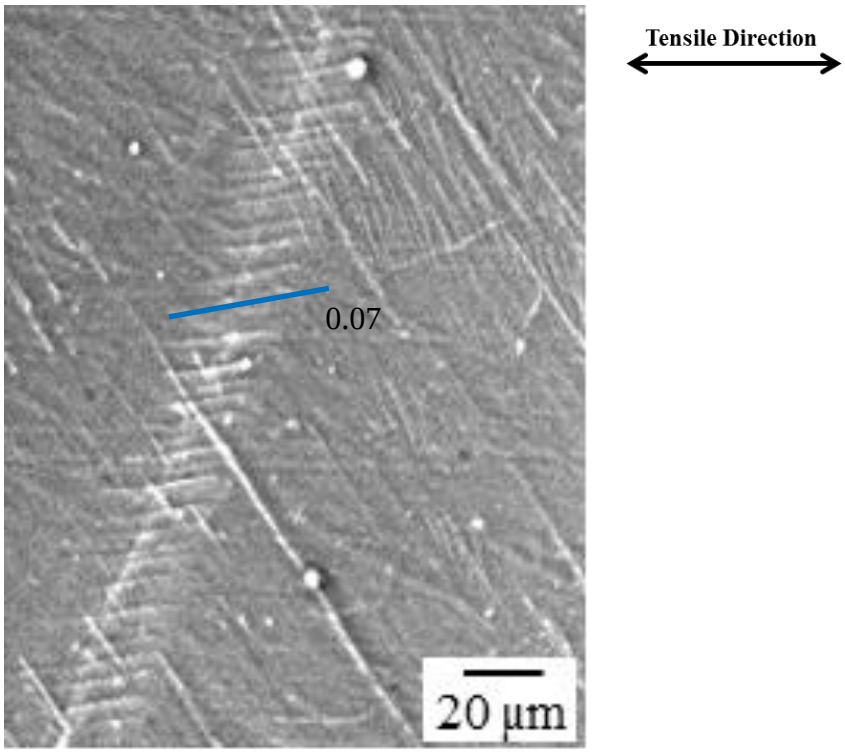

Figure 4.48 High magnification SE SEM image of the area highlighted by a black box in Figure 4.46c. The basal <a> slip observed within the extension twinned region at ~3.9% strain is marked along with its corresponding Schmid factor value.

Figure 4.49 plots the number of identified observations of a particular deformation versus the corresponding global Schmid factor range. 12 twin traces were observed. 11 of them were extension twins and one was a contraction twin. ~75% (12 out of 16) basal <a> slip was observed at Schmid factors higher than 0.25. Almost all of prismatic <a> slip (10 out of 11) and pyramidal <c+a> slip (6 out of 7) were observed at Schmid factors greater than 0.35.

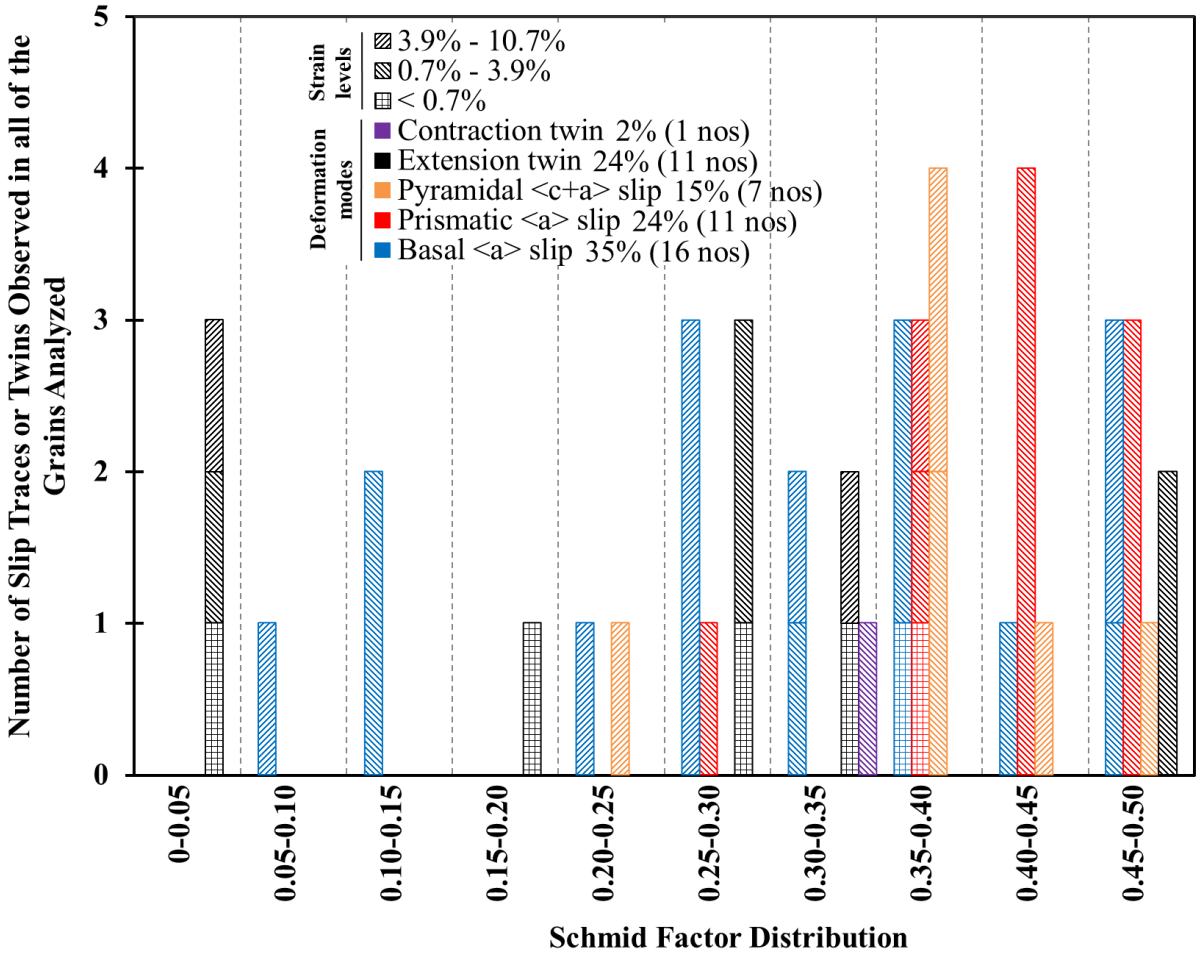

Figure 4.49 A histogram of the Schmid factor distribution of basal <a>, prismatic <a>, pyramidal <c+a>, extension twins, and contraction twins observed in the MN10 as-cast specimen tensile tested at 523K.

Figure 4.50a shows the orientation of the grains in which different deformation modes were identified plotted in a unit triangle along the tensile direction. Figure 4.50b shows the same data from Figure 4.50a plotted in a {0001} pole figure along the normal direction.

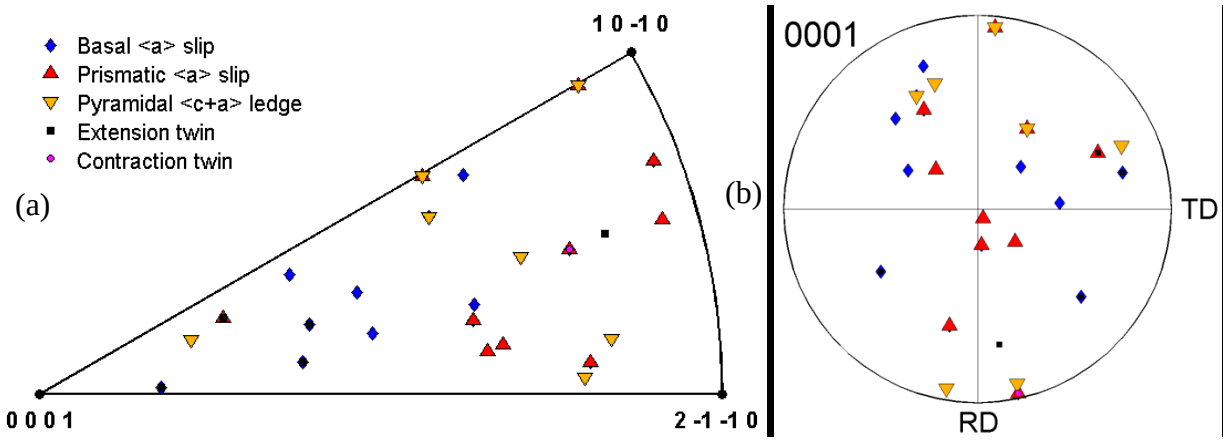

Figure 4.50 The individual grain orientations in which different deformation modes were observed for the MN10 as-cast specimen tensile tested at 523K, plotted in (a) unit triangle along the tensile direction and (b) {0001} pole figure along the normal direction.

4.3 Extruded Mg-1Mn-0.3Nd (MN10)

4.3.1 Microstructure and texture

Figure 4.51a and 4.51b show representative SE SEM and BF TEM images of the extruded MN10 microstructure, respectively. The average grain diameter was ~10±6μm based on ASTM standards for grain size measurement [ASTM E112-13 2013, Vander Voort 1999]. Figure 4.52 shows the grain size distribution for extruded MN10. As shown in Figure 4.51a, the grains were equiaxed suggesting that recrystallization occurred during the elevated-temperature extrusion process. The extrusion direction was horizontal in Figure 4.51a. Stringers of precipitates along the extrusion direction were observed in the microstructure suggesting that the cast billet may not have been homogeneous with respect to the alloying elements. The volume fraction of the second phase particles measured from the SE SEM images were ~0.49%. Both Mn-rich and Nd-rich precipitates were observed within the grains in the MN10 extruded microstructure (See Figure 4.51b). The average composition of the Mn-rich and Nd-rich precipitates were ~Mg-41Mn-1Nd and ~Mg-20Mn-51Nd, respectively. Table 4.7 and 4.8 lists the chemical composition of the 9 Mn rich and 6 Nd-rich precipitates analyzed, respectively. EDS performed on the extruded MN10 matrix suggested an average chemical composition of ~Mg-1Mn-0.4Nd. Table 4.9 lists the chemical compositions of the four observations from the matrix.

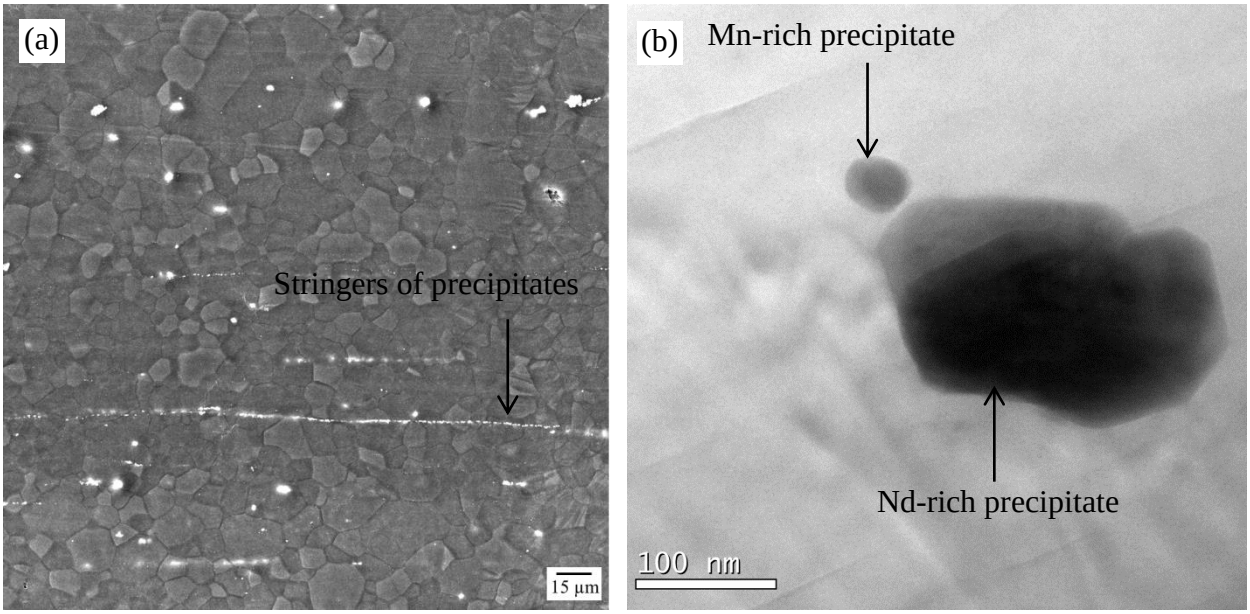

Figure 4.51 (a) SE SEM and (b) BF TEM image showing the microstructure of extruded MN10. The extrusion direction is horizontal. The extrusion direction is horizontal and out of the plane of paper in (a) and (b), respectively.

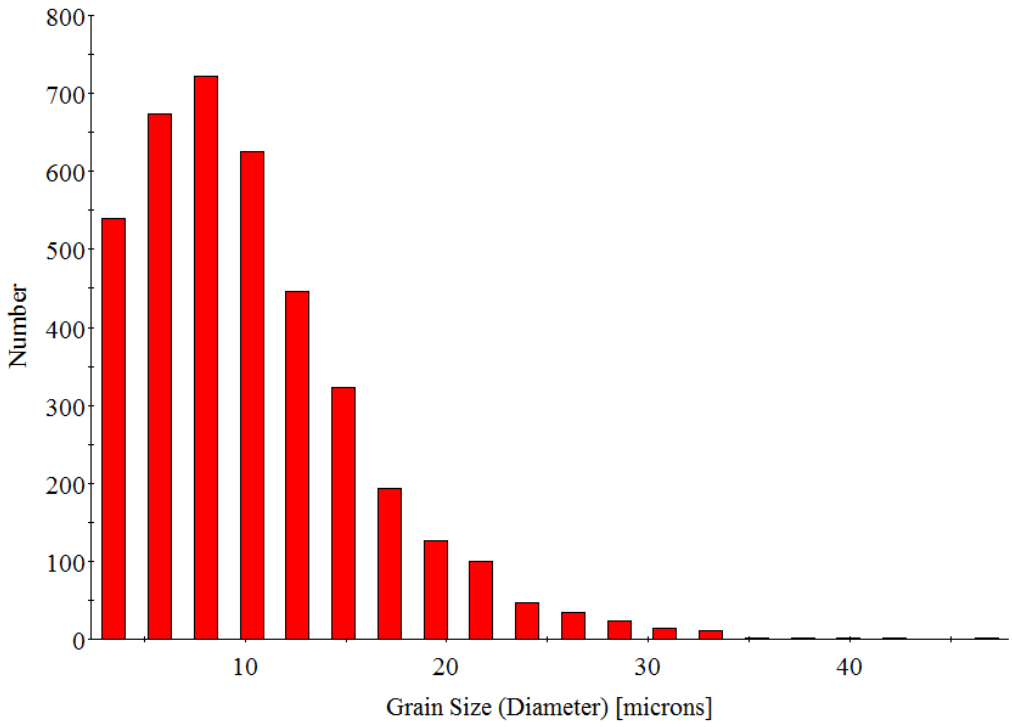

Figure 4.52 The grain size distribution of extruded MN10.

Table 4.7 The chemical composition of the 9 Mn-rich precipitates analyzed inside the grains in the extruded MN10 microstructure. The values are in wt%.

Observations	Mg	Mn	Nd
1	42.74	56.74	0.53
2	54.12	45.24	0.63
3	33.75	65.66	0.59
4	45.81	53.58	0.62
5	82.02	17.21	0.77
6	76.98	22.46	0.56
7	54.41	45.03	0.56
8	60.57	39.00	0.43
9	76.19	22.62	1.18
Average	58.51	40.84	0.65

Table 4.8 The chemical composition of the 6 Nd-rich precipitates analyzed inside the grains in the extruded MN10 microstructure. The values are in wt%.

Observations	Mg	Mn	Nd
1	32.80	0.27	66.93
2	19.22	29.99	36.49
3	22.20	34.55	43.25
4	34.95	41.41	23.24
5	47.17	10.03	40.33
6	3.28	0.49	96.23
Average	26.60	19.46	51.08

Table 4.9 The chemical composition of the extruded MN10 matrix. The values are in wt%.

Observations	Mg	Mn	Nd
1	98.89	0.70	0.41
2	98.62	0.81	0.58
3	98.80	0.81	0.39
4	98.95	0.69	0.36
Average	98.82	0.75	0.44

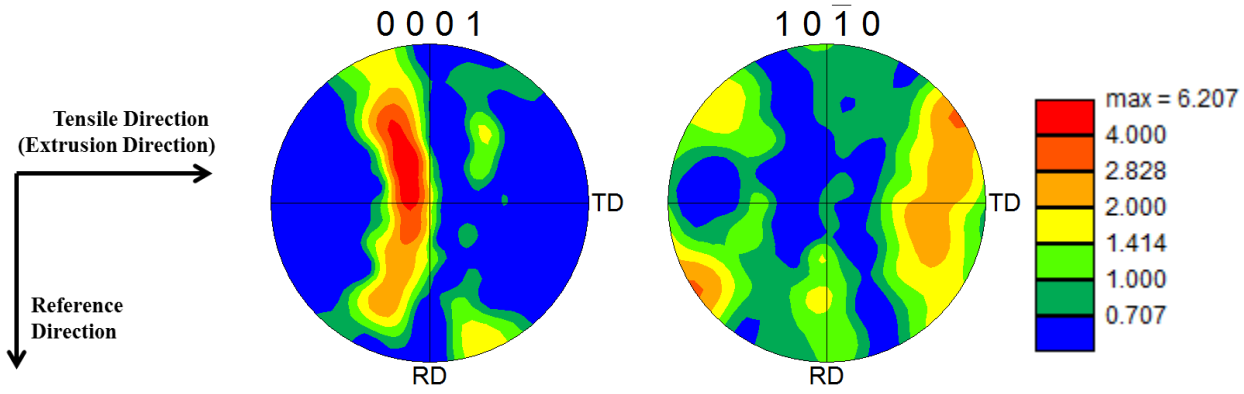

Figure 4.53 Representative texture of extruded MN10 microstructure in the form of {0001} and {10$\bar{1}$0} pole figures in the normal direction.

Figure 4.53 shows the representative texture of the extruded MN10 microstructure in the form of {0001} and {10$\bar{1}$0} pole figures in the normal direction. The texture shown in Figure 4.53 was obtained from an area containing ~3900 grains. The pole figures show a relatively strong basal <a> fiber texture where {0001} peaks were aligned almost perpendicular to the tensile direction. The relatively strong texture of the extruded MN10, similar to conventional wrought Mg alloys, suggest that 0.3 wt% Nd addition was not sufficient to randomize the grain orientations during the extrusion process.

4.3.2 In-situ tension

In-situ tensile tests were performed on extruded MN10 at 323K, 423K, and 523K. Three tests were performed at 323K, and two tests were performed at 423K and 523K. The engineering stress versus displacement curves for the 323K, 423K, and 523K tensile tests are illustrated in Figure 4.54. In Figure 4.54, the stress drops indicate the stress relaxation that occurred when the tests were paused for imaging. One specimen at each test temperature was taken to failure, for which slip trace analysis was performed. It is noted that twin trace analysis was not performed on those specimens due to the poor quality of the EBSD maps obtained due to

surface topography after deformation. Twin trace analysis was performed on separate tensile-tested specimens, which were deformed to ~6.4% strain at 323K, ~17.8% strain at 423K, and ~14.7% strain at 523K. These specimens were not taken to failure in order to facilitate EBSD mapping after deformation. Twin/slip trace analysis was performed on ~1800 grains for each test condition. The curve for the specimen not taken to failure at 423K was not recorded due to a glitch in the data acquisition system. The YS of the extruded MN10 material decreased with increasing temperature. Table 4.10 lists the approximate YS and UTS obtained, and the maximum strain levels achieved for each specimen.

Table 4.10 MN10 extruded tensile property comparison between different test conditions.

Test temperature	YS (MPa)	UTS (MPa)	Maximum strain (%)
323K	~118	~159	~34.9 (fractured)
323K	~125	~149	~6.4
323K	~113	~152	~19.4
423K	~81	~132	~44.5 (fractured)
423K	-	-	~17.8
523K	~64	~101	~39.4 (fractured)
523K	~67	~82	~14.7

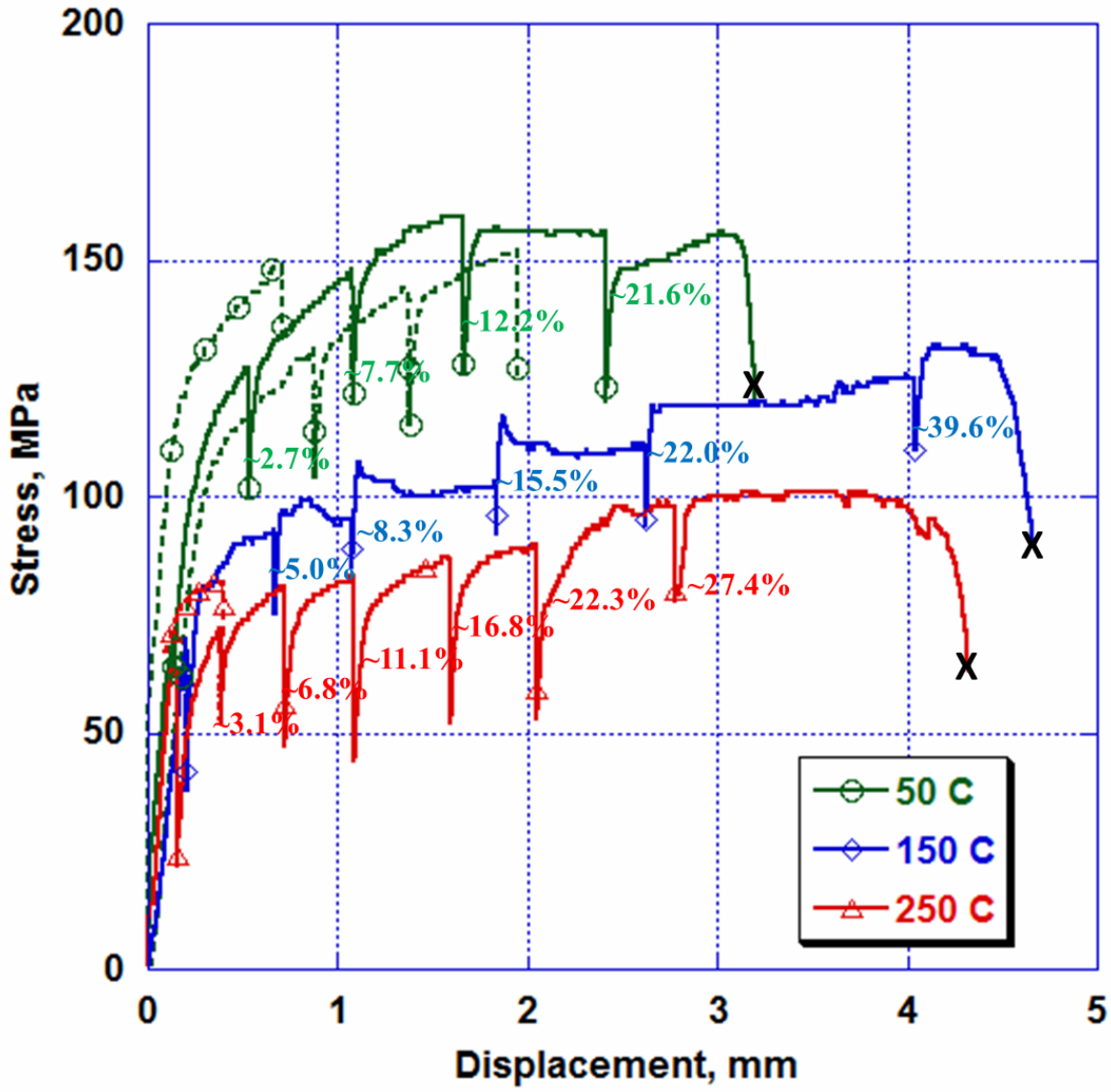

Figure 4.54 Representative stress vs. displacement plots for extruded MN10 samples tensile tested at 323K, 423K, and 523K. The stress drops indicate the stress relaxation that occurred when the tests were interrupted for imaging. The displacement values included displacements in both the gage section and the grip regions. The approximate strain values are indicated and "X" indicates when fracture occurred.

4.3.2.1 323K tension

Figure 4.55 shows sequential SE SEM images taken from the same area of the MN10 extruded specimen tensile tested at 323K. No obvious slip traces were observed even at strain levels close to failure. A few grain boundary cracks were observed at ~7.7% strain in the area analyzed (See Figure 4.55b-d). Both extension and contraction twinning were observed at less than ~6.4% strain. Figure 4.56 shows the EBSD IPF map in the normal direction of the same region from the gage section of the specimen both before and after deformation. An extension twin observed in this area is highlighted by the black arrow in Figure 4.56b.

(a) ε ≈ 0%

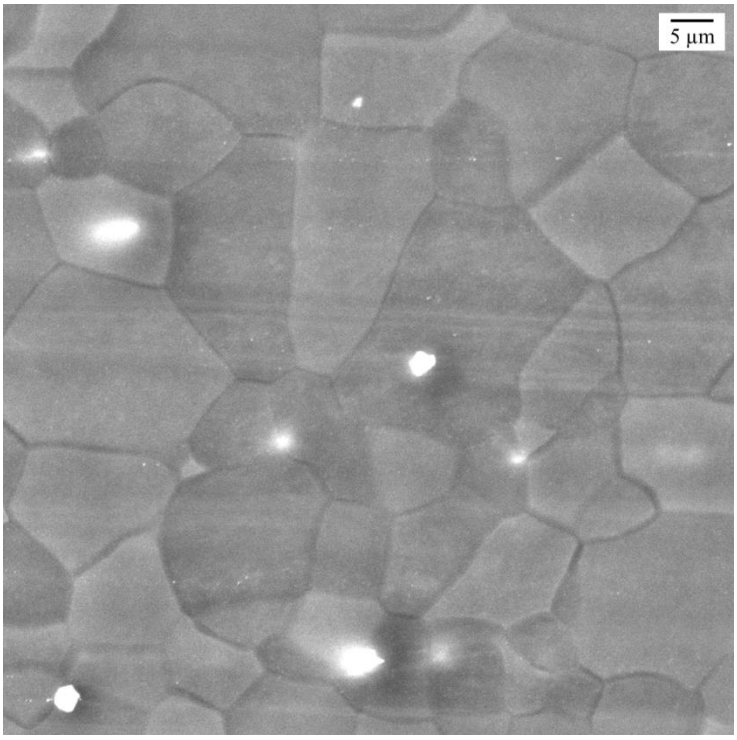

Tensile axis
↔
Extrusion direction

(b) ε ≈ 7.7%

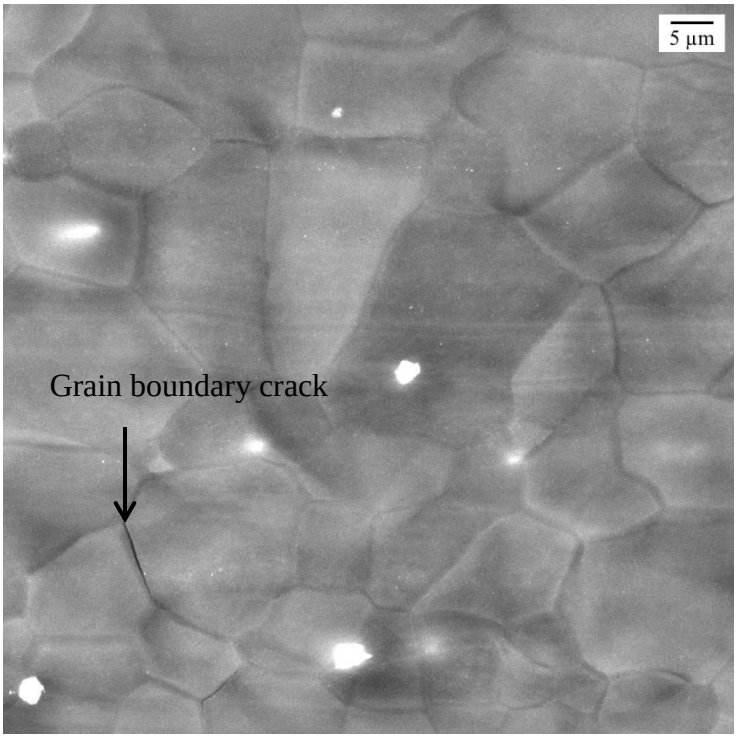

Figure 4.55 Sequential SE SEM images for the extruded MN10 tensile tested at 323K: (a) ~2.7% strain, (b) ~7.7% strain, (c) ~12.2% strain, and (d) ~21.6% strain. A grain boundary crack observed in this area at ~7.7% strain is indicated by the arrow. It is noted that no obvious slip traces were observed.

Figure 4.55 (cont'd)

(c) $\varepsilon \approx 12.2\%$

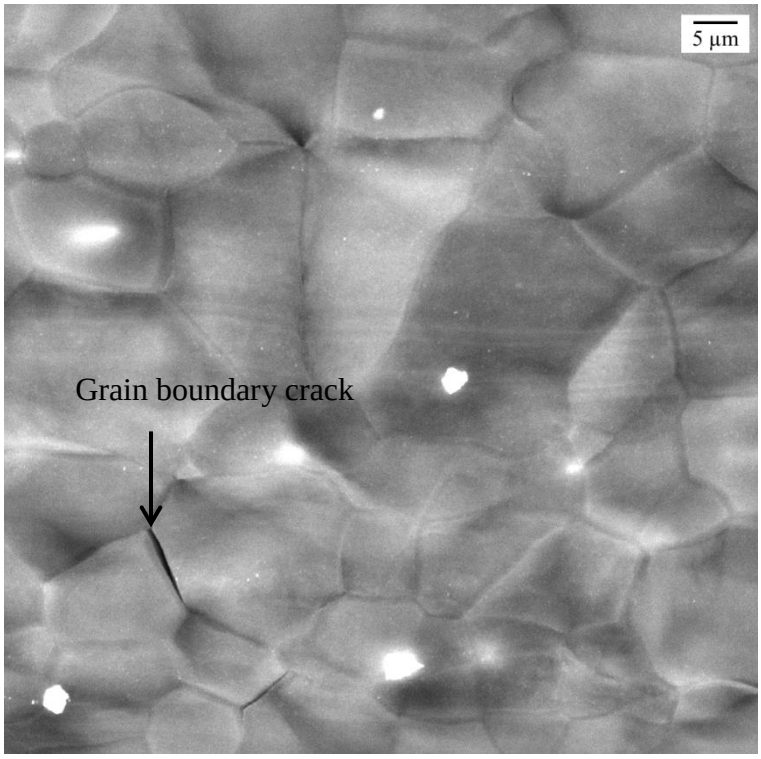

(d) $\varepsilon \approx 21.6\%$

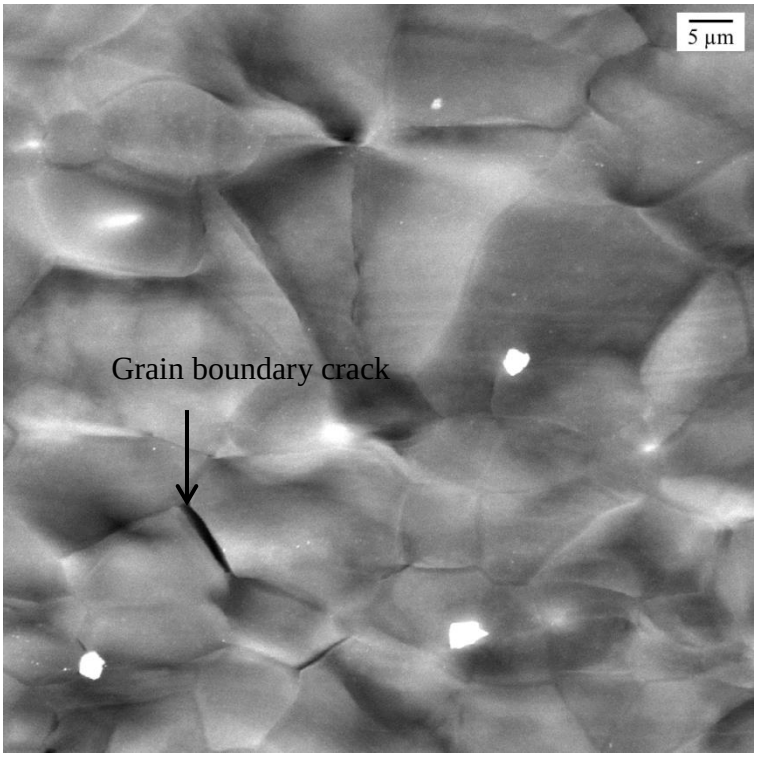

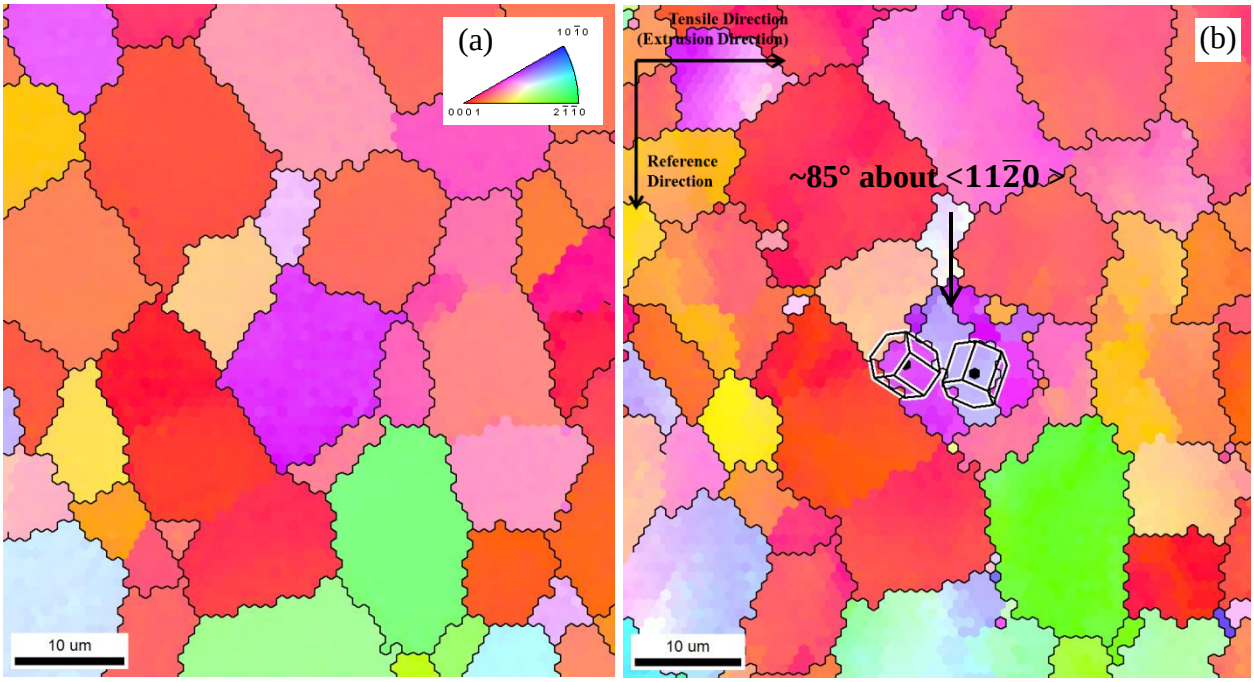

Figure 4.56 EBSD IPF map in the normal direction of the same area from the gage section of the extruded MN10 tensile tested specimen at 323K (a) before deformation and (b) at ~6.4% strain. An extension twin observed in this region is indicated by the black arrow in (b). The HCP unit cells are overlaid showing the misorientation between the parent grain and the twinned region and the rotation angles are indicated in (b).

19 extension twins and one contraction twin was observed in the area analyzed. Thus, extension twining appeared to be the dominant deformation mode at 323K. Figure 4.57 plots the number of identified observations of a particular deformation mode versus the corresponding global Schmid factor range. Extension twins were observed over the entire Schmid factor range. 6 of the extension twins were activated at a global Schmid factor of less than zero.

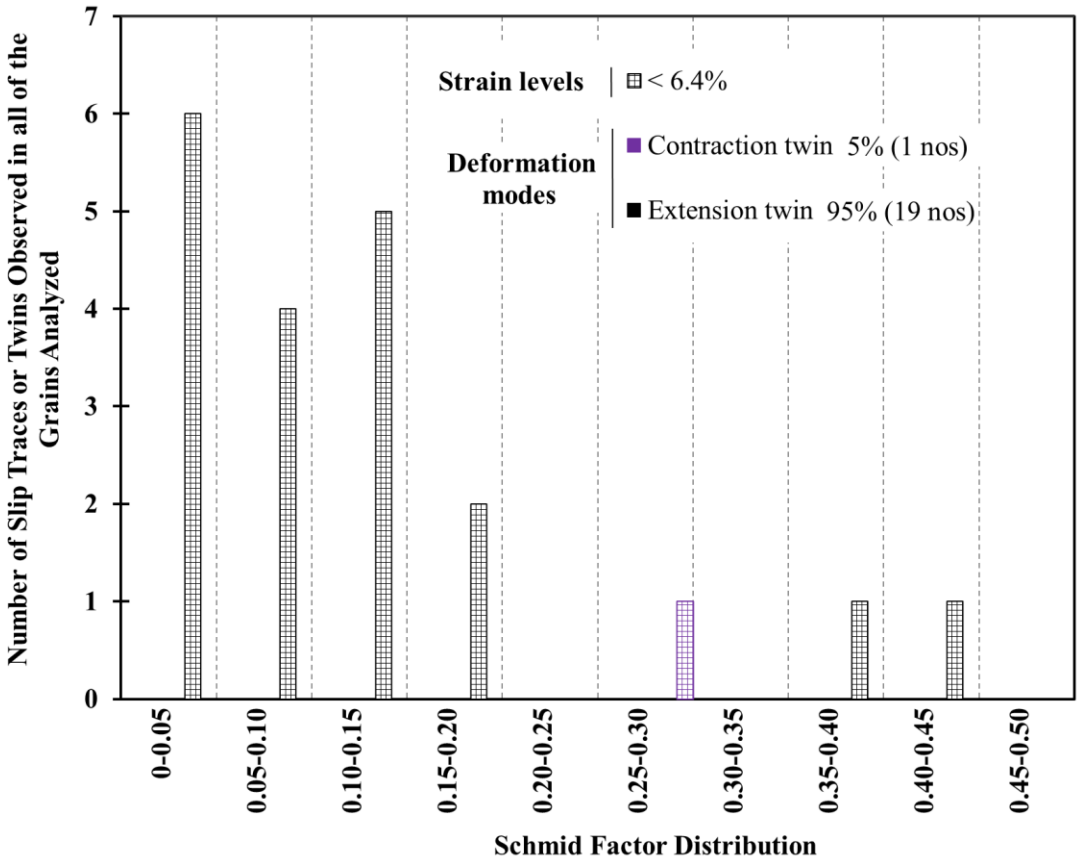

Figure 4.57 A histogram of the Schmid factor distribution of extension and contraction twin systems for the extruded MN10 323K tension experiment.

In Figure 4.58a, the orientation of the grains in which different twin systems were identified was plotted in a unit triangle along the tensile direction. The orientations of the grains on both sides of 6 grain boundary cracks, observed at ~7.7% strain, were plotted and connected by a line in Figure 4.58a. In Figure 4.58b the same data from 4.58a is plotted in a {0001} pole figure along the normal direction.

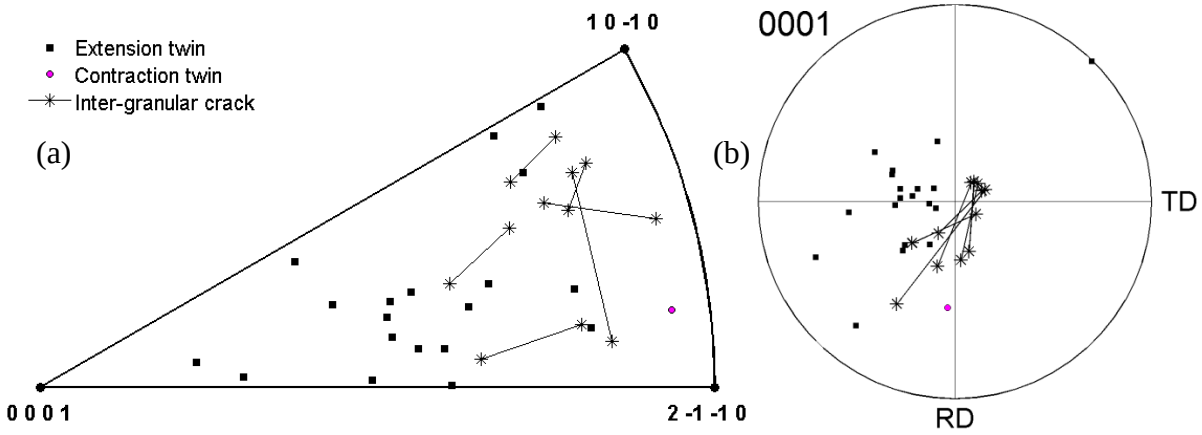

Figure 4.58 The individual grain orientations in which different deformation modes were observed for extruded MN10 tensile test at 323K, plotted in a (a) unit triangle along the tensile direction and (b) {0001} pole figure along the normal direction. The lines connect the grain orientations on both sides of the cracks observed.

4.3.2.2 423K tension

Figure 4.59 shows sequential SE SEM images taken from the same area of the MN10 extruded specimen tensile tested at 423K. Basal <a> slip, extension twinning, and contraction twinning were observed. Out of 7 slip and twin traces observed, five were identified to be basal <a> slip, 1 was an extension twin, and 1 was a contraction twin. Both extension and contraction twinning were observed at less than ~17.8% strain. Basal <a> slip traces were observed at strain levels close to failure at ~39.6% strain (highlighted by blue lines in Figure 4.59d). Figure 4.60 shows the EBSD IPF map in the normal direction of the same region from the gage section of the specimen before and after deformation. An extension twin observed in this area is highlighted by the black arrow in Figure 4.60b.

(a) ε ≈ 0%

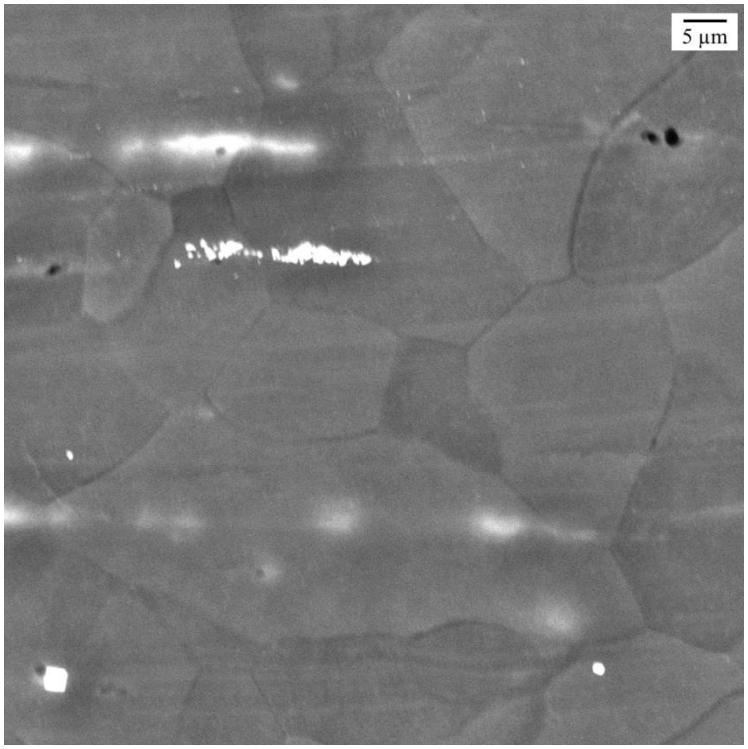

Tensile axis
↔
Extrusion direction

(b) ε ≈ 8.3%

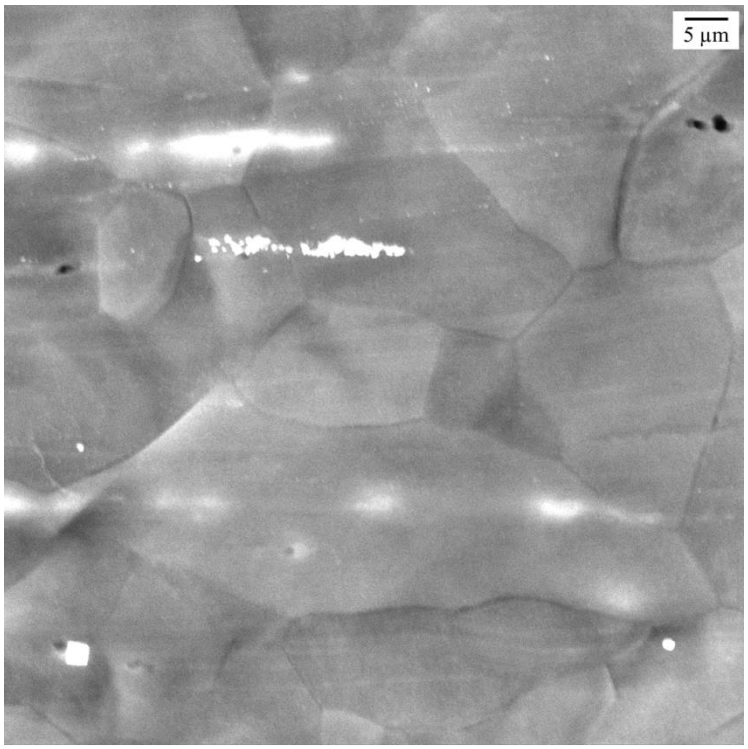

Figure 4.59 Sequential SE SEM images for the extruded MN10 tensile tested at 423K: (a) 0% strain, (b) ~8.3% strain, (c) ~22.0% strain, and (d) ~39.6% strain. Basal <a> slip observed in this region is highlighted by blue line and corresponding Schmid factor value is indicated in (d).

Figure 4.59 (cont'd)

(c) $\varepsilon \approx 22.0\%$

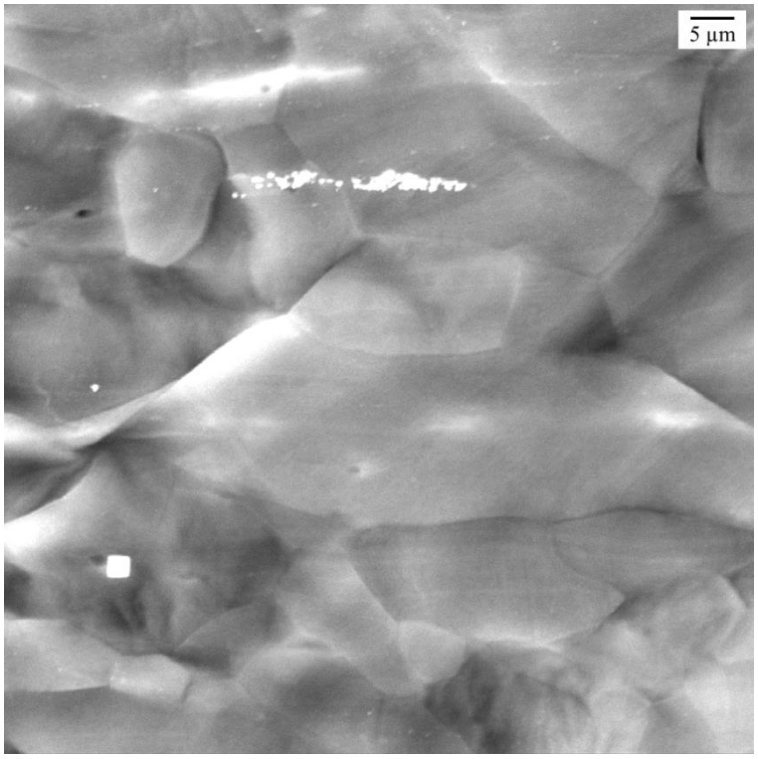

(d) $\varepsilon \approx 39.6\%$

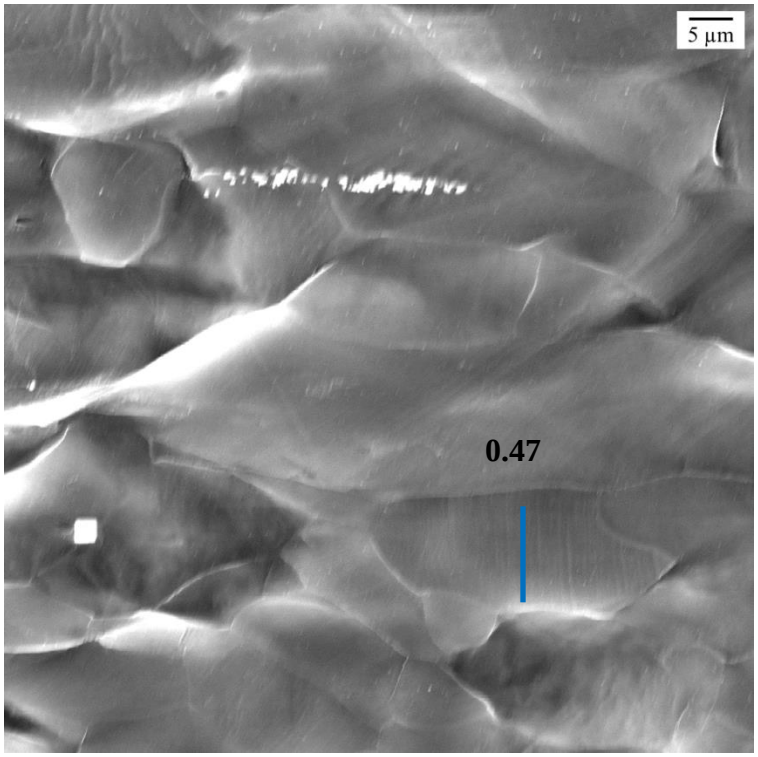

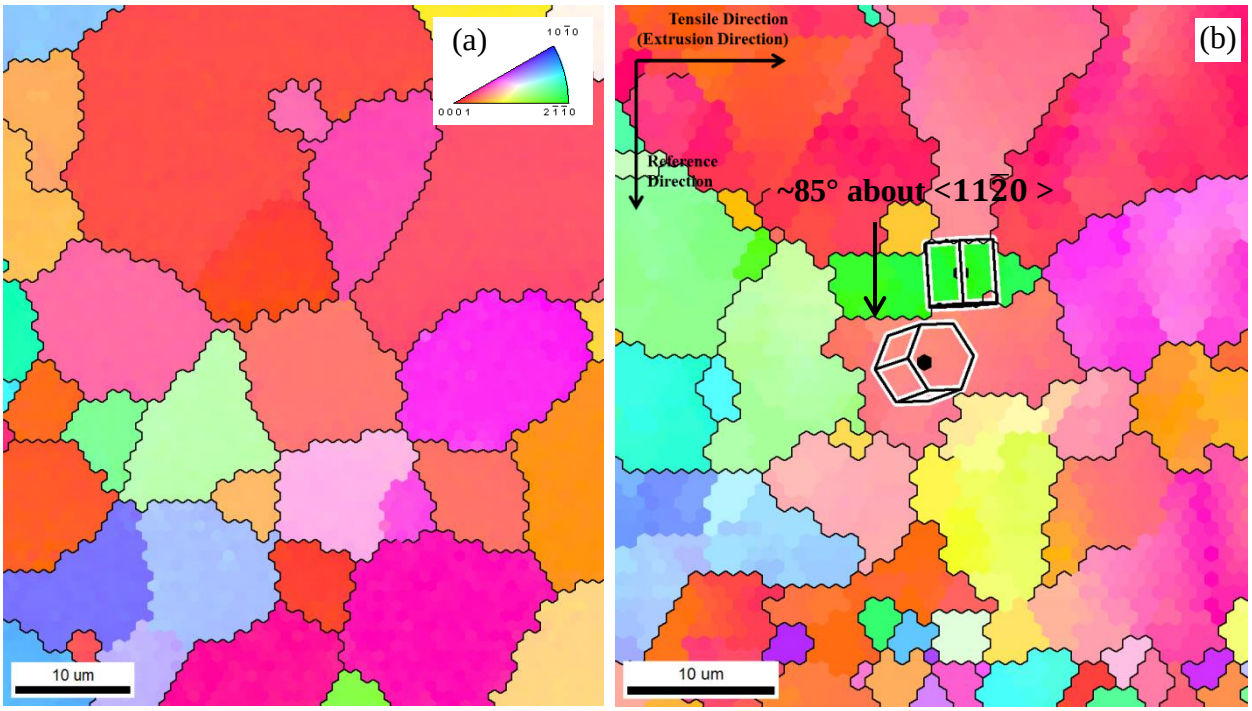

Figure 4.60 EBSD IPF map in the normal direction of the same area from the gage section of the extruded MN10 tensile tested specimen at 423K (a) before deformation and (b) at ~17.8% strain. An extension twin observed in this region is indicated by the black arrow in (b). The HCP unit cells are overlaid showing the misorientation between the parent grain and the twinned region and the rotation angles are indicated in (b).

Figure 4.61 plots the number of identified observations of a particular deformation mode versus the corresponding global Schmid factor range. Extension twins were observed at Schmid factors <0.1. All of the basal <a> slip traces were observed at Schmid factors >0.20. Three of the extension twins were activated at a global Schmid factor of less than zero.

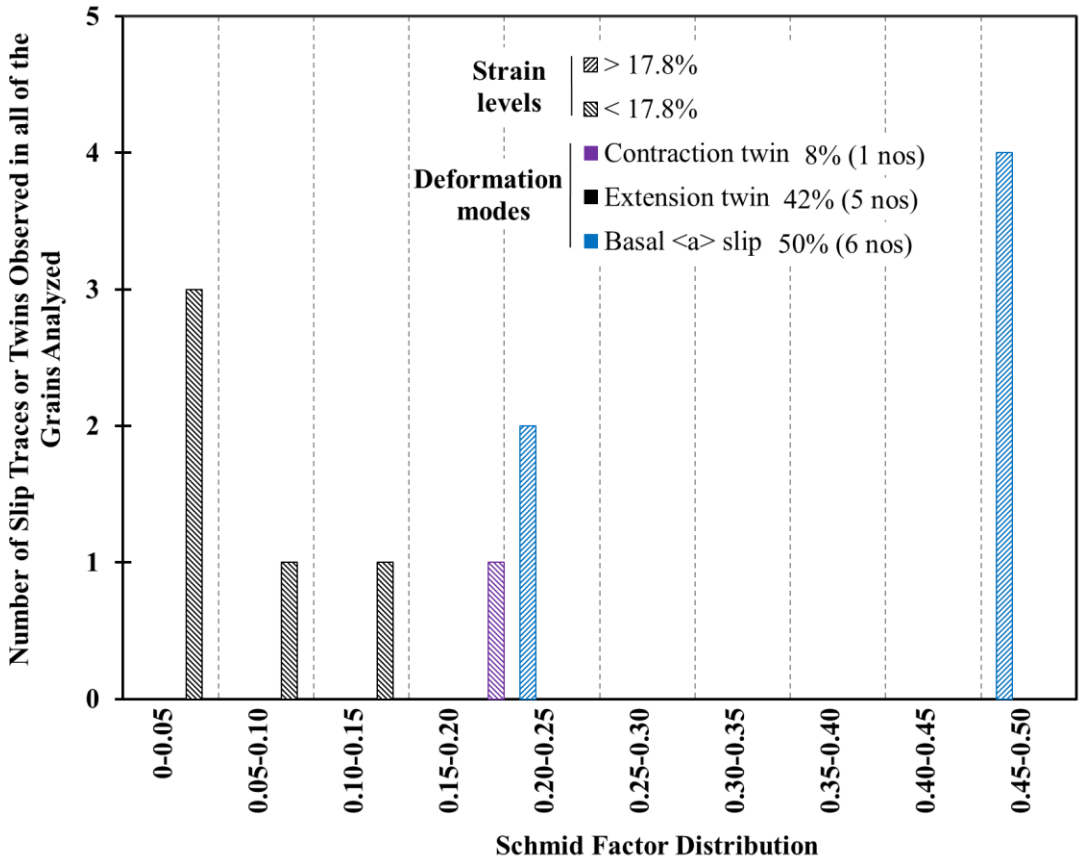

Figure 4.61 A histogram of the Schmid factor distribution of extension and contraction twin systems for the extruded MN10 423K tension experiment.

In Figure 4.62a, the orientation of the grains in which different twin systems were identified was plotted in a unit triangle along the tensile direction. In Figure 4.62b the same data from 4.62a is plotted in a {0001} pole figure along the normal direction.

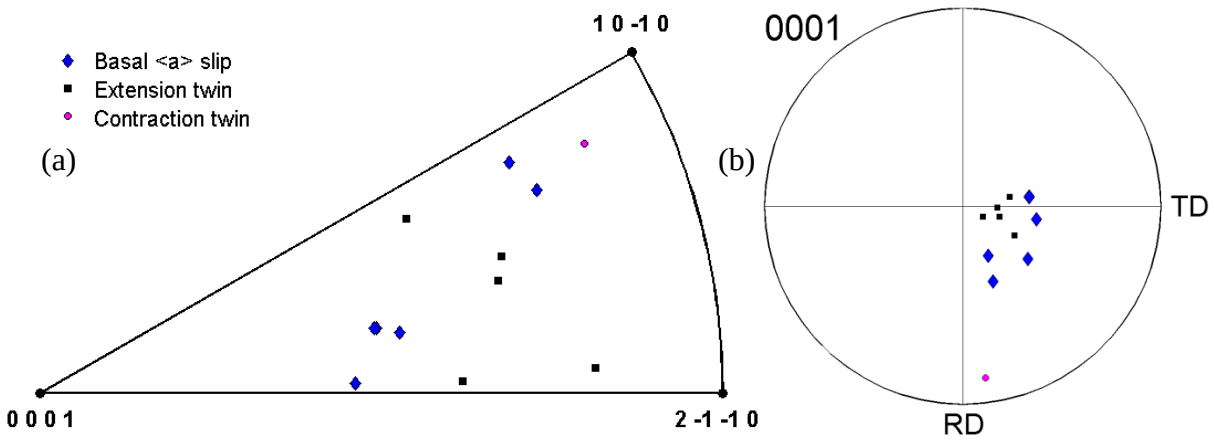

Figure 4.62 The individual grain orientations in which different deformation modes were observed for extruded MN10 tensile test at 423K, plotted in a (a) unit triangle along the tensile direction and (b) {0001} pole figure along the normal direction.

4.3.2.3 523K tension

Figure 4.63 shows sequential SE SEM images taken from the same area of the MN10 extruded specimen tensile tested at 523K. Basal <a> slip traces were first observed at ~6.8% strain. Basal <a> slip, prismatic <a> slip, and pyramidal <c+a> slip were observed, while no twinning was observed in the area analyzed. Out of 39 slip traces observed, 30 were identified to be basal <a> slip, 2 were prismatic <a> slip, and 7 were pyramidal <c+a> slip.

(a) ε ≈ 0%

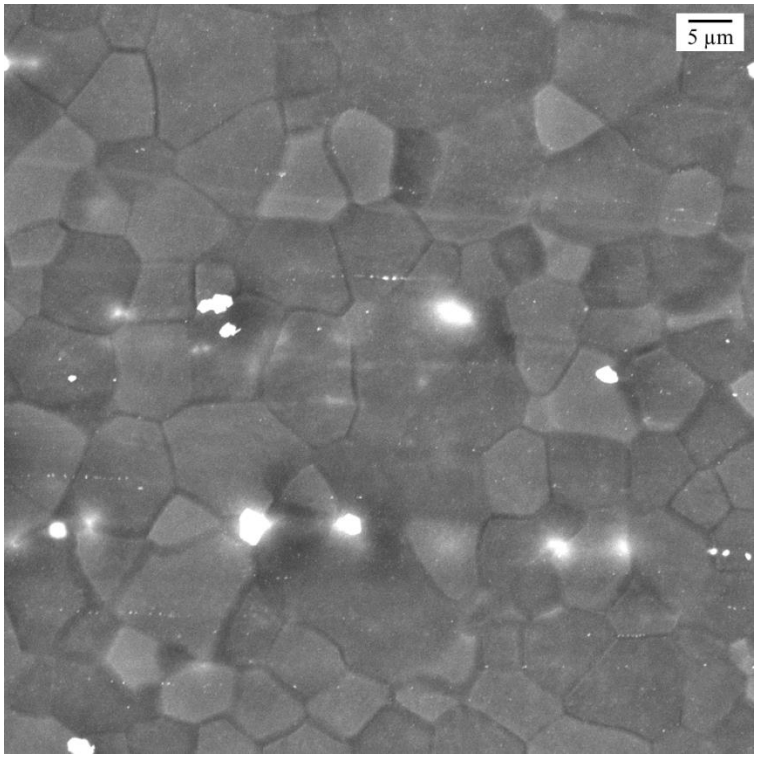

Tensile axis
↔
Extrusion direction

(b) ε ≈ 6.8%

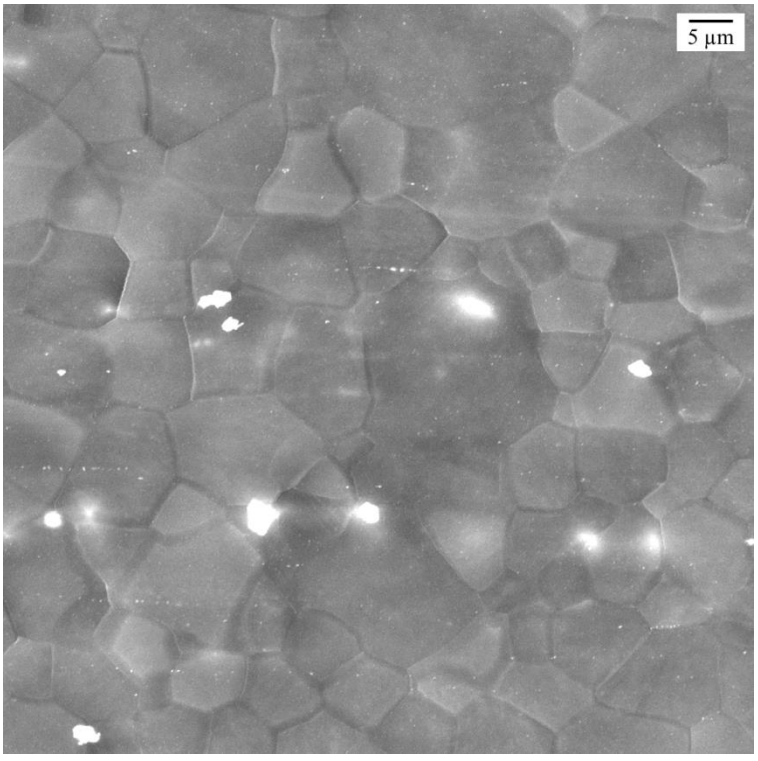

Figure 4.63 Sequential SE SEM images for the extruded MN10 tensile tested at 523K: (a) 0% strain, (b) ~6.8% strain, (c) ~22.3% strain, and (d) ~27.4% strain. Basal <a> slip and pyramidal <c+a> slip observed in this region are highlighted by blue and orange lines, respectively. The corresponding Schmid factor values are indicated in (c) and (d).

Figure 4.63 (cont'd)

(c) ε ≈ 22.3%

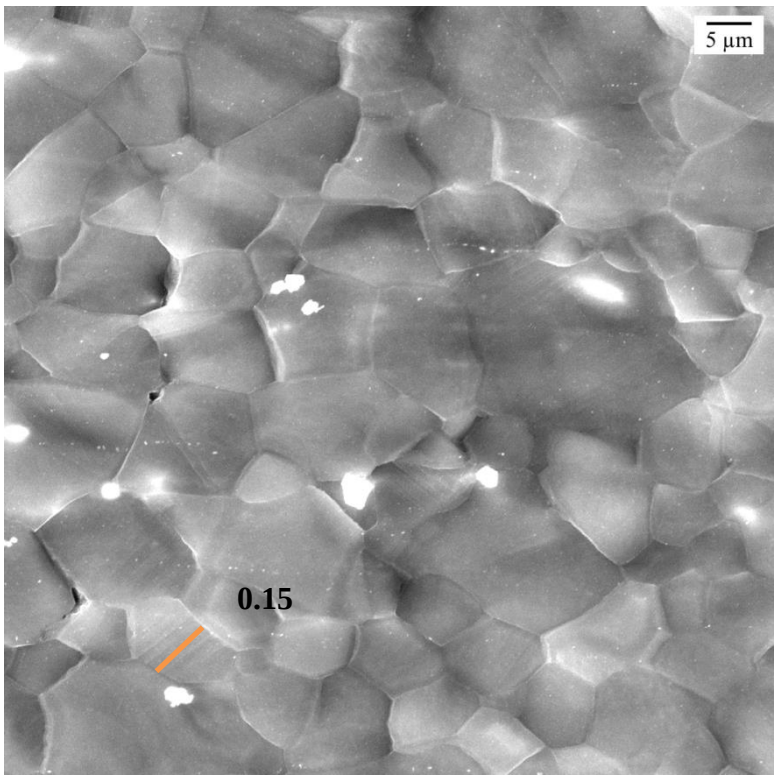

(d) ε ≈ 27.4%

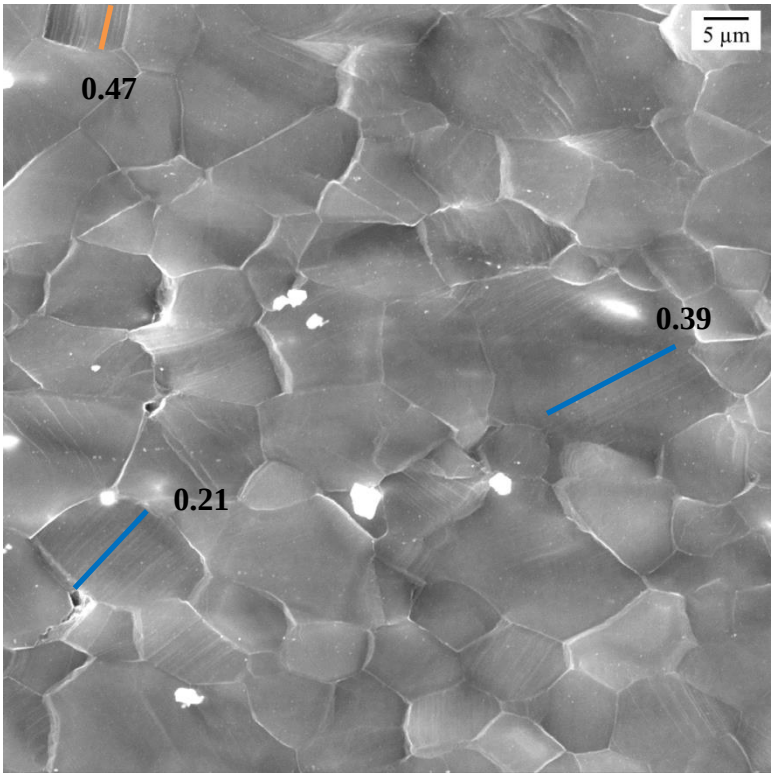

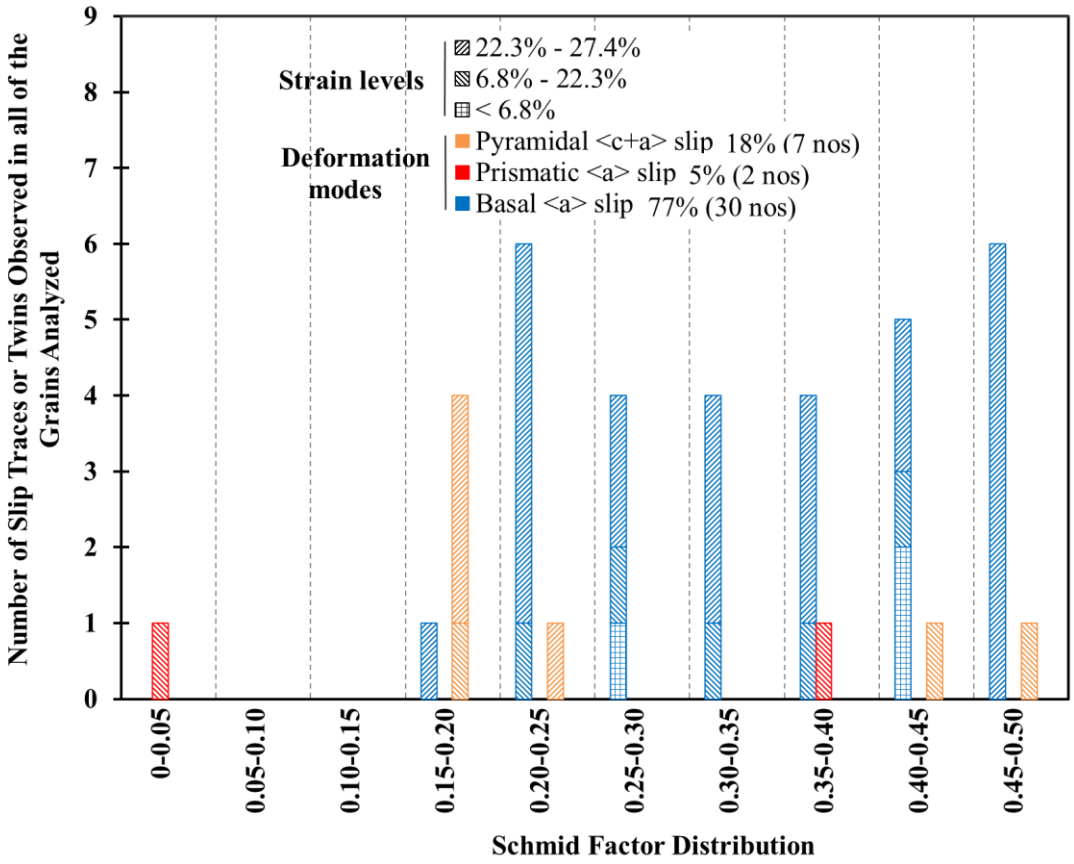

Figure 4.64 A histogram of the Schmid factor distribution of basal <a> slip, prismatic <a> slip, and pyramidal <c+a> slip for the extruded MN10 specimen tensile tested at 523K. No twinning was observed in the area analyzed.

Figure 4.64 plots the number of identified observations of a particular deformation mode versus the corresponding global Schmid factor range. Almost all of the basal <a> slip traces were observed at Schmid factors >0.20. The deformation was controlled by basal <a> slip.

In Figure 4.65a, the orientation of the grains in which different slip systems were identified was plotted in a unit triangle along the tensile direction. In Figure 4.65b the same data from 4.65a is plotted in a {0001} pole figure along the normal direction.

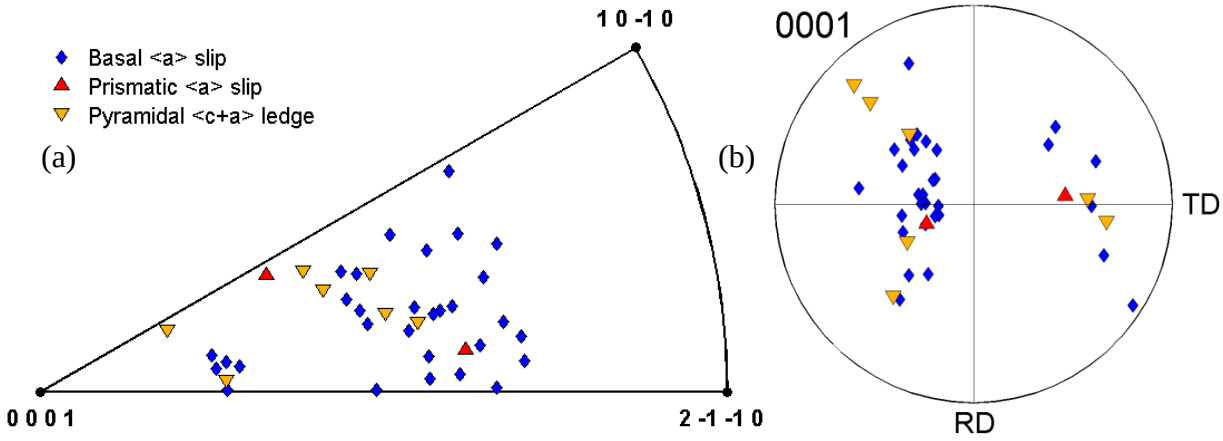

Figure 4.65 The individual grain orientations in which different deformation modes were observed for extruded MN10 tensile test at 523K, plotted in a (a) unit triangle along the tensile direction and (b) {0001} pole figure along the normal direction.

4.3.3 In-situ compression

In-situ compression tests were performed on extruded MN10 at 323K, 423K, and 523K. One test was performed at each temperature. The engineering stress versus displacement curves for the 323K compression test is illustrated in Figure 4.66. In figure 4.66, the stress drops indicate the stress relaxation that occurred when the tests were paused for imaging. The curves for the specimen tested at 423K and 523K were not recorded due to a glitch in the data acquisition system. None of the specimens were taken to failure in order to facilitate EBSD mapping after deformation. Twin trace analysis was performed on ~750 grains at each test condition. Slip traces were not observed at any of the tested temperatures at the given strain levels. However, twinning was observed. Table 4.11 lists the approximate YS and UTS obtained, and the maximum strain levels achieved for each experiment.

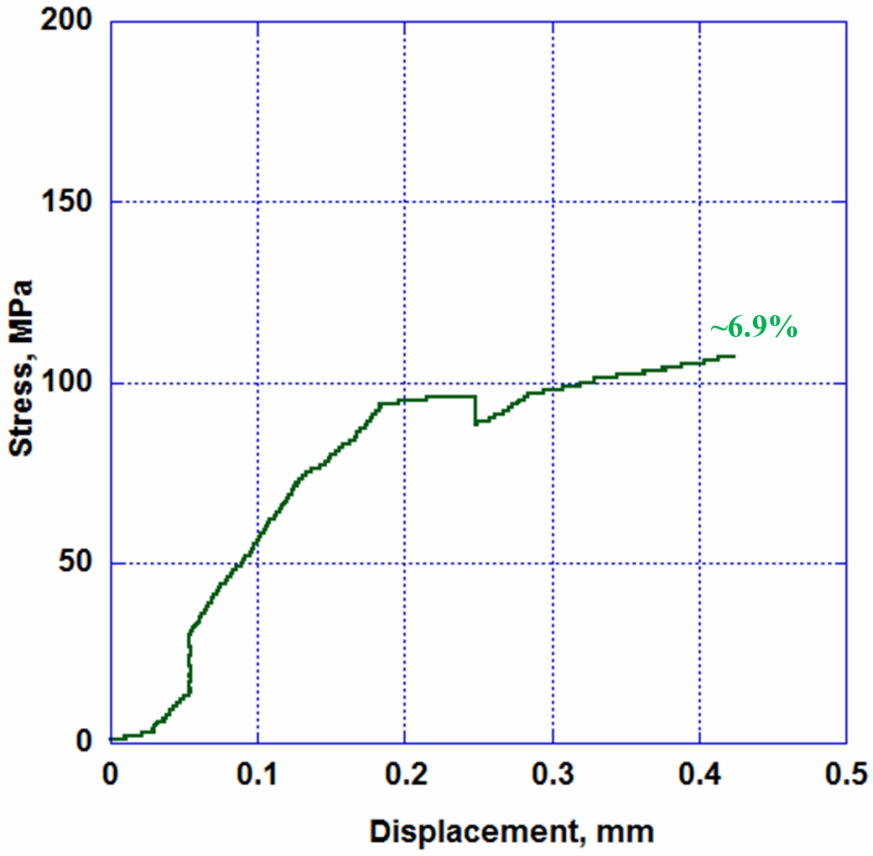

Figure 4.66 Representative stress vs. displacement plots for extruded MN10 samples compression tested at 323K. The displacement values included displacements in both the gage section and the grip regions. The approximate strain values are indicated.

Table 4.11 MN10 extruded compression property comparison between different test conditions.

Test temperature	YS (MPa)	UTS (MPa)	Maximum strain (%)
323K	~94	~108	~6.9
423K	-	-	~8.1
523K	-	-	~4.0

4.3.3.1 323K compression

Figure 4.67 shows the {0001} pole figures in the normal direction from the gage section of the specimen compression tested at 323K before and after deformation. The significant change in texture was expected to be due to the extension twinning activity.

In the microstructural patch analyzed, 96 extension twins were observed. No contraction twins were observed. Figure 4.68 shows the IPF map in the normal direction of the same area from the gage section of the MN10 extruded specimen compression tested at 323K taken at 0% and ~6.9% strain. The extension twin boundaries are highlighted in black in Figure 4.68b. Figure 4.69 plots the number of identified extension twins versus the corresponding global Schmid factor range. Extension twins with Schmid factors as low as 0.01 and as high as 0.50 were observed. 17 extension twins were observed at global Schmid factor values less than 0. The deformation was controlled by extension twinning in the extruded MN10 specimen compression tested at 323K.

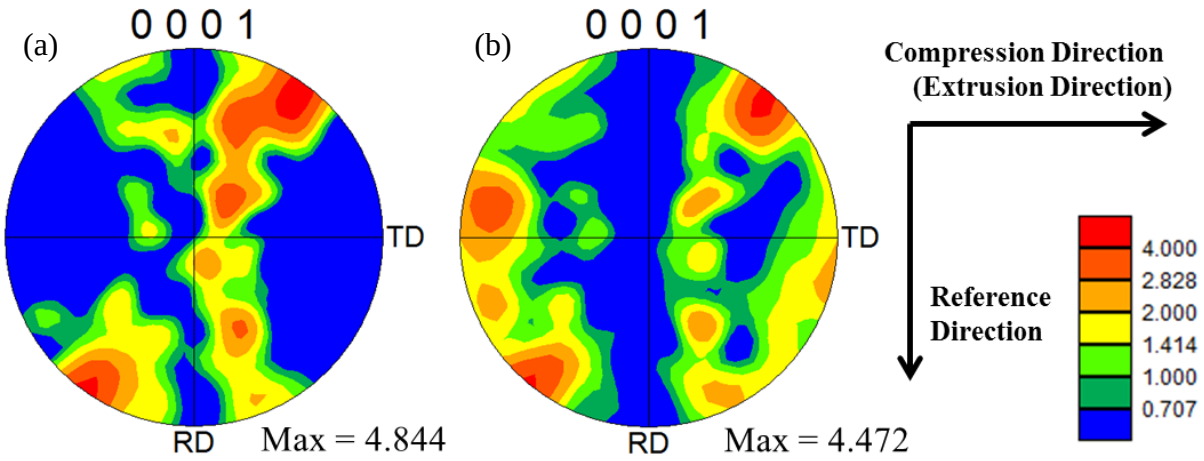

Figure 4.67 {0001} pole figures in the normal direction from the gage section of the MN10 extruded specimen compression tested at 323K (a) before and (b) after deformation (deformed to ~6.9% strain).

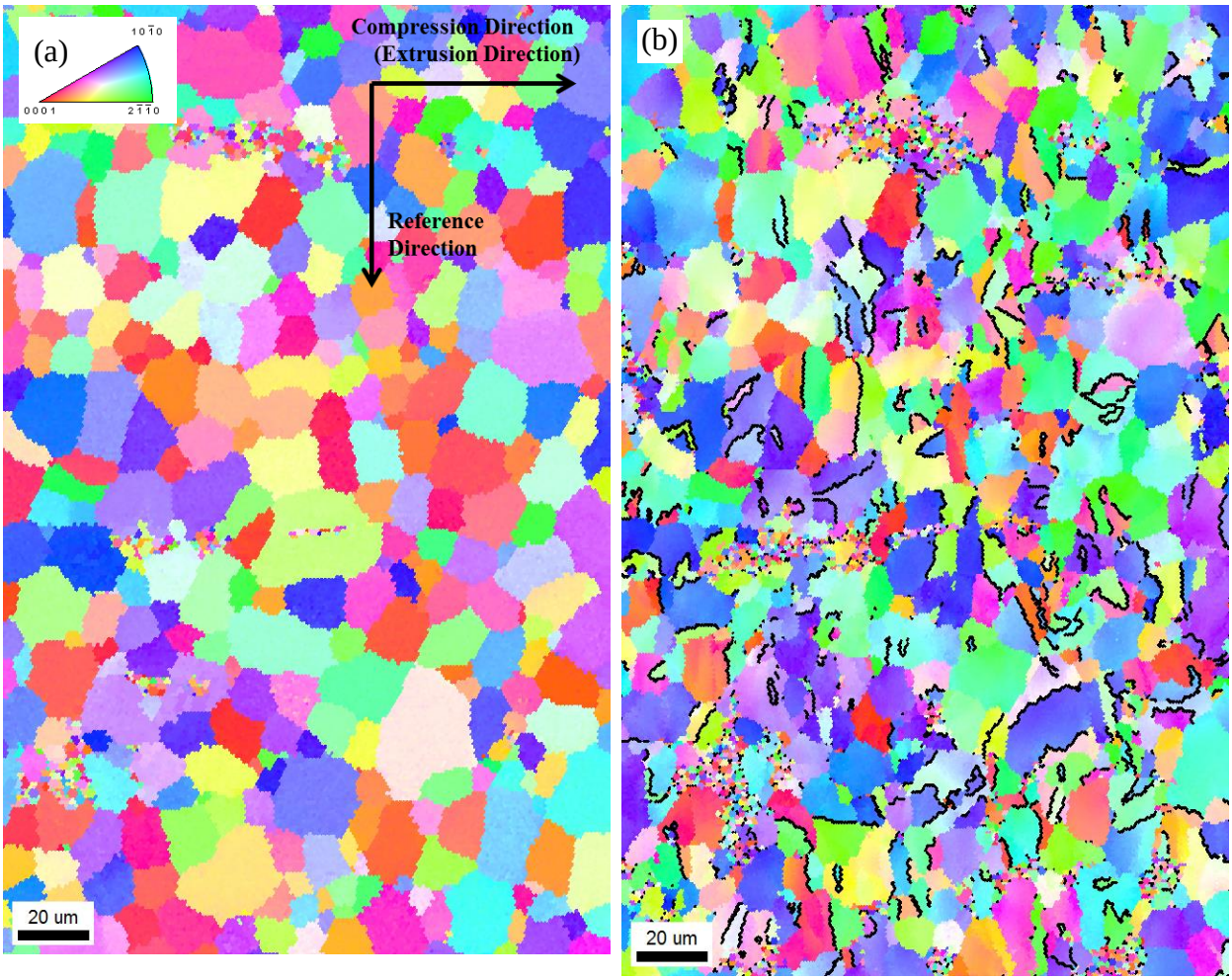

Figure 4.68 EBSD IPF map in the normal direction of the same area from the gage section of the extruded MN10 compression tested specimen at 323K (a) before deformation and (b) at ~6.9% strain. Extension twin boundaries (86°±5° misorientation about $< 11\bar{2}0 >$, twin plane $\{10\bar{1}2\}$±5° tolerance) are highlighted in black in (b).

In Figure 4.70a, the orientation of the grains in which extension twins were identified was plotted in a unit triangle along the compression direction. In Figure 4.70b the same data from 4.70a is plotted in a {0001} pole figure along the normal direction.

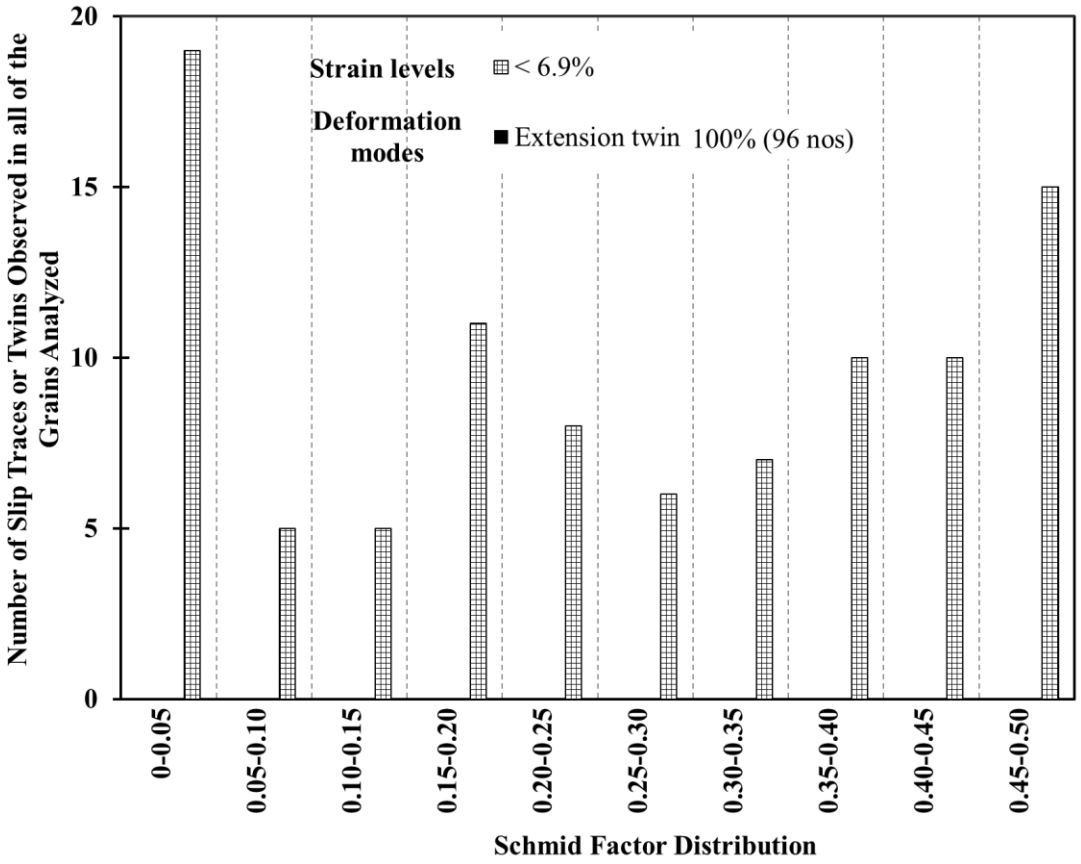

Figure 4.69 A histogram of the Schmid factor distribution of extension twins for the extruded MN10 323K compression experiment.

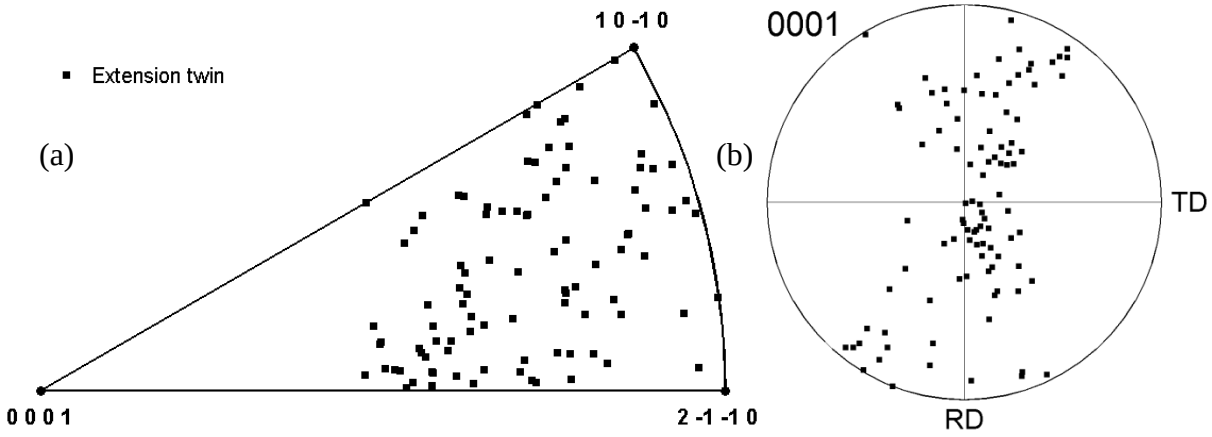

Figure 4.70 The individual grain orientations in which extension twins were observed for extruded MN10 compression test at 323K, plotted in a (a) unit triangle along the compression direction and (b) {0001} pole figure along the normal direction.

4.3.3.2 423K compression

Figure 4.71 shows the {0001} pole figures in the normal direction from the gage section of the specimen compression tested at 423K before and after deformation. The significant change in texture was expected to be due to the extension twinning activity.

In the microstructural patch analyzed, 67 extension twins were observed. No contraction twins were observed. Figure 4.72 shows the IPF map in the normal direction of the same area from the gage section of the MN10 extruded specimen compression tested at 423K taken at 0% and ~8.1% strain. The extension twin boundaries are highlighted in black in Figure 4.72b. Figure 4.73 plots the number of identified extension twins versus the corresponding global Schmid factor range. Extension twins with Schmid factors as low as 0.08 and as high as 0.50 were observed. 7 extension twins were observed at global Schmid factor values less than 0. The deformation was controlled by extension twinning in the extruded MN10 specimen compression tested at 423K.

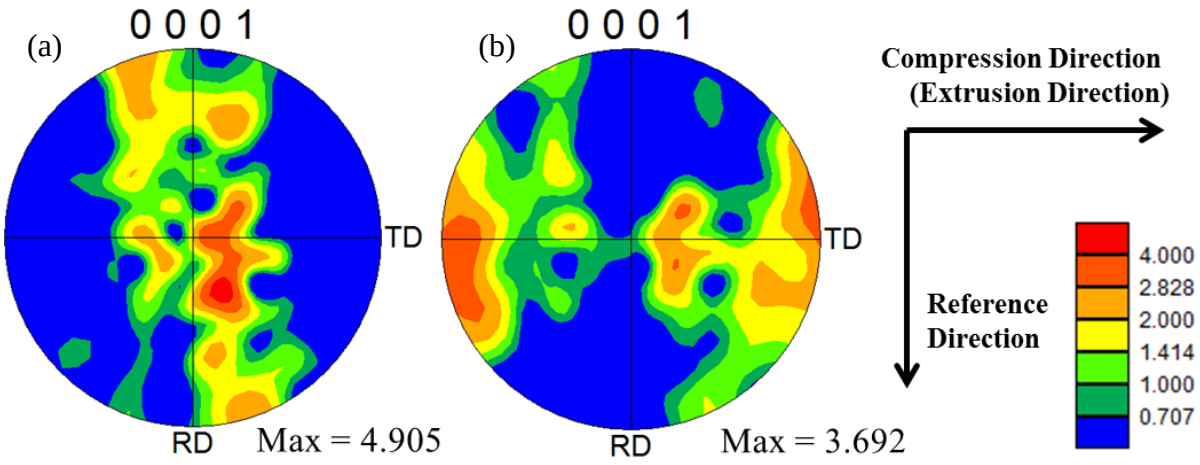

Figure 4.71 {0001} pole figures in the normal direction from the gage section of the MN10 extruded specimen compression tested at 423K (a) before and (b) after deformation.

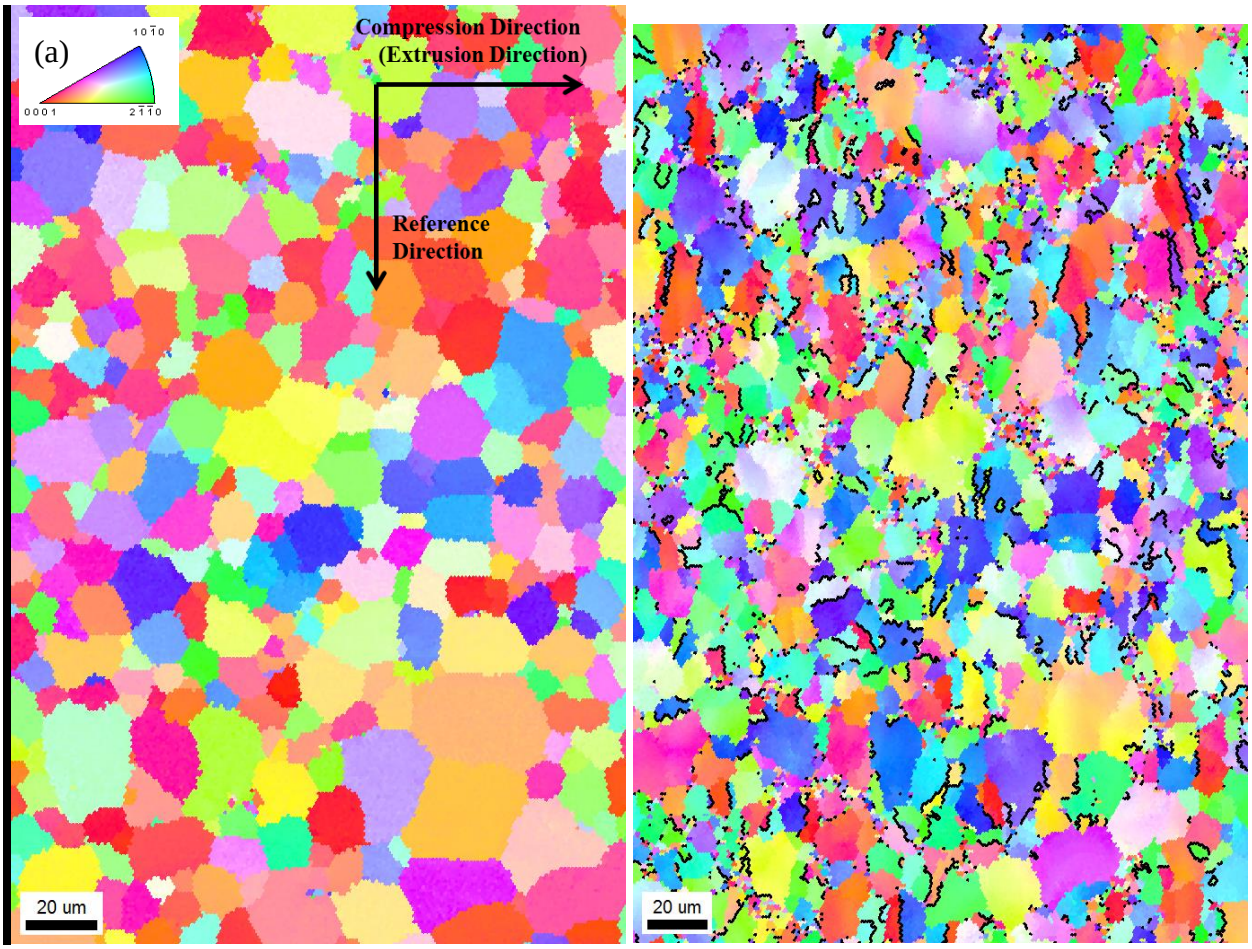

Figure 4.72 EBSD IPF map in the normal direction of the same area from the gage section of the extruded MN10 compression tested specimen at 423K (a) before deformation and (b) at ~8.1% strain. Extension twin boundaries (86°±5° misorientation about $< 11\bar{2}0 >$, twin plane $\{10\bar{1}2\}$±5° tolerance) are highlighted in black in (b).

In Figure 4.74a, the orientation of the grains in which extension twins were identified was plotted in a unit triangle along the compression direction. In Figure 4.74b the same data from 4.74a is plotted in a {0001} pole figure along the normal direction.

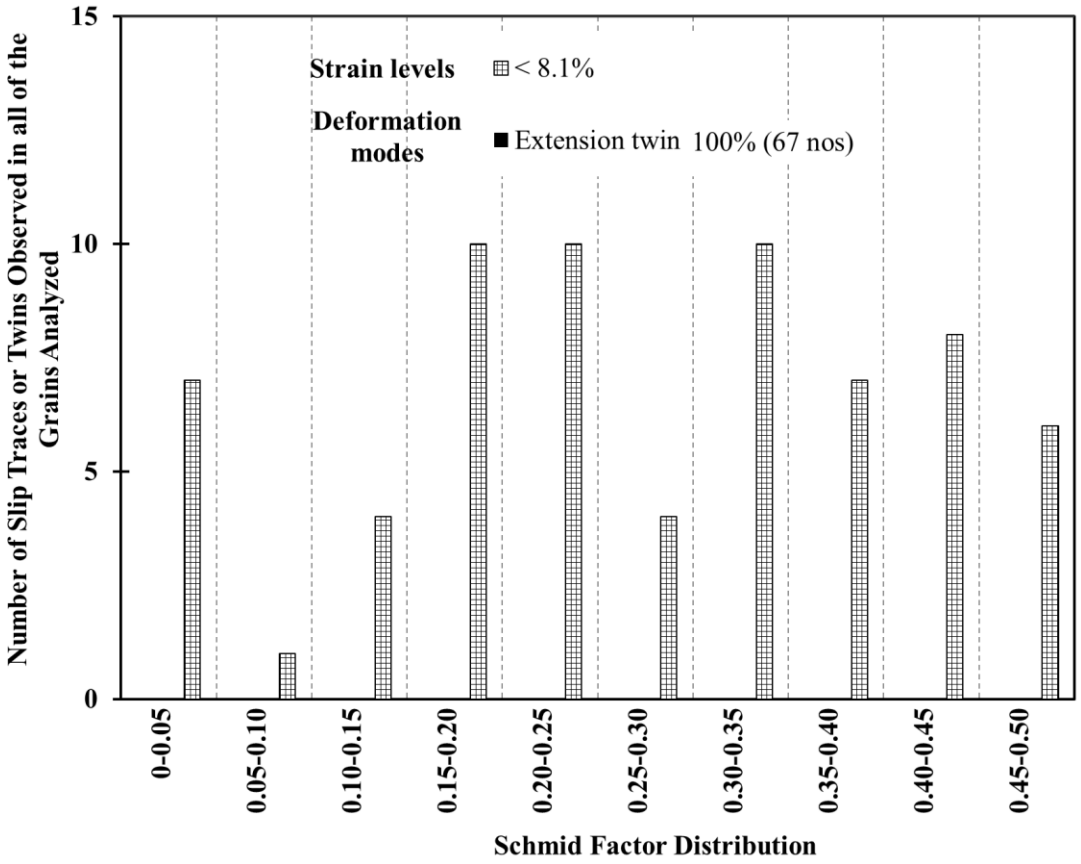

Figure 4.73 A histogram of the Schmid factor distribution of extension twins for the extruded MN10 423K compression experiment.

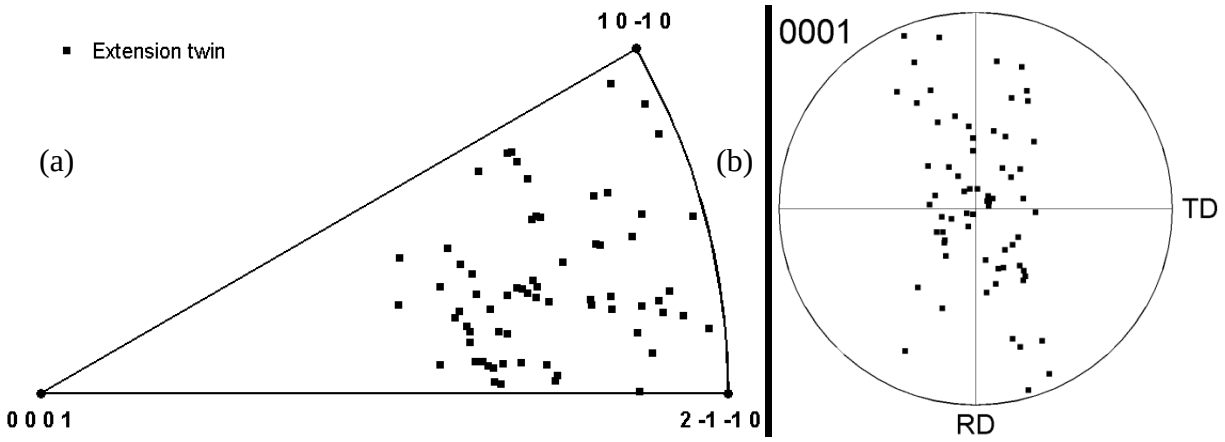

Figure 4.74 The individual grain orientations in which different extension twins were observed for extruded MN10 compression test at 423K, plotted in a (a) unit triangle along the compression direction and (b) {0001} pole figure along the normal direction.

4.3.3.3 523K compression

Figure 4.75 shows the {0001} pole figures in the normal direction from the gage section of the specimen compression tested at 523K before and after deformation. The change in texture was expected to be due to the extension twinning activity.

In the microstructural patch analyzed, 83 extension twins were observed. No contraction twins were observed. Figure 4.76 shows the IPF map in the normal direction of the same area from the gage section of the MN10 extruded specimen compression tested at 523K taken at 0% and ~4.0% strain. The extension twin boundaries are highlighted in black in Figure 4.76b. Figure 4.77 plots the number of identified extension twins versus the corresponding global Schmid factor range. Extension twins with Schmid factors as low as 0.01 and as high as 0.50 were observed. 10 extension twins were observed at global Schmid factor values <0. The deformation was controlled by extension twinning in the extruded MN10 specimen compression tested at 523K.

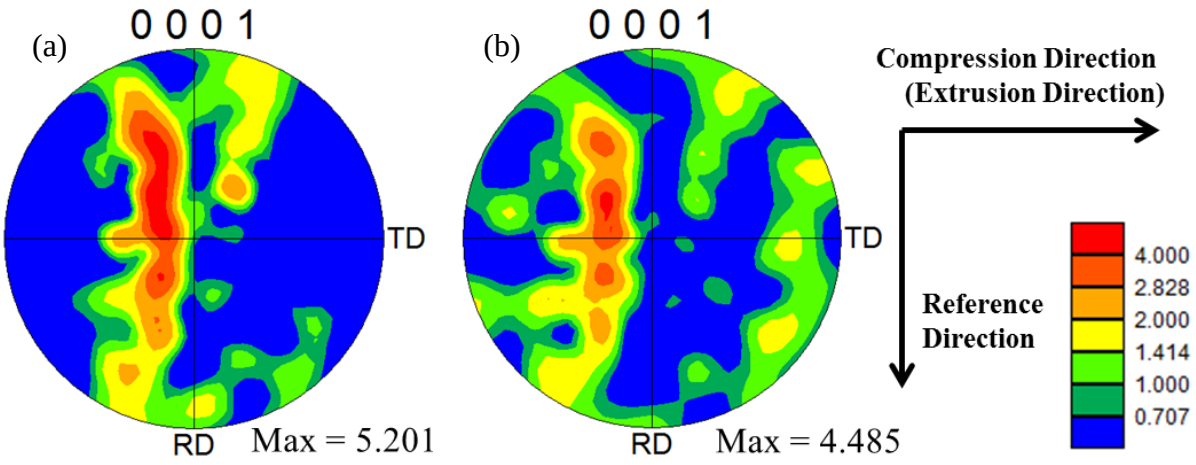

Figure 4.75 {0001} pole figures in the normal direction from the gage section of the MN10 extruded specimen compression tested at 523K (a) before and (b) after deformation.

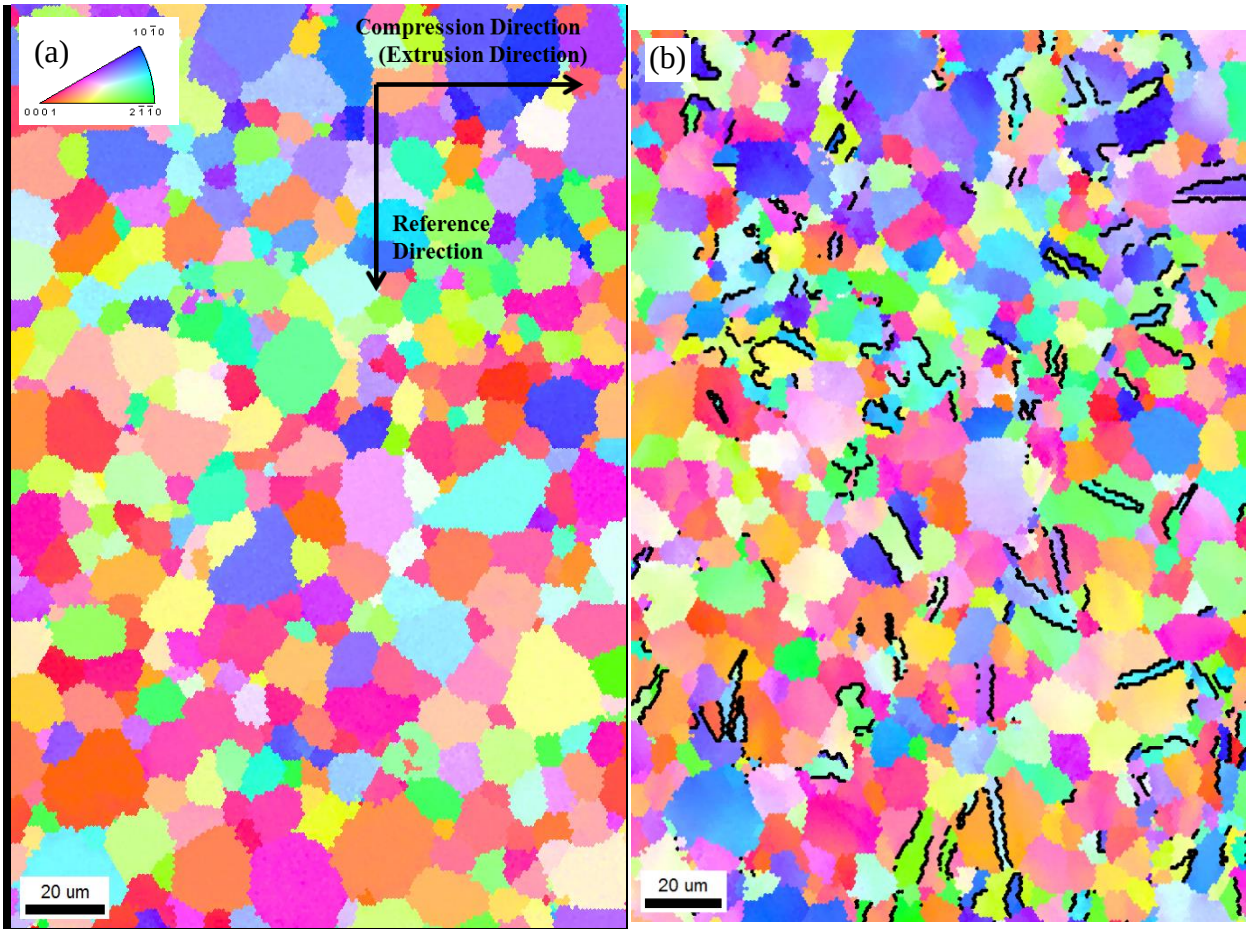

Figure 4.76 EBSD IPF map in the normal direction of the same area from the gage section of the extruded MN10 compression tested specimen at 523K (a) before deformation and (b) at ~4.0% strain. Extension twin boundaries (86°±5° misorientation about $< 11\bar{2}0 >$, twin plane $\{10\bar{1}2\}$±5° tolerance) are highlighted in black in (b).

In Figure 4.78a, the orientation of the grains in which extension twins were identified was plotted in a unit triangle along the compression direction. In Figure 4.78b the same data from 4.78a is plotted in a {0001} pole figure along the normal direction.

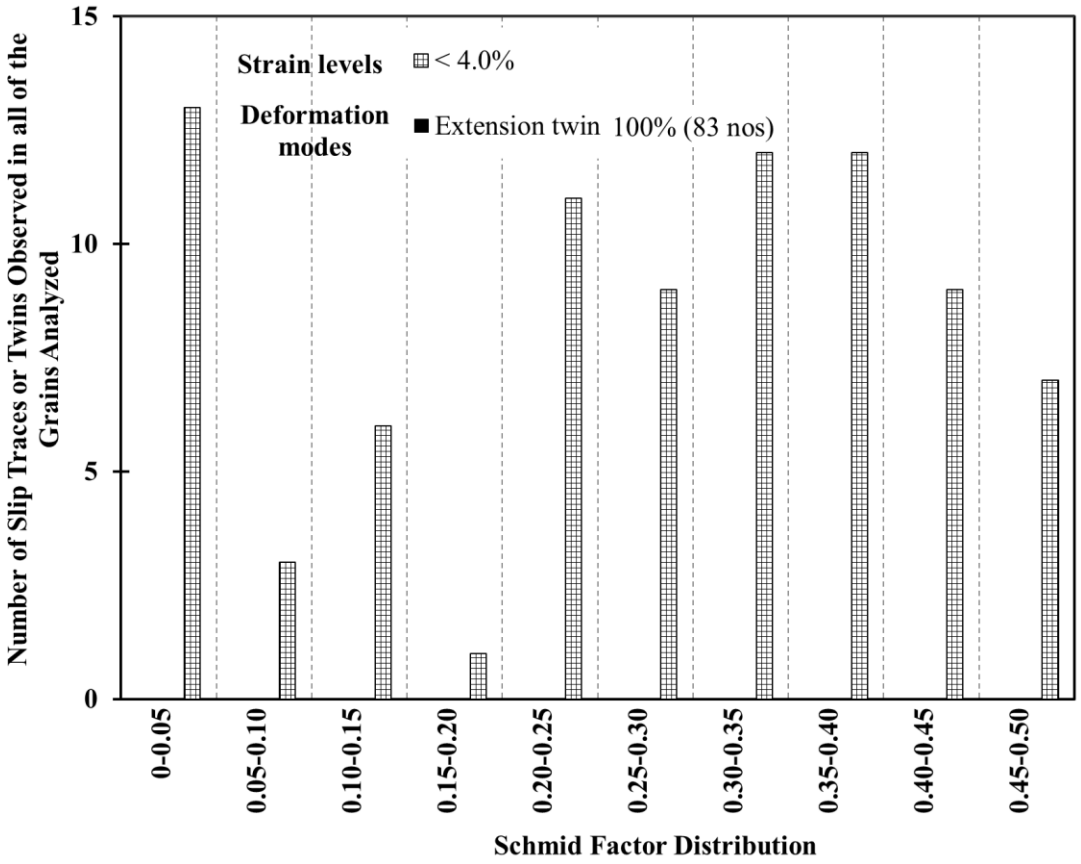

Figure 4.77 A histogram of the Schmid factor distribution of extension twins for the extruded MN10 523K compression experiment.

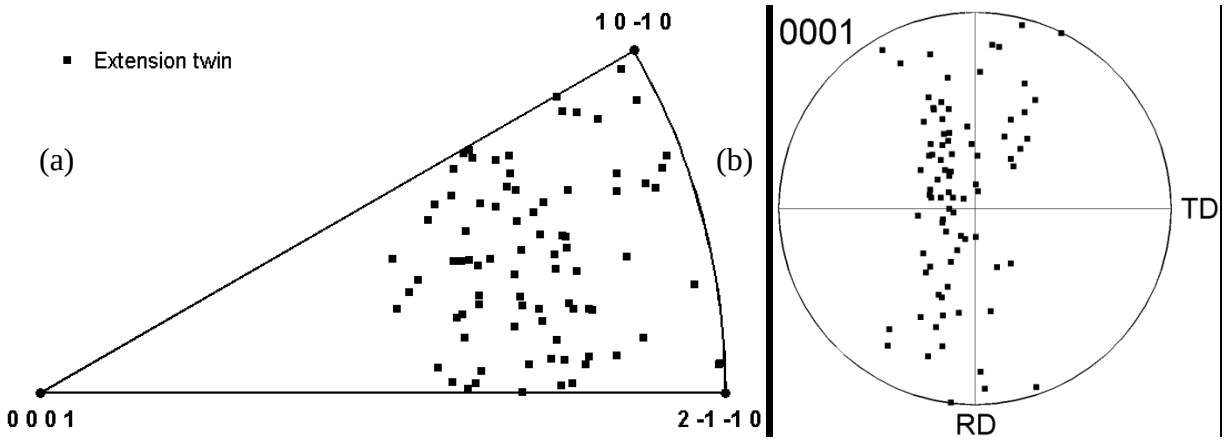

Figure 4.78 The individual grain orientations in which extension twins were observed for extruded MN10 compression test at 523K, plotted in a (a) unit triangle along the compression direction and (b) {0001} pole figure along the normal direction.

4.4 As-cast Mg-0.9Mn-0.8Nd (MN11)

4.4.1 Microstructure and texture

Figure 4.79 shows a representative SE SEM image of the as-cast MN11 microstructure. As shown in figure 4.79, equiaxed grains were observed. The average grain diameter was ~970±520µm based on ASTM standards for grain size measurement [ASTM E112-13 2013, Vander Voort 1999]. It is noted that the grain size measurement was performed on a microstructural patch containing ~220 grains. Figure 4.80 shows the grain size distribution of as-cast MN11. Grains with diameter ranging from ~315µm to ~2815µm were observed.

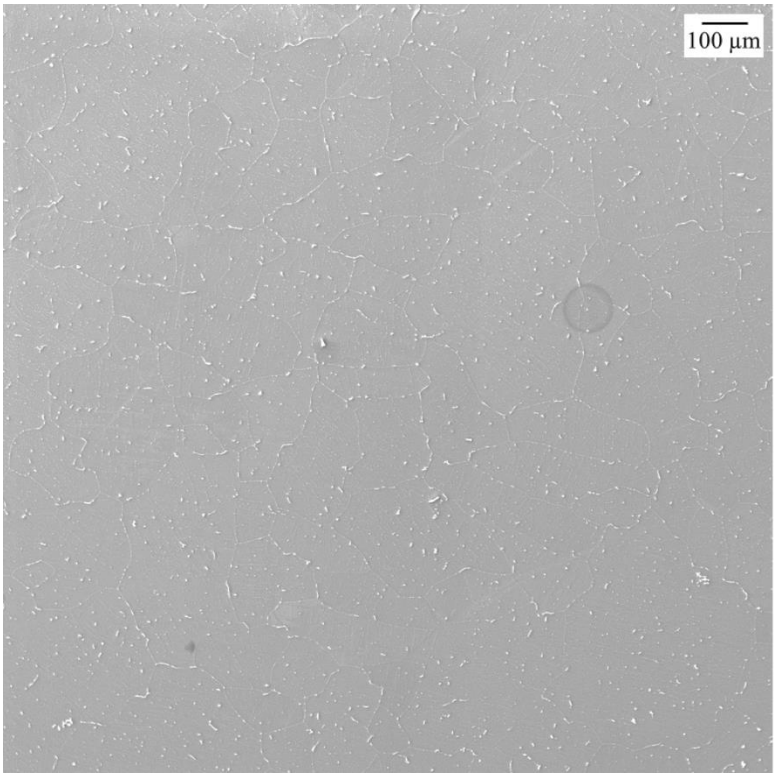

Figure 4.79 SE SEM image of as-cast MN11 microstructure.

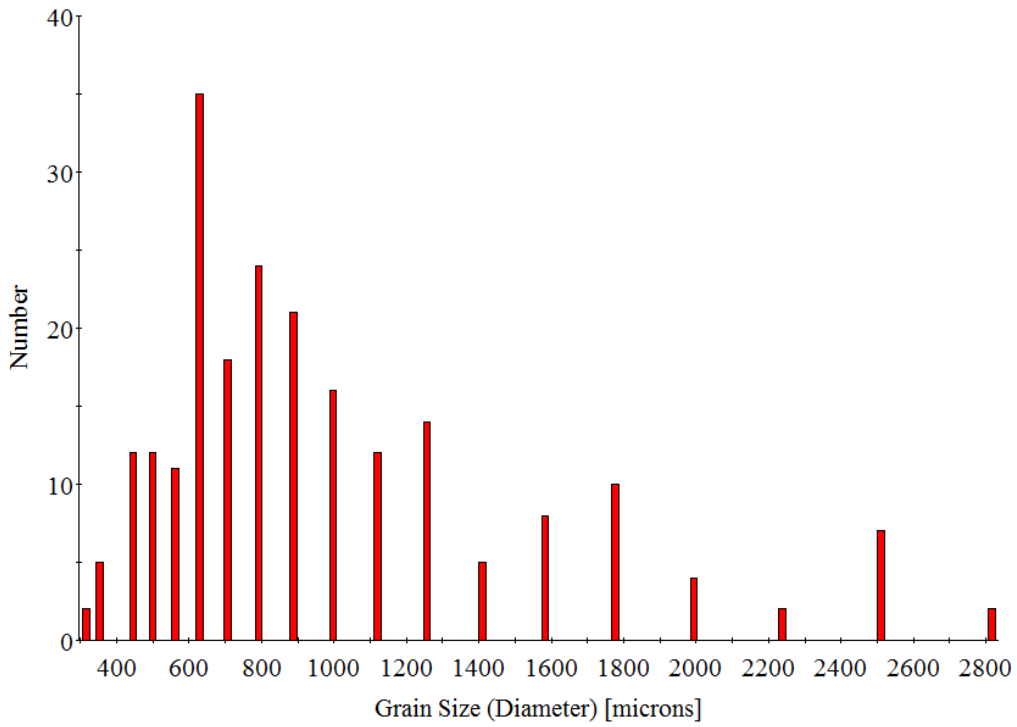

Figure 4.80 The grain size distribution of as-cast MN11. A total of ~220 grains were measured.

Stringers of precipitates were observed within grains in the MN11 as-cast microstructure (see Figure 4.81a). These precipitates appeared to be aligned parallel to the basal <a> planes. The orientation of the grains obtained from EBSD analysis is indicated in Figure 4.81a. The volume fraction of the second phase particles measured from the SE SEM images were ~2.05%. Figure 4.81b shows a DF TEM image of Mn-rich precipitates for which EDS analysis was performed. The average composition of 4 Mn-rich precipitates located inside grains was ~Mg-19Mn-1Nd (wt.%). Table 4.12 lists the chemical composition of the 4 Mn-rich precipitates analyzed.

Table 4.12 The chemical composition of the 4 Mn-rich precipitates analyzed inside the grains in the as-cast MN11 microstructure. The values are provided in wt%.

Observations	Mg	Mn	Nd
1	90.42	9.30	0.28
2	60.60	38.48	0.92
3	88.60	10.94	0.46
4	81.14	17.62	1.24
Average	80.19	19.09	0.73

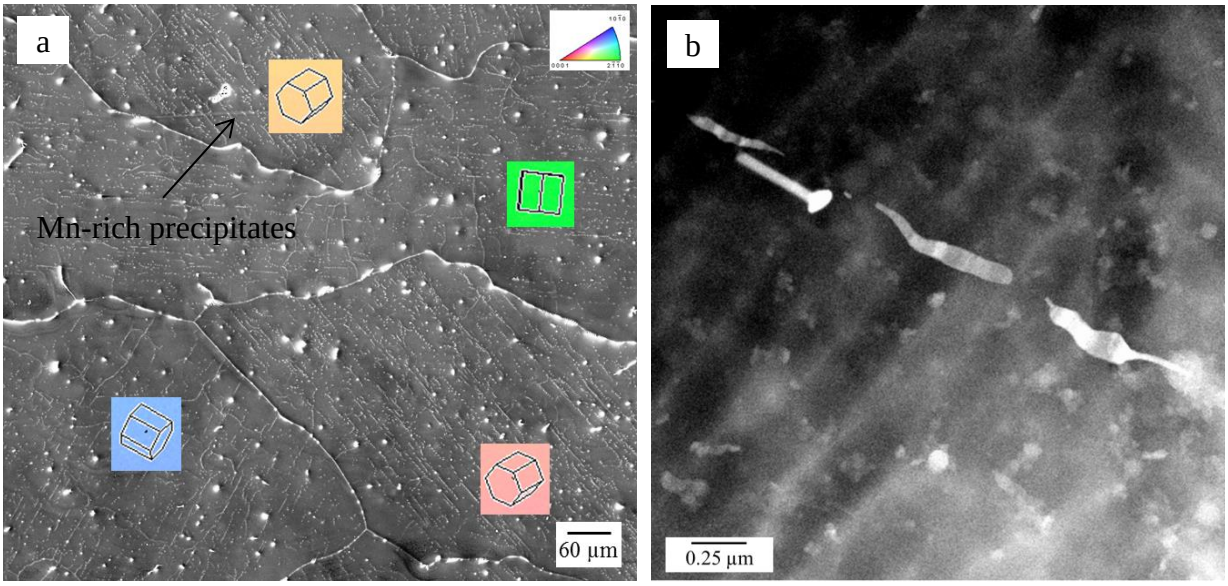

Figure 4.81 (a) SE SEM image showing the Mn-rich precipitates aligned parallel to the basal <a> planes and (b) DF TEM image of the Mn-rich precipitates in the MN11 as-cast microstructure. In (a), the orientation of the grains is indicated as HCP unit cells as obtained from the EBSD analysis.

Nd-rich precipitates were also observed within grains in the MN11 as-cast microstructure. Figure 4.82a shows the BF TEM image of a Nd-rich precipitate observed inside a grain. The chemical composition of this precipitate was measured to be Mg-1Mn-50Nd (wt.%). In addition, Nd-rich precipitates were also observed at the grain boundaries. Figure 4.82b shows the DF TEM image of Nd-rich precipitates observed at the grain boundaries in the MN11 as-cast microstructure. Three compositional measurements of Nd-rich precipitates at the

grain boundaries provided an average composition of ~Mg-2Mn-58Nd (wt.%). Table 4.13 shows the measured chemical composition of the three Nd-rich precipitates analyzed.

EDS performed on the matrix showed an average composition of ~Mg-1Mn-0.5Nd from 3 observations. Table 4.14 lists the chemical composition obtained from the 3 observations for the matrix.

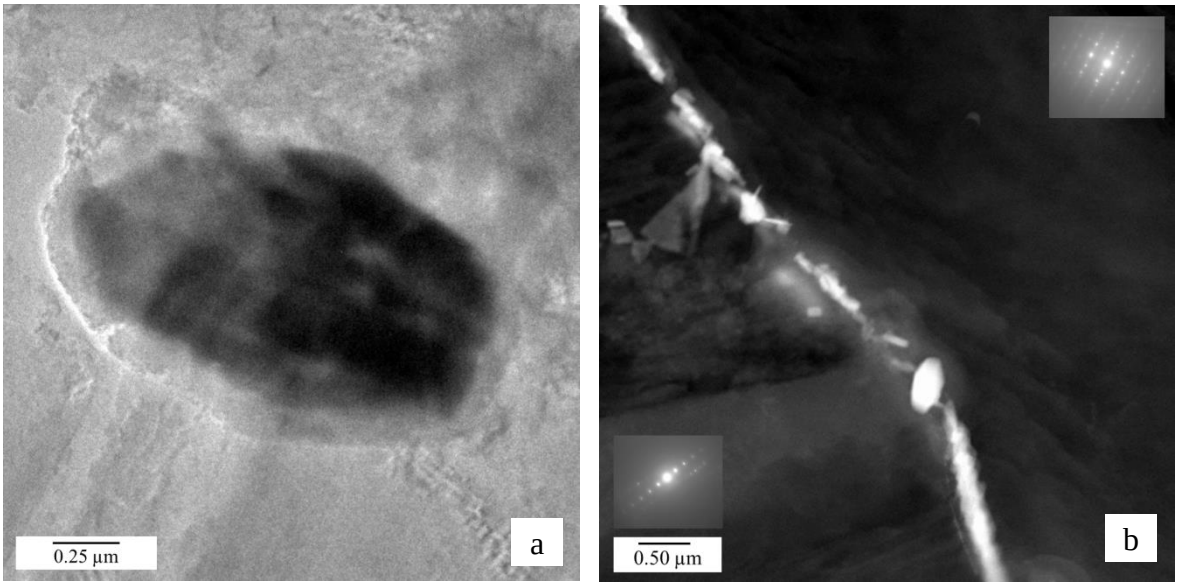

Figure 4.82 (a) BF TEM image of a Nd-rich precipitate observed within grains and (b) DF TEM image of Nd-rich precipitates observed at the grain boundaries in the MN11 as-cast microstructure. The SAD patterns from the two grains on either side of the grain boundary are shown in inset in (b).

Table 4.13 The chemical composition of the 3 Nd-rich precipitates analyzed at the grain boundaries in the as-cast MN11 microstructure. The values are in wt%.

Observations	Mg	Mn	Nd
1	36.70	1.01	62.28
2	32.35	4.01	63.63
3	50.30	0.83	48.87
Average	39.78	1.95	58.26

Table 4.14 The chemical composition of the as-cast MN11 matrix. The values are in wt%.

Observations	Mg	Mn	Nd
1	98.38	0.98	0.64
2	98.69	0.88	0.43
3	98.66	0.96	0.38
Average	98.58	0.94	0.48

Figure 4.83 shows the representative texture of the as-cast MN11 in the form of {0001} and $\{10\bar{1}0\}$ pole figures obtained using EBSD. The texture shown in Figure 4.83 was obtained from an area containing ~220 grains. Figure 4.84 shows the EBSD IPF map along the normal direction of the area from which the pole figures shown in Figure 4.83 was obtained. The image shown in Figure 4.84 was obtained by combining EBSD IPF maps of the gage section of 5 separate in-situ samples with similar orientations (normal direction of the sample perpendicular to the radial direction of the cast billet) but from different regions of the cast billet. The pole figures show a random texture. This type of texture is commonly observed in as-cast Mg alloys [Agnew et al. 2001, Pérez-Prado et al. 2004].

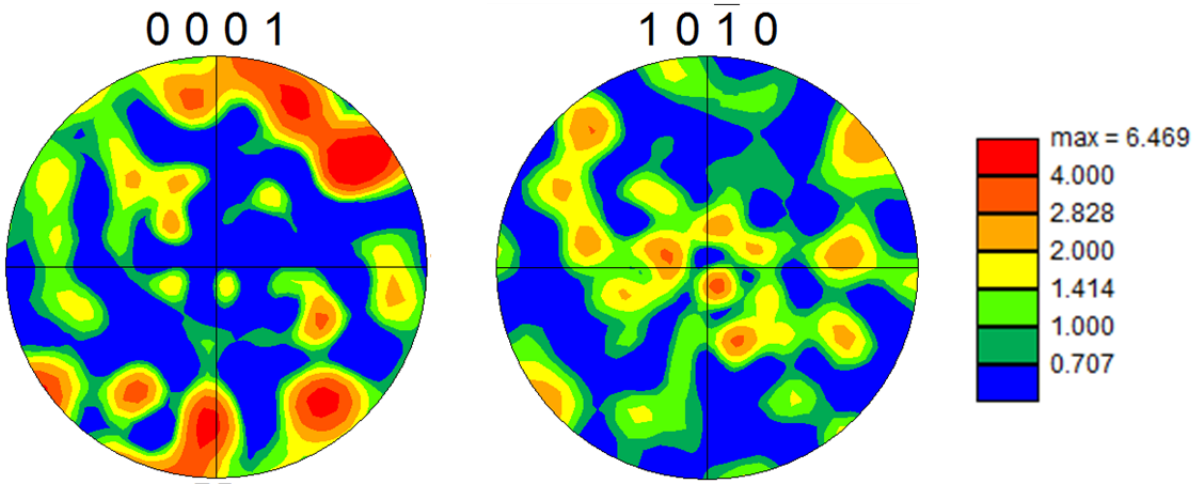

Figure 4.83 Representative texture of as-cast MN11 in the form of {0001} and $\{10\bar{1}0\}$ pole figures.

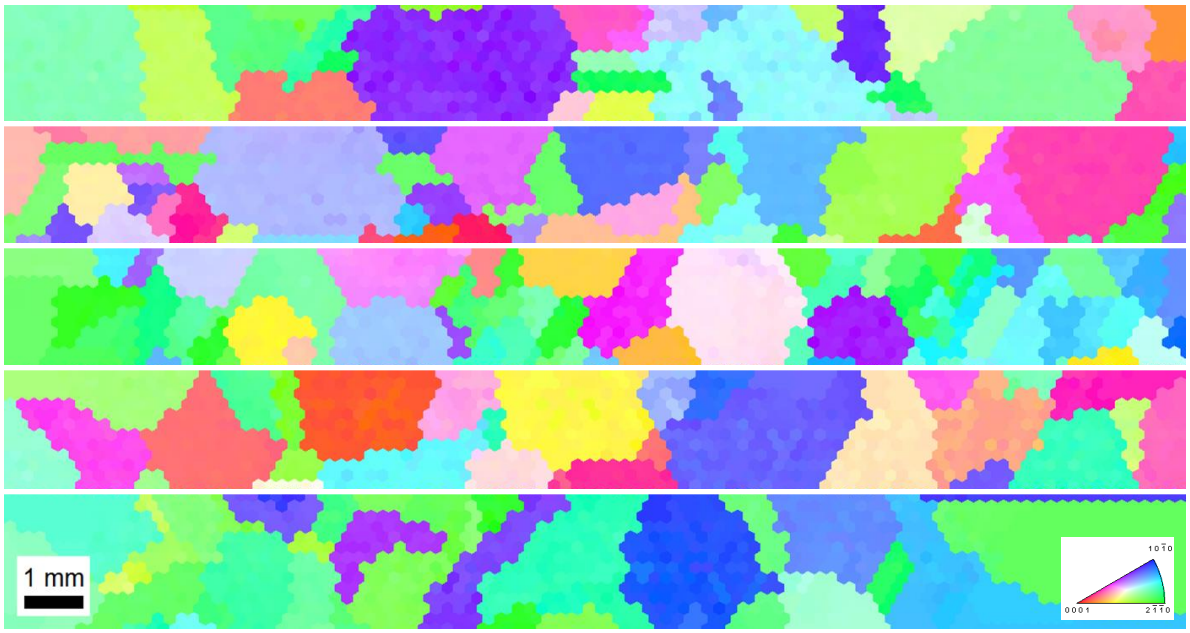

Figure 4.84 EBSD IPF map of the five different areas from which the pole figures shown in Figure 4.83 were obtained for as-cast MN11.

4.4.2 In-situ tension

In-situ tensile tests were performed on the as-cast MN11 at 323K, 423K, and 523K. One test was performed for each temperature. EBSD data was acquired before and after deformation, and slip/twin trace analysis was performed. Figure 4.85 shows the stress versus displacement plots for the 323K, 423K, and 523K tensile tests on the as-cast MN11. The stress drops indicate that stress relaxation occurred when the tests were paused for imaging. None of the specimens were taken to failure in order to facilitate EBSD mapping without further sample preparation. Table 4.15 lists the approximate YS, UTS, and the maximum strain levels attained for each experiment.

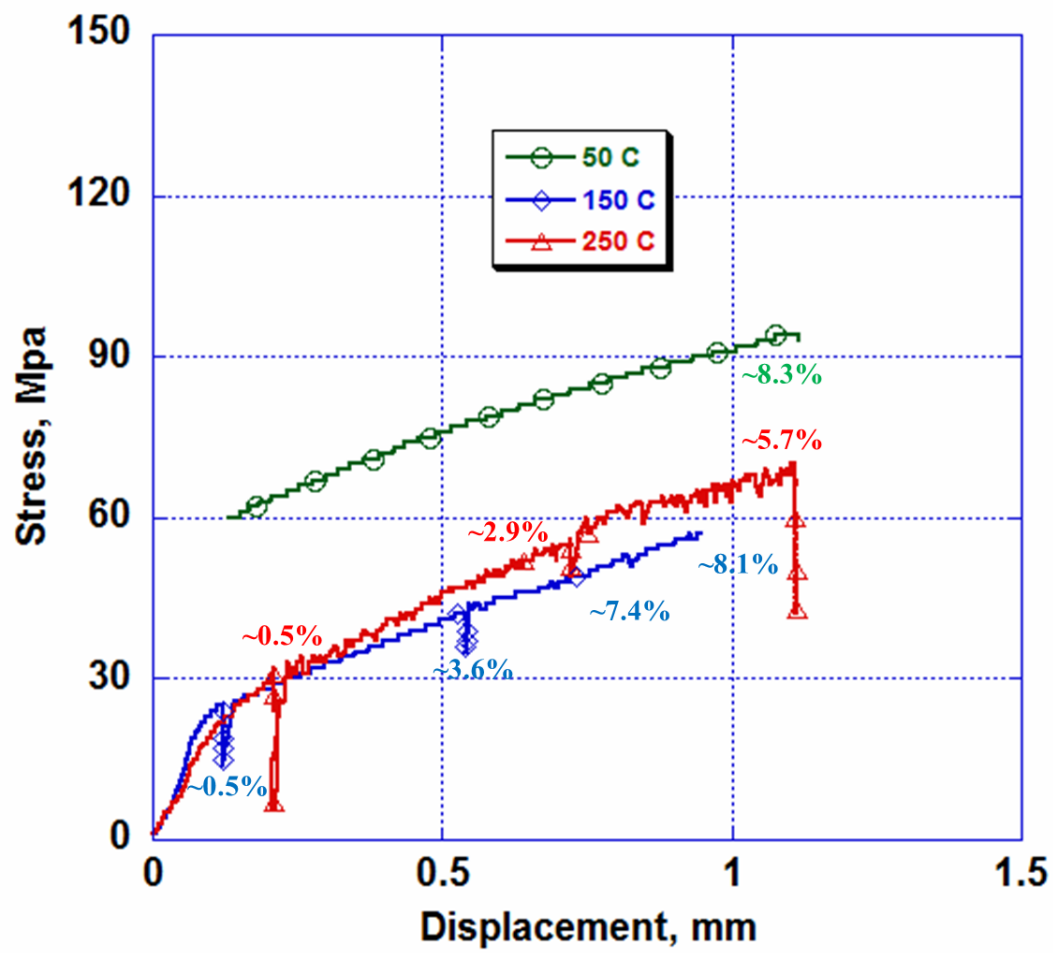

Figure 4.85 Representative stress vs. displacement plots for the as-cast MN11 sample tensile tested at 323K, 423K, and 523K. The stress drops indicate the stress relaxation that occurred when the tests were interrupted for imaging. The displacement values incorporate displacements in both the gage section and the grip region. Approximate local strain values are indicated in the plot.

Table 4.15 As-cast MN11 tensile property comparison between the different test conditions.

Test Temperature	YS(MPa)	UTS (MPa)	Maximum strain (%)
323K	-	~94	~8.3%
423K	~25	~57	~8.1%
523K	~23	~68	~5.7%

4.4.2.1 323K tension

Figure 4.86 shows the EBSD IPF map in the normal direction from the gage section of the 323K tensile tested sample before and after deformation.

Figure 4.87 shows the sequential SE SEM images taken from the same area of the 323K tensile-tested specimen. Basal <a> slip traces were observed in the area analyzed.

Figure 4.88 shows the area highlighted by the black box in Figure 4.6b. The extension twins observed in this region are highlighted in Figure 4.88. It is noted that multiple extension twin variants were activated in the grain shown in Figure 4.88.

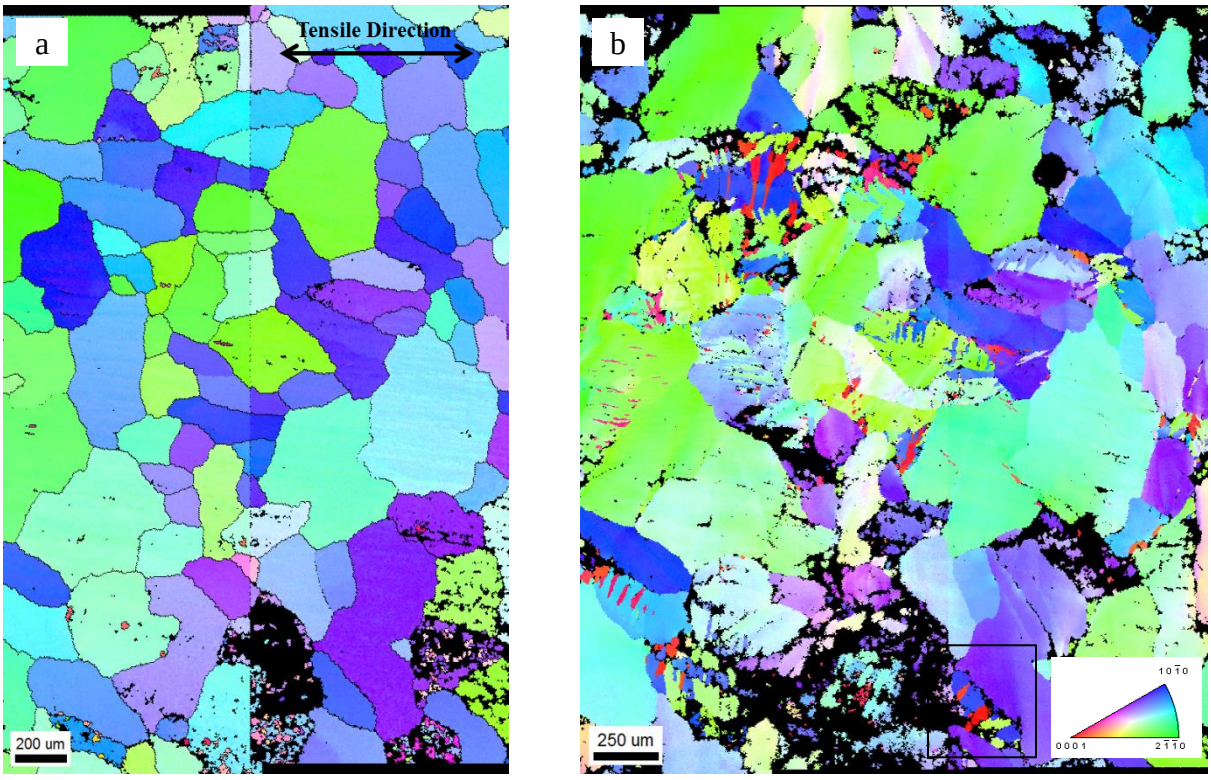

Figure 4.86 EBSD IPF map in the normal direction of the as-cast MN11 specimen tensile-tested at 323K (a) before deformation and (b) after deformation to ~8.3% strain.

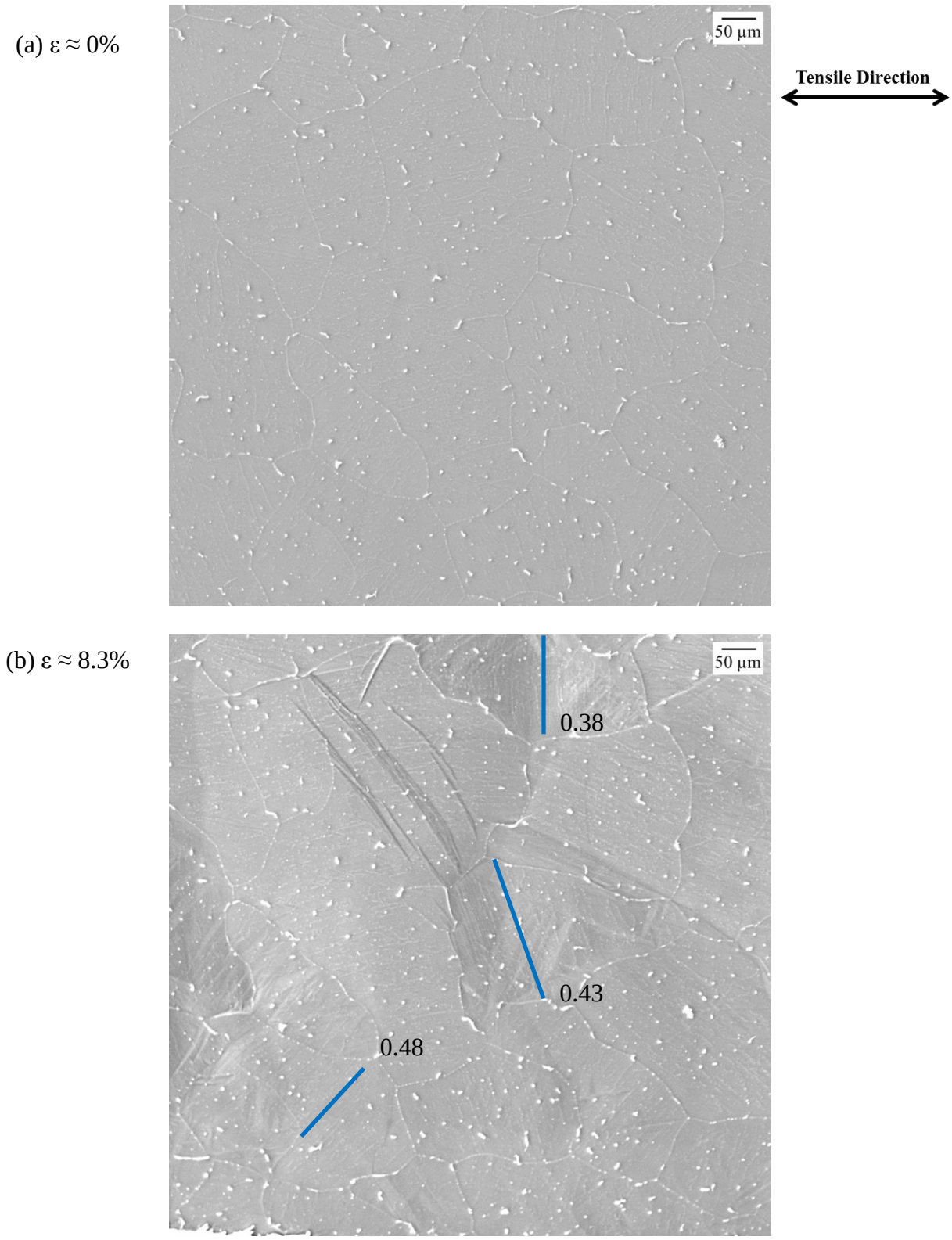

Figure 4.87 Sequential SE SEM images for the MN11 as-cast specimen tensile tested at 323K: (a) undeformed and (b) ~8.3% strain. In (b) the basal <a> slip traces observed in this region are highlighted and the corresponding Schmid factor values are provided.

Trace analysis was performed on ~100 grains from the microstructural patch shown in Figure 4.86a. 22 basal <a> slip traces and 17 extension twins were observed in this region. Figure 4.89 plots the number of identified observations of a particular deformation versus the corresponding global Schmid factor range. Two of the extension twins were observed at Schmid factors less than 0. All of the basal <a> slip was observed at Schmid factors higher than 0.25. Multiple slip/twin traces were observed in some of the grains. Extension twinning and basal <a> slip controlled the deformation in the MN11 as-cast specimen tensile tested at 323K.

Figure 4.90a shows the orientation of the grains in which different deformation modes were identified, plotted in a unit triangle along the tensile direction. Figure 4.90b shows the same data from Figure 4.90a plotted in a {0001} pole figure along the normal direction.

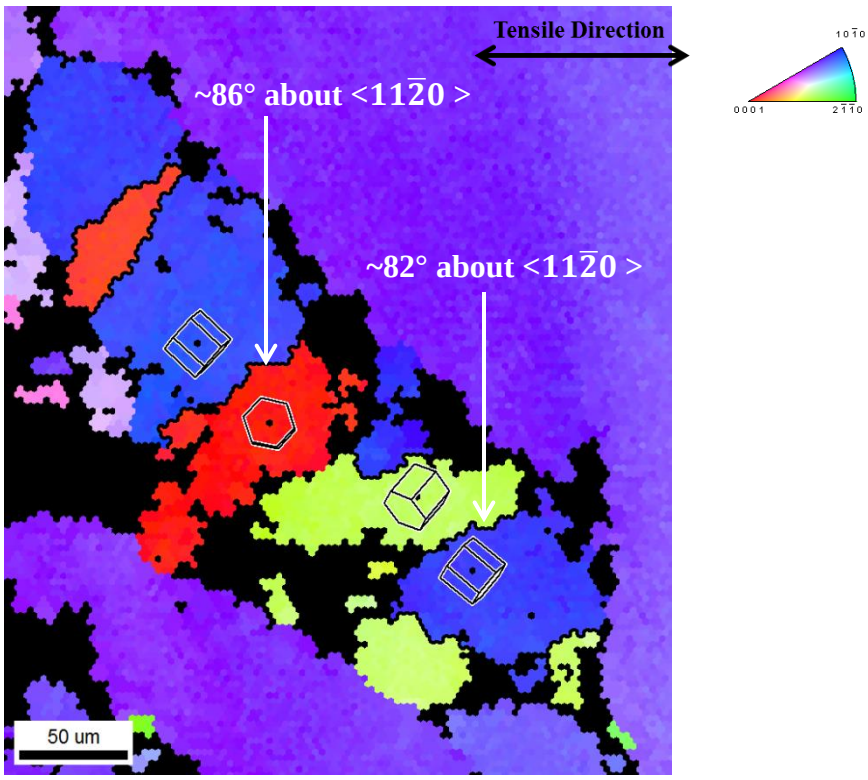

Figure 4.88 EBSD IPF map of the region highlighted by the black box in Figure 4.86b. The extension twin boundaries are highlighted by black lines. The HCP unit cells are overlaid indicating the misorientation between the parent grain and the twinned region.

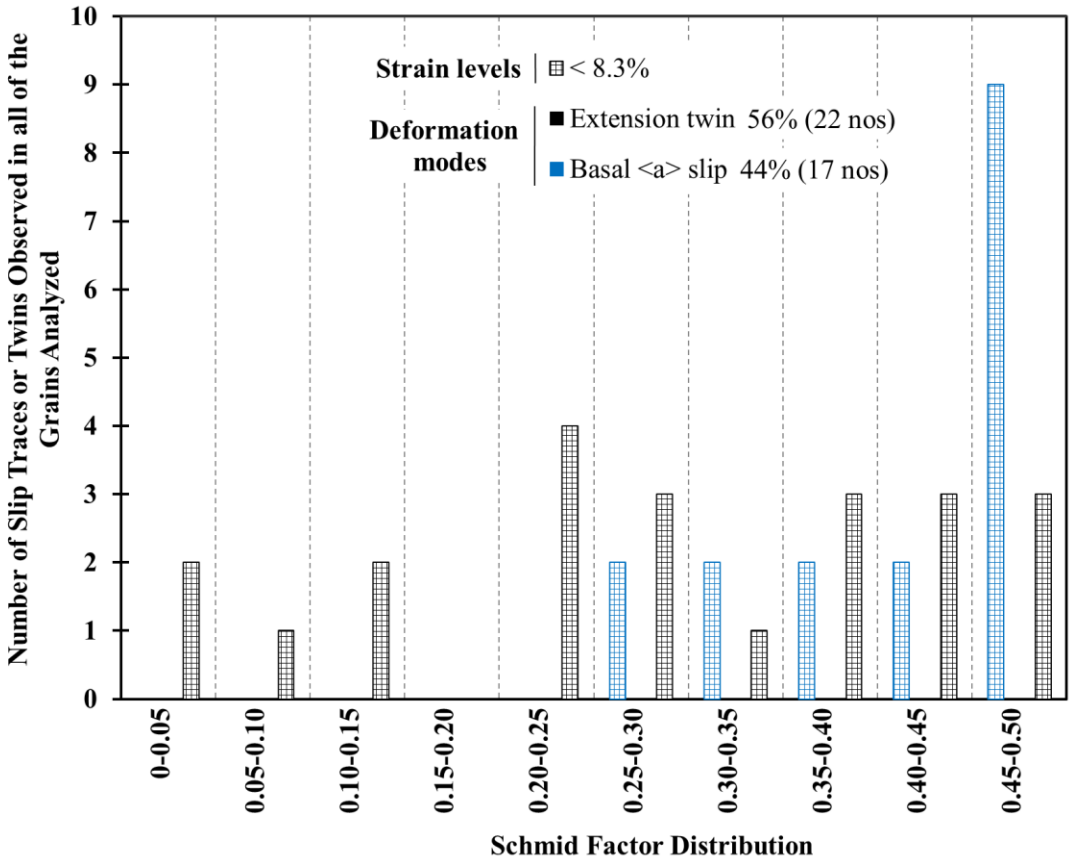

Figure 4.89 A histogram of the Schmid factor distribution of basal <a> slip and extension twins observed in the MN11 as-cast specimen tensile tested at 323K.

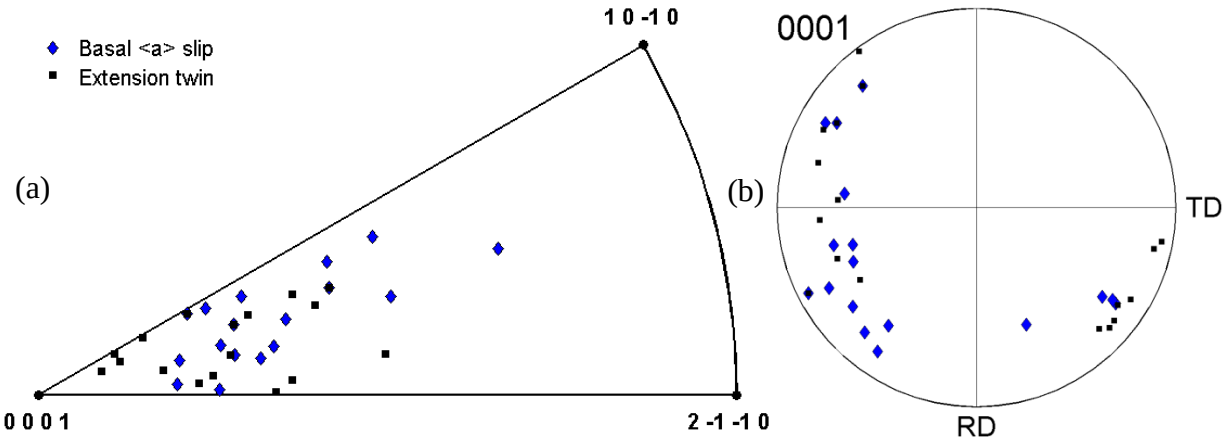

Figure 4.90 The individual grain orientations in which different deformation modes were observed for the MN11 as-cast specimen tensile tested at 323K, plotted in (a) unit triangle along the tensile direction and (b) {0001} pole figure along the normal direction.

4.4.2.2 423K tension

Figure 4.91 shows the EBSD IPF map in the normal direction from the gage section of the 423K tensile tested sample before and after deformation.

Figure 4.92 shows the sequential SE SEM images taken from the same area of the gage section of the 423K tensile-tested specimen. Basal <a> slip started to appear at ~0.5% strain. Prismatic <a> slip, pyramidal <c+a> slip, and extension twins were first observed to activate at ~3.6% strain.

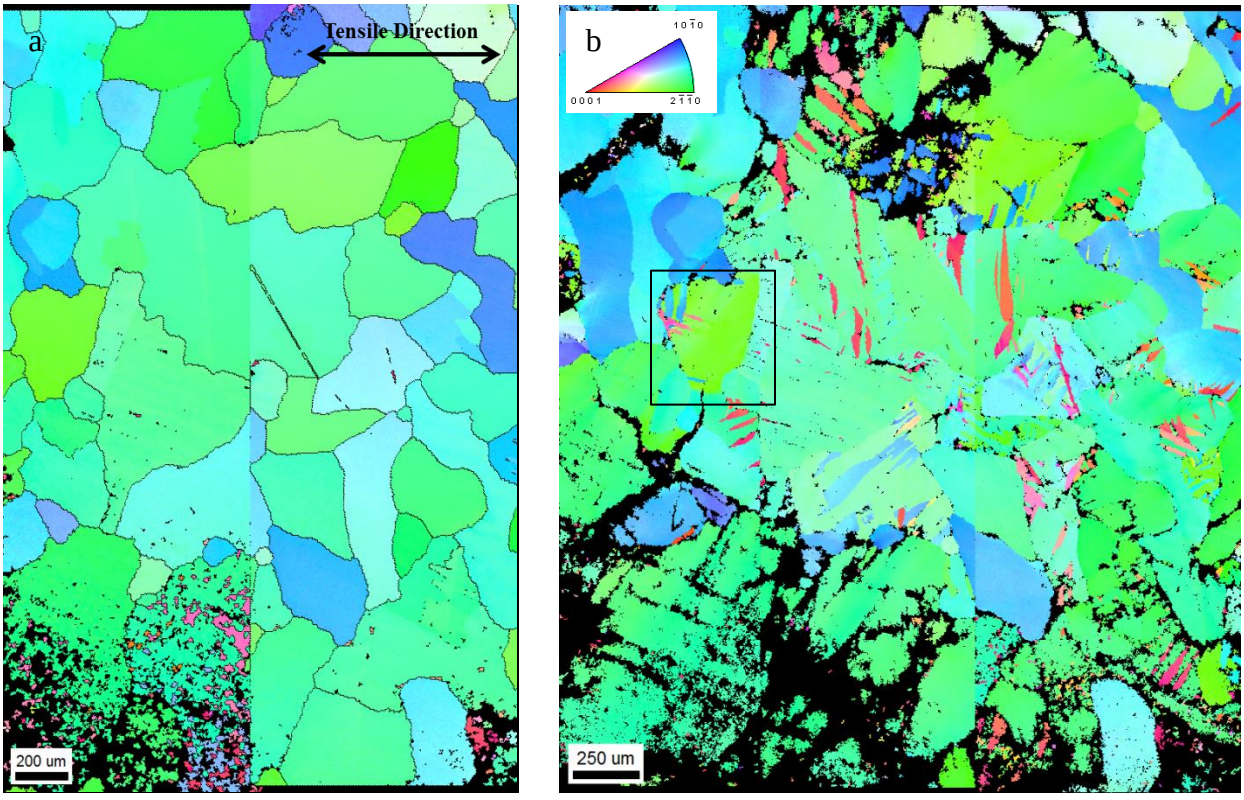

Figure 4.91 EBSD IPF map in the normal direction of the MN11 as-cast specimen tensile-tested at 423K (a) before deformation and (b) after deformation to ~8.1% strain.

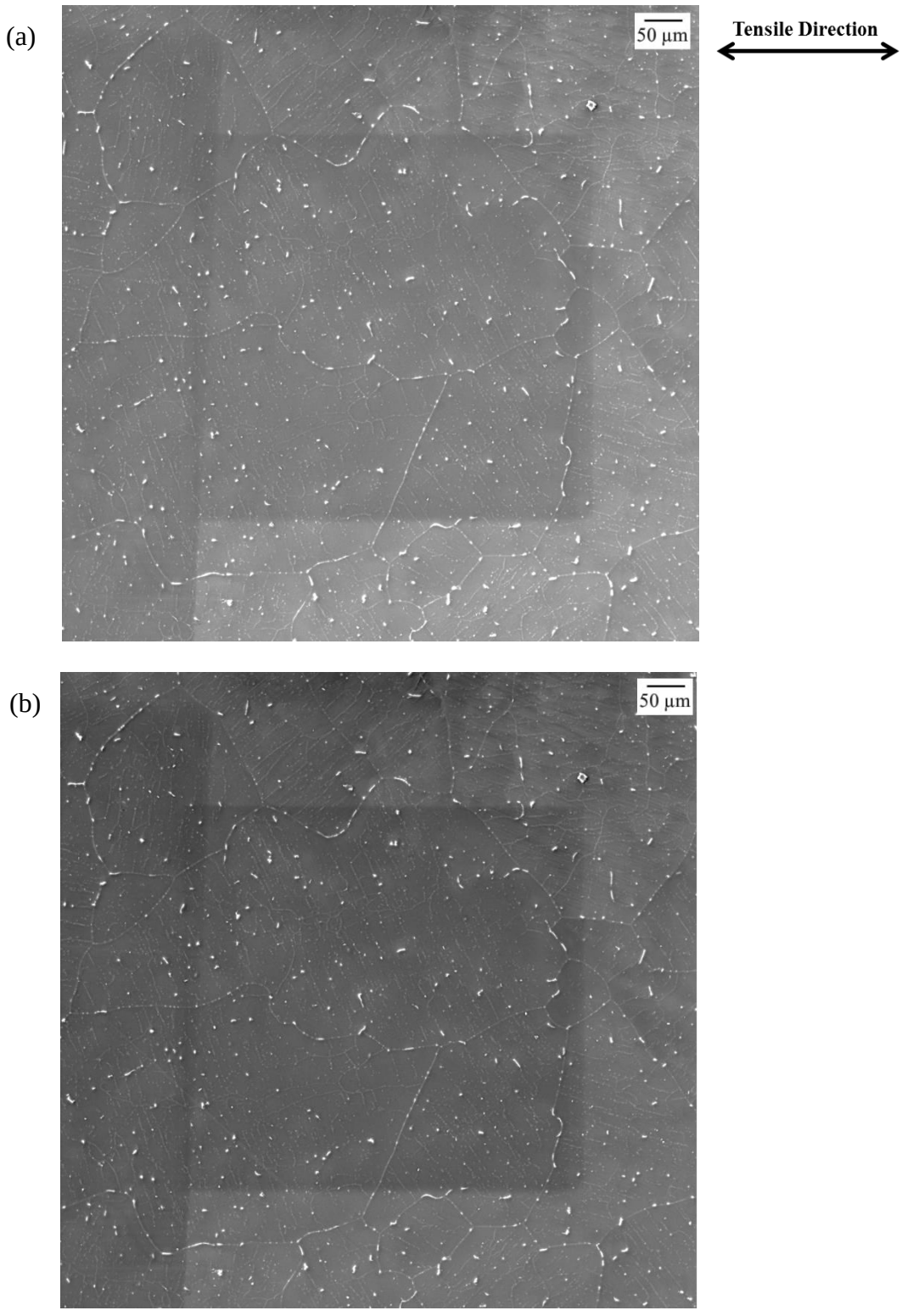

Figure 4.92 Sequential SE SEM images for the MN11 as-cast specimen tensile tested at 423K: (a) undeformed, (b) ~0.5% strain, (c) ~3.6% strain, and (d) ~8.1% strain. In (c) and (d), the slip traces are color coded for basal <a> slip (blue), and the corresponding Schmid factor values are given.

Figure 4.92 (cont'd)

(c)

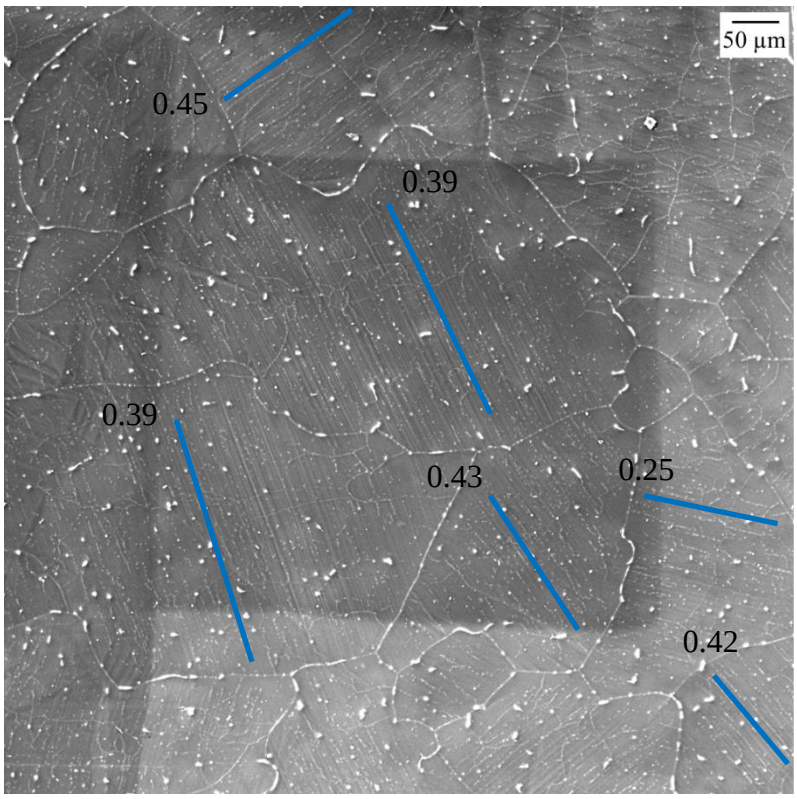

(d)

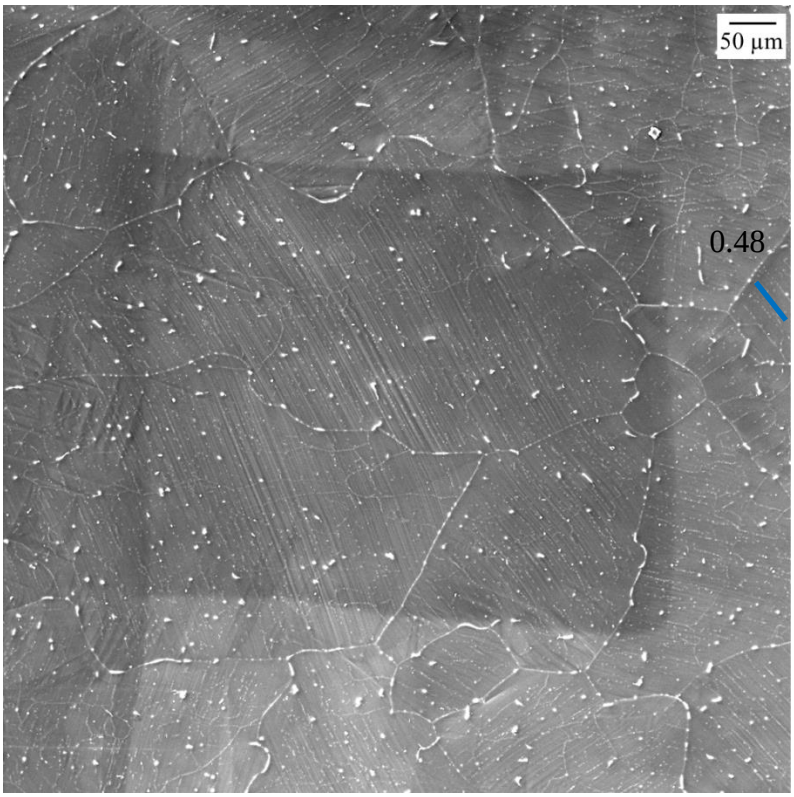

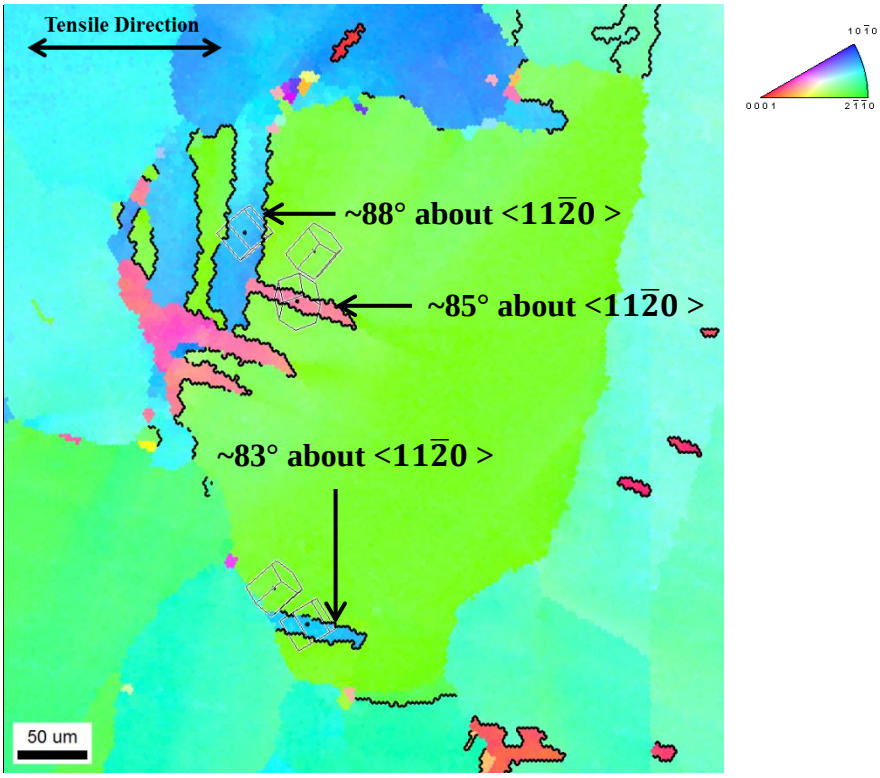

Figure 4.93 EBSD IPF map of the region highlighted by the black box in Figure 4.91b. The extension twin boundaries are highlighted by black lines. The HCP unit cells are overlaid indicating the misorientation between the parent grain and the twinned region.

Figure 4.93 shows the area highlighted by a black box in Figure 4.91b. The extension twins observed in this region are highlighted in Figure 4.93.

Trace analysis was performed on approximately 60 grains from the microstructural patch shown in Figure 4.91a. 32 slip traces were observed in this region in which 30 were basal <a> slip, 1 was prismatic <a> slip, and 1 was pyramidal <c+a> slip. 26 twin traces were observed and all of them were extension twins. Wavy slip traces were observed in 1 grain suggesting that cross-slip occured during deformation.

Figure 4.94 plots the number of identified observations of a particular deformation versus the corresponding global Schmid factor range. ~80% (24 out of 30) of the basal <a> slip traces

were observed at Schmid factors greater than 0.30. 9 extension twin traces were observed at Schmid factors less than 0. Similar to 323K, extension twinning and basal <a> slip controlled the deformation in the MN11 as-cast specimen tensile tested at 423K. It is noted that multiple slip and twin traces were observed in some of the grains analyzed.

Figure 4.95a shows the orientation of the grains in which different deformation modes were identified, plotted in a unit triangle along the tensile direction. Figure 4.95b shows the same data from Figure 4.95a plotted in a {0001} pole figure along the normal direction.

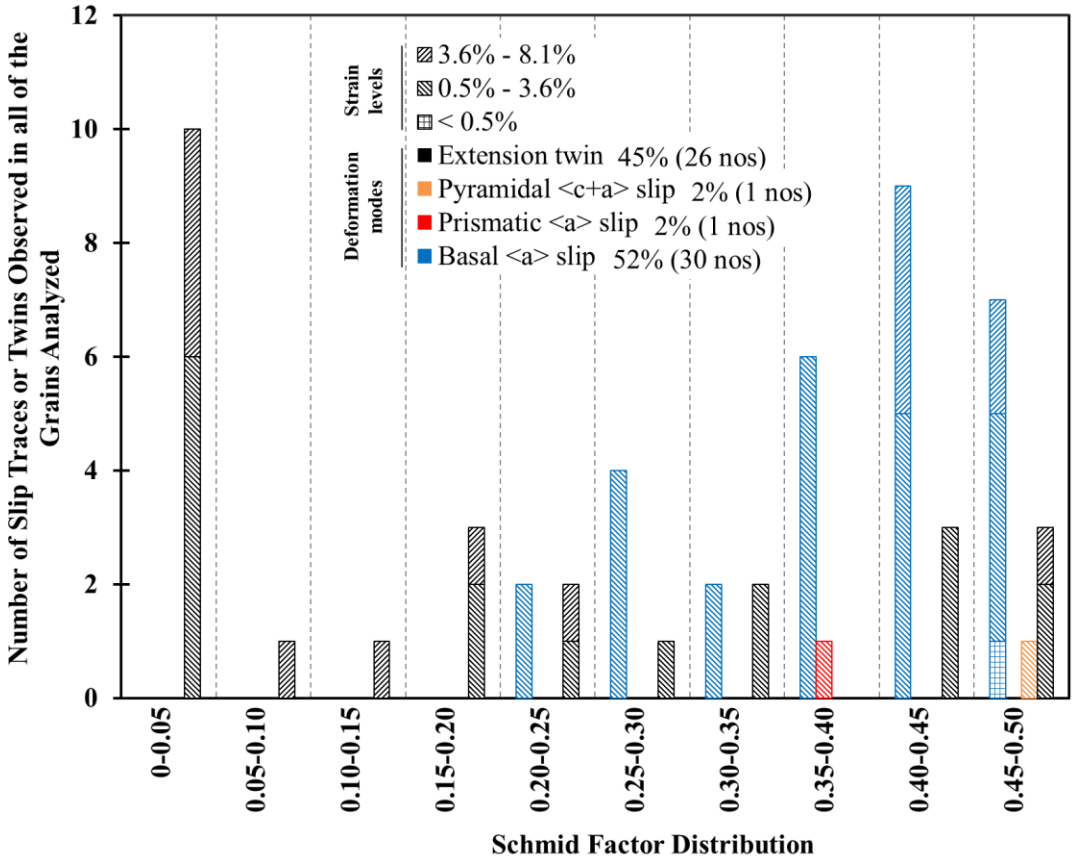

Figure 4.94 A histogram of the Schmid factor distribution of basal <a>, prismatic <a>, pyramidal <c+a>, and extension twins observed in the MN11 as-cast specimen tensile tested at 423K.

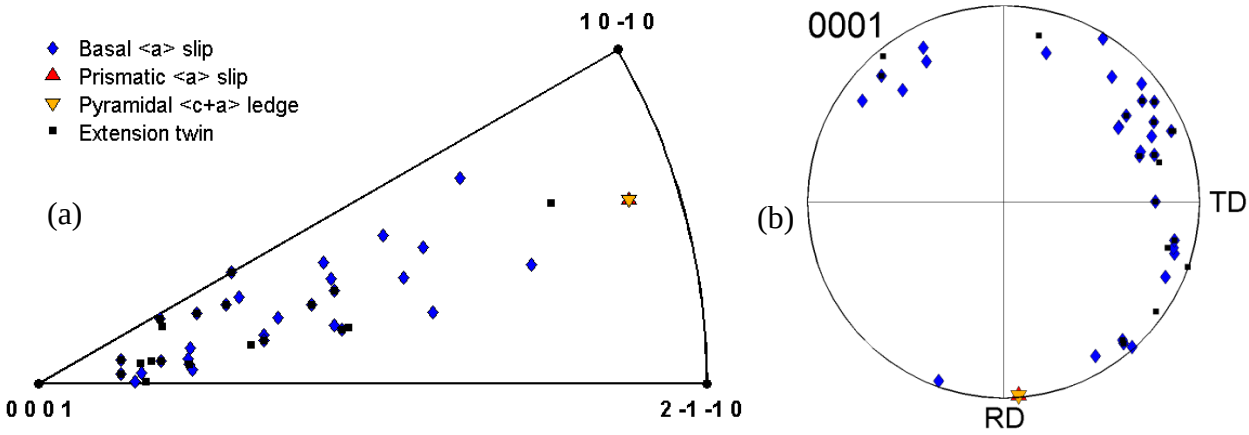

Figure 4.95 The individual grain orientations in which different deformation modes were observed for the MN11 as-cast specimen tensile tested at 423K, plotted in (a) unit triangle along the tensile direction and (b) {0001} pole figure along the normal direction.

4.4.2.3 523K tension

Figure 4.96 shows the EBSD IPF map in the normal direction from the gage section of the MN11 as-cast specimen, tensile tested at 523K, before and after deformation.

Figure 4.97 shows the sequential SE SEM images taken from the microstructural patch analyzed for slip and twin activity in the 523K tensile-tested specimen. Extension twins and basal <a> slip were first observed at ~0.7%. Prismatic <a> and pyramidal <c+a> slip traces were first observed at less than ~3.6% strain.

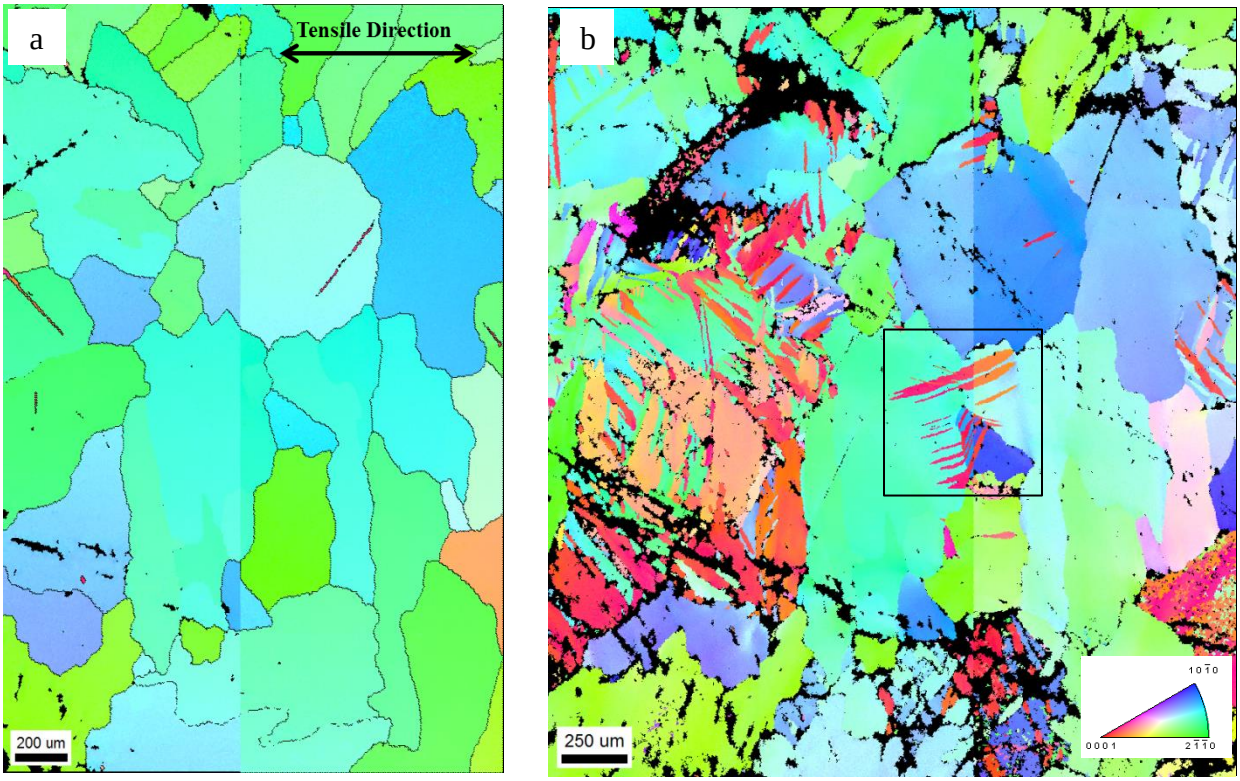

Figure 4.96 EBSD IPF map in the normal direction of the as-cast MN11 specimen tensile-tested at 523K (a) before deformation and (b) after deformation to ~6.7% strain.

Extension twins observed in the area highlighted by the black box in Figure 4.96b are shown in Figure 4.98. It is noted that multiple extension twin variants were activated in some of the grains.

Trace analysis was performed on approximately 50 grains from the microstructural patch shown in Figure 4.96a. 31 slip traces were observed in this region in which 15 were basal <a> slip, 6 were prismatic <a> slip, and 10 were pyramidal <c+a> slip. Wavy slip traces were observed in some grains. Multiple slip/twin traces were observed in most of the grains analyzed.

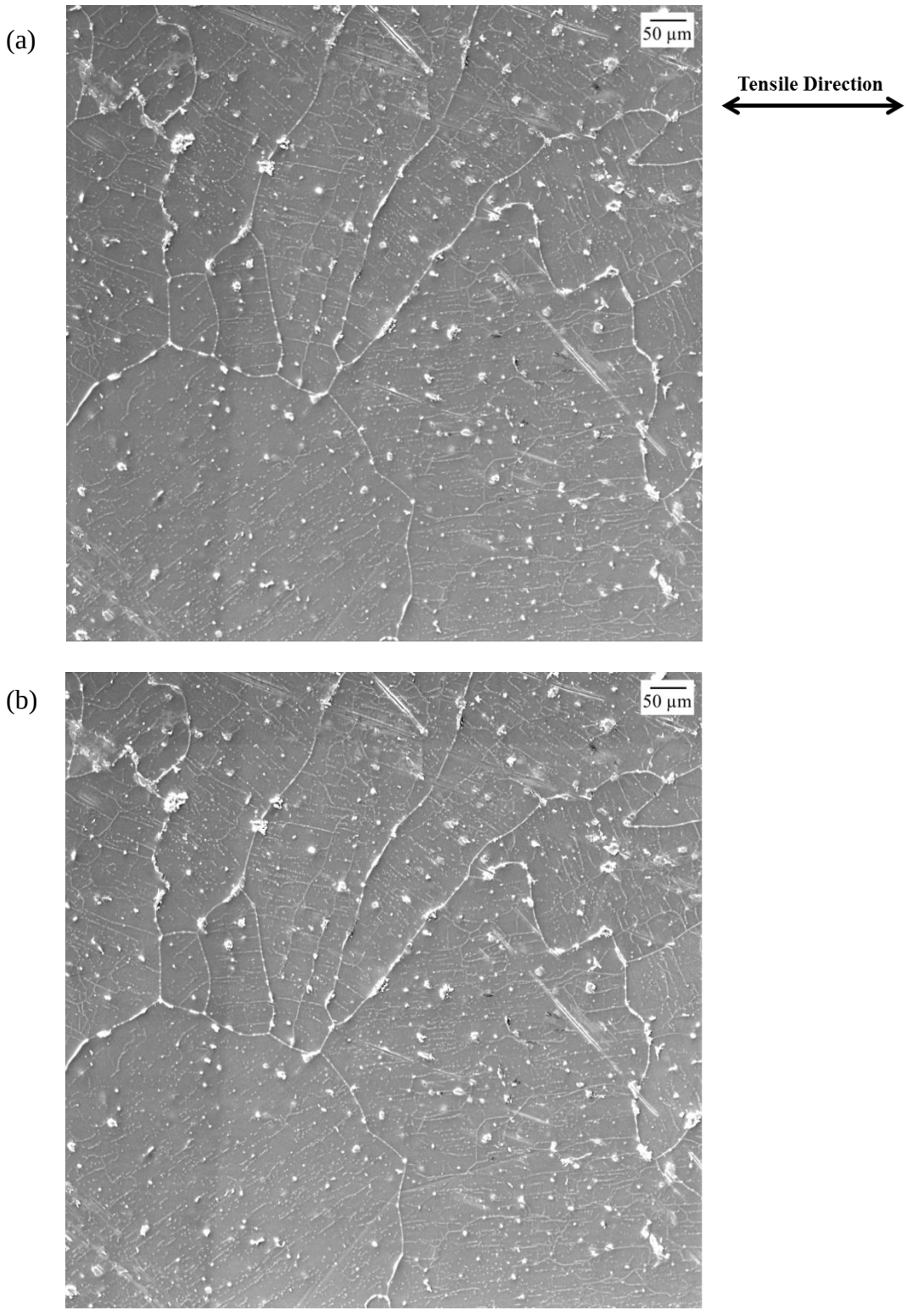

Figure 4.97 Sequential SE SEM images for the MN11 as-cast specimen tensile tested at 523K: (a) undeformed, (b) ~0.7% strain, (c) ~3.6% strain, and (d) ~6.7% strain. In (c) and (d), the slip traces are color coded for basal <a> slip (blue), prismatic <a> slip (red), and pyramidal <c+a> slip (orange). The corresponding Schmid factor values are provided in (c) and (d).

Figure 4.97 (cont'd)

(c)

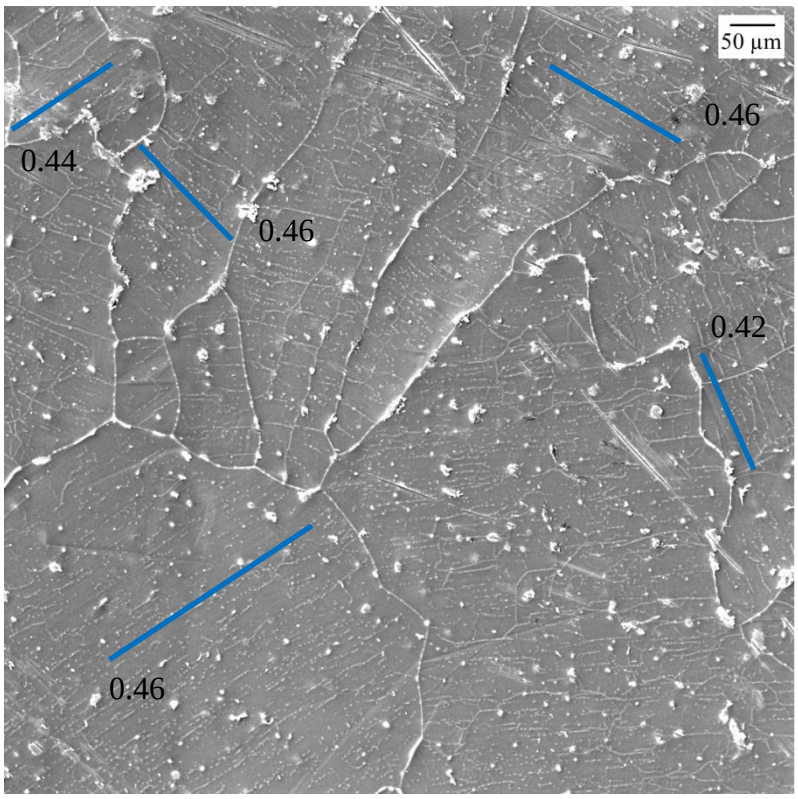

(d)

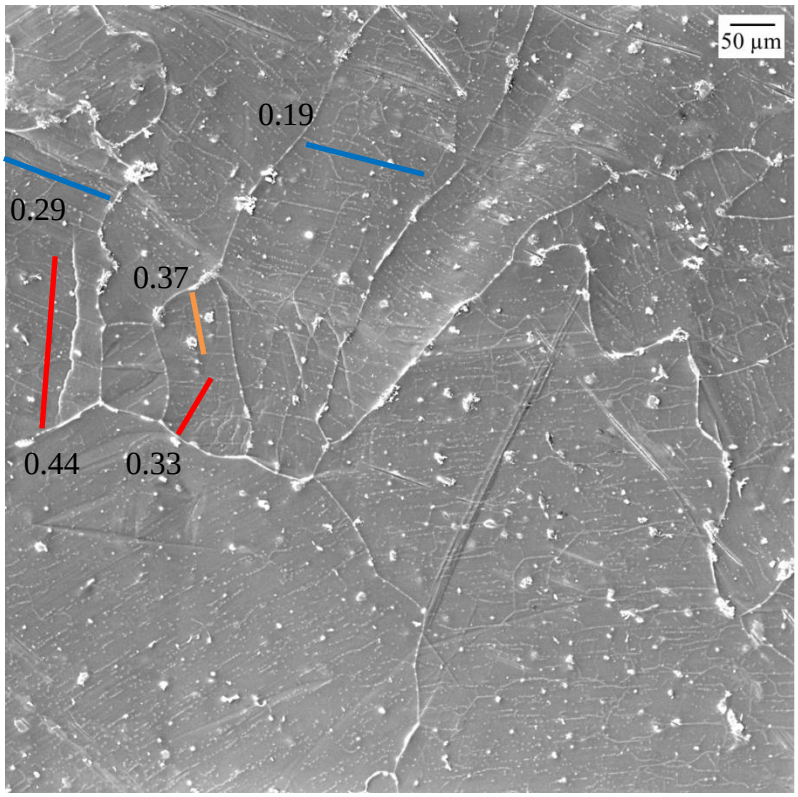

(a)

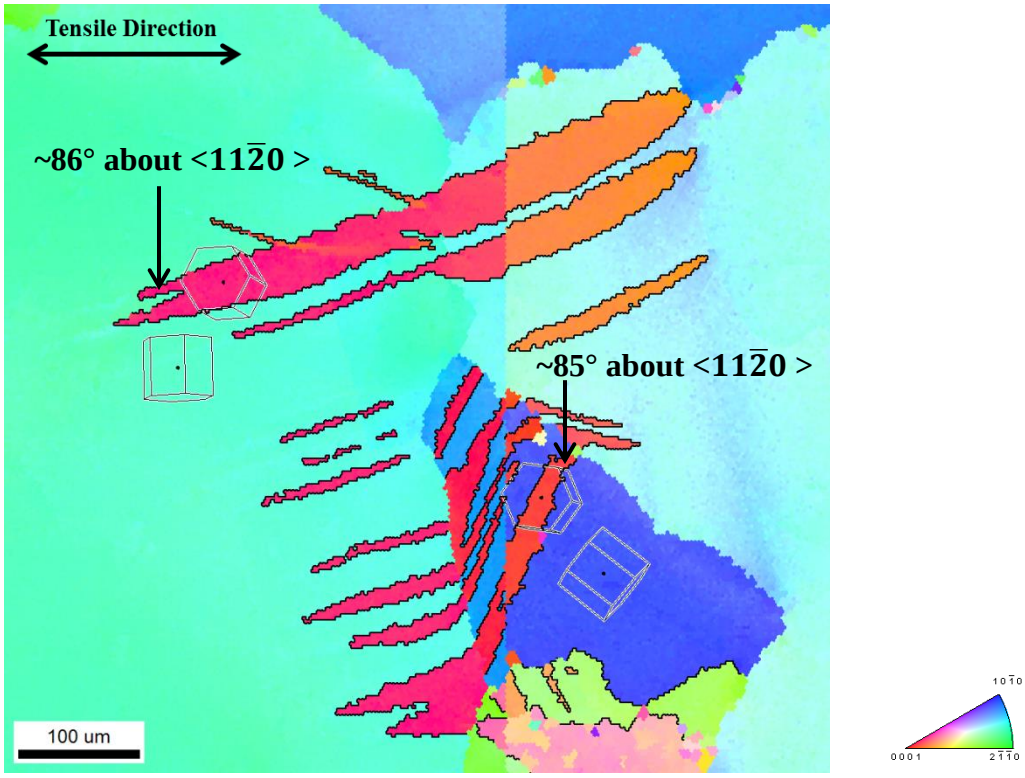

Figure 4.98 EBSD IPF map of the region highlighted in Figure 4.96b by the black box showing the extension twin. The extension twin boundaries are highlighted by black lines. The HCP unit cells are overlaid indicating the misorientation between parent grain and the twinned region.

Figure 4.99 plots the number of identified observations of a particular deformation versus the corresponding global Schmid factor range. 24 extension twin traces were observed. ~80% (12 out of 15) of the basal <a> slip traces were observed at Schmid factors higher than 0.35. Most of the prismatic <a> slip (3 out of 5) and pyramidal <c+a> slip (7 out of 10) were observed at Schmid factors greater than 0.35. 6 extension twins were observed at Schmid factors less than 0.

Figure 4.100a shows the orientation of the grains in which different deformation modes were identified plotted in a unit triangle along the tensile direction. Figure 4.100b shows the same data from Figure 4.100a plotted in a {0001} pole figure along the normal direction.

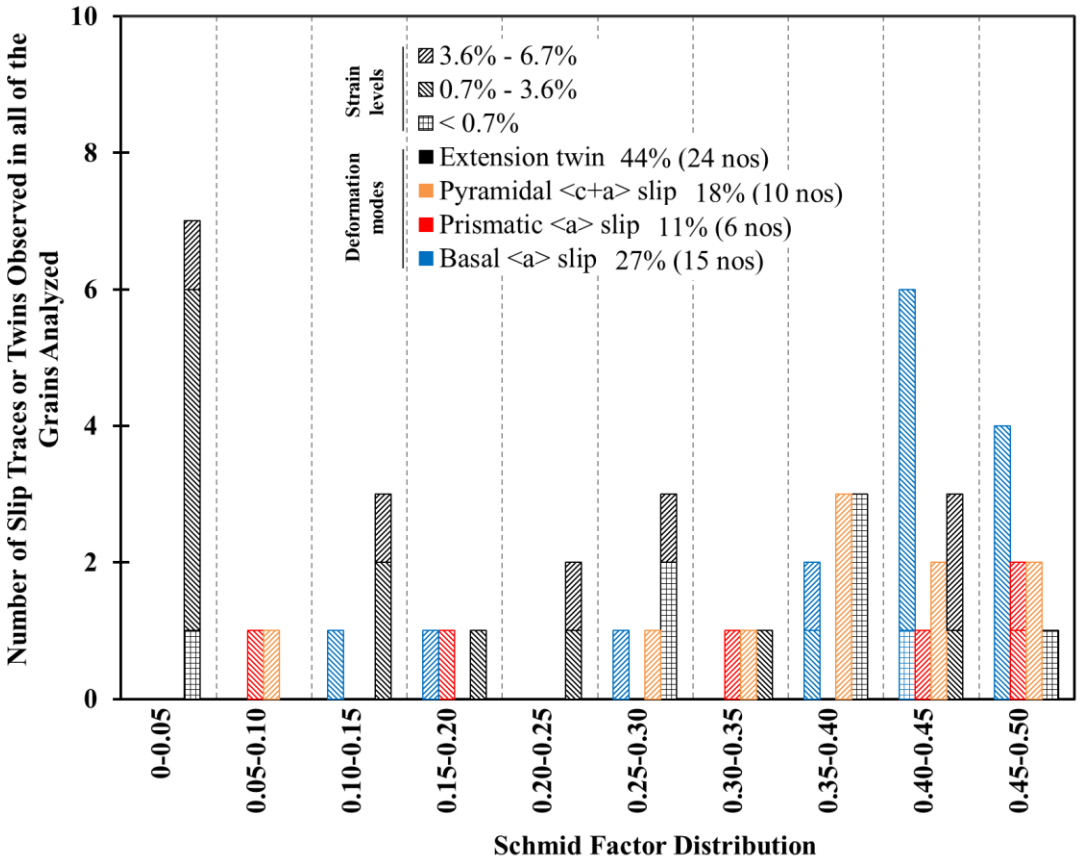

Figure 4.99 A histogram of the Schmid factor distribution of basal <a>, prismatic <a>, pyramidal <c+a>, and extension twins observed in the MN11 as-cast specimen tensile tested at 523K.

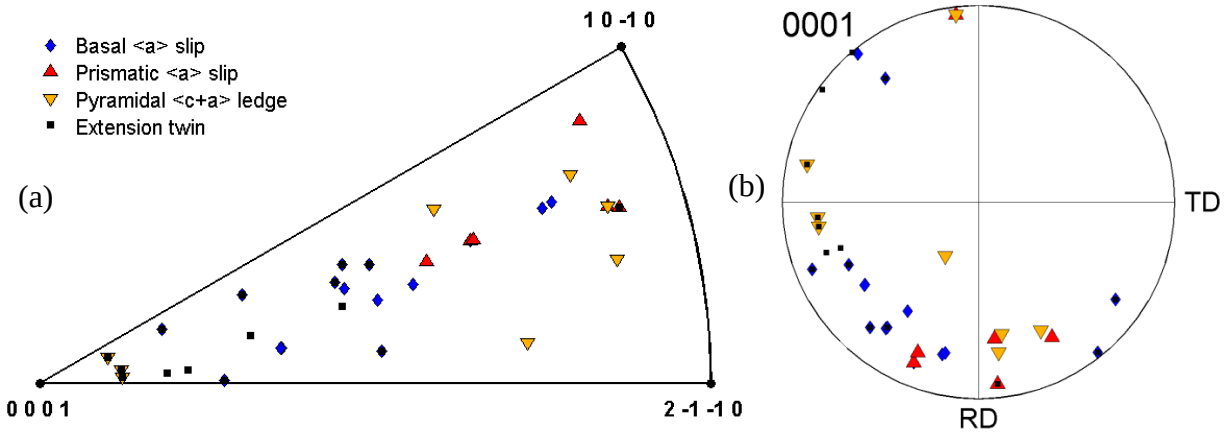

Figure 4.100 The individual grain orientations in which different deformation modes were observed for the MN11 as-cast specimen tensile tested at 523K, plotted in (a) unit triangle along the tensile direction and (b) {0001} pole figure along the normal direction.

4.5 Extruded Mg-1Mn-0.9Nd (MN11-300), Mg-1Mn-1Nd (MN11-275)

4.5.1 Microstructure and texture

Figures 4.101a and 4.101b show representative SE SEM images of the extruded MN11-300 and MN11-275 microstructure, respectively. The average grain diameter was ~12±5μm and ~11±5 μm for MN11-300 and MN11-275, respectively, based on ASTM standards for grain size measurement [ASTM E112-13 2013, Vander Voort 1999]. Figure 4.102a and 4.102b shows the grain size distribution for the extruded MN11-300 and MN11-275, respectively. As shown in Figure 4.101a and 4.101b, the grains were equiaxed suggesting that recrystallization occurred during the elevated-temperature extrusion process. The extrusion direction was horizontal in Figure 4.101. Stringers of precipitates along the extrusion direction were observed in both microstructures suggesting that the cast billet may not have been homogeneous with respect to the alloying elements. The volume fraction of the second phase particles measured from the SE SEM images were ~0.62% and ~0.48% for MN11-300 and MN11-275, respectively.

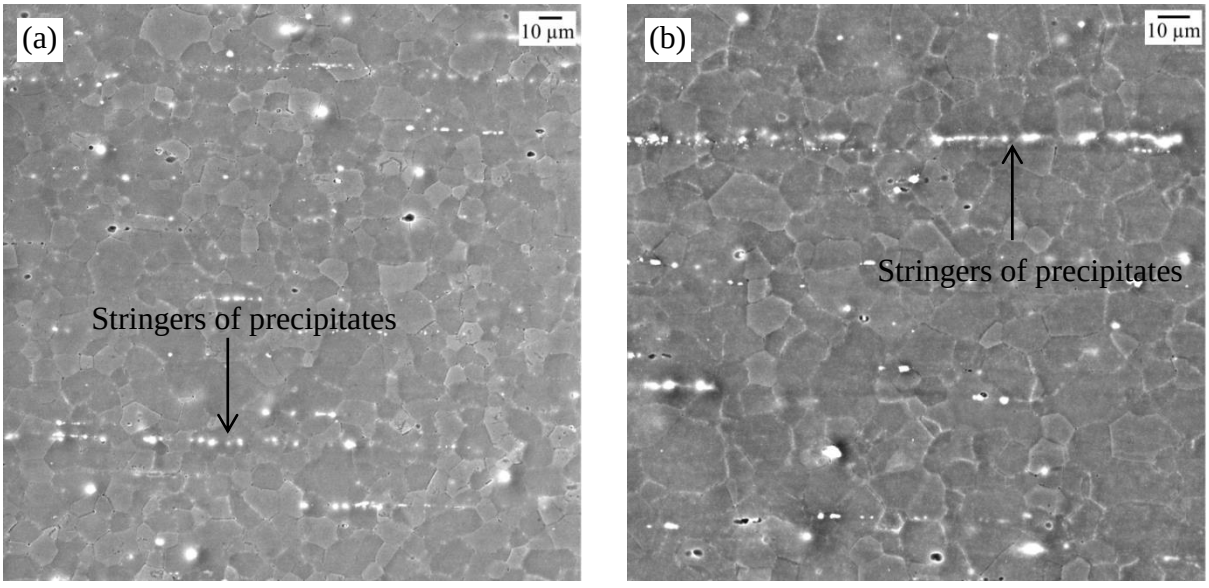

Figure 4.101 SE SEM images showing the microstructure of extruded (a) MN11-300 and (b) MN11-275. The extrusion direction is horizontal.

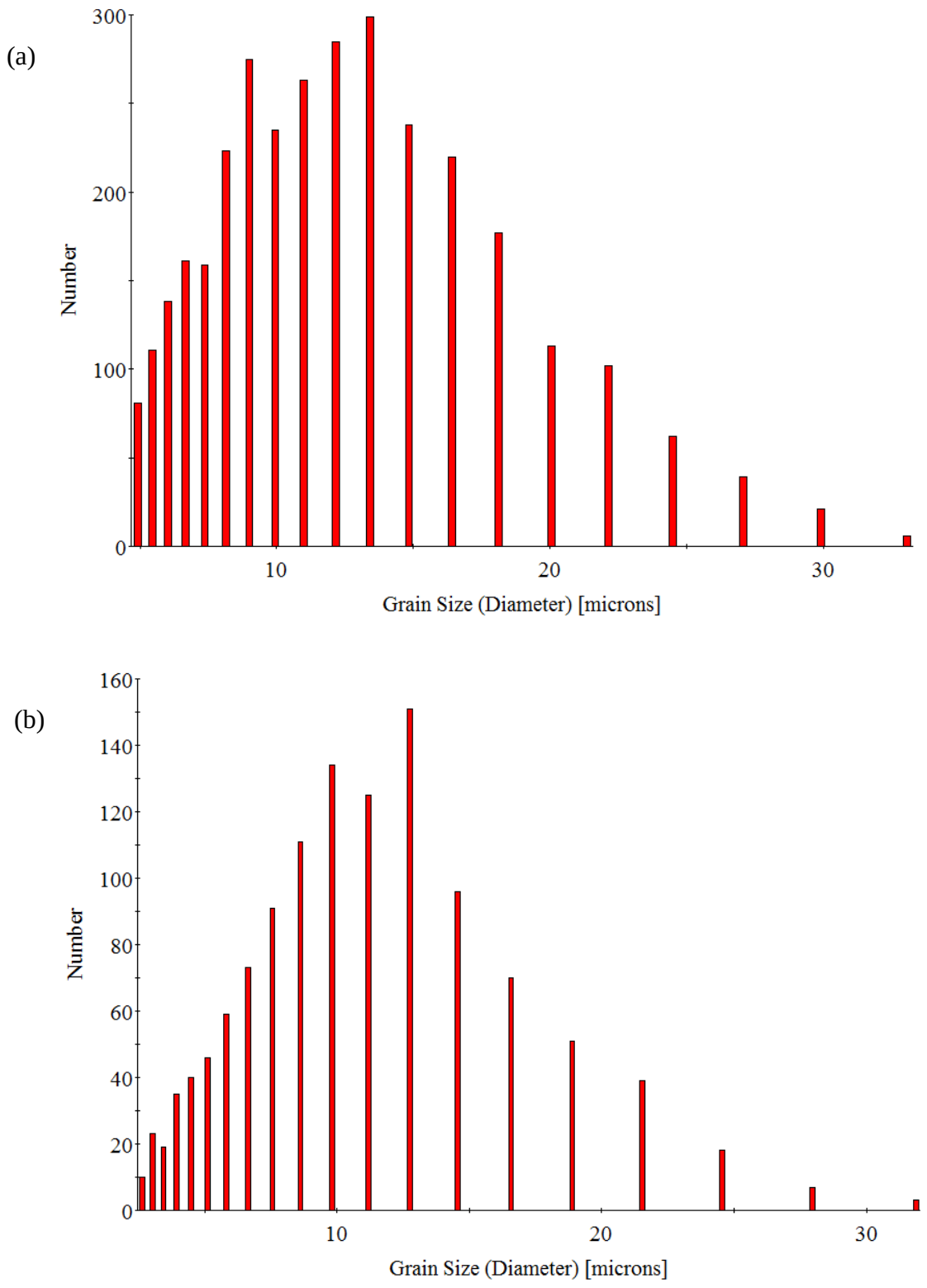

Figure 4.102 The grain size distribution of the extruded (a) MN11-300 and (b) MN11-275.

Both Mn-rich and Nd-rich precipitates were observed within the grains and at the grain boundaries in the MN11-300 microstructure (See Figure 4.103). The average composition of the Mn-rich and Nd-rich precipitates were ~Mg-40Mn-1Nd and ~Mg-40Mn-22Nd, respectively.

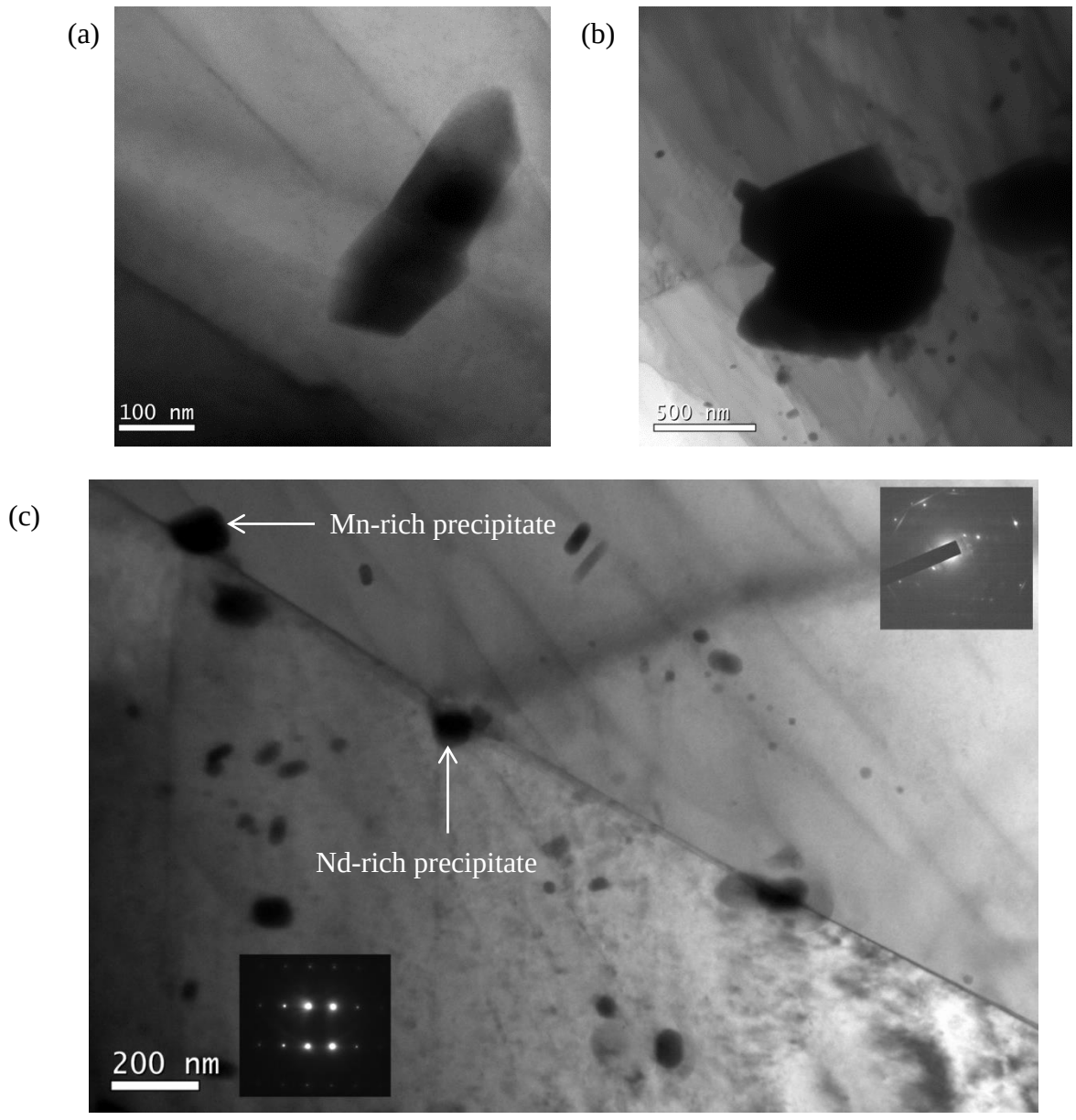

Figure 4.103 BF TEM images of (a) a Mn-rich precipitate and (b) a Nd-rich precipitate observed inside the grains in the extruded MN11-300 microstructure. In (c), a BF TEM image of a grain boundary is shown. The Mn-rich and Nd-rich precipitates are highlighted and the SAD pattern from both grains is given in the inset in (c).

Table 4.16 and 4.17 lists the chemical composition of the five Mn rich and four Nd-rich precipitates analyzed, respectively. EDS performed on the extruded MN11-300 matrix suggested an average chemical composition of ~Mg-0.7Mn-0.9Nd. Table 4.18 lists the two measurements of the chemical composition of the matrix.

Table 4.16 The chemical composition of the five Mn-rich precipitates analyzed in the extruded MN11-300 microstructure. The values are in wt%.

Observations	Mg	Mn	Nd
1	73.29	26.20	0.50
2	71.62	27.41	0.97
3	41.08	58.13	0.79
4	46.44	51.98	1.58
5	60.15	37.45	2.40
Average	58.52	40.23	1.25

Table 4.17 The chemical composition of the four Nd-rich precipitates analyzed in the extruded MN11-300 microstructure. The values are in wt%.

Observations	Mg	Mn	Nd
1	4.29	67.02	28.69
2	50.27	0.74	43.09
3	47.44	43.83	8.74
4	45.31	47.86	6.83
Average	36.83	39.86	21.84

Table 4.18 The chemical composition of the extruded MN11-300 matrix. The values are in wt%.

Observations	Mg	Mn	Nd
1	98.59	0.51	0.91
2	98.15	0.89	0.97
Average	98.37	0.70	0.94

Figure 4.104a and 4.104b show the representative texture of the extruded MN11-300 and MN11-275 microstructure, respectively, in the form of {0001} and {10$\bar{1}$0} pole figures in the normal direction. The texture shown in Figure 4.104a and 4104b was obtained from an area containing ~3200 and ~1200 grains, respectively. The pole figures show a random texture. A similar weak texture is observed in other wrought rare-earth containing Mg alloys [Bohlen et al. 2007, Bohlen et al. 2010].

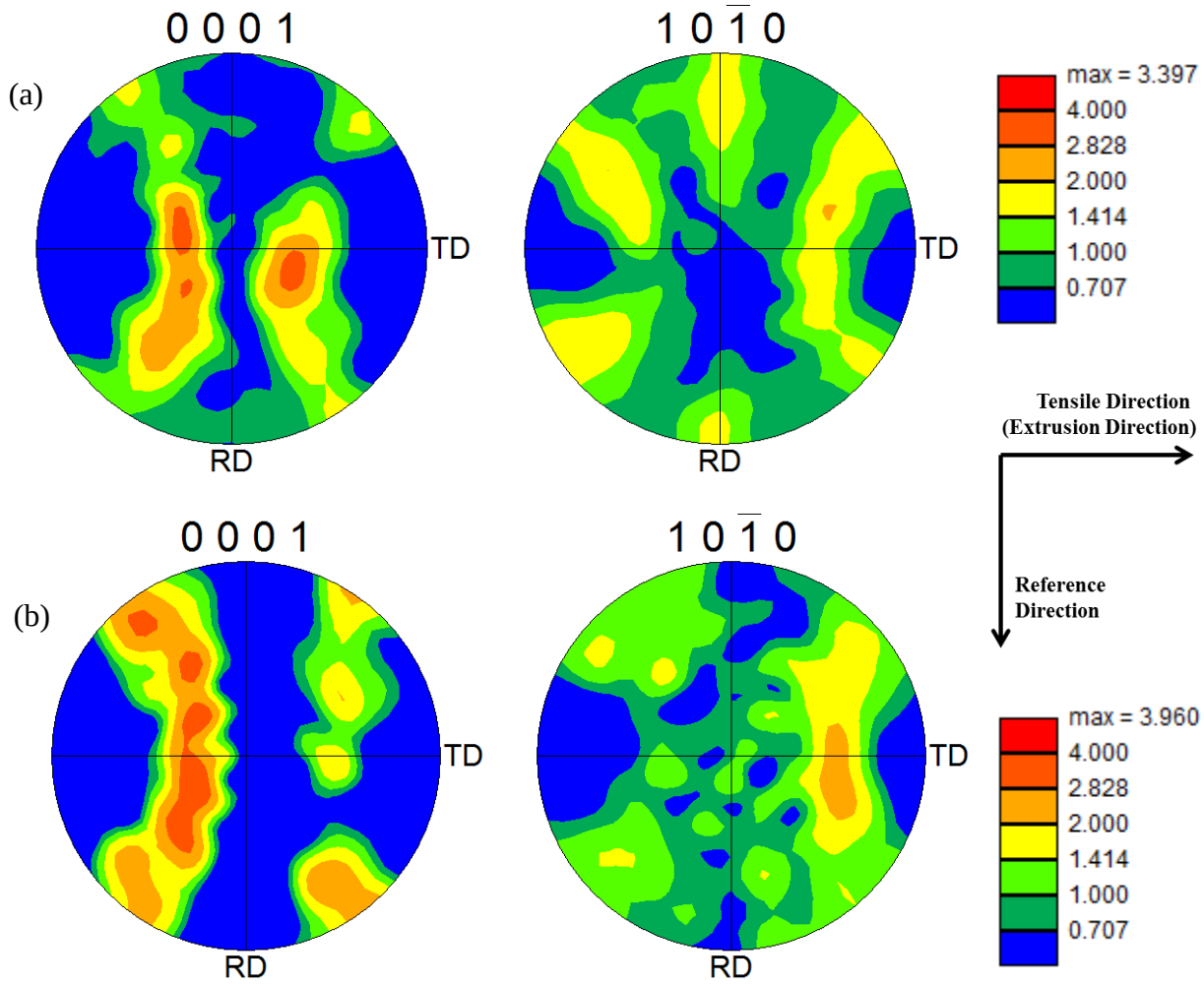

Figure 4.104 Representative texture of (a) MN11-300 and (b) MN11-275 microstructure in the form of {0001} and {10$\bar{1}$0} pole figures in the normal direction.

4.5.2 In-situ tension

In-situ tensile tests were performed on the extruded MN11-300 and MN11-275 alloys at 323K, 423K, and 523K. One test each was performed at 323K, 423K, and 523K for MN11-300 and these samples were taken to failure. Slip trace analysis was performed on those specimens. It is noted that twin trace analysis was not performed on those specimens due to the poor quality of the EBSD maps obtained due to surface topography after the deformation and fracture (at ~29% to ~43% strain). Approximately 150 grains were analyzed at 323K and 423K, and ~600 grains were analyzed at 523K for slip trace analysis.

In the case of MN11-275, two tests were performed at 323K, three tests were performed at 423K, and three tests were performed at 523K. One specimen at each test temperature was taken to failure. The rest of the samples were not taken to failure in order to facilitate EBSD mapping after deformation. Slip and twin trace analysis was performed on those specimens. Approximately ~450 grains were analyzed for the slip and twin trace analysis.

The engineering stress versus displacement curves for the 323K, 423K, and 523K tensile tests for MN11-300 (solid lines) and MN11-275 (dotted lines) are illustrated in Figure 4.105. In Figure 4.105, the stress drops indicate the stress relaxation that occurred when the tests were paused for imaging. Both materials exhibited superior strength retention and similar tensile properties at each test temperature. Table 4.19 lists the approximate YS and UTS obtained and the maximum strain levels achieved for each experiment. The curves for the MN11-300 523K specimen, which was taken to fracture, and the MN11-275 423K specimen, which did not fracture, were not recorded due to a glitch in the data acquisition system.

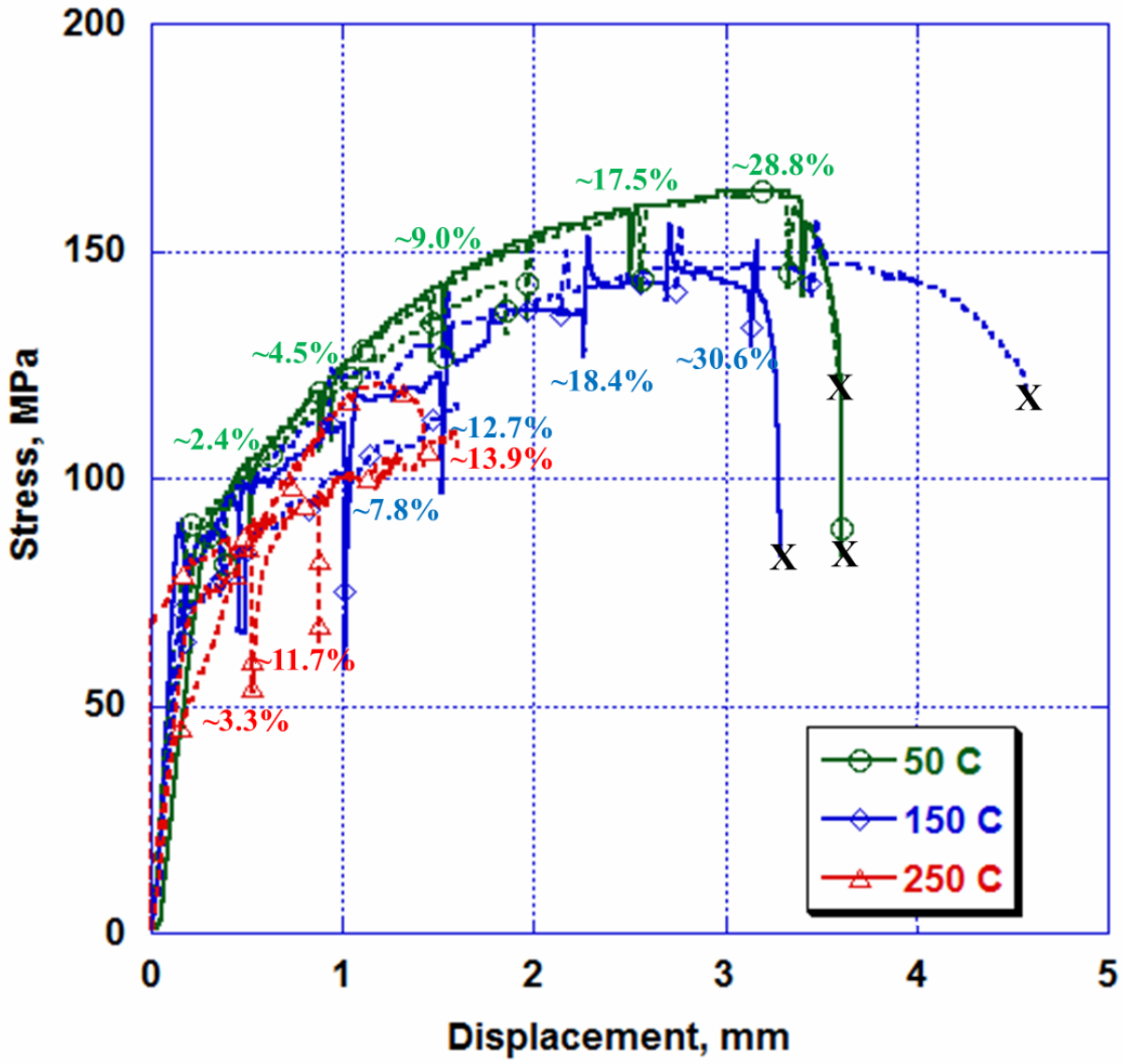

Figure 4.105 Representative stress vs. displacement plots for MN11-300 (solid lines) and MN11-275 (dotted lines) samples tensile tested at 323K, 423K, and 523K. The stress drops indicate the stress relaxation occurred when the tests were interrupted for imaging. "X" indicates fracture.

Table 4.19 MN11-300 and MN11-275 tensile property comparison for samples tested between 323-523K.

Material	Test temperature	YS (MPa)	UTS (MPa)	Maximum strain (%)
MN11-300	323K	~94	~163	~28.8 (fractured)
MN11-300	423K	~84	~145	~30.6 (fractured)
MN11-300	523K	-	-	~42.5 (fractured)
MN11-275	323K	~89	~163	~27.7 (fractured)
MN11-275	323K	~90	~143	~14.0
MN11-275	423K	~81	~147	~19.0 (fractured)
MN11-275	423K	~71	~116	~9.8
MN11-275	423K	-	-	~17.3
MN11-275	523K	~76	~96	~36.1 (fractured)
MN11-275	523K	-	~121	-
MN11-275	523K	~77	~110	~13.9

4.5.2.1 323K tension

Figure 4.106 shows sequential SE SEM images taken from the same area of the extruded MN11-300 specimen tensile tested at 323K. Slip traces started to appear at ~9.0% strain. Basal <a> slip and pyramidal <c+a> slip traces were observed in the area analyzed. Figure 4.107 shows the EBSD IPF map in the normal direction of the same region from the gage section of the extruded MN11-275 specimen both before and after the deformation. An extension twin observed in this area is highlighted by the black arrow in Figure 4.107b.

(a) ε ≈ 0%

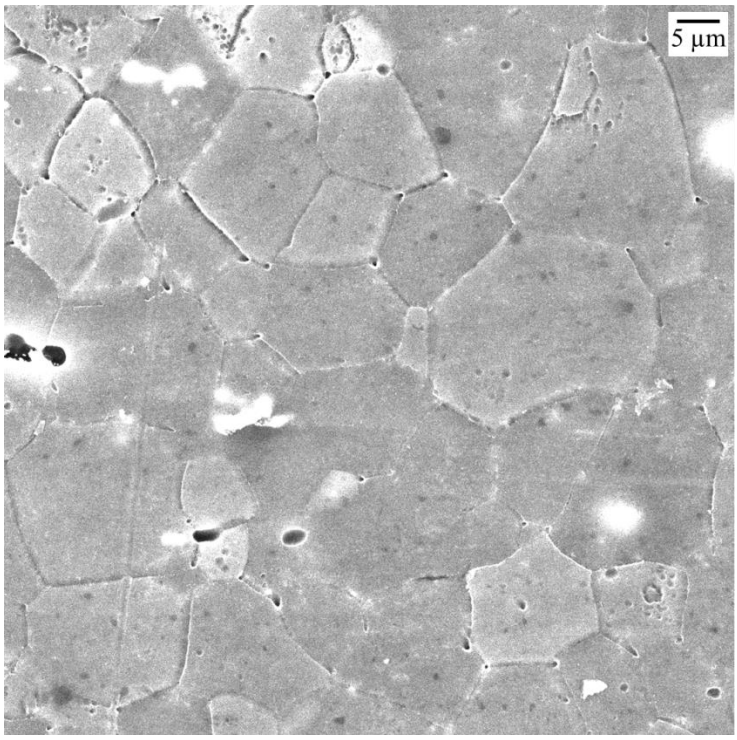

Tensile axis
↔
Extrusion direction

(b) ε ≈ 9.0%

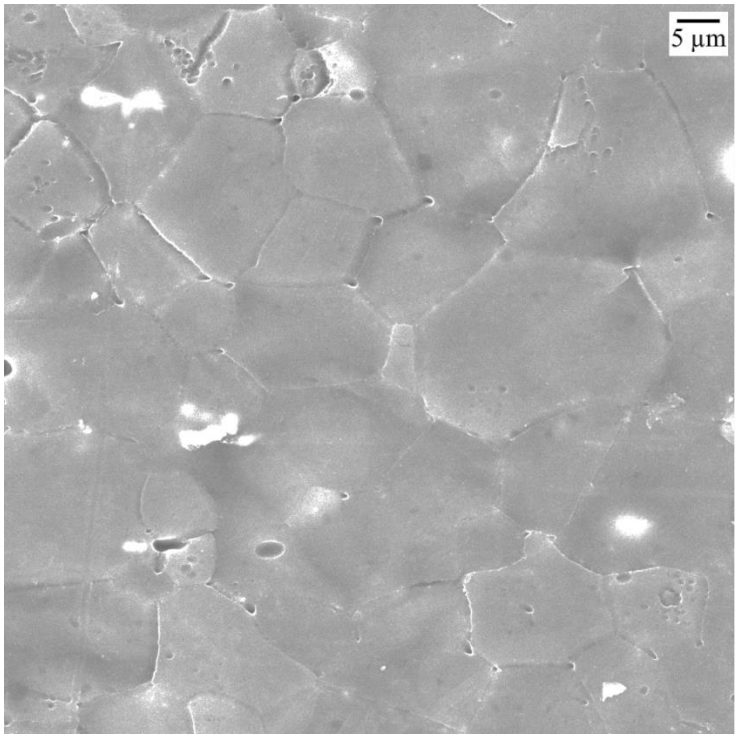

Figure 4.106 Sequential SE SEM images for the extruded MN11-300 specimen tensile tested at 323K: (a) 0% strain, (b) ~9.0% strain, (c) ~17.5% strain, and (d) ~29.7% strain. A basal <a> slip observed in this region is highlighted by blue line and the corresponding Schmid factor value is indicated in (d).

Figure 4.106 (cont'd)

(c) $\varepsilon \approx 17.5\%$

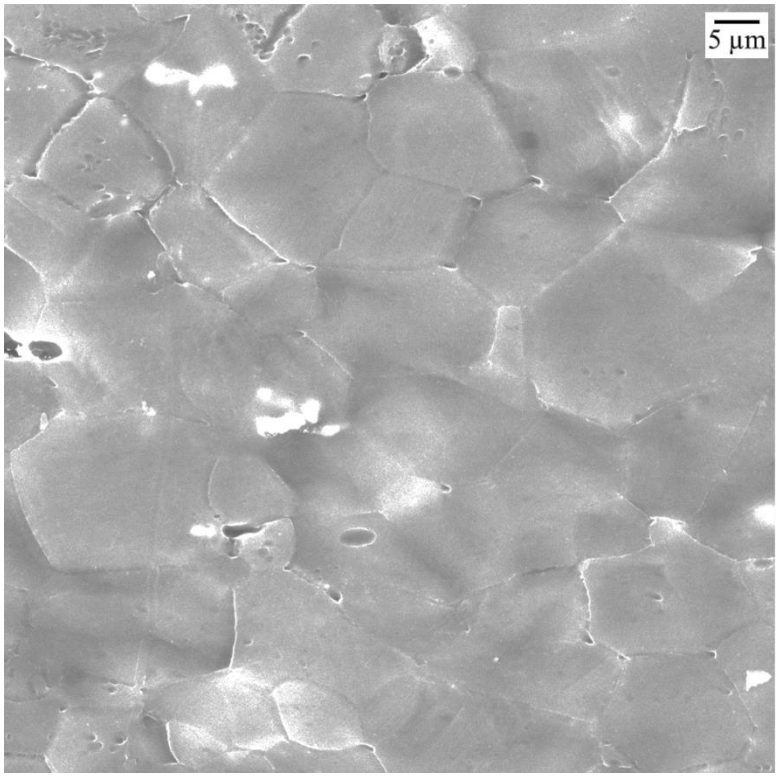

(d) $\varepsilon \approx 29.7\%$

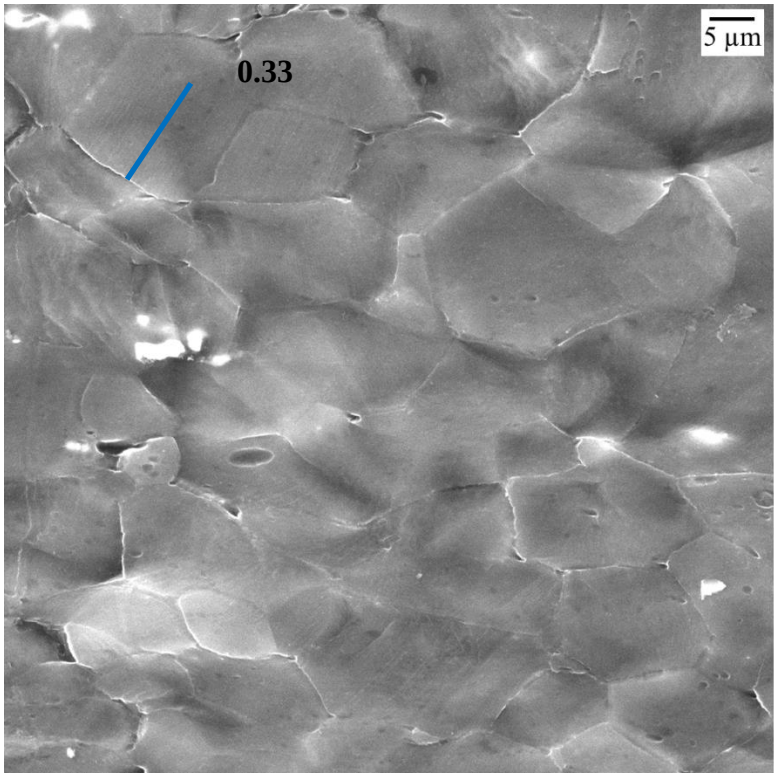

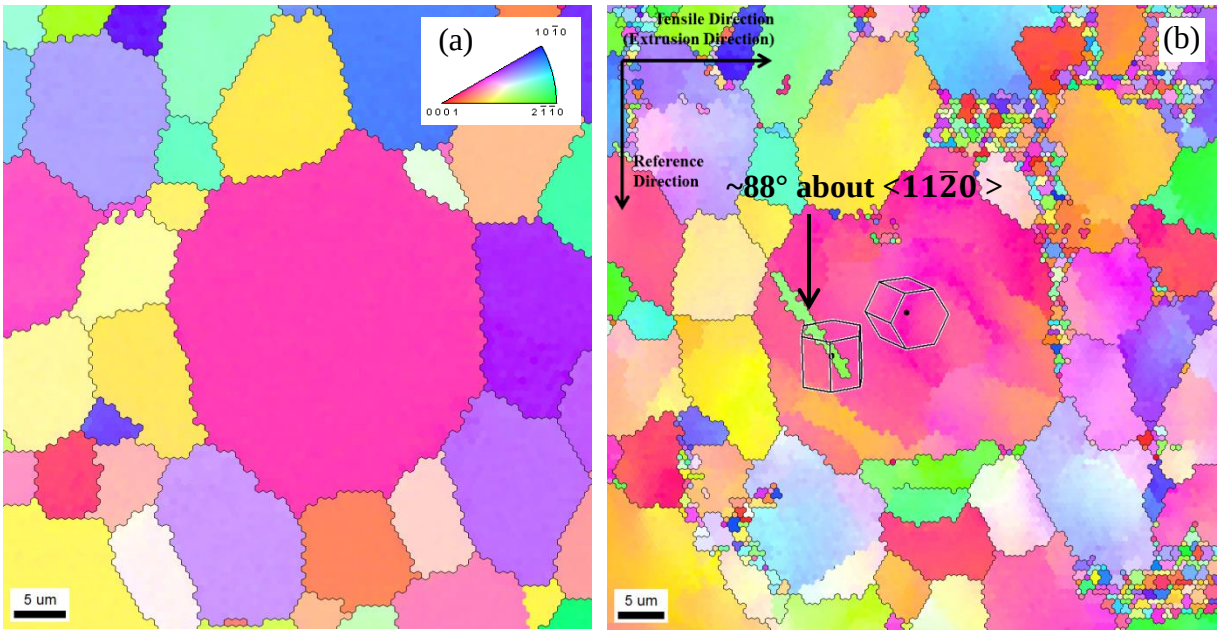

Figure 4.107 EBSD IPF map in the normal direction of the same area from the gage section of the extruded MN11-275 tensile tested specimen at 323K (a) before deformation and (b) at ~14.0% strain. An extension twin observed in this region is indicated by the black arrow in (b). The HCP unit cells are overlaid showing the misorientation between the parent grain and the twinned region and the rotation angles are indicated in (b).

In MN11-300 specimen, 6 basal <a> slip and one pyramidal <c+a> slip were observed. In the case of MN11-275 sample, 24 basal <a> slip, one prismatic <a> slip, three pyramidal <c+a> slip traces were observed. 27 extension twins were also observed. Thus, basal <a> slip and extension twinning appeared to be the dominant deformation modes at 323K. Figure 4.108a and 4.108b plots the number of identified observations of a particular deformation mode versus the corresponding global Schmid factor range for MN11-300 and MN11-275, respectively. Extension twins were observed over the entire Schmid factor range.

(a)

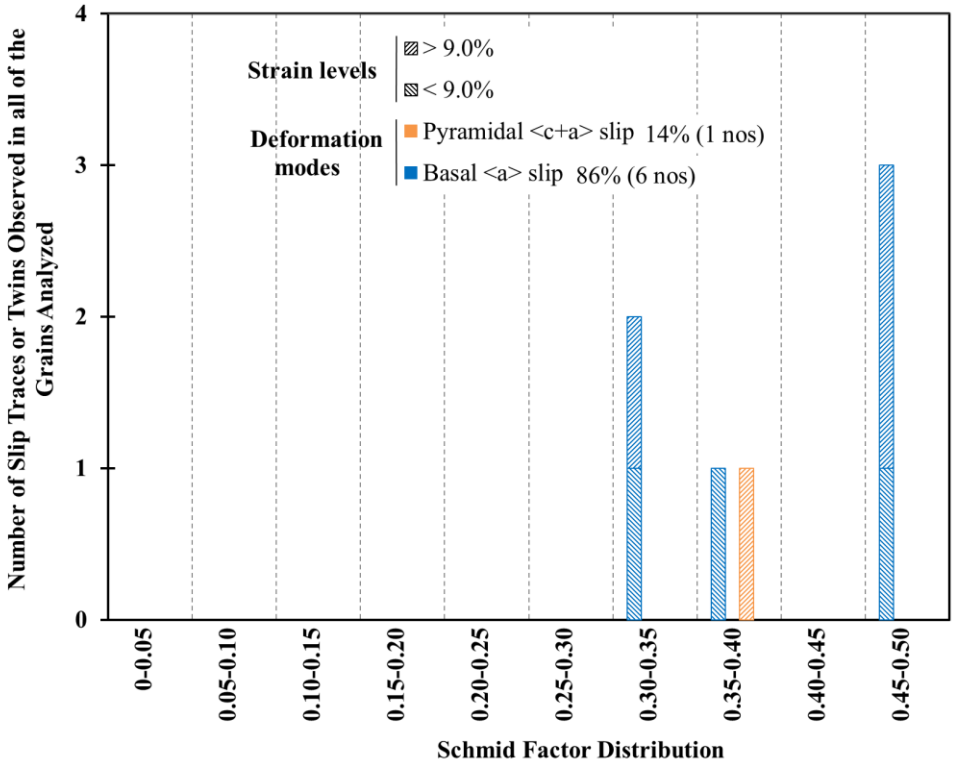

(b)

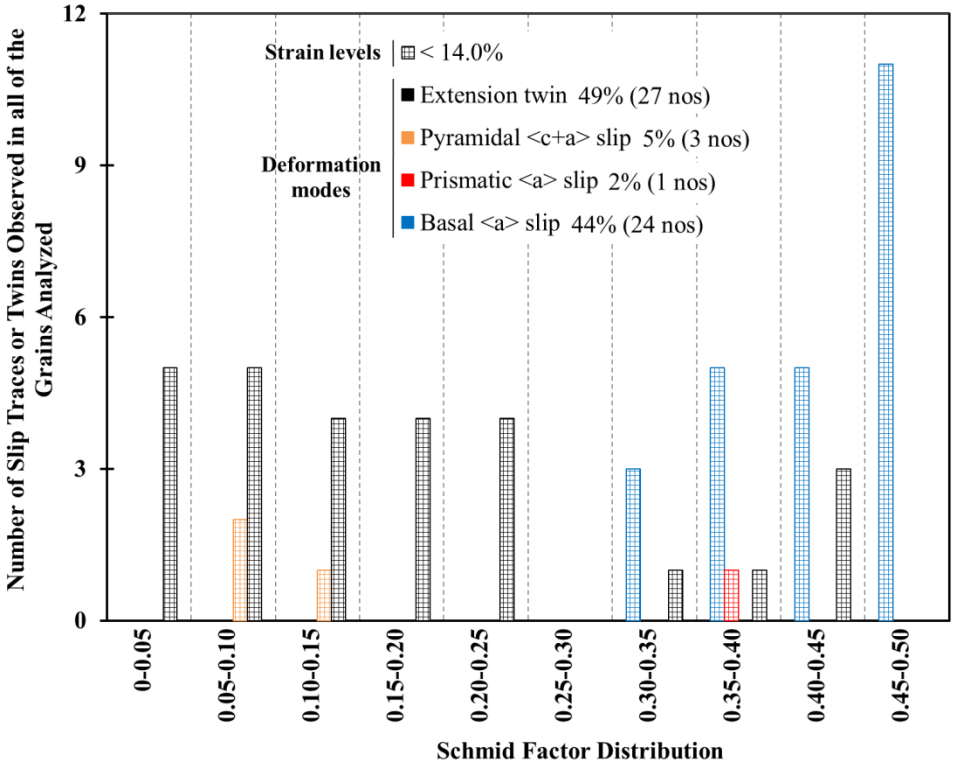

Figure 4.108 Histogram of the Schmid factor distribution of different deformation modes observed in extruded (a) MN11-300 and (b) MN11-275 specimens tensile tested at 323K.

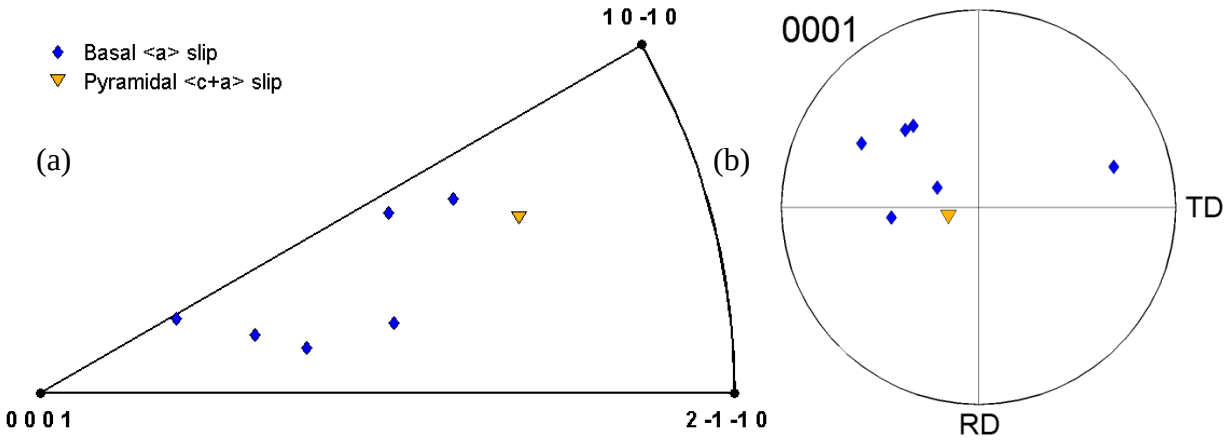

Figure 4.109 The individual grain orientations in which different slip modes were observed for extruded MN11-300 sample tensile test at 323K, plotted in a (a) unit triangle along the tensile direction and (b) {0001} pole figure along the normal direction.

In Figure 4.109a, the orientation of the grains in which different slip systems were identified in the extruded MN11-300 specimen was plotted in a unit triangle along the tensile direction. In Figure 4.109b the same data from 4.109a is plotted in a {0001} pole figure along the normal direction.

4.5.2.1.1 Estimated CRSS ratios

Table 4.20 lists the relative CRSS values of basal <a> slip, prismatic <a> slip, pyramidal <c+a> slip, and extension twinning, estimated based on the relative activity of these deformation modes in MN11-300 and MN11-275 at 323K. The estimated relative CRSS value for extension twinning with respect to basal <a> slip was <1, and the estimated relative CRSS value for prismatic <a> slip and pyramidal <c+a> slip with respect to basal <a> slip was >10 in both materials. For the CRSS ratios estimation for MN11-300, the tensile deformation results from this study were combined with results from a previous study [Chen 2012] to obtain a more statistically meaningful data set.

Table 4.20 The bootstrapped mean CRSS ratios and the corresponding 90% confidence intervals (listed in parenthesis) for prismatic <a> slip, pyramidal <c+a> slip, and extension twinning in the MN11-300 and MN11-275 alloys estimated using the tensile deformation results at 323K.

Material	Prismatic <a> slip / Basal <a> slip	Pyramidal <c+a> slip / Basal <a> slip	Extension twinning / Basal <a> slip
MN11-300	12.6 (3.1, 30.4)	12.2 (0.6, 40.0)	0.6 (0.2, 1.4)
MN11-275	11.0 (3.4, 18.7)	875.9 (29.8, 4033.5)	0.8 (0.3, 1.5)

4.5.2.2 423K tension

Figure 4.110 shows sequential SE SEM images taken from the same area of the MN11-300 specimen tensile tested at 423K. Slip traces started to appear at ~7.8% strain. Basal <a> slip, prismatic <a> slip, and pyramidal <c+a> slip traces observed in the area analyzed. Figure 4.111 shows the EBSD IPF map in the normal direction of the same region from the gage section of the specimen before and after deformation. An extension twin observed in this area is highlighted by the black arrow in Figure 4.111b.

(a) ε ≈ 0%

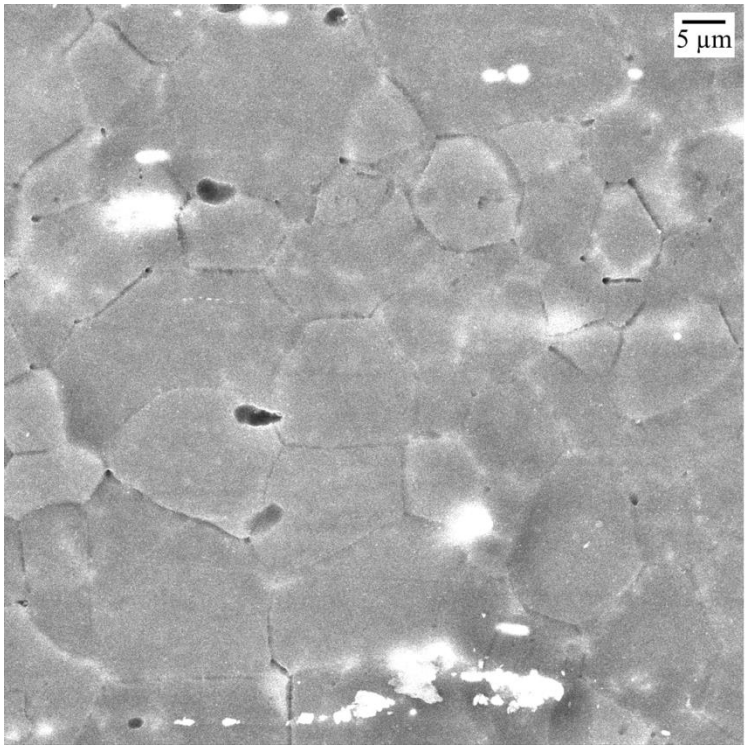

Tensile axis
↔
Extrusion direction

(b) ε ≈ 7.8%

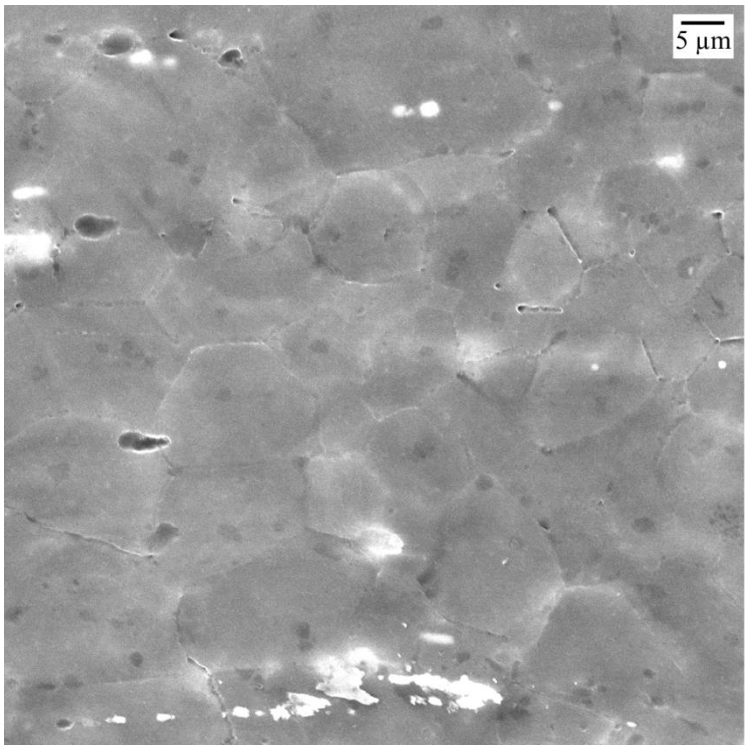

Figure 4.110 Sequential SE SEM images for the extruded MN11-300 specimen tensile tested at 423K: (a) 0% strain, (b) ~7.8% strain, (c) ~18.7% strain, and (d) ~30.6% strain. Basal <a> slip traces observed in this region are highlighted by blue line and corresponding Schmid factor values are indicated in (d).

Figure 4.110 (cont'd)

(c) $\varepsilon \approx 18.7\%$

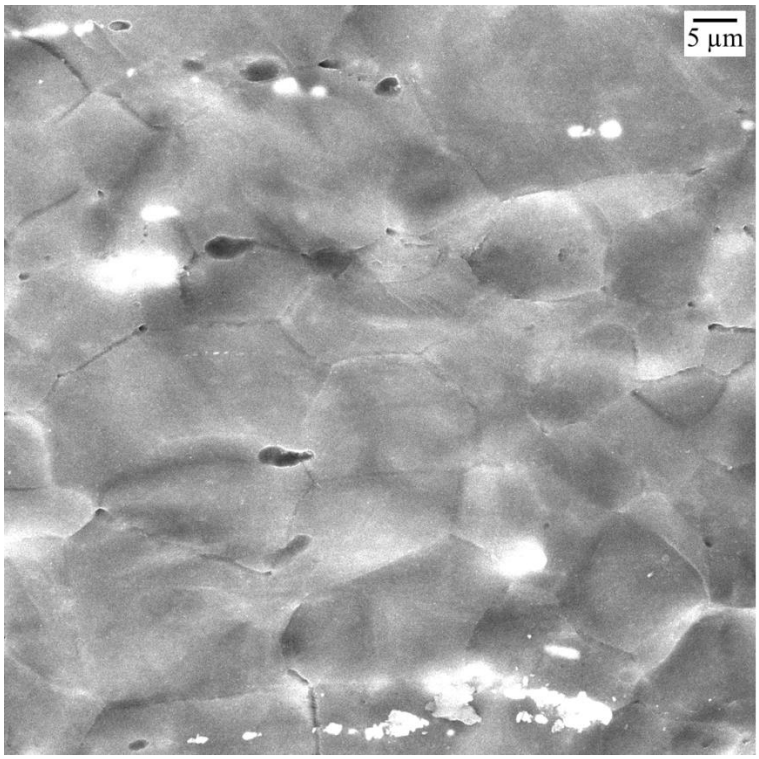

(d) $\varepsilon \approx 30.6\%$

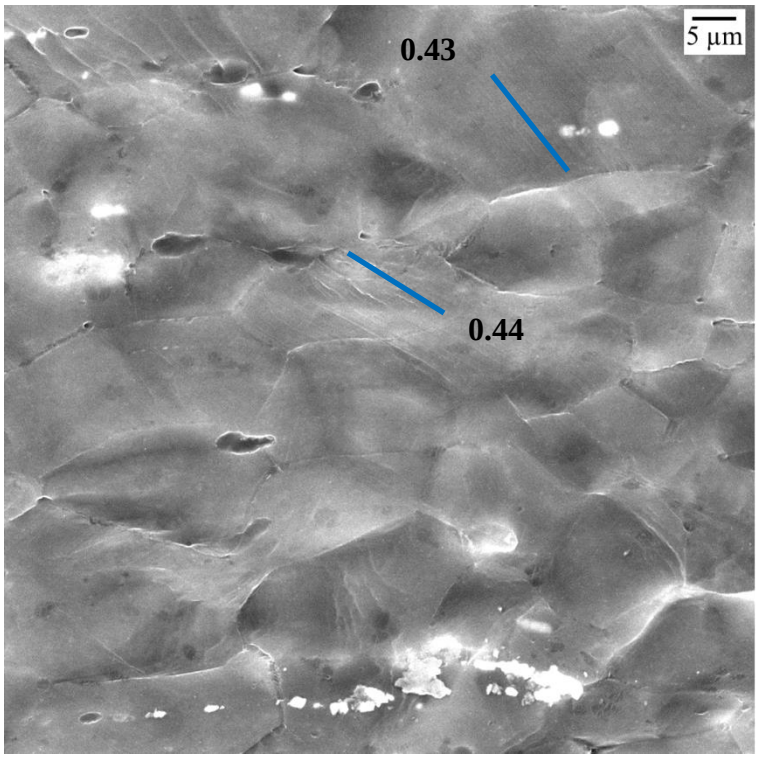

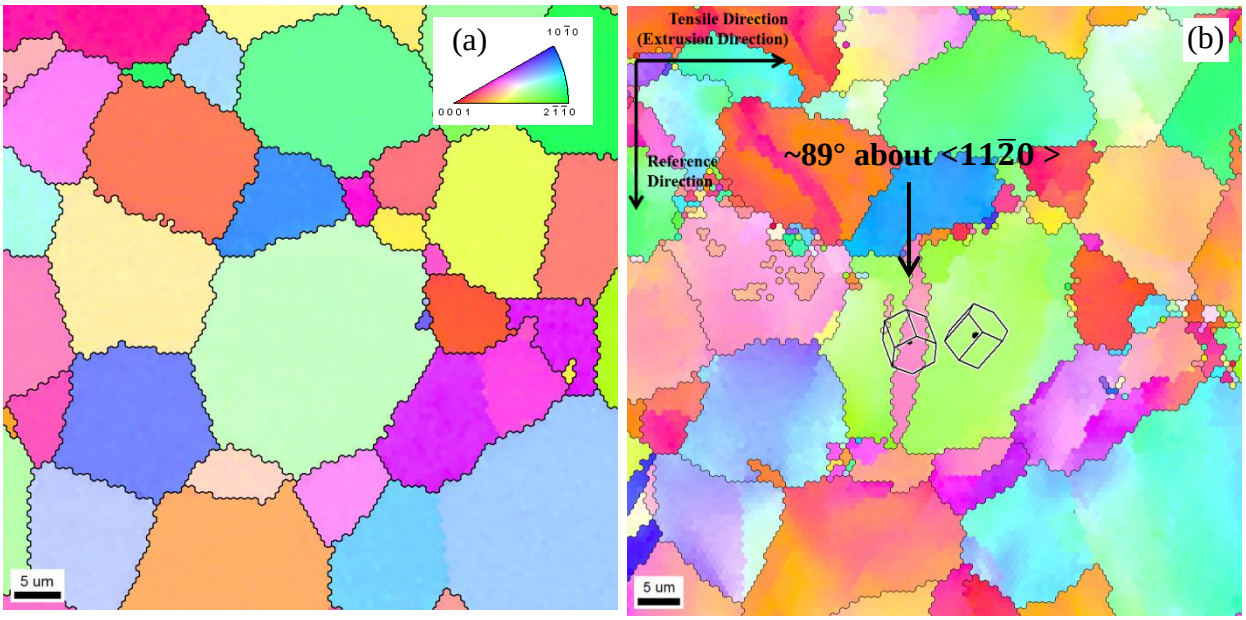

Figure 4.111 EBSD IPF map in the normal direction of the same area from the gage section of the extruded MN11-275 tensile tested specimen at 423K (a) before deformation and (b) at ~17.3% strain. An extension twin observed in this region is indicated by a black arrow in (b). The HCP unit cells are overlaid showing the misorientation between the parent grain and the twinned region and the rotation angles are indicated in (b).

In MN11-300 specimen, 9 basal <a> slip, one prismatic <a> slip, and two pyramidal <c+a> slip traces were observed. In the case of the MN11-275 sample, 29 basal <a> slip, three prismatic <a> slip, and four pyramidal <c+a> slip traces were observed. 17 extension twins were also observed. Thus, basal <a> slip and extension twinning appeared to be the dominant deformation modes at 423K. Figure 4.112a and 4.112b plots the number of identified observations of a particular deformation mode versus the corresponding global Schmid factor range for MN11-300 and MN11-275, respectively. Extension twins were observed over the entire Schmid factor range.

(a)

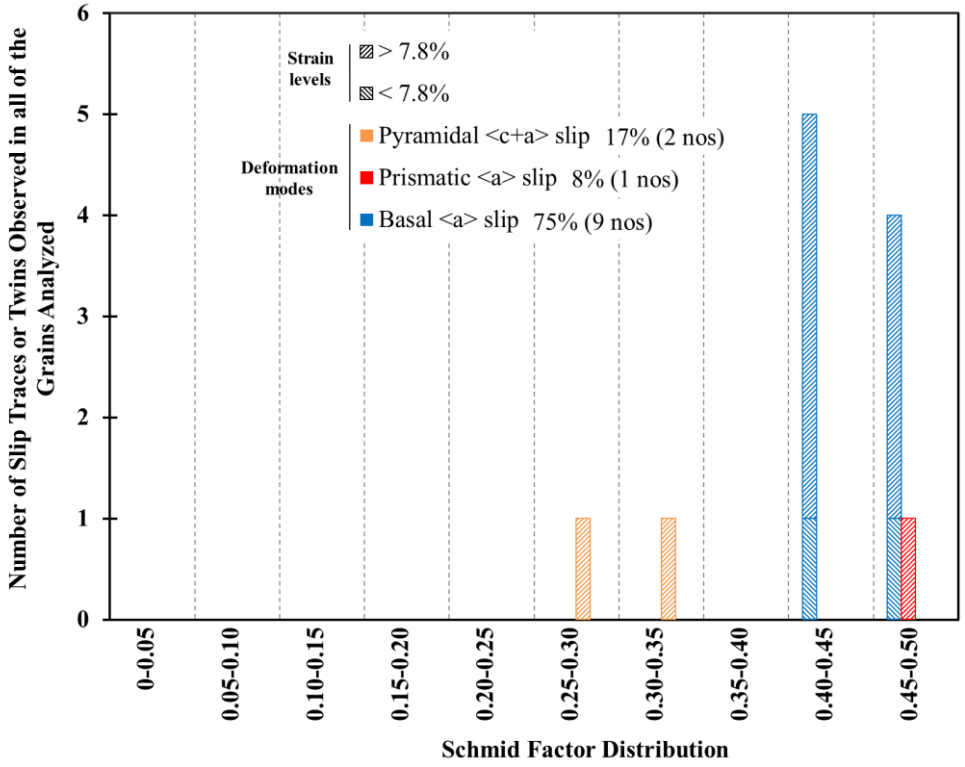

(b)

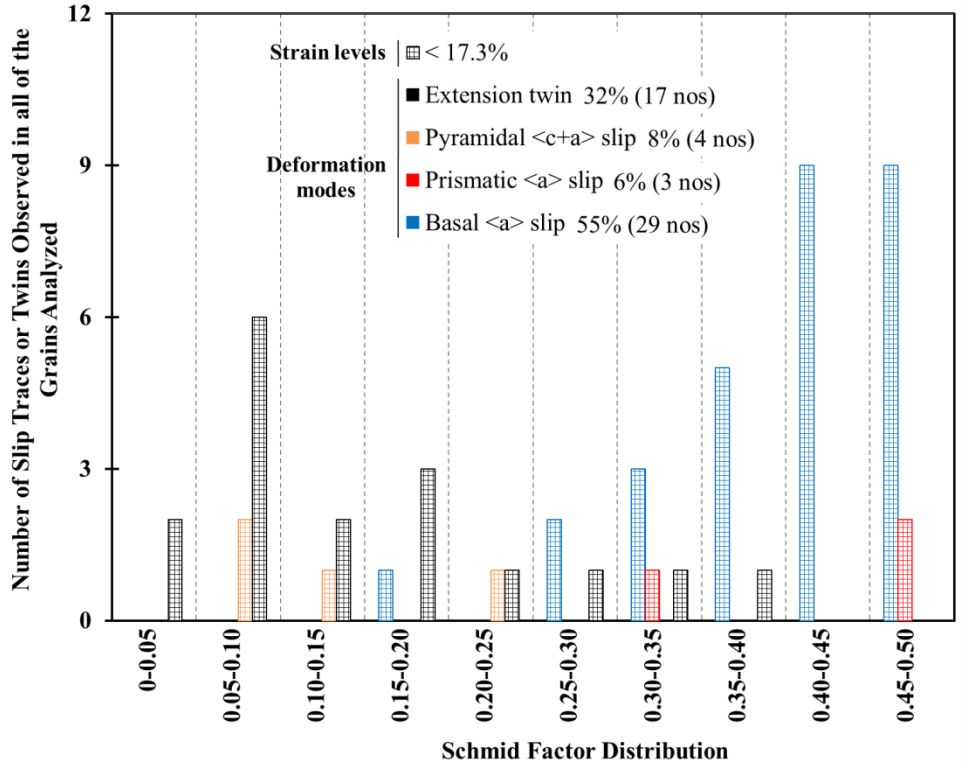

Figure 4.112 Histogram of the Schmid factor distribution of different deformation modes observed in extruded (a) MN11-300 and (b) MN11-275 specimens tensile tested at 423K.

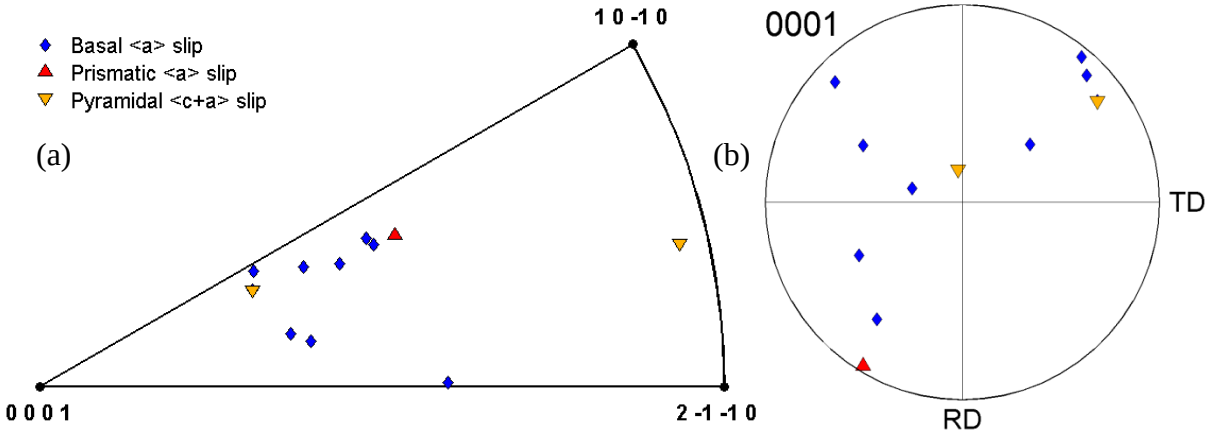

Figure 4.113 The individual grain orientations in which different slip modes were observed for extruded MN11-300 sample tensile test at 423K, plotted in a (a) unit triangle along the tensile direction and (b) {0001} pole figure along the normal direction.

In Figure 4.113a, the orientation of the grains in which different slip systems were identified in the MN11-300 specimen was plotted in a unit triangle along the tensile direction. In Figure 4.113b the same data from 4.113a is plotted in a {0001} pole figure along the normal direction.

4.5.2.3 523K tension

Figure 4.114 shows sequential SE SEM images taken from the same area of the MN11-300 specimen tensile tested at 523K. Basal <a> slip, prismatic <a> slip, and pyramidal <c+a> slip were observed. Figure 4.115 shows the EBSD IPF map in the normal direction of the same region from the gage section of the specimen before and after deformation. An extension twin observed in this area is highlighted by the black arrow in Figure 4.115b.

(a) ε ≈ 0%

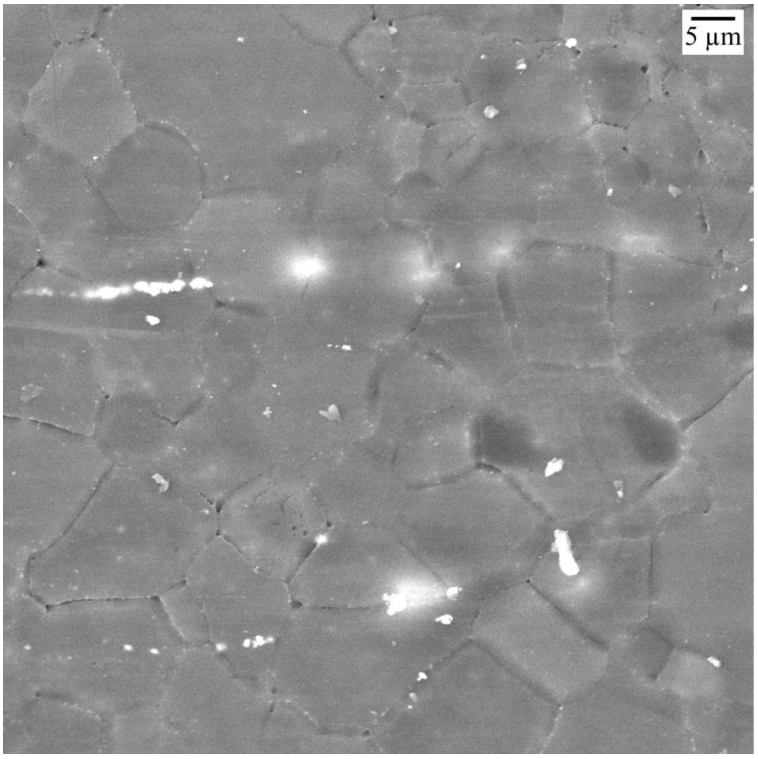

Tensile axis
↔
Extrusion direction

(b) ε ≈ 8.3%

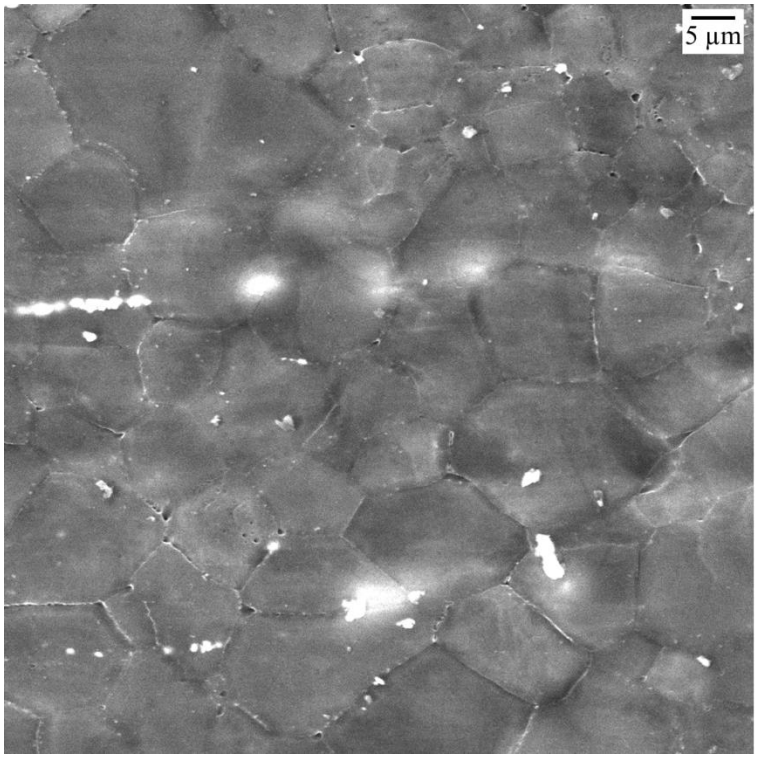

Figure 4.114 Sequential SE SEM images for the extruded MN11-300 sample tensile tested at 523K: (a) 0% strain, (b) ~8.3% strain, (c) ~19.2% strain, and (d) ~42.5% strain. Basal <a> slip traces observed in this region are highlighted by blue lines and the corresponding Schmid factor values are indicated in (d).

Figure 4.114 (cont'd)

(c) $\varepsilon \approx 19.2\%$

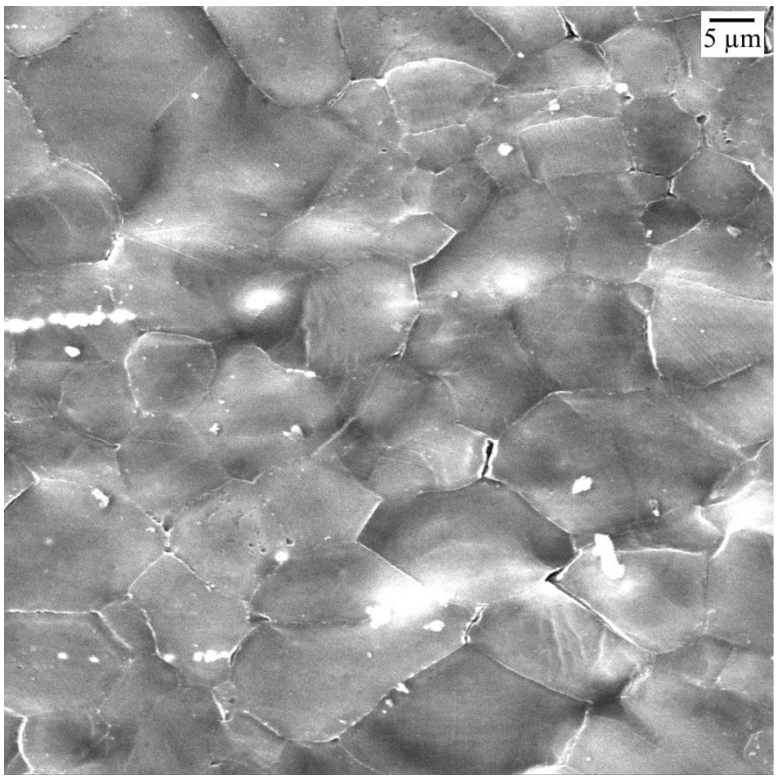

(d) $\varepsilon \approx 42.5\%$

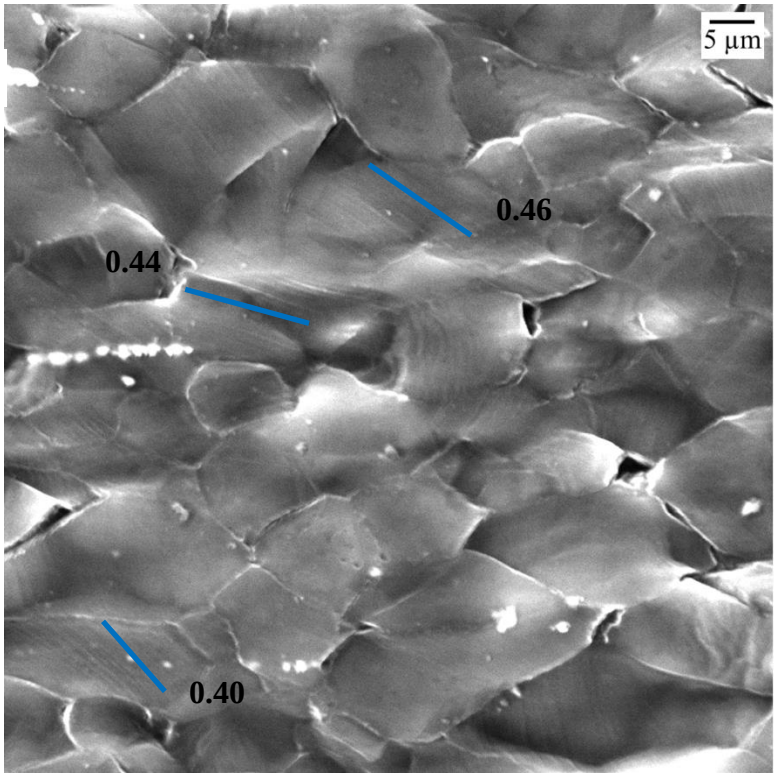

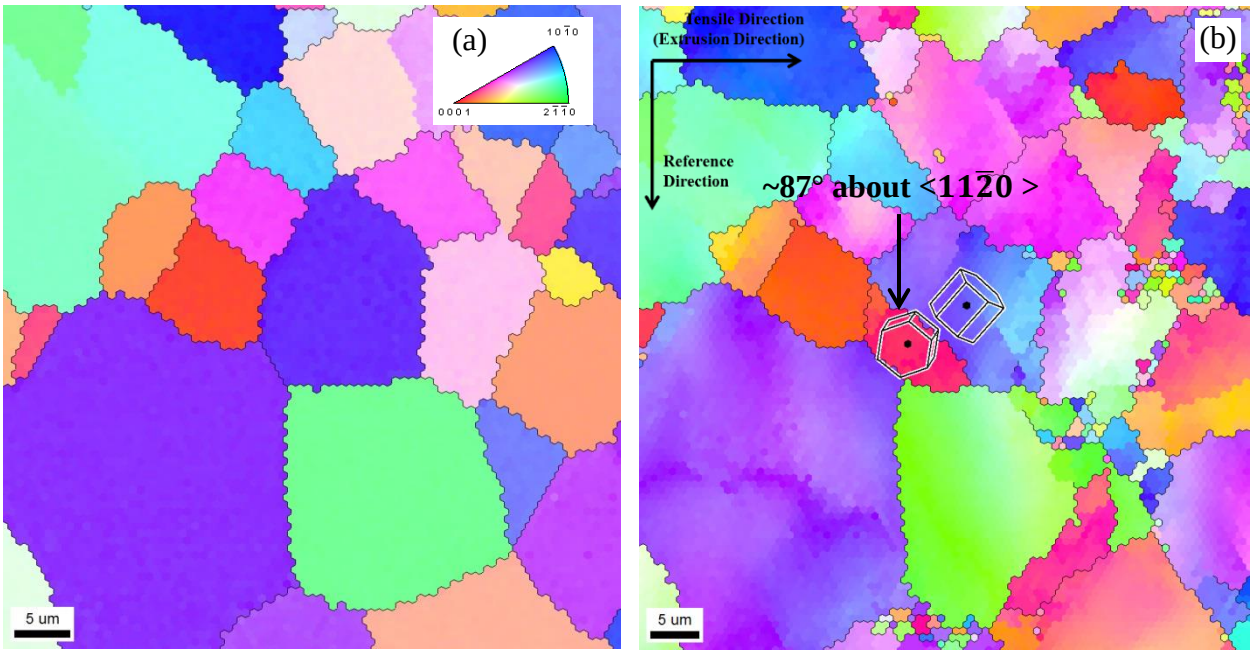

Figure 4.115 EBSD IPF map in the normal direction of the same area from the gage section of the extruded MN11-275 tensile tested specimen at 523K (a) before deformation and (b) at ~13.9% strain. An extension twin observed in this region is indicated by the black arrow in (b). The HCP unit cells are overlaid showing the misorientation between the parent grain and the twinned region and the rotation angles are indicated in (b).

In MN11-300 specimen, 58 basal <a> slip, four prismatic <a> slip, and four pyramidal <c+a> slip were observed. In the case of MN11-275 sample, 31 basal <a> slip, three prismatic <a> slip, and two pyramidal <c+a> slip traces were observed. 13 extension twins were also observed. Thus, basal <a> slip appeared to be the dominant deformation mode at 523K. Figure 4.116a and 4.116b plots the number of identified observations of a particular deformation mode versus the corresponding global Schmid factor range for MN11-300 and MN11-275, respectively. Extension twins were observed over the entire Schmid factor range.

(a)

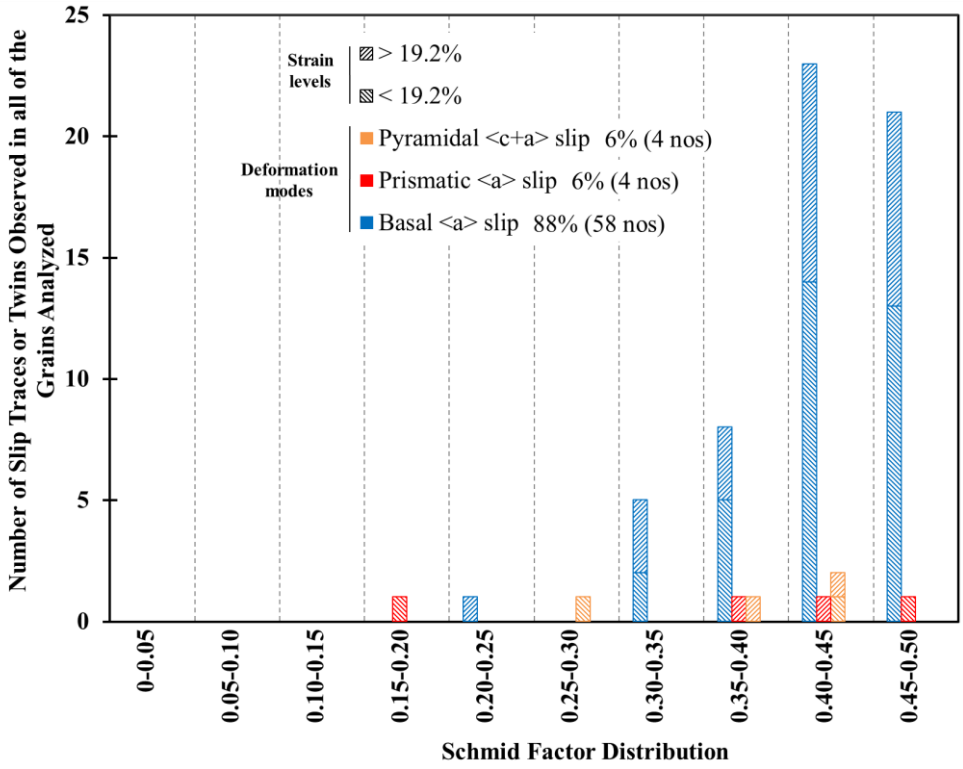

(a)

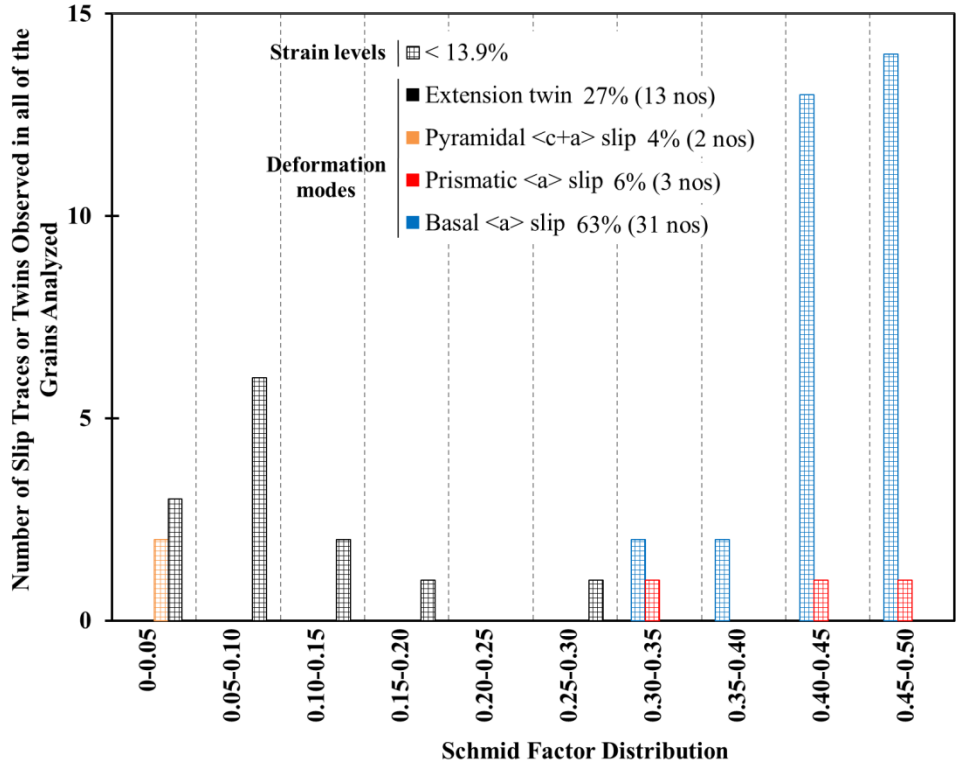

Figure 4.116 Histogram of the Schmid factor distribution of different deformation modes observed in the extruded (a) MN11-300 and (b) MN11-275 specimens tensile tested at 523K.

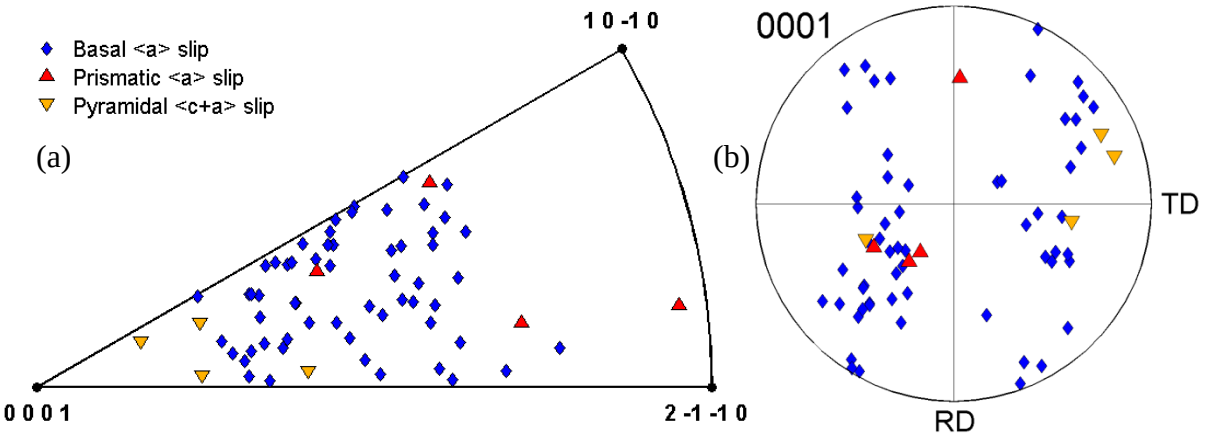

Figure 4.117 The individual grain orientations in which different deformation modes were observed for extruded MN11-300 tensile test at 523K, plotted in a (a) unit triangle along the tensile direction and (b) {0001} pole figure along the normal direction.

In Figure 4.117a, the orientation of the grains in which different slip systems were identified in extruded MN11-300 tensile deformed at 523K was plotted in a unit triangle along the tensile direction. In Figure 4.117b the same data from 4.117a is plotted in a {0001} pole figure along the normal direction.

4.5.3 In-situ compression

In-situ compression tests were performed on extruded MN11-300 at 298K, 423K, and 523K. One test was performed at each temperature. The engineering stress versus displacement curves for the compression tests are illustrated in Figure 4.118. In figure 4.118, the stress drops indicate the stress relaxation occurred when the tests were paused for imaging. None of the specimens were taken to failure in order to facilitate EBSD mapping after deformation. Twin trace analysis was performed on ~550, ~600, and ~750 grains for the samples tested at 298K, 423K, and 523K, respectively. Slip traces were not observed for any of the specimens at the given strain levels. However, twinning was observed. Table 4.21 lists the approximate YS and UTS obtained, and the maximum strain levels achieved for each experiment.

A separate MN11-300 sample was deformed in compression at 298K to study the evolution of extension twins. For this test, the loading was paused at ~0.8%, ~4.9%, and ~10.5% strain and EBSD orientation mapping was performed on the same microstructural patch while the sample was under load. The engineering stress versus displacement plot for this specimen is given (see dotted lines) in Figure 4.118.

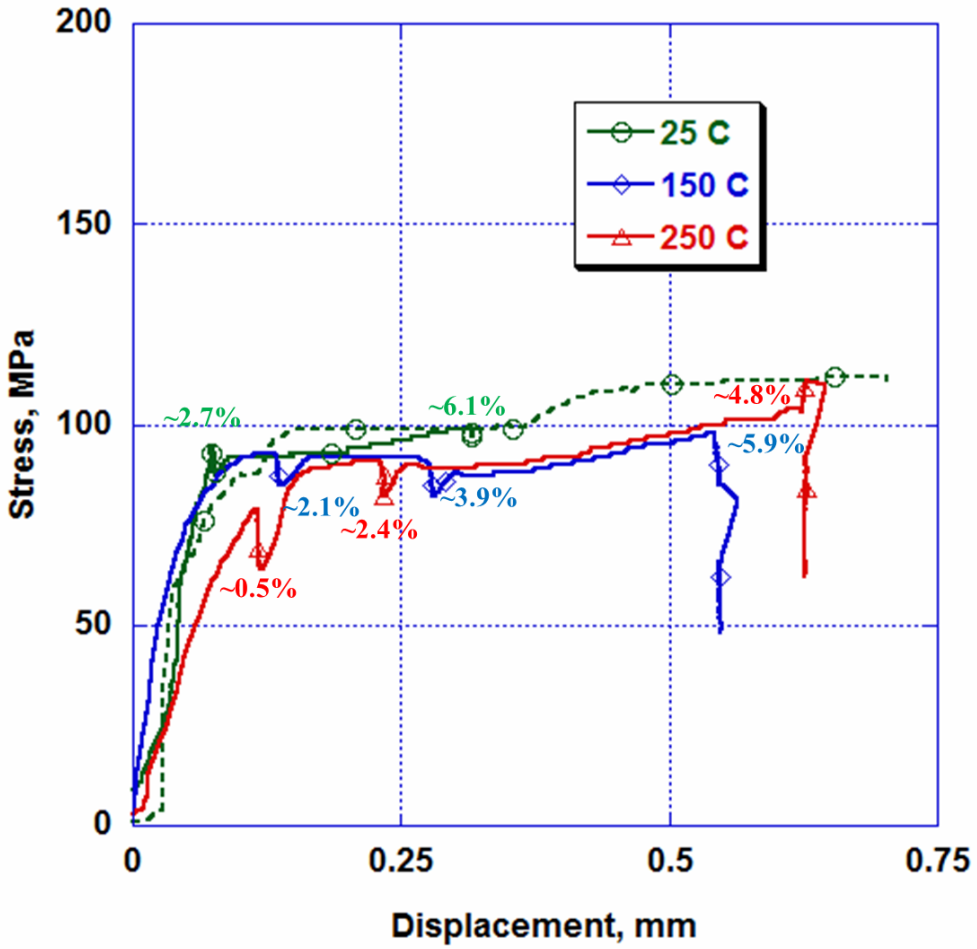

Figure 4.118 Representative stress vs. displacement plots for extruded MN11-300 samples compression tested at 298K, 423K, and 523K. The displacement values included displacements in both the gage section and the grip regions. The approximate strain values are indicated. The dotted line shows the stress vs. displacement plot for the MN11-300 specimen compression tested to study the evolution of twins. The stress drops indicated when the test was paused for imaging.

Table 4.21 MN11-300 extruded compression test property comparison for samples tested at 298K, 423K, and 523K.

Test temperature	YS (MPa)	UTS (MPa)	Maximum strain (%)
298K	~92	~99	~6.1
423K	~87	~98	~5.9
523K	~84	~98	~4.8

4.5.3.1 298K compression

Figure 4.119 shows the {0001} pole figures in the normal direction from the gage section of the specimen compression tested at 298K before and after deformation. The change in texture was expected to be due to the extension twinning activity.

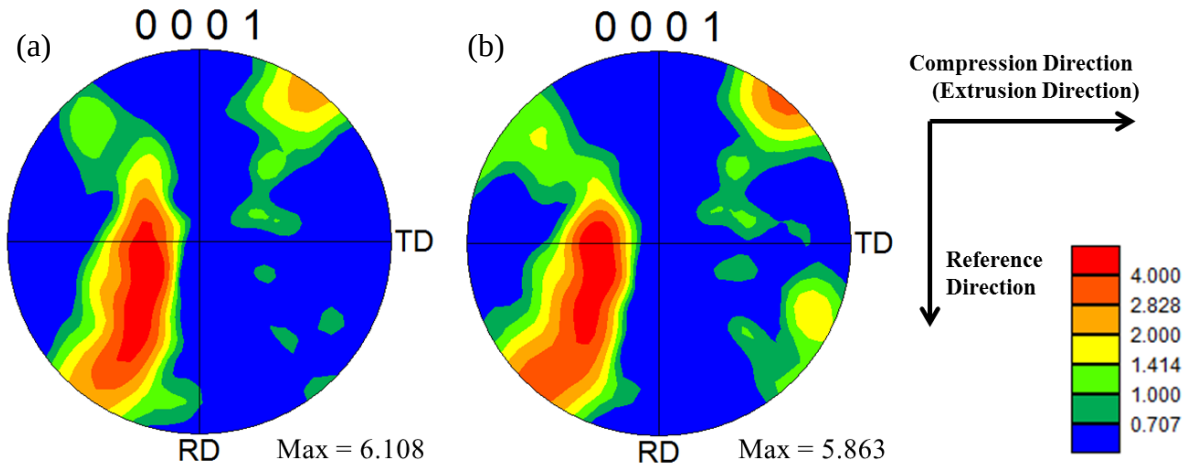

Figure 4.119 {0001} pole figures in the normal direction from the gage section of the MN11-300 extruded specimen compression tested at 298K (a) before and (b) after deformation (~6.1% strain).

In the microstructural patch analyzed, 24 extension twins were observed. No contraction twins were observed. Figure 4.120 shows the IPF map in the normal direction of the same area from the gage section of the MN11-300 extruded specimen compression tested at 298K, taken at 0% and ~6.1% strain. The extension twin boundaries are highlighted in black in Figure 4.120b. Figure 4.121 plots the number of identified extension twins versus the corresponding global Schmid factor range. Extension twins with Schmid factors as low as 0.03 and as high as 0.46 were observed. The deformation was controlled by extension twinning in the extruded MN11-300 specimen compression tested at 298K.

In Figure 4.122a, the orientation of the grains in which extension twins were identified was plotted in a unit triangle along the compression direction. In Figure 4.122b the same data from 4.122a is plotted in a {0001} pole figure along the normal direction.

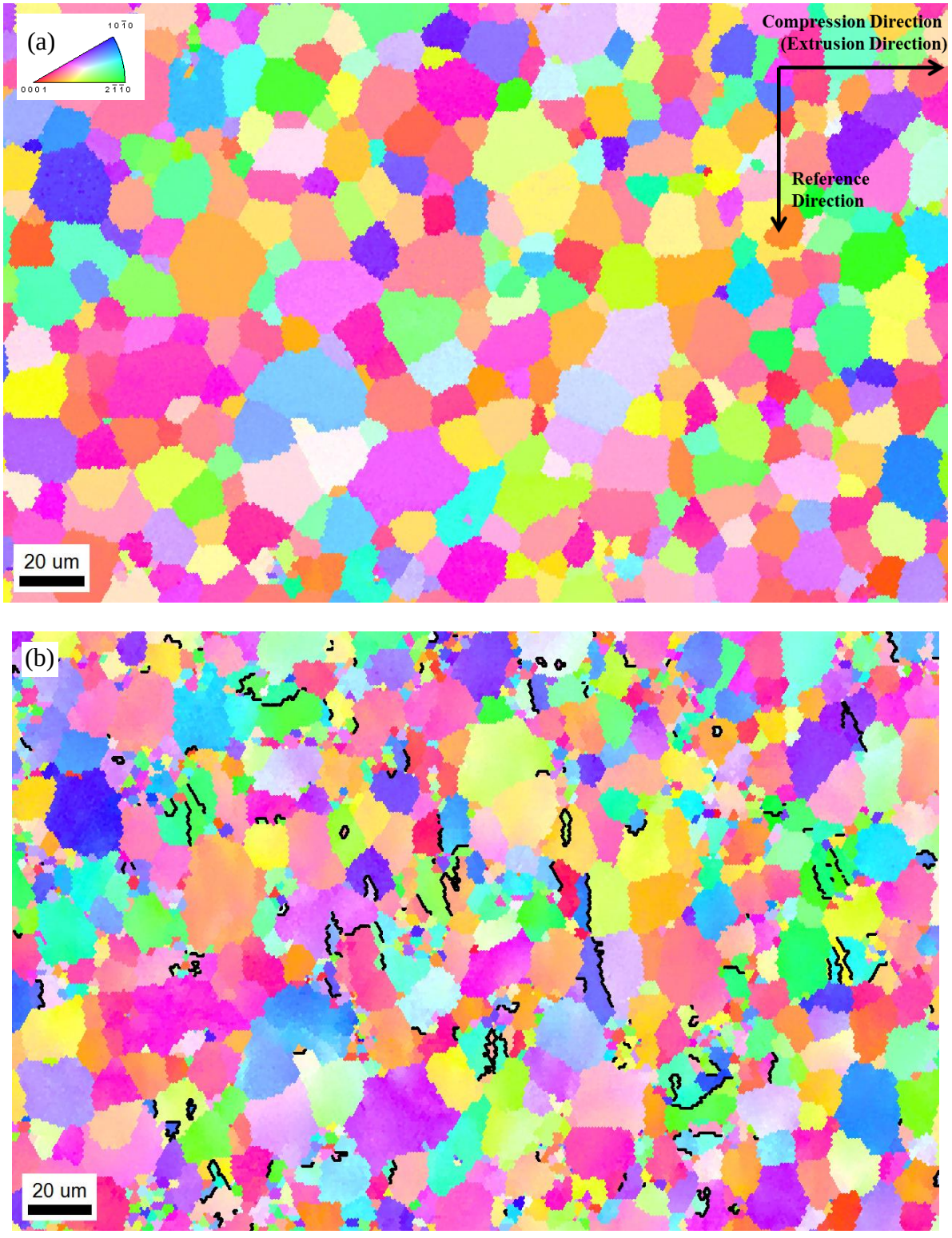

Figure 4.120 EBSD IPF map in the normal direction of the same area from the gage section of the extruded MN11-300 compression tested specimen at 298K (a) before deformation and (b) at ~6.1% strain. Extension twin boundaries (86°±5° misorientation about $< 11\bar{2}0 >$, twin plane $\{10\bar{1}2\}$±5° tolerance) are highlighted in black in (b).

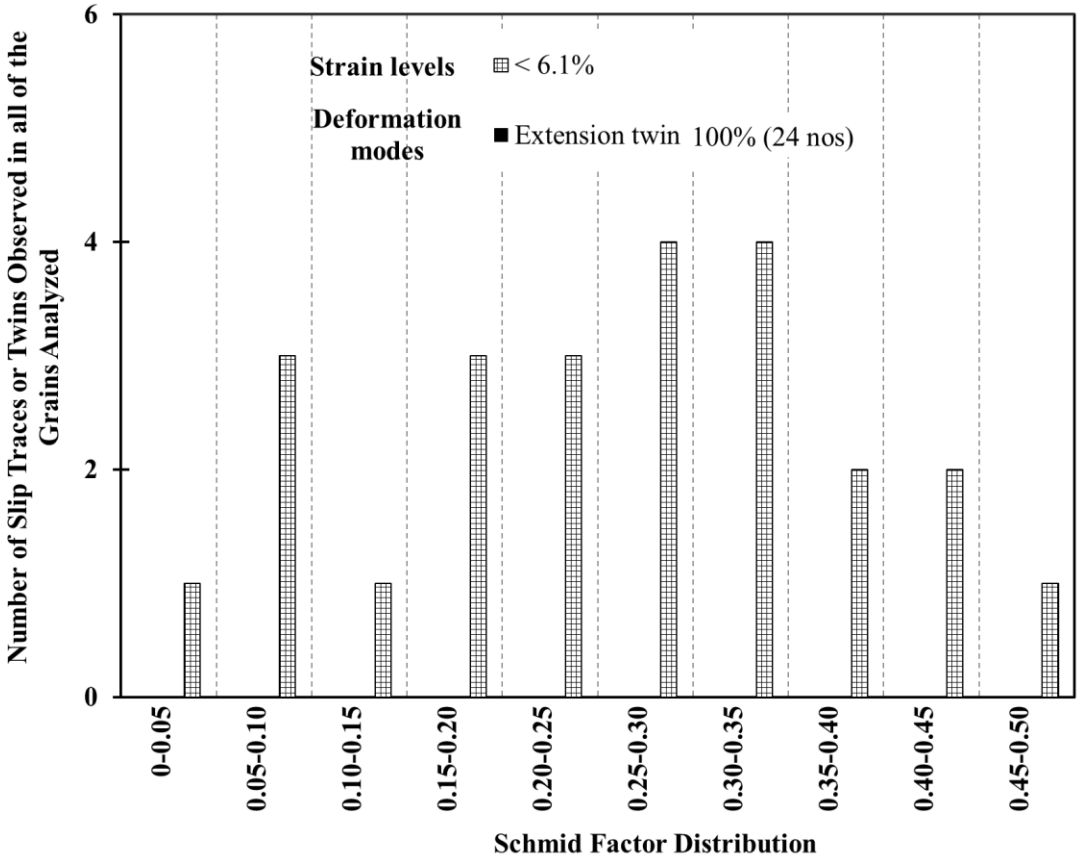

Figure 4.121 A histogram of the Schmid factor distribution of extension twins for the extruded MN11-300 298K compression sample.

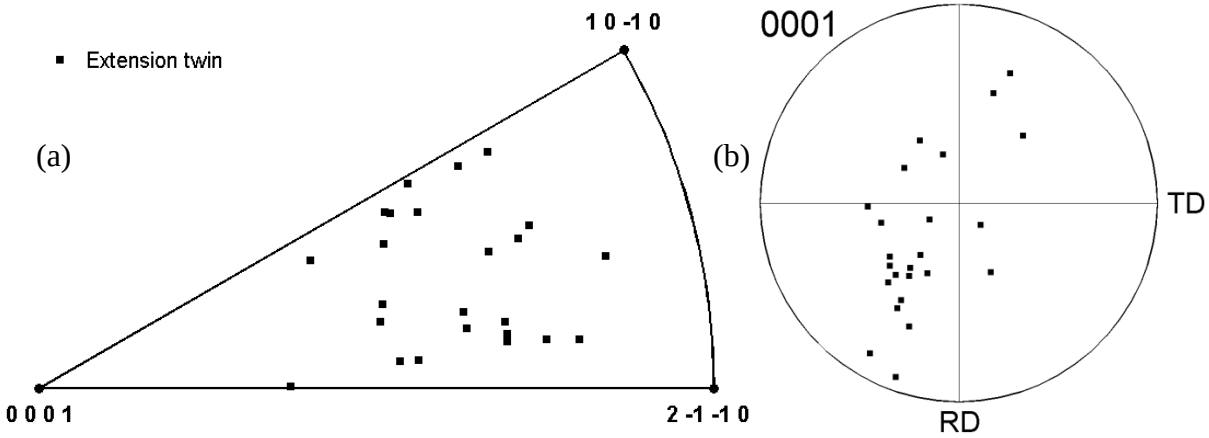

Figure 4.122 The individual grain orientations in which extension twins were observed for extruded MN11-300 compression test at 298K, plotted in a (a) unit triangle along the compression direction and (b) {0001} pole figure along the normal direction.

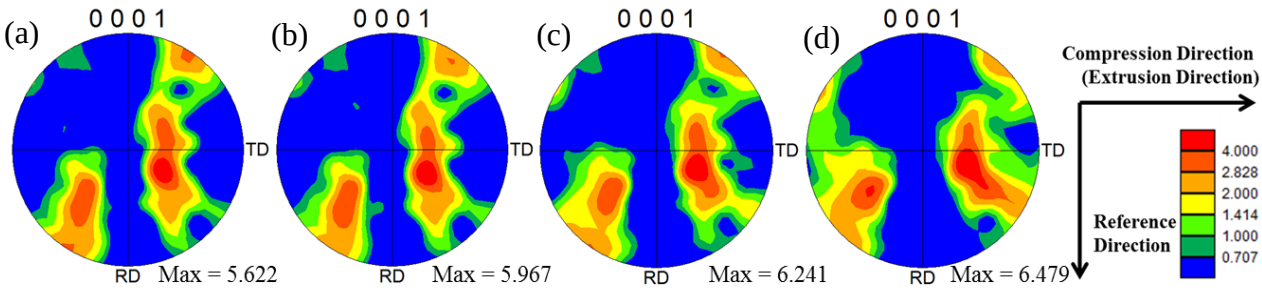

Figure 4.123 {0001} pole figures in the normal direction from the gage section of the MN11-300 extruded specimen compression tested at 298K to study the evolution of extension twins, at (a) 0%, (b) ~0.8%, (c) ~4.9%, and (d) ~10.5% strain.

Figure 4.123 shows the {0001} pole figures in the normal direction at 0%, ~0.8%, ~4.9%, and ~10.5% strain, from the gage section of the specimen compression tested at 298K to study the evolution of extension twins.

Approximately 1000 grains were analyzed for twin activity, and 46 extension twins were observed. Extension twins started to appear at ~0.8% strain, which was before global yielding, and the twin volume fraction increased with increasing strain. Figure 4.124 shows the EBSD IPF maps depicting the evolution of an extension twin of type $(01\bar{1}2)[0\bar{1}11]$ with a Schmid factor of 0.35. Figure 4.125 plots the number of identified extension twins versus the corresponding global Schmid factor range as function of strain for this specimen.

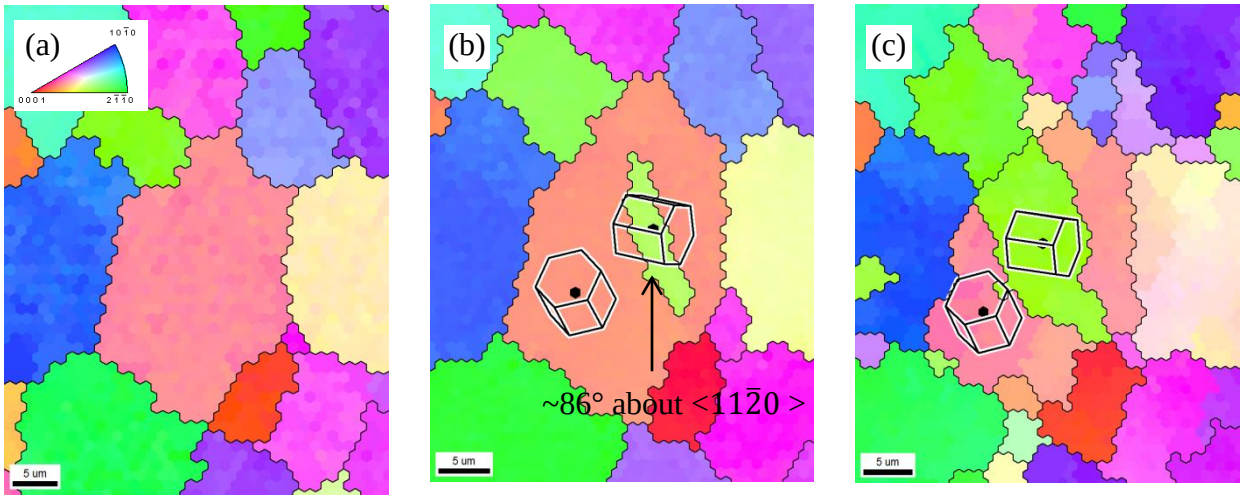

Figure 4.124 EBSD IPF map along the normal direction of an extension twin observed in MN11-300 specimen compression tested at 298K, at (a) 0%, (b) ~0.8%, and (c) ~4.9% strain, indicating the twin evolution. The HCP unit cells are overlaid showing the misorientation between the parent grain and the twinned region and the rotation angles are indicated in (b). Both the compression direction and then extrusion direction are horizontal.

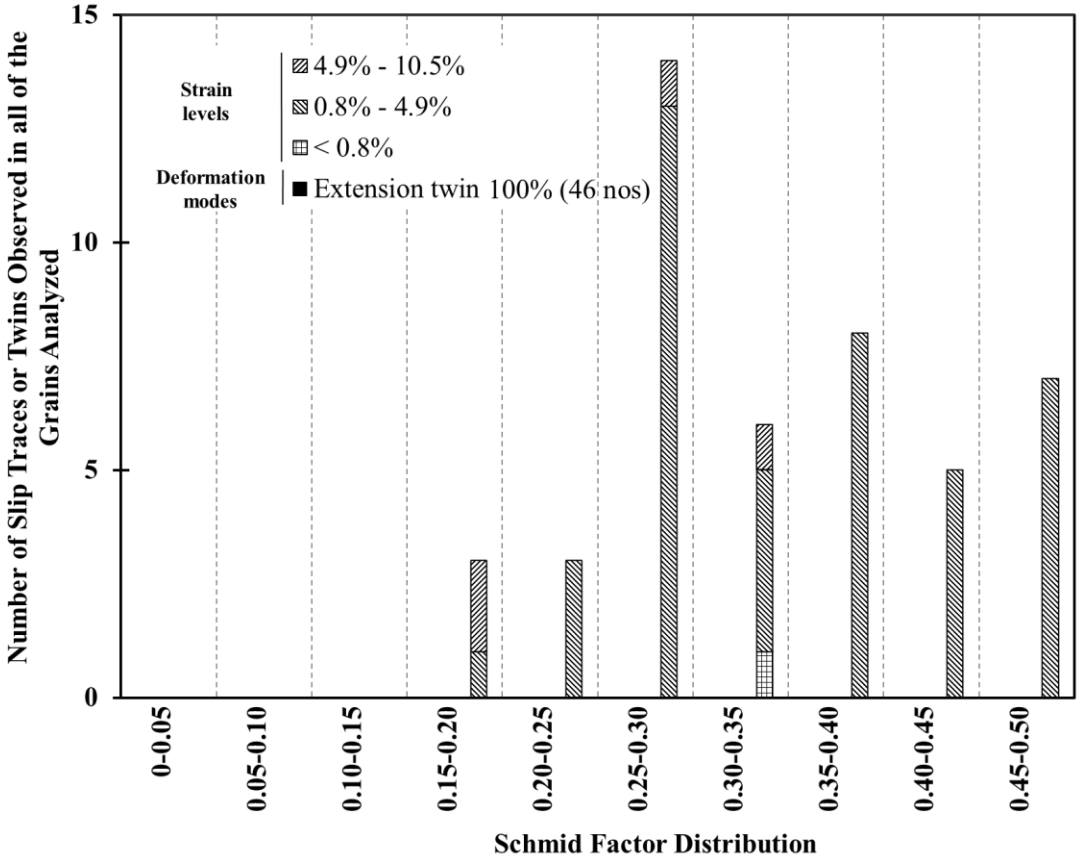

Figure 4.125 A histogram of the Schmid factor distribution of extension twins for the extruded MN11-300 298K compression experiment performed to study the evolution of extension twins.

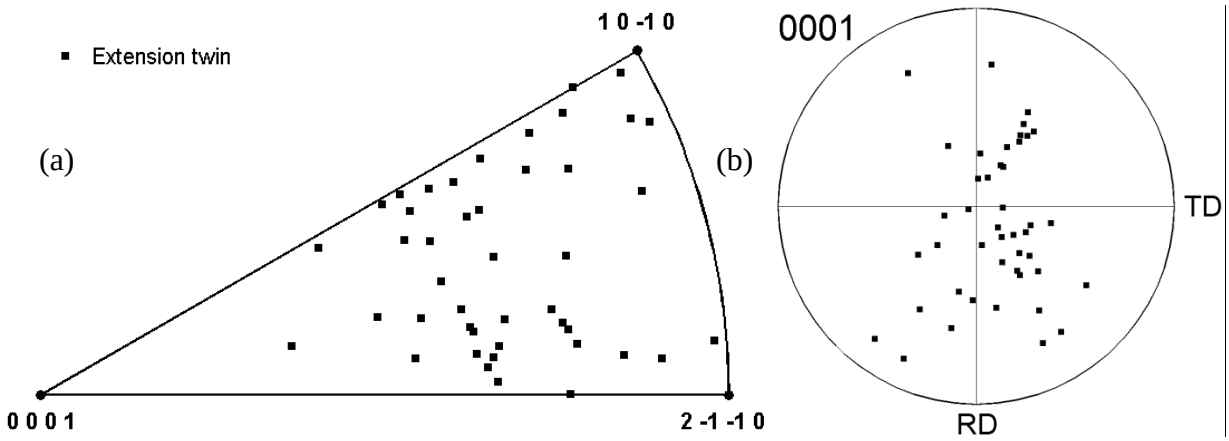

Figure 4.126 The individual grain orientations in which extension twins were observed for extruded MN11-300 compression test at 298K performed to study the evolution of extension twins, plotted in a (a) unit triangle along the compression direction and (b) {0001} pole figure along the normal direction.

In Figure 4.126a, the orientation of the grains in which extension twins were identified in this specimen was plotted in a unit triangle along the compression direction. In Figure 4.126b the same data from 4.126a is plotted in a {0001} pole figure along the normal direction.

4.5.3.2 423K compression

Figure 4.127 shows the {0001} pole figures in the normal direction from the gage section of the specimen compression tested at 423K before and after deformation. The significant change in texture was expected to be due to the extension twinning activity.

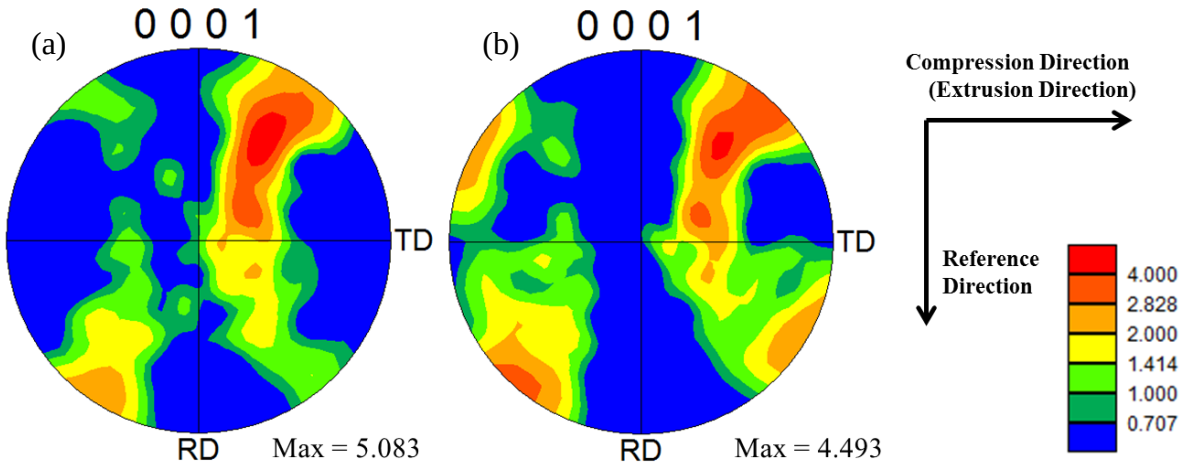

Figure 4.127 {0001} pole figures in the normal direction from the gage section of the MN11-300 extruded specimen compression tested at 423K (a) before and (b) after deformation (5.9% strain).

In the microstructural patch analyzed, 34 extension twins were observed. No contraction twins were observed. Figure 4.128 shows the IPF map in the normal direction of the same area from the gage section of the MN11-300 extruded specimen compression tested at 423K taken at 0% and ~5.9% strain. The extension twin boundaries are highlighted in black in Figure 4.128b. Figure 4.129 plots the number of identified extension twins versus the corresponding global Schmid factor range. Extension twins with Schmid factors as low as 0.04 and as high as 0.48 were observed. One extension twin was observed at a global Schmid factor value less than 0. The deformation was controlled by extension twinning in the extruded MN11-300 specimen compression tested at 423K.

In Figure 4.130a, the orientation of the grains in which extension twins were identified was plotted in a unit triangle along the compression direction. In Figure 4.130b the same data from 4.130a is plotted in a {0001} pole figure along the normal direction.

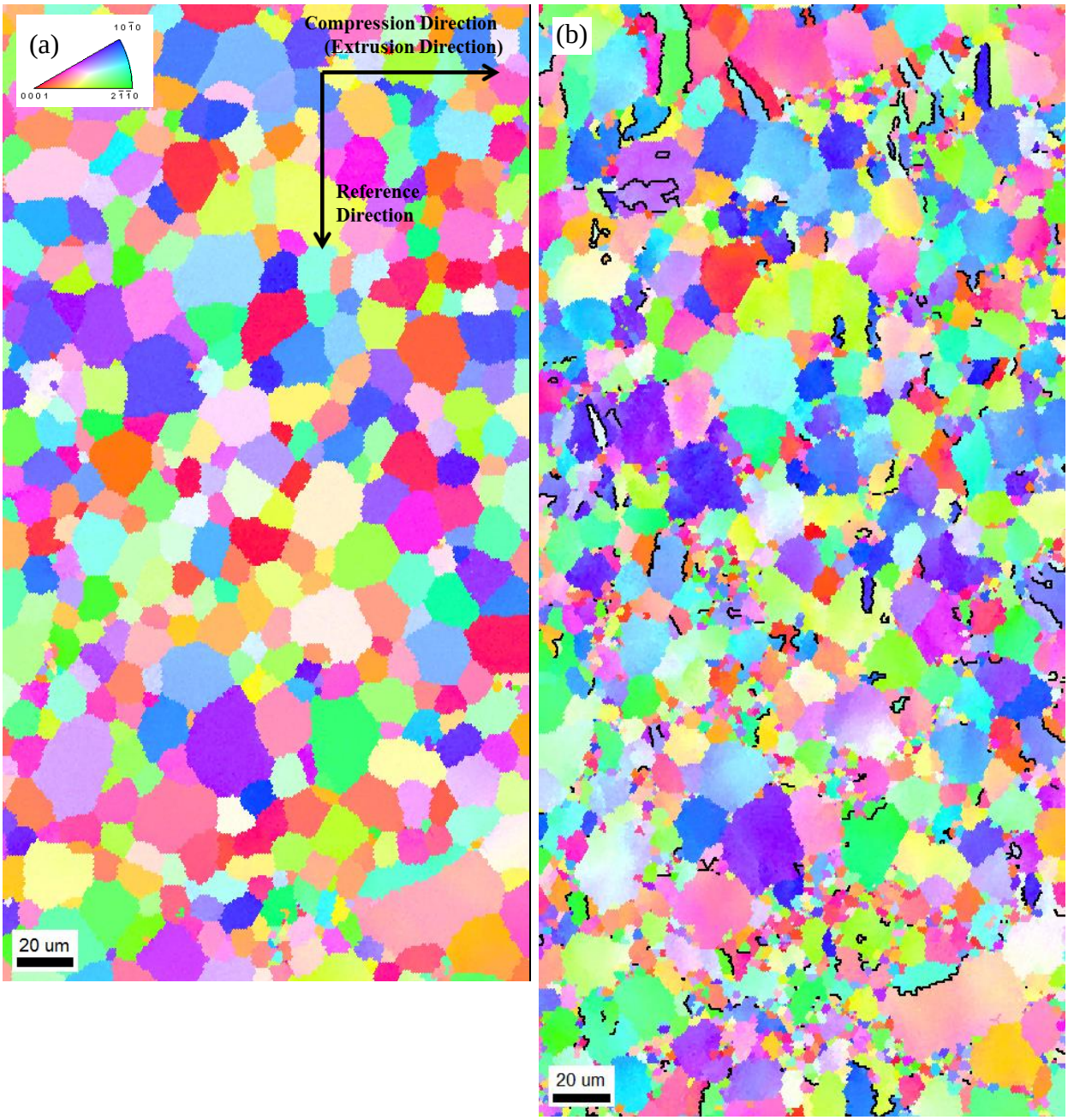

Figure 4.128 EBSD IPF map in the normal direction of the same area from the gage section of the extruded MN11-300 compression tested specimen at 423K (a) before deformation and (b) at ~5.9% strain. Extension twin boundaries (86°±5° misorientation about $< 11\bar{2}0 >$, twin plane $\{10\bar{1}2\}$±5° tolerance) are highlighted in black in (b).

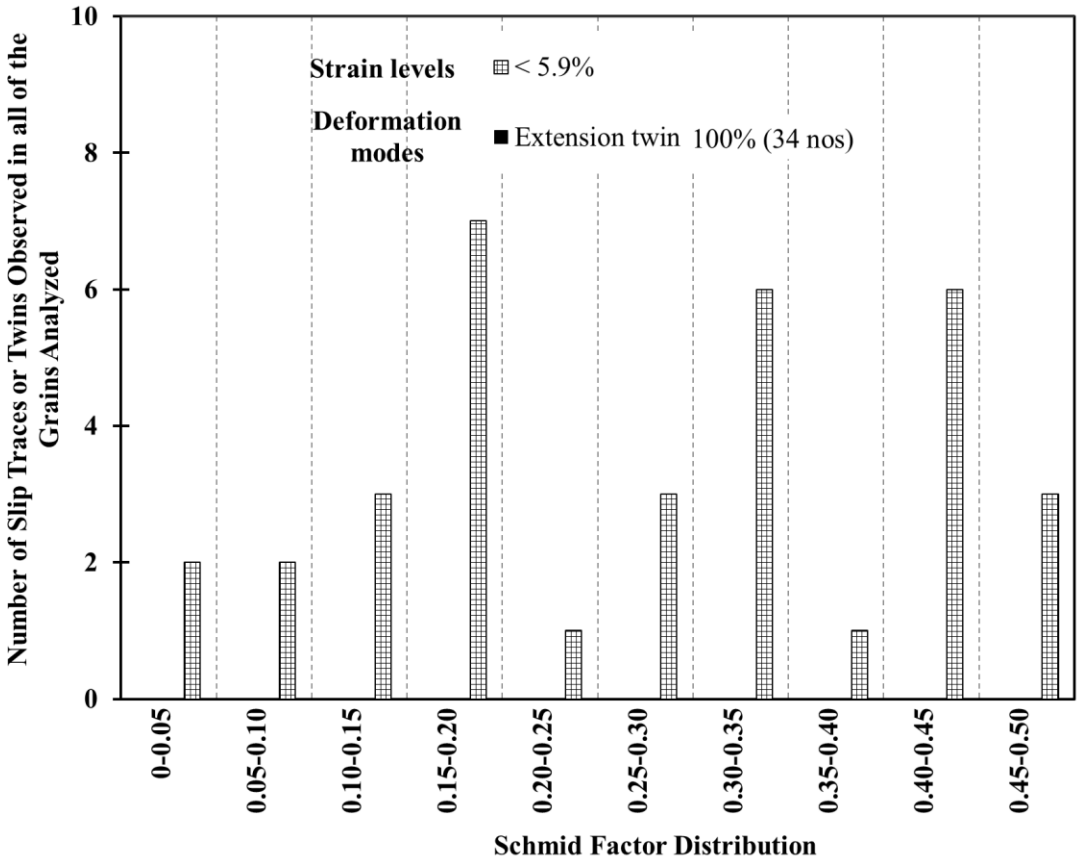

Figure 4.129 A histogram of the Schmid factor distribution of extension twins for the extruded MN11-300 423K compression sample.

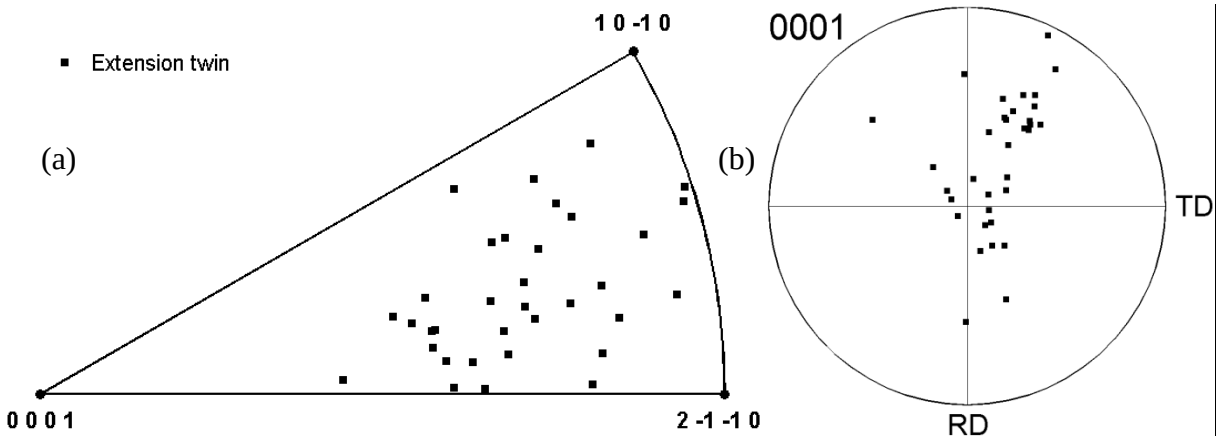

Figure 4.130 The individual grain orientations in which different extension twins were observed for extruded MN11-300 compression test at 423K, plotted in a (a) unit triangle along the compression direction and (b) {0001} pole figure along the normal direction.

4.5.3.3 523K compression

Figure 4.131 shows the {0001} pole figures in the normal direction from the gage section of the specimen compression tested at 523K before and after deformation. The change in texture was expected to be due to the extension twinning activity.

In the microstructural patch analyzed, 68 extension twins were observed. No contraction twins were observed. Figure 4.132 shows the IPF map in the normal direction of the same area from the gage section of the MN11-300 extruded specimen compression tested at 523K taken at 0% and ~4.8% strain. The extension twin boundaries are highlighted in black in Figure 4.132b. Figure 4.133 plots the number of identified extension twins versus the corresponding global Schmid factor range. Extension twins with Schmid factors as low as 0.03 and as high as 0.50 were observed. One extension twin was observed at a global Schmid factor value less than 0. The deformation was controlled by extension twinning in the extruded MN11-300 specimen compression tested at 523K.

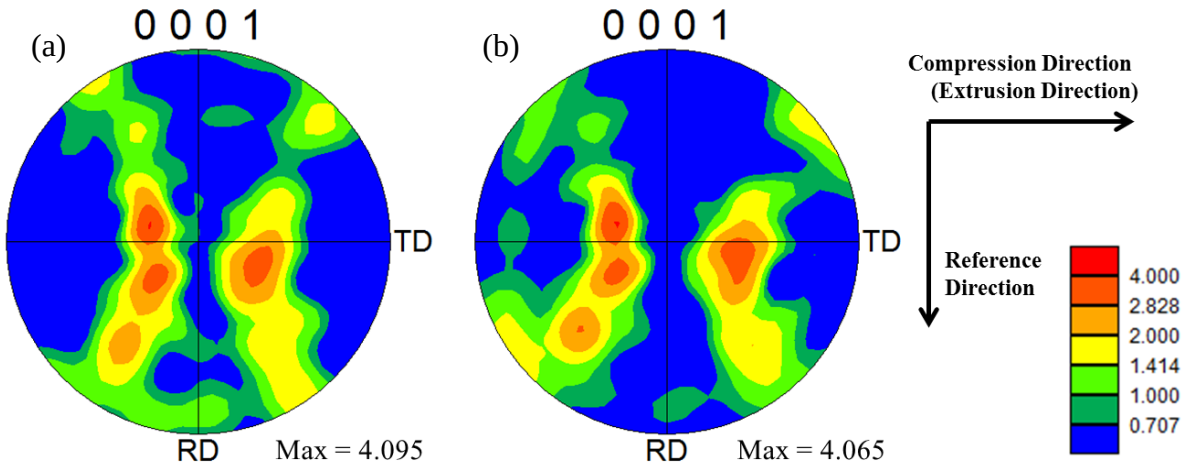

Figure 4.131 {0001} pole figures in the normal direction from the gage section of the MN11-300 extruded specimen compression tested at 523K (a) before and (b) after deformation (~4.8% strain).

Two variants of extension twins were observed in four grains. Extension twins of type $(0\bar{1}12)[01\bar{1}1]$ and $(01\bar{1}2)[0\bar{1}11]$ were active at the same time in three out of those four grains. One such grain is marked as "A" in Figure 4.132a and 4.132b. In the other grain, extension twins of type $(10\bar{1}2)[\bar{1}011]$ and $(01\bar{1}2)[0\bar{1}11]$ were observed. This grain is marked as "B" in Figure 4.132a and 4.132b. It is noted that multiple twin variants were not observed in the same grains for the MN11-300 samples tested at 298K and 423K.

In Figure 4.134a, the orientation of the grains in which extension twins were identified was plotted in a unit triangle along the compression direction. In Figure 4.134b the same data from 4.134a is plotted in a {0001} pole figure along the normal direction.

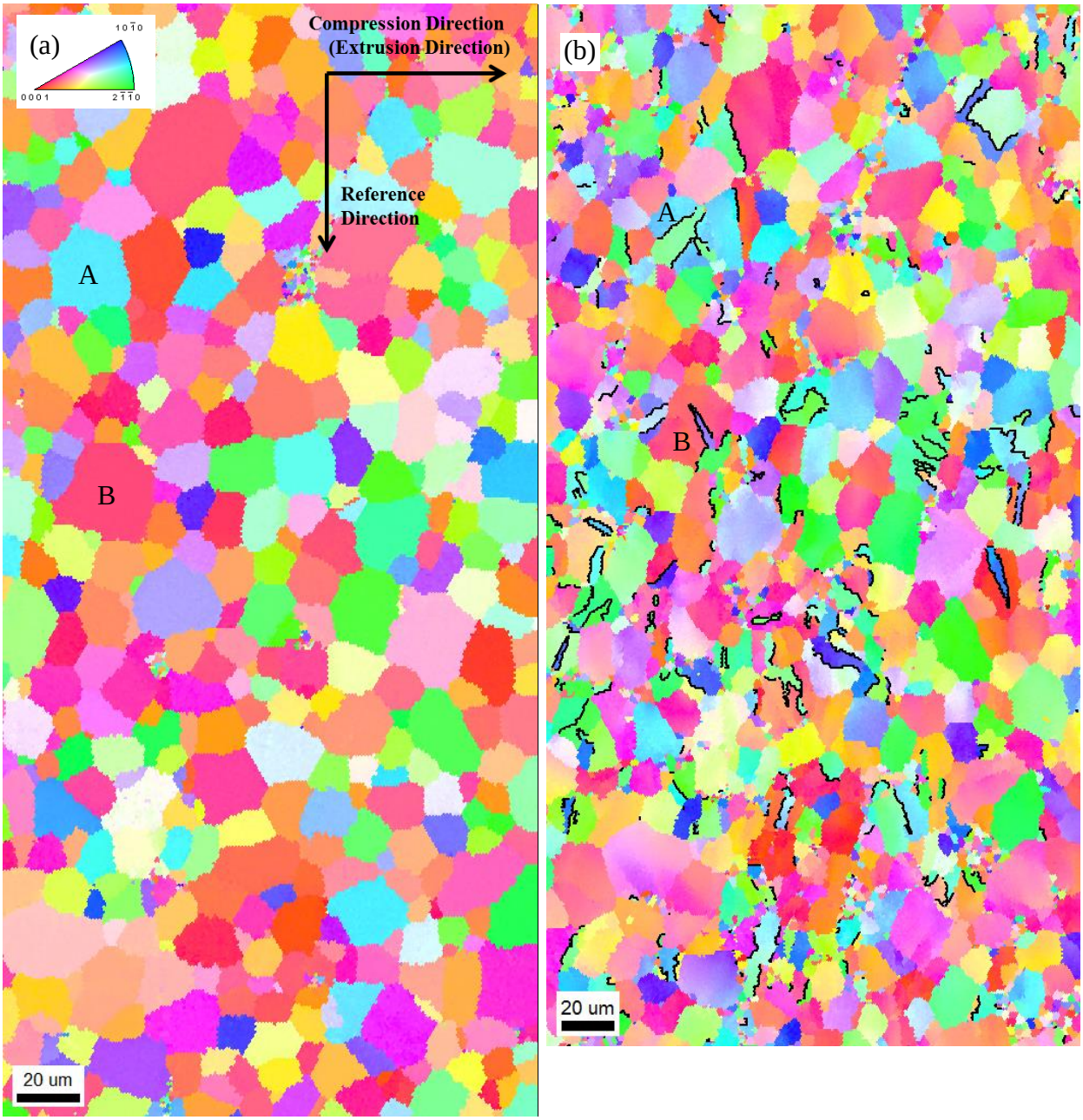

Figure 4.132 EBSD IPF map in the normal direction of the same area from the gage section of the extruded MN11-300 compression tested specimen at 523K (a) before deformation and (b) at ~4.8% strain. Extension twin boundaries (86°±5° misorientation about $< 11\bar{2}0 >$, twin plane $\{10\bar{1}2\}$±5° tolerance) are highlighted in black in (b). The grains in which multiple twin variants were observed are marked as "A" and "B" in (a) and (b).

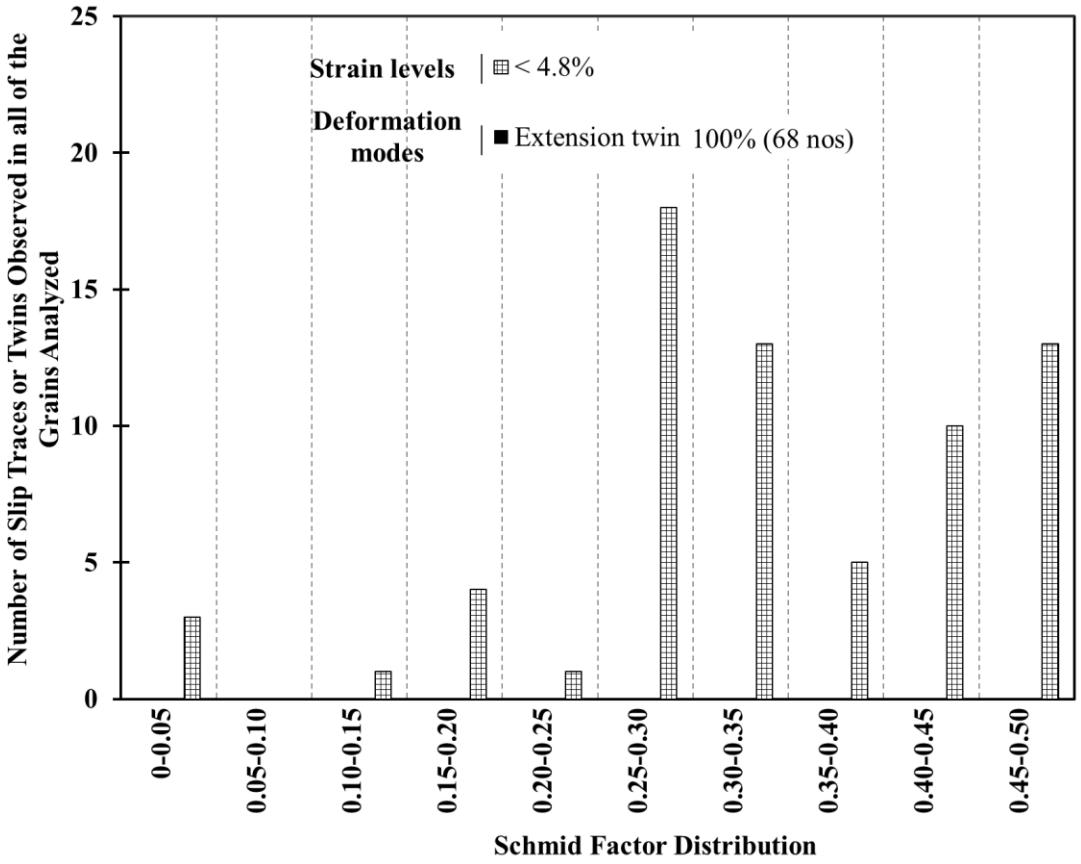

Figure 4.133 A histogram of the Schmid factor distribution of extension twins for the extruded MN11-300 523K compression sample.

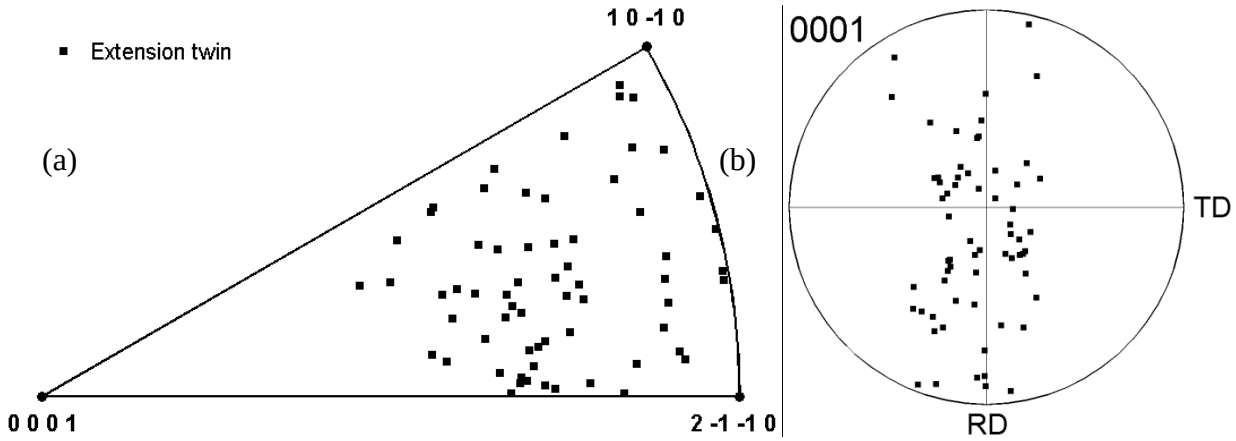

Figure 4.134 The individual grain orientations in which extension twins were observed for extruded MN11-300 compression test at 523K, plotted in a (a) unit triangle along the compression direction and (b) {0001} pole figure along the normal direction.

4.6 Rolled Mg-2Zn-0.2Ce and Mg-2Zn-0.6Ce (ZE20)

4.6.1 Microstructure and texture

Figure 4.135 shows the EBSD IPF map of the microstructure and the corresponding {0001} pole figures along the normal direction showing the texture in the as-rolled condition and after annealing at 673K for 60s for Mg-2Zn-0.2Ce and Mg-2Zn-0.6Ce. As shown in Figure 4.135, elongated grains along the RD were observed in the as-rolled microstructures of both materials and a fully recrystallized microstructure was observed after annealing. It is noted that these images were taken from different sections of the material, thus they do not represent the same microstructural patches before and after annealing. The average grain diameters for Mg-2Zn-0.2Ce and Mg-2Zn-0.6Ce after annealing at 673K for 60s were ~10μm and ~6μm, respectively.

Both materials exhibited a basal texture in the as-rolled condition in which the c-axis tends to align perpendicular to the rolling direction (See Figure 4.135a and 4.135c). Compared to Mg-2Zn-0.6Ce, a stronger basal texture was observed in Mg-2Zn-0.2Ce in the as-rolled condition (10.4 times random in Mg-2Zn-0.2Ce compared to 5.0 in Mg-2Zn-0.6Ce). The texture intensity decreased in both materials after annealing (from 10.4 and 5.0 times random in the as-rolled condition to 7.6 and 4.2 times random after annealing in Mg-2Zn-0.2Ce and Mg-2Zn-0.6Ce, respectively). This suggests that recrystallization helped in the weakening of texture. In order to understand the mechanisms responsible for the texture weakening during recrystallization, the same microstructural patch was monitored during annealing using the in-situ experimental technique described in Section 3.7. For the remainder of this sub-section, the results from those experiments are provided.

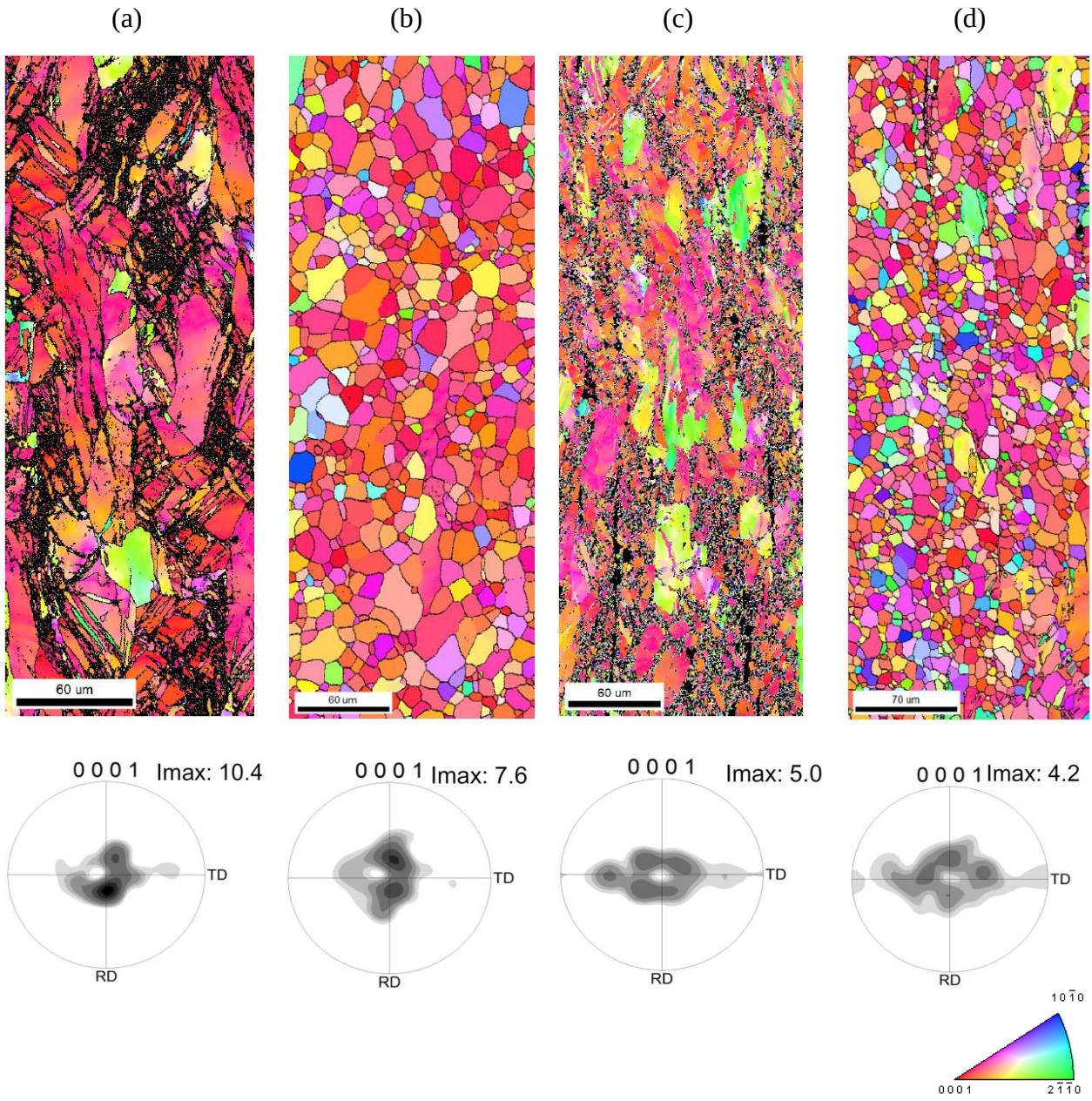

Figure 4.135 The EBSD IPF map of the microstructure and the texture in the form of {0001} pole figures along the normal direction for (a) as-rolled Mg-2Zn-0.2Ce, (b) Mg-2Zn-0.2Ce after annealing, (c) as-rolled Mg-2Zn-0.6Ce, and (d) Mg-2Zn-0.6Ce after annealing. The annealing was carried out at 673K for 60s for both materials. The rolling direction is vertical. It is noted that the images shown above were taken from different sections of the material, thus they do not represent the same microstructural patches before and after annealing.

4.6.2 In-situ annealing/recrystallization of Mg-2Zn-0.2Ce

Figure 4.136 shows the EBSD IPF map in the normal direction of the same microstructural patch depicting the evolution of microstructure in rolled Mg-2Zn-0.2Ce as a function of annealing temperature. It is noted that it took ~5-15 minutes to get to the annealing temperature and the EBSD orientation map was acquired in ~45 minutes for each subsequent heating step. The images given in Figure 4.136 were obtained after post-processing the EBSD raw data using a clean-up procedure in which a single iteration of grain dilation with a grain tolerance angle of 2° and minimum grain size of 2 pixels was performed. In the case of scans taken at temperatures less than 523K, ~20-25% points in the EBSD maps were modified during the clean-up procedure. For scans taken at temperatures greater than 523K, ~15% of the EBSD data points were changed during the clean-up. This was because the quality of EBSD indexing increased with an increase in temperature as the microstructure consisted mainly of newly recrystallized relatively strain-free grains. Furthermore, the EBSD data shown in Figure 4.136 were partitioned with a grain tolerance angle of 5 degrees and a minimum grain size of 2 pixels.

During the annealing process, new grains started to appear during the heating step from 423K to 473K in rolled Mg-2Zn-0.2Ce (See Figure 4.136). At ~573K, a completely recrystallized microstructure was observed. Figure 4.137 shows the grain orientation spread obtained from the EBSD data from the microstructural patch analyzed for Mg-2Zn-0.2Ce as a function of annealing temperature. It is noted that the post-processing procedures applied for the images given in Figure 4.137 are the same as that for Figure 4.136. As shown in Figure 4.137, the grain orientation spread was less than 1.5 degrees in the area analyzed after the heat treatment at 573K, suggesting that the grains were relatively free of the strain which accumulated during the rolling process.

The orientation relationship of the new grains formed during each heating step was investigated with respect to their neighbors. Specifically, the misorientation angles and the corresponding misorientation axis across the newly formed grain boundaries were examined. The grain boundaries with misorientation angles greater than 15 degrees were only considered for the analysis. A total of 59 new grains were formed during the four heating steps between 423K and 548K in the microstructural patch analyzed. This resulted in a total of 159 unique grain boundaries. It is noted that most of the new grains (~94%) appeared at temperatures between 423K and 548K. Thus only a few new grains appeared upon further heating from 548K to 598K.

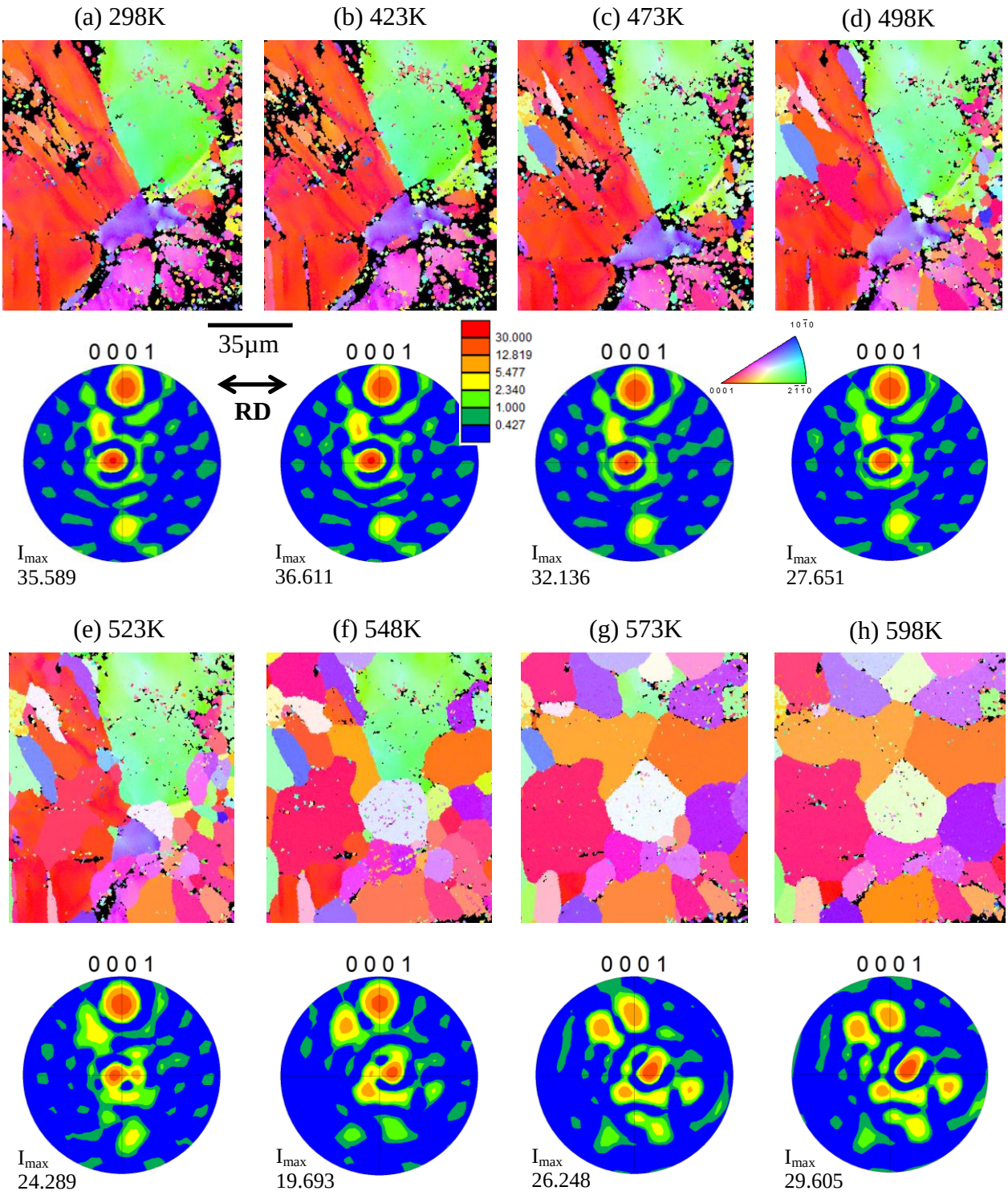

Figure 4.136 EBSD IPF maps and the corresponding {0001} pole figures in the normal direction depicting the microstructural evolution in rolled Mg-2Zn-0.2Ce as a function of annealing temperature. I_{max} is the maximum intensity values observed in the pole figures. It is noted that it took ~5-15 minutes to get to the annealing temperature and the EBSD orientation map was acquired in ~45 minutes for each subsequent heating step. The rolling direction is horizontal.

Figure 4.138 shows the distribution of the number fraction of the observed misorientation axis relationships for the newly formed grain boundaries in rolled Mg-2Zn-0.2Ce, annealed at temperatures between 423K and 548K, sorted into $< hki0 >$ and $< hkil >$ types. Among the misorientation relationships observed between the newly formed grain boundaries, rotation axis about $< 10\bar{1}0 >$ (~41%), $< 11\bar{2}0 >$ (~23%), and $< 10\bar{1}1 >$ (~12%) were prevalent. Grain boundaries with orientation relationships corresponding to $\{10\bar{1}2\}$ extension twinning (86° about $< 11\bar{2}0 >$), $\{10\bar{1}1\}$ contraction twinning (56° about $< 11\bar{2}0 >$), and $(10\bar{1}2) - (01\bar{1}2)$ extension double twin (60° about $< 10\bar{1}0 >$) were also commonly observed. That is, ~9%, ~6%, and ~18% of the newly formed grains boundaries had a misorientation relationship corresponding to $\{10\bar{1}2\}$ extension twinning, $\{10\bar{1}1\}$ contraction twinning, and $(10\bar{1}2) - (01\bar{1}2)$ extension double twinning, respectively. This was expected to be due to the recovery and growth of the twins formed during the rolling process.

During the heating cycles between 548K and 598K, 13 grains (corresponding to 42 grain boundaries) disappeared from the microstructural patch analyzed in rolled Mg-2Zn-0.2Ce. This was expected to be at the expense of the growth of some of the other grains. The misorientation axis involved in the grains which disappeared were mostly $< hki0 >$ type. That is, ~70% and ~74% of the misorientation axis associated with the grains which disappeared were $< hki0 >$ type at 548-573K and 573-598K, respectively. The rotation axis of the remainder of the grain boundaries were along a $< hkil >$ direction.

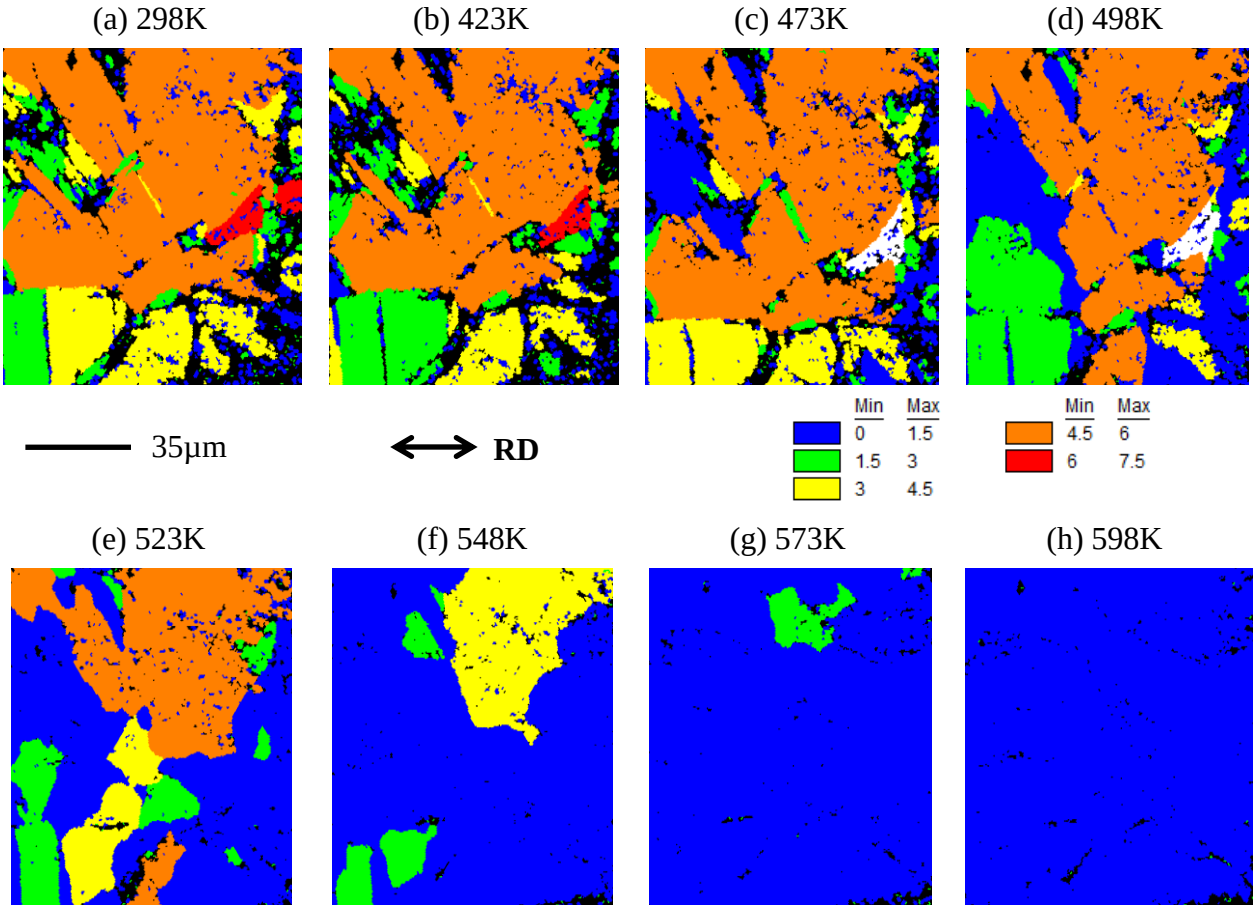

Figure 4.137 The grain orientation spread maps of the microstructural patch analyzed for rolled Mg-2Zn-0.2Ce as a function of temperature. It is noted that it took ~5-15 minutes to get to the annealing temperature and the EBSD orientation map was acquired in ~45 minutes for each subsequent heating step. The rolling direction is horizontal.

Overall, during the annealing of rolled Mg-2Zn-0.2Ce, the distribution of the misorientation axis across the newly formed grain boundaries at temperatures between 423-548K and the misorientation axis of the grain boundaries disappeared between 548-598K maintained a proportion of ~70% $< hki0 >$ and ~30% $< hkil >$ (See Figure 4.138). However, it is noted that the number of new grains which formed during the heating steps between 423-548K (59 grains) were higher than the number of grains which disappeared between 548-598K (13 grains).

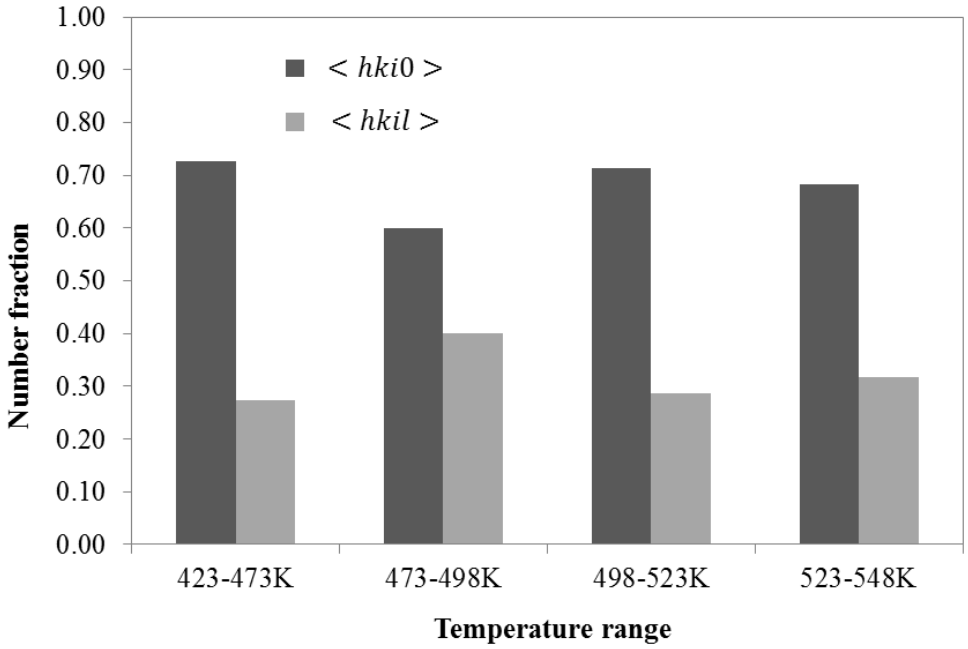

Figure 4.138 The number fraction of the $< hki0 >$ and $< hkil >$ type misorientation axis of the newly formed grain boundaries during the four heating cycles between 423K and 548K in the microstructural patch analyzed for rolled Mg-2Zn-0.2Ce.

4.6.3 In-situ annealing/recrystallization of Mg-2Zn-0.6Ce

Figure 4.139 shows the EBSD IPF map in the normal direction of the same microstructural patch depicting the evolution of microstructure in rolled Mg-2Zn-0.6Ce as a function of annealing temperature. It is noted that it took ~5-15 minutes to get to the annealing temperature and the EBSD orientation map was acquired in ~55 minutes for each subsequent heating step. The images given in Figure 4.139 were obtained after post-processing the EBSD raw data using a clean-up procedure same as that for Figure 4.136. In the case of scans taken at temperatures less than 523K, ~26-30% points in the EBSD maps were modified during the clean-up procedure. For scans taken at temperatures greater than 523K, ~22-25% of the EBSD data points were changed during the clean-up. The EBSD data shown in Figure 4.139 were partitioned with a grain tolerance angle of 5 degrees and a minimum grain size of 2 pixels.

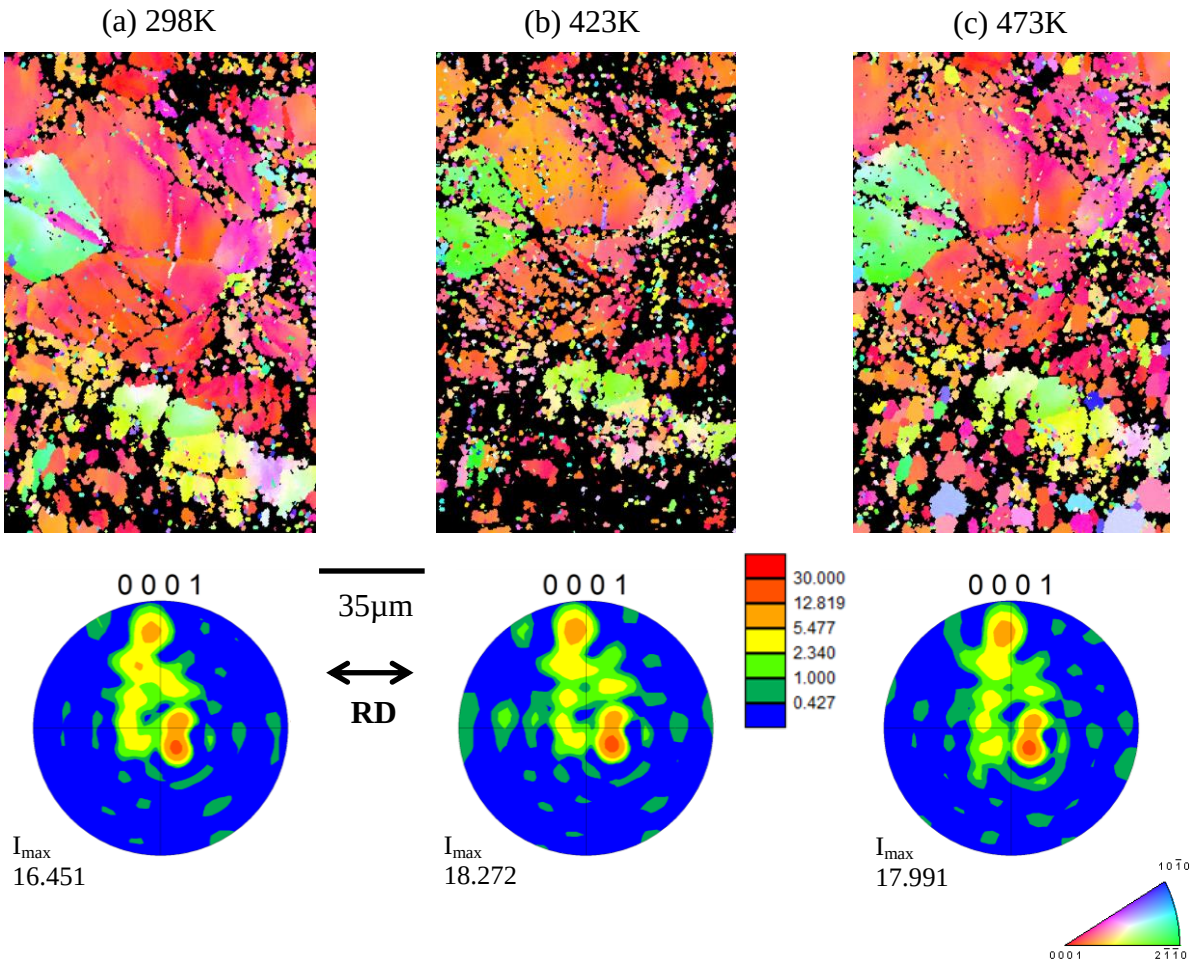

Figure 4.139 EBSD IPF maps and the corresponding {0001} pole figures in the normal direction depicting the microstructural evolution in rolled Mg-2Zn-0.6Ce as a function of annealing temperature. I_{max} is the maximum intensity values observed in the pole figures. It is noted that it took ~5-15 minutes to get to the annealing temperature and the EBSD orientation map was acquired in ~55 minutes for each subsequent heating step. The rolling direction is horizontal.

Figure 4.139 (cont'd)

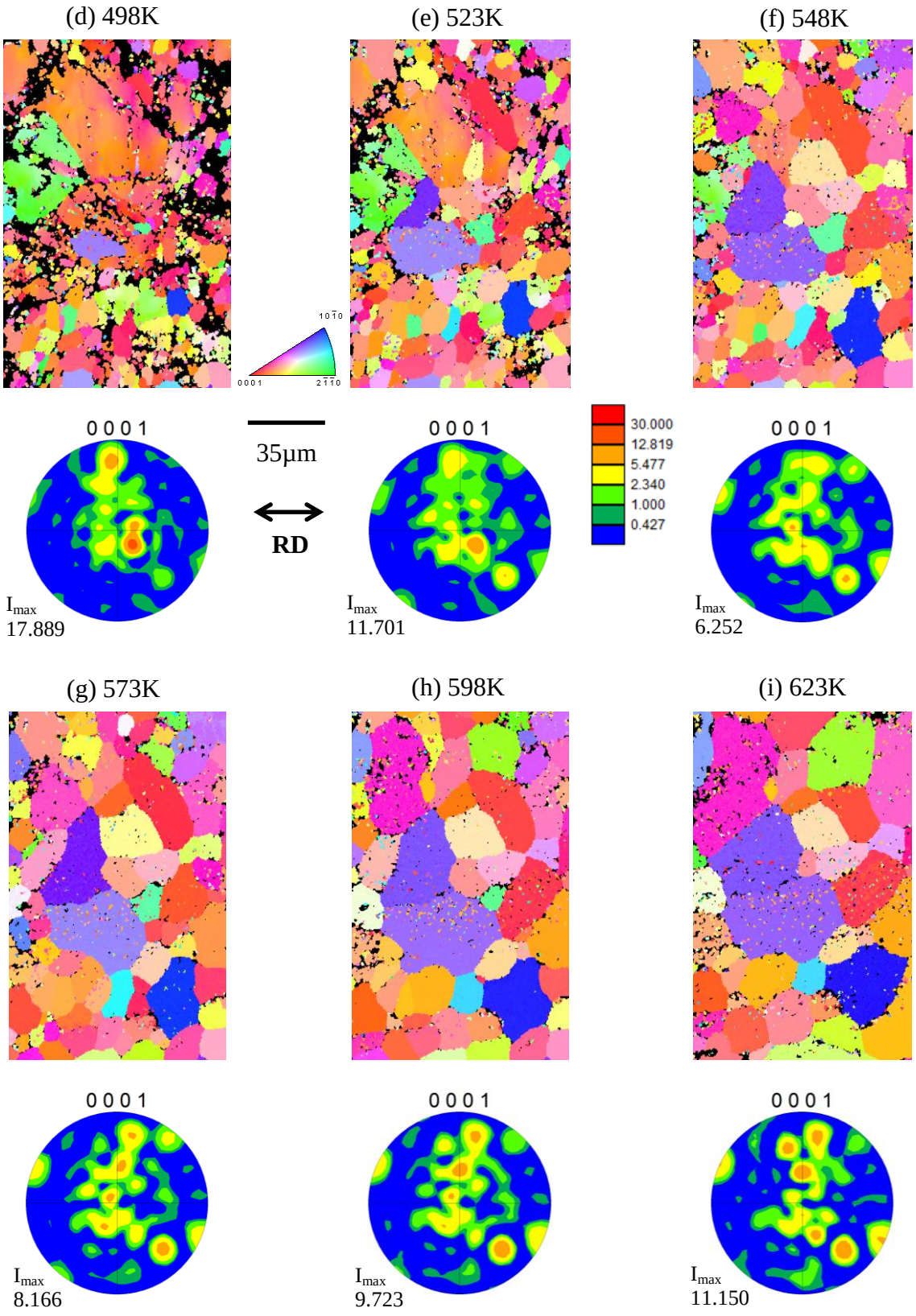

Similar to rolled Mg-2Zn-0.2Ce, during the annealing process, new grains started to appear during the heating step from 423K to 473K in rolled Mg-2Zn-0.6Ce (See Figure 4.139). At ~573K, a completely recrystallized microstructure was observed. Figure 4.140 shows the grain orientation spread obtained from the EBSD data from the microstructural patch analyzed for Mg-2Zn-0.6Ce as a function of annealing temperature. The post-processing procedures applied for the images given in Figure 4.140 are the same as that for Figure 4.136. As shown in Figure 4.140, the grain orientation spread was less than 1.5 degrees in the area analyzed after the heat treatment at 573K, suggesting that the grains were relatively free of the strain which accumulated during the rolling process.

The orientation relationship of the new grains formed during each heating step was investigated with respect to their neighbors. A total of 112 new grains were formed during the six heating steps between 423K and 598K in the microstructural patch analyzed. This resulted in a total of 300 unique grain boundaries. Figure 4.141 shows the distribution of the number fraction of the observed misorientation axis relationships for the newly formed grain boundaries in rolled Mg-2Zn-0.6Ce, annealed at temperatures between 423K and 598K, sorted into $< hki0 >$ and $< hkil >$ types. Among the misorientation relationships observed between the newly formed grain boundaries, rotation axis about $< 10\bar{1}0 >$ (~44%), $< 11\bar{2}0 >$ (~20%), and $< 10\bar{1}1 >$ (~14%) were prevalent. Grain boundaries with orientation relationships corresponding to $\{10\bar{1}2\}$ extension twinning (~7%) and $(10\bar{1}2) - (01\bar{1}2)$ extension double twin (~18%) were also commonly observed between the newly formed grains boundaries. This was expected to be due to the recovery and growth of the twins formed during the rolling process.

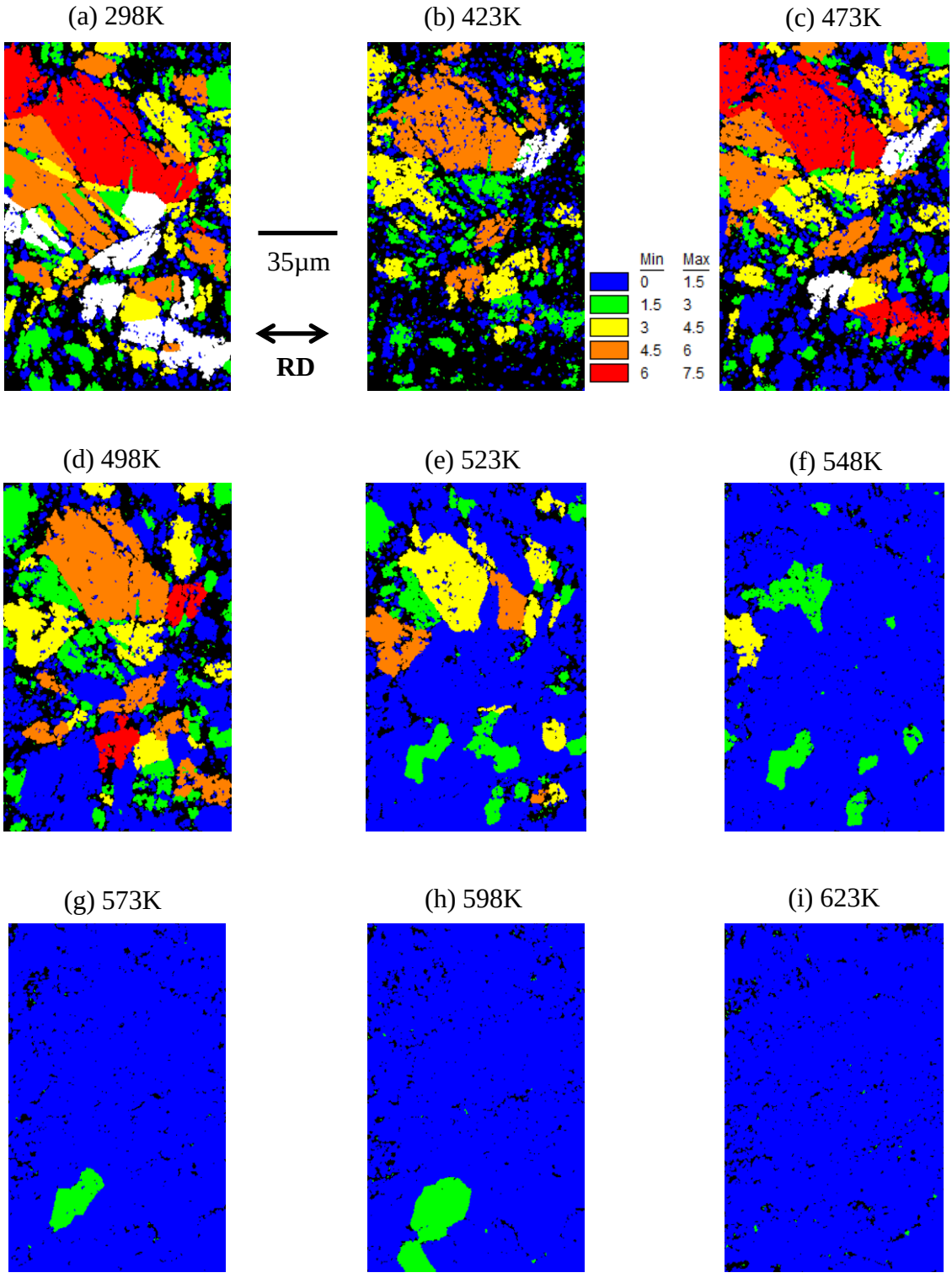

Figure 4.140 The grain orientation spread maps of the microstructural patch analyzed for rolled Mg-2Zn-0.6Ce as a function of annealing temperature. It took ~5-15 minutes to get to the annealing temperature and the EBSD orientation map was acquired in ~55 minutes for each subsequent heating step. The rolling direction is horizontal.

Overall, during the annealing of rolled Mg-2Zn-0.6Ce, the distribution of the misorientation axis across the newly formed grain boundaries at temperatures between 423K and 598K maintained a proportion of ~70% $< hki0 >$ and ~30% $< hkil >$ (See Figure 4.141). It is noted that this trend is similar to the one observed for rolled Mg-2Zn-0.2Ce (See Figure 4.138).

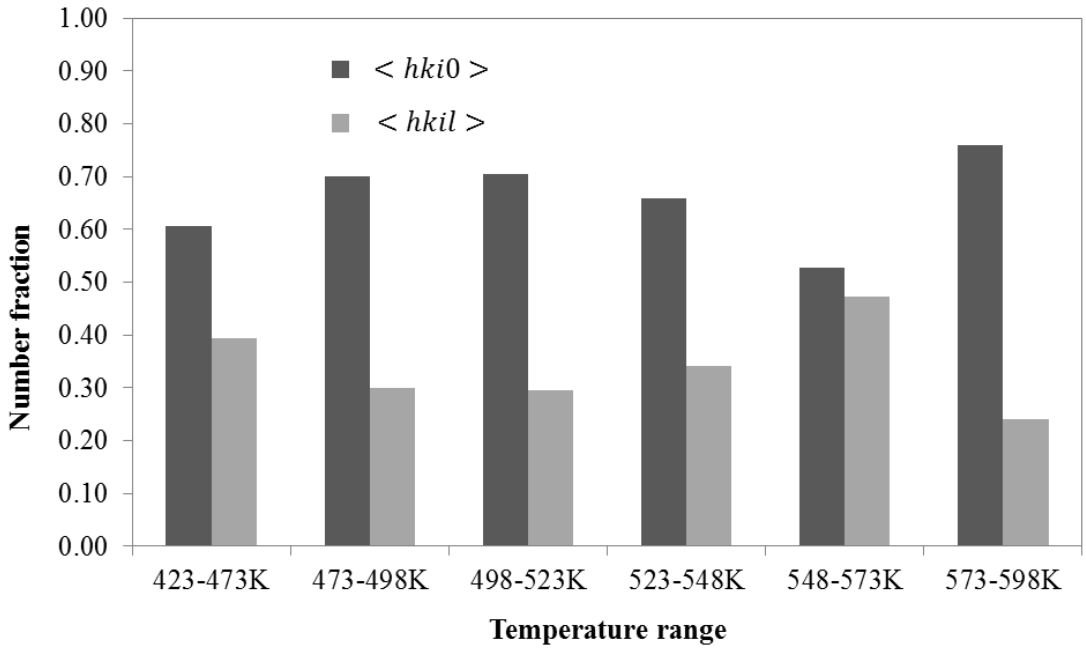

Figure 4.141 The number fraction of the $< hki0 >$ and $< hkil >$ type misorientation axis of the newly formed grain boundaries during the six heating cycles between 423K and 598K in the microstructural patch analyzed for rolled Mg-2Zn-0.6Ce.

CHAPTER 5

DISCUSSION

This chapter provides a detailed analysis and discussion of the results presented in Chapter 4. This chapter also compares the deformation behavior of the as-cast and cast-then-extruded M1, MN10, and MN11 alloys. First, the microstructure and texture of as-cast and cast-then-extruded M1, MN10, and MN11 are compared, with an emphasis on the effects of processing and Nd-content. Next, the effects of processing, temperature, and Nd-addition on the mechanical properties are discussed. Finally, the distribution of the active deformation mechanisms for each alloy at different temperatures are discussed and compared. During the tensile deformation of M1, contraction twinning and $\{10\bar{1}1\} - \{10\bar{1}2\}$ double twinning were observed. Crystal plasticity modeling and simulations were employed to explain the effect of contraction twinning and double twinning on the limited ε_f values obtained on specimens that exhibited such deformation modes. In addition, the recrystallization behavior of rolled ZE20 was discussed and compared with a rolled conventional Mg alloy, AZ31.

5.1 Microstructure

Table 5.1 lists the average grain size for the as-cast and cast-then extruded M1, MN10, and MN11 alloys. Extruded M1 exhibited grains with grain diameters ranging from ~10-190μm (See Figures 4.1 and 4.2) with an average grain size of ~42μm. The large range in grain sizes was expected to be due to the grain growth that may have happened during the elevated temperature extrusion process [Bohlen et al. 2010]. The as-cast MN10 and MN11 microstructures exhibited equiaxed grains with diameters ranging from a few hundred to one thousand micrometers. After extrusion, the wrought MN10 and MN11 alloys exhibited equiaxed

grains with an average grain diameter of ~10-12μm (See Figures 4.51, 5.42, 4.101, and 4.102). Microstructures with similar grain sizes and grain shapes after extrusion have been observed in Mg alloys with dilute addition (<1.5 wt.%) of RE elements such as Y, Ce, Gd, and La [Stanford 2010a]. Thus, similar to other RE elements, Nd-additions inhibit grain growth during extrusion of Mg alloys, which could then result in a refined microstructure with an average grain size of around 10 microns. The suppression of grain growth was expected to be due to the pinning effect of the RE elements at the grain boundaries [Nie et al. 2013]. It is interesting to note that both MN10 and MN11 exhibited similar grain size after extrusion, suggesting that dilute Nd addition of ~0.3 wt.% is sufficient to prevent grain growth and increasing Nd content did not significantly alter the resulting grain sizes.

Table 5.1 Summary of the average grain size of M1, MN10, and MN11 with different processing histories.

Material	Average grain diameter
Extruded M1	~42±30μm
Extruded MN10	~10±6μm
Extruded MN11-300	~12±5μm
Extruded MN11-275	~11±5μm
Cast MN10	~361±197μm
Cast MN11	~970±520μm

Table 5.2 Summary of the type, approximate size, and the location of the precipitates in the microstructure for M1, MN10, and MN11.

Material	Mn-rich precipitates	Nd-rich precipitates
Extruded M1	Inside grains (<0.5μm)	-
Cast MN10	Inside grains (<1μm) At grain boundaries (<1μm)	Inside grains (<1μm)
Cast MN11	Inside grains (<1μm)	Inside grains (<1μm) At grain boundaries (continuous network)
Extruded MN10	Inside grains (<0.5μm)	Inside grains (<0.5μm)
Extruded MN11	Inside grains (<0.5μm) At grain boundaries (<0.5μm)	Inside grains (<0.5μm) At grain boundaries (<0.5μm)

Mn-rich and Nd-rich precipitates were observed in the microstructure of the alloys studied. Table 5.2 lists the type of precipitates observed, approximate size, and their location in the microstructure. Mn-rich precipitates of <0.5μm size were observed in the extruded M1 microstructure in a randomly distributed fashion. Previous studies of extruded Mg-1.3Mn have reported the presence of particles enriched in Mn [Stanford 2010b]. In the case of MN10 and MN11, the size of the precipitates observed in the extruded microstructure (~0.5μm or less) was smaller compared to the cast material (~1μm or less) (see Table 5.2). This suggests that decomposition of the precipitates might have happened during the elevated-temperature extrusion process. Mn-rich and Nd-rich precipitates observed inside the grains in the as-cast MN10 and MN11 ingots were similar in shape and size. However, as opposed to the individual Mn-rich precipitates observed at the grain boundaries of the as-cast MN10, a continuous network of Nd-rich precipitates were observed along the grain boundaries in the as-cast MN11. The size and shape of the Mn-rich and Nd-rich precipitates observed in MN10 and MN11 after extrusion did not differ significantly. Precipitates with similar characteristics have been reported in other Nd-containing Mg alloys such as cast Mg-5Zn-2Al-xNd (x ranging between 0-4.12), cast Mg-3Nd-xZn (x ranging between 0-1.4), and rolled Mg-1.3Zn-0.25Zr-0.20Nd [Zou et al. 2005, Nie 2012, Min et al. 2014]. In addition, stringers of second phase particles, enriched in Mn, were observed within grains in the as-cast MN10 and MN11 alloys. From the EBSD orientation analysis, it appears that these stringers were aligned parallel to the basal planes of the HCP matrix grains (See Figures 4.27 and 4.81). It is expected that these stringers of precipitates would have an effect on the deformation behavior and the resulting texture formation during extrusion and this will be discussed in Section 5.4.2.

5.2 Texture

Extruded M1 rod exhibited a strong basal fiber texture (~9 times random) similar to the texture observed in other conventional Mg alloys after wrought processing. As-cast MN10 and MN11 exhibited a relatively weak texture and lacked any symmetric texture characteristics (See Figure 4.30 and 4.83). Such texture is common in cast Mg alloys [Agnew et al. 2001, Pérez-Prado et al. 2004]. With 0.3 wt% Nd addition, the extruded MN10 rod exhibited a moderate texture (~6 times random). A slight deviation from the basal fiber texture was observed, where the basal plane normals tended to be oriented almost perpendicular to the extrusion axis. With an increase in Nd, further texture weakening was observed, and MN11-300 and MN11-275 exhibited the weakest texture (~3 times random) among all the extruded rods analyzed. It is noted that the slight differences in the extrusion temperature between 548K and 573K did not have a significant effect on the texture as the extruded MN11-300 and MN11-275 textures were similar. Similar weak textures have been observed in other Mg alloys with dilute RE additions (<1.5 wt.%) [Stanford 2010a, Bohlen et al. 2010]. It has been reported that dilute additions of RE elements (<1.3 wt.%) can inhibit texture formation during extrusion in M1 [Bohlen et al. 2010]. However, the relatively strong texture in MN10 compared to the weak texture in MN11-300 and MN11-275 suggests that more than 0.3 wt.% Nd content is required to effectively weaken the wrought texture in M1 alloys during extrusion. It is also noted that the Nd content measured in the matrix in as-cast MN10 and MN11 were similar (See Table 4.4 and 4.14). However, more Nd-rich precipitates were observed at the grain boundaries in as-cast MN11 compared to as-cast MN10 (See Figure 4.27a, 4.29, 4.81, and 4.82b). Thus, the texture weakening in extruded MN10 and MN11 was expected to be due to the combined effect of Nd solute atoms and PSN assisted by the precipitates during extrusion.

5.3 Mechanical properties

The tensile YS changed with alloy composition and testing temperature. Figure 5.1 depicts the approximate tensile YS values of all the materials studied as a function of temperature. Among all the extruded materials studied, M1 exhibited the largest reduction in YS with increase in temperature, in which the YS at 423K and 523K was ~49% and ~29%, respectively, that of the YS at 323K. A similar reduction in tensile strength with an increase in temperature has been observed in other conventional wrought Mg alloys such as AZ31 [Boehlert et al. 2012]. The reduction in high-temperature tensile strength in extruded MN10 was less dramatic compared to extruded M1 (the YS at 423K and 523K were ~68% and ~54%, respectively, of that at 323K). Extruded MN11 was more effective in retaining high-temperature strength, and this was expected to be due to the greater Nd content. The YS for the extruded MN11 at 423K and 523K was ~89% of the YS at 323K. Other RE-containing Mg alloys, which contain greater than 1 wt.% RE, have also exhibited excellent elevated-temperature strength retention [Chang et al. 2001, Moreno et al. 2003]. An insufficient content of Nd for effective solid-solution strengthening is expected to be the reason behind the greater reduction in the elevated-temperature strength exhibited by extruded M1 and MN10 [Callister et al. 2009]. This suggests that the amount of Nd content plays an important role in retaining tensile strength at elevated temperatures in M1 alloys, and this effect is noticeable even with 1 wt.% Nd addition. It is noted that the tensile strength for extruded M1 and MN10 at 323K was slightly higher than that for extruded MN11. This is expected to be due to the stronger basal texture observed in M1 and MN10 compared to MN11, as the alignment of basal planes parallel to the tensile axis makes basal <a> slip difficult.

As-cast MN10 and MN11 exhibited a lower tensile YS compared to their extruded

counterparts at all the test temperatures. This was expected to be due to the significantly higher grain size of the as-cast material compared to the extruded material (~361-970μm in the as-cast material compared to ~10-12μm in the extruded material). Grain size reduction can result in an increase in the YS [Hall 1951, Petch 1953, Callister et al. 2009]. However, both as-cast MN10 and MN11 exhibited similar tensile strength at all tested temperatures (See Figure 5.1). It is worthwhile to note that the distribution of different deformation modes observed for as-cast MN10 and MN11 was also similar at all the test temperatures (See Section 5.4.2). Thus, the similarities of the deformation behavior at all the tested temperatures agree well with the similarity in the tensile strength observed in as-cast MN10 and MN11.

Among the alloys studied, extruded MN11 exhibited superior strength values compared to the Al 2024 alloy, on a density normalized basis, at temperatures upto 523K. The specific YS values for extruded MN11 were greater than ~42kNm/Kg at all test temperatures (the specific YS value for Al 2024 alloy was ~27kNm/Kg at RT [Friedrich et al. 2006]). In addition, the extruded MN11 alloy exhibited superior ε_f values (greater than ~25% at temperatures upto 523K) compared to the Al 2024 alloy (~12% at RT). Moreover, extruded MN11 exhibited similar tensile and compression strength (See Table 4.19 and 4.21) at all test temperatures. Similar behavior has been observed in other RE-containing Mg alloys [Ball et al. 1994]. This was expected to be due to the random texture exhibited by extruded MN11. However, this behavior is different from conventional Mg alloys where a strong tension-compression asymmetry is observed [Bettles et al. 2005]. Thus, extruded MN11 alloy could be an attractive candidate for lightweight structural applications.

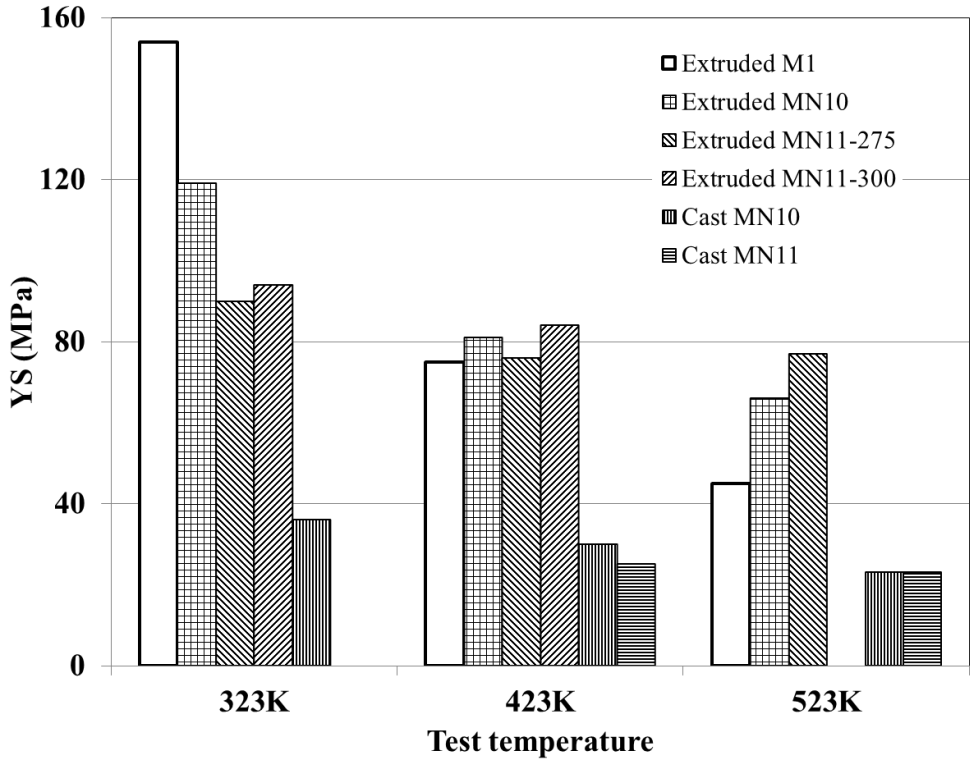

Figure 5.1 Approximate tensile YS values of M1, MN10, and MN11 as a function of test temperature.

5.4 Deformation mechanisms

The distribution of the deformation modes of the extruded M1, as-cast MN10 and MN11, and extruded MN10 and MN11 alloys during tensile/compression deformation are discussed in subsections 5.4.1, 5.4.2, and 5.4.3, respectively, based on the results presented in Chapter 4. In each case, the dominant deformation mechanisms and the effect of test condition are discussed.

5.4.1 Extruded M1

Before discussing the experimental results for extruded M1, the possible activity of different slip systems in a given microstructure was analyzed. Basal <a> slip and extension twinning exhibited low Schmid factors (typically <0.25) while prismatic <a> slip, pyramidal

<c+a> slip, and contraction twinning exhibited larger Schmid factors (typically >0.35) in a given extruded M1 microstructure. Figure 5.2 shows the possible Schmid factor distribution for all variants of basal <a> slip, prismatic <a> slip, and pyramidal <c+a> slip, calculated based on a uniaxial stress state assumption (tensile axis parallel to extrusion direction) for the given texture represented in Figure 4.3. The distribution shown in Figure 5.2 was obtained by analyzing all grains in a given un-deformed microstructure using EDAX TSL OIM Analysis 6.1 software. It is noted that the data provided in Figure 5.2 are not actual slip observations. As shown in Figure 5.2, the prismatic <a> and pyramidal <c+a> slip systems are favorably oriented for activation, and the opposite is true for the basal <a> slip systems. It is noted that among the slip systems mentioned above, only pyramidal <c+a> slip can accommodate strain along the c-axis. Nevertheless, contraction twinning can accommodate compression strain along the c-axis and extension twinning can accommodate tensile strain along c-axis [Yoo 1981]. When a tensile stress was applied perpendicular to the c-axis, the c-axis will experience an effective compressive stress. Hence, due to the strong basal <a> texture, where the c-axis of most of the grains was almost perpendicular to the tensile axis (See Figure 4.3), the grains are favorably oriented for the activation of contraction twinning or pyramidal <c+a> slip. This will be discussed with respect to the experimental observations in the following sections.

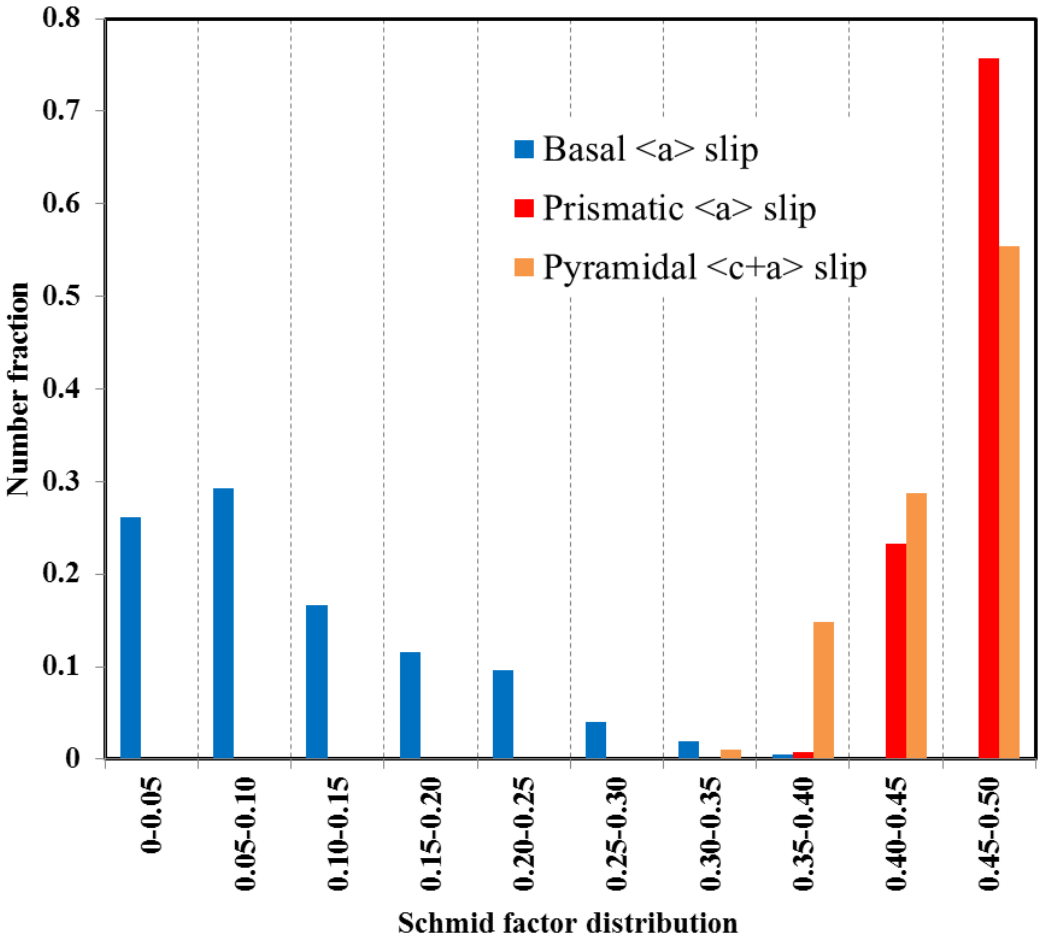

Figure 5.2 The Schmid factor distribution for all variants of basal <a> slip, prismatic <a> slip, and pyramidal <c+a> slip for all grains in a representative un-deformed extruded M1 microstructure calculated based on a uniaxial stress state assumption (tensile axis parallel to extrusion direction). The distribution was obtained using EDAX TSL OIM Analysis 6.1 software.

The actual deformation activity observed in extruded M1 during the experiments will be discussed in the following sections. Figure 5.3 shows the relative distribution of the different deformation modes identified in extruded M1 at 323K, 423K, and 523K. The deformation was dominated by twinning at 323K (i.e. ~75% of the observed deformation modes were for twinning), and at the higher temperatures, slip mechanisms controlled the deformation (i.e. only ~17% of the observed deformation modes were for twinning at 423K and no twinning was

observed at 523K). Thus, the transition from twinning-dominated deformation to slip-dominated deformation is expected to have occurred at temperatures around 423K.

As shown in Figure 5.3, contraction twinning dominated the deformation (~48%) at 323K. Extension twinning contributed to ~27% of all the deformation modes identified. The remaining deformation was contributed by slip (~25%). Limited basal <a> slip activity was observed at 323K. This was expected to be due to the lower Schmid factors for basal <a> slip due to the texture (See Figure 5.2), even though basal <a> slip is the easiest to activate due to significantly lower CRSS values compared to prismatic <a> and pyramidal <c+a> slip [Hutchinson et al. 2010, Chapius et al. 2011]. The limited activity of prismatic <a> and pyramidal <c+a> slip, despite their high Schmid factor values (See Figure 5.2), suggests that the CRSS of those systems were high compared to other deformation modes. It is noted that the pyramidal <c+a> slip traces were localized around grain boundaries or triple points, where stress concentrations were expected to be high (see Figure 4.6). Even though the activation of extension twinning was not favored under the above mentioned stress state, based on Schmid factor analysis, extension twins were observed. Approx. 27% of all the deformation modes observed at 323K were extension twins, and at 423K approx. 7% of all the deformation modes were extension twins. At 323K, ~81% of the identified extension twin traces were activated in grains in which the global Schmid factor for extension twinning, calculated based on an uniaxial stress state assumption, was less than 0. The remaining extension twins were activated with Schmid factors between 0 and 0.01. The negative value of Schmid factor is due to the polar nature of the twinning mechanism. Extension twinning is active only when the deformation conditions are such that extension along the c-axis takes place [Christian 1995]. Thus, the negative Schmid factor values are because the global stress state would favor “compression”

along the c-axis for extension twinning modes. This suggests that the local stress state was heterogeneous and the activation of pyramidal <c+a> slip and extension twinning was assisted by local stress concentrations. Extension twinning has been observed in other studies when the c-axis was placed under compression in rolled pure Mg and Mg alloys with a strong basal <a> texture [Koike et al. 2008, Barnett et al. 2008, Barnett et al. 2004, Ando et al. 2010, Nave et al. 2004]. Ando et al. [2014] recently showed that the negatively strained extension twins are formed to minimize the incompatibility of plastic strain caused by the activity of basal <a> slip. The low CRSS value for extension twinning is expected to have also assisted in its activation [Koike et al. 2005]. Most of the contraction twins (~86%) were activated at global Schmid factors greater than 0.25 suggesting a Schmid-type behavior. Similar observations regarding the activation of contraction twinning based on Schmid-type behavior has been reported previously [Barnett et al. 2008, Niknejad et al. 2016].

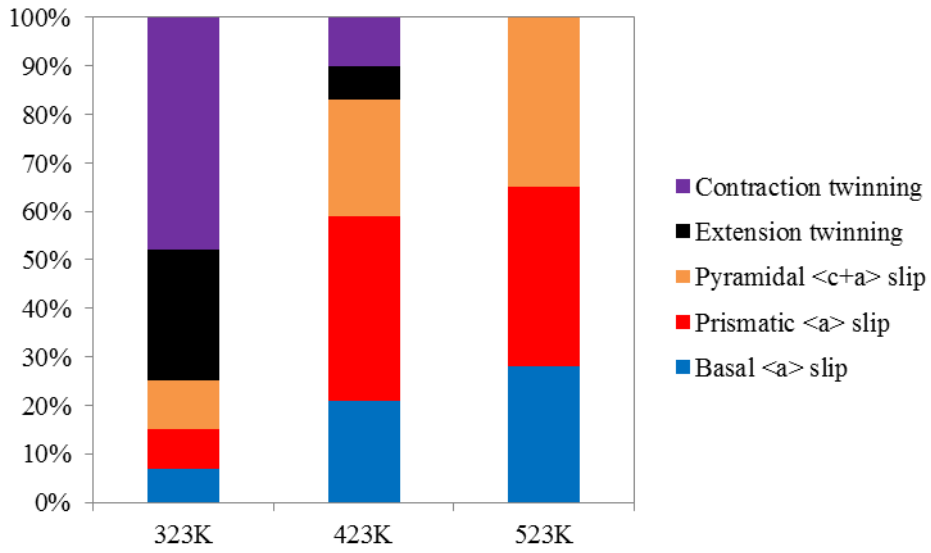

Figure 5.3 The relative distribution of different deformation modes observed in the extruded M1 specimen tensile tested at 323K, 423K, and 523K.

Among the deformation mechanisms considered in this study, only contraction twinning and pyramidal <c+a> slip can accommodate compression strain along the c-axis. Figure 5.4 plots the global Schmid factor values for the contraction twin variant activated in the M1 specimen tensile tested at 323K overlaid with the Schmid factor values for the contraction twin variant and pyramidal <c+a> slip variant with the highest Schmid factor in the same grain. In some grains the contraction twinning variant with the highest Schmid factor was not activated. Nevertheless, in all the grains in which contraction twinning was activated, pyramidal <c+a> slip had similar or higher Schmid factors. The enhanced activity of contraction twinning compared to pyramidal <c+a> slip (~48% compared to ~10%, respectively) as well as the preferred activation of contraction twinning in grains in which pyramidal <c+a> slip had similar Schmid factors (See Figure 5.4) suggest that the CRSS of contraction twinning was lower than that of pyramidal <c+a> slip at 323K. This observation is consistent with previous studies [Hutchinson et al. 2010, Chapuis et al. 2011].

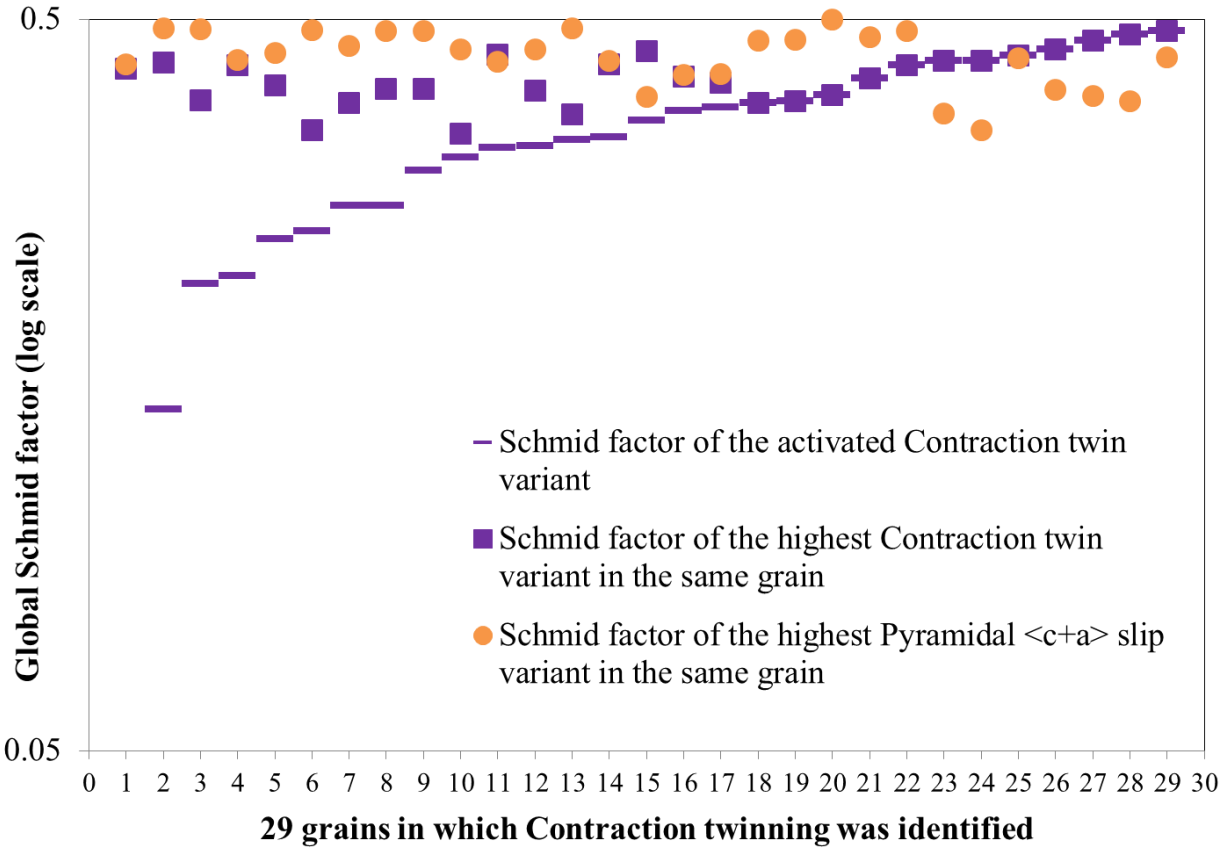

Figure 5.4 The global Schmid factor values of the contraction twin variants identified in the extruded M1 specimen tensile tested at 323K overlaid with the Schmid factor values for the contraction twin variant and pyramidal <c+a> slip variant with the highest Schmid factor in the same grain.

The contraction twins observed in the specimen tensile tested at 323K evolved into $\{10\bar{1}1\}-\{10\bar{1}2\}$ double twins with an increase in strain. It is noted that the primary $\{10\bar{1}1\}$ contraction twin trace did not change with deformation, and the secondary $\{10\bar{1}2\}$ extension twinning was confined within the primary twin boundaries. This is consistent with Barnett et al. [2008] and Ando et al. [2010]. Figure 4.12 depicts the double twin evolution. It is noted that the alloys in which $\{10\bar{1}1\}-\{10\bar{1}2\}$ double twins were reported previously had a similar average grain size (~50-80μm) as that of the alloy reported in this study [Barnett 2007, Ando et al. 2010]. In addition the texture and tensile strain rate used were also similar to the current study.

$\{10\bar{1}1\} - \{10\bar{1}2\}$ double twins were formed by the activation of a $\{10\bar{1}2\}$ extension twin inside the $\{10\bar{1}1\}$ contraction twinned region [Couling et al. 1959]. It was reported that the $\{10\bar{1}2\}$ extension twin within the $\{10\bar{1}1\}$ contraction twin was formed to accommodate and reduce the strain incompatibility with the surrounding matrix introduced due to the formation of primary $\{10\bar{1}1\}$ contraction twins [Koike et al. 2008, Ando et al. 2010]. The 56° misorientation about $< 11\bar{2}0 >$ caused by the activation of the $\{10\bar{1}1\}$ contraction twin and the subsequent misorientation of 86° about $< 11\bar{2}0 >$, caused by the activation of the $\{10\bar{1}2\}$ extension twin, resulted in an effective misorientation of 38° about $< 11\bar{2}0 >$ with respect to the matrix (See Figure 4.12c). The twin planes of the contraction twin and extension twin identified in Figure 4.12 were $\{10\bar{1}1\}$ and $\{10\bar{1}2\}$, respectively. However, the habit plane for the $\{10\bar{1}1\} - \{10\bar{1}2\}$ double twin (38° misorientation about $< 11\bar{2}0 >$) is a subject of debate. Previous studies have reported the habit plane for $\{10\bar{1}1\} - \{10\bar{1}2\}$ double twins to be $\{30\bar{3}4\}$ or $\{10\bar{1}3\}$ [Cizek et al. 2008, Yoshinaga et al. 1973]. The habit plane of the double twin shown in Figure 4.12c was found to be $\{10\bar{1}3\}$. Figure 5.5 shows the pole figures indicating the $\{10\bar{1}3\}$ poles for the regions marked "C" (double twinned region) and "D" (matrix) in Figure 4.12c.

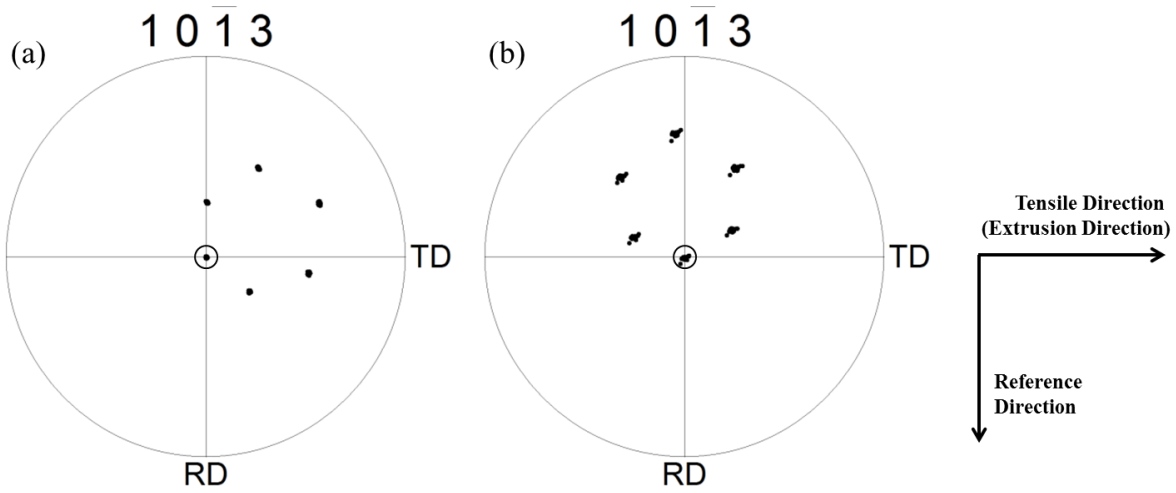

Figure 5.5 The pole figures indicating the $\{10\bar{1}3\}$ poles for (a) the region marked "C" (double twinned region) and (b) "D" (matrix) in Figure 4.12c for the 323K tension-tested extruded M1 specimen deformed to ~9.9% strain. The common poles are circled.

Surface steps were observed in the double twinned regions (See Figure 4.12a). Twinning can form surface steps depending on the magnitude of the shear strain [Ando et al. 2010]. However, the surface relief caused by the $\{10\bar{1}1\}$ contraction twin, $\{10\bar{1}2\}$ extension twin, and $\{10\bar{1}3\}-\{10\bar{1}2\}$ double twins were reported to be smaller compared to the surface relief formed due to $\{10\bar{1}1\}-\{10\bar{1}2\}$ double twins with an identical plane of shear [Ando et al. 2010]. This was attributed to localized shear deformation within such twins [Ando et al. 2007]. The reason for localized shear deformation in the $\{10\bar{1}1\}-\{10\bar{1}2\}$ twin type was explained to be due to the larger slip length inside the twinned volume as opposed to other twin types [Ando et al. 2010]. Thus, the magnitude of the localized slip in the $\{10\bar{1}1\}-\{10\bar{1}2\}$ twin type is expected to be high. This is expected to form large surface relief, which can lead to crack formation and premature failure [Ando et al. 2010]. The experimental observations of the surface step in the $\{10\bar{1}1\}-\{10\bar{1}2\}$ double twinned regions were consistent with the previous reports [Ando et al. 2010].

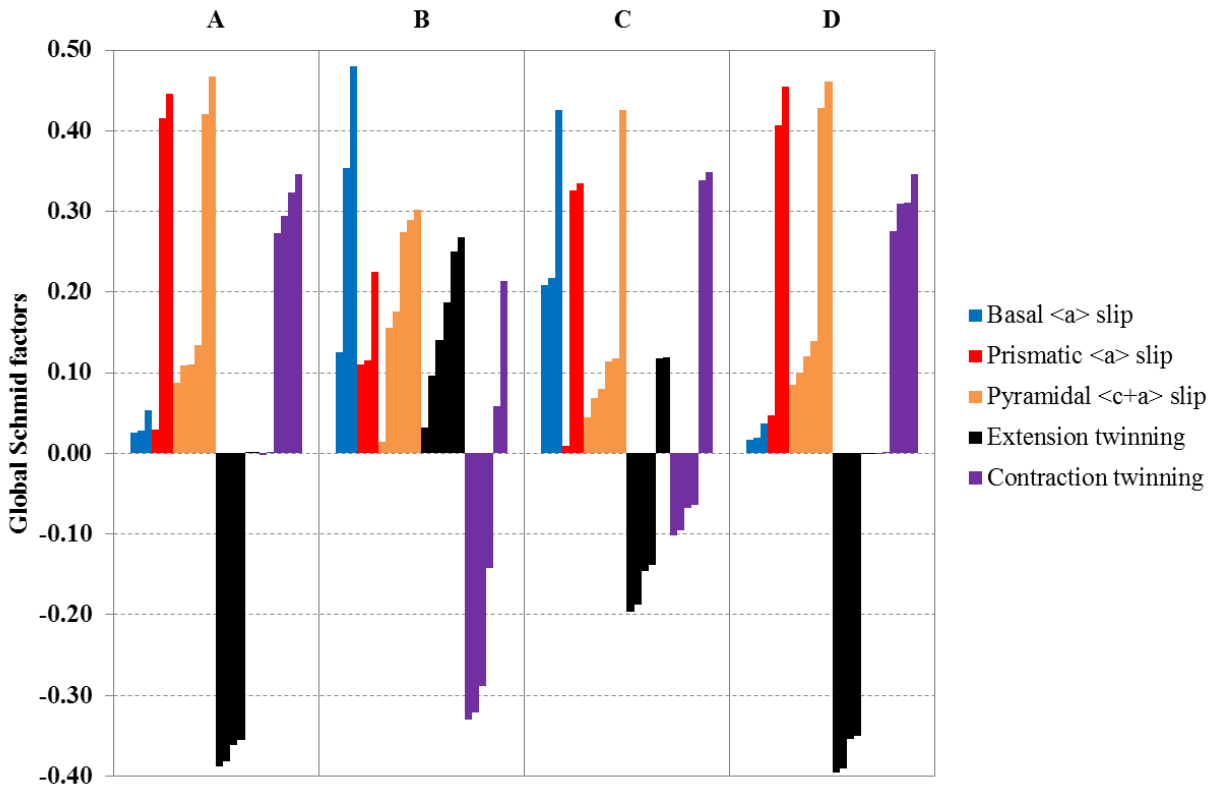

Figure 5.6 The Schmid factor values calculated based on a uniaxial stress state assumption for different deformation modes in the regions indicated as "A", "B", "C", and "D", in Figure 4.12c for the 323K tension-tested extruded M1 specimen deformed to ~9.9% strain. Note that "A" and "D" represent the matrix, "B" represents the primary $\{10\bar{1}1\}$ contraction twinned region, and "C" represents the $\{10\bar{1}1\} - \{10\bar{1}2\}$ double twinned region.

Cracks developed in the double twinned regions as the strain increased (See Figure 4.13). Previous studies have reported the formation of localized shear regions inside $\{10\bar{1}1\} - \{10\bar{1}2\}$ double twins in Mg single crystals, and this was attributed to the large amount of basal <a> slip inside the twinned volume [Couling et al. 1959]. Figure 5.6 shows the Schmid factor values calculated based on a uniaxial stress state assumption for different deformation modes in the regions indicated as "A", "B", "C", and "D", in Figure 4.12c. The Schmid factor for basal <a> slip variants in the twinned regions were relatively high compared to the matrix. This suggests that the $\{10\bar{1}1\} - \{10\bar{1}2\}$ double twinning orients the crystal in such a way that basal <a> slip

variants are oriented for easy activation (See Figure 5.6). The high Schmid factor of basal <a> slip inside the twinned regions combined with their low CRSS values [Hutchinson et al. 2010, Chapius et al. 2011] creates a "soft" region inside the twinned volume. Figure 5.7 shows the Schmid factor plot for basal <a> slip for the area shown in Figure 4.12b. It is noted that the Schmid factor for basal <a> slip in the parent region (matrix) on either side of the twinned region is close to 0 (See Figure 5.7). Thus, the formation of a "soft" region surrounded by "hard" regions is expected to result in the enhanced activity of basal <a> slip in the twinned volume. This could then explain the formation of localized shear regions within the twinned region and eventual crack formation (See Figure 4.13). Enhanced activity of basal <a> slip inside a twin has been suggested to result in premature fracture in Mg single crystals [Reed-Hill 1957, Couling et al. 1959]. Figure 5.8 shows the unit cells indicating the Burger's vectors for the 3 variants of basal <a> slip in the twin volume shown in Figure 4.12c. The basal <a> slip variants and the corresponding global Schmid factor calculated based on the uniaxial stress state assumption are also given in Figure 5.8. Thus, the surface steps observed in the double twinned region (See Figure 4.12a) were expected to be due to the enhanced activity of basal <a> slip in the component of its Burger's vectors along the normal direction of the sample.

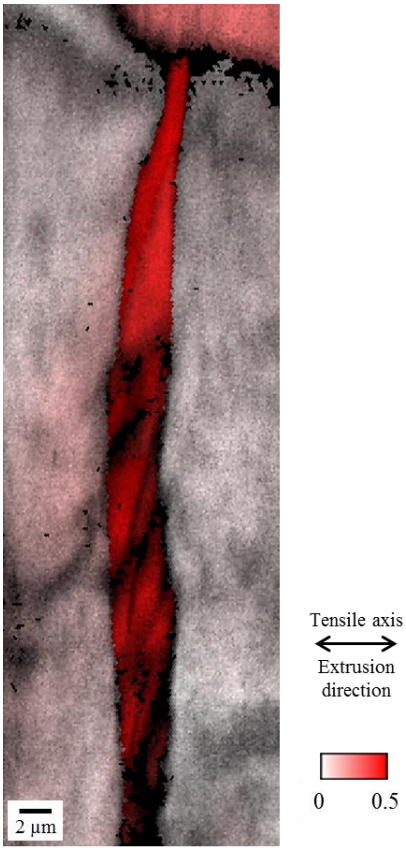

Figure 5.7 The Schmid factor map for basal <a> slip, calculated based on a uniaxial stress state assumption, for the area shown in Figure 4.12b for the 323K tension-tested extruded M1 specimen deformed to ~9.9% strain.

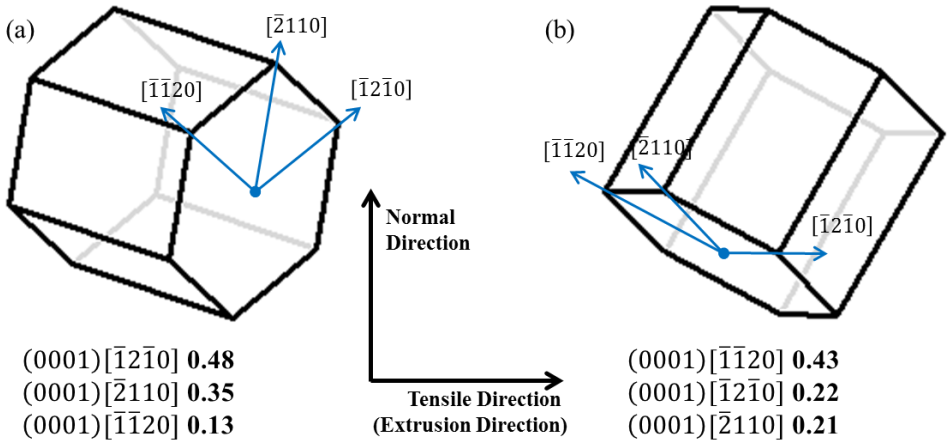

Figure 5.8 The unit cells indicating the Burger's vectors for the 3 variants of basal <a> slip in the twinned volume (a) indicated as "B" and (b) indicated as "C" in Figure 4.12c for the 323K tension-tested extruded M1 specimen deformed to ~9.9% strain. The basal <a> slip variants and the corresponding global Schmid factors calculated based on a uniaxial stress state assumption are listed.

It is noted that out of the 29 contraction twins observed at 323K, 13 (~45%) were formed at strains between 0.7-5.2%, while the remaining contraction twins formed at strains greater than 5.2% strain (see Figure 4.9). Fracture occurred at ~9.9% strain at 323K. The increase in frequency of contraction twins might have led to an increase in the frequency of double twins as well because of the propensity of contraction twins to evolve into double twins with an increase in strain. The increase in frequency of double twins is expected to lead to a lower ε_f value as crack nucleation within the double twinned region can occur due to shear localization. Thus, it is believed that once a threshold level of contraction twinning is achieved, crack initiation occurs and failure is imminent. It is interesting to note that some of the localized shear bands were observed to traverse a number of grains, especially close to the fracture surface (See Figure 4.13). A similar observation was made in previous reports [Barnett 2007]. This severe shear localization might be sufficient to lead to failure.

With increased temperature, the twin activity decreased (see Figure 5.3). Significantly less twinning activity was observed at 423K compared to 323K, and at 523K the deformation was dominated by slip deformation (see Figure 5.3). No twinning was observed at 523K. Thus, the transition from twin-dominated deformation to slip-dominated deformation was expected to happen around 423K. This is expected to be due to the reduction in the CRSS values for prismatic <a> and pyramidal <c+a> slip systems at elevated temperatures [Hutchinson et al. 2010, Chapius et al. 2011]. It can be expected that at elevated temperatures, the CRSS of pyramidal <c+a> slip would become lower than that of contraction twinning and this would result in a decreased amount of contraction twinning, thereby enabling an increased ε_f [Barnett 2007].

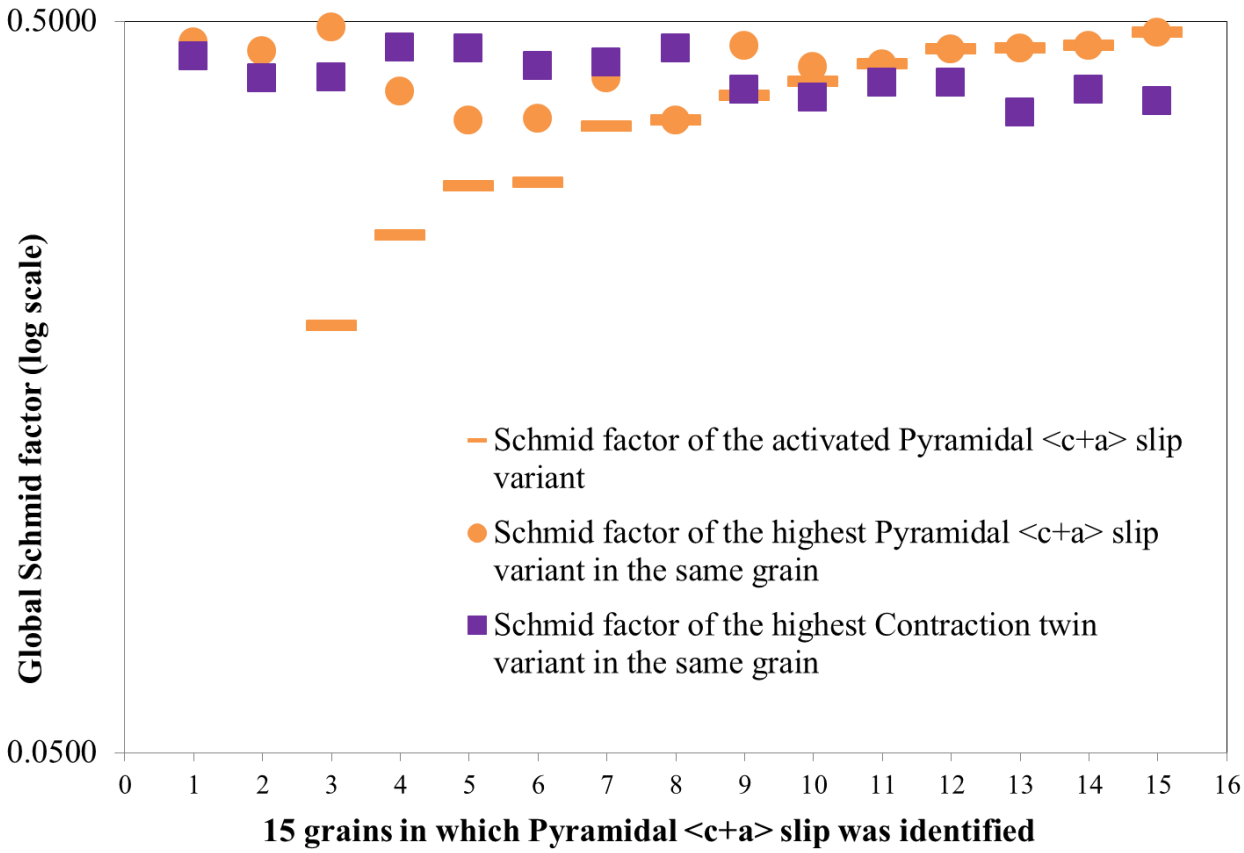

Figure 5.9 The global Schmid factor values of the pyramidal <c+a> slip variants identified in the extruded M1 specimen tensile tested at 523K overlaid with the Schmid factor values for the contraction twin variant and pyramidal <c+a> slip variant with the highest Schmid factor in the same grain.

The specimens tensile tested at 423K and 523K exhibited higher ε_f values compared to the specimen tested at 323K (see Figure 4.4). This was expected to be due to the limited activity of contraction twinning, which led to the formation of double twins and subsequent cracking as explained previously, at elevated temperatures. Figure 5.9 shows the global Schmid factor values of the pyramidal <c+a> slip variant identified in the specimen tensile tested at 523K overlaid with the Schmid factor values for the contraction twin variant and pyramidal <c+a> slip variant with the highest Schmid factor in the same grain. In some grains, the pyramidal <c+a> variant with the highest Schmid factor was not activated. Nevertheless, in all the grains in which

pyramidal <c+a> slip was activated, the contraction twin had similar or higher Schmid factors. The lack of contraction twinning at 523K, as well as the preferred activation of pyramidal <c+a> slip in grains in which the contraction twins had similar Schmid factors (see Figure 5.9), suggest that the CRSS of pyramidal <c+a> slip was lower than that of contraction twinning at 523K. If this were the case, it would be expected that pyramidal <c+a> slip would be more prevalent than contraction twinning at elevated temperatures. This could help explain the higher ε_f values observed at elevated temperatures compared to that at 323K. Moreover, it is noted that the distribution of the activity of different deformation modes did not change significantly as a function of strain levels under tension in extruded M1 at all tested temperatures (See Figure 4.9, 4.19, and 4.23).

5.4.1.1 Crystal plasticity modeling and simulation of twins

In order to understand the effect of contraction twinning and $\{10\bar{1}1\} - \{10\bar{1}2\}$ double twinning on the shear localization observed at 323K, the deformation behavior of the twins within the matrix under the influence of tensile loading was simulated using the crystal plasticity model described in Section 3.6. The tensile axis was chosen in order to reflect the experimental setup. For this simulation, only the slip systems given in Table 3.3 were considered in the matrix and the twinned volume. Figure 5.10 shows the stress and strain response of the contraction twin and the parent grain (see area marked "B" in Figure 4.12c) when pulled along the Y axis, after 4.0% strain. The parent-twin interface was parallel to $(01\bar{1}1)$, which was obtained from the twin trace analysis. Some stress concentrations along the parent-twin boundary were observed. However, the strain values appeared to be distributed uniformly across the contraction twinned region. The strain within the twinned volume was ~8.0% while the total strain from the combined matrix and twinned region was only 4.0%. This suggests that, after the nucleation of

the contraction twin, the twinned volume could act like a localized shear band. Figure 5.11 shows the accumulated shear from different slip systems after 4.0% strain. As expected from the Schmid factor analysis shown in Figure 5.6 and 5.8, $(0001)[\bar{1}2\bar{1}0]$ was the most active basal <a> slip variant due to the high Schmid factor value for this system compared to other systems. Step formation within the twinned volume was observed, and this was expected to be due to the component of the Burger's vector for $(0001)[\bar{1}2\bar{1}0]$ slip along the normal direction (see Figure 5.8).

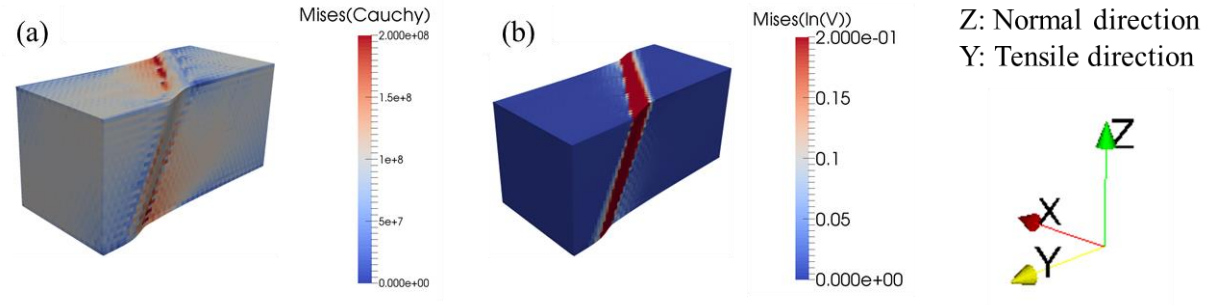

Figure 5.10 (a) the stress and (b) strain response of the contraction twin and the parent grain, shown in Figure 4.12c, when pulled along the Y axis, after 4.0% strain (see Section 3.6 for the details of the simulation).

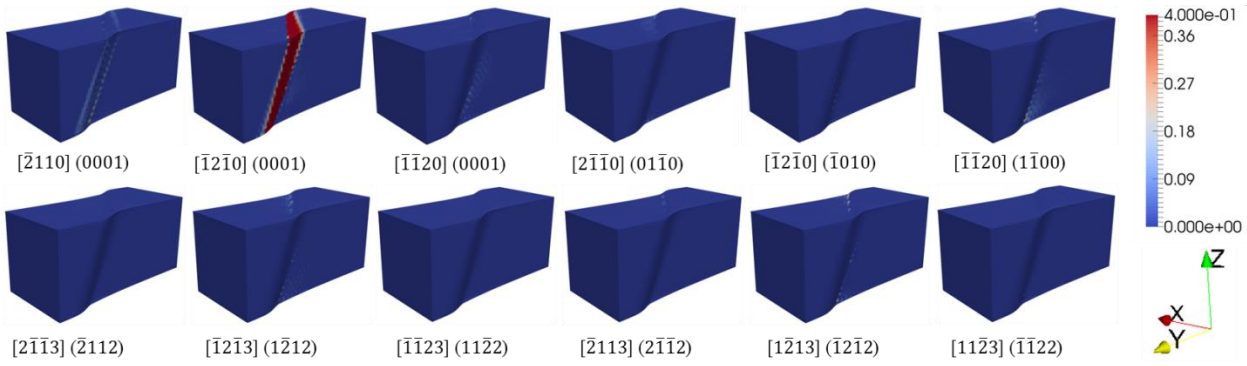

Figure 5.11 The accumulated shear from different slip systems in the contraction twin and parent grain after 4.0% strain along the Y direction simulated using the crystal plasticity model given in Section 3.6. Z is the normal direction.

A second simulation was performed with the same material configuration, but using the $\{10\bar{1}1\}-\{10\bar{1}2\}$ double twin orientation instead of the contraction twin to study the deformation behavior of $\{10\bar{1}1\}-\{10\bar{1}2\}$ double twins. Similar to the previous case, the parent-twin interface was parallel to $(01\bar{1}1)$ in this simulation in order to reflect the observation that $\{10\bar{1}1\}-\{10\bar{1}2\}$ double twins were formed within the primary contraction twin, and the primary contraction twin boundary did not change with an increase in strain during the experiments. Figure 5.12 shows the stress and strain response from this simulation after 5.0% strain, when pulled along the Y axis. Significantly higher stress values were observed in the matrix compared with the case including the contraction twin, and this was expected to be due to the localization of strain along the parent-twin interface (See Figure 5.12b). This suggests that once the contraction twins evolve into double twins, strain localization starts to happen along the matrix-twin interface. This is expected to lead to the nucleation of cracks along the matrix-twin interface, suggesting that $\{10\bar{1}1\}-\{10\bar{1}2\}$ double twins lead to a decrease in the ε_f value compared to $\{10\bar{1}1\}$ contraction twins. This is consistent with the previous experimental studies in which micro-cracks at the $\{10\bar{1}1\}-\{10\bar{1}2\}$ twin-matrix interface were detected using TEM [Cizek et al. 2008]. Ando et al. [2010] has also reported that crack initiation occurs along the $\{10\bar{1}1\}-\{10\bar{1}2\}$ twin-matrix interface. This helps explain the experimentally observed orientation of the cracks in this study. They were parallel to the contraction twin traces, suggesting crack nucleation along the matrix-twin interface (see Figure 4.13). Figure 5.13 shows the accumulated shear from different slip systems after 5.0% strain within the $\{10\bar{1}1\}-\{10\bar{1}2\}$ double twin and matrix (see area "C" indicated in Figure 4.12c). As expected, $(0001)[\bar{1}\bar{1}20]$ was the most active basal <a> slip variant due to the high Schmid factor value for this system compared to other systems (see Figure 5.8). Basal <a> slip activity confined within the

extension twinned regions were observed in as-cast MN10 tensile tested at 323K and 523K (See Figure 4.36 and 4.48). However, basal <a> slip within the double twins were not experimentally observed due to the significant ledges that happened from the shearing, and the difficulty in doing EBSD in that region because of the topography after deformation.

Small steps formed within the twinned volume, and this was expected to be due to the component of the Burger's vector for $(0001)[\bar{1}\bar{1}20]$ slip along the normal direction (see Figure 5.8). It is noted that the size of the surface step formed at the $\{10\bar{1}1\} - \{10\bar{1}2\}$ double twin was significantly smaller than that of the contraction twin.

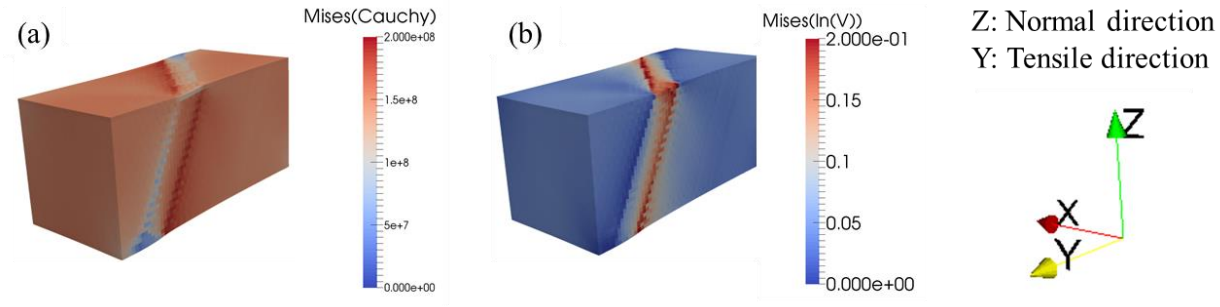

Figure 5.12 (a) the stress and (b) strain response of the $\{10\bar{1}1\} - \{10\bar{1}2\}$ double twin and the parent grain, shown in Figure 4.12c, when pulled along the Y axis. The maximum strain was 5.0% (see Section 3.6 for the details of the simulation).

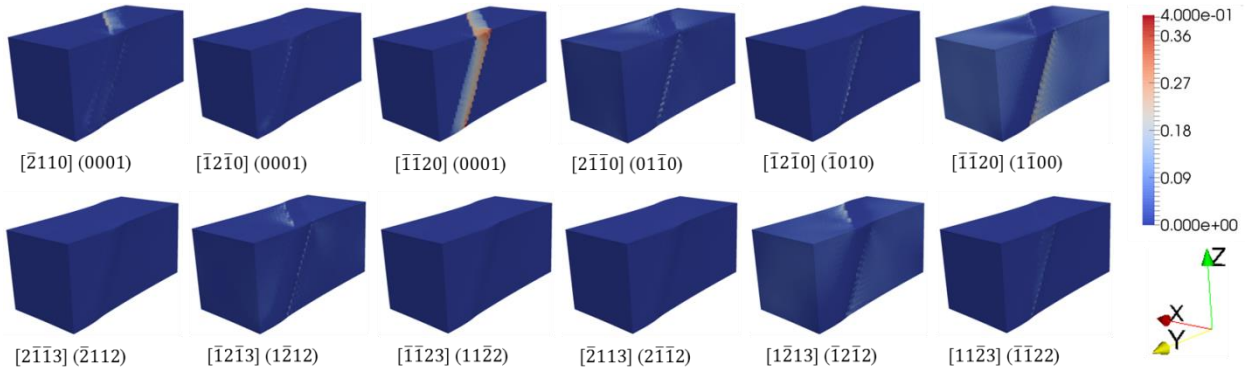

Figure 5.13 The accumulated shear from different slip systems in the $\{10\bar{1}1\} - \{10\bar{1}2\}$ double twin and parent grain after 5.0% strain along the Y direction simulated using the crystal plasticity model given in Section 3.6. Z is the normal direction.

Figure 5.14 shows the change in the orientation of the matrix (highlighted in Figure 4.12c as "A" or "D"), and the contraction twin and the $\{10\bar{1}1\} - \{10\bar{1}2\}$ double twin (highlighted in Figure 4.12c as "B" and "C", respectively), before and after the simulations, in the form of {0001} pole figures along the normal direction. In both cases, the matrix orientation did not change much during the deformation. In the case of the contraction twin, the orientation did not change significantly after the deformation. However, a significant change in the orientation of the $\{10\bar{1}1\} - \{10\bar{1}2\}$ double twin was observed after the deformation. The orientation of the $\{10\bar{1}1\} - \{10\bar{1}2\}$ double twin appeared to shift towards the matrix orientation (See Figure 5.14b), for which basal <a> slip is hard to activate (See Figure 5.6 and 5.7). This orientation gradient was expected to be formed due to the activity of $(0001)[\bar{1}\bar{1}20]$ basal <a> slip. Thus, the localization of stress and strain along the matrix-twin interface after the formation of double twins was assumed to be due to the rotation of the crystal to an orientation in which basal <a> slip variants are not oriented for easy activation. The relatively small strain values observed within the double twinned volume compared to the contraction twinned volume (See Figure 5.10 and 5.12) suggests that contraction twins cannot accommodate much strain after the transformation into double twins. This could then result in lower ε_f values. From the simulation results, the early fracture of the material at 323K was attributed to the enhanced activity of contraction twins and their subsequent evolution into double twins. This is in agreement with the experimental observation of relatively low ε_f values of this material at 323K and the observation of cracks parallel to the contraction twin traces (see Figure 4.13). In addition, the simulation results shows good agreement with the nature of the surface steps (see Figure 4.12a) observed within the twins.

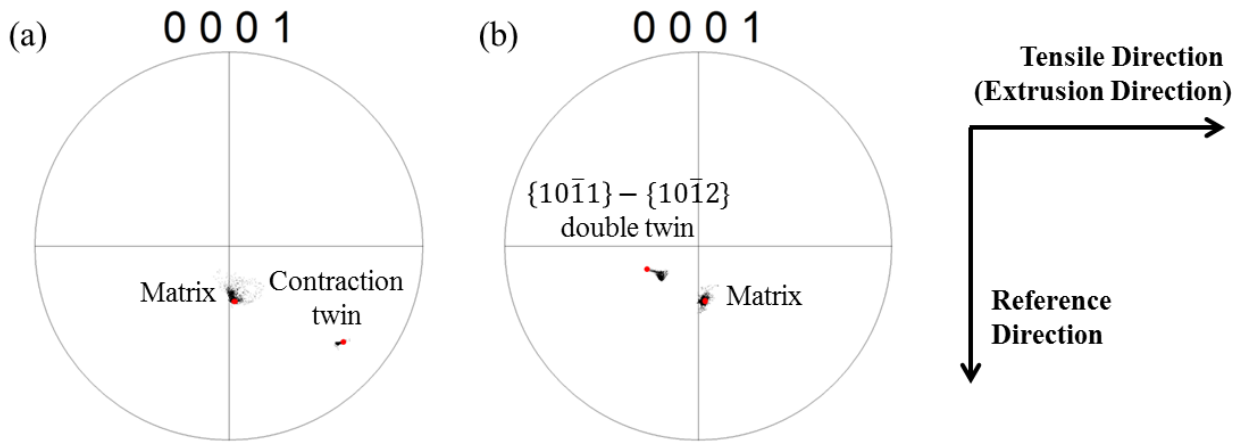

Figure 5.14 The change in the orientation of the matrix and (a) the contraction twin and (b) the $\{10\bar{1}1\} - \{10\bar{1}2\}$ double twin before and after the crystal plasticity simulations in the form of 0001 pole figures along the normal direction. The red dots indicate the orientation before deformation and the black dots indicate the orientation after (a) 4.0% and (b) 5.0% strain.

5.4.2 As-cast MN10 and MN11

Figure 5.15 shows the relative distribution of the different deformation modes identified in as-cast MN10 and MN11 tensile tested at 323K, 423K, and 523K. At all tested temperatures, the deformation was dominated by extension twinning and basal <a> slip. The profuse twinning activity observed in both alloys was expected to be due to the large grain size. A strong dependence of mechanical twinning on grain size was reported in Mg alloys where an increase in twinning activity with an increase in grain size was observed [Barnett 2008]. In addition, multiple twinning events, including $(10\bar{1}2) - (01\bar{1}2)$ extension–extension double twinning, were observed in the same grains in both alloys at all the test temperatures (See Section 4.2.2 and 4.4.2). This is in agreement with the previous studies in which the number of twins per grain tends to increase markedly with an increase in grain size [Barnett 2008]. Thus, the extensive activity of twinning in cast MN10 and MN11 can be attributed to the relatively large grain size exhibited by these materials.

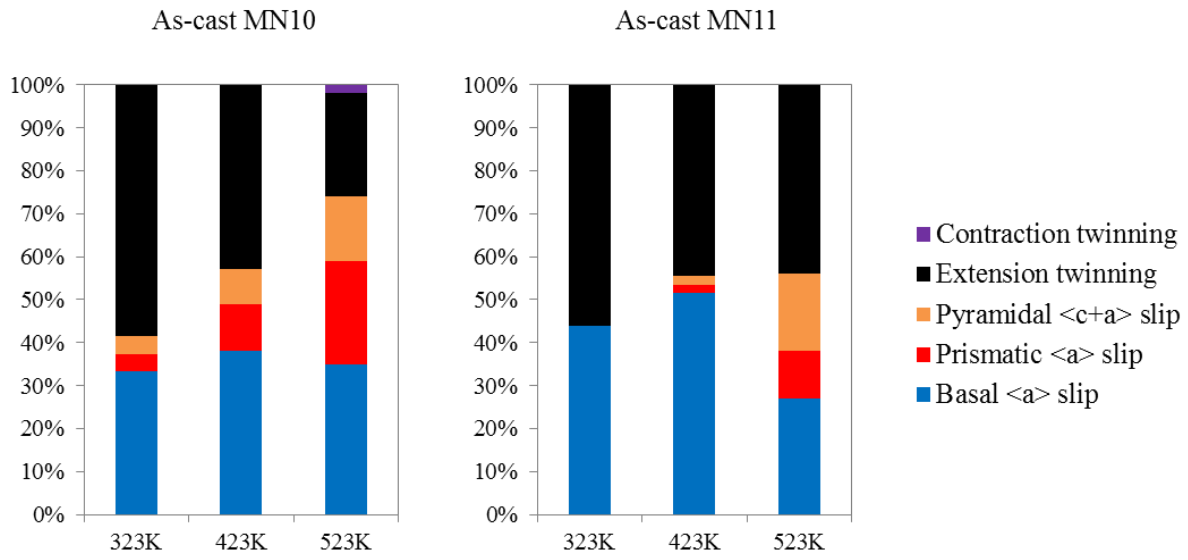

Figure 5.15 The relative distribution of the different deformation modes identified in as-cast MN10 and MN11 tensile tested at 323K, 423K, and 523K.

The non-basal slip activity increased with an increase in temperature in both alloys. This was expected to be due to the decrease in the CRSS values of non-basal systems with an increase in temperature [Hutchinson et al. 2010, Chapuis et al. 2011]. However, non-basal slip shows a significant contribution (>30%) towards deformation only at 523K. This suggests that the CRSS of non-basal systems become close to that of basal slip only at temperatures above 423K. In both materials, the basal <a> slip activity was similar at all test temperatures. It is also noted that the basal slip traces observed in both alloys were parallel to the stringers of particles observed within the grains (See Section 4.2.2 and 4.4.2). Thus, the stingers of second phase particles, aligned parallel to the basal planes in both alloys, might have served as stress concentrators and might have assisted in the activation of basal <a> slip. It is noteworthy that the similar deformation behavior exhibited by the as-cast MN10 and MN11 alloys at all tested temperatures resulted in a similar macroscopic tensile behavior in these alloys (See Figure 4.32 and 4.85). In addition, it is noted that the distribution of the activity of different deformation modes did not

change significantly as a function of strain levels under tension in as-cast MN10 and MN11 at all tested temperatures (See Section 4.2 and 4.4).

5.4.3 Extruded MN10 and MN11

The deformation behavior of the extruded MN10 and MN11 alloys was significantly different from the as-cast material. Figure 5.16 shows the relative distribution of the different deformation modes identified in extruded MN10, MN11-275, and MN11-300 tensile tested at 323K, 423K, and 523K. In the case of extruded MN10, no obvious slip traces were observed at 323K under tensile loading. This might be due to the strong basal texture observed in this alloy. The alignment of basal planes parallel to the tensile axis makes basal <a> slip difficult. However, both extension and contraction twinning were observed. At 423K, basal <a> slip, extension twinning, and contraction twinning were observed. At 523K, basal <a>, prismatic <a>, and pyramidal <c+a> slip were observed, and no twinning was observed. In the case of MN11-300 and MN11-275, a similar deformation mode distribution was observed at all the test temperatures. At 323K, basal <a> slip, prismatic <a> slip, pyramidal <c+a> slip, and extension twinning were observed. With an increase in temperature, the twinning activity was decreased, and at 423K and 523K, basal <a>, prismatic <a>, and pyramidal <c+a> slip dominated the deformation. Thus, the extruded MN10 and MN11 exhibited similar deformation mode distributions at elevated temperatures.

It is noted that, due to the weak texture exhibited by extruded MN10 and MN11, the number of grains that are aligned favorable for the activation of contraction twinning and $\{10\bar{1}1\} - \{10\bar{1}2\}$ double twinning in a given microstructure are expected to be low. Thus, the limited activity of these twin types in extruded MN10 and MN11, compared to extruded M1, was

attributed to the relatively random texture exhibited by these alloys.

At ambient temperature, substantial activity of extension twinning was observed in the extruded MN10 and MN11 specimens under tensile loading. However, the amount of twinning activity decreased with increased temperature. At the same time, the amount of slip, especially basal <a> slip, increased with increasing temperature in both materials. This suggests that the CRSS of basal <a> slip could be higher than that of extension twinning at lower temperatures and the opposite would be true at elevated temperature. The relative distribution of basal <a> slip and extension twinning, shown in Figure 5.16, suggest that the CRSS transition may occur at a temperature around 423K. However, this suggestion is contrary to the belief that the CRSS values for both twinning and basal <a> slip are relatively insensitive to temperature, where the CRSS for twinning is expected to be slightly higher than that for basal <a> slip [Reed-Hill et al. 1957a, Reed-Hill et al. 1957b, Kelley et al. 1968, Barnett 2003, Chapuis et al. 2011, Guillemer et al. 2011].

According to the Taylor based model by Barnett [2003], the CRSS of extension twinning is approximately 6 times than that of basal <a> slip in AZ31 polycrystals. Other authors have reported that the CRSS of extension twinning is approximately two times that of basal <a> slip in a Mg single crystal at temperatures close to 294K [Reed-Hill et al. 1957a, Reed-Hill et al. 1957b, Kelley et al. 1968, Chapuis et al. 2011]. Guillemer et al. [2011] reported that the CRSS value of extension twinning is higher than that of basal <a> slip at 294K based on Mg polycrystal experimental studies. A recent study by Kim et al. [2012] showed that the addition of non-RE elements increases the CRSS of basal <a> slip in Mg binary alloy single crystals. However, the effect of RE elements on the relative CRSS values of the different deformation modes in Mg has not been studied extensively.

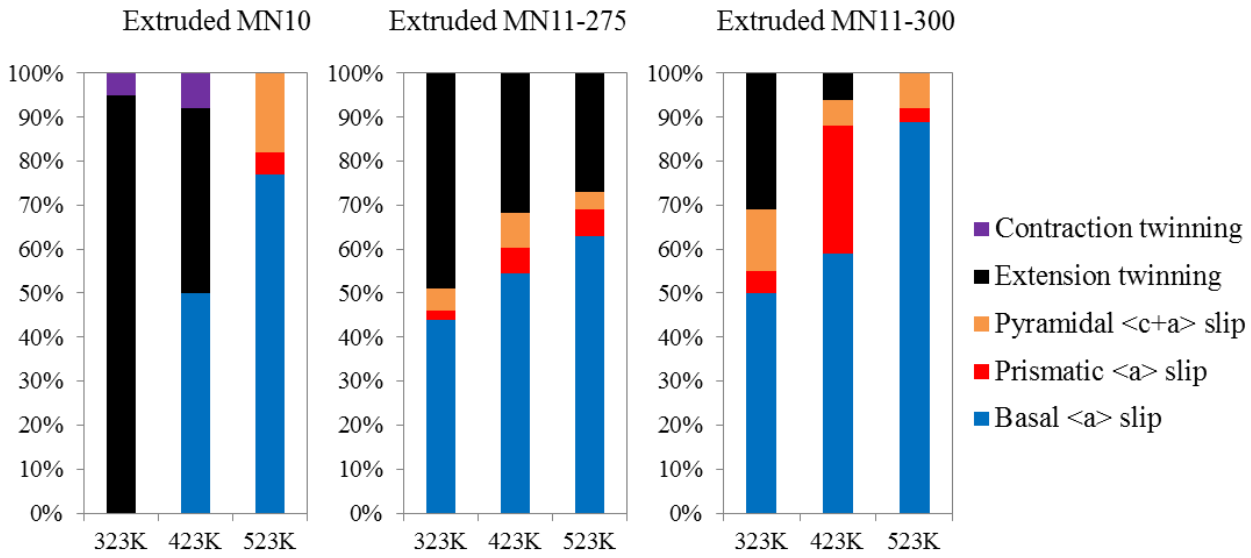

Figure 5.16 The relative distribution of the different deformation modes identified in extruded MN10, MN11-275, and MN11-300 tensile tested at 323K, 423K, and 523K.

Based on the relative distribution of the different deformation modes observed in MN11-300 and MN11-275 at 323K, the relative CRSS value of extension twinning and non-basal <a> slip (prismatic <a> and pyramidal <c+a> slip) with respect to basal <a> slip was estimated to be <1 and >10, respectively (See Section 4.5). This suggests that the CRSS value of extension twinning can be very close or even less than that of basal <a> slip in RE-containing Mg alloys at temperatures close to RT. This is consistent with the CRSS values estimated for basal <a> slip and extension twinning in Mg-0.2Ce by Ye et al. [2011] using in-situ TEM uniaxial nano-compression experiments on single crystals. This could then explain the substantial activity of extension twinning observed at ambient temperatures. On the other hand, at elevated temperatures, basal <a> slip was the dominant deformation mode in MN10 and MN11 (See Figure 5.16). However, MN11 exhibited better elevated-temperature strength retention compared to MN10. This suggests that Nd addition strengthens basal <a> slip and this was expected to be one of the factors responsible for improved elevated temperature strength

retention. The relative CRSS ratio of >10 for non-basal slip with respect to basal <a> slip for MN11 estimated from this study is similar to the data reported for other Mg alloys [Yoshinaga et al. 1963, Wonsiewicz et al. 1967, Obara et al. 1973, Barnett 2003, Chapuis et al. 2011].

More than 90% of the basal <a> slip observed in extruded MN11-275 and MN11-300 was associated with high Schmid factors (>0.30). Thus, basal <a> slip appeared to follow Schmid law in extruded MN11 at all tested temperatures. A wider distribution of Schmid factors for basal <a> slip was observed in extruded MN10 at 423K and 523K. However, basal <a> slip occurred more frequently at lower Schmid factors (though typically >0.20) at 423K and 523K. The wider distribution of Schmid factors for basal <a> slip in extruded MN10 might be due to the strong basal <a> texture of this material. Prismatic <a> and pyramidal <c+a> slip with low Schmid factors (<0.15) were observed in both extruded MN11 and MN10. However, they did not occur frequently.

The validity of Schmid law for twinning systems in Mg has often been a subject of debate, and for modeling purposes it is often assumed that Schmid law is valid for twinning [Godet et al. 2006, Barnett et al. 2008, Beyerlein et al. 2010, Hong et al. 2010, Chapuis et al. 2011, Tome et al. 2011, Mu et al. 2012]. In extruded MN10, more than 90% of the extension twins were observed at Schmid factors <0.20 under tensile loading at 323K and 423K. A similar trend was observed in extruded MN11-275 under tensile loading at all the test temperatures, in which more than ~67% of the extension twins were associated with Schmid factors <0.20. Under compression, the extension twinning observed in both extruded MN10 and MN11 was distributed over the entire Schmid factor range, 0 to 0.50, at all the test temperatures. The lack of basal <a> slip in MN11 and MN10 under compression at any of the tested temperatures might be due to the lower strain values in which the compression samples were subjected to compared

with the tension-tested samples. The earliest that the slip traces were observed in MN11 and MN10 under tension at any of the test temperatures was ~9% strain. In the case of MN10, the strong basal <a> texture makes the activation of basal <a> slip even more difficult under compression at low strain levels. Nevertheless, the results from this study show that the activation of extension twinning does not follow the Schmid law. This is in agreement with a recent study in which a strong dependence of extension twinning on Schmid law was not observed in HCP polycrystalline Mg [Tome et al. 2011].

As stated in section 3.4, the slip trace analysis technique used in this work only identifies slip activity indirectly through the observation of surface slip traces. This approach has the possibility to miss the observation of some deformation systems. For example, slip systems with Burgers vectors parallel to the sample surface will not develop observable traces. Also, diffuse slip will not lead to well-defined slip traces. In addition, slip bands will not develop if the magnitude of slip is small. It is therefore likely that not all of the slip activated in the deformed specimens was observed, especially when one considers the amount of strain achieved by the samples.

In addition, in some Mg alloys, it is challenging to observe obvious slip traces in SEM images in the deformed grains, especially at ambient temperatures [Boehlert et al. 2012, Chen 2012]. One of the reasons might be because Mg is a light element and perhaps we are getting fewer signals compared to other heavier alloys which may account for the observation of better slip traces. For example, in Ti alloys, slip traces were consistently observed in 85-95% of the grains analyzed even after the same local strains as measured in the current work [Li et al. 2013, Li 2013]. Thus, from the slip trace analysis on Ti alloys, more statistically significant data can be extracted from fewer grains and this may lead to a more reliable CRSS value after only testing

a few samples and examining a few microstructural patches. In contrast, in the tensile deformed microstructure of extruded MN10 and MN11 (see Section 4.3 and 4.5), among a few hundred grains analyzed, obvious slip/twin traces were observed only in ~1-10% of the grains. Thus, the slip trace analysis cannot have accounted for all the deformation occurring in the samples based on the local strain measurements.

However, EBSD orientation maps revealed orientation gradients (up to 5 degrees) within the grains after deformation. Thus, a methodology (see Appendix C) was developed in an effort to account for more active slip systems in the grains which did not show clear evidence of slip, based on the orientation gradients within grains obtained from EBSD orientation mapping. If this methodology is successfully verified, this allow more active slip to be identified despite no surface traces, and obtain confidence that the local strains achieved can be accounted for. Furthermore, the methodology described in Appendix C demonstrates that the lack of observations of obvious slip traces does not imply the lack of slip activity. It is noted that the slip activity identified using the slip trace analysis technique in this study might have underestimated the overall slip activity in the deformed microstructure for extruded MN10 and MN11, especially at ambient temperatures.

Nevertheless, the methodology described in Appendix C was used to estimate the slip activity in the extruded MN10 tensile tested at 323K for grains which did not exhibit obvious surface slip traces. In Figure 5.17, the deformed microstructure of extruded MN10 tensile tested at 323K after 6.4% strain was partitioned based on the orientation of the grains in which basal <a> slip traces were observed during the tensile test at 523K. As obvious basal <a> slip traces with Schmid factors >0.40 were observed in similar orientations during the tensile test at 523K, it can be assumed that basal <a> slip is more likely to be active in similar orientations during the

tensile test at 323K. It was observed that in most of the grains shown in Figure 5.17, basal <a> slip had relatively high Schmid factors. In Figure 5.17, an example of the analysis performed on the grain highlighted by the white box in the EBSD IPF map is shown. In the example shown in Figure 5.17, the streaks observed in the {0001} and $\{11\bar{2}2\}$ match fairly well with the simulated arcs for basal <a> slip system number 2 with Schmid factor 0.37. In addition, no streaking was observed in the $\{10\bar{1}0\}$ and $\{11\bar{2}0\}$ pole figures along the simulated arcs for prismatic <a> slip. Thus, it can be stated with a fair degree of confidence that basal <a> slip with a Schmid factor of ~0.37 was the predominant active in the grain of interest. However, as the pyramidal <c+a> slip systems also have relatively high Schmid factors in this grain, the possible activity of this slip system cannot be ruled out completely. The analysis of the streaks for the other grains shown in Figure 5.17 suggested possible activity of basal <a> slip as well. Thus, the simultaneous activity of basal <a> slip and pyramidal <c+a> slip in the grains shown in Figure 5.17 would then help explain the high elongation-to-failure value of ~35% strain exhibited by extruded MN10 at 323K.

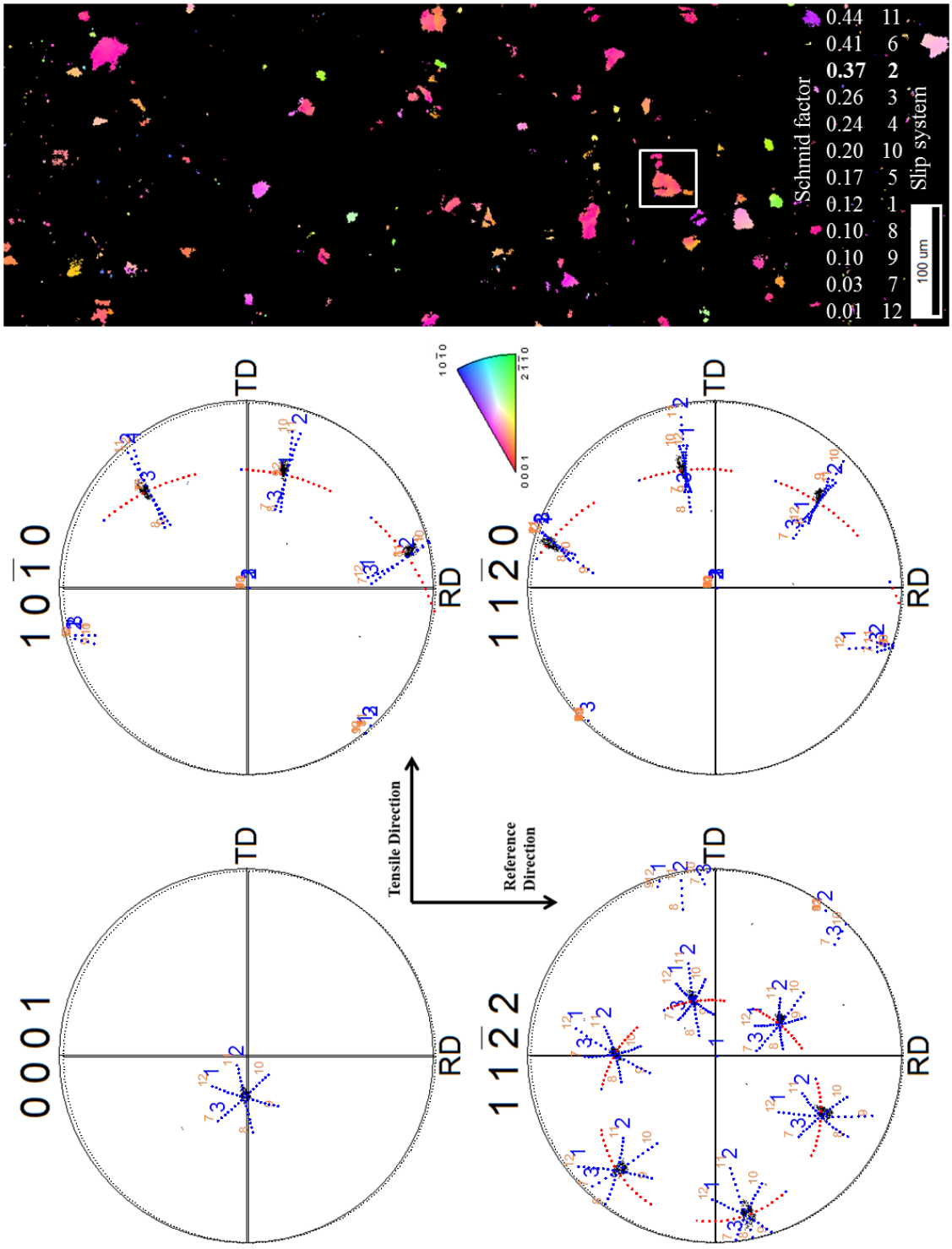

Figure 5.17 The EBSD IPF map for extruded MN10 tensile tested at 323K after 6.4% strain. The grains are partitioned using the orientations for which basal <a> slip traces were observed during the tensile test at 523K. The pole figures for the grain highlighted by the white box are overlaid with the simulated arcs for different slip systems. By analyzing the streaks in the pole figures, it is likely that basal <a> slip system number 2 with a Schmid factor of 0.37 was active.

5.5 Recrystallization in rolled ZE20

The recrystallization behavior of both Mg-2Zn-0.2Ce and Mg-2Zn-0.6Ce alloys followed similar trends. As shown in Figure 4.136 and 4.139, new grains started to appear at temperatures between 423-473K in both alloys. As expected, with the formation of new grains, the texture intensity in the microstructural patches decreased (See Figure 4.136 and 4.139). However, it is noted that the texture intensity increased slightly during the final annealing steps, which include temperatures above 548K. This was expected to be due to grain growth and therefore fewer grains were present in the given microstructural patch analyzed. Nevertheless, in both materials, relatively equiaxed and strain-free grains were observed after the annealing step between 548-573K, suggesting that recrystallization was complete by 573K (See Figure 4.137 and 4.140).

In the microstructural patch monitored during the in-situ experiments, only 159 and 300 unique grain boundaries from 59 and 112 newly formed grains were observed in Mg-2Zn-0.2Ce and Mg-2Zn-0.6Ce, respectively. To obtain a more statistically meaningful dataset, a larger area from the final microstructure (after the last annealing step) was analyzed for Mg-2Zn-0.2Ce and Mg-2Zn-0.6Ce. Furthermore, the final microstructure of the rolled Mg-2Zn-0.2Ce and Mg-2Zn-0.6Ce was compared with a rolled conventional Mg alloy, Mg-3Al-1Zn (AZ31) [Chen 2012]. It is noted that the rolling parameters and annealing conditions for AZ31 were different from the alloys in the current study. Figure 5.18 compares the EBSD IPF map in the normal direction, the corresponding texture in the form of {0001} pole figures, and the misorientation angle distribution in the final annealed microstructure for Mg-2Zn-0.2Ce, Mg-2Zn-0.6Ce, and AZ31. The pole figures and the misorientation angle distribution shown in Figure 5.18 were obtained from an area containing ~2800, ~1400, and ~4800 grains in Mg-2Zn-0.2Ce, Mg-2Zn-0.6Ce, and AZ31, respectively.

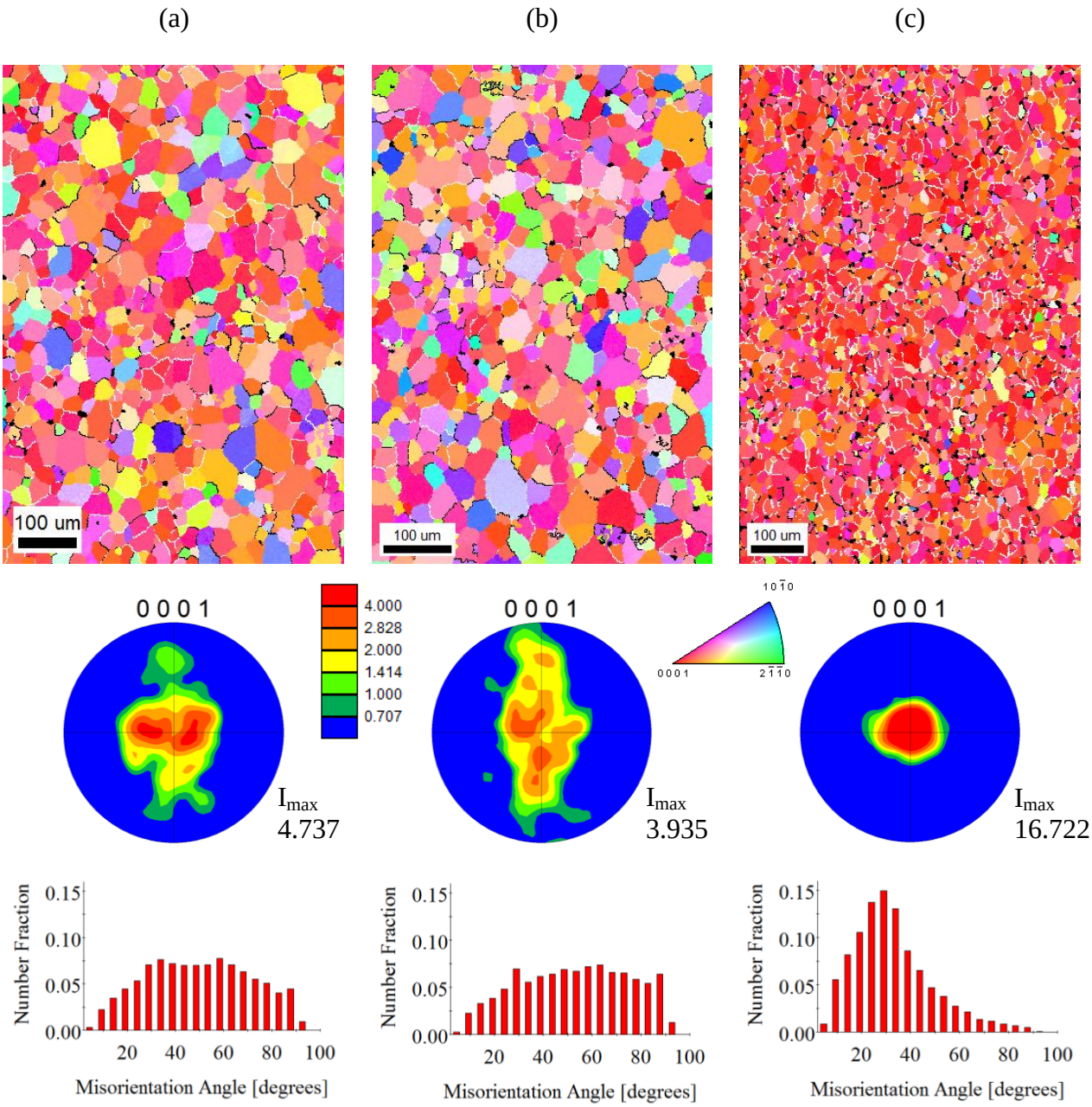

Figure 5.18 The EBSD IPF map in the normal direction, the corresponding texture in the form of {0001} pole figures, and the misorientation angle distribution in the final annealed microstructure in rolled (a) Mg-2Zn-0.2Ce, (b) Mg-2Zn-0.6Ce, and (c) AZ31. The grain boundaries highlighted by white lines in the EBSD IPF correspond to $< 11\bar{2}0 >$ and $< 10\bar{1}0 >$ type, and the black ones correspond to $< 10\bar{1}1 >$ type rotation axis. I_{max} is the maximum texture intensity values observed. The rolling direction is horizontal. The EBSD data was post-processed using a clean-up procedure in which multiple iteration of grain dilation with a grain tolerance angle of 5 degrees and minimum grain size of 5 pixels was performed. Furthermore, the EBSD data were partitioned with a grain tolerance angle of 5 degrees and a minimum grain size of 15-25 pixels.

The average grain sizes after the final annealing step in rolled Mg-2Zn-0.2Ce and Mg-2Zn-0.6Ce were ~28μm and ~24μm, respectively. The slightly smaller grain size observed in the 0.6-Ce containing alloy, compared to the 0.2Ce-containing alloy, was expected to be due to the increased amount of RE-content, which might have assisted in the prevention of grain growth during annealing [Bohlen et al. 2010]. It is noted that the average grain size in rolled AZ31 microstructure after annealing was ~16μm and this might be due to the different processing history and annealing conditions for this alloy. Nevertheless, a weaker texture was observed in rolled Mg-2Zn-0.2Ce and Mg-2Zn-0.6Ce after annealing compared to AZ31 (See Figure 5.18). In addition, the texture intensity observed in the 0.6-Ce containing alloy was smaller compared to the 0.2Ce-containing alloy, suggesting that an increase in RE content assists texture weakening in Mg alloys [Bohlen et al. 2010].

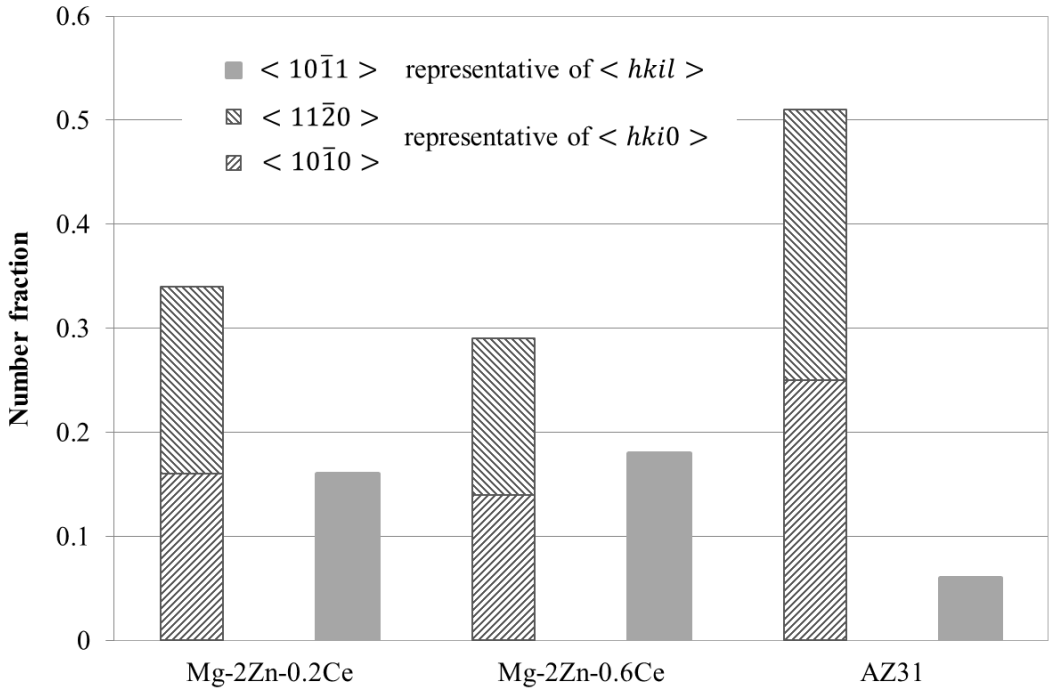

Figure 5.19 The distribution of the grain boundaries with $< 11\bar{2}0 >$, $< 10\bar{1}0 >$, and $< 10\bar{1}1 >$ type rotation axis in Mg-2Zn-0.2Ce, Mg-2Zn-0.6Ce, and AZ31 in the final annealed microstructure.

The distribution of the misorientation axis across the newly formed grain boundaries in Mg-2Zn-0.2Ce and Mg-2Zn-0.6Ce was ~70% $< hki0 >$ and ~30% $< hkil >$ (See Figure 4.138 and 4.141). As $< 11\bar{2}0 >$, $< 10\bar{1}0 >$, and $< 10\bar{1}1 >$ type rotation axis accounted for ~76% and ~78% of all the rotation axis observed among the newly formed grain boundaries in Mg-2Zn-0.2Ce and Mg-2Zn-0.6Ce, respectively, orientation relationships of neighboring grains in the final annealed microstructure were analyzed.

Figure 5.19 shows the distribution of $< 11\bar{2}0 >$, $< 10\bar{1}0 >$, and $< 10\bar{1}1 >$ type rotation axis in the microstructure after annealing in Mg-2Zn-0.2Ce, Mg-2Zn-0.6Ce, and AZ31. As shown in Figure 5.19, a significantly different distribution of $< hki0 >$ and $< hkil >$ type rotation axis were observed for AZ31 compared to Mg-2Zn-0.2Ce and Mg-2Zn-0.6Ce. Specifically, a significantly higher proportion of $< hkil >$ type rotation axis was observed in the Ce-containing alloys compared to AZ31 (a number fraction of 0.16 and 0.18 for Mg-2Zn-0.2Ce and Mg-2Zn-0.6Ce, respectively, compared to 0.06 for AZ31). This difference might be due to the different type of deformation systems activated during the rolling process, in which the activity of the different type of slip systems could result in a difference in the characteristics of the new grains formed in the deformed regions. For example, RE additions are expected to enhance the non-basal slip activity during deformation [Chino et al. 2008a, Stanford et al. 2010, Sandlobes et al. 2011]. However, the distribution of the deformation modes was not investigated during rolling of the alloys in this study. In addition, as shown in Figure 5.18, the misorientation angle distribution among the grain boundaries in AZ31 was concentrated around 30 degrees, whereas, a uniform distribution of misorientation angles was observed in rolled Mg-2Zn-0.2Ce and Mg-2Zn-0.6Ce. Thus, it can be concluded that the enhanced number of grain boundaries with $< hkil >$ rotation axis and a uniform distribution of misorientation angles

between grains resulted in a more random texture for Ce-containing Mg alloys compared to the more conventional Al-containing Mg alloy, such as AZ31.

CHAPTER 6

SUMMARY AND CONCLUSIONS

6.1 Summary

In this dissertation, a systematic study of the effect of alloying, processing, and temperature on the microstructure, mechanical properties, and the deformation behavior of a few newly developed RE-containing Mg alloys was performed. The effect of Nd additions (0-1wt.%) and temperature (298-523K) on the active deformation modes in as-cast and cast-then-extruded Mg-1Mn alloys was investigated and compared using an in-situ technique which involves testing inside a SEM combined with EBSD analysis. The microstructure, texture, and YS of each of the above mentioned alloys were also investigated and compared. In addition, crystal plasticity modeling and simulations were used to understand the evolution of $\{10\bar{1}1\}-\{10\bar{1}2\}$ double twinning and its effect on the limited ε_f in the extruded M1 alloy. Finally, a novel in-situ experimental technique which involves annealing inside a SEM combined with EBSD analysis was developed and employed to understand the effect of Ce additions (0.2-0.6wt.%) on the recrystallization behavior of rolled Mg-2Zn alloys. Overall, the work performed in this dissertation has provided new insights on the effects of RE alloying on the deformation mechanisms and microstructural evolution of these newly developed Mg alloys.

6.2 Conclusions

6.2.1 Extruded M1

(1) The extruded M1 alloy exhibited an average grain size of ~42μm. The relatively larger grain size of extruded M1, compared to the Nd-containing extruded alloys studied, was

expected to be due to the absence of RE elements. This suggests that RE additions assist in the prevention of grain growth during the extrusion process in Mg alloys.

(2) A strong basal texture (maximum intensity of ~7.8), was observed in the extruded M1 alloy (where the c-axis of the HCP unit cells was aligned perpendicular to the extrusion direction). This is similar to the wrought texture observed in other conventional Mg alloys.

(3) With an increase in temperature, the tensile YS of the extruded M1 alloy decreased significantly (a tensile YS of ~45MPa and ~75MPa at 523K and 423K, respectively, compared to ~154MPa at 323K). Similar reduction in YS has been observed in other conventional Mg alloys.

(4) The extruded M1 specimen tensile tested at 323K fractured at ~9.9% strain whereas failure was not observed at 423K and 523K even at much higher strain levels.

(5) The tensile deformation at 323K was dominated by contraction twinning. Extension twinning was also prominent at 323K. The twinning activity decreased with an increase in temperature, and at 523K no twinning activity was observed. A combination of basal <a> slip, prismatic <a> slip, and pyramidal <c+a> slip dominated the elevated temperature tensile deformation.

(6) The enhanced activity of contraction twinning at ambient temperature was expected to be due to its lower CRSS values compared to pyramidal <c+a> slip. At elevated temperatures (>423K), the CRSS of pyramidal slip was expected to be lower than that for contraction twinning.

(7) The contraction twins observed at 323K evolved into $\{10\bar{1}1\} - \{10\bar{1}2\}$ double twins with an increase in strain. Crystal plasticity modeling and simulation studies showed that contraction twinning and $\{10\bar{1}1\} - \{10\bar{1}2\}$ double twinning are detrimental to the ε_f due to the enhanced activity of basal <a> slip within the twinned volume. The twin-matrix interface was

identified to be a potential crack initiation cite. Thus, the limited ε_f of the extruded M1 alloy at ambient temperature was attributed to the profuse activity of contraction twinning.

(8) It is noteworthy that extension twins were formed in the extruded M1 microstructure during mechanical polishing. This suggests that extra care should be taken during the metallographic preparation of Mg alloys for accurate microstructure characterization.

6.2.2 As-cast MN10

(1) The as-cast MN10 microstructure exhibited equiaxed grains with an average grain size of ~361μm. Stringers of Mn-rich precipitates aligned parallel to the HCP basal planes.

(2) A random texture (maximum intensity of ~3.0) with no preference to any particular texture component was observed in the as-cast MN10. This type of texture has been commonly observed in other as-cast Mg alloys.

(3) The tensile YS did not significantly decrease with an increase in temperature (~23MPa and ~30MPa at 523K and 423K, respectively, compared to ~36MPa at 323K).

(4) The tensile deformation was dominated by basal <a> slip and extension twinning at 323K, 423K, and 523K. The stringers of precipitates aligned parallel to the basal planes might have served as stress concentrators, which might have assisted in the activation of basal <a> slip. The Schmid factors of the extension twins observed at all test temperatures were distributed over the entire Schmid factor range. Some of the extension twins evolved into $(10\bar{1}2)-(01\bar{1}2)$ double twins. The profuse activity of twinning was expected to be due to the relatively large grain size. The similarities of the deformation behavior at all the tested temperatures agree well with the similarity in the tensile strength observed.

6.2.3 Extruded MN10

(1) A completely recrystallized microstructure with an average grain size of ~10μm was observed in the extruded MN10. This suggests that ~0.3wt.% Nd addition is sufficient to prevent grain growth during extrusion in M1.

(2) A relatively strong basal texture was observed in extruded MN10 (maximum intensity of ~6.2 compared to ~7.8 in extruded M1) where the basal planes aligned parallel to the extrusion direction. This suggests that ~0.3wt.% is not sufficient to significantly weaken the texture in M1 alloys during extrusion.

(3) Although not as dramatic as that for extruded M1, the tensile YS of extruded MN10 decreased with an increase in temperature (~66MPa and ~81MPa at 523K and 423K, respectively, compared to ~119MPa at 323K). This suggests that ~0.3wt.% Nd addition is not sufficient to retain the strength at elevated temperatures. However, the tensile strength of extruded MN10 was higher compared to the as-cast MN10. This was expected to be due to the significantly smaller grain size in extruded MN10 compared to the as-cast material.

(4) The tensile deformation at 323K was dominated by extension twinning. With an increase in temperature, the twinning activity decreased. At elevated temperatures, the deformation was dominated by slip mechanisms, particularly basal <a> slip.

(5) The compression YS was ~94MPa at 323K (the YS was ~119MPa at 323K in tension) and the deformation was dominated by extension twinning at all tested temperatures. The extension twins observed at all test temperatures under compression was distributed over the entire Schmid factor range, suggesting that extension twins in Mg do not follow Schmid's law. A similar trend was observed for the extension twins identified under tension at 323K.

6.2.4 As-cast MN11

(1) A relatively large average grain size of ~970μm was observed in the as-cast MN11. Stringers of Mn-rich precipitates aligned parallel to the HCP basal planes. In addition, a continuous network of Nd-rich precipitates was observed at the grain boundaries in as-cast MN11.

(2) A relatively weak texture (maximum texture intensity of ~6.5) was observed in the as-cast MN11. The prevalence of any particular texture component was not observed.

(3) As-cast MN11 exhibited similar tensile YS values at all tested temperatures (~23MPa and ~25MPa at 523K and 423K, respectively) compared to as-cast MN10.

(4) Similar to as-cast MN10, the tensile deformation was dominated by basal <a> slip and extension twinning at 323K, 423K, and 523K. The stringers of precipitates aligned parallel to the basal planes might have served as stress concentrators, which might have eventually assisted in the activation of basal <a> slip. The profuse activity of twinning was expected to be due to the relatively large grain size observed. The extension twins identified did not follow Schmid's law at all tested temperatures.

6.2.5 Extruded MN11

(1) A completely recrystallized microstructure with an average grain size of ~12μm was observed in the extruded MN11, suggesting that grain growth did not occur during the extrusion process.

(2) Extruded MN11 exhibited the weakest texture among the alloys studied in this work. A weak texture (maximum intensity of ~3.4-4.0) with no preference for any particular texture component was observed. This suggests that ~1wt.% is sufficient to prevent strong basal texture

formation in M1 alloys during extrusion.

(3) Extruded MN11 exhibited excellent elevated-temperature strength retention (the tensile YS was ~77MPa and ~80MPa at 523K and 423K, respectively, compared to ~92MPa at 323K). In addition, the tensile strength of extruded MN11 was higher than as-cast MN11, which was expected to be due to the significantly smaller grain size in the extruded material compared to the as-cast material.

(4) The tensile deformation at 323K was dominated by basal <a> slip and extension twinning. With an increase in temperature, the twinning activity decreased. At elevated temperatures, the deformation was dominated by slip mechanisms, with basal <a> slip being the most prominent mode. This suggests that Nd-additions strengthen the basal <a> slip in M1 alloy which could then result in excellent elevated temperature strength retention.

(5) The CRSS ratio of extension twinning with respect to basal <a> slip was estimated to be <1 at 323K, whereas the CRSS ratios of non-basal slip relative to basal <a> slip was >10.

(6) The compression YS of extruded MN11 was similar to the tensile YS values (~92MPa, ~87MPa, and ~84MPa at 323K, 423K, and 523K, respectively). Thus, a significant tension-compression asymmetry, commonly observed in conventional Mg alloys, was not observed in extruded MN11. The deformation was dominated by extension twinning under compression at all tested temperatures, and the corresponding Schmid factors were distributed over the entire Schmid factor range. This suggests that extension twins in Mg do not follow Schmid law. A similar trend was observed for the extension twins identified under tension.

6.2.6 Rolled ZE20

(1) A completely recrystallized microstructure with relatively equiaxed and strain-free grains were observed after the annealing step between 548-573K, suggesting that

recrystallization was complete by 573K in rolled Mg-2Zn-0.2Ce and Mg-2Zn-0.6Ce alloys.

(2) The average grain sizes after the final annealing step at 598K and 623K in rolled Mg-2Zn-0.2Ce and Mg-2Zn-0.6Ce were ~28μm and ~24μm, respectively. This suggests that RE additions assists in the prevention of grain growth in Mg alloys.

(3) A weaker texture was observed in rolled Mg-2Zn-0.2Ce (maximum texture intensity of ~4.7) and Mg-2Zn-0.6Ce (maximum texture intensity of ~3.9) after annealing compared to a rolled conventional alloy, such as AZ31 (maximum texture intensities typically >15). This suggests that RE additions assists in texture weakening in Mg alloys. During the annealing, an enhanced number of grain boundaries with $< hkil >$ rotation axis formed.

6.3 Summary of the novel aspects of this work

(1) Using the in-situ testing technique, the evolution of contraction twinning into $\{10\bar{1}1\} - \{10\bar{1}2\}$ double twinning was captured in the M1 alloy tensile tested at 323K. In addition, an understanding of the decreasing activity of contraction twinning with an increase in temperature, and its effect on increased ε_f of Mg alloys was obtained. In the literature, there has been no evidence for the activity of double twinning in M1 alloy and the effects of temperature on its activity. By using crystal plasticity modeling and simulations, it was shown that the effect of contraction twinning and $\{10\bar{1}1\} - \{10\bar{1}2\}$ double twinning on the limited ε_f of Mg alloys was due to the strain localization due to the enhanced activity of basal <a> slip within the twinned volume. In addition, the twin-matrix interface was identified to be a potential crack initiation site. Although, there have been speculation about these phenomenon derived from experimental studies, a computational study on this subject was lacking in the literature prior to this work.

(2) The effect of Nd-additions on the activity of different deformation modes in the M1 alloy was characterized as a function of temperature in this study. It was found out that the strengthening of basal <a> slip by Nd-additions was one of the reasons behind the excellent elevated-temperature strength retention observed in the extruded MN11 alloy. In addition, clear experimental evidence on the decreasing activity of extension twinning with an increase in temperature was obtained from this study. It was observed that extension twinning does not follow the Schmid law in the Mg alloys studied. This is in good agreement with the similar trends being reported in the literature recently [Tome et al. 2011]. Moreover, the CRSS ratio estimation methodology developed by Li et al. [2013] was successfully employed to calculate the relative CRSS values of extension twinning and non-basal slip with respect to basal <a> slip (<1 and >10 respectively) in the extruded MN11 alloy at 323K. By using in-situ TEM studies, Ye et al. [2011] recently measured the CRSS value of extension twinning to be strikingly close to that for basal <a> slip in Mg-0.2Ce alloy. A CRSS ratio typically greater than 10 for non-basal slip systems with respect to basal <a> slip has been reported for Mg alloys in the literature [Barnett 2003, Chapuis et al. 2011]. Thus, the results from this work on the newly developed Nd-containing Mg alloys are in good agreement with the studies on other RE-containing Mg alloys. The insights gained from these studies have a broad impact on understanding the deformation behavior of RE-containing Mg alloys and also on the development of accurate crystal plasticity models.

(3) A novel in-situ annealing technique was developed and successfully employed to understand the mechanisms responsible for texture weakening observed in RE-containing Mg alloys during wrought processing. Although the effect of RE elements on the random texture development in Mg alloys during wrought processing have been demonstrated previously

[Bohlen et al. 2007, Bohlen et al. 2010], an investigation on the underlying mechanisms responsible for this effect during annealing was lacking in the literature prior to this work. It was identified that the formation of an enhanced number of grain boundaries with $< hkil >$ rotation axis during recrystallization is a key factor responsible for the texture weakening observed in RE-containing Mg alloys during annealing. The methodology developed for this part of the dissertation work will be valuable for future recrystallization studies on Mg and other alloy systems.

6.4 Recommendations for future work

(1) To gain a deeper understanding of the effect of contraction twinning and $\{10\bar{1}1\} - \{10\bar{1}2\}$ double twinning on the macroscopic mechanical properties of the extruded M1 alloy, future work can focus on the crystal plasticity modeling and simulation of a representative microstructural patch containing a few hundred grains. In addition, the TEM analysis of the twins identified in the extruded M1 sample tensile deformed at 323K will be useful to support the computational observations made in this study.

(2) To obtain a more statistical data set for obtaining the distribution of the deformation modes, larger microstructural patches could be analyzed during the in-situ tests and/or multiple tests could be performed, especially for the early stages of the deformation process at ambient temperatures. This would be particularly beneficial for the accurate estimation of the CRSS ratios for different deformation modes as a function of strain and/or temperature.

(3) To gain a better understanding of the deformation activity beneath the sample surface, future work may use other methods such as TEM or in-situ XRD to study the subsurface deformation activity. The results and conclusions made on the deformation activity in this work are based on the analysis of slip/twin traces observed on the surface. It is not clear how well the

observations on the surface reflect the sub-surface deformation activity. Thus, studying the sub-surface deformation activity may be a subject for future work.

(4) The MN11 alloy, which exhibited excellent elevated temperature strength retention, could be an attractive candidate for powertrain applications. As creep is one of the dominant mechanisms of deformation during the extended operation at elevated-temperatures, it will be beneficial to investigate the creep deformation behavior of the MN11 alloy using in-situ studies.

(5) The in-situ annealing technique developed in this work may be used to investigate the recrystallization behavior of conventional Mg alloys, such as AZ31, during in-situ annealing. In addition, this methodology may be used to investigate the recrystallization behavior of other RE-containing Mg alloy systems. The comparison of the results from such studies will be beneficial to understand the difference in the effect of various alloying elements on the texture and microstructure evolution in Mg alloys.

APPENDICES

Appendix A

Methodology for slip/twin trace analysis and Schmid factor calculation

The crystallographic orientation of each individual grains with respect to the sample/lab coordinate system was obtained from the EBSD data in the form of three Euler angles $(\varphi_1, \Phi, \varphi_2)$. The rotation matrix ($g$) between the crystal coordinate system and the sample/lab coordinate system was calculated using the formula given below:

$$g = \begin{bmatrix} cos\ \varphi_2 & \sin\varphi_2 & 0 \\ -\sin\varphi_2 & \cos\varphi_2 & 0 \\ 0 & 0 & 1 \end{bmatrix} \begin{bmatrix} 1 & 0 & 0 \\ 0 & \cos\Phi & \sin\Phi \\ 0 & -\sin\Phi & \cos\Phi \end{bmatrix} \begin{bmatrix} \cos\varphi_1 & \sin\varphi_1 & 0 \\ -\sin\varphi_1 & \cos\varphi_1 & 0 \\ 0 & 0 & 1 \end{bmatrix}$$

For a given slip/twin system, the slip/twin plane and the slip/twin direction can be expressed as ($h\ k\ l$)[$u\ v\ w$] in the crystal coordinate system using the Miller indices. The transformation of the slip/twin plane and the slip/twin direction from the crystal coordinate system to the sample/lab coordinate system can be achieved using the equations given below:

$$n = g^T . \begin{bmatrix} h \\ k \\ l \end{bmatrix}$$

$$b = g^T . \begin{bmatrix} u \\ v \\ w \end{bmatrix}$$

where n and b are the corresponding slip/twin plane normal and the slip/twin direction of a given slip/twin system presented in the sample/lab coordinate system. The plane trace was then calculated using the cross product of the slip/twin plane normal (n), expressed in the sample/lab coordinate, and the sample normal direction, [001]. The reason for using the cross product of the slip/twin plane normal and the sample normal to calculate the plane trace is that if slip/twin

occurred, the intersection line between the slip/twin plane of a given deformation system and the sample surface should be parallel to the experimentally-observed slip/twin traces.

Assuming a uniaxial stress state, represented as σ, the global Schmid factor (m) of each slip/twin system in an individual grain could be calculated by resolving the stress in the slip/twin direction (Burgers vector direction) of a particular slip/twin plane, expressed as below:

$$m = n.\sigma.b^T$$

Appendix B

Matlab™ code for slip trace analysis and Schmid factor calculation

This Matlab™ code provides a visualization of the calculated plane traces for all the slip systems, as well as a calculation of the corresponding Schmid factors for all the slip systems, for a given orientation. The input parameter is the orientation of a particular grain in the form of three Euler angles, $(\varphi_1, \Phi, \varphi_2)$, given by the EDAX EBSD software. In this example, $\varphi_1 = 10$, $\Phi = 60$, and $\varphi_2 = 20$. The variable "ssa" contains the 12 common slip systems in Mg, where the slip plane normals and slip directions are stored in 12 cells of this variable. For example, basal slip systems are stored in cells 1 to 3, prismatic slip systems in cells 4 to 6, and pyramidal <c+a> slip systems are stored in cells 7 to 12. In the EBSD coordinate system, x-axis is pointing down and y-axis is pointing right. Therefore, the stress tensor is defined to be $\begin{bmatrix} 0 & 0 & 0 \\ 0 & 1 & 0 \\ 0 & 0 & 0 \end{bmatrix}$. However, in the lab coordinate system, x-axis is pointing right and y-axis is pointing up. In order to compare the calculated slip traces based on the EBSD coordinate with the SE SEM images based on the lab coordinates, additional 90 degree counterclockwise rotation was performed on the calculated slip traces. The Global coordinate system was chosen such that the x-axis was parallel with the horizontal direction (loading axis) in the in-situ images. Therefore, the stress state is assumed as uniaxial along the x direction. It is noted that the twin plane trace and the corresponding Schmid factors are calculated in a similar manner.

```
% Code modified from Dr. Thomas Bieler's and Dr. Zhe Chen's version in 2012
clc
clear
%  basal <a>-glide
ssa(:,:,1) = [0 0 0 1; -2 1 1 0];
ssa(:,:,2) = [0 0 0 1; -1 2 -1 0];
ssa(:,:,3) = [0 0 0 1; -1 -1 2 0];
ibas = 1;
fbas = 3;
%  prism <a>-glide
ssa(:,:,4) = [0 1 -1 0; 2 -1 -1 0];
ssa(:,:,5) = [1 0 -1 0; 1 -2 1 0];
ssa(:,:,6) = [-1 1 0 0; 1 1 -2 0];
iprs = 4;
fprs = 6;
%  second order pyramidal <c+a>
ssa(:,:,7) = [1 1 -2 2; -1 -1 2 3];
ssa(:,:,8) = [-1 2 -1 2; 1 -2 1 3];
ssa(:,:,9) = [-2 1 1 2; 2 -1 -1 3];
ssa(:,:,10) = [-1 -1 2 2; 1 1 -2 3];
ssa(:,:,11) = [1 -2 1 2; -1 2 -1 3];
ssa(:,:,12) = [2 -1 -1 2; -2 1 1 3];
ispy = 7;
fspy = 12;

euler=[ 10 60 20 ]; % input three euler angles here

sliptrace=[0,0,0];
phi1=euler(1,1);
PHI=euler(1,2);
phi2=euler(1,3);
g11=cosd(phi1)*cosd(phi2)-sind(phi1)*sind(phi2)*cosd(PHI);
g12=sind(phi1)*cosd(phi2)+cosd(phi1)*sind(phi2)*cosd(PHI);
g13=sind(phi2)*sind(PHI);
g21=-cosd(phi1)*sind(phi2)-sind(phi1)*cosd(phi2)*cosd(PHI);
g22=-sind(phi1)*sind(phi2)+cosd(phi1)*cosd(phi2)*cosd(PHI);
g23=cosd(phi2)*sind(PHI);
g31=sind(phi1)*sind(PHI);
g32=-cosd(phi1)*sind(PHI);
g33=cosd(PHI);
g=[g11,g12,g13;g21,g22,g23;g31,g32,g33];
sigma=[0,0,0;0,1,0;0,0,0];
c_a=1.62;

for i=1:1:12            % Change n & m to unit vector
    n=[ssa(1,1,i)  (ssa(1,2,i)*2+ssa(1,1,i))/3^.5  ssa(1,4,i)/c_a]; % Plane
normal /c_a
    m=[ssa(2,1,i)*1.5  3^.5/2*(ssa(2,2,i)*2+ssa(2,1,i))  ssa(2,4,i)*c_a]; %
Slip direction *c_a
    ss(1,:,i) = n/norm(n);  % alpha plane
    ss(2,:,i) = m/norm(m);  % alpha direction
end

for k=1:1:12
burger(1,:,k)=ss(2,:,k);
rot_burger(:,1,k)=g'*burger(1,:,k)';
```

```
z=[0 0 1];
burger_z(k)=rot_burger(:,1,k)'*z';
end
hold off
for j=1:1:12;
plane=ss(1,:,j);
plane=plane';
rot_plane=g'*plane;
z=[0,0,1];
sliptrace(:,:,j)=cross(rot_plane',z);
    rot = [0 -1 0; 1 0 0; 0 0 1]; % rotation matrix to correct "rotation"
    sliptrace(:,:,j)=sliptrace(:,:,j)*rot; % rotation corrected slip traces
x=sliptrace(1,1,j);
y=sliptrace(1,2,j);

X=[0,x];
Y=[0,y];
axis([-1.2 1.2 -1.2 1.2])
if j<4
    k=j;
elseif j<=6
    k=j-4;
elseif j<=12;
    k=j-7;
end
  axis square
if j>=7
plot(X,Y,'k','LineWidth',1); text(x,y,num2str(j),'FontSize',10);
else
   plot(X,Y,'k','LineWidth',1); text(x,y,num2str(j),'FontSize',10);
end
hold on
end;

axis square
rot_c=g'*[0 0 1]';
angle_C=acosd([0 1 0]*rot_c);
if angle_C>90
    angle_C=180-angle_C;
else
end

SF=zeros(12,1);
sigma=g*sigma*g';
for i=1:1:12
a=ss(1,:,i);  % alpha plane
b=ss(2,:,i); % alpha direction
N=g'*a';
M=g'*b';
SF(i)=N(2)*M(2);
schmidfactor(i)=a*sigma*b';
sf_temp(i,1) = schmidfactor(i);
sf_temp(i,2) = i;
end
clc
sortedSF = sortrows(abs(sf_temp), -1)
```

Appendix C

Methodology for speculating slip activity based on orientation gradients within deformed grains

The orientation gradients observed in selected deformed grains are plotted in {0001}, $\{10\bar{1}0\}$, $\{11\bar{2}2\}$, and $\{11\bar{2}0\}$ pole figures. Due to the gradient in the orientation, the points in the pole figures look like arcs or streaks. Using a Matlab™ code (given at the end), the possible arcs that could be formed in these pole figures due to the activity of different slip systems were simulated. This was accomplished by rotating (± a few degrees) the given orientation around an axis given by the cross product of the slip plane normal and the slip direction for different slip systems, because crystal rotations will occur about this axis if there is a strain gradient arising from this slip system. The experimentally-observed streaks in the pole figures are then compared with the simulated arcs for different slip systems. Thus, using this methodology, the slip activity in grains without obvious slip traces can be analyzed.

The slip systems given in Table 3.3 were considered in the analysis. As the cross product of the slip plane normal and the slip direction is identical for basal <a> slip and pyramidal <c+a> slip, the arcs generated for these systems in the pole figures are identical. Thus, it is impossible to differentiate between basal <a> slip and pyramidal <c+a> slip by analyzing the arcs in the pole figures. However, for orientations in which the Schmid factors for these two systems are significantly different, it can be assumed with some degree of certainty that the system with the highest Schmid factor is more likely to be active. Due to the unique rotation axis for prismatic <a> slip, compared to other slip systems, the arcs in the pole figure due the prismatic <a> slip activity can be unambiguously identified.

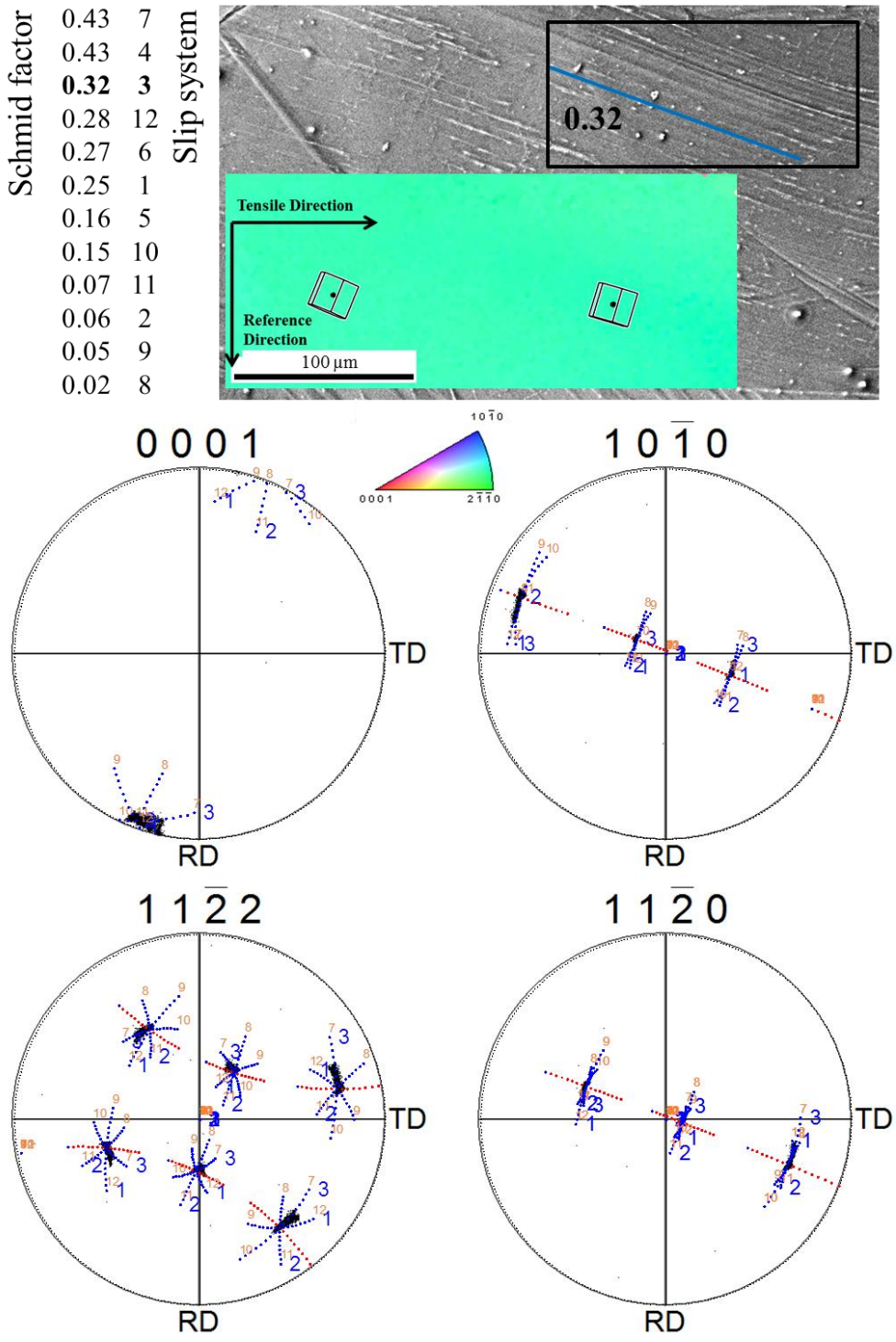

Figure C.1 The SEM image and the corresponding EBSD IPF of the area in which basal <a> slip traces were observed (see blue line in upper right hand side image) after 8.2% strain in the as-cast MN10 tensile-tested at 323K. The pole figures obtained from this region are overlaid with the simulated arcs for different slip systems. The Schmid factors for different slip systems are also listed. The bold slip system was identified based on the slip trace analysis. By comparing the streaks observed in the pole figures with the simulated arcs for different slip systems, basal <a> slip on system 3 was identified to be active in this grain.

Figure C.1 demonstrates this methodology in a grain in which the slip system was already identified using the slip trace analysis technique described in Section 3.4. The example given in Figure C.1 is for basal <a> slip observed in as-cast MN10 tensile-tested at 323K after 8.2% strain. In Figure C.1, the SEM image of the grain in which slip traces were observed and the EBSD IPF map of the area highlighted by a black box in the SEM image are given. The Schmid factors for different slip systems, calculated using a uniaxial stress state assumption, are given along with the corresponding slip systems (represented with numbers 1-12). Numbers 1-3, 4-6, and 7-12 represent the 3 variants of basal <a> slip, the 3 variants of prismatic <a> slip, and the 6 variants of pyramidal <c+a> slip, respectively (see Figure 3.4 for the slip plane and slip direction of these systems). In Figure C.1, the pole figures are obtained from the area highlighted by the black box in the SEM image. The black dots in the pole figures (seen as a continuous arc) correspond to the orientation gradient observed in the area shown in the EBSD IPF map. The blue dots and the red dots in the pole figures represent the arcs simulated due to the activity of basal <a> slip and prismatic <a> slip, respectively (note that the arcs formed due to the activity of the pyramidal <c+a> slip will be identical to that for basal <a> slip). In addition, as the rotation axis for the three variants of prismatic <a> slip is same (along the c-axis), only one arc can be observed in the pole figures for the 3 variants of this slip system.

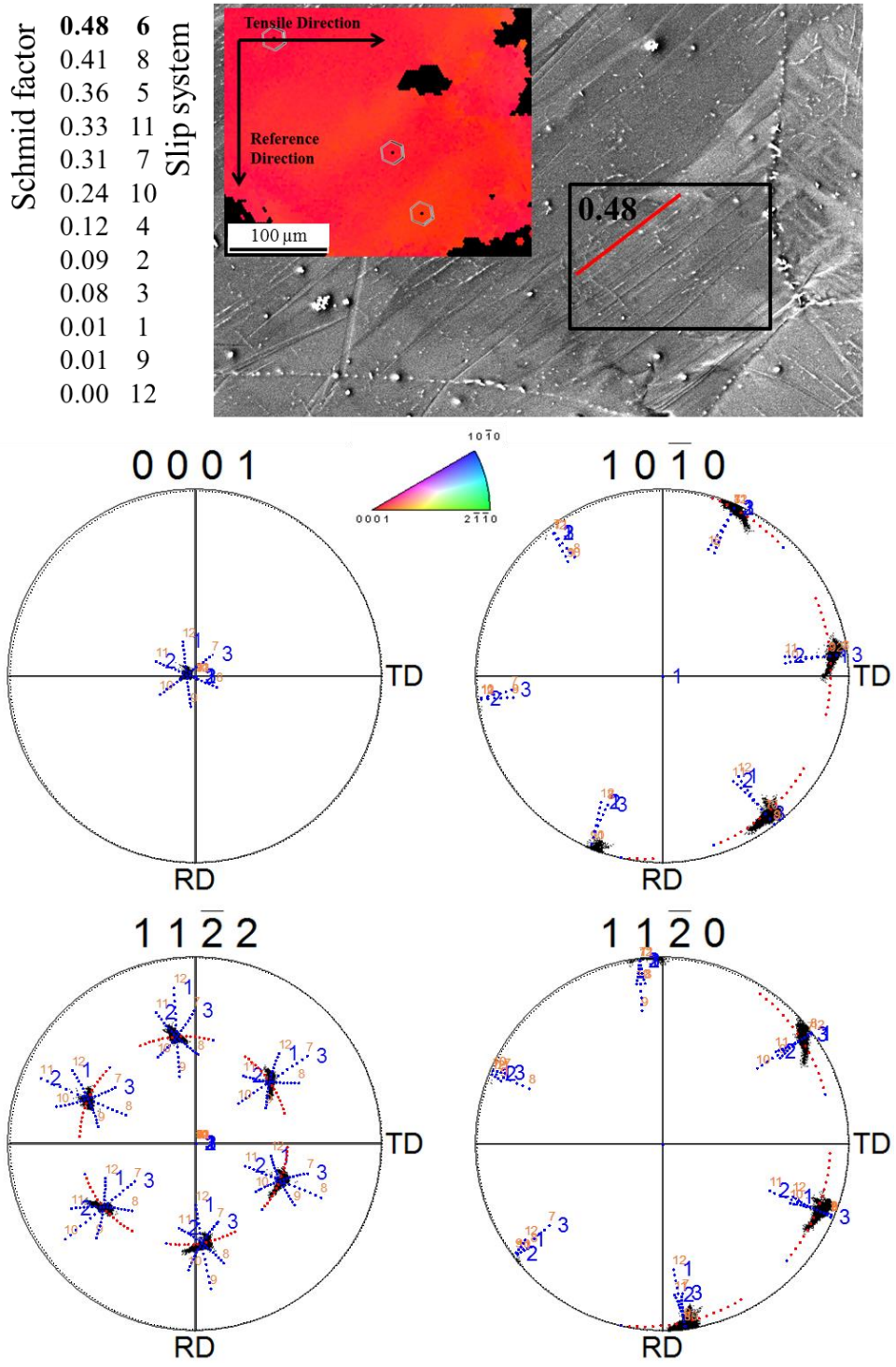

Figure C.2 The SEM image and the corresponding EBSD IPF of the area in which prismatic <a> slip traces were observed after 8.2% strain in the as-cast MN10 tensile-tested at 323K. The pole figures obtained from the area highlighted by the black box are overlaid with the simulated arcs for different slip systems. The Schmid factors for different slip systems are also listed. The bold slip system was chosen based on the slip trace analysis. By comparing the streaks observed in the pole figures with the simulated arcs for different slip systems, prismatic <a> slip was identified to be active in this grain.

As shown in Figure C.1, the simulated arc for the basal <a> slip system number 3 matches with most of the streaks observed in the {0001} and $\{11\bar{2}2\}$ pole figures. Using the slip trace analysis technique, the slip system was identified to be basal <a> slip (number 3) with a Schmid factor of 0.32 (highlighted as a blue line in the SEM image) in this grain. Thus, the slip system identified using the analysis of streaks in the pole figures agrees with the slip system identified using the slip trace analysis technique. It can also be assumed that significant prismatic <a> slip activity has not occurred as the streaks in the $\{10\bar{1}0\}$ and $\{11\bar{2}0\}$ pole figures do not tend to spread along the simulated arcs for prismatic <a> slip.

In Figure C.2, an example for prismatic <a> slip observed in as-cast MN10 tensile tested at 323K after 8.2% strain is given. The slip traces observed were identified to be prismatic <a> slip with Schmid factor of 0.48 using the slip trace analysis technique. The streaks in the $\{10\bar{1}0\}$, $\{11\bar{2}2\}$, and $\{11\bar{2}0\}$ pole figures match fairly well with the simulated arcs for prismatic <a> slip systems. Furthermore, the nonexistence of streaks in {0001} pole figures indicates that the activity of prismatic <a> slip led to the rotation axis of this particular slip system that is parallel to the <0001> direction, and such rotations will not show up as streaks in {0001} pole figure. However, it is impossible to identify which variant of prismatic <a> slip is active from the pole figures. In addition, as some of the streaks in the pole figures tend to orient towards the simulated arcs for basal <a> and pyramidal <c+a> slip system, the simultaneous activity of these systems is likely. However, it can be stated with some confidence that prismatic <a> slip system is the most prominent system. This agrees with the slip system identified using the slip trace analysis technique.

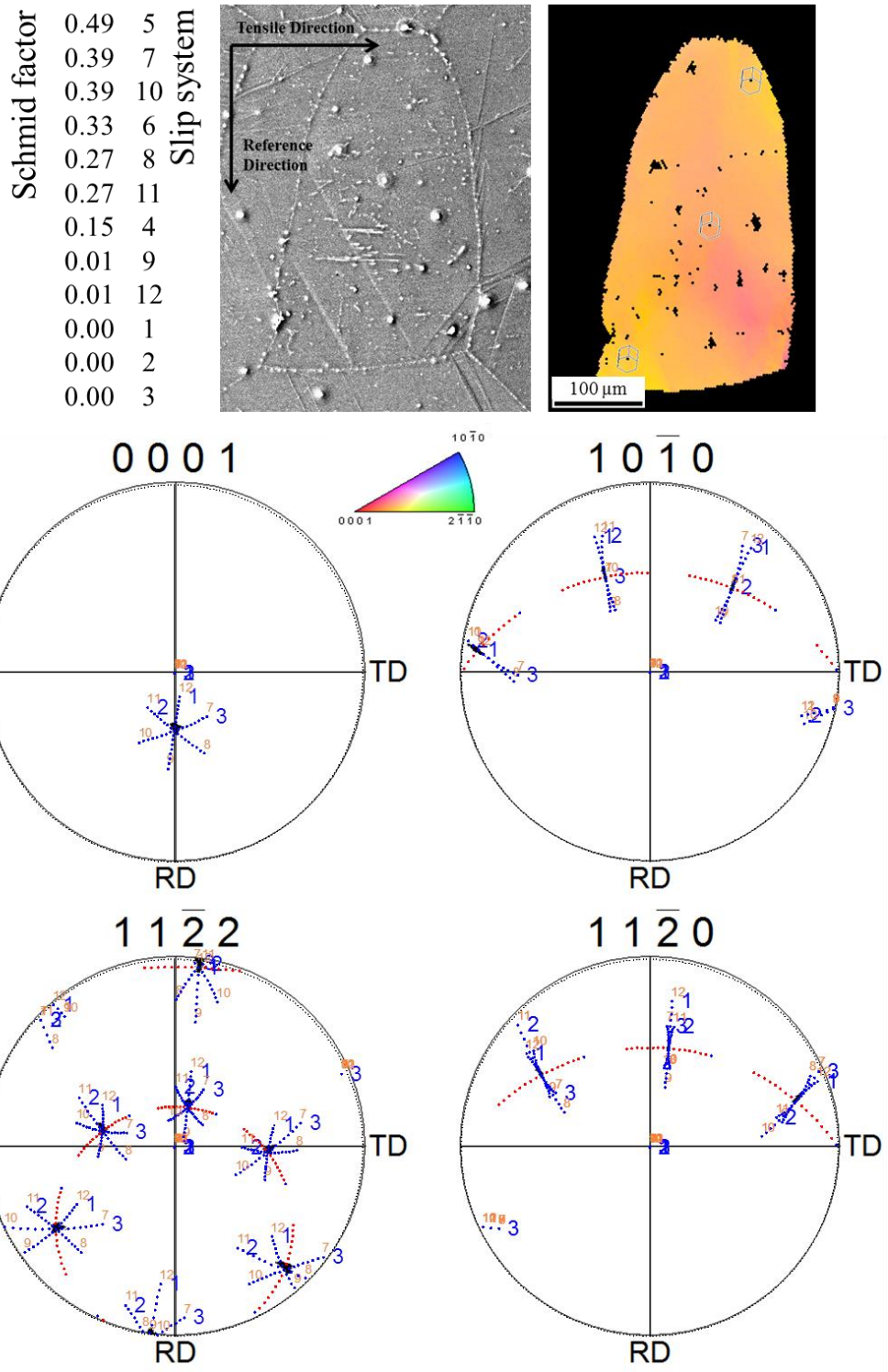

Figure C.3 The SEM image and the EBSD IPF map of the grain in which obvious slip traces were not observed after 8.2% strain in as-cast MN10 tensile-tested at 323K. The pole figures obtained from the grain are overlaid with the simulated arcs for different slip systems. The Schmid factors for different slip systems are also listed. By comparing the streaks observed in the pole figures with the simulated arcs for different slip systems, multiple variants of pyramidal <c+a> slip system were probably active in this grain.

In Figure C.3, this methodology was used to speculate on the active slip systems in a grain in which obvious slip traces were not observed. The SEM image and the EBSD IPF map was for an as-cast MN10 tensile tested at 323K after 8.2% strain. From the streaks observed in the $\{10\bar{1}0\}$ and $\{11\bar{2}0\}$ pole figures, the possibility of prismatic <a> slip can be ruled out as the streak does not orient parallel to the arcs simulated for prismatic <a> slip variants. The possibility of basal <a> slip can also be ruled out as the Schmid factors for the basal <a> slip variants in the grain of interest were 0. Thus, a pyramidal <c+a> system can best account for the active slip system in this grain. However, it is challenging to identify which variant of pyramidal <c+a> system is active as the streak does not uniquely match with any one of the simulated arcs for the 6 variants of pyramidal <c+a> slip systems in the {0001} and $\{11\bar{2}2\}$ pole figure. Thus, it can be suggested that simultaneous activation of more than one variant of pyramidal <c+a> slip probably occurred in the grain of interest.

In order to successfully verify the methodology described above, future work could focus on analyzing more grains in the deformed microstructures for which the active slip systems were already identified using the slip trace analysis technique described in Section 3.4. In addition, to validate this methodology with a statistically meaningful dataset, one could deform a representative 3D microstructure using crystal plasticity modeling and simulations and compare the streak directions observed in the pole figures due to slip activity with the simulated arcs for different slip systems in the simulation as well. Overall, the methodology described here will be useful to identify probable slip activity in many of the deformed grains in which obvious slip traces were not observed.

Matlab™ code for simulating the arcs formed in the {0001}, {$10\bar{1}0$}, {$11\bar{2}2$}, and {$11\bar{2}0$} pole figures due to the activity of different slip systems in Mg:

```
clear all; clc; close all;

% Code to plot the arcs in pole figures due to slip activity
% Code written by Ajith Chakkedath, last modified on 3/6/2016
% parts of the code adapted from Dr. Thomas Bieler and Mr. Harsha Phukan

for k = 1:1:4
    if k == 1
        % npln is number of members in the plane family
        planes = [0 0 0 1; 0 0 0 -1];
        npln = 2;
    elseif k == 2
        planes = [0 1 -1 0; 1 0 -1 0; -1 1 0 0;  0 -1 1 0; -1 0 1 0; 1 -1 0
0];
        npln = 6;
    elseif k == 3
        planes = [1 1 -2 2; -1 2 -1 2; -2 1 1 2; -1 -1 2 2; 1 -2 1 2; 2 -1 -1
2];
        planes = [planes; -1*planes];
        npln = 12;
    else
        planes = [1 1 -2 0; -1 2 -1 0; -2 1 1 0; -1 -1 2 0; 1 -2 1 0; 2 -1 -1
0];
        planes = [planes; -1*planes];
        npln = 12;
    end
    figure
    hold on
    axis square
    axis([-1.2 1.2 -1.2 1.2])

    for ideg = 1:1:360
        plot(cosd(ideg),sind(ideg),'k.','MarkerSize',3); % plot unit circle
        plot([-1 1], [0 0], 'k-'); % plot horizontal line
        plot([0 0], [-1 1], 'k-'); % plot vertical line
    end
    axis off

    % text for TS, RD, and the type of pole figures
    % text(-0.25,1.1,mat2str(planes(1,:)),'FontSize',30); % Label pole figure
with type of plane
    % text(-.09,-1.1,'RD','FontSize',30);
    % text (1.05, 0, 'TD','FontSize',30); % Note that X is down and Y is to
the right

    % Ang is the variable holding Euler angles
    Eang = [30 60 90];

    % for each orientation, convert the plane normal direction to a Cartesian
direction,
    % and then normalize it to make a unit vector, e.g. unit_vector =
vector/norm(vector).
```

```
    c_a =0.52/0.32; % ratio of lattice parameters for Mg
    % Initialize matrices to store Cartesian Coordinates for each plane:
    CartPlane=zeros(2,3);

    for kpln = 1:1:npln % convert 4 index (hkil) to Cartesian unit vectors)
        CartPlane(kpln,1) = planes(kpln,1);
        CartPlane(kpln,2) = (planes(kpln,1)+2*planes(kpln,2))/sqrt(3);
        CartPlane(kpln,3) = planes(kpln,4)/c_a;
        uvect(kpln,:) = CartPlane(kpln,:)/norm(CartPlane(kpln,:));
    end

    % Compute Bunge orientation matrix g
    gPhi1(:,:)=[cosd(Eang(1,1)) sind(Eang(1,1)) 0;-sind(Eang(1,1))
cosd(Eang(1,1)) 0; 0 0 1];
    gPhi(:,:)=[1 0 0;0 cosd(Eang(1,2)) sind(Eang(1,2)); 0 -sind(Eang(1,2))
cosd(Eang(1,2))];
    gPhi2(:,:)=[cosd(Eang(1,3)) sind(Eang(1,3)) 0;-sind(Eang(1,3))
cosd(Eang(1,3)) 0; 0 0 1];
    g(:,:)=gPhi2(:,:)*gPhi(:,:)*gPhi1(:,:); % assemble entire g matrix

    % compute rotated plane normal vectors (in sample coordinate system)
    for kpln = 1:1:npln; % express each plane normal in Sample coordinate
system, X(sam) = x(crys) * g
        X(kpln,:)=uvect(kpln,:)*g(:,:);
        if  X(kpln,3)>0 % If X3 > 0 plot X(sam) on stereographic projection
            Xst(kpln)=X(kpln,1)/(1+X(kpln,3)); % , set plot variables for
stereographic projection
            Yst(kpln)=X(kpln,2)/(1+X(kpln,3));
            % plotting the original orientation
            % plot(Yst,-Xst,'ok','MarkerSize',15,'LineWidth',2.5);
        end % Xst down, Yst right
    end

    % Plotting slip trace arcs
    %  basal <a>-glide
    ssa(:,:,1) = [0 0 0 1; -2 1 1 0];
    ssa(:,:,2) = [0 0 0 1; -1 2 -1 0];
    ssa(:,:,3) = [0 0 0 1; -1 -1 2 0];
    ibas = 1;
    fbas = 3;
    %  prism <a>-glide
    ssa(:,:,4) = [0 1 -1 0; 2 -1 -1 0];
    ssa(:,:,5) = [1 0 -1 0; 1 -2 1 0];
    ssa(:,:,6) = [-1 1 0 0; 1 1 -2 0];
    iprs = 4;
    fprs = 6;
    %  second order pyramidal <c+a>
    ssa(:,:,7) = [1 1 -2 2; -1 -1 2 3];
    ssa(:,:,8) = [-1 2 -1 2; 1 -2 1 3];
    ssa(:,:,9) = [-2 1 1 2; 2 -1 -1 3];
    ssa(:,:,10) = [-1 -1 2 2; 1 1 -2 3];
    ssa(:,:,11) = [1 -2 1 2; -1 2 -1 3];
    ssa(:,:,12) = [2 -1 -1 2; -2 1 1 3];
    ispy = 7;
    fspy = 12;
```

```
    for i=1:1:12 % Change n & m to unit vector
        n=[ssa(1,1,i)  (ssa(1,2,i)*2+ssa(1,1,i))/3^.5  ssa(1,4,i)/c_a]; %
Plane normal /c_a
        m=[ssa(2,1,i)*1.5  3^.5/2*(ssa(2,2,i)*2+ssa(2,1,i))  ssa(2,4,i)*c_a];
% Slip direction *c_a
        ss(1,:,i) = n/norm(n); % alpha plane
        ss(2,:,i) = m/norm(m); % alpha direction
        ss(3,:,i) = cross(n,m)/norm(cross(n,m));
        % % plotting the rotation axis for different slip systems
        % % compute rotated plane normal vectors for the rotation axis (in
sample coordinate system)
        % for kpln = 1:1:npln; % express each plane normal in Sample
coordinate system, X(sam) = x(crys) * g
        % X(kpln,:)=ss(3,:,i)*g(:,:);
        % if  X(kpln,3)>0 % If X3 > 0 plot X(sam) on stereographic projection
        % Xst(kpln)=X(kpln,1)/(1+X(kpln,3)); % , set plot variables for
stereographic projection
        % Yst(kpln)=X(kpln,2)/(1+X(kpln,3));
        % if i < 4
        % plot(Yst,-Xst,'ok','MarkerSize',7);
        % hold on
        % elseif i < 7
        % plot(Yst,-Xst,'or','MarkerSize',9);
        % hold on
        % % else
        % % plot(Yst,-Xst,'oy','MarkerSize',4);
        % % hold on
        % end
        % end % Xst down, Yst right
        % end
    end

    for j = 1:1:12
        for i = -20:2.5:20
            RA = i;
            RV = ss(3,:,j); % Rotation Vector
            R = [cosd(RA)+RV(1)^2*(1-cosd(RA)),          RV(1)*RV(2)*(1-
cosd(RA))-RV(3)*sind(RA), RV(1)*RV(3)*(1-cosd(RA))+RV(2)*sind(RA);
                RV(1)*RV(2)*(1-cosd(RA))+RV(3)*sind(RA), cosd(RA)+RV(2)^2*(1-
cosd(RA)),           RV(2)*RV(3)*(1-cosd(RA))-RV(1)*sind(RA);
                RV(3)*RV(1)*(1-cosd(RA))-RV(2)*sind(RA), RV(2)*RV(3)*(1-
cosd(RA))+RV(1)*sind(RA), cosd(RA)+RV(3)^2*(1-cosd(RA))];
            for kpln = 1:1:npln; % express each plane normal in Sample
coordinate system, X(sam) = x(crys) * g
                X(kpln,:)=uvect(kpln,:)*R(:,:)*g(:,:);
                if  X(kpln,3)>0 % If X3 > 0 plot X(sam) on stereographic
projection
                    Xst(kpln)=X(kpln,1)/(1+X(kpln,3)); % set plot variables
for stereographic projection
                    Yst(kpln)=X(kpln,2)/(1+X(kpln,3));
                    if j>3 & j<7
                        plot(Yst,-Xst,'r.','MarkerSize',5)
                    else
                        plot(Yst,-Xst,'b.','MarkerSize',5)
                    end
                end % Xst down, Yst right
            end
```

```
        end
        if j<4
            text(Yst+0.05,-Xst,mat2str(j),'FontSize',25,'Color',[0 0 1])
            % elseif j<7
            % text(Yst,-Xst,mat2str(j),'FontSize',20,'Color',[1 0 0])
        elseif j>6
            text(Yst,-Xst+0.05,mat2str(j),'FontSize',15,'Color',[1 0.5 0.2])
        end
    end
    % Schmid factor calculation
    SF=zeros(12,1);
    sigma=[0,0,0;0,1,0;0,0,0];
    sigma=g*sigma*g';
    for i=1:1:12
        a=ss(1,:,i);  % alpha plane
        b=ss(2,:,i); % alpha direction
        N=g'*a';
        M=g'*b';
        SF(i)=N(2)*M(2);
        schmidfactor(i)=a*sigma*b';
        sf_temp(i,1) = schmidfactor(i);
        sf_temp(i,2) = i;
    end
    sortedSF = sortrows(abs(sf_temp), -1)
    clear all;
end
```

BIBLIOGRAPHY

BIBLIOGRAPHY

Agnew, S. R., Yoo, M. H., & Tome, C. N. (2001). Application of texture simulation to understanding mechanical behavior of Mg and solid solution alloys containing Li or Y. Acta Materialia, 49(20), 4277-4289.

Agnew, S. R., Brown, D. W., & Tomé, C. N. (2006). Validating a polycrystal model for the elastoplastic response of magnesium alloy AZ31 using in situ neutron diffraction. Acta Materialia, 54(18), 4841-4852.

Akhtar, A., & Teghtsoonian, E. (1969). Solid solution strengthening of magnesium single crystals—I alloying behaviour in basal slip. Acta Metallurgica, 17(11), 1339-1349.

Akhtar, A., & Teghtsoonian, E. (1969). Solid solution strengthening of magnesium single crystals—II the effect of solute on the ease of prismatic slip. Acta Metallurgica, 17(11), 1351-1356.

Akhtar, A., & Teghtsoonian, E. (1972). Substitutional solution hardening of magnesium single crystals. Philosophical Magazine, 25(4), 897-916.

Al-Samman, T., & Li, X. (2011). Sheet texture modification in magnesium-based alloys by selective rare earth alloying. Materials Science and Engineering: A, 528(10), 3809-3822.

Ando, D., & Koike, J. (2007). Relationship between Deformation-Induced Surface Relief and Double Twinning in AZ 31 Magnesium Alloy. Journal of the Japan Institute of Metals, 71(9), 684-687.

Ando, D., Koike, J., & Sutou, Y. (2010). Relationship between deformation twinning and surface step formation in AZ31 magnesium alloys. Acta Materialia, 58(13), 4316-4324.

Ando, D., Koike, J., & Sutou, Y. (2014). The role of deformation twinning in the fracture behavior and mechanism of basal textured magnesium alloys. Materials Science and Engineering: A, 600, 145-152.

Asada, H., & Yoshinaga, H. (1958). Nonbasal slips and twins of magnesium coarse grains. Journal of Japan Institute Metals, 23(1), 67-71.

ASTM (2012) E112-12 Standard Test Methods for Determining Average Grain Size.

Avedesian, M. M., & Baker, H. (Eds.). (1999). ASM specialty handbook: magnesium and magnesium alloys. ASM international.

Ball, E. A., & Prangnell, P. B. (1994). Tensile-compressive yield asymmetries in high strength wrought magnesium alloys. Scripta Metallurgica et Materialia, 31(2), 111-116.

Barnett, M. R. (2003). A Taylor model based description of the proof stress of magnesium AZ31 during hot working. Metallurgical and materials transactions A, 34(9), 1799-1806.

Barnett, M. R., Nave, M. D., & Bettles, C. J. (2004). Deformation microstructures and textures of some cold rolled Mg alloys. Materials Science and Engineering: A, 386(1), 205-211.

Barnett, M. R., Keshavarz, Z., Beer, A. G., & Atwell, D. (2004). Influence of grain size on the compressive deformation of wrought Mg–3Al–1Zn. Acta materialia, 52(17), 5093-5103.

Barnett, M. R. (2007). Twinning and the ductility of magnesium alloys: Part II."Contraction" twins. Materials Science and Engineering: A, 464(1), 8-16.

Barnett, M. R. (2008). A rationale for the strong dependence of mechanical twinning on grain size. Scripta materialia, 59(7), 696-698.

Barnett, M. R., Keshavarz, Z., Beer, A. G., & Ma, X. (2008). Non-Schmid behaviour during secondary twinning in a polycrystalline magnesium alloy. Acta Materialia, 56(1), 5-15.

Beals, R. S., Tissington, C., Zhang, X., Kainer, K., Petrillo, J., Verbrugge, M., & Pekguleryuz, M. (2007). Magnesium global development: Outcomes from the TMS 2007 annual meeting. JOM, 59(8), 39-42.

Bettles, C., & Gibson, M. (2005). Current wrought magnesium alloys: strengths and weaknesses. Jom, 57(5), 46-49.

Beyerlein, I. J., & Tomé, C. N. (2010, September). A probabilistic twin nucleation model for HCP polycrystalline metals. In Proceedings of the Royal Society of London A: Mathematical, Physical and Engineering Sciences (Vol. 466, No. 2121, pp. 2517-2544). The Royal Society.

Boehlert, C. J., Chen, Z., Gutiérrez-Urrutia, I., Llorca, J., & Pérez-Prado, M. T. (2012). In situ analysis of the tensile and tensile-creep deformation mechanisms in rolled AZ31. Acta Materialia, 60(4), 1889-1904.

Bohlen, J., Nürnberg, M. R., Senn, J. W., Letzig, D., & Agnew, S. R. (2007). The texture and anisotropy of magnesium–zinc–rare earth alloy sheets. Acta Materialia, 55(6), 2101-2112.

Bohlen, J., Yi, S., Letzig, D., & Kainer, K. U. (2010). Effect of rare earth elements on the microstructure and texture development in magnesium–manganese alloys during extrusion. Materials Science and Engineering: A, 527(26), 7092-7098.

Busk, R. S. (1950). Lattice parameters of magnesium alloys. Trans. Aime, 188, 1460-1464.
Callister Jr, W. D. (2009). Materials Science and Engineering - An Introduction, 8th Edition, Wiley, New York.

Chang, S. Y., Nakagaido, T., Hong, S. K., Shin, D. H., & Sato, T. (2001). Effect of Yttrium on High Temperature Strength of Magnesium. Materials Transactions, 42(7), 1332-1338.

Chapuis, A., & Driver, J. H. (2011). Temperature dependency of slip and twinning in plane strain compressed magnesium single crystals. Acta Materialia, 59(5), 1986-1994.

Chen, Z. (2012). A study of the effects of processing and alloying on the microstructure and deformation behavior of wrought magnesium alloys. PhD Dissertation, Michigan State University.

Chino, Y., Kado, M., & Mabuchi, M. (2008). Enhancement of tensile ductility and stretch formability of magnesium by addition of 0.2 wt%(0.035 at%) Ce. Materials Science and Engineering: A, 494(1), 343-349.

Chino, Y., Kado, M., & Mabuchi, M. (2008). Compressive deformation behavior at room temperature–773K in Mg–0.2 mass%(0.035 at.%) Ce alloy. Acta materialia, 56(3), 387-394.

Christian, J. W., & Mahajan, S. (1995). Deformation twinning. Progress in materials science, 39(1), 1-157.

Cizek, P., & Barnett, M. R. (2008). Characteristics of the contraction twins formed close to the fracture surface in Mg–3Al–1Zn alloy deformed in tension. Scripta Materialia, 59(9), 959-962.

Cottam, R., Robson, J., Lorimer, G., & Davis, B. (2008). Dynamic recrystallization of Mg and Mg–Y alloys: crystallographic texture development. Materials Science and Engineering: A, 485(1), 375-382.

Couling, S. L., & Roberts, C. S. (1956). New Twinning systems in magnesium. Acta Crystallographica, 9(11), 972-973.

Couling, S. L., Pashak, J. F., & Sturkey, L. (1959). Unique deformation and aging characteristics of certain magnesium-base alloys. American Society for Metals Transactions, 51, 94-107.

Datta, A., Waghmare, U. V., & Ramamurty, U. (2008). Structure and stacking faults in layered Mg–Zn–Y alloys: A first-principles study. Acta Materialia, 56(11), 2531-2539.

Dobrzański, L. A., Tański, T., Čížek, L., & Brytan, Z. (2007). Structure and properties of magnesium cast alloys. Journal of Materials Processing Technology, 192, 567-574.

Ecob, N., & Ralph, B. (1983). The effect of grain size on deformation twinning in a textured zinc alloy. Journal of Materials Science, 18(8), 2419-2429.

Eisenlohr, P., Diehl, M., Lebensohn, R. A., & Roters, F. (2013). A spectral method solution to crystal elasto-viscoplasticity at finite strains. International Journal of Plasticity, 46, 37-53.

Ernst, T., & Laves, F. (1949). On the Deformation of Magnesium and Its Alloys. Zeitschrift fiir Melallkunde, 40, 1-12.

Flynn, P. W., Mote, J. E. D. J., & Dorn, J. E. (1961). On the thermally activated mechanism of prismatic slip in magnesium single crystals. Transactions of the Metallurgical Society of AIME, 221(6), 1148-1154.

Friedrich, H. E., Mordike, B. L. (2006). Magnesium Technology Metallurgy, Design Data, Applications, Springer Springer-Verlag, Berlin, 317.

Godet, S., Jiang, L., Luo, A. A., & Jonas, J. J. (2006). Use of Schmid factors to select extension twin variants in extruded magnesium alloy tubes. Scripta materialia, 55(11), 1055-1058.

Gu, X. N., & Zheng, Y. F. (2010). A review on magnesium alloys as biodegradable materials. Frontiers of Materials Science in China, 4(2), 111-115.

Guillemer, C., Clavel, M., & Cailletaud, G. (2011). Cyclic behavior of extruded magnesium: Experimental, microstructural and numerical approach. International Journal of Plasticity, 27(12), 2068-2084.

Gupta, M., & Sharon, N. M. L. (2011). Magnesium, magnesium alloys, and magnesium composites. John Wiley & Sons.

Hadorn, J. P., Hantzsche, K., Yi, S., Bohlen, J., Letzig, D., Wollmershauser, J. A., & Agnew, S. R. (2012). Role of solute in the texture modification during hot deformation of Mg-rare earth alloys. Metallurgical and Materials Transactions A, 43(4), 1347-1362.

Hall, E. O. (1951). The deformation and ageing of mild steel: III discussion of results. Proceedings of the Physical Society. Section B, 64(9), 747.

Hantzsche, K., Bohlen, J., Wendt, J., Kainer, K. U., Yi, S. B., & Letzig, D. (2010). Effect of rare earth additions on microstructure and texture development of magnesium alloy sheets. Scripta Materialia, 63(7), 725-730.

Hartt, W. H., & Reed-Hill, R. E. (1967). The irrational habit of second-order 1011-1012 twins in magnesium. AIME, Transactions, 239, 1511-1517.

Hartt, W. H., & Reed-Hill, R. E. (1968). Internal deformation and fracture of second-order 1011-1012 twins in magnesium. Trans. Met. Soc. AIME, 242(6).

Hehmann, F., Sommer, F., & Predel, B. (1990). Extension of solid solubility in magnesium by rapid solidification. Materials science and engineering: A, 125(2), 249-265.

Hidalgo-Manrique, P., Yi, S. B., Bohlen, J., Letzig, D., & PÚrez-Prado, M. T. (2014). Control of the Mechanical Asymmetry in an Extruded MN11 Alloy by Static Annealing. Metallurgical and Materials Transactions A, 45(8), 3282-3291.

Hong, S. G., Park, S. H., & Lee, C. S. (2010). Role of {10–12} twinning characteristics in the deformation behavior of a polycrystalline magnesium alloy. Acta Materialia, 58(18), 5873-5885.

Hort, N., Huang, Y. D., & Kainer, K. U. (2006). Intermetallics in magnesium alloys. Advanced Engineering Materials, 8(4), 235-240.

Hutchinson, J. W. (1976, February). Bounds and self-consistent estimates for creep of polycrystalline materials. In Proceedings of the Royal Society of London A: Mathematical, Physical and Engineering Sciences (Vol. 348, No. 1652, pp. 101-127). The Royal Society.

Hutchinson, W. B., & Barnett, M. R. (2010). Effective values of critical resolved shear stress for slip in polycrystalline magnesium and other hcp metals. Scripta materialia, 63(7), 737-740.

Inoue, A., Kawamura, Y., Matsushita, M., Hayashi, K., & Koike, J. (2001). Novel hexagonal structure and ultrahigh strength of magnesium solid solution in the Mg–Zn–Y system. Journal of Materials Research, 16(07), 1894-1900.

Jain, A., Duygulu, O., Brown, D. W., Tomé, C. N., & Agnew, S. R. (2008). Grain size effects on the tensile properties and deformation mechanisms of a magnesium alloy, AZ31B, sheet. Materials Science and Engineering: A, 486(1), 545-555.

Jiang, L., Jonas, J. J., Luo, A. A., Sachdev, A. K., & Godet, S. (2006). Twinning-induced softening in polycrystalline AM30 Mg alloy at moderate temperatures. Scripta materialia, 54(5), 771-775.

Jiang, L., Jonas, J. J., & Mishra, R. (2011). Effect of dynamic strain aging on the appearance of the rare earth texture component in magnesium alloys. Materials Science and Engineering: A, 528(21), 6596-6605.

Kelley, E. W., & Hosford, W. (1968). Plane-strain compression of magnesium and magnesium alloy crystals. Trans Met Soc AIME, 242(1), 5-13.

Kim, H. L., Park, J. S., & Chang, Y. W. (2012). Effects of lattice parameter changes on critical resolved shear stress and mechanical properties of magnesium binary single crystals. Materials Science and Engineering: A, 540, 198-206.

King, J. F. (2007). Magnesium: commodity or exotic?. Materials science and technology, 23(1), 1-14.

Koike, J., Kobayashi, T., Mukai, T., Watanabe, H., Suzuki, M., Maruyama, K., & Higashi, K. (2003). The activity of non-basal slip systems and dynamic recovery at room temperature in fine-grained AZ31B magnesium alloys. Acta materialia, 51(7), 2055-2065.

Koike, J. (2005). Enhanced deformation mechanisms by anisotropic plasticity in polycrystalline Mg alloys at room temperature. Metallurgical and Materials Transactions A, 36(7), 1689-1696.

Koike, J., Sato, Y., & Ando, D. (2008). Origin of the anomalous 1012 twinning during tensile deformation of Mg alloy sheet. Materials transactions, 49(12), 2792-2800.

Kulekci, M. K. (2008). Magnesium and its alloys applications in automotive industry. The International Journal of Advanced Manufacturing Technology, 39(9-10), 851-865.

Letzig, D., Swiostek, J., Bohlen, J., Beaven, P. A., & Kainer, K. U. (2008). Wrought magnesium alloys for structural applications. Materials science and technology, 24(8), 991-996.

Li, H., Mason, D. E., Bieler, T. R., Boehlert, C. J., & Crimp, M. A. (2013). Methodology for estimating the critical resolved shear stress ratios of α-phase Ti using EBSD-based trace analysis. Acta Materialia, 61(20), 7555-7567.

Li, H. (2013). Analysis of the deformation behavior of the hexagonal close-packed alpha phase in titanium and titanium alloys. PhD Dissertation, Michigan State University.

Lütjering, G., & Williams, J. C. (2003). Titanium (Vol. 2). Berlin: Springer.

Lyon, P., Syed, I., & Heaney, S. (2007). Elektron 21–an aerospace magnesium alloy for sand cast and investment cast applications. Advanced Engineering Materials, 9(9), 793-798.

Ma, Q., El Kadiri, H., Oppedal, A. L., Baird, J. C., Horstemeyer, M. F., & Cherkaoui, M. (2011). Twinning and double twinning upon compression of prismatic textures in an AM30 magnesium alloy. Scripta Materialia, 64(9), 813-816.

Mackenzie, L. W. F., & Pekguleryuz, M. O. (2008). The recrystallization and texture of magnesium–zinc–cerium alloys. Scripta Materialia, 59(6), 665-668.

Martin, G., Sinclair, C. W., Poole, W. J., & Azizi-Alizamini, H. Local Plastic-Strain Heterogeneities and Their Impact on the Ductility of Mg. JOM, 1-13.

Meyers, M. A., Vöhringer, O., & Lubarda, V. A. (2001). The onset of twinning in metals: a constitutive description. Acta materialia, 49(19), 4025-4039.

Mezbahul-Islam, M., Mostafa, A. O., & Medraj, M. (2014). Essential magnesium alloys binary phase diagrams and their thermochemical data. Journal of Materials, 2014.

Min, J., Hector, L. G., Lin, J., Carter, J. T., & Sachdev, A. K. (2014). Spatio-temporal characteristics of propagative plastic instabilities in a rare earth containing magnesium alloy. International Journal of Plasticity, 57, 52-76.

Mishra, R. K., Gupta, A. K., Rao, P. R., Sachdev, A. K., Kumar, A. M., & Luo, A. A. (2008). Influence of cerium on the texture and ductility of magnesium extrusions. Scripta Materialia, 59(5), 562-565.

Moreno, I. P., Nandy, T. K., Jones, J. W., Allison, J. E., & Pollock, T. M. (2003). Microstructural stability and creep of rare-earth containing magnesium alloys. Scripta Materialia, 48(8), 1029-1034.

Mu, S., Jonas, J. J., & Gottstein, G. (2012). Variant selection of primary, secondary and tertiary twins in a deformed Mg alloy. Acta Materialia, 60(5), 2043-2053.
Nave, M. D., & Barnett, M. R. (2004). Microstructures and textures of pure magnesium deformed in plane-strain compression. Scripta Materialia, 51(9), 881-885.

Nayeb-Hashemi, A. A., & Clark, J. B. (1985). The Mg− Mn (Magnesium-Manganese) system. Bulletin of Alloy Phase Diagrams, 6(2), 160-164.

Nayeb-Hashemi, A. A., & Clark, J. B. (1988). The Mg− Nd system (Magnesium-Neodymium). Journal of Phase Equilibria, 9(5), 618-623.

Nayeb-Hashemi, A. A., & Clark, J. B. (1988). The Ce− Mg (Cerium-Magnesium) system. Journal of Phase Equilibria, 9(2), 162-172.

Nie, J. F. (2012). Precipitation and hardening in magnesium alloys. Metallurgical and Materials Transactions A, 43(11), 3891-3939.

Nie, J. F., Zhu, Y. M., Liu, J. Z., & Fang, X. Y. (2013). Periodic segregation of solute atoms in fully coherent twin boundaries. Science, 340(6135), 957-960.

Niknejad, S., Esmaeili, S., & Zhou, N. Y. (2016). The role of double twinning on transgranular fracture in magnesium AZ61 in a localized stress field. Acta Materialia, 102, 1-16.

Obara, T., Yoshinga, H., & Morozumi, S. (1973). {11$\bar{2}$2}< 1123> Slip system in magnesium. Acta Metallurgica, 21(7), 845-853.

Omori, G. (1979). A Fundamental Study on Magnesium--Rare Earth Alloys(Mainly on those with Lanthanum and Cerium). Trans. Natl. Res. Inst. Met.(Jpn.), 21(4), 192-205.

Pei, Z., Zhu, L. F., Friák, M., Sandlöbes, S., von Pezold, J., Sheng, H. W., ... & Neugebauer, J. (2013). Ab initio and atomistic study of generalized stacking fault energies in Mg and Mg–Y alloys. New Journal of Physics, 15(4), 043020.

Peirce, D., Asaro, R. J., & Needleman, A. (1982). An analysis of nonuniform and localized deformation in ductile single crystals. Acta metallurgica, 30(6), 1087-1119.

Pérez-Prado, M. T., Del Valle, J. A., Contreras, J. M., & Ruano, O. A. (2004). Microstructural evolution during large strain hot rolling of an AM60 Mg alloy. Scripta Materialia, 50(5), 661-665.

Petch, N. J. (1953). The cleavage strength of polycrystals. J. Iron Steel Inst., 174, 25-28.

Polmear, I. J. (1994). Magnesium alloys and applications. Materials science and technology, 10(1), 1-16.

Reed-Hill, R. E., & Robertson, W. D. (1957). Additional modes of deformation twinning in magnesium. Acta Metallurgica, 5(12), 717-727.
Reed-Hill, R. E., & Robertson, W. D. (1957). Deformation of magnesium single crystals by nonbasal slip. Journal of Metals-Transactions AIME, 220, 496-502.

Reed-Hill, R. E., & Robertson, W. D. (1957). The crystallographic characteristics of fracture in magnesium single crystals. Acta Metallurgica, 5(12), 728-737.

Reed-Hill, R. E. (1960). A study of 1011 and 1013 twinning modes in magnesium. Trans. AIME, 218, 554-558.

Robson, J. D., Twier, A. M., Lorimer, G. W., & Rogers, P. (2011). Effect of extrusion conditions on microstructure, texture, and yield asymmetry in Mg–6Y–7Gd–0.5 wt% Zr alloy. Materials Science and Engineering: A, 528(24), 7247-7256.

Rokhlin, L. L. (2003). Magnesium alloys containing rare earth metals: structure and properties. Crc Press.

Rokhlin, L. L. (2006). Structure and properties of alloys of the Mg-REM system. Metal science and heat treatment, 48(11-12), 487-490.

Roters, F., Eisenlohr, P., Hantcherli, L., Tjahjanto, D. D., Bieler, T. R., & Raabe, D. (2010). Overview of constitutive laws, kinematics, homogenization and multiscale methods in crystal plasticity finite-element modeling: Theory, experiments, applications. Acta Materialia, 58(4), 1152-1211.

Sandlöbes, S., Zaefferer, S., Schestakow, I., Yi, S., & Gonzalez-Martinez, R. (2011). On the role of non-basal deformation mechanisms for the ductility of Mg and Mg–Y alloys. Acta Materialia, 59(2), 429-439.

Sandlöbes, S., Friák, M., Zaefferer, S., Dick, A., Yi, S., Letzig, D., ... & Raabe, D. (2012). The relation between ductility and stacking fault energies in Mg and Mg–Y alloys. Acta Materialia, 60(6), 3011-3021.

ASTM (2011) B951-11 Standard Practice for Codification of Unalloyed Magnesium and Magnesium-Alloys, Cast and Wrought.

Stanford, N., & Barnett, M. (2008). Effect of composition on the texture and deformation behaviour of wrought Mg alloys. Scripta materialia, 58(3), 179-182.

Stanford, N., Atwell, D., Beer, A., Davies, C., & Barnett, M. R. (2008). Effect of microalloying with rare-earth elements on the texture of extruded magnesium-based alloys. Scripta materialia, 59(7), 772-775.

Stanford, N., & Barnett, M. R. (2008). The origin of “rare earth” texture development in extruded Mg-based alloys and its effect on tensile ductility. Materials Science and Engineering: A, 496(1), 399-408.
Stanford, N., Atwell, D., & Barnett, M. R. (2010). The effect of Gd on the recrystallisation, texture and deformation behaviour of magnesium-based alloys. Acta materialia, 58(20), 6773-6783.

Stanford, N. (2010). Micro-alloying Mg with Y, Ce, Gd and La for texture modification—A comparative study. Materials Science and Engineering: A, 527(10), 2669-2677.

Stanford, N. (2010). The effect of calcium on the texture, microstructure and mechanical properties of extruded Mg–Mn–Ca alloys. Materials Science and Engineering: A, 528(1), 314-322.

Stanford, N., Sha, G., Xia, J. H., Ringer, S. P., & Barnett, M. R. (2011). Solute segregation and texture modification in an extruded magnesium alloy containing gadolinium. Scripta Materialia, 65(10), 919-921.

Tański, T., Dobrzański, L. A., & Labisz, K. (2010). Investigations of microstructure and dislocations of cast magnesium alloys. Issues, 1, 2.

Tomé, C. N., Beyerlein, I. J., Wang, J., & McCabe, R. J. (2011). A multi-scale statistical study of twinning in magnesium. JOM, 63(3), 19-23.

Trojanová, Z., & Lukáč, P. (2005). Compressive deformation behaviour of magnesium alloys. Journal of Materials Processing Technology, 162, 416-421.

Ulacia, I., Dudamell, N. V., Gálvez, F., Yi, S., Pérez-Prado, M. T., & Hurtado, I. (2010). Mechanical behavior and microstructural evolution of a Mg AZ31 sheet at dynamic strain rates. Acta materialia, 58(8), 2988-2998.

Vander Voort, G. F. (1999). Metallography Principles and Practice. Materials Park, OH: ASM International, pp. 442-446.

von-Mises, R. (1928). Mechanik der plastischen Formänderung von Kristallen. ZAMM-Journal of Applied Mathematics and Mechanics/Zeitschrift für Angewandte Mathematik und Mechanik, 8(3), 161-185.

Wonsiewicz, B. C., & Backofen, W. A. (1967). Plasticity of magnesium crystals. Transactions of the Metallurgical Society AIME, 239, 1422-1431.

Ye, J., Mishra, R. K., Sachdev, A. K., & Minor, A. M. (2011). In situ TEM compression testing of Mg and Mg–0.2 wt.% Ce single crystals. Scripta Materialia, 64(3), 292-295.

Yoo, M. H. (1981). Slip, twinning, and fracture in hexagonal close-packed metals. Metallurgical Transactions A, 12(3), 409-418.

Yoshinaga, H., & Horiuchi, R. (1963). Deformation mechanisms in magnesium single crystals compressed in the direction parallel to hexagonal axis. Transactions of the Japan Institute of Metals, 4(1), 1-8.

Yoshinaga, H., & Horiuchi, R. (1964). On the nonbasal slip in magnesium crystals. Transactions of the Japan Institute of Metals, 5(1), 14-21.

Yoshinaga, H., Obara, T., & Morozumi, S. (1973). Twinning deformation in magnesium compressed along the C-axis. Materials Science and Engineering, 12(5), 255-264.

Zaluzec, M. (2014). Personal communication. Ford Motor Company, MI, USA.

Zou, H., Zeng, X., Zhai, C., & Ding, W. (2005). Effects of Nd on the microstructure of ZA52 alloy. Materials Science and Engineering: A, 392(1), 229-234.